MARTIN MARIETTA ENERGY SYSTEMS LIBRARIES
3 4456 0155371 8

ORNL-4979

Cy 4

Health Physics DIVISION

Annual Progress Report

Period Ending July 31, 1974

OAK RIDGE NATIONAL LABORATORY
CENTRAL RESEARCH LIBRARY
CIRCULATION SECTION
4500N ROOM 175
LIBRARY LOAN COPY
DO NOT TRANSFER TO ANOTHER PERSON.
if you wish someone else to see this report, send in name with report and the library will arrange a loan.
ORNL-118 (6-97)
(3 5-60)

OAK RIDGE NATIONAL LABORATORY
OPERATED BY UNION CARBIDE CORPORATION • FOR THE U.S. ATOMIC ENERGY COMMISSION

Printed in the United States of America. Available from
National Technical Information Service
U.S. Department of Commerce
5285 Port Royal Road, Springfield, Virginia 22151
Price: Printed Copy $7.60; Microfiche $1.45

This report was prepared as an account of work sponsored by the United States Government. Neither the United States nor the United States Atomic Energy Commission, nor any of their employees, nor any of their contractors, subcontractors, or their employees, makes any warranty, express or implied, or assumes any legal liability or responsibility for the accuracy, completeness or usefulness of any information, apparatus, product or process disclosed, or represents that its use would not infringe privately owned rights.

ORNL-4979
UC-41 — Health and Safety

Contract No. W-7405-eng-26

HEALTH PHYSICS DIVISION
ANNUAL PROGRESS REPORT

For Period Ending July 31, 1974

J. A. Auxier, Director
D. M. Davis, Assistant Director
W. S. Snyder, Assistant Director
J. E. Turner, Associate Director

SEPTEMBER 1974

OAK RIDGE NATIONAL LABORATORY
Oak Ridge, Tennessee 37830
operated by
UNION CARBIDE CORPORATION
for the
U.S. ATOMIC ENERGY COMMISSION

MARTIN MARIETTA ENERGY SYSTEMS LIBRARIES
3 4456 0155371 8

Reports previously issued in this series are as follows:

ORNL-2384	Period Ending July 31, 1957
ORNL-2590	Period Ending July 31, 1958
ORNL-2806	Period Ending July 31, 1959
ORNL-2994	Period Ending July 31, 1960
ORNL-3189	Period Ending July 31, 1961
ORNL-3347	Period Ending July 31, 1962
ORNL-3492	Period Ending July 31, 1963
ORNL-3697	Period Ending July 31, 1964
ORNL-3849	Period Ending July 31, 1965
ORNL-4007	Period Ending July 31, 1966
ORNL-4168	Period Ending July 31, 1967
ORNL-4316	Period Ending July 31, 1968
ORNL-4446	Period Ending July 31, 1969
ORNL-4584	Period Ending July 31, 1970
ORNL-4720	Period Ending July 31, 1971
ORNL-4811	Period Ending July 31, 1972
ORNL-4903	Period Ending July 31, 1973

Contents

FOREWORD xi

SUMMARY xiii

PART I. MEDICAL PHYSICS AND INTERNAL DOSIMETRY

1. TABULATIONS OF ABSORBED DOSE PER MICROCURIE-DAY RESIDENCE OF VARIOUS RADIONUCLIDES IN SOURCE ORGANS OF AN ADULT 1

2. REVISION OF MIRD PAMPHLET NO. 5 ENTITLED "ESTIMATES OF ABSORBED FRACTIONS FOR MONOENERGETIC PHOTON SOURCES UNIFORMLY DISTRIBUTED IN VARIOUS ORGANS OF A HETEROGENEOUS PHANTOM" 5

   Exterior of the Phantom 5

   Description of Organs 7

3. REPORT OF THE TASK GROUP ON REFERENCE MAN 12

4. DOSE TO A DYNAMIC BLADDER FOR ADMINISTERED RADIONUCLIDES 13

5. INTERNAL DOSIMETRY OF SPONTANEOUSLY FISSIONING NUCLIDES 17

   Fission-Fragment Dosimetry 17

   Neutron Dosimetry 18

   Gamma-Ray Dosimetry 21

   Beta Dosimetry 24

   Discussion of the Results 25

6. DOSIMETRIC DATA FOR LEAD 27

   Metabolism 27

   Metabolic Models 27

   Chemical Toxicity 29

7. DOSIMETRIC DATA FOR COPPER 30

   Metabolism 30

   Metabolic Models 31

   Chemical Toxicity 32

8. MEASUREMENT OF ABOSRBED FRACTIONS FOR PHOTON SOURCES DISTRIBUTED UNIFORMLY IN VARIOUS ORGANS OF A HETEROGENEOUS PHANTOM 33

Experimental Apparatus and Procedures 34

Results and Discussion 37

9. ABSORBED DOSE IN MALE HUMANOID PHANTOMS FROM EXTERNAL SOURCES OF PHOTONS AS A FUNCTION OF AGE 40

10. GENERIC ENVIRONMENTAL STATEMENT FOR PLUTONIUM-238-POWERED CARDIAC PACEMAKERS 46

11. MEDICAL X-RAY DOSE ESTIMATION PROGRAM 47

12. ABSORBED DOSE TO SELECTED INTERNAL ORGANS FROM TYPICAL DIAGNOSTIC X-RAY EXPOSURES 60

13. X-RAY EXPOSURE FACILITY 68

14. AN AaI(Tl) SCINTILLATION DETECTOR FOR SPECTROMETRY AND DOSIMETRY OF MEDICAL DIAGNOSTIC X RAYS 70

15. MODIFICATIONS TO THE MR. ADAM PHANTOM 73

16. A COMPARISON OF THE GTC CROSS SECTIONS WITH ENDF/B III 77

PART II. CIVIL DEFENSE RESEARCH

17. EFFECTS OF ELECTROMAGNETIC PULSE (EMP) FROM HIGH-ALTITUDE DETONATIONS 79

Transmission Through Underground Cables 79

A Versatile Pulser for Proof-Testing EMP Hardness by Pulse Injection 79

Response of an Infinitely Long Perfectly Conducting Cylindrical Antenna to an Electromagnetic Plane Wave Pulse 80

Transient Response of Low-Frequency (LF) Vertical Antennas to High-Altitude Nuclear Electromagnetic Pulse 81

18. STRATEGIC DEFENSE 83

Strategic Implications of Expedient Shelter 83

Expedient Shelter Handbook (ORNL-4941) 91

Development and Construction of Aboveground Expedient Shelters 91

Soviet Civil Defense Studies 97

19. NUCLEAR REACTOR SAFETY STUDIES 101

Emergency Planning for Accidental Radioactivity Releases From a Licensed Nuclear Facility 101

Calculation of Site Population Factor (SPF) 106

PART III. FUNDAMENTAL HEALTH PHYSICS RESEARCH

20. ELECTRON AND ION COLLISION PHYSICS 111

Collisional Ionization of Cesium by Molecules: Determination of Molecular Electron Affinities 111

Cesium Collisions with CO_2 112

Cesium Collisions with Some Octahedral Hexafluoride Molecules 113

Electron Attachment and Cesium Collisional Ionization Studies of Organic Molecules (Benzoquinones) 114

Electron Attachment and Cesium Collisional Ionization Studies of Tetrafluorosuccinic and Hexafluoroglutaric Anhydrides 115

Dissociation and Autoionization Lifetimes 116

Energy Pathways in the Rare Gases 116

Dissociative Ionization of Molecules by Electron Impact 117

Dissociative Ionization of D_2 117

Dissociative Ionization of N_2 120

Predissociation of the $B^2\Sigma^-_g$ State of O_2^+ 121

Mass Analysis of Negative Ions Produced in Swarm Experiments: Ion Clustering Reactions in Ammonia 122

Low-Energy-Electron-Induced Sputtering of Alkali Halides 122

21. INTERACTION OF RADIATION WITH LIQUIDS AND SOLIDS 125

Ultraviolet Optical Properties of Lithium 125

Electron Attenuation Lengths in Carbon Films 128

Plasmon Resonance Photoemission from Aluminum 129

Determination of Electron Scattering Lengths in Aluminum from Measurements of Photoemission Escape Depths 130

Radiation-Induced Changes in the Soft X-Ray Emission from LiF and NaCl 132

Electrical Conductivity and Optical Properties of (TTF)(TCNQ) 132

Effect of Damping on Surface-Plasmon Dispersion 134

A Concentric Angle Doubler for Vacuum Ultraviolet Studies 136

Photon Scattering from Cylinders 137

22. PHYSICS OF TISSUE DAMAGE 140

Collective Electron Effects in Molecular Liquids 140

Collective Oscillation in Liquid Water 143

Optical Properties of Organic Liquids 145

Index of Refraction of Aqueous Solutions of Alkali Halides in the Ultraviolet 146

Electron Slowing-Down Studies 147

Radiation Interactions with Nucleic Acid Bases 148

Optical and Dielectric Properties of DNA in the Extreme Ultraviolet 149

Optical Properties of Chloroplasts and Red Blood Cells in the Vacuum Ultraviolet 151

23. ATOMIC AND MOLECULAR RADIATION PHYSICS 153

Attachment of Slow (<1 eV) Electrons to O_2 in Very High Pressures of Nitrogen, Ethylene, and Ethane 153

Low-Energy (<1 eV) Electron Attachment to Molecules in Very-High-Pressure Gases: C_6H_6 154

Low-Energy (<3 eV) Electron Attachment to Molecules in Very-High-Pressure Gases: C_2H_5Br 158

Mobilities of Slow Electrons in Low- and High-Pressure Gases and in Liquids 158

Mobilities of Thermal Electrons in Low-Pressure Organic Vapors 161

Electron Mobilities in High-Pressure Gases ("Quasi Liquids") 162

Direct Measurement of the Mobility of Excess Electrons in Liquids 162

Potential Energy Function for an Excess Electron in a Nonpolar Liquid 163

Compound Negative Ion Resonant States and Threshold Electron Excitation Spectra of Monosubstituted Benzene Derivatives 163

Lifetimes of Long-Lived Monosubstituted Nitrobenzenes 165

Dual Fluorescence of Aromatic Hydrocarbons in Solution 167

24. THEORETICAL RADIATION PHYSICS 168

Pion Beam Dosimetry 168

Conversion Factors for Estimating Dose and Dose Equivalent from ^{11}C Activation 173

Comments on the Theory of Radiation Risk 173

Two-Component Models of Cellular Survival 173

Mathematical Analyses of Cell Survival Mechanisms 174

Molecular Scattering: Convergence of Close-Coupling Expansions in the Presence of Many Open Channels 174

Scattering of Electromagnetic Waves by a Cylinder 176

X-Ray Excitation of Surface Plasmons on Spheres and Cylinders 177

Dispersion Relations of Collective States When Damping Is Present 178

Energy Gain from Surface Plasmons in Electron Energy Loss Experiments 180

The Impact Parameter Representation of Charged-Particle Energy Losses in Condensed Media 181

Radiative Capture of Electrons by Swift Ions in Solids 183

Surf-Riding Electron States Trailing Swift Ions in Condensed Matter 186

PART IV. RADIATION RESEARCH AND DEVELOPMENT

25. DOSIMETRY FOR HUMAN EXPOSURES AND RADIOLOGICAL IMPACT 189

Study of Radiation Exposure to Atomic Bomb Survivors Residing in the United States 189

In-Vivo Dose Estimates for Atomic Bomb Survivors in Hiroshima and Nagasaki 190

Cesium Distribution in Soil of the Oak Ridge Area 196

In-Situ Gamma-Ray Measurements 197

Measurements of Radon Daughter Concentrations in Air 202

Shielding Materials for High-Yield Neutron Source Carriers 207

26. SOLID-STATE DOSIMETRY RESEARCH 209

Objectives 209

Spark Counting of Neutron-Induced Recoil Particles 209

Precision of Fast-Neutron Dosimetry by Track Etching 210

Thermoluminescence of Ancient Ceramics 211

Environmental Dosimetry Intercomparisons 213

TLD Measurements with Terbium-Activated Magnesium Orthosilicate 213

TL Dosimetry with Ceramic BeO 214

Computational Extension of the Dynamic Range of TL and TSEE Readers 215

Proportional Counting of TSEE Dosimeters 216

Relationships Between EPR, TL, and TSEE in Ceramic BeO 216

Dosimetric Properties of BeO TSEE Dosimeters 217

TSEE Monitoring of Beta Emitters 219

TSEE in Personnel Monitoring 220

Miscellaneous 221

27. ATOMIC PHYSICS 222

Symposium on the Jesse Effect and Related Phenomena 222

Jesse Effect in Helium 226

Energy Transfer from the Resonance States Ar($^1P_1$) and Ar($^3P_1$) to Ethylene 229

Energy Transfer from the Resonance States Ar($^1P_1$) and Ar($^3P_1$) to Nitrogen 230

Resonance Ionization Spectroscopy 230

Microdosimetry 233

Theoretical Models for Low-LET Cell-Survival Studies 235

28. SPECTROMETRIC DOSIMETRY 241

Application of Pulse-Shape Discrimination to Liquid Scintillation Alpha Spectroscopy 241

Spectra of Unscattered Gamma Rays with Energies Greater Than 1.8 MeV That Come from the Health Physics Research Reactor during Its Operation 243

Organic Scintillator Research 243

29. HPRR AND ACCELERATOR OPERATIONS 247

Introduction 247

Health Physics Research Reactor (HPRR) 247

Use of HPRR in Nuclear Engineering Experiments 249

DOSAR Low Energy Accelerator (DLEA) 250

ORNL 3-MV Van de Graaff Accelerator 250

PART V. EDUCATION AND INFORMATION

30. EDUCATION AND VOCATIONAL TRAINING 253

31. HEALTH PHYSICS INFORMATION SYSTEM (HPIS) 255

THESES, PAPERS, PUBLICATIONS, AND LECTURES

THESES 257

PAPERS 257

PUBLICATIONS 262

LECTURES 270

MISCELLANEOUS STAFF ACTIVITIES

ACADEMIC APPOINTMENTS 275

SERVICE IN PROFESSIONAL ORGANIZATIONS 275

GUESTS AND TRAINEES 276

- Faculty Institute Participants 276
- Health Physics Technologists 277
- ORAU Trainees 277
- Graduate Students 277
- Foreign Guests 277

ORGANIZATION CHART 279

Foreword

This annual report covers the research activities of the Health Physics Division between August 1, 1973, and July 31, 1974. As in the past, the Division's work in applied health physics is reported separately by calendar year. The latest report, for 1973, is ORNL-4974.

The Urban Research Section of the Health Physics Division was transferred to the new Energy Division of the Laboratory when it was formed in May 1974. The close working relationship existing with this group is being maintained under the new administrative structure.

W. S. Snyder retired at the end of February 1974. We are fortunate in maintaining his continued services as a consultant.

Several new administrative changes were made in the Division during the year. J. E. Turner was appointed Associate Director; J. C. Hart, Chief of the Education and Information Section; J. W. Poston, Chief of the Medical Physics and Internal Dosimetry Section; A. D. Warden, Chief of the Industrial Safety and Special Projects Section; and J. S. Carver, Administrative Assistant.

As this report will document, the research programs of the Health Physics Division continue to be exciting and productive. The highlights are described in the opening Summary. Detailed descriptions of the work are presented in the five parts of this report. The reader is invited to contact individual investigators whose names are associated with parts of the work. Numerous references to the open literature are given, and a list of the Division's publications is included.

The basic long-term research programs of the Division have continued during the year. In addition, efforts were made to strengthen collaboration within the Division itself in order to initiate new needed programs. For example, D. G. Jacobs, who returned to the Division after an extended assignment with the International Atomic Energy Agency, has established an environmental health physics program within the Radiation Monitoring Section. Contacts with investigators in other disciplines outside the Division have been strengthened. Cooperative programs with the Biology and Environmental Sciences Divisions and with the University of Tennessee Comparative Animal Research Laboratory are in various stages of development and implementation.

The Division continues its broad approach to health physics – an approach that ranges from basic research to the day-to-day practice of radiation protection. The Division's programs will remain dynamic and responsive to the needs and goals of the Laboratory, the AEC, and the nation.

Summary

PART I. MEDICAL PHYSICS AND INTERNAL DOSIMETRY

(Chapters 1–16)

The report of the Section for this year illustrates the merging of several disciplines necessary in this particular research area. Further, the summaries presented demonstrate that the Section is expanding its interests outside of the traditional area once labeled "internal dose." Without question, the importance of internal dosimetry to the practice of the profession of health physics has not diminished. However, as more stringent demands are put upon the dose estimation, more refinements must be added to the models and codes used to produce these estimates. In addition, the developments made over the last ten years in the Section are being applied in areas outside the estimation of internal dose received in an occupational situation. All these efforts require additional information and input from the many disciplines which together represent our area of research – medical physics and internal dosimetry.

The dose equivalent to a target organ per microcurie-day of residence in a source organ corresponds essentially to the effective energy values used in computing dose and/or maximum permissible concentration (MPC) values recommended at the present time by the NCRP and ICRP. "Tabulations of Absorbed Dose per Microcurie-Day Residence of Various Radionuclides in Source Organs of an Adult" is a summary of two reports in draft form, which present a tabulation of the average dose equivalent in various target organs per microcurie-day of activity in the source organ. One report will contain information on about 100 radionuclides of particular interest in nuclear medicine, while the second report will give data on many more radionuclides (400 to 500) of interest to the applied health physicist.

The "Revision of MIRD Pamphlet No. 5. . ." presents a summary of the revisions to the Snyder-Fisher phantom which have taken place since the original design in 1967. These revisions include the separation of the legs, the rounding of the head, the addition of clavicles and scapulae to the skeleton, as well as the addition of walls to many of the internal organs. In addition, this pamphlet will present estimates of absorbed fractions for 12 monoenergetic photon sources distributed uniformly in various organs of the phantom.

Other significant results reported include the "Report of the Task Group on Reference Man," "Dose to a Dynamic Bladder for Administered Radionuclides," and "Internal Dosimetry of Spontaneously Fissioning Nuclides." The report on reference man has been completed and sent to the publisher. This extensive compilation of data on the human should be invaluable to the health physicist. The effects of voiding schedule, rate of formation, and biological rates of elimination of the radionuclide have been studied in the dynamic situation represented by the bladder. This study is a continuation of earlier studies for monoenergetic photon sources. Calculations were made for both the photon and beta dose from ^{89}Sr and ^{131}I in the contents of the bladder. A comparison of surface dose and a dose averaged over the wall of the bladder as a result of beta exposure is also given. The assessment of the radiation hazard associated with radionuclides that decay partly by spontaneous fission has become more important in the last few years. The study by Dillman and Jones, reported herein, represents a significant contribution to the evaluation of internal dose due to the transuranium isotopes.

The "Dosimetric Data for Lead" and "Dosimetric Data for Copper" delineate the kinds of metabolic information which result from the careful analysis of the existing literature. These models and their retention functions represent an important input to the calculation of internal dose. A program designed to provide

experimental data for comparison with our Monte Carlo results is summarized in "Measurement of Absorbed Fractions for Photon Sources Distributed Uniformly in Various Organs of a Heterogeneous Phantom." This experiment is the first attempt to measure absorbed fractions in a geometry that matches closely the Snyder-Fisher mathematical phantom. The research on exposure to a semi-infinite cloud has been extended to include phantoms representing children of five different ages. The results presented in "Absorbed Dose in Male Humanoid Phantoms from External Sources of Photons as a Function of Age" indicate that the dose to the genitalia of a newborn might be three times greater than the dose to the genitalia of an adult at higher emitter energies and 30 times greater at the lowest emitter energy. In general, from one year old upward in age the dose decreases with age.

The remaining summaries represent the newer research areas of the Medical Physics and Internal Dosimetry Section. The "Generic Environmental Statement for Plutonium-238-Powered Cardiac Pacemakers" will include an incremental benefit assessment, a risk assessment, a benefit-risk balance, and suggestions of protective measures. The research agreement with the Food and Drug Administration (FDA) is reviewed in the "Medical X-Ray Dose Estimation Program." This research has provided FDA with valuable data that have been folded into a program aimed at controlling and reducing population exposure to diagnostic x-ray sources. "Absorbed Dose to Selected Internal Organs from Typical Diagnostic X-Ray Exposures" presents results of a study of two typical diagnostic x-ray examinations for a number of beam sizes and x-ray spectra.

Additional experimental work is outlined in the next three summaries – "X-Ray Exposure Facility," "An NaI(Tl) Scintillation Detector . . . ," and "Modifications fo the MR. ADAM Phantom." The objective here is to provide a facility for simulating typical x-ray exposure, to design a detector suitable for measurements of x-ray spectra in a phantom, and to modify the original physical representation of the Snyder-Fisher phantom to conform to the latest design. "A Comparison of the GTC Cross Sections with ENDF/B III" delineates an initial step in the modification of the existing neutron code to include the heterogeneous mathematical phantom. One of the first hurdles was to assemble and compare cross sections that have been used over the past ten years with the latest cross sections available. The ultimate goal is a computer code, similar to the existing photon code, suitable for use with neutrons in the energy range from thermal to 20 MeV.

PART II. CIVIL DEFENSE RESEARCH

17. Effects of Electromagnetic Pulse (EMP) from High-Altitude Detonations

The response of top-loaded vertical low-frequency antennas to electromagnetic pulse (EMP) was studied. Several antenna models were applied to calculate the response. Among the models employed were the infinite cylindrical antenna, the singularity expansion method and the quasi-first-order theory of King for the electrically short antenna, and the theory of Wu for the electrically long antenna. The computed curves were checked by comparing the results from the various antenna models.

The infinite cylindrical antenna model was developed to obtain very accurate early-time results for the EMP response of long antennas. The Norton equivalent current used in the derivation was from the EMP-induced current on an infinite circular cylinder. The Norton equivalent antenna admittance used in the derivation was that of an infinitely long cylindrical antenna excited by a finite uniform distributed source.

The propagation of EMP surges by underground power lines was studied. Maxwell's equations were solved directly for a three-media model of underground transmission lines. The result leads to an iterative procedure as simple as that of Sunde's formula for transmission lines.

A very versatile and convenient pulser for simulating EMP surges was built to our specifications by Maxwell Laboratories of San Diego, California. The peak amplitude of the voltage pulse is 150 kV. The rise time is selectable and ranges from 10 to 1000 nsec. The fall time (to $1/e$) is also selectable from a range of 0.5 to 10 μsec.

18. Strategic Defense

The family of expedient shelter designs that has been developed by this project has the potential to change qualitatively the outcome of a nuclear war. The shelters provide high-grade radiation protection and significant blast protection and can be constructed by almost anyone almost anywhere with existing resources of tools and materials. Employed in conjunction with an urban evacuation plan, the shelters can reduce U.S. fatalities in a nuclear war from over half the population to a few percent or less, depending on conditions.

A handbook for the construction of expedient shelters was published. It gives pictorial design drawings and detailed written step-by-step instructions that can be used by persons who have had little or no construction

experience to build for themselves and their families, within 48 hr, shelters that can give them adequate protection from fallout. Some of these shelters can protect against low levels of blast overpressure.

Civil defense officials in Florida, Louisiana, and other areas with very high water tables for years have recognized the need for *aboveground* expedient shelters that average citizens could build within a day or two by using only widely available local materials and common hand tools. However, civil defense publications do not contain such designs. Therefore, as part of the continuing research and development of expedient shelters for all major environments in the United States, contractors' workers and untrained families were hired to build new and improved designs of aboveground shelters in Flagler County, Florida. The most practical of these aboveground types were built successfully by untrained families guided only by step-by-step illustrated written instructions. These types were the door-covered shelter (which for walls has earth-filled "rolls" made of bed sheets and/or other home fabrics), the ridge-pole shelter, the crib-walled shelter, and the A-frame pole shelter.

Our research in the area of Soviet civil defense has continued to reveal that the Russian leaders are convinced that preparations to evacuate, disperse, and shelter their population are a very necessary part of their defense planning. There has been a new directive to the effect that the civilian population must be given practical training in civil defense measures. As a result of this, Col. Gen. Altunin, Deputy Defense Minister for U.S.S.R. Civil Defense, has stated that all civil defense services must prepare the necessary training and material base to implement this directive by December 1, 1973. In January 1974 a new program was announced for the construction of additional underground "spaces" in Moscow. The aim of this project was stated as "to put underground those structures which do not require daylight." Examples given are garages, shopping plazas, and bus terminals adjacent to subway entrances.

19. Reactor Nuclear Safety Studies

Two factors which determine the time available to institute emergency procedures after a water-cooled power-reactor core meltdown were examined. First, a realistic calculation of fission product release as a function of time was made. The release time function can determine, in part, the speed and type of response that is necessary. Second, the time-dependent meteorological dispersion and deposition of the radioactive aerosol released to the environment were calculated. Inhalation dose as a function of time was also estimated because it is the immediate concern of emergency planning for the population surrounding a licensed nuclear facility.

A formula was devised for calculating a number, the site population factor (SPF), which indicates the suitability of a specific location relative to others for the location of power reactors, in terms of population at risk from a potential nuclear reactor accident. This formula was used to prepare maps of the United States which show contour lines of equal values of the SPF.

PART III. FUNDAMENTAL HEALTH PHYSICS RESEARCH

20. Electron and Ion Collision Physics

Many new results have been obtained in experiments with our cesium charge-exchange apparatus. In these experiments, well-controlled beams of ground-state cesium atoms are collided with neutral target atoms over a wide range of relative energies. Due to its small ionization potential, electrons can be easily transferred from cesium to another atom or molecule. Studies of chemi-ionizing collisions between fast cesium atoms and molecules are yielding important information on structures of molecular negative ions. The electron affinities of many polyatomic molecules have been determined by measuring the threshold for the formation of ion pairs in collisions of cesium with the target molecules. Among these are O_2, NO, NO_2, SF_6, TeF_6, and a number of organic molecules.

New insight into dissociation and autoionization lifetimes of collision-induced unimolecular dissociations has been achieved through a statistical theory. A unified treatment for species of low angular momentum, such as produced by electron or photon impact, and those of high angular momentum, as in ion-molecule collision complexes, has been obtained.

More detailed results on dissociative ionization of molecules by electron impact have been obtained in the complex crossed-beam collision chamber described last year. Quadrupole mass spectrometric capabilities have been added to the experimental apparatus, which now yields angular and energy distributions of mass-identified positive ions under low- to medium-energy electron impact. Most recent results include ionic distributions from H_2, D_2, O_2, and N_2.

Measurements of ion clustering reactions, reported last year for H_2O, have been extended, and results have been obtained for clustering of ammonia about NH_2^-. This information should prove to be very valuable for studies of the radiation chemistry of gases.

Members of the Health Physics Division are interested in the evolution of chlorine gas from irradiated rock salt, with application to the storage of radioactive wastes in salt mine repositories. In an experiment conducted in collaboration with the Chemistry Division, alkali halide single crystals were bombarded with 100- to 2000-eV electrons, and the sputtered neutral particles were analyzed.

21. Interaction of Radiation with Liquids and Solids

As a continuation of our studies on the alkali metals, the reflectances of evaporated films of lithium were measured as functions of angle of incidence for photon energies between 3 and 10.7 eV. It has been found that special care must be exercised in order to obtain bulk optical parameters from the data, since anomalous surface roughness effects must be eliminated by preparing smooth films, or the roughness must be accurately measured and its effects on the optical measurements must be modeled and used to correct the observed data. Electron escape depths of photoexcited electrons in thick carbon films have been obtained from measurements of the total photoelectric yield as a function of photon angle of incidence over an energy range of 20 to 64 eV. In a separate study, the effects of a plasmon resonance peak on photoemission yields from aluminum have been determined. A yield has been measured at 50° from normal incidence that is more than 100 times that obtained at normal incidence. The scattering lengths of low-energy electrons in aluminum were determined in another photoemission experiment. A new method of analyzing photoemission data was developed in order to obtain the scattering length from a ratio of measurements taken with a vacuum-aluminum interface and with an MgF_2-aluminum interface.

A brief account was given last year of some work in this section on organic molecular constituents of high-conductivity charge-transfer compounds such as (TTF)(TCNQ). Single crystals of this and a few other related compounds show extraordinarily high electrical conductivity at a temperature of approximately 60°K. Single crystals of (TTF)(TCNQ) were prepared at this Laboratory, and dc electrical conductivity and optical reflectivity and transmission measurements were made. Similar work on related compounds is under way in a cooperative effort between this Division and other divisions of ORNL.

We have discovered and explained an unexpected behavior of surface-plasmon dispersion in the presence of damping. If damping is included in the equation that defines the surface-plasmon dispersion curve, the resulting curve does not increase monotonically as the surface-plasmon wave vector increases. A dramatic departure from monotonicity is observed in the analysis of data for silver taken at our laboratory and elsewhere. Theoretical discussion of this phenomenon is included in the theoretical radiation physics portion of this report.

22. Physics of Tissue Damage

Theoretical studies of the electronic structure of liquids have been continued. We note that the peak in the imaginary part of the dielectric function at 13.5 eV for water vapor is identified with a peak at 21 eV in the energy loss function for liquid water. This behavior is indicative of a strong collective electronic resonance in liquid water, as discussed previously by Platzman. New optical data were obtained on the molecules tetramethylbenzene and pentafluorobenzene, and their electronic and optical behavior in the liquid state was contrasted with that of benzene itself.

The indices of refraction of the alkali halides LiCl, NaCl, NaI, and KCl have been measured in aqueous solution through a range of wavelengths in the ultraviolet.

The electron fluxes due to beta rays from the isotope ^{166}Dy slowing down in aluminum oxide have been determined and compared with a Monte Carlo slowing-down calculation. The agreement between theory and experiment is generally good below 100 eV and above 1000 eV electron energy. Experimental fluxes exceed theoretical calculations by as much as a factor of 3 in the intermediate energy region. The reasons for this discrepancy are not known.

Studies have continued on the optical and electronic properties of the nucleic acid bases guanine and adenine over the energy region from 2 to 84 eV. Electronic transitions have been assigned to some of the structure found in the dielectric functions of these two materials. The most prominent characteristics are strong peaks in the energy loss function at 25.5 and 24.4 eV for guanine and adenine, respectively, indicating a strong collective electronic excitation contribution to the energy absorptions at these energies.

The optical and dielectric properties of dry films of DNA have been determined for photon energies between 2 and 82 eV. Peaks in various dielectric parameters are found at several energies, and these are generally identifiable. The most prominent characteristic, as in the cases of the nucleic acid bases themselves, is the peak in the energy loss function at 21.6 eV.

The studies described last year on the optical behavior of chloroplasts were extended this year to include the somewhat similar molecule heme. The chloroplasts were in the form of a solid dry deposited layer, whereas the heme was suspended in a liquid medium. Interesting similarities were found between the optical behavior of chloroplasts and that of red blood cells.

23. Atomic and Molecular Radiation Physics

Over the past year an intensive effort has been maintained in our research program on the attachment of slow electrons to a number of different molecules in very-high-pressure gases. As has been indicated in earlier reports, this effort represents an attempt to span the gap between electron swarm experiments performed at ordinary gas pressures and experiments involving irradiated liquids. In recent experiments we have studied the attachment of slow electrons to oxygen in very high pressures of various carrier gases including nitrogen, ethylene, and ethane. Electron capture mechanisms and reaction schemes for these phenomena, consistent with the observed dependences of the attachment rates on the density of each medium, have been developed. In complementary experiments, low-energy electron attachment to various molecules has been studied under a common high-pressure carrier gas such as nitrogen or argon. In these experiments, studies have been made of electron attachment to benzene and to bromoethane. Our research efforts on the behavior of electrons in high-density media are being expanded through the design and construction of two additional experiments for the study of the mobility of thermal electrons in high-pressure gases and in liquids. The design of these experiments is described briefly, and their role in our program is outlined.

Our efforts in the study of compound negative ion resonant states in low-energy electron-molecule collisions is continuing. Threshold electron excitation spectra have been obtained for monosubstituted benzene derivatives. The number and positions of a number of observed resonances have been interpreted in terms of the net π-electron charge transfer between the substituent and the benzene ring. In another experiment the lifetimes of long-lived monosubstituted nitrobenzene negative ions have been determined in mass spectrometric studies of these molecules.

24. Theoretical Radiation Physics

Theoretical dosimetry. The computer code PION-1, which was discussed in last year's annual report, has been further improved and used for several calculations related to the use of pions for cancer radiotherapy and also to radiation protection. Research in the pion beam dosimetry program includes calculations to estimate dose equivalent and average quality factors for both positive and negative pion beams typical of those currently being used in radiobiological experiments. For a π^- beam of Gaussian momentum distribution with a mean momentum of 175 MeV/c, it was found that the average quality factor is approximately 1.5 between the surface and a depth of 15 cm; thereafter, it rises to a maximum of about in the stopping region around 21 cm depth. Detailed calculations have been made of the distributions of absorbed dose in a soft-tissue phantom containing regions of both bone and air. In a further refinement of the computer code PION-1, provision has been made to include the cell survival model of Robert Katz. With this new capability, calculations have been made of the survival of T-1 kidney cells as a function of position in a tissue phantom irradiated by a pion beam.

In another related study, which involves members of the Fundamental Health Physics Research Section and members of the Radiation Research and Development Section of the Health Physics Division, a number of mathematical models of cell survival have been developed and applied to a number of experimental studies. In these models, particular attention has been given to the mathematical formulation of specific biological mechanisms, including (1) the effects of statistical fluctuations associated with both the direct and indirect effects of radiation, (2) chemical kinetics associated with the indirect effect and/or repair and recovery, (3) possible effects of radiation on the repair mechanisms, (4) the effect of chemicals which are believed to either stop repair or fix reparable cell damage, (5) the effect of fixation time or other cell cycle effects, (6) the accumulation of reparable damage to a given lesion, and (7) the possible requirement of multihits or multitargets in accounting for cell death.

Theoretical atomic and molecular physics. For low-energy collisions in atomic and molecular scattering phenomena, one of the most powerful and useful theoretical methods for obtaining detailed cross-section information is the target-eigenstate-expansion or close-coupling method. It is well established that application of the usual close-coupling method to low-energy atomic scattering does not yield completely reliable results unless all open channels are retained in the eigenstate expansion. We have shown that the opposite is true for low-energy molecular scattering below the thresholds for vibrational and electronic excitation in the target molecule. That is, the close-coupling methods do indeed converge for molecular scattering involving

rotational excitation, even in the presence of a large number of open channels. This result is particularly significant for a study of rotational resonances in low-energy electron collisions for simple molecules, such as those reported last year, which have been proposed to explain anomalies in electron swarm experiments at very high pressures. Theoretical and experimental studies of these high-pressure scattering phenomena are continuing in the Fundamental Health Physics Research Section of this Division.

Theoretical radiation physics of solids. In our continuing effort to a reach a theoretical understanding of the properties of surface plasmons, we have made a theoretical study of a recent experiment involving the reflection of a laser beam from a small aluminum cylinder at small angles of incidence with respect to the cylinder axis. In this study the generation of surface plasmons is proposed to explain anomalous dips that are observed in the reflected intensity of the light as a function of the angle of incidence on the cylindrical surface. In another study we have examined theoretically the excitation of surface plasmons by x rays incident on very small spherical and cylindrical surfaces. Interest in this particular problem was generated by the experimental work of Koumelis on the inelastic scattering of x rays from colloidal graphite particles, where the energy loss of the photon was attributed to surface-plasmon excitation. Analytical expressions for the surface-plasmon excitation cross section have been obtained, and suggestions have been made for further experimental work which will allow x-ray inelastic scattering with surface-plasmon excitation to be studied in more detail. In another study a detailed theoretical explanation is given for the experimentally demonstrated fact that the dispersion relation of the surface plasmon when inferred from certain optical measurements may be drastically different from that deduced from the electron energy loss determinations.

A theory has been given which accounts quantitatively for the heretofore unexplained energy gain observations of Schilling and Raether [*J. Phys. C* **6**, L358 (1973)]. The energy gain process is described successfully in terms of the exchange of quanta of collective electron oscillations by two fast electrons. A new theory of the impact parameter representation of energy deposition in matter by swift charged particles has been proposed. Expressed in terms of the linear response function of a medium, our new representation describes both close and distant collisions in a consistent manner.

Recent experiments in the Solid State and Chemistry Divisions of this Laboratory and elsewhere have established the surprising fact that photons resulting from the capture of electrons by swift ions traversing solids can now be measured. We have used a standard radiation theory together with a statistical model of the electron states in a crystal lattice in order to analyze the results of Appleton et al. of ORNL. In the experimental data for channeled O^{8+} and O^{7+} ions in a single-crystal silver target, further refinements in both the experimental data and the theoretical analysis are anticipated in future efforts at this Laboratory.

A new physical phenomenon has been predicted in radiation processes involving the penetration of swift ions through condensed matter (solids or liquids). The energy loss of a fast charged particle moving in condensed matter can be described in terms of the complex dielectric function of the medium. Physically, the target response manifests itself as a cylindrically symmetric wake of electron density fluctuations behind the particle. Its axis defines the particle track. The wake consists of a series of domains, at distinct distances behind the projectile, in which the electron density is alternately enhanced and depleted relative to the mean density in the medium. Domains of density enhancement create regions of negative electron potential, and domains of depletion create regions of positive potential. If sufficiently deep, these potential troughs can trap, respectively, positive or negative particles and sweep them along in states we define as surf-riding states, which trail behind the projectile. Experimental verification of surf-riding states would contribute significantly to the understanding of the dynamic many-body response of condensed matter to moving charged particles. Moreover, projectile trailing by surf-riding particles may contribute to several important phenomena associated with the penetration of charged particles through dense matter. We have made variational estimates of the binding energy of electrons in surf-riding states and find values which range from less than 10 eV for H^+ to more than a kilovolt for S^{16+}.

PART IV. RADIATION RESEARCH AND DEVELOPMENT

25. Dosimetry for Human Exposures and Radiological Impact

Research on techniques for the dosimetry of human exposures and for assessing the radiological impact of low-level occupational and environmental exposures makes up the major areas of interest to the group. To evaluate the radiological impact of low-level exposures, large populations receiving varying levels of exposures must be studied. Because the Japanese populations of

Hiroshima and Nagasaki are unique in this respect, close liaison has been maintained with the Atomic Bomb Casualty Commission (ABCC).

In the past year, liaison studies with the ABCC have involved (1) the calculation of depth-dose distributions for application in thyroid carcinoma and nodule formation studies of atomic-bomb survivors and for studies of survivors exposed in utero and (2) a study of the radiation exposure to survivors of Hiroshima and Nagasaki who are now residing in the United States.

The study of radiation exposure to survivors residing in the United States was started in 1973 at the request of the U.S. Atomic Energy Commission. In preliminary work completed in the past year, tentative estimates of radiation exposure were made for 44 survivors in the Los Angeles area, using recent survey information obtained from several sources in this country. Based on the results of this work, the study has been enlarged to include additional survivors in the Los Angeles area and has been extended to the San Francisco area. The survivors in these two areas represent approximately one-half of the estimated 500 survivors residing in the United States. Results of this larger study are of interest in local public health programs and are desirable as supporting information in making budget estimates for funding a bill such as H.R. 17112. If passed by Congress, this bill would provide financial support toward the medical care of some survivors now living in the United States.

Techniques have been developed for estimating doses to the thyroid and foetus of a survivor using T65D dose assignments that have been compiled for most of the 117,000 survivors in the Master Sample of the ABCC. The T65D doses, which actually predict dose to an infinitesimal amount of human tissue under exact analog exposure conditions except for the absence of the survivor, are generally not adequate to assess in vivo doses, because attenuation and multiple scattering in the body of the survivor are neglected. Applications of depth-dose calculations in phantoms from gamma rays and neutrons with energy and angular distributions typical of fission spectra are illustrated by the use of a survivor specific example. In this example, the importance of correlating radiation effects observed in survivor studies with in vivo dose estimates rather than T65D assignments is clearly demonstrated by the decrease in dose, especially that from neutrons, in the body.

In the past year, dose rates from natural radionuclides and ^{137}Cs in soils of the Oak Ridge area have been investigated using in situ and core-sample measurements. In situ gamma-ray measurements were made with a spectrometer consisting of a 4096-channel analyzer and a 50-cm^3 Ge(Li) detector. Information such as composition, density, and moisture content of the soil and the distribution of ^{137}Cs in the soil, needed in the analysis of the in situ gamma-ray spectra, were obtained from core-sample measurements. Results of some measurements that were made in support of an aerial survey of the Oak Ridge area are given. At most sites the dose rate from radionuclides determined from our data was about 5 microrads/hr (44 millirads/year).

Other topics discussed are a technique for measuring low levels of radon daughter radionuclides in air by alpha-particle spectrometry, results of radon daughter measurements made in structures in Grand Junction, Colorado, and research on a suitable shielding replacement for paraffin in neutron source carriers.

26. Solid-State Dosimetry Research

In recent years, emphasis of the track-etching fast-neutron dosimetry work has been on the detector sensitivity, with the measurability of the low doses encountered in personnel dosimetry being the most important goal. There is, however, frequently a need for precise measurements of doses in the 50-to-500-rad range, for example, in accident dosimetry, in radiobiological or radiotherapeutical work, or for the intercomparison of neutron sources by mail. The latter application is the subject of a current research agreement between ORNL and IAEA. With repeated exposures and etchings, standard deviations of 2 to 3.5% have been obtained for both spark counting and visual counting of fission fragment tracks from natural thorium or ^{237}Np. In applications where the use of fissionable materials is undesirable, the efficient automatic spark counting of fast-neutron-induced recoil particle tracks in thin polymer foils, such as cellulose nitrate and polycarbonate, is possible if the foils undergo extended etching to the point where electric breakdown begins to occur even in unexposed foils.

The measurement of high radiation doses with TL or TSEE readers is often limited, not by the response characteristics of the detector (saturation), but by the maximum light intensity or count rate which the readout instrument can handle. It has been demonstrated that it is possible to "reconstruct" an incompletely recorded glow peak, and to determine the area under it as if it were recorded in full, by using one of several methods. For example, one can assume that the glow curves scale approximately linearly in both the X and Y coordinates. A standard curve is adopted, its area is determined, and then the scaling factors required to

transform an arbitrary TSEE curve to the standard curve can be used to find the area under the former curve. This is done by using a coordinate digitizer and programmed calculator.

It is known that the environmental dose rate is subject to daily, seasonal, and other long-term fluctuations. In order to obtain values which have been averaged over hundreds or thousands of years, the TL signal in large (0.1 to 0.2 mm) quartz grains extracted from ancient ceramics, such as potsherds from Central America, Egypt, and Asia, has been investigated. The alpha-radiation effect at their surface had to be eliminated by etching away the alpha-exposed surface layer, and the "internal" beta-radiation dose had to be subtracted for precise measurements. If a faker of ancient artifacts should try to simulate old age by external irradiation, this can, incidentally, also be detected by etching of the large quartz grains.

The results obtained in conventional environmental monitoring with TLD by different investigators using different types of detectors rarely agree within the accuracy limits claimed for each method. In order to standardize the techniques, a workshop on this subject was organized as part of the Annual Dosimetry Intercomparison Study. In a test, the results of five groups varied by more than a factor of 2. A more comprehensive study of this type is, therefore, being organized in cooperation with the AEC Health and Safety Laboratory and the University of Texas.

27. Atomic Physics

During the past year, there have been several opportunities to put a perspective on our research on energy pathways in the noble gases. This program is concerned with the interaction of radiation with matter and, in particular, with the interaction of fast protons with the noble gases.

In a broad sense, the program is radiation chemistry conducted at the atomic physics level. The close relationship between this work and other fields of radiation chemistry has been developed in a chapter entitled "Elementary Processes in Irradiated Noble Gases" to be published in *Advances in Radiation Chemistry,* Vol. 4, edited by M. Burton and J. L. Magee.

Because of the understanding which has developed on energy transfer processes, it was found that the research has two very important applications to problems of great interest.

Charged-particle excitation appears to be a useful approach to gas-laser pumping. Excitation of high-pressure noble gases by accelerated electrons is one approach being intensively investigated. The work being pursued at ORNL on the energy pathways following proton interaction with noble gases is, thus, very directly relevant to the laser problem. It has been shown, for instance, that fast charged particles excite the resonance states of these gases, whereas gas discharges cause mainly the excitation of optically forbidden (metastable) levels. Therefore the large body of older literature on gas discharge excitation is not nearly so relevant to the laser problem.

The fact that, in general, noble-gas resonance states are converted to long-lived excited molecular states by three-body collisions has been used as the basis for looking for laser action in noble gases. Laser oscillations have already been demonstrated in xenon and in argon. The exceptionally high yield of these diatomic species follows from the fact that the oscillator strengths for the resonance states are large and that, once formed, all resonance states are converted to molecules at high pressure.

It is quite natural that the work done at ORNL on the interaction of radiation with matter has application to the characterization of the modern atmosphere. Work conducted here on the interaction of protons with the noble gases suggests a number of interesting and useful new methods for the determination of low levels of atmospheric pollution. The scope of this work includes the study of energy transfer from excited atomic and molecular states of the noble gases to other gases added in small concentrations, the development of a laser technique for laboratory analysis of the modern atmosphere, and the development of simple electronic monitoring equipment for field application.

We have solved the stochastic problem associated with a rather large family of cell-survival models which may be appropriate to low-LET radiation. The latter work emphasizes the importance of incorporating repair, recovery, and various cell-cycle effects into models of cell survival. Some special cases of the models mentioned above have been generalized to arbitrary-LET radiation. In particular, we have developed a microdosimetric version of the model due to Roesch.

28. Spectrometric Dosimetry

Spectrometric dosimetry is the study and use of the methods of spectrometry as they apply to problems in radiation protection. The program involves the study and improvement of components of spectrometry systems and the development of related electronic circuitry and data-handling techniques. For example,

the techniques used to distinguish between electron- and proton-produced pulses in a scintillator were applied to discriminate against electron-produced pulses in liquid organic scintillators used to measure alpha activity. This work, done in conjunction with the ORNL Chemical Technology Division, resulted in a counter capable of detecting a tenth as much alpha activity as that produced by the ^{239}Pu that exists in most soil samples. In support of other dosimetry programs that use the Health Physics Research Reactor as a radiation source, particularly the Nuclear Accident Dosimetry Intercomparison Program, the high-energy gamma-ray spectrum produced by the reactor was measured. Measurements behind the steel and Lucite shields used to modify the reactor spectrum for intercomparison studies were included. Work was completed on the synthesis and purification of parasexiphenyl (PSP). Fractional sublimation was chosen as the best means for purifying the PSP. Crystals of anthracene, stilbene, and paraquaterphenyl were grown for use in determining their light output as a function of incident particle energy. Preliminary measurements of the distribution of energy losses of low-energy protons in gases have begun. As the gases become available, this information will be recorded to determine how energy losses are affected by molecular bonding. The present experiment will also consider the effect of molecular bonds on Bragg additivity, because other evidence exists that molecular binding may affect its application.

29. HPRR and Accelerator Operations

The principal activity of this group is the operation of the Section's radiation facilities in support of research in dosimetry, radiation biology, other radiation effects, and nuclear safety.

The Health Physics Research Reactor (HPRR) continues to play an important role in the efforts to correlate radiation dose with biological effect. Scientists from the ORNL Biology Division, UT-AEC Comparative Animal Research Laboratory, and several other laboratories comprise the list of "most frequent" users. In addition, the HPRR is also used for nuclear engineering studies and for nuclear safety through the dosimetry intercomparison studies, which are designed to evaluate nuclear accident dosimetry systems.

Most of the operation of the DOSAR Low Energy Accelerator has been in support of an experiment designed to determine the stopping of protons, in the energy range of 50 to 150 keV, in tissue-constituent gases. Considerable modifications have been made to the beam handling apparatus, and differentially pumped regions of the beam tube have been added. Neutrons from the $^{3}H(d, n)^{4}He$ reaction have been generated for dosimetry tests by a small sealed-tube neutron generator manufactured by Philips Electronic Instruments.

Significant improvements have been made to the Section's 3-MV Van de Graaff. A second experimental station is being added. Equipment additions at this station will permit the measurement of resonance radiation both in the visible and ultraviolet regions.

PART V. EDUCATION AND INFORMATION SECTION

30. Education and Vocational Training

Studies carried out last year by staff personnel showed that a critical shortage of B.S.-level health physics technologists would occur very early in the next decade if college curricula were not developed by the mid-seventies that would produce skilled technicians capable of assuming job responsibilities immediately following graduation. A Faculty Institute program was conceived and approved for operation by the AEC at ORNL, and selected college faculty members were brought into the program in early June of 1974.

The Institute provides for a 12-week course, which has as its principal objective the development of B.S.-level curricula that will produce undergraduates capable of qualifying eventually for certification by the American Board of Health Physics. Up to ten participants are enrolled in the Institute each year during the summer months. The program is scheduled to run through about 1980 with the expectation that participating colleges will be able to fulfill projected needs for B.S.-level graduates commensurate with a projected growth-requirement time curve.

The training of B.S.-level health physics technologists, continued at ORNL through most of calendar year 1973, has been discontinued in favor of the Faculty Institute program. However, graduate training continues to be an important part of the program of the Section. Nine faculty, ten undergraduates, and seven graduate trainees from 22 college campuses participated in various training programs during the reporting period.

31. Health Physics Information System

The Health Physics Information System (HPIS) completed its plans for utilizing computerized techniques and was interfaced with other technical information systems operating in the Oak Ridge area. The HPIS assumed responsibility for information input in mammalian metabolism, monitoring, and waste management

when these areas were discontinued by the Nuclear Safety Information Center (NSIC) program. During the period, the HPIS moved from a design pilot stage to an operational stage with partial capability on video terminals via the ORLOOK program of the Computer Sciences Division.

Part I. Medical Physics and Internal Dosimetry

W. S. Snyder J. W. Poston

1. Tabulations of Absorbed Dose Per Microcurie-Day Residence of Various Radionuclides in Source Organs of an Adult

W. S. Snyder M. R. Ford S. B. Watson[1]

The authors have two reports in draft form which present a tabulation of the average dose equivalent in various target organs per microcurie-day of activity in the source organ. One report is being prepared for publication as a Medical Internal Radiation Dose Committee (MIRD) pamphlet, and the other is expected to be issued, perhaps in loose-leaf form, as a Laboratory report. The MIRD pamphlet will list estimates of total dose for approximately 100 radionuclides of particular interest in nuclear medicine. The Laboratory report will contain the same type of data except for a larger number of radionuclides, perhaps 400 to 500, and more detail will be given; for example, separate listings of dose will be included for each type of radiation.

The tabulated values are the dose equivalent imparted to the target organ for 1 μCi-day in the source organ and correspond in principle to the effective energy values used in computing dose and/or maximum permissible concentration (MPC) values recommended at the present time by the National Committee on Radiation Protection (NCRP) and the International Commission on Radiological Protection (ICRP). This effective energy is the weighted energy absorbed in an organ per disintegration of the radionuclide, the weighting factors being those related to the biological effectiveness of the radiation, the linear energy transfer (LET), or other conditions of exposure. Thus the tabulated quantity, termed S, may be used to obtain dose equivalent in the target organ by the simple formula

$$\mathrm{DE} = U \times S\,, \tag{1}$$

where U represents the time integral of activity in the source organ, expressed in microcurie-days, and S is the dose equivalent per microcurie-day tabulated in this report for the source and target organs and nuclide considered. Thus S, more precisely $S(X \leftarrow Y)$, for source organ Y and target organ X, is given by

$$S = 51.15 \sum_i f_i \bar{E}_i \Phi_i(X \leftarrow Y) Q_i(X) N_i(X) \tag{2}$$

Here $\bar{E}_i$ is the average energy or unique energy of the ith type of particle, f_i is the yield in particles of type i per disintegration, $\Phi_i(X \leftarrow Y)$ is the specific absorbed fraction of energy (or fraction of energy absorbed per gram of the target organ) for ith type particles and for the source and target organs considered, and $Q_i(X)$ and $N_i(X)$ are the quality factor and modifying factor for i-type radiation in the target organ. The factor $Q_i(X)$ is generally assumed in internal dose estimations to be 1 for beta particles, monoenergetic electrons, and gamma and x rays; 10 for alpha particles; and 20 for recoil nuclei associated with alpha emission. $N_i(X)$ is used for alpha emitters in bone, and is taken equal to

1. Computer Sciences Division.

5. For alpha particles emitted in the contents of the gastrointestinal (GI) tract, $N_i(X)$ is taken as 0.01. The latter factor is recommended by the ICRP and the NCRP because of the demonstrated inefficiency of alpha particles in irradiating the mitosing cells of the tract.[2]

Actually, the tabulated values of S are much more general than the effective energy values given by NCRP and ICRP in that a value of S is given when the source and target organs are distinct. Generally, only the photons will make a contribution to this dose if the organs are well separated, but for tissues in close proximity (e.g., bone and active bone marrow) the contribution of electrons or beta rays should not be ignored. The use of the quality factor, Q, is a convenience for the health physicist, who will usually be interested in estimating dose equivalent or dose commitment. For any nuclide that does not produce alpha particles, $Q = 1$, and the results are equivalent to doses in rads. The user who wishes to compute an absorbed dose in rads will find it easy to convert from the values listed in the Laboratory report to the appropriate values for alpha particles and recoil ions. A general discussion of the computational method used in forming these estimates of S follows. A detailed account is given in the text accompanying the tabulations.

Estimation of the energy absorbed by an organ implies knowledge of all the energy emitted. However, the usual decay schemes found in compilations of decay data, for example, the compilation by Lederer et al.,[3] do not include radiations such as x rays and Auger electrons resulting from rearrangements in the electron shells, and these contributions are quite tedious to compute. Fortunately, Dillman[4] has published detailed decay data of this kind with average beta energies for many radionuclides of interest, and he has designed a computer code which produces these data. This code is the source of the decay data used in these compilations.

Apart from the difficulty involved in arriving at a complete listing of all radiations emitted per decay, considerable tedious calculations may be required to compute the total energy absorbed in body organs, particularly for photons. The authors have published in MIRD Pamphlet No. 5 (ref. 5) absorbed fractions of photon energies for 12 monoenergetic photons ranging in energy from 0.01 to 4 MeV and distributed uniformly in 16 source organs of a mathematical anthropomorphic phantom with organs approximating those of their prototypes in size, shape, composition, and density. A Monte Carlo-type computer code was used in estimating the absorbed fraction for some 20 target organs. Thus absorbed fractions for various organs can be estimated for all photons emitted in the decay of a particular radionuclide by interpolating on energy. However, many photons may be emitted per disintegration, and dose may be required for a variety of source organs to many target organs. For example, if a radionuclide can emit ten x rays and four gamma rays – not an unusual case – and is present in six source organs, 84 simple multiplications and interpolations are required in the table of absorbed fractions[5] to determine the total photon contribution for just one target organ. If there are a number of target organs, these calculations become quite lengthy, and the tendency could be to neglect the low-energy, low-intensity emissions. Although any such photon alone might make a negligible contribution to the overall dose, all such emissions in a decay, taken together, may be quite significant.

The tabulated values of S include the above-mentioned interpolations, multiplications, and additions for all the photons emitted. Also, the energy contributions from other types of emissions are weighted by the proper quality and/or modifying factors as recommended by the ICRP and the NCRP and are included.

The absorbed fraction of photons was calculated principally by the Monte Carlo method described in MIRD Pamphlet No. 5,[5] but new computer runs were made using a revised phantom and twice as many (60,000) source photons for each source organ and photon energy as were used previously.

Revisions in the phantom include (1) changes of the GI tract and bladder to include walls and contents separately, except for the small intestine, which is still defined as a wall plus contents since it is essentially a tube free to move except at the two ends and has no fixed position; (2) modification of the skeleton to

2. M. F. Sullivan and R. C. Thompson, "Absence of Lethal Effects Following Massive Oral Administration of Plutonium," *Nature (London)* **180**, 651–52 (1957).

3. C. M. Lederer et al., *Table of Isotopes*, 6th ed., John Wiley & Sons, Inc., New York, 1967.

4. L. T. Dillman, "Radionuclide Decay Schemes and Nuclear Parameters for Use in Radiation-Dose Estimation," *J. Nucl. Med., Suppl. No. 2* **10** (March 1969); *Suppl. No. 4* **11** (March 1970).

5. W. S. Snyder, M. R. Ford, G. G. Warner, and H. L. Fisher, Jr., "Estimates of Absorbed Fractions for Monoenergetic Photon Sources Uniformly Distributed in Various Organs of a Heterogeneous Phantom," MIRD Pamphlet No. 5, *J. Nucl. Med., Suppl. No. 3* **10** (August 1969).

provide a more realistic estimate of dose to red bone marrow and to endosteal cells, including addition of the clavicles and scapulae, rounding of the tissues covering the skull, and designation of areas corresponding to red bone marrow and yellow bone marrow; and (3) division of the combined configuration of the legs into two separate regions to provide a more realistic location for the testes.

Although the increase in sample size did improve the statistics somewhat, the accuracy was not sufficient to warrant use of the Monte Carlo estimates in every case. The method of estimating absorbed fractions of photon energies by use of Berger's[6] buildup factor for a point source of monoenergetic photons in an infinite medium of soft tissue was explored. Integrating the corresponding dose formula over regions representing the source and target organs yielded statistically reliable estimates which were plausibly an overestimate since buildup is maximal in the infinite space. However, compared with reliable Monte Carlo estimates, they differed by no more than 30% in most cases and were rarely high by more than a factor of 2. The justification of this method is discussed more fully by Snyder et al.[7]

Thus absorbed fractions estimated by the Berger buildup factor were used in cases where the Monte Carlo estimates were not statistically reliable. However, Berger's tabulations only extend to 15 keV. At lower energies, values have been obtained by extrapolation based on the concept that as the photon energy approaches 0, the absorbed fraction approaches 1 or 0, depending on whether the source and target organs coincide or are distinct.

Certain other absorbed fractions were obtained by use of the reciprocity theorem. This occurs in a few cases where an organ is programmed as a target organ but not as a source organ. For example, the values for muscle with kidney as the source organ were used for kidney with muscle as the source organ. This approach is discussed in more detail by Snyder.[8]

For beta particles and monoenergetic electrons, the energy contributions of this short-range radiation are generally taken equal to 0 or to $\bar{E}$ depending on whether source and target organs are different or whether they coincide. Among exceptions to this general rule are the organs with walls when the source is in the contents. This occurs in the four sections of the GI tract as well as in the bladder. In all such cases the energy contribution is taken as $\bar{E}/2$, where $\bar{E}$ is the average energy of the beta or positron or equals the energy in the case of a monoenergetic electron. This amounts to using the dose on the surface of a half space containing the source at a uniform concentration equal to that in the source tissue. Certainly this appears to be conservative in that the critical cells for the GI tract are frequently taken to be the mitosing cells which lie at some depth in the tissue.

The contributions of beta particles and monoenergetic electrons to the active bone marrow and to the endosteal cells are based on calculations of Spiers.[9] The ICRP has recommended that endosteal cells be considered the radiosensitive cells for exposure to bone. The estimates of Spiers are shown in Fig. 1.1. They are expressed as the ratio of the desired doses, D_S (endosteal cells) and D_M (active bone marrow), to a dose D_0 based on complete absorption of energy. These ratios, D_S/D_0 and D_M/D_0, averaged over cortical and trabecular bone, have been given by Spiers for the following radionuclides: ^{90}Y ($\bar{E}$ = 0.927), ^{90}Sr ($\bar{E}$ = 0.200), ^{14}C ($\bar{E}$ = 0.049), ^{45}Ca ($\bar{E}$ = 0.076), ^{22}Na ($\bar{E}$ = 0.218), ^{18}F ($\bar{E}$ = 0.253), and ^{32}P ($\bar{E}$ = 0.695). The values for ^{18}F and ^{22}Na were not considered to differ significantly from the values for ^{90}Sr; hence the dashed line was used for this portion of the graph. Estimates for other beta emitters are interpolated or extrapolated on $\bar{E}$.

For alpha particles and recoil nuclei, the energy is assumed to be absorbed in the source tissue except for organs with walls where, again, the energy contribution is estimated for a surface dose, that is, $\bar{E}/2$, and this contribution is weighted by the appropriate quality factors and modifying factors mentioned earlier. However, recoil nuclei emitted in the contents of the GI tract are assumed not to penetrate the mucus and irradiate the mitosing cells; thus the dose from these nuclei is considered to be zero.

It should be noted that the use of the absorbed fractions, as calculated by the Monte Carlo method,

6. Martin J. Berger, "Energy Deposition in Water by Photons from Point Isotropic Sources," *J. Nucl. Med., Suppl. No. 1* **15** (February 1968).

7. W. S. Snyder, M. R. Ford, and G. G. Warner, "Estimates of Absorbed Fractions for Photon Emitters within the Body," *Health Physics Problems of Internal Contamination,* Second European Congress on Radiation Protection, May 3–5, 1972, Budapest, Hungary. Also, *Health Phys. Div. Annu. Progr. Rep. July 31, 1972,* ORNL-4822, p. 86.

8. W. S. Snyder, "Estimation of Absorbed Fraction of Energy from Photon Sources in Body Organs," *Medical Radionuclides: Radiation Dose and Effects,* USAEC report CONF-691212 (1970), pp. 33–49.

9. F. W. Spiers, *Radioisotopes in the Human Body, Physical and Biological Aspects,* Academic Press, New York, 1968.

implies that the corresponding doses are estimated for a uniform distribution of activity in the source organ and only an average dose to the target organ is obtained. Dose contributions from electrons, alpha particles, and recoil nuclei are also estimated only in the sense of an average dose. No inherent limitation of the method is involved, since it would be feasible to estimate dose for other distributions of activity the biological data might indicate. However, these are the assumptions generally used by health physicists, and the paucity of data on the distribution of activity in the source organs is so prevalent that it does not appear worth while to provide data for other distributions which would be based largely on little more than guesses.

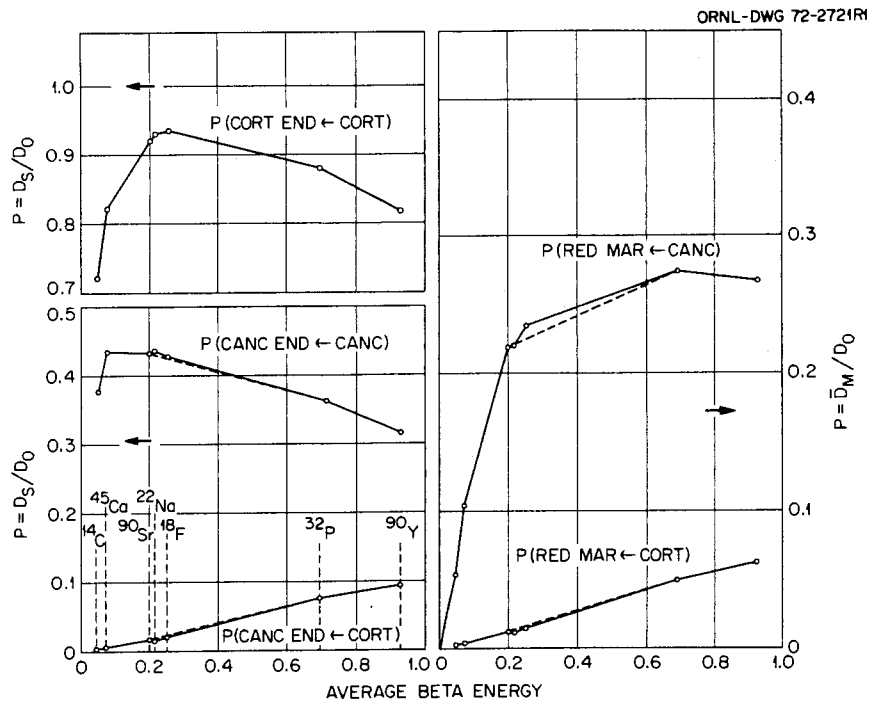

Fig. 1.1. Ratios of average endosteal dose and of average red marrow dose to the equilibrium dose in bone from beta emitters. Data from: F. W. Spiers, *Radioisotopes in the Human Body, Physical and Biological Aspects,* Academic Press, New York, 1968.

2. Revision of MIRD Pamphlet No. 5 Entitled "Estimates of Absorbed Fractions for Monoenergetic Photon Sources Uniformly Distributed in Various Organs of a Heterogeneous Phantom"

W. S. Snyder Mary R. Ford G. G. Warner[1]

MIRD Pamphlet No. 5 by Snyder et al.[2] presents estimates of absorbed fractions for 12 monoenergetic photon sources distributed uniformly in some 16 different body organs of a mathematical phantom simulating an adult. These estimates were made with a Monte Carlo computer code designed to take account of (1) the geometrical shape of the body and of the major internal organs, (2) the different densities and compositions of the various tissues of the body, especially of the skeleton and lungs, and (3) the multiple scattering of photons in the body. New computer runs have been made, and the revision of MIRD Pamphlet No. 5 has been drafted.

The decision to issue a revision of the pamphlet is due principally to the following considerations:

1. There are a number of blanks in the published tables which should be filled. These blanks occurred where the estimates were judged to be statistically unreliable. Increasing the sample size improved the statistics somewhat but was not sufficient to warrant use of the Monte Carlo method in every case. Berger's[3] buildup factor method for estimating photon absorbed fractions was explored and, when compared with reliable Monte Carlo estimates, was found by Snyder et al.[4] to differ by no more than 30% in most cases and seldom by more than a factor of 2. Thus this method was used to fill many blanks. In certain other cases the reciprocity theorem as presented by Snyder[5] was used, for example, where an organ was programmed as a target organ but not as a source organ.

2. There have been considerable changes made in the anthropomorphic phantom used in the Monte Carlo calculations, so that it is now more nearly representative of the actual situation. Consequently, the new values should provide better estimates of absorbed fractions for several tissues, for example, red bone marrow, gastrointestinal tract, bladder, etc.

A detailed description of the exterior of the revised phantom and of the modified or added organs follows.

EXTERIOR OF THE PHANTOM

The body is represented as erect with the z axis directed upward toward the head. The x axis is directed to the phantom's left (the reader's right in Fig. 2.1), and the y axis is directed toward the posterior side of the phantom. The origin is taken at the center of the base of the "trunk" section of the phantom. The axes are calibrated in centimeters.

The "trunk" is a solid elliptical cylinder specified by

$$(x/20)^2 + (y/10)^2 \leqslant 1 ,$$

$$0 \leqslant z \leqslant 70 ,$$

so that the "trunk" includes the arms as well as the pelvic and hip bones from the point where the separation of the legs begins. The volume of the trunk section is 43,982 cm^3, and the mass is 42,701 g.

1. Computer Sciences Division.

2. W. S. Snyder, M. R. Ford, G. G. Warner, and H. L. Fisher, Jr., "Estimates of Absorbed Fractions for Monoenergetic Photon Sources Uniformly Distributed in Various Organs of a Heterogeneous Phantom," MIRD Pamphlet No. 5, *J. Nucl. Med., Suppl. No. 3* **10** (August 1969).

3. M. J. Berger, "Energy Deposition in Water by Photons from Point Isotropic Sources," MIRD Pamphlet No. 2, *J. Nucl. Med., Suppl. No. 1* **15** (February 1968).

4. W. S. Snyder, M. R. Ford, and G. G. Warner, "Estimates of Absorbed Fractions for Photon Emitters within the Body," *Health Physics Problems of Internal Contamination,* Second European Congress on Radiation Protection, May 3–5, 1972, Budapest, Hungary. Also, *Health Phys. Div. Annu. Progr. Rep. July 31, 1972,* ORNL-4822, p. 86.

5. W. S. Snyder, "Estimation of Absorbed Fraction of Energy from Photon Sources in Body Organs," *Medical Radionuclides: Radiation Dose and Effects,* USAEC report CONF-691212 (1970), pp. 33–49.

The head section is a right elliptical cylinder topped by half an ellipsoid. The locus is specified by

$$(x/7)^2 + (y/10)^2 \leqslant 1, \quad 70 \leqslant z \leqslant 85.5 ,$$

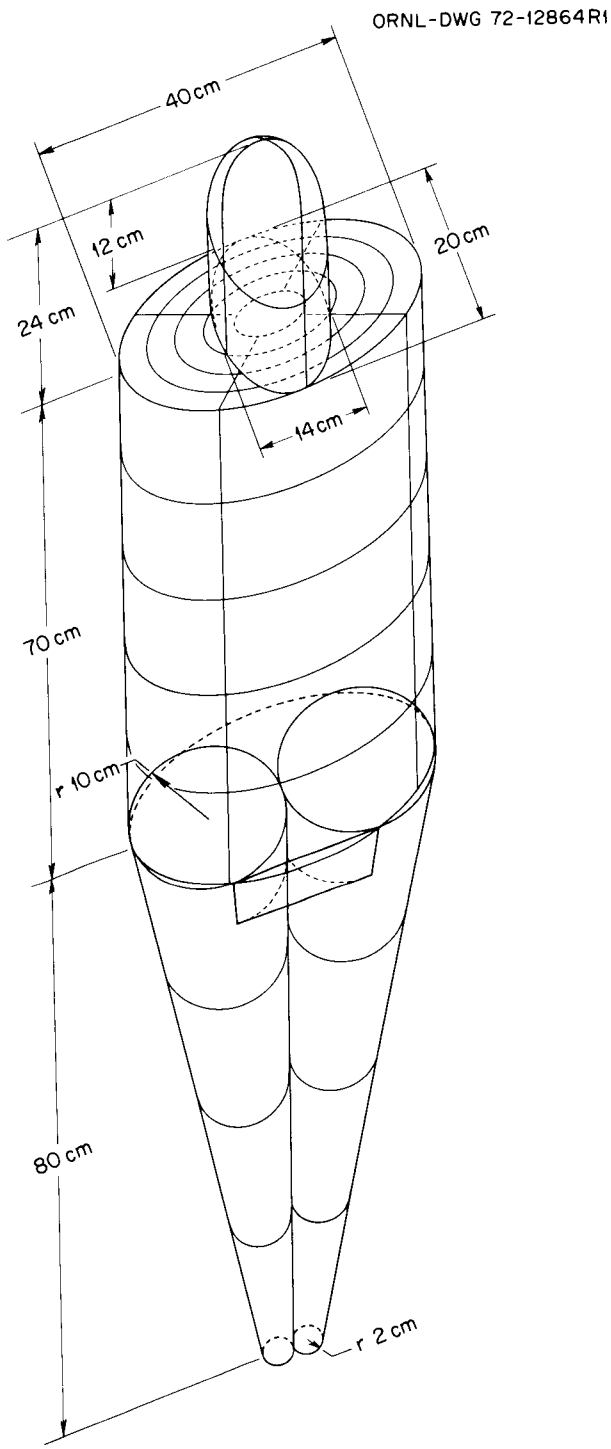

Fig. 2.1. The adult human phantom.

and

$$\left(\frac{x}{7}\right)^2 + \left(\frac{y}{10}\right)^2 + \left(\frac{z - 85.5}{8.5}\right)^2 \leqslant 1, \quad 85.5 \leqslant z \leqslant 94 .$$

The total volume is 4655 cm^3, and the mass is 5083 g.

The leg region of the phantom consists of the frustums of two circular cones specified by

$$x^2 + y^2 \leqslant \pm x \left(20 + \frac{z}{5}\right) ,$$

$$-80 \leqslant z \leqslant 0 ,$$

where the plus sign defines the left leg and the minus sign the right. The total volume of both legs is 20,776 cm^3, and the mass, as discussed below, is 21,901 g. It is apparent that the leg region does not join smoothly to the trunk region because the legs protrude slightly beyond the ellipse defining the trunk in the plane $z = 0$.

The genitalia region (male) of the phantom consists of the region specified by

$$-4.8 \leqslant z \leqslant 0 ,$$

$$-\left(10 + \frac{z}{10}\right) \leqslant x \leqslant 10 + \frac{z}{10} ,$$

$$-\left(10 + \frac{z}{10}\right) \leqslant y \leqslant 0 ,$$

and

$$x \pm \left(10 + \frac{z}{10}\right)^2 + y^2 \geqslant \left(10 + \frac{z}{10}\right)^2 ,$$

and this last inequality must hold for either choice of sign; that is, the genitalia region lies outside both legs. The genitalia region has a volume of 196.3 cm^3 and a mass of 193.7 g.

The phantom is divided into subregions by a geometrical grid. In the trunk, this region is formed by the planes z = 0, 14, 28, 42, 56, and 70, planes $x = \pm y$, and concentric elliptic cylinders

$$(x/20)^2 + (y/10)^2 = \rho^2 ,$$

where ρ = 0.2, 0.4, 0.6, and 0.8. The head is divided into eight regions defined by $x = \pm y$, $70 \leqslant z \leqslant 85.5$, and $85.5 \leqslant z \leqslant 94$. The legs are subdivided into regions by the planes z = −20, −40, −60, and −80. Although no data are given in this report for the subregions

defined by this grid, the computer code provides estimates of dose and absorbed fraction for each such subregion. These values are often useful in deciding whether to accept a given value or to program another calculation.

DESCRIPTION OF ORGANS

Urinary Bladder and Contents

The bladder is regarded as an ellipsoid, and the defining inequalities are

$$\left(\frac{x}{4.958}\right)^2 + \left(\frac{y+4.5}{3.458}\right)^2 + \left(\frac{z-8}{3.458}\right)^2 \leqslant 1$$

and

$$\left(\frac{x}{4.706}\right)^2 + \left(\frac{y+4.5}{3.206}\right)^2 + \left(\frac{z-8}{3.206}\right)^2 \geqslant 1 .$$

The volume is 45.73 cm^3, and the mass is 45.13 g. The contents have a volume of 202.6 cm^3 and mass of 200 g, representing a moderately full bladder.

Clavicles

The clavicles (Fig. 2.2) are represented as two portions of a torus which lie along the circular arc $x^2 + (y - 11.1)^2 = 10^2$, $z = 68.25$ and have a smaller radius of 0.7883 cm. The clavicles include only the portion of the torus between the planes $11.1 - y = |x| \cot \theta$ with $\theta = 8°5.5'$ and $\theta = 48°12'$. The absolute value sign on x allows for both a right and a left clavicle. The volume of both clavicles is 54.7 cm^3, and the mass is about 82 g.

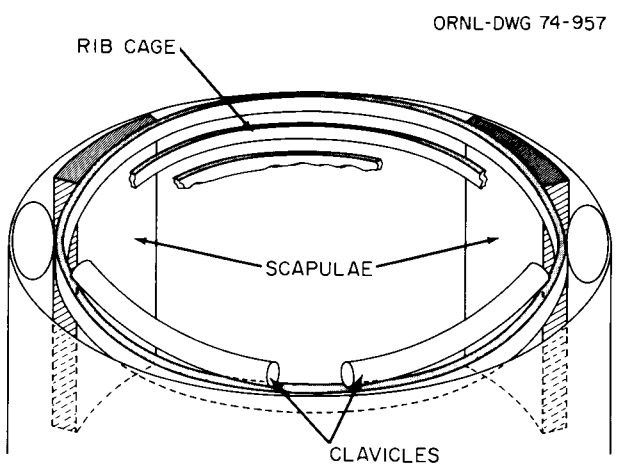

Fig. 2.2. Detailed view of scapulae and clavicles.

The equations can be reduced to the form

$$(z - 68.25)^2 + [20 - \sqrt{x^2 + (y - 11.1)^2}]^2 \leqslant 0.7883^2 ,$$

$$0.89415 \leqslant \frac{11.1 - y}{|x|} \leqslant 7.0342 ,$$

$$y \leqslant 0 .$$

The clavicles lie slightly inside the cylinder defining the rib cage and just above the top rib.

Scapulae

The scapulae (Fig. 2.2) extend from $z = 64.5$ cm (the top of the 12th rib) to $z = 48.1$ cm and lie between two elliptical cylinders

$$(x/17)^2 + (y/9.8)^2 = 1 \quad \text{(outer surface of ribs)}$$

and

$$(x/19)^2 + (y/9.8)^2 = 1 \quad \text{(a somewhat larger cylinder)} .$$

Although the lower portion of the scapula is somewhat smaller than the upper, this distinction is ignored here, and the left scapula will occupy all the above space between the planes $y = 0.25x$ and $y = 0.80x$.

Thus the test for point (x,y,z) to be in the left scapula is the following:

$$50.9 \leqslant z \leqslant 67.3 ,$$

$$(x/19)^2 + (y/9.8)^2 \leqslant 1 ,$$

$$(x/17)^2 + (y/9.8)^2 > 1 ,$$

$$y > 0 ,$$

$$0.25 < y/x < 0.80 .$$

For the right scapula, only the last inequality needs to be replaced by

$$0.25 < y/-x < 0.80 .$$

For both scapulae, one uses

$$0.25 < y/|x| < 0.80 ,$$

the other inequalities being unaltered. Consider the ellipse

$$(x/a)^2 + (y/b)^2 = 1 .$$

The point (ρ, θ) lies on this ellipse if

$$\frac{\rho^2 \cos^2 \theta}{a^2} + \frac{\rho^2 \sin^2 \theta}{b^2} = 1 ,$$

or, equivalently, if

$$\rho = \frac{ab}{\sqrt{a^2 \sin^2 \theta + b^2 \cos^2 \theta}} .$$

The area of a sector of the ellipse is given by

$$A(\theta_1, \theta_2) = \int_{\theta_1}^{\theta_2} \frac{\rho^2}{2} d\theta$$

$$= \int_{\theta_1}^{\theta_2} \frac{a^2 b^2 \, d\theta}{2(a^2 \sin^2 \theta + b^2 \cos^2 \theta)}$$

$$= \frac{ab}{2} \left(\arctan \frac{a \tan \theta_2}{b} - \arctan \frac{a \tan \theta_1}{b} \right) .$$

The volume of a "wedge" of height h with the base as indicated above is then

$$V = \frac{abh}{2} \left(\arctan \frac{a \tan \theta_2}{b} - \arctan \frac{a \tan \theta_1}{b} \right) .$$

The volume of one scapula is then

$$V\,(\text{scapula}) = V_2 - V_1 ,$$

where V_2 is obtained from the above formula by substituting $a = 19$, $b = 9.8$, $h = 16.4$, $\tan \theta_2 = 0.8$, and $\tan \theta_1 = 0.25$, and the same values are used for V_1 except that $a = 17$. Thus

$$V\,(\text{scapula}) = V_2 - V_1$$

$$= 834.47 - 733.76 = 100.7 \text{ cm}^3 .$$

For a density of 1.4862 g/cm^3, one scapula has a mass of 150.0 g. The scapulae, as defined, do not intersect the arm bones, the ribs, or other designated organs of the phantom.

In Fig. 2.3 a human adult skeleton has been sketched, and the areas that contain active bone marrow (red bone marrow) have been crosshatched. The idealized skeleton used for the phantom is sketched also, with the corresponding areas crosshatched. The red, or active, bone marrow is assigned a total weight of 1500 g, and the same weight is assigned to yellow bone marrow. The weights of the two marrow types are given in Table 2.1, and they are assigned to the corresponding regions of bone and are assumed to be uniformly distributed in these regions. In calculating an absorbed

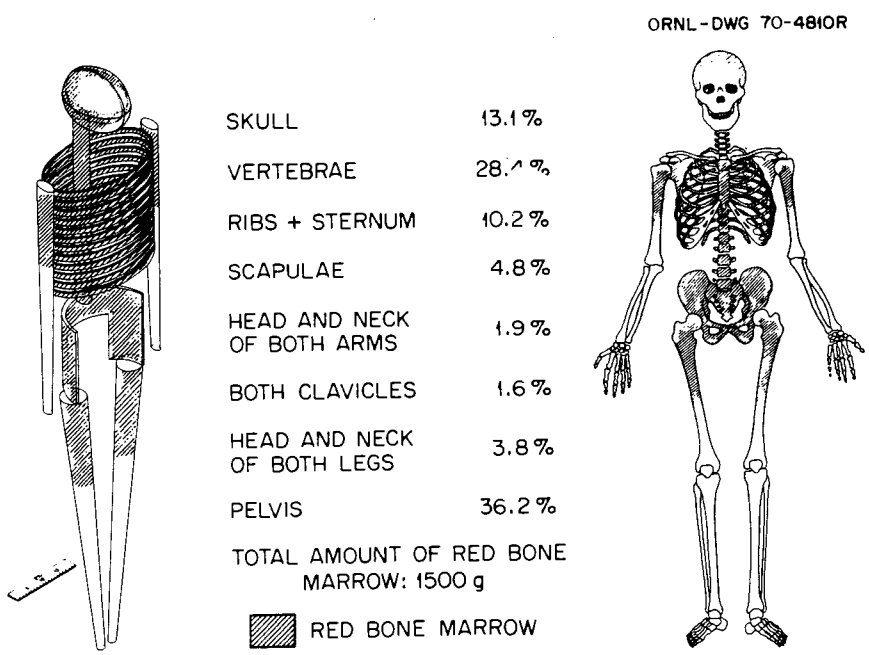

Fig. 2.3. Idealized model of the skeleton for computer calculations (left) and a more realistic representation (right) with percentages of red bone marrow found in the shaded portions of the bones.

Table 2.1. Masses of red and yellow marrow and bone in the phantom

Bone region	Mass (g)		
	Red marrow	Bone	Yellow marrow
Arms			
Upper[a]	28.5	474	9.5
Lower	0	520	389
Clavicles	24	49.2	8
Legs			
Upper[b]	57	2036	19
Lower	0	1588	461
Pelvis	543	177	181
Ribs	153	677	201
Scapulae	72	206	24
Skull			
Cranium[c]	178.5	557	59.5
Mandible	18	439	6
Spine			
Upper[d]	51	130	17
Middle	211.5	533	70.5
Lower[e]	163.5	87.8	54.5
Total	1500.0	7474.0	1500.0

[a] $69 \geqslant z \geqslant 52.6$.
[b] $0 \geqslant z \geqslant -22.8$.
[c] $z \geqslant -3y + 77$.
[d] $70 \leqslant z \leqslant 78.5$.
[e] $0 \leqslant z \leqslant 35.1$.

fraction for red and for yellow marrow in these regions, it is assumed that the marrow absorbs energy per gram as efficiently as does bone. This assumption is not grossly wrong at energies of 200 keV or more, but it is increasingly inaccurate at energies below 100 keV. The effect is to somewhat overestimate the dose to marrow and to somewhat underestimate the dose to bone. This difficulty is due to the failure to find ways to program the intricate intermixture of bone and marrow spaces in a more realistic fashion. The composition of the skeleton has a specific gravity of 1.4862 and thus is to be regarded as a homogeneous mixture of true bone and marrow and other organic constituents of the skeleton.

Gastrointestinal Tract and Contents – Stomach (S)

The stomach (see Fig. 2.4) is represented as the mass between two ellipsoids:

$$\left(\frac{x-8}{4}\right)^2 + \left(\frac{y+4}{3}\right)^2 + \left(\frac{z-35}{8}\right)^2 \leqslant 1$$

and

$$\left(\frac{x-8}{3.387}\right)^2 + \left(\frac{y+4}{2.387}\right)^2 + \left(\frac{z-35}{7.387}\right)^2 \geqslant 1 .$$

The volume is 151.9 cm^3 and the mass 150 g. The contents have a volume of 250.2 cm^3 and a mass of 246.9 g. The thickness of the stomach wall is about 0.613 cm.

The stomach represented here is a "full" stomach, and the average dose rate, even for the same activity present, probably varies greatly depending on the degree of extension of the stomach, presence of air spaces, etc.

Small Intestine (SI)

The small intestine (see Fig. 2.4) does not seem to remain in any "standard position" except the ends, which are relatively fixed. Thus the small intestine is to be regarded as occupying a volume within which it is free to move. No attempt to determine a specific configuration is made here, and thus the wall and contents are not distinguished for estimation of photon dose. The small intestinal wall has a mass of 640 g, and the contents have a mass of 400 g. Thus the total mass is 1040 g, and the corresponding volume is about 1054 cm^3. This volume, which lies in the pelvic region, is a section of a circular cylinder given by

$$x^2 + (y + 3.8)^2 \leqslant (11.3)^2 ,$$

$$-4.86 \leqslant y \leqslant 2.2 ,$$

$$17 \leqslant z \leqslant 27 ,$$

but the portion of the large intestine within this region is excluded. The thickness of the wall is generally 0.3 to 0.4 cm, although the thickness of the duodenum is approximately one-tenth of these values.

Upper Large Intestine (ULI)

The upper large intestine (see Fig. 2.4) consists of an ascending colon and a transverse colon. The ascending colon is defined by the inequalities

$$(x + 8.5)^2 + (y + 2.36)^2 \leqslant 2.5^2 ,$$

$$(x + 8.5)^2 + (y + 2.36)^2 \geqslant 1.7915^2 ,$$

$$14.45 \leqslant z \leqslant 24 .$$

ORNL-DWG 73-12124

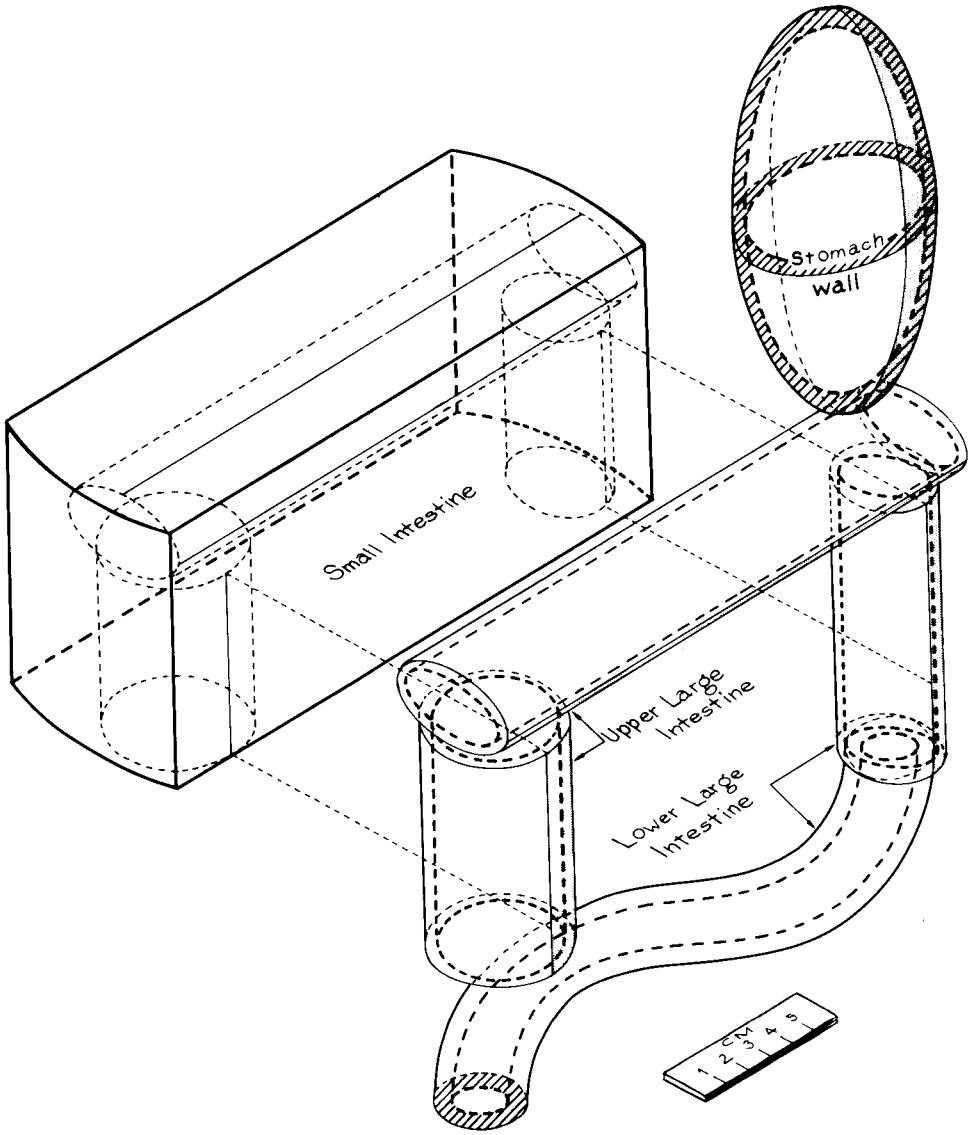

Fig. 2.4. Gastrointestinal tract.

The wall has a total volume of 91.22 cm^3 and a mass of 90.02 g. The inequalities

$$(x + 8.5)^2 + (y + 2.36)^2 \leqslant 1.7915^2 ,$$

$$14.45 \leqslant z \leqslant 24$$

define the contents of the ascending colon. The volume is 96.29, the mass is 95.03 g, and the thickness of the wall according to this model is 0.7085 cm.

The transverse colon is of elliptical cross section and is defined by

$$\left(\frac{y + 2.36}{2.5}\right)^2 + \left(\frac{z - 25.5}{1.5}\right)^2 \leqslant 1 ,$$

$$\left(\frac{y + 2.36}{1.973}\right)^2 + \left(\frac{z - 25.5}{0.973}\right)^2 \geqslant 1 ,$$

$$-10.5 \leqslant x \leqslant 10.5 .$$

The volume of the wall is 120.7 cm^3, and the mass is 119.2 g. By this model the thickness is about 0.53 cm. The contents are specified by

$$\left(\frac{y+2.36}{1.973}\right)^2+\left(\frac{z-25.5}{0.973}\right)^2 \leqslant 1 ,$$

$$-10.5 \leqslant x \leqslant 10.5 .$$

The volume is 126.7 cm^3, and the mass is 125 g.

Lower Large Intestine (LLI)

The lower large intestine (see Fig. 2.4) consists of a descending colon and a sigmoid colon. The descending colon is described by the inequalities

$$\left(\frac{x-x_0}{1.88}\right)^2+\left(\frac{y-y_0}{2.13}\right)^2 \leqslant 1 ,$$

$$\left(\frac{x-x_0}{1.58}\right)^2+\left(\frac{y-y_0}{1.34}\right)^2 \geqslant 1 ,$$

$$8.72 \leqslant z \leqslant 24 ,$$

where

$$x_0 = 9+\frac{0.28(z-24)}{15.28} ,$$

$$y_0 = \frac{2.5(8.72-z)}{15.28} .$$

The descending colon has a volume of 90.59 cm^3 and a mass of 89.40 g. The thickness would vary between 0.3 and 0.79 cm according to this model.

The sigmoid colon consists of portions of two tori and is defined by the inequalities:

upper portion

$$[\sqrt{(x-3)^2+(z-8.72)^2}-5.72]^2+y^2 \leqslant 1.57^2 ,$$

$$[\sqrt{(x-3)^2+(z-8.72)^2}-5.72]^2+y^2 \geqslant 0.91^2 ,$$

$$x \geqslant 3 ,$$

$$z \leqslant 8.72 ;$$

lower portion

$$[\sqrt{(x-3)^2+z^2}-3]^2+y^2 \leqslant 1.57^2 ,$$

$$[\sqrt{(x-3)^2+z^2}-3]^2+y^2 \geqslant 0.91^2 ,$$

$$x \leqslant 3 ,$$

$$z \geqslant 0 .$$

The volume of the sigmoid colon is 70.42 cm^3, and the mass is 69.50 g. The thickness of the wall would be 0.66 cm according to this model.

Skin

Skin is represented as a layer 0.2 cm thick extending over the entire exterior of the phantom. Thus this corresponds to the dermis as well as the epidermis. The back is the only major body area where the thickness is larger, being about double. The volume of skin is 2828 cm^3, and the mass is 2791 g.

3. Report of the Task Group on Reference Man

W. S. Snyder G. S. Hill M. J. C. Hilyer[1]

In cooperation with the special International Commission on Radiological Protection (ICRP) Task Group on Reference Man, of which W. S. Snyder is chairman, members of the Medical Physics and Internal Dosimetry Section have been involved to an important extent in the compilation, editing, and general preparation of the Report of the Task Group on Reference Man. The report is now in the hands of the publisher and will be issued as an ICRP publication by Pergamon Press sometime in 1974.

The report is an enormously comprehensive work and includes extensive background data and bibliographies used in establishing the reference man values. It is anticipated that the report will have wide and varied uses, but its primary use will be as a research tool in both radiological and nonradiological investigations. It establishes fixed parameters for the anatomical and physiological values and the elemental composition of man, which may be used as reference points from which other changes and effects may be recognized, measured, and compared. While the report, from necessity, deals primarily with the reference male, data for the reference female and the reference child are given where such information became available within the scope of the report.

1. Retired.

4. Dose to a Dynamic Bladder for Administered Radionuclides

W. S. Snyder J. W. Poston G. G. Warner[1] L. W. Owen[1]

The urinary bladder is one of the more dynamic of the body organs in that it undergoes marked changes in size during the course of a filling, and the dose per disintegration of a nuclide present in urine may change by an order of magnitude as the volume of urine increases. The dose is thus affected by the schedule of voiding, by the rate of formation of urine, by the biological rates of elimination of the radionuclide, and by the decay scheme of the radionuclide. The influence of these variables has been discussed in detail,[2] and it has been shown that substantial reductions in dose are possible if one can optimize on these parameters. There may be cases where reduced dose would not be possible without interfering with the clinical regime, but frequently this is not the case.

The bladder is represented as an ellipsoid which preserves its shape as it fills. The mass of the bladder walls is taken as 45 g, and the volume of urine may vary from 0 to 500 ml.

Assuming that a source of photons is distributed uniformly in the urine content, Monte Carlo calculations have been used to determine the dose per photon for seven volumes of urine. The dose per photon can be approximated by a sum of two exponentials with the urine volume as the independent variable. The doses have been computed for each of 12 photon energies ranging from 10 keV to 4 MeV. The coefficients and exponential factors vary with energy and have been reported previously.[3] A computer code has been written which can be used to compute the dose for an arbitrary filling with the activity entering the bladder at an arbitrary exponential rate. A sum of such exponentials can represent most elimination patterns that have been observed.

Calculations at the 12 photon energies mentioned above with four, seven, and ten voids per day, with urine outputs of 1000, 1400, and 2000 ml/day, and for biological elimination half-times ranging from 1 hr to 10 days indicate three broad generalizations:

1. As the urine output changes from 1000 to 2000 ml/day, the dose reduction ranges from 25 to 50%.
2. Increasing the number of voids per day results in a further dose reduction, although it generally is not large.
3. If the radionuclide can be administered at a time when the bladder is about half full, an additional reduction of dose of 15 to 50% is realized.

The above results assume complete emptying of the bladder with each void. If emptying is not complete, the dose may be greater (if radioactive half-time and biological elimination half-times are long) or the dose may be less (if one or both half-times are short). The effect does not appear to be great, being, for example, about a 10% change in dose for a 10% carry-over of urine.

Beta dose and dose from monoenergetic electrons have been computed for the same bladder model. The variation of dose rate with depth is estimated by use of Berger's point kernel[4] in an infinite slab of tissue for unit source density in the half space exterior to one side of the slab. The average dose in the slab having a thickness equal to the bladder thickness is then calculated. This is integrated over time with weighting factors to represent the number of disintegrations occurring in the bladder content during the various time intervals. This neglect of curvature is not rigorous, but the errors made would be greatest when the contents were small and relatively few photons were emitted.

1. Computer Sciences Division.
2. W. S. Snyder and J. W. Poston, "Medical Physics and Internal Dosimetry," *Health Phys. Div. Annu. Progr. Rep. July 31, 1973,* ORNL-4903.
3. W. S. Snyder, "Internal Dosimetry," *Health Phys. Div. Annu. Progr. Rep. July 31, 1970,* ORNL-4584.
4. M. J. Berger, "Distribution of Absorbed Dose around Point Sources of Electrons and Beta Particles in Water and Other Media," *J. Nucl. Med., Suppl. No. 5* **12** (March 1971).

For the larger bladder sizes the curvature would not seem to be a major influence in view of the short range of most beta rays. For completeness, the surface dose is also given. Generally, it is found that the surface dose from electrons or from beta rays far exceeds the average dose in the walls, as might be expected. The discrepancy is often by an order of magnitude or more. The results somewhat parallel those for the photons, although in some cases the dose reduction appears to be somewhat smaller for betas than for photons.

As examples, ^{131}I and ^{99m}Tc pertechnetate have been programmed using standard excretion models; these data are presented in Tables 4.1 and 4.2. The dose to the bladder from ^{99m}Tc is found to be among the higher doses received following administration, and dose reduction by use of such procedures as those mentioned should be considered by clinicians. Of course, these procedures are suggested for use only when they do not conflict with other clinical purposes for which the radionuclide is administered.

By way of illustration, some of the data for ^{131}I and ^{99m}Tc are shown in Figs. 4.1 and 4.2 respectively. These data are for a filling rate of 1400 ml/day, and results for four, seven, and ten voids per day are shown. In general, the surface dose is about one to two orders of magnitude greater than the average depth dose in each case. These data indicate also only a small effect on the absorbed dose to the bladder wall due to incomplete voiding (carry-over) of the bladder. The percent change in dose is usually less than the percent of carry-over; that is, for 10% carry-over the change in the absorbed dose is less than 10%.

Table 4.1. Absorbed dose in bladder wall for ^{131}I present in the urine

Half-life = 8.06 days
In rads per microcurie per cubic centimeter

Filing rate (ml/day)	No. of voids per day	Percent carryover	Photon dose	Beta dose		Total dose	
				Average depth	Surface	Photon plus av. depth	Photon plus surface
1000	4	0	6.17 −4	2.07 −4	3.83 −3	8.23 −4	4.45 −3
		10	6.67 −4	2.25 −4	3.61 −3	8.92 −4	4.28 −3
		20	7.09 −4	2.43 −4	3.52 −3	9.53 −4	4.23 −3
		30	7.51 −4	2.61 −4	3.46 −3	1.01 −4	4.22 −3
	7	0	4.46 −4	1.43 −4	3.55 −3	5.89 −4	4.00 −3
		10	4.87 −4	1.57 −4	3.43 −3	6.44 −4	3.92 −3
		20	5.19 −4	1.69 −4	3.38 −3	6.89 −4	3.90 −3
		30	5.48 −4	1.82 −4	3.34 −3	7.30 −4	3.89 −3
	10	0	3.77 −4	1.19 −4	3.48 −3	4.95 −4	3.85 −3
		10	4.14 −4	1.29 −4	3.39 −3	5.43 −4	3.80 −3
		20	4.41 −4	1.40 −4	3.36 −3	5.81 −4	3.80 −3
		30	4.63 −4	1.49 −4	3.33 −3	6.13 −4	3.80 −3
1400	4	0	5.21 −4	1.79 −4	2.74 −3	7.00 −4	3.26 −3
		10	5.61 −4	1.96 −4	2.58 −3	7.57 −4	3.14 −3
		20	5.95 −4	2.13 −4	2.52 −3	8.06 −4	3.11 −3
		30	6.27 −4	2.28 −4	2.47 −3	8.55 −4	3.10 −3
	7	0	3.73 −4	1.22 −4	2.54 −3	4.95 −4	2.91 −3
		10	4.09 −4	1.35 −4	2.45 −3	5.44 −4	2.86 −3
		20	4.38 −4	1.46 −4	2.41 −3	5.84 −4	2.85 −3
		30	4.66 −4	1.58 −4	2.39 −3	6.23 −4	2.85 −3
	10	0	3.08 −4	1.00 −4	2.48 −3	4.09 −4	2.79 −3
		10	3.39 −4	1.10 −4	2.42 −3	4.49 −4	2.76 −3
		20	3.63 −4	1.19 −4	2.40 −3	4.82 −4	2.76 −3
		30	3.84 −4	1.28 −4	2.38 −3	5.12 −4	2.76 −3
2000	4	0	4.25 −4	1.55 −4	1.92 −3	5.80 −4	2.34 −3
		10	4.51 −4	1.70 −4	1.81 −3	6.22 −4	2.26 −3
		20	4.73 −4	1.85 −4	1.76 −3	6.58 −4	2.23 −3
		30	4.90 −4	1.99 −4	1.73 −3	6.89 −4	2.22 −3
	7	0	3.13 −4	1.05 −4	1.78 −3	4.17 −4	2.09 −3
		10	3.43 −4	1.16 −4	1.71 −3	4.58 −4	2.06 −3
		20	3.67 −4	1.26 −4	1.69 −3	4.94 −4	2.06 −3
		30	3.91 −4	1.36 −4	1.67 −3	5.27 −4	2.06 −3
	10	0	2.55 −4	8.47 −4	1.74 −3	3.40 −4	1.99 −3
		10	2.82 −4	9.37 −4	1.70 −3	3.75 −4	1.98 −3
		20	3.03 −4	1.02 −4	1.68 −3	4.05 −4	1.98 −3
		30	3.23 −4	1.10 −4	1.67 −3	4.33 −4	1.99 −3

Table 4.2. Absorbed dose in bladder wall for ^{99m}Tc present in the urine

Half-life = 6.031 hr

In rads per microcurie per cubic centimeter

Filling rate (ml/day)	No. of voids per day	Percent carryover	Photon dose	Beta dose		Total dose	
				Average depth	Surface	Photon plus av. depth	Photon plus surface
1000	4	0	3.17 −5	5.98 −7	5.19 −5	3.23 −5	8.36 −5
		10	3.18 −5	6.03 −7	4.43 −5	3.24 −5	7.61 −5
		20	3.20 −5	6.15 −7	4.04 −5	3.26 −5	7.24 −5
		30	3.23 −5	6.25 −7	3.75 −5	3.29 −5	6.98 −5
	7	0	2.44 −5	4.97 −7	5.11 −5	2.49 −5	7.56 −5
		10	2.55 −5	4.67 −7	4.63 −5	2.59 −5	7.18 −5
		20	2.62 −5	4.86 −7	4.37 −5	2.67 −5	6.99 −5
		30	2.68 −5	5.03 −7	4.17 −5	2.73 −5	6.85 −5
	10	0	2.16 −5	3.84 −7	5.13 −5	2.14 −5	7.23 −5
		10	2.24 −5	4.04 −7	4.78 −5	2.28 −5	7.02 −5
		20	2.31 −5	4.23 −7	4.58 −5	2.36 −5	6.90 −5
		30	2.38 −5	4.41 −7	4.42 −5	2.42 −5	6.80 −5
1400	4	0	2.69 −5	5.17 −7	3.71 −5	2.74 −5	6.40 −5
		10	2.69 −5	5.26 −7	3.16 −5	2.74 −5	5.85 −5
		20	2.70 −5	5.37 −7	2.89 −5	2.75 −5	5.58 −5
		30	2.70 −5	5.48 −7	2.68 −5	2.76 −5	5.38 −5
	7	0	2.06 −5	3.83 −7	3.65 −5	2.10 −5	5.71 −5
		10	2.16 −5	4.02 −7	3.31 −5	2.20 −5	5.47 −5
		20	2.23 −5	4.20 −7	3.12 −5	2.27 −5	5.35 −5
		30	2.30 −5	4.36 −7	2.98 −5	2.34 −5	5.28 −5
	10	0	1.74 −5	3.24 −7	3.66 −5	1.78 −5	5.41 −5
		10	1.85 −5	3.43 −7	3.41 −5	1.89 −5	5.27 −5
		20	1.93 −5	3.62 −7	3.27 −5	1.97 −5	5.20 −5
		30	2.00 −5	3.78 −7	3.16 −5	2.04 −5	5.16 −5
2000	4	0	2.20 −5	4.47 −7	2.60 −5	2.25 −5	4.80 −5
		10	2.18 −5	4.57 −7	2.21 −5	2.22 −5	4.39 −5
		20	2.16 −5	4.69 −7	2.02 −5	2.20 −5	4.18 −5
		30	2.12 −5	4.79 −7	1.88 −5	2.16 −5	3.99 −5
	7	0	1.74 −5	3.27 −7	2.56 −5	1.77 −5	4.30 −5
		10	1.82 −5	3.45 −7	2.32 −5	1.86 −5	4.14 −5
		20	1.88 −5	3.62 −7	2.18 −5	1.92 −5	4.07 −5
		30	1.94 −5	3.78 −7	2.08 −5	1.98 −5	4.03 −5
	10	0	1.46 −5	2.74 −7	2.56 −5	1.48 −5	4.02 −5
		10	1.56 −5	2.92 −7	2.39 −5	1.58 −5	3.94 −5
		20	1.63 −5	3.10 −7	2.29 −5	1.66 −5	3.92 −5
		30	1.70 −5	3.25 −7	2.21 −5	1.73 −5	3.91 −5

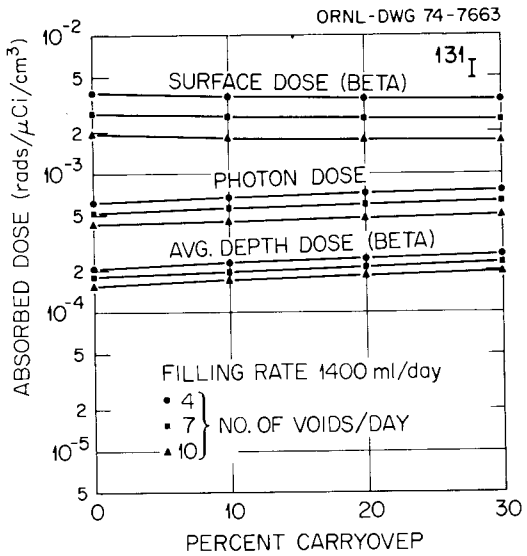

Fig. 4.1. Absorbed dose in bladder wall for ^{131}I present in the urine.

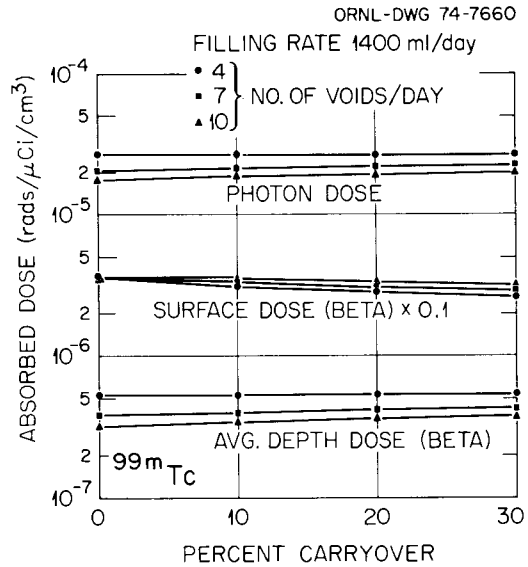

Fig. 4.2. Absorbed dose in bladder wall for ^{99m}Tc present in the urine.

5. Internal Dosimetry of Spontaneously Fissioning Nuclides

L. T. Dillman[1] T. D. Jones

Due to the increased amounts of transuranium isotopes produced in recent years, the assessment of the radiation hazard associated with radionuclides that decay partly by spontaneous fission has become more important. Even if a nuclide decays via spontaneous fission only 1% of the time, the associated dose will be comparable with or larger than the dose due to all other modes of decay. In the report of Committee II of the International Commission on Radiological Protection,[2] the physical aspects of the internal dosimetry for spontaneous fission consisted merely of crudely estimating the total energy released per fission. All this energy was assumed to be absorbed in the source organ. Such an assumption neglects the cross irradiation of organs due to the neutrons and gamma rays concomitant with fission. Since approximately 80% of the energy emitted in fission occurs as kinetic energy of the fission fragments, the source organ will absorb a major portion of the total emitted radiation. However, for the gastrointestinal (GI) tract, the fission fragments fail to penetrate the mucosa to an appreciable extent. In this case, the neutron, gamma, and beta radiations associated with fission are responsible for an appreciable fraction of the dose to the GI tract walls. Cross-irradiation effects are significant in this situation and are also important in determining genetic doses.

FISSION-FRAGMENT DOSIMETRY

Unik and Gindler[3] have made a comprehensive review of experimental data concerning the energy released in nuclear fission and have provided a rather complete bibliography through 1970. In regard to fission fragments, they give an expression for the kinetic energy, E_{FF}, associated with fission fragments as

$$E_{FF} = 0.139601 Z^2/A^{1/3} - 21.975 \text{ MeV} , \qquad (1)$$

where Z and A are the atomic and mass numbers, respectively, of the fissioning nuclide. This equation is accurate to ±2 MeV, or approximately 1%, since the total energy of the fission fragments is of the order of 200 MeV.

It is a well-known fact that spontaneous fission or fission induced by thermal neutrons is asymmetric,[4] and there is significant spread of kinetic energies of fission fragments and their associated ranges; however, according to the heavy-ion data of Northcliffe and Schilling,[5] 25 μ is a reasonable upper bound on the range in water of the fission fragments associated with any fissioning nuclide.

On the other hand, the kinetic energies of alpha particles from alpha decay vary from 4 to 10 MeV. The corresponding span of alpha-particle ranges in water is from 24 to 103 μ; thus fission-fragment ranges are comparable with or less than alpha-particle ranges that result from alpha decay. Hence, as is common practice in alpha-particle dosimetry, it shall be assumed that fission-fragment energy is absorbed locally at the site of the fission process. For a time integral of activity of 1 μCi-day, the fission-fragment average dose equivalent, DE_{FF}, to a source organ is given by

$$DE_{FF} = 51.15 f E_{FF}(\text{QF})/M_s \text{ rems } (\mu\text{Ci-day})^{-1} , \qquad (2)$$

where f is the fraction of the disintegrations of the nuclide which occur via spontaneous fission, E_{FF} is as given by Eq. (1), QF is the quality factor for fission

1. Consultant, Ohio Wesleyan University.
2. *Recommendations of the International Commission on Radiological Protection,* ICRP Publication 2, Pergamon Press, Oxford, 1959.
3. J. P. Unik and J. E. Gindler, *A Critical Review of the Energy Released in Nuclear Fission,* ANL-7748 (1971).
4. A. Prince, "Nuclear and Physical Properties of Cf-252," *Proceedings of a Symposium on Californium-252,* USAEC report CONF-681032 (1969).
5. L. C. Northcliffe and R. F. Schilling, *Nuclear Data Tables* A7, 233 (1970).

fragments, and M_s is the mass of the source organ in grams. The constant 51.15 is a conversion factor from units of MeV per gram per fission to units of rads per microcurie-day. A QF of 20 for fission fragments was used in this work.

Application of Eq. (2) to the GI tract requires modification since we desire the dose to the walls of the GI tract rather than the dose to the contents. Due to the extremely short range of fission fragments in tissue-equivalent material, the boundary between the walls and contents is assumed flat, and the surface dose to the wall is approximately one-half the equilibrium dose to the contents. The ICRP[2] used a modifying factor, MF, of 0.01 for alpha particles in the contents of the GI tract. The use of such a modifying factor is justified because alpha particles do not penetrate the mucosa of the GI tract wall to an appreciable extent; so the radiosensitive crypt cells of the GI tract walls are irradiated only slightly, if at all. Because the range of fission fragments is comparable with or less than that for alpha particles, a modifying factor of 0.01 will also be used for fission fragments. With these considerations in mind, the dose equivalent to any of the four sections of the GI tract walls is given by

$$DE_{FF} = 25.57 f E_{FF}(\mathrm{QF})(\mathrm{MF})/M_s \quad \text{rems } (\mu\text{Ci-day})^{-1} , \qquad (3)$$

where M_s is the mass of the contents, not the walls.

The masses of the various source organs used in the present study are those currently in use with the reference man phantom developed by Fisher and Snyder.[6] The small intestine of the Fisher-Snyder phantom does not have separate compartments for walls and contents; so an overall mass of 400 g was used in Eq. (3).

NEUTRON DOSIMETRY

During the fission process, both prompt and delayed neutrons are emitted. The ratio of delayed neutrons to prompt neutrons is of the order of 0.005, and the two groups were combined because the energy distributions are similar. Let $\bar{\nu}$ be the average number of neutrons emitted per fission. An approximate expression (taken from ref. 7) for the average energy, $\bar{E}_n$, associated with an emitted neutron is

$$\bar{E}_n = 0.75 + 0.65(\bar{\nu} + 1)^{1/2} \text{ MeV} . \qquad (4)$$

Data from Unik and Gindler[3] indicate that Eq. (4) gives results that are in excellent agreement with experimental values of $\bar{E}_n$. In order to implement Eq. (4), it is necessary to know $\bar{\nu}$. Attempts to determine $\bar{\nu}$ from theoretical considerations have had quite limited success; however, a significant body of experimental data on $\bar{\nu}$ is available. Table 5.1 summarizes the presently available values of $\bar{\nu}$ for nuclides that decay by spontaneous fission. For cases other than those given in Table 5.1 a rather crude approximation for $\bar{\nu}$ may be

Table 5.1. Data on neutron multiplicity and on fraction of decays that occur via spontaneous fission

Isotope	Fission decay fraction, f[a]	Average number of neutrons per fission, $\bar{\nu}$	Source of $\bar{\nu}$ data[b,c]
Th-232	$<10^{-11}$	2.37 ± 0.14	ANL
U-238	4.55×10^{-7}	2.07 ± 0.07	Orth–ANL[d]
Pu-236	8×10^{-10}	2.23 ± 0.19	Orth
Pu-238	1.7×10^{-9}	2.28 ± 0.06	Orth–ANL[d]
Pu-240	4.9×10^{-8}	2.21 ± 0.03	Orth–ANL[d]
Pu-242	5.5×10^{-6}	2.24 ± 0.08	Orth–ANL[d]
Pu-244	1.0×10^{-3}	2.28 ± 0.19	Orth
Cm-242	6.8×10^{-8}	2.59 ± 0.06	Orth–ANL[d]
Cm-244	1.3×10^{-6}	2.77 ± 0.04	Orth–ANL[d]
Cm-246	3×10^{-4}	2.86 ± 0.06	Stoughton
Cm-248	9×10^{-2}	3.14 ± 0.06	Stoughton
Cm-250	1.0×10^{0}	3.31 ± 0.08	Orth
Bk-249	$<7 \times 10^{-10}$	3.67 ± 0.16	ANL
Cf-246	2×10^{-6}	2.83 ± 0.19	Orth
Cf-250	8×10^{-4}	3.49 ± 0.09	Orth
Cf-252	3.1×10^{-2}	3.73 ± 0.03	Stoughton
Cf-254	9.98×10^{-1}	3.89 ± 0.05	Orth
Fm-254	5.9×10^{-4}	4.00 ± 0.19	Orth
Fm-257	2×10^{-3}	3.97 ± 0.13	Cheifetz

[a]All f values are from *Nuclear Data* **B3-2** (1969) and **B4-6** (1970), Academic Press, New York.

[b]Sources: R. W. Stoughton, *Nucl. Sci. Eng.* **50**, 169 (1973); C. J. Orth, *Nucl. Sci. Eng.* **43**, 54 (1971); Argonne National Laboratory, *Reactor Physics Constants*, ANL-5800 (1963); E. Cheifetz, H. R. Bowman, J. B. Hunter, and S. G. Thompson, *Phys. Rev.* **C3**, 2017 (1971).

[c]Data of Orth are renormalized to $\bar{\nu} = 3.73$ for ^{252}Cf.

[d]Tabulated value is an average of the best values in Orth and ANL-5800.

6. W. S. Snyder, M. R. Ford, G. G. Warner, and H. L. Fisher, Jr., "Estimates of Absorbed Fractions for Monoenergetic Photon Sources Uniformly Distributed in Various Organs of a Heterogeneous Phantom," MIRD Pamphlet No. 5, *J. Nucl. Med., Suppl. No. 3* **10** (August 1969).

7. J. Terrell, *Proceedings of the Symposium on the Physics and Chemistry of Fission, Salzburg, Austria*, International Atomic Energy Agency, Vienna, Austria, 1965, vol. II, p. 3.

obtained from the theoretical work of Bondarenko.[8] Bondarenko presents a convenient graph that indicates the dependence of $\bar{\nu}$ on mass number and atomic number for fissionable nuclei.

Stoddard[9] and Prince[4] present data which indicate that the shapes of the neutron energy spectra are quite similar and, to a first approximation, are given by a Maxwellian distribution. The effective temperature of the Maxwellian distribution is given by $2\bar{E}_n/3k$, where k is the Boltzmann constant. The number of neutrons in an energy interval dE about energy E is given by

$$N(E)\,dE = CE^{1/2}e^{-3E/2\bar{E}_n}\,dE\,, \tag{5}$$

where C is a constant and $N(E)$ is the number of neutrons per MeV per unit fission event at energy E. Since the integral of $N(E)\,dE$ from zero to infinity is equal to $\bar{\nu}$, C can be evaluated analytically. The result is

$$C = \left(\frac{3}{2\bar{E}_n}\right)^{3/2} \frac{\bar{\nu}}{\Gamma(3/2)} = \frac{2.073\bar{\nu}}{\bar{E}_n{}^{3/2}}\,. \tag{6}$$

The only datum needed to make a plot of $N(E)$ as a function of E is $\bar{\nu}$ since $\bar{E}_n$ is a function of $\bar{\nu}$ as given by Eq. (4). $N(E)$ as calculated from Eq. (5) is shown in Fig. 5.1 for ^{238}U, ^{244}Cm, and ^{252}Cf. Also shown in Fig. 5.1 are selected points on the curve

$$N(E) = 1.392e^{-0.88E}\sinh(2.0E)^{1/2}\,, \tag{7}$$

which is an excellent empirical fit to the experimental data for ^{252}Cf. For ^{252}Cf, it will be noted that, compared with experimental data, Eq. (5) predicts too many neutrons at low energies and not enough neutrons at high energies. This same tendency occurs for other nuclides where comparisons with experimental data have been made; however, for our purposes, Eq. (5) is sufficiently accurate because it shows the features of the neutron spectrum. It is apparent that the spectral shapes for ^{238}U, ^{244}Cm, and ^{252}Cf are quite similar.

The similarity of the neutron spectral shapes is fortunate because it permits one to calculate neutron doses for a particular nuclide and then to scale the results to give reasonably good estimates of neutron dose for any other spontaneously fissioning nuclide. Scaling is done simply on the basis of the ratio of $\bar{\nu}$ for the nuclide under consideration to $\bar{\nu}$ for the nuclide used as the standard.

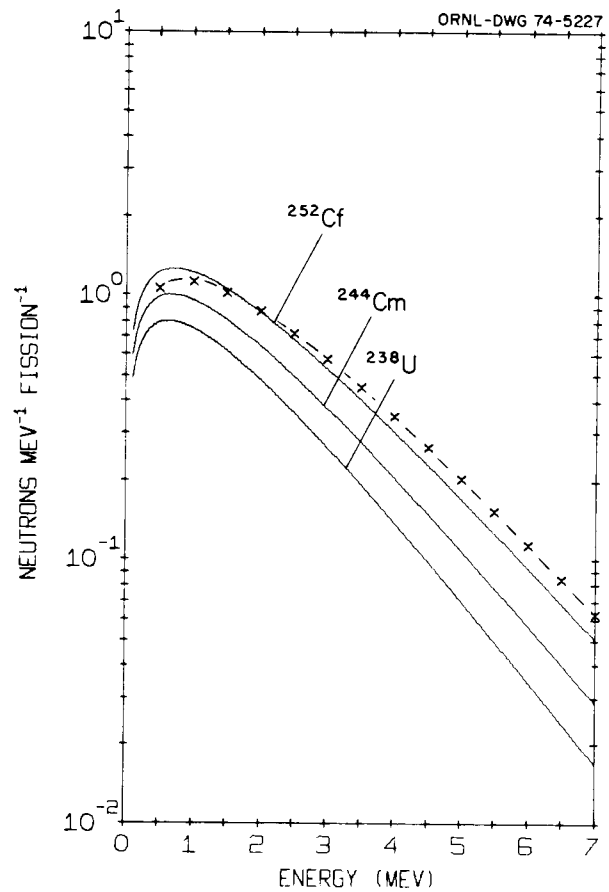

Fig. 5.1. Spectral distribution of emitted neutrons in fission.

The choice of ^{252}Cf as a standard was made primarily because Jones and Auxier[10] have made Monte Carlo calculations of the absorbed dose distribution about a point isotropic ^{252}Cf source implanted at the center of a tissue-equivalent phantom representative of the human torso. The central portion of the phantom was divided into 103 volume elements where doses were recorded. The dose in rads per neutron from recoil ions was recorded as a function of the distance from the source to the centroid of the volume element, and similar data were recorded for the neutron-produced gamma rays. The calculations permitted the determination of the average dose to a particular target organ of

8. I. I. Bondarenko, B. D. Kuzminov, L. S. Kutsayeva, L. I. Prokhorova, and G. N. Smirenkin, "Average Number and Spectrum of Prompt Neutrons in a Fast-Neutron-Induced Fission," P/2187, *Proceedings of the Second Conference on the Peaceful Uses of Atomic Energy*, Geneva, Switzerland, 1958.

9. D. H. Stoddard, *Radiation Properties of ^{244}Cm Produced for Isotopic Power Generators*, USAEC report DP-939 (1964).

10. T. D. Jones and J. A. Auxier, *Phys. Med. Biol.* 17, 206 (1972).

the reference man phantom for a ^{252}Cf source uniformly distributed in a specified source organ. This was done in Monte Carlo fashion by picking points randomly in the source and target organs, recording the sum of the recoil-ion and neutron-produced gamma-ray doses corresponding to these distances, and finally averaging over many such trials. This process essentially computes the mean dose to the target organ.

For distances greater than 1 cm, the recoil-ion dose, D_{RI}, was given very closely by the equation

$$D_{RI} = ae^{-br}/r^2 \quad (r > 1 \text{ cm}) , \tag{8}$$

where r is the distance from the source and a and b are constants. Similarly, the neutron-induced gamma-ray dose, $D_{n\gamma}$, is given approximately by

$$D_{n\gamma} = ce^{-dr} \quad (r > 3 \text{ cm}) , \tag{9}$$

where c and d are constants. By least-squares fit of the data of Jones and Auxier[10] to Eqs. (8) and (9), the constants a, b, c, and d were determined to be 2.912×10^{-10}, 0.07536, 2.045×10^{-12}, and 0.1370, respectively, if r is measured in centimeters and D in rads per neutron. Equations (8) and (9) were used whenever extrapolations were required.

For the recoil-ion dose, the neutron attenuation was assumed to be small, and, therefore, from the inverse-square law,

$$D_{RI} = (0.25)^2 \, D_{RI}(0.25)/r^2 \quad (r < 0.25 \text{ cm}) , \tag{10}$$

where $D_{RI}(0.25)$ is the dose given by Jones and Auxier at 0.25 cm. The assumption of negligible neutron attenuation seems reasonable since an effective energy-absorption coefficient is 0.07536 cm^{-1} as demonstrated by the numerical value of b in Eq. (8). For distances less than 0.25 cm from the source, the neutron-produced gamma-ray dose was determined on the basis of a linear extrapolation to zero dose at $r = 0$. Although the dose at $r = 0$ will not vanish, it will be small compared with distances of a few millimeters. That is,

$$D_{n\gamma} = r\, D_{n\gamma}(0.25)/0.25 \quad (r < 0.25 \text{ cm}) . \tag{11}$$

Equation (10) can become unbounded if the source and target regions have a common boundary or if they overlap. This problem was avoided in the Monte Carlo calculations by recording the average dose over a small sphere of radius 0.1 cm centered about the target point if the source-target distance was less than 0.1 cm. In every case the results from this averaging procedure were quite close to the results obtained when no averaging was used.

The average doses to target organs for a source uniformly distributed in an organ were determined by this procedure for all possible combinations of a set of seven source organs and nine target organs. The seven source organs, in which spontaneously fissioning nuclides are most likely to reside, are the four sections of the GI tract, lungs, liver, and skeleton. For target organs, the ovaries and testes were added to the above list so that a genetic dose could be estimated. The results of the Monte Carlo computer runs are shown in Table 5.2, where each entry in the table is the result of averaging 60,000 pairs of source and target points. The coefficients of variation of the numbers given in Table 5.2 were less than 1% for most source-target combinations. As expected, the coefficients of variation were largest when source and target were identical, since the estimator had a large dynamic range. The largest coefficient of variation, 6.7%, was for the liver-liver source-target combination.

The results of Table 5.2 and the equation

$$DE_n = 3.1968 \times 10^{-3} \bar{\nu}^2 f D_{0n}(\text{QF})/\bar{\nu}_0 \quad \text{rems } (\mu\text{Ci-day})^{-1} \tag{12}$$

may be used to find the neutron dose equivalent, DE_n, for any spontaneously fissioning nuclide, where D_{0n} is the appropriate entry in Table 5.2 for ^{252}Cf, $\bar{\nu}_0$ equals 3.73 and is $\bar{\nu}$ for the ^{252}Cf reference nuclide, f is the fraction of decays that occur by spontaneous fission, and the constant 3.1968×10^{-3} is the product of 3.7×10^4 dis sec^{-1} μCi^{-1} times 8.64×10^4 sec/day times 10^{-12} rad/picorad. The quality factor, QF, for neutrons is 10. A quality factor of 8 has been recommended by the ICRP[11] for spontaneous fission neutrons; however, values of 10, based on the probability density functions given in ref. 12, were calculated for ^{252}Cf and ^{244}Cm.

11. *Radiation Protection: Recommendations of the International Commission on Radiological Protection,* ICRP Publication 6, Pergamon Press, Oxford, 1962.

12. J. J. Barker, ed., *Californium-252,* USAEC report CONF-681032, p. 48 (1969).

Table 5.2. Neutron doses for a ^{252}Cf source

Table entries are in units of picorads per neutron and are the sum of the contributions due to recoil ions and neutron-produced gamma rays. Doses shown are averages over the target organ for uniform concentration of activity in the source organ.

Target organ	Dose when source organ is –						
	Stomach contents	Small intestine	Upper large intestine contents	Lower large intestine contents	Liver	Lungs	Skeleton
Stomach wall	18.6	0.999	1.12	0.490	0.574	0.763	0.174
Small intestine	0.901	9.79	6.69	2.81	0.530	0.0681	0.228
Upper large intestine wall	1.04	7.37	10.1	1.30	0.730	0.0672	0.220
Lower large intestine wall	0.350	2.44	0.999	7.8	0.0739	0.0268	0.352
Liver	0.561	0.527	0.570	0.0874	9.04	0.221	0.216
Lungs	0.679	0.0687	0.0591	0.0332	0.22	8.82	0.284
Skeleton	0.164	0.243	0.388	0.326	0.228	0.291	1.13
Testes	0.0242	0.145	0.607	1.74	0.0180	0.0292	0.305
Ovaries	0.232	3.23	1.85	5.93	0.166	0.0246	0.270

GAMMA-RAY DOSIMETRY

The division point between prompt and delayed gamma rays associated with fission is somewhat arbitrary, but beta decay with its associated gamma rays is energetically unfavorable until the fission fragments are deexcited. The time of 10^{-3} sec for the fission fragments to become deexcited was the division point chosen here.

Unik and Gindler[3] have analyzed available data, and they have concluded that the total energy release in prompt gamma rays for the fission of ^{236}U caused by thermal neutrons is 7.64 ± 0.75 MeV. This is somewhat lower than the value of 8.01 ± 0.87 MeV,[13] which was based on the analysis by Holden et al.;[14] however, the values agree within experimental error, and for this work the value given by Unik and Gindler was adopted.

Except for ^{236}U, data on the prompt fission spectra of nuclides are meager. Stoddard[9] compared the prompt fission gamma-ray spectra of ^{252}Cf, ^{244}Cm, and ^{236}U and found them to be similar. In his review article, James[13] indicated that ^{239}U gives a prompt-gamma-ray spectrum which deviates from that of ^{236}U by less than 3% over the range of energies investigated. There was early evidence that the total energy release in the form of prompt gamma rays for ^{252}Cf was greater than for ^{236}U;[15] however, in more recent measurements, Verbinski et al.[16] found a total energy release of prompt gamma rays of 8.03 ± 0.94 MeV for ^{252}Cf. Within experimental error, this is the same as the result for ^{236}U.

In view of the above discussion, the approximation was used that the total energy release in the form of prompt gamma rays for any spontaneously fissioning nuclide is the same as that for the thermal-neutron-induced fission of ^{236}U. Furthermore, the prompt-gamma-ray spectral measurements of Peelle and Maienschein[17] for ^{236}U were adopted as being representative of any fissioning isotope. In order to use the data of Peelle and Maienschein conveniently, the spectrum was approximated by a series of mono-energetic gamma rays. The final array of photon energies used in this work is shown in Table 5.3.

For delayed photons, this work used the energy spectral information of Zigman and Mackin[18] for ^{236}U, which provides information on the rate of

13. M. F. James, *J. Nucl. Energy* **23**, 517 (1969).
14. N. E. Holden, M. R. Mendelson, and T. D. Dudley, *Nucl. Sci. Eng.* **30**, 461 (1967).
15. E. K. Hyde, *A Review of Nuclear Fission – Part I, Fission Phenomena at Low Energies*, UCRL-9036 (1960).
16. V. V. Verbinski, H. Weber, and R. E. Sund, *Proceedings of the Second IAEA Symposium on the Physics and Chemistry of Fission*, International Atomic Energy Agency, Vienna, Austria, 1969, p. 929.
17. R. W. Peelle and F. C. Maienschein, *The Absolute Spectrum of Photons Emitted in Coincidence with Thermal-Neutron Fission of Uranium-235*, ORNL-4457 (1970).
18. P. Zigman and J. Mackin, *Health Phys.* **5**, 79 (1961).

Table 5.3. Prompt gamma rays in the fission of ^{236}U

This table is based upon the work of R. W. Peelle and F. C. Maienschein, *The Absolute Spectrum of Photons Emitted in Coincidence with Thermal-Neutron Fission of Uranium-235*, ORNL-4457 (1970). Their data have been renormalized to give a total energy release by prompt gamma rays of 7.64 MeV.

Photon energy (MeV)	Photons per fission	Photon energy (MeV)	Photons per fission
0.0148	0.0947	0.749	0.565
0.0314	0.247	0.849	0.474
0.0453	0.00716	0.949	0.396
0.0553	0.0102	1.049	0.332
0.0753	0.0208	1.149	0.277
0.0853	0.0295	1.25	0.232
0.0953	0.0421	1.35	0.194
0.11	0.14	1.45	0.162
0.13	0.14	1.73	0.575
0.15	0.14	2.23	0.334
0.17	0.14	2.73	0.193
0.19	0.14	3.23	0.112
0.225	0.351	3.73	0.0650
0.275	0.351	4.23	0.0377
0.325	0.351	4.73	0.0218
0.375	0.351	5.23	0.0127
0.425	0.351	5.91	0.0116
0.475	0.351	6.91	0.0039
0.525	0.351	7.91	0.0013
0.575	0.351	8.91	0.00044
0.649	0.676	9.91	0.00015

Table 5.4. Delayed gamma rays in the fission of ^{236}U

This table is based upon the work of P. Zigman and J. Mackin, *Health Phys.* 5, 79 (1961), and L. R. Bunney and D. Sam, *Nucl. Sci. Eng.* 39, 81 (1970). Entries are the integral of the photon emission rate from 10^{-3} sec to infinity. Normalization is to a total energy release of 7.2 MeV.

Photon energy (MeV)	Photons per fission	Photon energy (MeV)	Photons per fission
0.03	0.11	0.54	0.59
0.05	0.11	0.64	0.46
0.07	0.11	0.74	0.36
0.09	0.11	0.84	0.28
0.11	0.11	1.10	1.18
0.13	0.11	1.56	0.72
0.15	0.11	2.00	0.38
0.17	0.11	2.40	0.28
0.19	0.11	2.80	0.16
0.225	0.27	3.25	0.12
0.275	0.27	3.75	0.086
0.325	0.27	4.25	0.042
0.375	0.27	4.75	0.020
0.44	0.76	5.25	0.0095

photon emission for a series of energy intervals and a series of time intervals from 1 to 10^8 sec. Data have been integrated to obtain the total energy release by delayed gamma rays in the interval from 10^{-3} to 10^8 sec for several energy intervals; however, data in the energy interval 0.01 to 0.4 MeV are subject to large experimental error. It was estimated on the basis of more recent spectra by Bunney and Sam[19] that the value of Zigman and Mackin in the 0.02 to 0.4 MeV interval is perhaps a factor of 2 too low, and the estimate of energy release in this region was adjusted accordingly. For lack of better evidence, the photons per MeV per fission were assumed constant for 0.02 to 0.4 MeV. It was also assumed that the photon spectra for time intervals less than 1 sec after fission were similar in shape to the photon spectrum at 1 sec. Unik and Gindler[3] analyzed the literature on the total energy released in delayed gamma rays by ^{236}U from 10^{-3} sec to infinity and concluded that 7.2 ± 1.3 is the best value. This value was used in normalizing our spectral distribution for ^{236}U. The delayed-gamma-ray spectral shapes, integrated over time, are somewhat dependent upon the nuclide undergoing fission; however, the ^{236}U spectral shape was adopted for all nuclides. As in the case of prompt gamma rays, the essentially continuous delayed-gamma-ray spectrum was approximated by a series of monoenergetic gamma rays; the data for ^{236}U are shown in Table 5.4.

Although the spectral shapes of the energy distribution of delayed gamma rays are nearly the same for all nuclides, the total energy release by delayed gamma rays varies from one nuclide to another. James[13] and Griffin[20] have derived expressions for the total energy release by delayed gamma rays which involve the average chain length to reach stability for the fission fragments. Their theory is summarized by Unik and Gindler.[3] The basic result is that the total delayed-gamma-ray energy is approximately proportional to the square of the total chain length of both fission fragments, $N_{\beta T}$. An expression for the ratio of the total energy release by delayed gamma rays for any fissioning nuclide to the corresponding energy release for ^{236}U is

19. L. R. Bunney and D. Sam, *Nucl. Sci. Eng.* **39**, 81 (1970).

20. J. J. Griffin, *Beta Decays and Delayed Gamma from Fission Fragments*, LA-2811 (1963).

$$R = (N_{\beta T})^2 / [N_{\beta T}(^{236}\mathrm{U})]^2 \ . \qquad (13)$$

An expression for $N_{\beta T}$ is given by

$$N_{\beta T} = N_{\beta T}(^{236}\mathrm{U}) + A\left(\frac{92}{236} - \frac{Z}{A}\right) , \qquad (14)$$

where Z and A are the atomic and mass numbers of the fissioning nuclide. Combining Eqs. (13) and (14) and substituting an experimental value[3] of 5.98 for $N_{\beta T}(^{236}\mathrm{U})$, the result is

$$R = 0.02796\left(5.98 + \frac{92}{236}A - Z\right)^2 \ . \qquad (15)$$

Equation (15) is compared with experimental results for several nuclides in Table 5.5, and it is seen that theory and experiment are in good agreement. The ratio computed by Eq. (15) was adopted, and the photon intensities were normalized accordingly.

In order to obtain doses, the spectra of prompt and delayed gamma rays given in Tables 5.3 and 5.4 have been used in conjunction with the extensive tabulation by Snyder et al.[6] of absorbed fractions of energy in a target organ for a source uniformly distributed in a source organ. To obtain dose, D_γ, for any particular gamma ray, one may use the equation

$$D_\gamma = 51.15 E_\gamma f_\gamma (\mathrm{AF})/M_t \ \ \mathrm{rads\ (\mu Ci\text{-}day)^{-1}} \ , \qquad (16)$$

where E_γ is the gamma-ray energy in MeV, f_γ is the number of such gamma rays per fission, and AF is the absorbed fraction of energy in the target organ of mass M_t.

The resultant doses from Eq. (16) for all possible combinations of the source and target organs are shown in Table 5.6 for prompt gamma rays of ^{236}U fission and in Table 5.7 for delayed gamma rays of ^{236}U fission.

The total gamma dose, $D_{\gamma T}$, due to both prompt and delayed gamma rays from any nuclide and for any source-target combination can be found by using the equation

$$D_{\gamma T} = [D_{\gamma p}(^{236}\mathrm{U}) + R\, D_{\gamma d}(^{236}\mathrm{U})] f(\mathrm{QF}) \ \ \mathrm{millirads\ (\mu Ci\text{-}day)^{-1}} \ , \qquad (17)$$

Table 5.5. The ratio, R, of total delayed-gamma-ray energy for a fissioning nuclide to the corresponding total delayed-gamma-ray energy for ^{236}U

Fissioning nuclide	R (theory), Eq. (14)	R (experimental)[a,b]
Th-233	1.30	1.27 ± 0.21
U-234	0.76	0.83 ± 0.18
U-236	1.00	1.00
U-239	1.43	1.27 ± 0.21
Pu-240	0.86	0.96 ± 0.21

[a]Values have been extrapolated to include the time interval from 10^{-3} sec to infinity.

[b]P. C. Fisher and L. B. Engle, "Delayed Gammas from First Neutron Fission of Th^{232}, U^{233}, U^{235}, U^{238}, and Pu^{239}," *Phys. Rev. B.* 134, 796 (1964).

Table 5.6. Fission-produced prompt-gamma-ray doses for a ^{236}U source

Table entries are in units of millirads per microcurie-day of fission events.

Target organ	Dose when source organ is –						
	Stomach contents	Small intestine	Upper large intestine contents	Lower large intestine contents	Liver	Lungs	Skeleton
Stomach wall	59.8	4.12	4.13	2.09	2.39	2.27	0.700
Small intestine	3.08	35.4	18.2	10.4	1.95	0.410	0.970
Upper large intestine wall	3.88	26.4	49.8	4.86	2.82	0.552	0.910
Lower large intestine wall	1.59	8.18	3.53	59.3	0.426	0.106	1.21
Liver	2.42	2.21	3.01	0.492	29.4	2.83	0.920
Lungs	2.13	0.444	0.494	0.213	2.90	16.8	1.20
Skeleton	0.736	0.961	0.864	1.24	0.899	1.20	4.08
Testes	0.181	0.639	0.639	2.14	0.211	0.0506	0.976
Ovaries	1.19	11.1	11.3	19.5	0.818	0.218	1.14

Table 5.7. Fission-produced delayed-gamma-ray doses for a ^{236}U source

Table entries are in units of millirads per microcurie-day of fission events.

Target organ	Dose when source organ is –						
	Stomach contents	Small intestine	Upper large intestine contents	Lower large intestine contents	Liver	Lungs	Skeleton
Stomach wall	55.7	3.85	3.84	1.96	2.25	2.13	0.659
Small intestine	2.88	32.9	16.9	9.76	1.82	0.391	0.910
Upper large intestine wall	3.62	24.6	46.2	4.53	2.63	0.522	0.854
Lower large intestine wall	1.50	7.62	3.27	54.7	0.401	0.0981	1.12
Liver	2.28	2.07	2.81	0.467	27.4	2.63	0.869
Lungs	1.98	0.417	0.468	0.208	2.71	15.5	1.12
Skeleton	0.690	0.895	0.808	1.16	0.843	1.12	3.78
Testes	0.179	0.619	0.603	2.01	0.195	0.0492	0.961
Ovaries	1.11	10.2	10.6	18.2	0.797	0.208	1.06

where $D_{\gamma p}(^{236}U)$ is the appropriate entry in Table 5.6, $D_{\gamma d}$ is the appropriate entry in Table 5.7, R is given by Eq. (15), and f is the fraction of the decays that occur by spontaneous fission.

BETA DOSIMETRY

Similarly to the case of delayed gamma rays following fission, the total average beta energy emitted following fission is proportional to $N_{\beta T}{}^2$. Unik and Gindler[3] adopted a value of 7.36 MeV for the total fission-produced beta energy released by ^{236}U, and, again, ^{236}U is used as a standard. Thus, substituting numerical values into Eq. (14) gives

$$E_{\beta T} = 0.2058\left(5.98 + \frac{92}{236}A - Z\right)^2 . \qquad (18)$$

Although beta radiation is much more penetrating than fission fragments, the maximum range in tissue is short; for example, the range at 4 MeV is only 2 cm and decreases rapidly as the beta energy decreases. As for fission fragments, it is assumed that the beta energy is absorbed locally in the source organ; however, there will be significant penetration of the mucosa of the GI tract walls except for beta particles of low energy. Hence, in contrast to fission fragments, a modifying factor of unity was used for the GI tract. The approximation that the surface dose to the walls of the GI tract is one-half the equilibrium dose to the contents was retained, although this result is not as rigorously correct as for the case of fission fragments. The beta dose equivalent values which correspond to Eqs. (2) and (3) for fission fragments are

$$DE_\beta = 51.15 f E_{\beta T}(\mathrm{QF})/M_s \text{ rems } (\mu\text{Ci-day})^{-1} \qquad (19)$$

and

$$DE_\beta = 25.57 f E_{\beta T}(\mathrm{QF})/M_s \text{ rems } (\mu\text{Ci-day})^{-1} , \qquad (20)$$

respectively, where $E_{\beta T}$ is given by Eq. (18).

This beta-dosimetry model is somewhat oversimplified when the skeleton is a source organ. It is well known from the work of Spiers[21] that the beta dose is not uniformly distributed in the various tissues of the skeleton, even if the source is uniformly distributed. It is useful to consider that the skeleton comprises four separate source tissues, which are cortical bone, cancellous bone, red bone marrow, and yellow bone marrow. The target tissues are taken as bone (cortical and cancellous bone are not distinguished from each other as target organs), endosteal cells near bone surfaces, red bone marrow, and yellow bone marrow. Snyder[22] has developed a dosimetric schema based on these 16 source-target combinations. The results of this model for the betas associated with the fission of ^{236}U are given in Table 5.8 and correspond to 0.0359 rad $(\mu\text{Ci-day})^{-1}$ as given by Eq. (19) for the skeleton.

21. F. W. Spiers, *Radioisotopes in the Human Body – Physical and Biological Aspects,* Academic Press, New York, 1968.

22. W. S. Snyder, 1974, private communication of unpublished work in progress.

Table 5.8. Fission-produced beta doses in skeletal tissues for ^{236}U

Table entries are in units of millirads per microcurie-day of fission events. The average dose to the skeleton is 35.9 millirads $(\mu\text{Ci-day})^{-1}$ as computed by Eq. (19).

Target organ	Dose when source organ is –			
	Cortical bone	Cancellous bone	Red bone marrow	Yellow bone marrow
Bone	75.0	42.8	21.5	0
Endosteal cells	45.8	63.7	82.7	62.6
Red bone marrow	6.2	107	179	0
Yellow bone marrow	0	0	0	250

Table 5.9. Organ doses due to ^{252}Cf for radiation components that have small penetration distances in tissue

For the GI-tract parts the source organs are the respective contents. For the liver, lungs, and skeleton the source and target are identical.

Organ	Dose [millirems $(\mu\text{Ci-day})^{-1}$]			
	Alpha particles	Recoil ions	Fission fragments	Beta particles
Stomach wall	61.3	0	122	25.5
Small intestine	37.8	0	75.4	15.8
Upper large intestine wall	68.8	0	137	28.7
Lower large intestine wall	111	0	221	46.1
Liver	1670	53.9	3340	6.97
Lungs	3030	97.6	6040	12.6
Skeleton	1450	46.6	576	1.2[a]

[a]This entry is the average dose to the skeleton as given by Eq. (19). For doses to subregions of the skeleton, this entry is scaled according to the data in Table 5.8. For example, the dose to bone for cortical bone as a source is 75.0/35.9 times this entry, or 2.5 millirems $(\mu\text{Ci-day})^{-1}$.

DISCUSSION OF THE RESULTS

As an example of our model for the internal dosimetry of spontaneously fissioning nuclides, the methods described above were applied to ^{252}Cf, which decays by spontaneous fission 3.1% of the time and by alpha decay 96.9% of the time. For completeness, the alpha dose and the dose due to recoil ions in alpha decay were included, in addition to the various components of the spontaneous fission dose. Also, an MF of 0.01 was used for alpha particles in the GI tract. An MF of zero was used for recoil ions in the GI tract; furthermore, MF was taken as 5 for the skeleton as a source organ. There are several L x rays, internal conversion electrons, Auger electrons, and very low intensity gamma rays associated with the alpha decay of ^{252}Cf. The total dose contribution from these sources is negligible compared with the alpha-particle dose or the components of the spontaneous fission dose; thus they were omitted from further consideration.

The fission-fragment doses were calculated from Eqs. (2) and (3), the neutron doses from Eq. (12), the total gamma doses from Eq. (17), and the beta doses from Eqs. (19) and (20). The results are tabulated in Table 5.9 for alpha particles, recoil ions, fission fragments, and fission-produced beta particles. The fission neutrons and fission-produced gamma-ray doses are given separately in Table 5.10 since there is cross irradiation of organs in these two cases. The total doses due to all radiation components, including those given in Table 5.9, are also listed in Table 5.10.

In cases where the dose to the source organ itself is being evaluated, fission-fragment and alpha-particle doses dominate over the dose from all other radiation components, except for the GI tract. Here the fission-fragment doses are still larger than that due to any other type of radiation. However, the fission-produced neutron and beta doses are now quite significant compared with the alpha-particle and fission-fragment doses. The neutron-produced gamma-ray dose is relatively small in all cases. Furthermore, it is noted that, for the GI tract, cross-irradiation effects due to fission-produced neutrons can be significant. As an example, for a source in the small intestine, the dose to the upper large intestine is 17% of the dose to the small intestine itself. Obviously, cross-irradiation effects account for most of the genetic dose.

We recognize the limitations of the dosimetric model that has been outlined, and, while further refinements of the present dosimetric model for internal deposition of spontaneously fissioning nuclides are certainly possible, such further developments will be of limited value until significant improvements are made in required biological data. The accuracy of the final dose values is much more likely to be limited by the uncertainties in source strength and uncertainties concerning uniformity of activity in the source organ than by the uncertainties in the physical model presented in this paper.

Table 5.10. Fission-produced neutron and gamma doses for a ^{252}Cf source

Table entries are in units of millirems per microcurie-day. Each entry consists of three numbers. The first number is the fission-produced neutron dose, and the second number is the fission-produced gamma-ray dose. The third number is the total dose from all radiation components, including those listed in Table 5.9.

Target organ	Dose when source organ is –						
	Stomach contents	Small intestine	Upper large intestine contents	Lower large intestine contents	Liver	Lungs	Skeleton
Stomach wall	68.6 3.72 281	3.69 0.257 3.95	4.13 0.257 4.39	1.81 0.131 1.94	2.12 0.149 2.27	2.82 0.142 2.96	0.642 0.0438 0.686
Small intestine	3.33 0.192 3.52	36.2 2.20 167	24.7 1.13 25.8	10.4 0.650 11.1	1.96 0.121 2.08	0.252 0.0258 0.278	0.844 0.0606 0.905
Upper large intestine wall	3.83 0.241 4.07	27.3 1.64 28.9	37.1 3.09 275	4.79 0.303 5.09	2.70 0.175 2.88	0.248 0.0346 0.283	0.814 0.0568 0.871
Lower large intestine wall	1.29 0.0996 1.39	9.01 0.509 9.52	3.69 0.219 3.91	65.9 3.67 448	0.273 0.0266 0.300	0.0991 0.00658 0.106	1.30 0.0752 1.38
Liver	2.07 0.151 2.22	1.95 0.138 2.09	2.11 0.187 2.30	0.323 0.0309 0.354	33.4 1.83 5110	0.818 0.176 0.994	0.797 0.0576 0.855
Lungs	2.51 0.132 2.64	0.254 0.0277 0.282	0.218 0.0310 0.249	0.123 0.0135 0.137	0.821 0.181 1.00	32.6 1.04 9210	1.05 0.0747 1.12
Skeleton	0.607 0.0459 0.653	0.899 0.0597 0.959	1.43 0.0538 1.48	1.20 0.0774 1.28	0.842 0.0561 0.898	1.07 0.0749 1.14	4.17 0.253 2080[a]
Testes	0.0896 0.0116 0.101	0.538 0.0405 0.579	2.24 0.0400 2.28	6.44 0.134 6.57	0.0664 0.0131 0.0795	0.0108 0.00322 0.0140	1.13 0.0624 1.19
Ovaries	0.856 0.0739 0.930	11.9 0.684 12.6	6.82 0.704 7.52	21.9 1.21 23.1	0.615 0.0521 0.667	0.0909 0.0137 0.105	0.999 0.0711 1.07

[a]The average beta dose to skeleton was used in obtaining this total (see footnote *a* of Table 5.9).

6. Dosimetric Data for Lead

S. R. Bernard

METABOLISM

Reference man[1] has approximately 120 mg of lead in his body. About 110 mg are in his skeleton, and the remaining 10 mg are assumed to be distributed in soft tissues. The average concentration in soft tissues is approximately 0.2 μg per gram of wet tissue. The liver and kidneys have 6 to 8 times this average, the aorta has 10 times, the skeleton has 50 times, and the hair has 250 times, all other tissues have about 0.25 to 3 times the average of 0.2 μg/g. Reference man's food intake of lead is 0.44 mg/day. About 0.04 mg/day is excreted in urine, and 0.3 mg is excreted in feces; the balance is in sweat excretion and hair loss.

Data on both small animals (rats) and large animals (baboons) are available in the experiments of Bolonowska et al.,[2] Lucas and Standford,[3] Castellino and Aloj,[4] and Cohen.[5] From Bolonowska's data, a power function retention equation for the total body, $0.8t^{-0.2}$ ($t \geqslant 1$ day), and an excretion equation, $0.16t^{-1.2}$ ($t \geqslant 1$ day), are obtained for injected lead acetate. Lucas and Standford's data on rats that had been given $^{210}PbCl_2$ yielded a slightly different retention function, $0.8t^{-0.09}$ ($t \geqslant 1$ day), and excretion equation, $0.1t^{-1.09}$ ($t \geqslant 1$ day). This experiment also showed that blood cells concentrate the lead almost two orders of magnitude higher than plasma. The data of Castellino and Aloj on rats sacrificed at times between 0 and 12 days after injection showed that lead favored uptake in the kidneys and the liver, followed by a slower decline than for blood, and then a tendency toward leveling off in uptake. In Cohen's study on baboons, there was approximately a 4 to 20% initial uptake, each, in the liver and kidneys and a decline with about a 10- to 20-day half-life out to 60 days following injection of $^{210}PbCl_2$. The total-body retention out to about 300 days was fitted with a two-exponential retention equation, $0.3e^{-0.093t/10} + 0.7e^{-0.693t/320}$ (t in days).

Hursh's[6] data on dogs give whole-body retention and excretion out to 10 days following intravenous injection of $^{210}PbCl_2$. Four exponentials were used to represent the total-body retention data:

$$0.457e^{-0.120t} + 0.230e^{-0.0315t} + 0.178e^{-0.00815t} + 0.135e^{-0.00085t} \quad (t \text{ in days}).$$

Hursh noted a more slowly decreasing retention in the total-body data when estimated from total excretion data, suggesting a loss of activity from excreta. The urine-to-fecal ratio was also estimated, and a value of about 1:0.5 was indicated.

Studies of the absorption of ^{212}Pb trapped in beer (from bubbling thoron gas into this fluid) from the GI tract of three men were also made by Hursh and Suomela.[7] Here it can be estimated that about 0.08 is the expected absorption and the standard deviation is about 0.06, indicating a wide spread in values.

METABOLIC MODELS

Uptake to Blood from GI Tract.

In Publication 2 of ICRP,[8] the value of 0.08 was adopted. It is used here too for the usual inorganic compounds of lead and for food bearing lead.

1. ICRP Task Group Report on a Reference Man, Pergamon Press, in press.
2. W. Bolonowska et al., *Proceedings, 14th International Congress on Occupational Health, 1964, Madrid, Spain,* p. 420.
3. H. F. Lucas and J. E. Standford, ANL-7360 (1967), p. 105.
4. N. Castellino and S. Aloj, UCRL-Trans-1196(L) (1965).
5. N. Cohen, NYO-3806-9 (1970).
6. J. B. Hursh, *Health Phys.* **25,** 29 (1973).
7. J. B. Hursh and J. Suomela, *Acta Radiol. Ther. Phys. Biol.* **7,** 108 (1968).
8. *Recommendations of the International Commission on Radiological Protection,* ICRP Publication 2, Pergamon Press, Oxford, 1959.

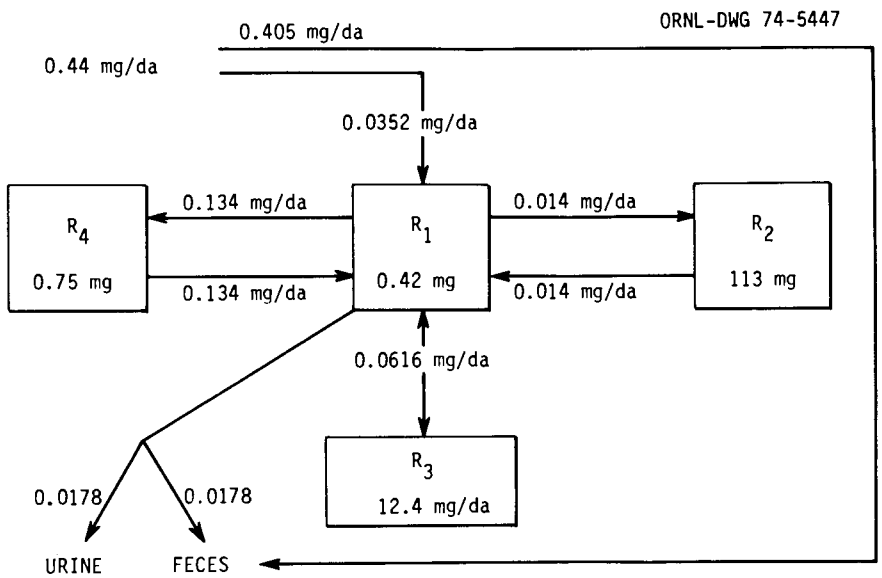

Fig. 6.1. Basic mammillary model for lead in man.

Inhalation Classes

The sulfides, oxides and hydroxides, halides, and nitrates of lead are in class W. No class D or class Y compounds are recognized. For class W compounds, the value of 0.08 is used for f_1.

Retention Equations for Unit Intake to Blood

A mammillary compartment model has been used, together with data on the baboons and reference man, to generate equations for retention in organs and tissues. The model is seen in Fig. 6.1. The total-body retention equation for a single injection into blood is

$$R(t) = 0.1e^{-0.693t} + 0.20e^{-0.693t/10} + 0.4e^{-0.693t/320} + 0.3e^{-0.793t/8000} \quad (t \text{ in days}) .$$

The mean residence time obtained from this equation is the same as would be found from the tissue data and dietary intake data on reference man.

The following equations express the retention in organs and tissues obtained from the above compartment model.

Blood

$$R(t) = 0.00125e^{-\mu_1 t} + 0.0642e^{-\mu_2 t} + 0.128e^{-\mu_3 t} + 0.808e^{-\mu_4 t}$$

Bone (with blood)

$$R(t) = 0.265e^{-\mu_1 t} + 0.303e^{-\mu_2 t} - 0.0287e^{-\mu_3 t} - 0.384e^{-\mu_4 t}$$

Liver (with blood)

$$R(t) = 0.0069e^{-\mu_1 t} + 0.0129e^{-\mu_2 t} + 0.0922e^{-\mu_3 t} - 0.0852e^{-\mu_4 t}$$

Kidney (with blood)

$$R(t) = 0.000605e^{-\mu_1 t} + 0.00178e^{-\mu_2 t} + 0.0493e^{-\mu_3 t} + 0.618e^{-\mu_4 t}$$

Other tissues (with blood)

$$R(t) = 0.0275e^{-\mu_1 t} + 0.0825e^{-\mu_2 t} + 0.101e^{-\mu_3 t} + 0.618e^{-\mu_4 t}$$

In the above, with t in days,

$\mu_1 = 0.693/8000$,

$\mu_2 = 0.00217$,

$\mu_3 = 0.0693$,

$\mu_4 = 0.693$.

Also, the constraints on the retention equations obtained from the mammillary model are:

$$\text{Bone} = 0.636R_4(t) + 0.800R_3(t) + 0.889R_2(t)$$

$$\text{Liver} = 0.2R_4(t) + 0.02R_3(t) + 0.02R_2(t)$$

$$\text{Kidneys} = 0.1R_4(t) + 0.002R_2(t)$$

$$\text{Tissues} = 0.0636R_4(t) + 0.0800R_3(t) + 0.0889R_2(t)$$

$$\text{Blood} = R_1(t) + 0.1R_3(t)$$

CHEMICAL TOXICITY

The American Conference of Governmental Industrial Hygienists[9] recommends 0.2 mg/m^3 for metallic lead and 0.15 mg/m^3 for lead arsenate [$Pb_3(AsO_4)_2$].

9. *Documentation of the Threshold Limit Values for Substances in Workroom Air,* American Conference of Governmental Industrial Hygienists (1971).

7. Dosimetric Data for Copper

S. R. Bernard

METABOLISM

A mathematical model for retention and elimination of copper in and from the body was generated from the data of Cartwright and Wintrobe,[1] from their schematic diagram of metabolism (shown in Fig. 7.1), and from data on reference man.[2] The body level of copper is taken at approximately 70 mg, and the dietary intake is taken at approximately 3.5 mg/day. The average concentration in the body is approximately 1 μg per gram of wet tissue. Concentrations in the liver and the brain are higher than the average by a factor of about 6. Experimental data on rats given a single intravenous injection of ^{64}Cu as the acetate corroborate the equations in this model for humans.[3] Also, data have been reported in which ^{67}Cu-labeled ceruloplasmin was intravenously injected into rats and its distribution was followed in organs and tissues.[4] In general, copper seems to be removed from the blood and to find its way into the tissues, but whether it exists as ^{67}Cu-labeled ceruloplasmin in the tissues is not known.

Studies have been made on the absorption and excretion of ^{64}Cu in rats after intravenous injection of the acetate.[5] Only about one-half to two-thirds of doses up to 1 μg of copper were absorbed; the site of absorption seemed to be the upper portion of the small intestine. With larger doses the percentage of absorption fell, but the absolute amount increased.[5] Much less copper was excreted in the feces when the rat had a biliary fistula. In general, excretion into the GI tract seemed to occur all along the tract, with more excretion occurring near the duodenum and less near the cecum. Practically all the dietary copper is excreted in feces.

1. G. E. Cartwright and M. M. Wintrobe, *Amer. J. Clin. Nutr.* **14**, 224 (1964); **15**, 94 (1964).
2. *Report on a Reference Man*, ICRP Publication 23, Pergamon Press (in press).
3. C. A. Owen, *Amer. J. Physiol.* **209**, 900 (1965).
4. N. Marceau and N. Aspin, *Amer. J. Physiol.* **222**, 106 (1972).
5. C. A. Owen, *Amer. J. Physiol.* **107**, 1203 (1964).

Mention is also made of the inherited disease of copper metabolism in humans called Wilson's disease (hepatolenticular degeneration).[6] In subjects homozygous for the disease, secretion of ceruloplasmin by the liver into the bloodstream ceases, and, evidently the excretion of copper into the gut is decreased. The concentration of copper in the liver, brain, other tissues, and urine increases, and, without treatment with penicillamine (used within the past decade), the patient dies. Uptake from the gut to blood seems to be the same as in nonaffected persons. It is also pointed out that copper and molybdenum have an interface in the body, as do copper and iron (see Underwood[7]).

6. C. A. Owen, Jr., *Wilson's Disease*, vol. IV, No. 2, D. Bergsma, ed., National Foundation March of Dimes, April 1968.
7. E. J. Underwood, *Trace Elements in Human and Animal Nutrition*, Academic Press, New York and London, 1971.

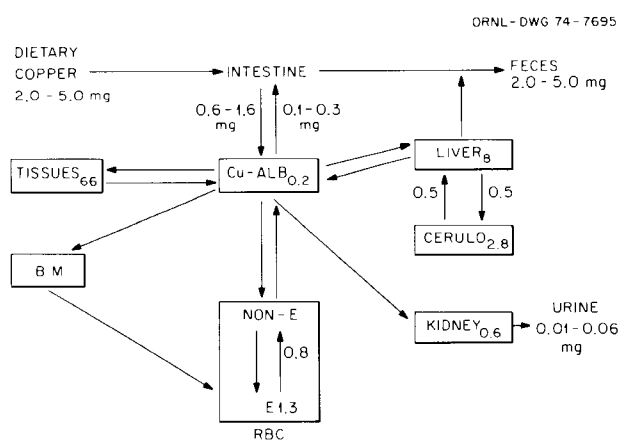

Fig. 7.1. Schematic representation of some metabolic pathways of copper in man. The numbers in the boxes refer to milligrams of copper in the pool. The numbers next to the arrows refer to milligrams of copper transversing the pathway each day. Cu-ALB = direct-reacting fraction; Cerulo = ceruloplasmin; Non-E- = nonerythrocuprein; BM = bone marrow; RBC = red blood cell. Source: G. E. Cartwright and M. M. Wintrobe, *Amer. J. Clin. Nutr.* **14**, 224 (1964) and **15**, 94 (1964).

METABOLIC MODELS

Uptake to Blood from the Gut

In ICRP Publication 2[8] the value of 0.28, obtained from studies by Comar, was used. Here, for the acetate and chloride and general dissociable inorganic compounds of copper, the value of 0.35 is used.[7] This value does not differ much from the 0.28 used previously.

Inhalation Classes[9]

The oxides and hydroxides are in class Y, the sulfides are in class W, and the sulfates, carbonates, phosphates, and nitrates are in class D. For all class W and class D compounds, use $f_1 = 0.35$; for class Y, assume that f_1 is approximately 0.20.

Retention for Unit Intake to Blood

The metabolic model of Cartwright and Wintrobe is used, and the values for transfer to and from compartments are shown in Fig. 7.2. It was assumed that residences in the compartments were distributed exponentially, and the corresponding equations were found as follows:

Blood (Cu-alb fraction)

$$R(t) = 0.0016e^{-\lambda_1 t} + 0.00012e^{-\lambda_2 t} + 0.000036e^{-\lambda_3 t} + 0.996e^{-\lambda_5 t} + 0.0027e^{-\lambda_6 t}$$

Blood (RBC fraction)

$$R(t) = 0.0030e^{-\lambda_1 t} + 0.029e^{-\lambda_2 t} + 0.0015e^{-\lambda_3 t} - 0.735e^{-\lambda_5 t} + 0.70e^{-\lambda_6 t}$$

Blood (ceruloplasmin fraction)

$$R(t) = -0.021e^{-\lambda_1 t} + 0.27e^{-\lambda_2 t} + 0.006e^{-\lambda_3 t} + 0.0060e^{-\lambda_5 t} - 0.26e^{-\lambda_6 t}$$

Liver

$$R(t) = 0.00092e^{-\lambda_1 t} + 0.00044e^{-\lambda_2 t} + 0.00011e^{-\lambda_3 t} + 0.025e^{-\lambda_4 t} - 0.023e^{-\lambda_5 t} - 0.0038e^{-\lambda_6 t}$$

Kidney

$$R(t) = 0.0021e^{-\lambda_1 t} + 0.0021e^{-\lambda_2 t} + 0.00041e^{-\lambda_3 t} - 0.039e^{-\lambda_5 t} - 0.0052e^{-\lambda_6 t}$$

Tissues

$$R(t) = -0.0044e^{-\lambda_1 t} - 0.0085e^{-\lambda_2 t} + 0.1091e^{-\lambda_3 t} - 0.086e^{-\lambda_5 t} - 0.0099e^{-\lambda_6 t}$$

8. *Recommendations of the International Commission on Radiological Protection,* ICRP Publication 2, Pergamon Press, Oxford, 1959.

9. "Report of ICRP Task Group on Lung Dynamics," *Health Phys.* **12**(2), 173 (1966).

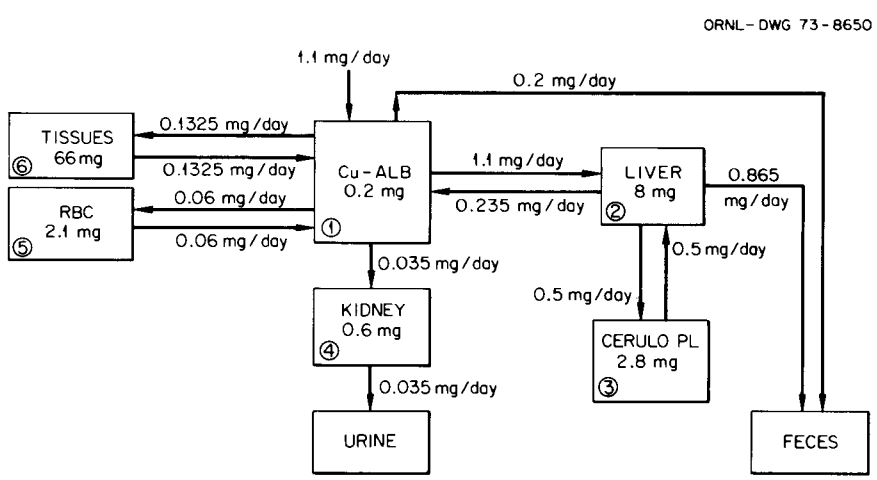

Fig. 7.2. Cartwright and Wintrobe copper model.

where

$\lambda_1 = 0.027\ \text{day}^{-1}$,

$\lambda_2 = 0.011\ \text{day}^{-1}$,

$\lambda_3 = 0.0018\ \text{day}^{-1}$,

$\lambda_4 = 0.058\ \text{day}^{-1}$,

$\lambda_5 = 7.66\ \text{day}^{-1}$,

$\lambda_6 = 0.185\ \text{day}^{-1}$.

The above function for the Cu-alb fraction in blood is for loosely bound copper attached to albumin in blood. The RBC fraction is for copper present in the cells, and the ceruloplasmin fraction is for copper bound to the protein ceruloplasmin present in blood. The above functions do not apply if a mass effect (regulation of uptake or elimination) is operative, as suggested from studies by Owen[6] on perfused liver of rats. For the present, it will be assumed that linear superposition is operating.

CHEMICAL TOXICITY

The American Conference of Governmental Industrial Hygienists[10] recommends 0.1 mg of Cu per cubic meter of air for fumes of copper, whereas 1 mg/m^3 is recommended for dusts and mists of copper salts.

---

10. *Documentation of the Threshold Limit Values for Substances in Workroom Air,* 3d ed., American Conference of Governmental Industrial Hygienists, 1971.

8. Measurement of Absorbed Fractions for Photon Sources Distributed Uniformly in Various Organs of a Heterogeneous Phantom

S. M. Garry[1] P. S. Stansbury[2] J. W. Poston

Monte Carlo calculations provide a direct and accurate means of determining the gamma-ray energy deposition in phantoms from internal emitters. Formulation of Monte Carlo results into absorbed fractions and specific absorbed fractions allows direct calculation of the average gamma dose delivered to a given target region or to a point region respectively. Extensive tables of absorbed fractions and specific absorbed fractions applicable to bounded tissue regions containing point- or uniform-source distributions of radioactivity have been published.[3-7]

There are two limitations on the accuracy of Monte Carlo results: (1) the statistical uncertainty due to sampling variation and (2) the adequacy of the mathematical model being sampled as a representation of the physical processes involved.[8] The number of photon histories followed in the Monte Carlo calculation may be the limiting factor for statistical uncertainty, for example, when source and target organs are small and are separated by an appreciable distance. In practice, this is an important limitation on the accuracy of the Monte Carlo calculations.[9] In some cases, however, the statistical limitation may not be as important as the limitations of the mathematical model. The adequacy of the mathematical model being sampled as a representation of the physical process involved can only be determined by experimental verification.

No experimental work has been published which gives the absorbed doses in phantom organs from internal gamma sources. Although depth-dose distributions have been measured,[10-12] these have not been correlated with the absorbed dose in organs. The simple geometric phantoms that have been used do not accurately represent the reference man.[13] Hubiak[14] experimentally determined the energy absorption for gamma sources in tissue-equivalent cylinders. Jones[15] used a Rando phantom to make measurements of the absorbed doses in various organs as a function of the external gamma exposure; however, these techniques do not give an assessment of the absorbed dose in organs from internal sources, and experimentation was not done in a reference man phantom. This paper describes a program that was undertaken in the Section to:

1. design and construct a physical representation of the Snyder-Fisher heterogeneous mathematical phantom (based on reference man),

1. USAEC Special Fellowship in Health Physics, Physics Dept., University of Tennessee. Present address: Tennessee Valley Authority, River Oaks Building, Muscle Shoals, Ala. 35660.

2. ORAU Laboratory Graduate Participation Grant, School of Nuclear Engineering, Georgia Institute of Technology.

3. W. S. Snyder, M. R. Ford, G. G. Warner, and H. L. Fisher, Jr., "Estimates of Absorbed Fractions for Monoenergetic Photon Sources Uniformly Distributed in Various Organs of a Heterogeneous Phantom," MIRD Pamphlet No. 5, *J. Nucl. Med., Suppl. No. 3* **10** (August 1969).

4. W. H. Ellett, *Phys. Med. Biol.* **14**, 615 (1969).

5. W. H. Ellett, A. B. Callahan, and G. L. Brownell, *Brit. J. Radiol.* **37**, 45 (1964).

6. W. H. Ellett, A. B. Callahan, and G. L. Brownell, *Brit. J. Radiol.* **38**, 541 (1965).

7. A. R. Reddy, W. H. Ellett, and G. L. Brownell, *Brit. J. Radiol.* **40**, 512 (1967).

8. W. H. Ellett, G. L. Brownell, and A. R. Reddy, *Phys. Med. Biol.* **13**, 219 (1968).

9. H. L. Fisher, Jr., and W. S. Snyder, *Health Phys. Div. Annu. Progr. Rep. July 31, 1967,* ORNL-4168, p. 245.

10. L. L. Meisberger, R. J. Keller, and R. J. Shalek, *Radiology* **90**, 953 (1960).

11. V. Krishnaswamy, *Radiology* **105**, 181 (1972).

12. P. Wootton, R. J. Shalek, and G. H. Fletcher, *Amer. J. Roentgenol.* **71**, 683 (1954).

13. International Commission on Radiological Protection, *Report on a Reference Man,* Pergamon Press, 1974.

14. R. J. Hubiak, Sc.D. thesis, University of Cincinnati, 1971.

15. A. R. Jones, Atomic Energy of Canada, Limited, report AECL-2240 (October 1964).

2. determine dose distributions within the phantom resulting from photon emitters uniformly distributed in selected organs,
3. utilize these dose distributions to determine absorbed fractions, and
4. compare these experimentally determined absorbed fractions with the results of Monte Carlo calculations.

EXPERIMENTAL APPARATUS AND PROCEDURES

Phantom

The phantom used in this research was fabricated according to the design of the mathematical phantom described by Fisher and Snyder, but of modified composition.[16] Some perturbations in the design were necessary for the construction of a physical phantom. The exterior phantom shells were fabricated from Lucite in three sections: (1) an elliptical cylinder containing the arms, torso, and hips; (2) a truncated elliptical cone containing both the legs and the feet; and (3) an elliptical cylinder containing the head and neck. A more complete description of the phantom, the materials of construction, etc., has been published.[17,18] The phantom is shown in Fig. 8.1.

A mixture of various chemicals was used to simulate the elemental composition of each phantom region. The soft tissue substitute, composed of 80.0% water, 18.0% methanol, 1.8% sucrose, and 0.2% sodium chloride, had a mass density of 1.0 g/cm^3. Shavings of Shonka A-150 tissue-equivalent plastic[19] were used as the lung substitute, resulting in a mass density of 0.3 g/cm^3. The homogeneous bone substitute, composed of 27.0% water, 19.5% bone flour,[20] 39.5% sucrose, 8.0% ammonium phosphate, and 6.0% ammonium nitrate, had a mass density of 1.5 g/cm^3. A nonionic surfactant,

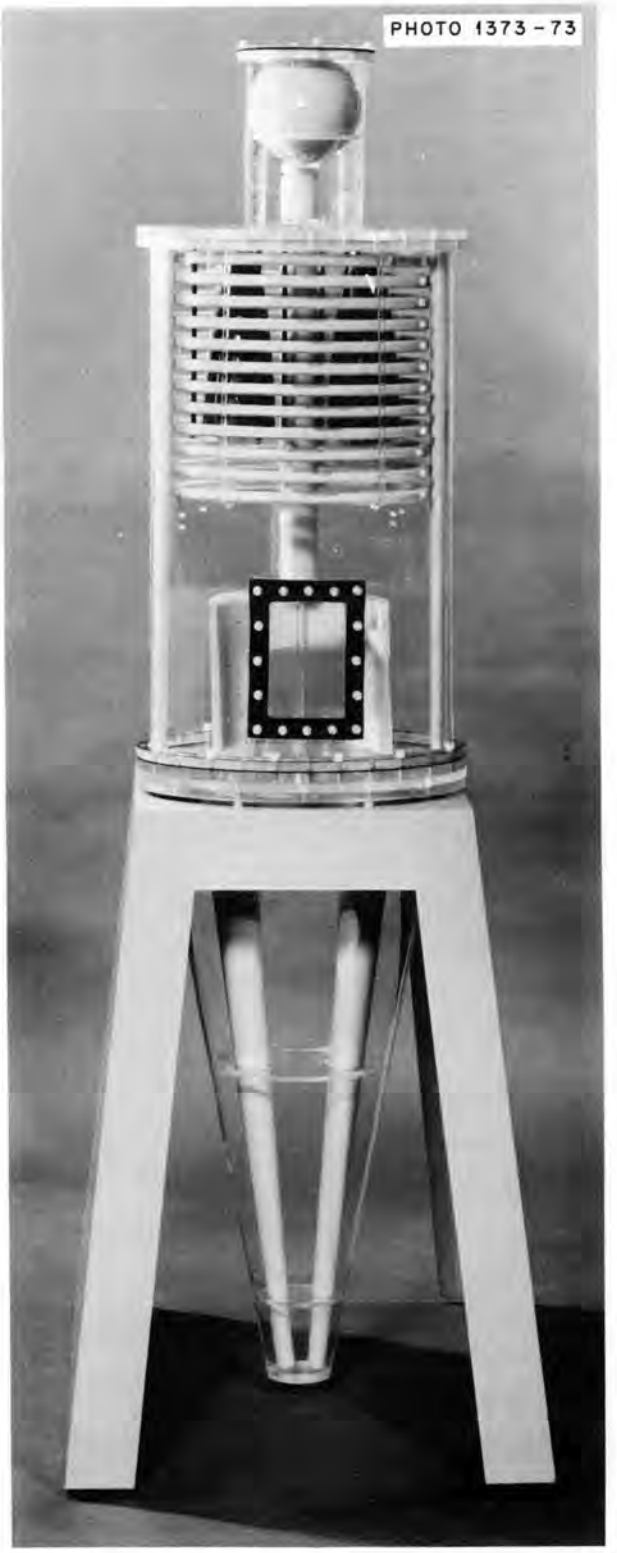

Fig. 8.1. The physical representation of the mathematical Snyder-Fisher phantom.

16. W. S. Snyder, M. R. Ford, and G. G. Warner, *Health Phys. Div. Annu. Progr. Rep. July 31, 1968,* ORNL-4316, p. 274.
17. S. M. Garry, *Measurement of Absorbed Fractions for Photon Sources Distributed Uniformly in Various Organs of a Heterogeneous Phantom,* M.S. thesis, University of Tennessee, Physics Dept., 1973.
18. S. M. Garry, P. S. Stansbury, and J. W. Poston, *Measurement of Absorbed Fractions for Photon Sources Distributed Uniformly in Various Organs of a Heterogeneous Phantom,* ORNL-TM-4411 (January 1974).
19. J. J. Spokas, Physical Sciences Laboratory, Illinois Benedictine College, Lisle, Ill.
20. Nutritional Biochemical Co., 26201 Miles Road, Cleveland, Ohio 44128.

Sterox DJ,[21] was added at a concentration of 3 drops per 20 g of bone substitute to retain regional homogeneity. A surface tension breaker, 1 drop of Tergitol[22] per 100 g of bone substitute, was added also. A small amount of bromthymol blue was added to the liquids to prevent bacterial growth. The selection of these mixtures was determined by use of a computer program[23] which may be used to calculate Compton, coherent, and photoelectric mass attenuation coefficients.

The stomach and bladder source organs were each loaded with cesium chloride (^{137}Cs) solutions, and a bladder source organ was loaded with a cobalt chloride (^{60}Co) solution for the different measurements. A viscous "filler" solution was prepared by blending 2.0% Cellosize hydroxyethyl cellulose[22] with 98.0% water. After the concentrated cobalt chloride and cesium chloride solutions were mixed uniformly with the "filler" solution, the solutions were injected into the source organ shells, which were sealed permanently.

Dosimetry

The gamma dosimeter[24] used in this experiment, commonly called the "Phil" counter, was a small Geiger-Mueller (GM) counter shielded with lead, tin, and fluorothene. The GM tube was filled with neon, argon, and a halogen quenching agent. The shielding of tin and lead, with the stainless steel cathode, provided the necessary material such that the counter response per roentgen of exposure was independent of energy over an energy range of 150 keV to 8 MeV.[25]

The original preamp circuit design of Wagner and Hurst was modified to allow the separation of the GM tube and shielding from the preamp. The preamp was located approximately 1 m from the GM tube, which eliminated scattering effects and bulkiness inside the phantom. The modified design of the preamp provided an impedance matching device with essentially no gain.[26] The pulses from the preamp were large enough to drive a scaler without further amplification. This detector was selected for use in the experiment primarily because of its low-dose-rate response (0.1 mR/hr), readout characteristics, accuracy, and physical characteristics, which allowed positioning of the dosimeter within the phantom.

Dosimeter positioning within the phantom was accomplished by the use of a grid plate with a series of holes for locating and supporting the dosimeter. The holes formed a 2- by 2-cm grid system in the grid plate into which the dosimeter was inserted. The plate was suspended from the top cover of the trunk region by four Bakelite rods, which allowed the vertical adjustment of the plate for varying z positions. A typical situation using the bladder source organ is shown in Fig. 8.2. Several sets of plates were necessary in order to obtain measurements in the various regions of the phantom. The dosimeter was repositioned in the grid plate by inserting a Lucite rod into the phantom, attaching the rod to the dosimeter, and moving the dosimeter to a new location in the grid plate. This enabled positioning of the dosimeter without draining and refilling the phantom for each detector position. However, not all positions could be attained with the dosimeter in the grid holes. Certain positions (e.g., in the immediate vicinity below the lungs) required the use of another dosimeter orientation because of the physical height of the dosimeter itself. In these cases, the dosimeter was laid on its side over the position of interest on the grid and then positioned vertically.

Organ Dose

Fisher and Snyder defined 22 major target organs; however, experimental estimates of the absorbed fraction in some of these organs were not made. These organs, the lungs, the brain, the skeleton, and the source organs themselves, presented experimental difficulty beyond the scope of the present research. However, they were physically included in the phantom. In certain other cases, the position of a target organ with respect to the source organ presented a dosimeter-positioning difficulty which prevented measurements from being made.

An averaging technique was devised to determine the target organ absorbed fraction from the "point" measurements of exposure. Representative positions in the target organs were selected from a consideration of the volume and shape of each target organ. For example, the stomach was defined mathematically by the equation

21. Monsanto Corporation, 800 N. Lindberg Blvd., St. Louis, Mo. 63166.

22. Union Carbide Corporation, 17 Executive Park Dr., N.E., Atlanta, Ga.

23. P. S. Stansbury, *TECALC – a Program to Calculate Compton, Coherent, and Photoelectric Mass Attenuation Coefficients for Photons with Energies Less Than 1 MeV and to Assist in the Evaluation and Formulation of Photon-Equivalent Materials,* ORNL-TM-4451 (January 1974).

24. E. B. Wagner and G. S. Hurst, *Health Phys.* 5, 20 (1961).

25. J. H. Thorngate and D. R. Johnson, *Health Phys.* 11, 133 (1965).

26. J. H. Thorngate, ORNL, personal communication, 1972.

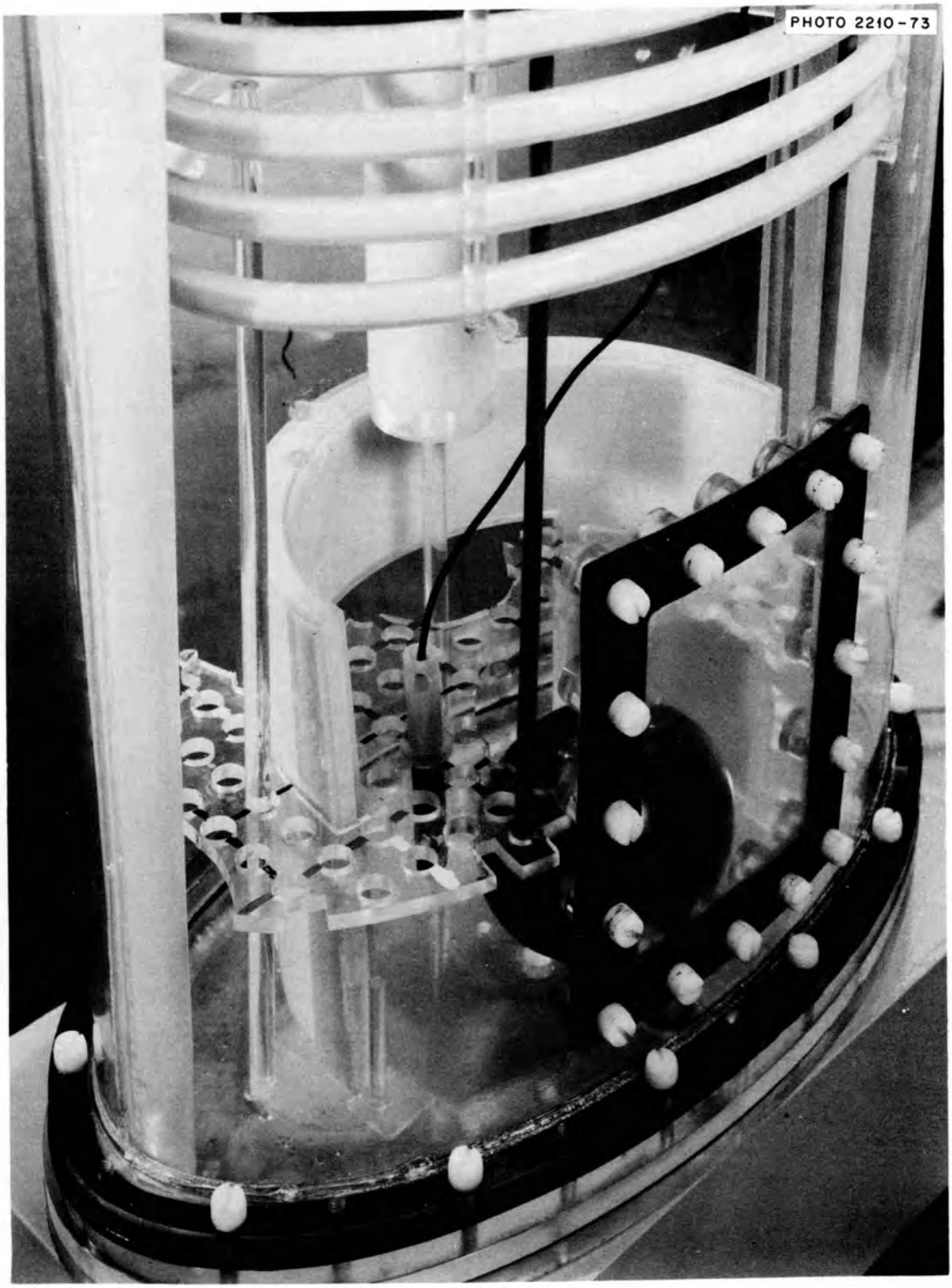

Fig. 8.2. Internal view of phantom showing the dosimeter located in the positioning grid near the bladder source organ.

$$\left(\frac{x-8}{4}\right)^2+\left(\frac{y+4}{3}\right)^2+\left(\frac{z-35}{8}\right)^2 \leqslant 1 .$$

The choice of representative positions within the stomach was made by dividing the stomach by four planes parallel to the *x-y* plane at the *z* coordinates of 29, 33, 37, and 41. These cross-sectional views were superimposed over a drawing of the *x-y* dosimeter grid network. The representative positions chosen within the stomach target organ in the z = 33 cm and z = 37 cm planes were (12, -4), (10, -2), (10, -4), (10, -6), (8, -2), (8, -4), (8, -6), (6, -2), (6, -4), (6, -6), and (4, -4). The *x-y* positions in the z = 29 cm and z = 41 cm planes were (10, -4), (8, -2), (8, -4), (8, -6), and (6, -4). These representative measurements, taken within the target organ, were averaged and multiplied by the appropriate conversion factors to obtain an estimate of the target organ absorbed fraction.

The number of positions at which measurements were to be taken varied from one measurement at the center of each testis and one at the center of the thyroid gland to 40 measurements throughout the volume of the liver.

RESULTS AND DISCUSSION

Comparisons between calculated and measured absorbed fractions for the three source organs are given in Tables 8.1–8.3. The calculated estimates do not include a contribution from that component of the absorbed fraction which is due to photons having an energy less than 150 keV (the approximate low-energy cutoff for the detector). The position of the testes is the same as that defined by Snyder et al.[16] Listed also are the number of measurements taken in each target organ, the coefficient of variation of the Monte Carlo estimate, and the percent difference between the measured and calculated estimates. The column labeled "difference" is the numerical difference between the two estimates multiplied by 100% and divided by the experimental estimate. The comparison of measured and calculated results is made only when the coefficient of variation of the Monte Carlo estimate is less than 20.0%.

Table 8.1. Absorbed fractions for uniform cesium-137 source in bladder

Target organ	Number of measurements	Measured A.F.[a]	Calculated A.F.	C.V.[b] of calculation	Difference[c] (%)	C.V. of difference
L. adrenal	6	0.365E-05				
R. adrenal	6	0.365E-05				
Adrenals	12	0.730E-05				
Bladder	0		0.630E-01	<0.02		
GI(stomach)	32	0.359E-03	0.447E-03	<0.10	32.9	15.9
GI(ULI)	23	0.194E-02	0.264E-02	<0.05	36.1	13.4
GI(LLI)	0		0.608E-02	<0.03		
GI(SI)	39	0.700E-02	0.869E-02	0.022	24.1	12.6
Heart	12	0.959E-04	0.115E-03	0.186	19.9	22.4
L. kidney	18	0.146E-03	0.149E-03	0.152	2.1	19.6
R. kidney	18	0.146E-03	0.183E-03	0.131	25.3	18.0
Kidneys	36	0.293E-03	0.332E-03	0.099	13.3	15.9
Liver	40	0.135E-02	0.130E-02	0.055	−3.7	13.6
L. ovary	5	0.706E-04	0.646E-04	0.248		
R. ovary	5	0.706E-04	0.624E-04	0.255		
Ovaries	10	0.141E-03	0.127E-03	0.178	−9.9	21.7
Pancreas	7	0.392E-04	0.377E-04	0.259		
Spleen	24	0.990E-04	0.159E-03	0.160	60.6	20.2
L. testis	1	0.290E-03	0.344E-03	0.108	18.6	22.4
R. testis	1	0.290E-03	0.395E-03	0.103	36.2	
Testes	2	0.580E-03	0.738E-03	0.075	27.2	
Thymus	5	0.161E-05				
Thyroid	1	0.431E-06				
Uterus	10	0.230E-02	0.324E-02	0.036	40.9	12.9

[a]Absorbed fraction.

[b]Coefficient of variation.

[c]Calculated values with coefficients of variation greater than 20.0% are not included in the comparison.

Table 8.2. Absorbed fractions for uniform cobalt-60 source in bladder

Target organ	Number of measurements	Measured A.F.[a]	Calculated A.F.	C.V.[b] of calculation	Difference[c] (%)	C.V. of difference
L. adrenal	6	0.439E-05				
R. adrenal	6	0.439E-05				
Adrenals	12	0.878E-05				
Bladder	0		0.578E-01	<0.02		
GI(stomach)	32	0.412E-03	0.531E-03	<0.02	28.9	12.6
GI(ULI)	23	0.198E-02	0.292E-02	<0.05	47.5	13.4
GI(LLI)	0		0.599E-02	<0.03		
GI(SI)	39	0.718E-02	0.886E-02	0.023	23.4	12.6
Heart	12	0.143E-03	0.183E-03	0.150	28.0	19.5
L. kidney	18	0.166E-03	0.217E-03	0.134	30.7	18.3
R. kidney	18	0.166E-03	0.209E-03	0.138	25.9	18.6
Kidneys	36	0.332E-03	0.427E-03	0.096	28.6	15.7
Liver	40	0.160E-02	0.182E-02	0.050	13.8	13.4
L. ovary	5	0.664E-04	0.711E-04	0.253		
R. ovary	5	0.664E-04	0.580E-04	0.240		
Ovaries	10	0.133E-03	0.129E-03	0.176	−3.0	21.5
Pancreas	7	0.471E-04	0.497E-04	0.269		
Spleen	24	0.118E-03	0.149E-03	0.164	26.3	20.6
L. testis	1	0.329E-03	0.256E-03	0.125	−22.2	17.6
R. testis	1	0.329E-03	0.410E-03	0.110	24.6	16.6
Testes	2	0.658E-03	0.666E-03	0.083	1.2	14.9
Thymus	5	0.274E-05				
Thyroid	1	0.881E-06				
Uterus	10	0.217E-02	0.308E-02	0.040	41.9	13.0

[a]Absorbed fraction.

[b]Coefficient of variation.

[c]Calculated values with coefficients of variation greater than 20.0% are not included in the comparison.

Inspection of these tables indicates that, in general, the Monte Carlo estimates are greater than the experimental estimates. However, direct correlation between these estimates is hampered not only by experimental uncertainties but also by the statistical variance associated with the calculated estimates. Snyder[27] has indicated that the absorbed fraction estimates provided by the Monte Carlo calculation may vary about the calculated value by approximately twice the coefficient of variation. If one employs this criterion, the agreement between experiment and calculation appears acceptable. For example, in Table 8.1 the calculated absorbed fractions for the left and right kidneys are 0.149×10^{-3} and 0.183×10^{-3} respectively. The coefficient of variation for these estimates is approximately 14%. Since the kidneys are located symmetrically in relation to the bladder, one would expect that these two values would be essentially equal. Using the average value for kidneys and applying a factor equal to twice the coefficient of variation, one finds that the range of absorbed fractions, determined by an additional Monte Carlo calculation, might vary from 0.212×10^{-3} to 0.119×10^{-3}. A check of the experimental estimates for the kidneys shows that these estimates lie within the expected range of the calculated absorbed fractions.

27. W. S. Snyder, *Medical Radionuclides: Radiation Dose and Effects*, p. 33, USAEC Division of Technical Information, Oak Ridge, Tenn., 1970.

Table 8.3. Absorbed fractions for uniform cesium-137 source in stomach

Target organ	Number of measurements	Measured A.F.[a]	Calculated A.F.	C.V.[b] of calculation	Difference[c] (%)	C.V. of difference
L. adrenal	6	0.986E-04	0.123E-03	0.174	24.7	21.4
R. adrenal	6	0.348E-04	0.302E-04	0.380		
Adrenals	12	0.133E-03	0.154E-03	0.158	15.8	20.1
Bladder	7	0.238E-03	0.282E-03	<0.10		
GI(stomach)	0		0.109E-00	<0.02		
GI(ULI)	0		0.440E-02	<0.03		
GI(LLI)	0		0.125E-02	<0.06		
GI(SI)	0		0.812E-02	0.023		
Heart	12	0.201E-02	0.389E-02	0.033	93.5	12.8
L. kidney	18	0.235E-02	0.222E-02	0.043	−5.5	13.1
R. kidney	18	0.581E-03	0.685E-03	0.075	17.9	14.5
Kidneys	36	0.294E-02	0.290E-02	0.037	−1.4	12.9
Liver	40	0.013E-00	0.108E-01	0.020	−16.9	12.6
L. ovary	5	0.125E-04	0.240E-04	0.376		
R. ovary	5	0.707E-05				
Ovaries	10	0.195E-04	0.332E-04	0.312		
Pancreas	0		0.306E-02	0.037		
Spleen	0		0.517E-02	0.029		
L. testis	1	0.618E-05				
R. testis	1	0.562E-05				
Testes	2	0.118E-04				
Thymus	5	0.272E-04	0.558E-04	0.304		
Thyroid	1	0.618E-05				
Uterus	10	0.141E-03	0.183E-03	0.142	29.8	18.9

[a]Absorbed fraction.

[b]Coefficient of variation.

[c]Calculated values with coefficients of variation greater than 20.0% are not included in the comparison.

9. Absorbed Dose in Male Humanoid Phantoms from External Sources of Photons as a Function of Age

G. G. Warner[1] J. W. Poston W. S. Snyder

Various computer studies have been made at the Oak Ridge National Laboratory which have indicated that variations of dose exist among various aged humans when the sources of radiation were within the body. Hilyer[2-4] has reported on estimates of dose to infants and children from a photon emitter in the lungs and on estimates of dose to infants and children from the medical uses of ^{133}Xe.[5] It has been found that the dose from internal sources to internal organs has been greater for younger individuals, that the specific absorbed fraction of source energy decreases as age increases, and that the specific absorbed fraction decreases as energy increases.

We have now investigated the effect of age on absorbed dose and on specific absorbed fraction when six phantoms of various ages have been immersed in infinite external sources of photons. An IBM 360/91 computer was used for these studies. At each of 12 energies, 60,000 monoenergetic photons were initiated externally and allowed to impinge on the surface of each of the six phantoms which represented a newborn, a 1-year-old, a 5-year-old, a 10-year-old, a 15-year-old, and an adult. The adult phantom has been much publicized and is familiar to many people.[6] The younger phantoms were created by reducing the adult in similitude; that is, a coordinate point in the adult was transformed to a coordinate point in a younger phantom by factors separate for each coordinate axis. Loci which were nonintersecting in the adult were also nonintersecting in a younger phantom. Figure 9.1 shows the relative sizes of the various phantoms.

Data were taken in many internal organs, but interest in the gonads has prompted us to report here on the genitalia regions. Figure 9.2 shows part of the legs and the male genitalia of the adult phantom. Genitalia in the younger phantoms are similar. Data were taken on the testes separately, but generally the statistics were poor enough to cause suspicion of their reliability; therefore, data for the genitalia regions, which include the testes, were chosen. Figure 9.3 shows a comparison of testes data with genitalia data indicating errant testes data. Table 9.1 shows that the coefficients of variation for data on the testes are higher than coefficients of variation for data on the genitalia region.

Figure 9.4 shows the specific absorbed fraction of initial energy in the genitalia as a function of initial energy. The absorbed fractions decrease with increase in energy for all phantoms. The absorbed dose (Fig. 9.5), however, shows an increase in dose (rads/photon) with energy at initial energies above 0.100 MeV for all phantoms. Table 9.2 shows the absorbed dose for the genitalia regions of five younger phantoms normalized to the absorbed dose for the genitalia region of the adult. These data indicate how much more dose at each energy is obtained in the younger phantom than in an adult. For instance, depending on the energy, the dose to the newborn genitalia might be from $3\frac{1}{2}$ to 31 times the dose to the adult genitalia. These factors decrease as age increases. Indications are that for initial energies above 0.030 MeV, the normalized data are fairly constant; that is, above 0.030 MeV, for instance, the 1-year-old received 5.7 times as much dose as the adult; the 5-year-old received 3.2 times as much dose; the 10-year-old, 1.8 times as much; and the 15-year-old, 1.1 times as much. In Fig. 9.6, where the data from Table 9.3 are shown, the amount of energy absorbed in the genitalia is compared with that absorbed in the whole phantom. Again, because the data are fairly constant

1. Computer Sciences Division.
2. *Health Phys. Div. Annu. Progr. Rep. July 31, 1971*, ORNL-4720, p. 116.
3. *Health Phys. Div. Annu. Progr. Rep. July 31, 1972*, ORNL-4811, p. 91.
4. *Health Phys. Div. Annu. Progr. Rep. July 31, 1973*, ORNL-4903, p. 119.
5. "Health Physics in the Healing Arts," p. 131 in *Proceedings of the Health Physics Society Seventh Midyear Topical Symposium, San Juan, Puerto Rico, December 1972*, (FDA) 73-8029, March 1973.
6. G. G. Warner, "BRHGAM: A Medical X-Ray Dose Estimation Program," ORNL-TM-4393 (October 1973).

above 0.030 MeV of the energy absorbed in the whole body of each phantom, 0.13% was absorbed in the genitalia of the 1-year-old, 0.20% in the 5-year-old, 0.22% in the 10-year-old, and 0.26% in the 15-year-old.

Figures 9.7 and 9.8 show that both the specific absorbed fraction of initial energy in the genitalia and the absorbed dose in rads per photon in the genitalia vary inversely with age. Figure 9.8 does not show every energy; however, the lines for energies not shown do follow the pattern.

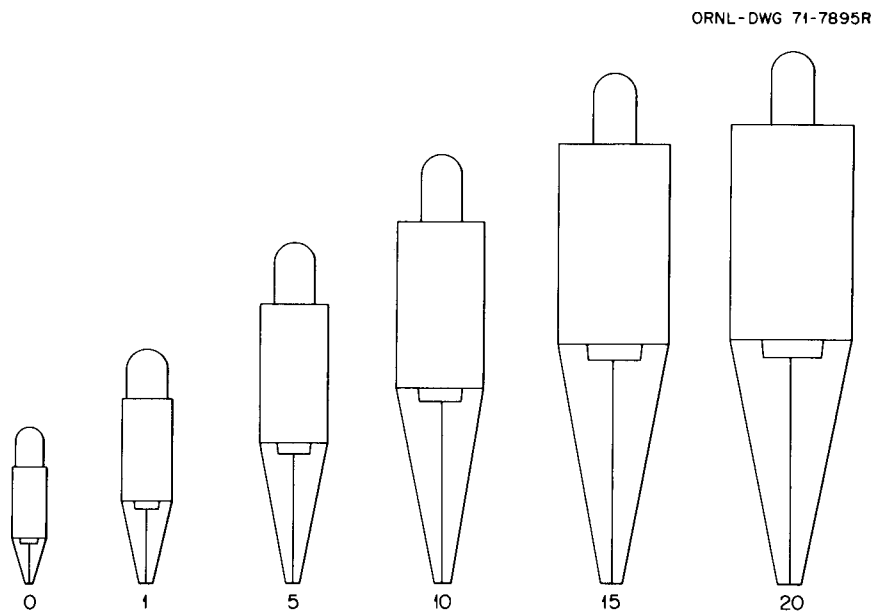

Fig. 9.1. Relative size of phantoms for 0, 1, 5, 10, 15, and 20 years.

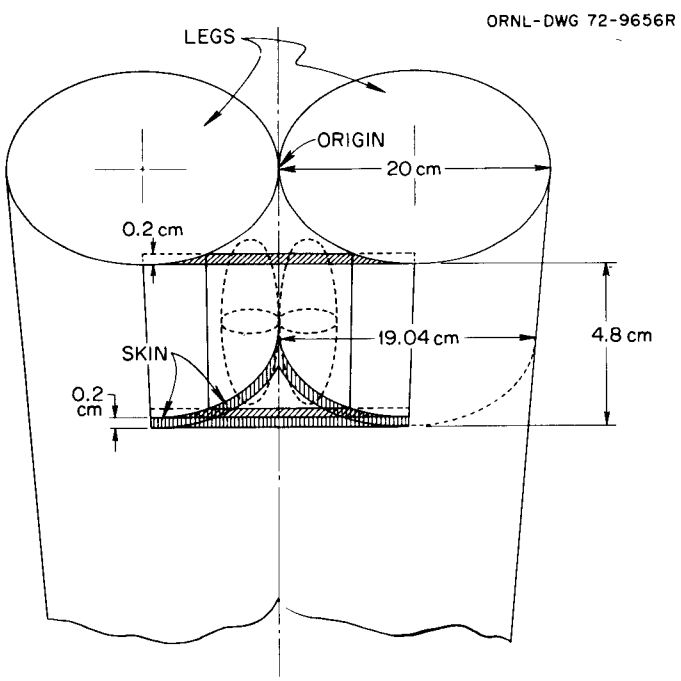

Fig. 9.2. Legs and male genitalia of phantom.

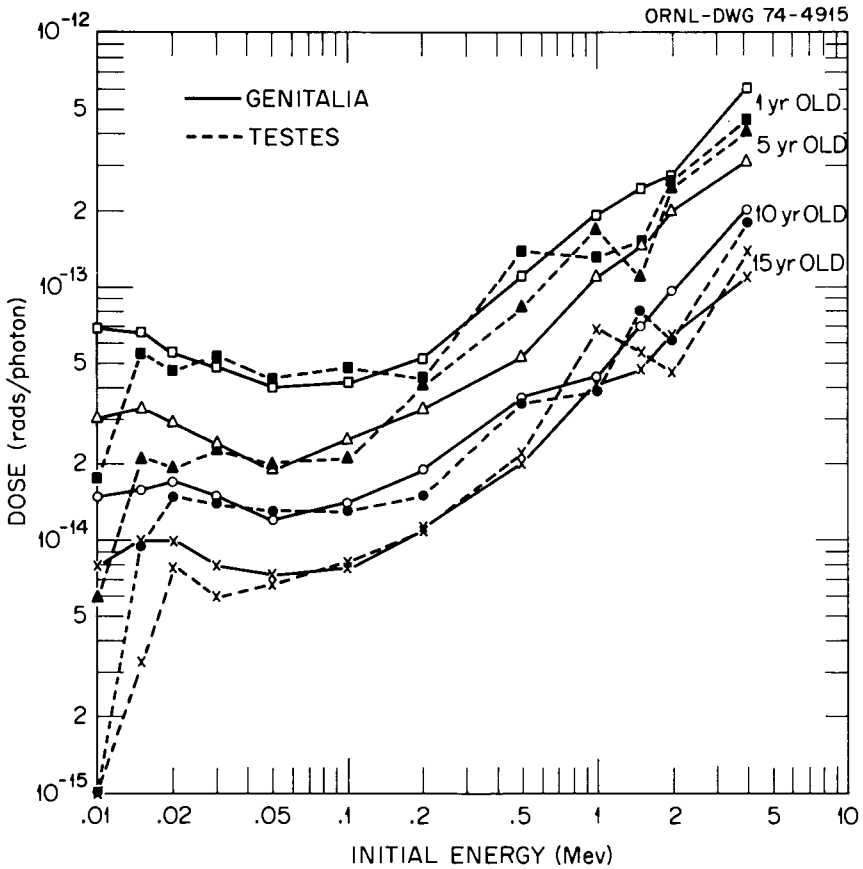

Fig. 9.3. Dose vs initial energy of 12 monoenergetic infinite external sources of photons.

Table 9.1. Ranges of coefficients of variation of dose from all ages according to initial energy of source

Initial energy (MeV)	Coefficient of variation (%) when target region is –	
	Testes	Genitalia
0.010	26–42	5–7
0.100	25–45	8–18
1.00	25–43	13–40

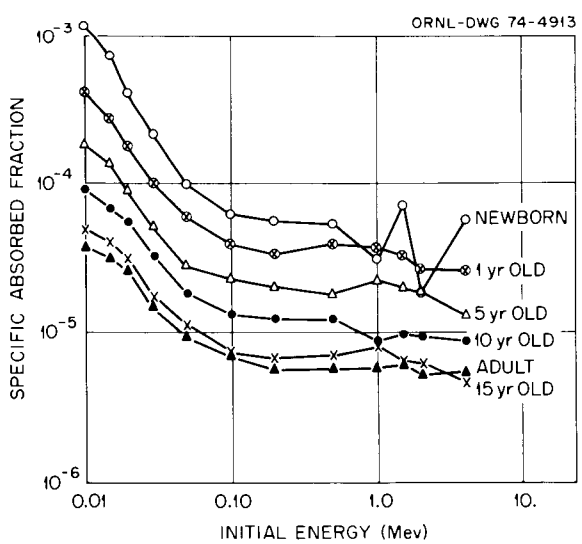

Fig. 9.4. Specific absorbed fraction of energy absorbed in genitalia as a function of initial energy for 12 monoenergetic infinite external sources of photons.

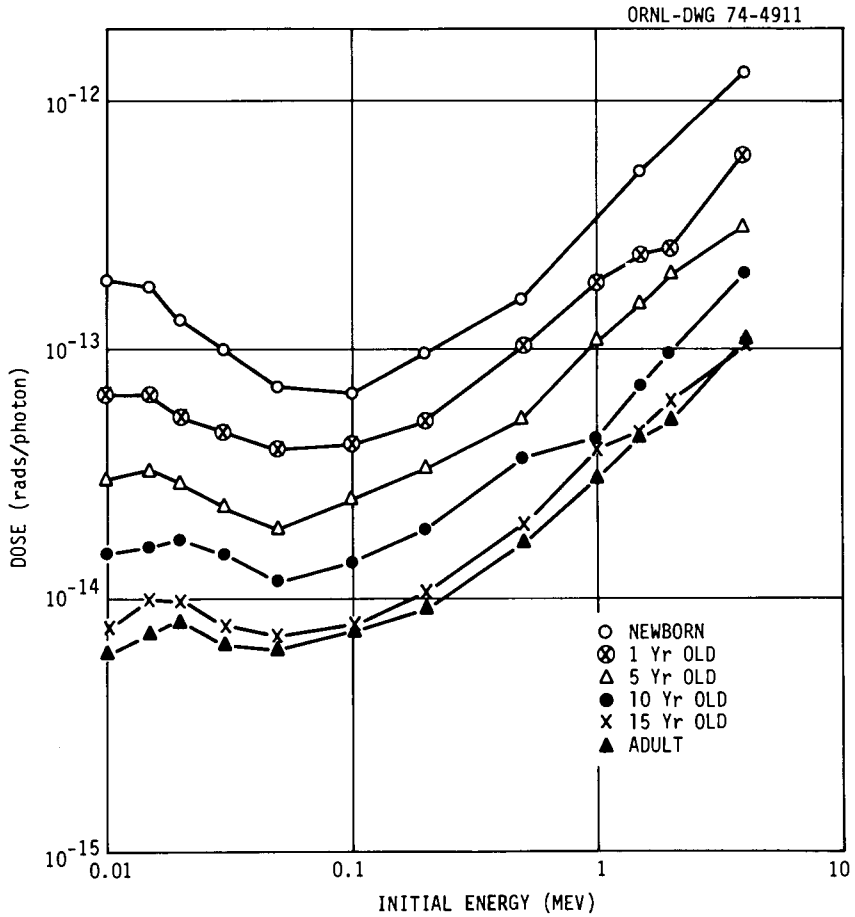

Fig. 9.5. Dose (rads/photon) in genitalia region as a function of initial energy of 12 monoenergetic infinite external sources of photons.

Table 9.2. Doses for genitalia of phantoms of all ages normalized to doses for adult genitalia at all initial energies

Initial energy (MeV)	Normalized dose				
	Newborn	1-year-old	5-year-old	10-year-old	15-year-old
0.010	31.0	11.0	4.9	2.5	1.3
0.015	24.0	9.1	4.5	2.2	1.3
0.020	16.0	6.8	3.6	2.1	1.2
0.030	15.0	7.2	3.6	2.2	1.2
0.050	11.0	6.2	2.9	1.8	1.1
0.10	8.9	5.6	3.3	1.9	1.0
0.20	9.8	5.6	3.5	2.0	1.2
0.50	9.4	6.5	3.1	2.1	1.2
1.0	5.0	6.3	3.7	1.5	1.4
1.5	12.0	5.3	3.3	1.6	1.0
2.0	3.5	5.0	3.8	1.8	1.2
4.0	11.0	5.0	2.6	1.7	0.92

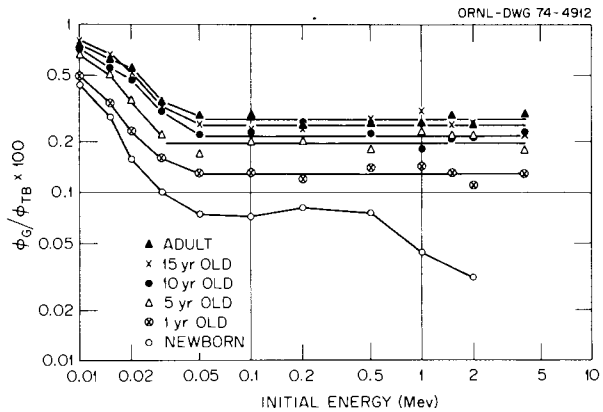

Fig. 9.6. Amount of energy absorbed in genitalia compared with amount of energy absorbed in total body from 12 monoenergetic infinite external sources of photons.

Table 9.3. Amount of energy absorbed in genitalia of phantoms as percent of amount of energy absorbed in total body for all phantoms at every initial energy

Initial energy (MeV)	Percent of absorbed energy absorbed in genitalia					
	Newborn	1-year-old	5-year-old	10-year-old	15-year-old	Adult
0.010	0.43	0.49	0.66	0.72	0.78	0.76
0.015	0.28	0.34	0.50	0.55	0.66	0.63
0.020	0.16	0.23	0.35	0.47	0.53	0.55
0.030	0.10	0.16	0.22	0.31	0.33	0.35
0.050	0.075	0.13	0.17	0.22	0.26	0.29
0.10	0.072	0.13	0.20	0.23	0.24	0.29
0.20	0.081	0.12	0.20	0.24	0.24	0.25
0.50	0.076	0.14	0.18	0.26	0.27	0.26
1.0	0.044	0.14	0.23	0.18	0.30	0.26
1.5	0.11	0.13	0.22	0.21	0.25	0.29
2.0	0.031	0.11	0.22	0.22	0.26	0.25
4.0	0.11	0.13	0.18	0.23	0.22	0.29

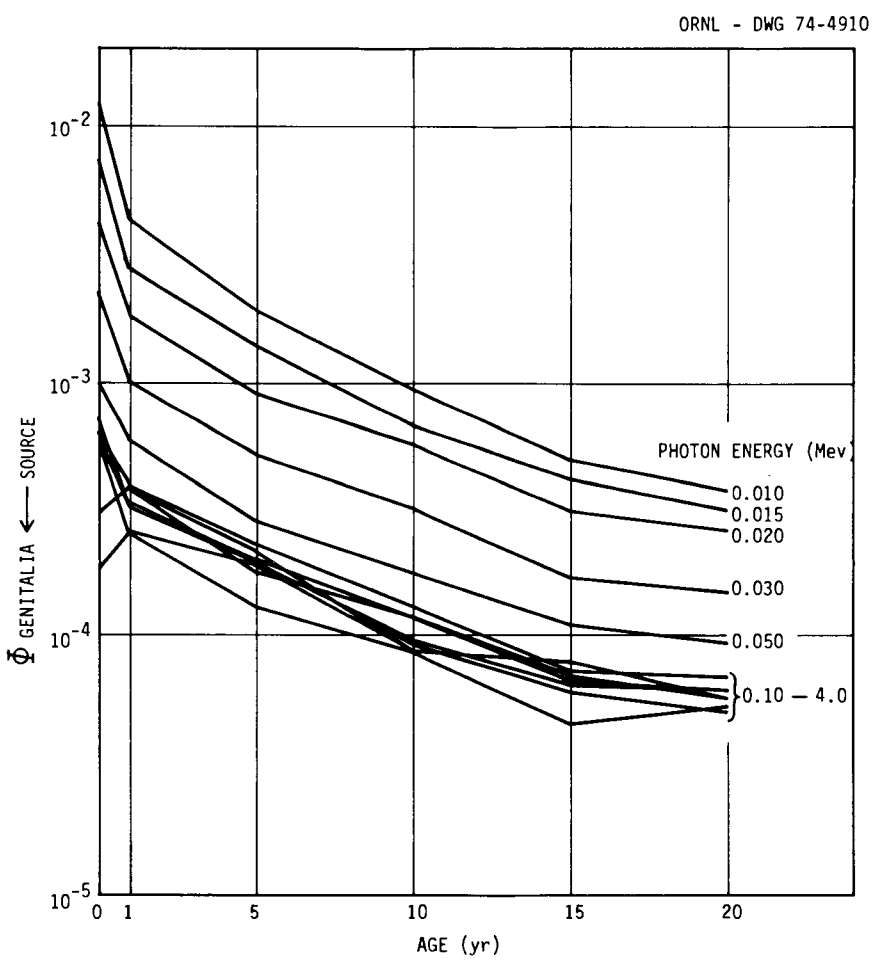

Fig. 9.7. Specific absorbed fraction of initial energy absorbed in genitalia region as a function of age (monoenergetic infinite external sources of photons).

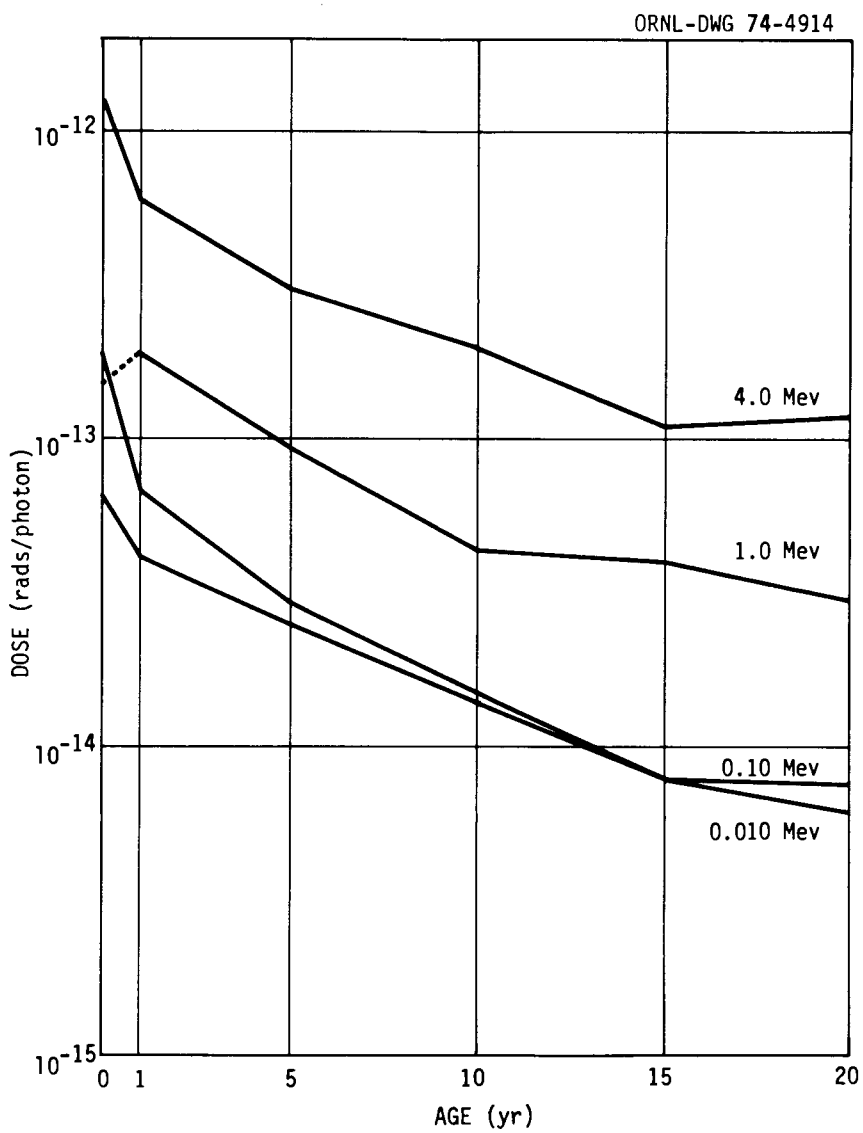

Fig. 9.8. Dose (rads/photon) in genitalia region as a function of age (monoenergetic infinite external sources of photons).

10. Generic Environmental Statement for Plutonium-238-Powered Cardiac Pacemakers

R. L. Shoup

For some patients suffering from certain forms of cardiac disease, the implantation of pacemakers with long-lived batteries appears to be desirable. It has now been several years since the development of pacemakers powered by radioisotopic batteries, which have a relatively long lifetime, theoretically, as compared with conventional devices in use up to the present time. Implantations of this type of pacemaker have been authorized in various countries and in the United States for essentially investigational purposes.[1]

Although it is desirable to increase the life of cardiac pacemakers to avoid the risks and drawbacks of repeated and frequent operations, it is not possible to determine the useful lifetime and the reliability of the different new types of devices without sufficient experience in their use. Such experience is required, in particular, to assess the merits of nuclear batteries as compared with other devices. Interim safety standards have been developed to enable this experience to be acquired with the necessary protection for the public.[1,2]

The implantation of plutonium-powered cardiac pacemakers is being restricted for the time being to a limited number of patients until an environmental statement has been completed. Data must be obtained to establish (1) that the general use of these pacemakers will not subject the public to undue risk and (2) that the incremental benefits to be derived from such pacemakers as compared with nonnuclear pacemakers will outweigh both the risk, however small, to the public and the social costs, including those of the necessary accountability and control measures. The salient parts of a generic environmental statement for the ^{238}Pu-powered cardiac pacemaker are presently being written for the U.S. Atomic Energy Commission. These include an incremental benefit assessment, a risk assessment, a benefit-risk balance, and the necessary protective measures. The generic environmental statement will be instrumental in solidifying the Commission's position on the use of these pacemakers and will support the necessary USAEC amendment changes, should wide-scale distribution of these pacemakers be authorized.

The publication of the draft environmental statement is scheduled for the end of summer, 1974; and, after a public comment period and resolution of comments, a final statement will be issued.

---

1. *Interim Radiation Protection Standards for the Design, Construction, Testing and Control of Radioisotopic Cardiac Pacemakers,* Organization for Economic Co-operation and Development/Nuclear Energy Agency, OECD/NEA Publication C(74)101, May 21, 1974.

2. *Interim Safety Guide for the Design and Testing of Nuclear Powered Cardiac Pacemakers,* Materials Branch, Directorate of Licensing, U.S. Atomic Energy Commission, March 1974.

11. Medical X-Ray Dose Estimation Program

J. W. Poston G. G. Warner[1]

In March 1972 the Section undertook a study to determine the feasibility of obtaining absorbed doses to internal organs of the body due to external sources of x-ray beams in the energy range 20 to 150 keV. This study was initiated as the result of an interagency agreement between the U.S. Atomic Energy Commission and the Food and Drug Administration (FDA). The primary objective of this research was the calculation of absorbed dose in several critical internal organs per unit surface radiation exposure for normally incident external x-ray beams. Organs of primary interest were the ovaries, testes, thyroid, lenses of the eyes, and the red bone marrow.

During the past year, work on this program has continued in the same manner as that described in ref. 2. Calculations for 4 X 4 cm beams incident on the front (anterior-posterior, AP) of the phantom were completed for monoenergetic photons of 30, 55, and 80 keV.[3] Several modifications were made to the existing phantom geometry, and a duplicate set of calculations for beams incident on the rear (posterior-anterior, PA) of the phantom were completed.[4] These data are presented in tabular form in Tables 11.1–11.3; Figs. 11.1–11.3 are to be used in conjunction with the tables.

Figure 11.1 and Table 11.1 will be discussed here to show how these data tables are to be used. Figure 11.1 is a plan view of the phantom used in the calculations. A grid network is shown on the right side of the phantom. The number in each block is the run number and corresponds to the point of incidence of the beam for that calculation. By selecting a beam location, the calculated absorbed dose to the organs of interest can be obtained by looking up the run number (given in the square) in the table of results. Presented in the table are the absorbed dose (rads/R) and the coefficient of variation for the thyroid gland, ovaries, testes, lenses of the eyes, and red bone marrow. These values represent the absorbed dose due to direct and/or scattered radiation delivered to the particular organ by a beam of photons impinging at the designated location.

Calculations for photons with an energy of 25 keV incident both AP and PA on the phantom are under way. Upon completion of these calculations, at least one more energy (probably 100 keV) will be selected for study before the data set will be complete.

Data from all these calculations are transmitted to the FDA in tabular form, as well as on magnetic tapes. The FDA is presently using these data to construct exposure situations of varying beam size and spectral distribution.

---

1. Computer Sciences Division.
2. W. S. Snyder and J. W. Poston, "Medical Physics and Internal Dosimetry," *Health Phys. Div. Annu. Progr. Rep. July 31, 1973,* ORNL-4903.
3. J. W. Poston and G. G. Warner, *Medical X-Ray Dose Estimation Program,* ORNL-TM-4217 (April 1973).
4. J. W. Poston and G. G. Warner, *Medical X-Ray Dose Estimation Program,* ORNL-TM-4429 (January 1974).

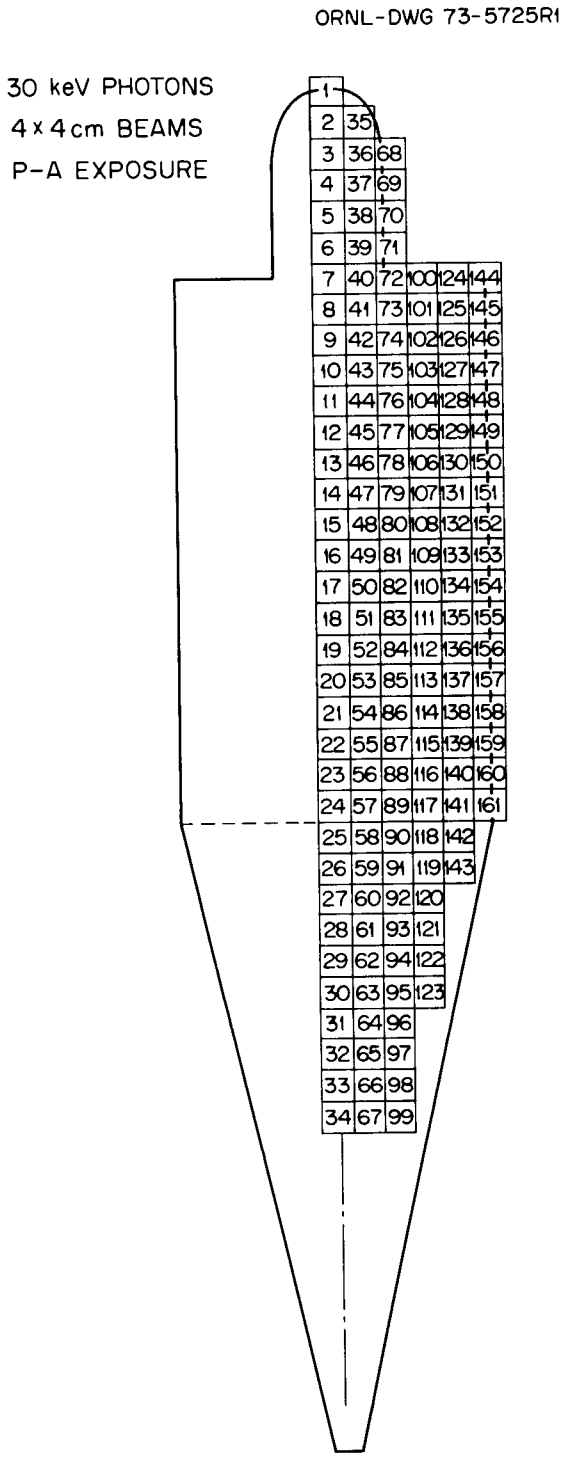

Fig. 11.1. Beam location diagram for calculations of absorbed dose due to 30-keV photons.

Table 11.1. Summary of calculated absorbed dose to organs of interest: 30-keV photons

Posterior/anterior exposure
4 × 4 cm beam
Note: 2.8E–05 read as 2.8×10^{-5} rads/R

Run number	Thyroid		Ovaries		Testes		Lens of eye		Red bone marrow	
	Dose (rads/R)	C. of var. (%)	Dose (rads/R)	C. of var. (%)	Dose (rads/R)	C. of var. (%)	Dose (rads/R)	C. of var. (%)	Dose (rads/R)	C. of var. (%)
1	0.0	0.0	0.0	0.0	0.0	0.0	7.9E–05	51.7	4.5E–03	0.8
2	1.1E–07	100.0	0.0	0.0	0.0	0.0	1.4E–04	25.8	7.6E–03	0.4
3	3.3E–09	100.0	0.0	0.0	0.0	0.0	3.8E–04	25.0	8.4E–03	0.4
4	0.0	0.0	0.0	0.0	0.0	0.0	1.9E–04	35.5	9.2E–03	0.4
5	1.8E–04	55.2	0.0	0.0	0.0	0.0	1.7E–05	96.4	7.3E–03	0.5
6	2.8E–04	57.5	0.0	0.0	0.0	0.0	5.7E–06	91.7	8.0E–03	0.5
7	1.1E–04	68.8	0.0	0.0	0.0	0.0	2.5E–07	100.0	8.0E–03	0.5
8	1.6E–06	68.0	0.0	0.0	0.0	0.0	4.0E–08	100.0	8.6E–03	0.4
9	1.3E–06	81.2	0.0	0.0	0.0	0.0	0.0	0.0	8.6E–03	0.4
10	0.0	0.0	0.0	0.0	0.0	0.0	0.0	0.0	8.5E–03	0.4
11	9.2E–08	100.0	0.0	0.0	0.0	0.0	0.0	0.0	8.6E–03	0.4
12	2.1E–06	100.0	0.0	0.0	0.0	0.0	0.0	0.0	8.4E–03	0.4
13	0.0	0.0	0.0	0.0	0.0	0.0	0.0	0.0	8.6E–03	0.4
14	0.0	0.0	0.0	0.0	0.0	0.0	0.0	0.0	8.5E–03	0.4
15	0.0	0.0	0.0	0.0	0.0	0.0	0.0	0.0	8.6E–03	0.4
16	0.0	0.0	1.0E–04	99.2	0.0	0.0	0.0	0.0	1.5E–02	0.5
17	0.0	0.0	6.2E–05	100.0	0.0	0.0	0.0	0.0	1.6E–02	0.5
18	0.0	0.0	2.1E–05	68.8	0.0	0.0	0.0	0.0	1.7E–02	0.5
19	0.0	0.0	3.2E–04	63.6	0.0	0.0	0.0	0.0	2.0E–02	0.4
20	0.0	0.0	2.0E–04	37.9	3.5E–06	100.0	0.0	0.0	2.4E–02	0.4
21	0.0	0.0	1.1E–03	26.5	2.3E–07	74.4	0.0	0.0	1.2E–02	0.7
22	0.0	0.0	8.7E–04	26.9	7.0E–05	49.4	0.0	0.0	5.5E–04	2.8
23	0.0	0.0	1.5E–04	40.6	1.4E–04	30.3	0.0	0.0	1.9E–04	4.4
24	0.0	0.0	6.8E–05	45.3	5.1E–04	19.8	0.0	0.0	1.1E–04	5.3
25	0.0	0.0	3.4E–05	77.3	2.6E–02	4.1	0.0	0.0	7.6E–05	6.0
26	0.0	0.0	0.0	0.0	4.5E–03	7.9	0.0	0.0	4.0E–05	5.6
27	0.0	0.0	0.0	0.0	1.1E–03	13.0	0.0	0.0	3.3E–05	4.0
28	0.0	0.0	0.0	0.0	6.1E–04	17.0	0.0	0.0	3.3E–05	2.7
29	0.0	0.0	0.0	0.0	3.3E–04	25.9	0.0	0.0	3.2E–05	2.7
30	0.0	0.0	0.0	0.0	1.3E–04	32.7	0.0	0.0	2.3E–05	3.0
31	0.0	0.0	0.0	0.0	1.0E–04	45.8	0.0	0.0	7.7E–06	4.9
32	0.0	0.0	0.0	0.0	4.5E–05	96.4	0.0	0.0	1.5E–06	10.7
33	0.0	0.0	0.0	0.0	1.3E–04	38.5	0.0	0.0	5.0E–07	18.5
34	0.0	0.0	0.0	0.0	0.0	0.0	0.0	0.0	7.7E–08	37.4
35	1.1E–08	100.0	0.0	0.0	0.0	0.0	2.6E–04	24.2	8.1E–03	0.4
36	0.0	0.0	0.0	0.0	0.0	0.0	8.6E–04	19.2	9.8E–03	0.3
37	3.0E–05	78.6	0.0	0.0	0.0	0.0	5.6E–04	26.3	8.5E–03	0.4
38	3.9E–04	31.5	0.0	0.0	0.0	0.0	6.5E–05	55.2	2.2E–03	1.0
39	1.1E–03	18.7	0.0	0.0	0.0	0.0	1.1E–05	77.2	1.0E–03	1.4
40	9.6E–04	18.4	0.0	0.0	0.0	0.0	1.4E–05	74.7	9.2E–04	1.5
41	1.4E–04	37.4	0.0	0.0	0.0	0.0	2.7E–09	100.0	2.5E–03	0.8
42	5.5E–05	58.9	0.0	0.0	0.0	0.0	9.3E–09	71.9	2.8E–03	0.7
43	7.9E–05	91.0	0.0	0.0	0.0	0.0	0.0	0.0	2.3E–03	0.8
44	1.4E–05	95.1	0.0	0.0	0.0	0.0	0.0	0.0	3.1E–03	0.7
45	0.0	0.0	0.0	0.0	0.0	0.0	0.0	0.0	2.3E–03	0.8
46	0.0	0.0	0.0	0.0	0.0	0.0	0.0	0.0	2.9E–03	0.7
47	0.0	0.0	0.0	0.0	0.0	0.0	0.0	0.0	2.6E–03	0.8
48	0.0	0.0	0.0	0.0	0.0	0.0	0.0	0.0	2.6E–03	0.8
49	0.0	0.0	3.0E–08	88.3	0.0	0.0	0.0	0.0	2.2E–03	1.2
50	0.0	0.0	1.6E–05	67.5	0.0	0.0	0.0	0.0	1.7E–03	1.6
51	0.0	0.0	1.4E–04	73.6	1.3E–06	100.0	0.0	0.0	1.9E–03	1.5
52	0.0	0.0	5.4E–04	39.7	0.0	0.0	0.0	0.0	1.2E–02	0.7

Table 11.1 (continued)

Run number	Thyroid		Ovaries		Testes		Lens of eye		Red bone marrow	
	Dose (rads/R)	C. of var. (%)	Dose (rads/R)	C. of var. (%)	Dose (rads/R)	C. of var. (%)	Dose (rads/R)	C. of var. (%)	Dose (rads/R)	C. of var. (%)
53	0.0	0.0	1.3E−03	27.1	0.0	0.0	0.0	0.0	2.1E−02	0.4
54	0.0	0.0	7.8E−03	12.3	0.0	0.0	0.0	0.0	1.1E−02	0.8
55	0.0	0.0	1.8E−03	18.1	3.8E−05	62.8	0.0	0.0	7.7E−04	2.4
56	0.0	0.0	7.0E−04	34.2	1.4E−04	33.9	0.0	0.0	4.7E−04	3.0
57	0.0	0.0	2.2E−04	54.4	3.8E−04	23.5	0.0	0.0	3.4E−04	3.5
58	0.0	0.0	9.3E−08	100.0	1.8E−03	11.7	0.0	0.0	1.8E−04	4.3
59	0.0	0.0	4.6E−08	100.0	8.2E−04	17.0	0.0	0.0	8.5E−05	4.2
60	0.0	0.0	0.0	0.0	4.2E−04	23.2	0.0	0.0	7.8E−05	2.9
61	0.0	0.0	0.0	0.0	1.9E−04	28.4	0.0	0.0	9.0E−05	1.9
62	0.0	0.0	0.0	0.0	5.3E−05	56.8	0.0	0.0	1.1E−04	1.7
63	0.0	0.0	0.0	0.0	3.8E−05	47.1	0.0	0.0	9.1E−05	1.9
64	0.0	0.0	0.0	0.0	1.4E−05	98.6	0.0	0.0	9.8E−06	6.0
65	0.0	0.0	0.0	0.0	7.0E−06	82.3	0.0	0.0	1.8E−06	23.5
66	0.0	0.0	0.0	0.0	1.1E−05	79.8	0.0	0.0	2.4E−07	39.6
67	0.0	0.0	0.0	0.0	0.0	0.0	0.0	0.0	1.3E−07	30.8
68	1.0E−04	54.1	0.0	0.0	0.0	0.0	8.8E−04	16.5	1.9E−03	1.3
69	1.4E−04	40.1	0.0	0.0	0.0	0.0	8.0E−04	16.1	8.1E−04	1.9
70	6.1E−04	23.3	0.0	0.0	0.0	0.0	3.2E−04	29.2	1.7E−04	3.2
71	1.1E−03	17.4	0.0	0.0	0.0	0.0	2.3E−04	29.6	1.1E−04	4.2
72	3.0E−04	29.6	0.0	0.0	0.0	0.0	1.6E−05	83.3	2.5E−04	2.8
73	6.0E−05	45.3	0.0	0.0	0.0	0.0	1.0E−05	99.4	2.0E−03	0.9
74	9.4E−05	51.2	0.0	0.0	0.0	0.0	4.6E−07	100.0	2.4E−03	0.8
75	4.4E−05	61.2	0.0	0.0	0.0	0.0	1.9E−06	85.2	1.9E−03	0.9
76	1.5E−05	98.0	0.0	0.0	0.0	0.0	0.0	0.0	2.7E−03	0.7
77	1.4E−08	100.0	0.0	0.0	0.0	0.0	0.0	0.0	1.8E−03	0.9
78	0.0	0.0	0.0	0.0	0.0	0.0	0.0	0.0	2.4E−03	0.8
79	0.0	0.0	0.0	0.0	0.0	0.0	0.0	0.0	2.0E−03	0.9
80	0.0	0.0	0.0	0.0	0.0	0.0	0.0	0.0	2.0E−03	0.9
81	0.0	0.0	1.9E−07	93.0	0.0	0.0	0.0	0.0	1.0E−03	1.5
82	0.0	0.0	1.4E−07	72.8	0.0	0.0	0.0	0.0	2.9E−04	3.5
83	0.0	0.0	1.4E−04	63.3	0.0	0.0	0.0	0.0	5.7E−04	2.7
84	0.0	0.0	3.7E−04	42.8	0.0	0.0	0.0	0.0	7.6E−03	1.0
85	0.0	0.0	1.2E−03	31.4	6.2E−06	100.0	0.0	0.0	1.4E−02	0.6
86	0.0	0.0	8.4E−03	13.3	1.1E−05	73.1	0.0	0.0	1.0E−02	0.8
87	0.0	0.0	1.6E−03	21.9	4.9E−06	56.0	0.0	0.0	6.4E−03	1.1
88	0.0	0.0	3.5E−04	45.3	3.5E−05	48.8	0.0	0.0	6.2E−03	1.1
89	0.0	0.0	9.1E−06	84.1	1.1E−04	35.9	0.0	0.0	5.8E−03	1.2
90	0.0	0.0	0.0	0.0	7.7E−05	41.7	0.0	0.0	5.6E−04	2.3
91	0.0	0.0	0.0	0.0	2.9E−05	43.0	0.0	0.0	3.1E−04	1.5
92	0.0	0.0	0.0	0.0	1.9E−05	69.1	0.0	0.0	3.2E−04	1.1
93	0.0	0.0	0.0	0.0	4.4E−06	82.0	0.0	0.0	3.4E−04	1.1
94	0.0	0.0	0.0	0.0	1.2E−05	71.2	0.0	0.0	3.6E−04	1.0
95	0.0	0.0	0.0	0.0	1.5E−05	99.5	0.0	0.0	2.7E−04	1.2
96	0.0	0.0	0.0	0.0	4.1E−09	84.8	0.0	0.0	9.4E−06	4.8
97	0.0	0.0	0.0	0.0	0.0	0.0	0.0	0.0	1.1E−06	13.5
98	0.0	0.0	0.0	0.0	0.0	0.0	0.0	0.0	1.1E−07	29.4
99	0.0	0.0	0.0	0.0	0.0	0.0	0.0	0.0	9.2E−09	68.4
100	4.7E−04	27.0	0.0	0.0	0.0	0.0	4.7E−05	44.5	3.4E−04	2.7
101	3.3E−05	55.9	0.0	0.0	0.0	0.0	6.2E−05	50.8	6.5E−03	0.5
102	2.5E−06	66.8	0.0	0.0	0.0	0.0	0.0	0.0	7.8E−03	0.4
103	4.4E−08	90.5	0.0	0.0	0.0	0.0	2.7E−07	100.0	7.5E−03	0.5
104	1.0E−07	86.9	0.0	0.0	0.0	0.0	0.0	0.0	8.0E−03	0.4
105	0.0	0.0	0.0	0.0	0.0	0.0	0.0	0.0	3.5E−03	0.8
106	0.0	0.0	0.0	0.0	0.0	0.0	0.0	0.0	2.2E−03	0.9
107	1.4E−07	100.0	0.0	0.0	0.0	0.0	0.0	0.0	1.8E−03	1.0
108	1.3E−07	100.0	1.8E−09	100.0	0.0	0.0	0.0	0.0	1.8E−03	1.0

Table 11.1 (continued)

Run number	Thyroid		Ovaries		Testes		Lens of eye		Red bone marrow	
	Dose (rads/R)	C. of var. (%)	Dose (rads/R)	C. of var. (%)	Dose (rads/R)	C. of var. (%)	Dose (rads/R)	C. of var. (%)	Dose (rads/R)	C. of var. (%)
109	0.0	0.0	5.0E–07	100.0	0.0	0.0	0.0	0.0	8.7E–04	1.5
110	0.0	0.0	1.3E–06	90.2	0.0	0.0	0.0	0.0	9.8E–05	5.4
111	0.0	0.0	3.6E–05	100.0	5.9E–09	100.0	0.0	0.0	2.9E–04	3.8
112	0.0	0.0	7.4E–05	57.9	0.0	0.0	0.0	0.0	2.3E–03	1.8
113	0.0	0.0	4.4E–04	42.2	0.0	0.0	0.0	0.0	4.2E–03	1.3
114	0.0	0.0	5.3E–04	32.3	2.3E–07	100.0	0.0	0.0	4.3E–03	1.3
115	0.0	0.0	1.9E–04	50.0	4.1E–07	99.5	0.0	0.0	4.1E–03	1.3
116	0.0	0.0	0.0	0.0	1.3E–05	73.0	0.0	0.0	4.1E–03	1.3
117	0.0	0.0	4.5E–06	97.5	1.1E–05	70.6	0.0	0.0	3.7E–03	1.4
118	0.0	0.0	9.3E–07	100.0	3.2E–06	95.0	0.0	0.0	4.9E–04	2.4
119	0.0	0.0	0.0	0.0	1.8E–05	99.8	0.0	0.0	2.4E–04	2.0
120	0.0	0.0	0.0	0.0	8.7E–06	55.1	0.0	0.0	1.9E–04	1.6
121	0.0	0.0	0.0	0.0	7.1E–07	100.0	0.0	0.0	1.7E–04	1.5
122	0.0	0.0	0.0	0.0	4.5E–06	91.0	0.0	0.0	1.3E–04	1.6
123	0.0	0.0	0.0	0.0	3.3E–06	90.6	0.0	0.0	7.3E–05	2.0
124	9.3E–05	40.1	0.0	0.0	0.0	0.0	1.5E–04	40.7	3.9E–04	2.1
125	6.8E–06	68.5	0.0	0.0	0.0	0.0	2.6E–05	48.1	6.3E–03	0.5
126	2.9E–05	84.5	0.0	0.0	0.0	0.0	0.0	0.0	7.5E–03	0.5
127	5.4E–07	93.5	0.0	0.0	0.0	0.0	6.7E–07	72.7	7.3E–03	0.5
128	2.9E–07	100.0	0.0	0.0	0.0	0.0	0.0	0.0	7.4E–03	0.5
129	0.0	0.0	0.0	0.0	0.0	0.0	0.0	0.0	3.0E–03	0.9
130	0.0	0.0	0.0	0.0	0.0	0.0	8.0E–06	99.8	1.6E–03	1.0
131	0.0	0.0	0.0	0.0	0.0	0.0	0.0	0.0	1.4E–03	1.1
132	0.0	0.0	0.0	0.0	0.0	0.0	0.0	0.0	1.4E–03	1.1
133	0.0	0.0	0.0	0.0	0.0	0.0	0.0	0.0	6.6E–04	1.7
134	0.0	0.0	1.2E–05	100.0	0.0	0.0	0.0	0.0	4.6E–05	6.8
135	0.0	0.0	4.8E–06	73.7	0.0	0.0	0.0	0.0	1.1E–04	6.2
136	0.0	0.0	1.1E–04	97.4	0.0	0.0	0.0	0.0	3.3E–04	3.6
137	0.0	0.0	3.0E–05	53.4	0.0	0.0	0.0	0.0	5.4E–04	2.9
138	0.0	0.0	6.9E–05	58.2	2.5E–07	100.0	0.0	0.0	5.8E–04	2.7
139	0.0	0.0	1.6E–04	64.2	3.2E–06	98.6	0.0	0.0	6.0E–04	2.7
140	0.0	0.0	2.3E–05	83.3	0.0	0.0	0.0	0.0	5.8E–04	2.7
141	0.0	0.0	0.0	0.0	4.0E–07	97.1	0.0	0.0	4.5E–04	3.1
142	0.0	0.0	0.0	0.0	2.3E–06	98.9	0.0	0.0	1.5E–04	4.8
143	0.0	0.0	0.0	0.0	4.6E–05	61.8	0.0	0.0	5.3E–05	4.6
144	6.4E–05	63.4	0.0	0.0	0.0	0.0	1.3E–04	41.0	3.6E–04	1.6
145	1.2E–06	76.2	0.0	0.0	0.0	0.0	5.3E–05	57.5	1.2E–03	0.8
146	1.8E–06	85.0	0.0	0.0	0.0	0.0	3.5E–06	89.6	1.2E–03	0.8
147	0.0	0.0	0.0	0.0	0.0	0.0	0.0	0.0	1.2E–03	0.8
148	0.0	0.0	0.0	0.0	0.0	0.0	0.0	0.0	1.0E–03	0.9
149	0.0	0.0	0.0	0.0	0.0	0.0	2.5E–05	100.0	6.6E–05	4.1
150	0.0	0.0	0.0	0.0	0.0	0.0	0.0	0.0	5.2E–05	4.4
151	0.0	0.0	0.0	0.0	0.0	0.0	0.0	0.0	5.1E–05	4.5
152	0.0	0.0	0.0	0.0	0.0	0.0	0.0	0.0	5.2E–05	4.6
153	0.0	0.0	0.0	0.0	0.0	0.0	0.0	0.0	2.8E–05	6.6
154	0.0	0.0	0.0	0.0	3.8E–08	100.0	0.0	0.0	1.2E–05	13.7
155	0.0	0.0	0.0	0.0	0.0	0.0	0.0	0.0	1.2E–05	14.4
156	0.0	0.0	3.0E–06	100.0	0.0	0.0	0.0	0.0	3.0E–05	10.8
157	0.0	0.0	3.3E–07	100.0	0.0	0.0	0.0	0.0	5.0E–05	8.8
158	0.0	0.0	4.5E–06	73.8	0.0	0.0	0.0	0.0	6.0E–05	7.8
159	0.0	0.0	0.0	0.0	2.4E–08	100.0	0.0	0.0	5.9E–05	8.1
160	0.0	0.0	0.0	0.0	3.1E–08	97.4	0.0	0.0	5.7E–05	8.0
161	0.0	0.0	9.9E–09	100.0	1.5E–08	100.0	0.0	0.0	4.3E–05	9.1

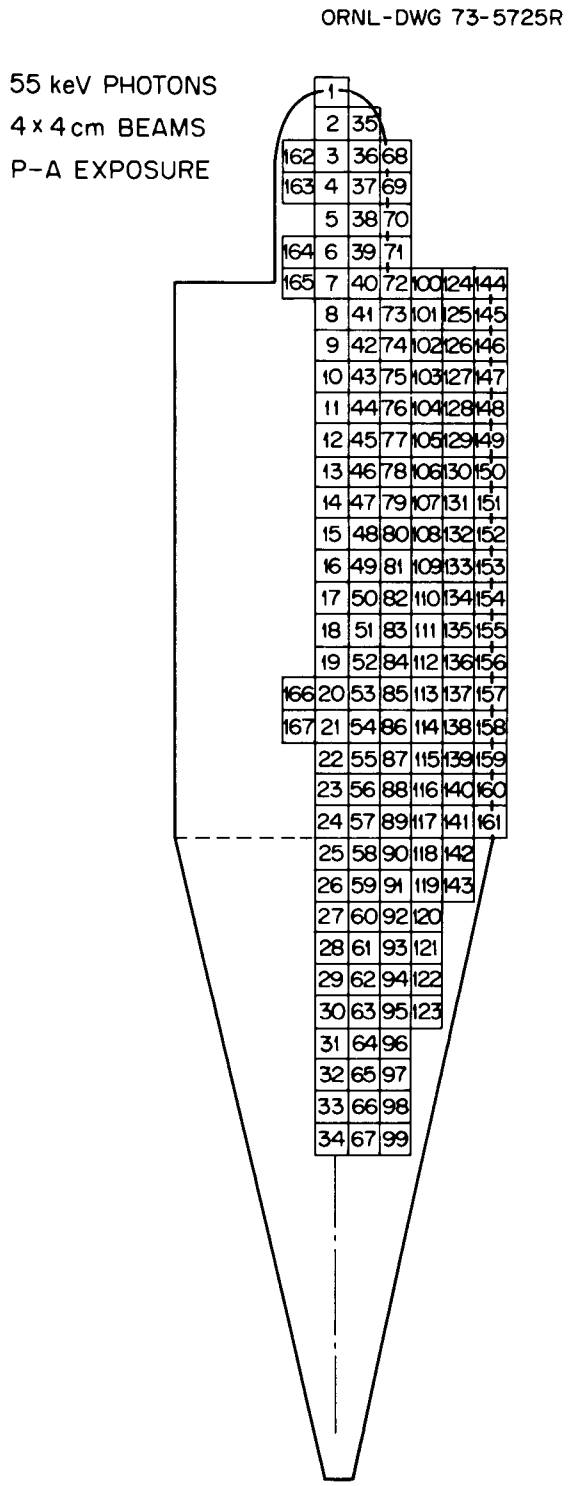

Fig. 11.2. Beam location diagram for calculations of absorbed dose due to 55-keV photons.

Table 11.2. Summary of calculated absorbed dose to organs of interest: 55-keV photons

Posterior/anterior exposure
4 × 4 cm beam
Note: 2.8E−05 read as 2.8×10^{-5} rads/R

Run number	Thyroid		Ovaries		Testes		Lens of eye		Red bone marrow	
	Dose (rads/R)	C. of var. (%)	Dose (rads/R)	C. of var. (%)	Dose (rads/R)	C. of var. (%)	Dose (rads/R)	C. of var. (%)	Dose (rads/R)	C. of var. (%)
1	3.1E−05	70.8	0.0	0.0	0.0	0.0	9.7E−04	20.6	1.0E−02	0.9
2	3.7E−04	53.0	0.0	0.0	0.0	0.0	5.0E−03	10.3	1.4E−02	0.7
3	5.3E−04	42.3	0.0	0.0	0.0	0.0	1.1E−02	7.5	1.7E−02	0.6
4	7.7E−04	31.7	0.0	0.0	0.0	0.0	9.2E−03	7.8	2.7E−02	0.4
5	2.8E−03	17.9	0.0	0.0	0.0	0.0	1.9E−03	15.0	2.9E−02	0.5
6	2.2E−02	8.9	0.0	0.0	0.0	0.0	8.3E−04	28.6	2.8E−02	0.5
7	2.0E−02	8.8	0.0	0.0	0.0	0.0	1.2E−04	38.6	2.8E−02	0.5
8	5.1E−03	14.3	0.0	0.0	0.0	0.0	3.9E−05	53.0	2.9E−02	0.5
9	1.9E−03	25.4	0.0	0.0	0.0	0.0	5.9E−05	59.3	2.9E−02	0.5
10	7.8E−04	30.6	0.0	0.0	0.0	0.0	3.3E−05	76.5	2.9E−02	0.5
11	5.1E−04	56.8	0.0	0.0	0.0	0.0	8.5E−05	58.2	2.9E−02	0.5
12	1.8E−04	50.3	0.0	0.0	0.0	0.0	2.0E−05	100.0	2.9E−02	0.5
13	1.5E−04	70.1	0.0	0.0	0.0	0.0	0.0	0.0	2.9E−02	0.5
14	0.0	0.0	1.0E−04	100.0	0.0	0.0	1.2E−05	75.6	2.9E−02	0.5
15	2.5E−07	100.0	0.0	0.0	0.0	0.0	0.0	0.0	3.0E−02	0.5
16	5.7E−05	100.0	2.7E−04	57.6	1.3E−06	100.0	0.0	0.0	4.9E−02	0.5
17	0.0	0.0	1.0E−03	30.1	7.3E−07	75.7	0.0	0.0	5.6E−02	0.5
18	7.3E−06	100.0	2.5E−03	25.6	7.4E−05	55.6	0.0	0.0	5.8E−02	0.5
19	0.0	0.0	6.7E−03	17.3	9.1E−05	57.0	0.0	0.0	5.6E−02	0.5
20	0.0	0.0	1.3E−02	12.9	2.7E−04	33.0	0.0	0.0	5.2E−02	0.6
21	0.0	0.0	2.0E−02	12.2	5.7E−04	25.1	0.0	0.0	3.0E−02	0.8
22	0.0	0.0	1.1E−02	14.6	1.7E−03	18.5	0.0	0.0	7.1E−03	1.7
23	0.0	0.0	5.3E−03	19.5	3.7E−03	12.7	0.0	0.0	4.4E−03	2.0
24	0.0	0.0	3.9E−03	22.9	8.4E−03	9.1	0.0	0.0	3.0E−03	2.5
25	0.0	0.0	1.8E−03	37.7	1.3E−01	2.6	0.0	0.0	2.0E−03	2.7
26	0.0	0.0	3.7E−04	60.9	2.5E−02	5.7	0.0	0.0	1.1E−03	3.2
27	0.0	0.0	7.5E−05	98.7	8.2E−03	9.5	0.0	0.0	7.7E−04	3.3
28	0.0	0.0	0.0	0.0	5.3E−03	11.4	0.0	0.0	5.9E−04	2.8
29	0.0	0.0	3.8E−07	100.0	2.4E−03	16.9	0.0	0.0	4.7E−04	2.5
30	0.0	0.0	0.0	0.0	1.3E−03	23.6	0.0	0.0	3.1E−04	2.5
31	0.0	0.0	0.0	0.0	5.4E−04	28.2	0.0	0.0	1.4E−04	4.1
32	0.0	0.0	0.0	0.0	3.0E−04	44.9	0.0	0.0	6.0E−05	6.5
33	0.0	0.0	0.0	0.0	1.5E−04	49.3	0.0	0.0	2.6E−05	14.6
34	0.0	0.0	0.0	0.0	1.9E−04	60.5	0.0	0.0	1.0E−05	22.2
35	1.3E−04	58.7	0.0	0.0	0.0	0.0	4.0E−03	11.2	1.7E−02	0.6
36	3.8E−04	39.7	0.0	0.0	0.0	0.0	1.8E−02	6.1	2.1E−02	0.5
37	1.8E−03	28.4	0.0	0.0	0.0	0.0	1.8E−02	6.1	2.7E−02	0.4
38	8.2E−03	12.8	0.0	0.0	0.0	0.0	3.5E−03	12.2	1.2E−02	0.9
39	1.3E−02	9.4	0.0	0.0	0.0	0.0	1.4E−03	19.1	7.0E−03	1.2
40	1.4E−02	10.4	0.0	0.0	0.0	0.0	5.9E−04	27.2	6.7E−03	1.2
41	6.5E−03	14.2	0.0	0.0	0.0	0.0	1.3E−04	49.6	8.9E−03	0.9
42	2.2E−03	21.1	3.0E−07	100.0	0.0	0.0	5.2E−05	72.5	9.3E−03	0.9
43	1.1E−03	33.1	0.0	0.0	0.0	0.0	6.7E−05	89.0	8.9E−03	0.9
44	6.4E−04	36.0	0.0	0.0	0.0	0.0	7.1E−07	87.9	9.6E−03	0.9
45	6.2E−05	72.8	7.9E−07	100.0	0.0	0.0	3.7E−05	100.0	8.7E−03	0.9
46	2.0E−05	76.2	0.0	0.0	0.0	0.0	0.0	0.0	9.3E−03	0.9
47	0.0	0.0	5.6E−05	99.8	0.0	0.0	0.0	0.0	9.0E−03	1.0
48	9.9E−06	100.0	1.5E−04	60.1	0.0	0.0	0.0	0.0	9.7E−03	1.0
49	0.0	0.0	1.9E−04	67.7	1.1E−08	100.0	0.0	0.0	1.1E−02	1.2
50	1.5E−06	100.0	1.3E−03	42.6	8.3E−07	100.0	0.0	0.0	1.2E−02	1.3
51	0.0	0.0	5.3E−03	19.9	8.8E−05	64.8	0.0	0.0	1.4E−02	1.2
52	0.0	0.0	7.4E−03	16.7	9.2E−05	65.4	0.0	0.0	3.3E−02	0.8

Table 11.2 (continued)

Run number	Thyroid		Ovaries		Testes		Lens of eye		Red bone marrow	
	Dose (rads/R)	C. of var. (%)	Dose (rads/R)	C. of var. (%)	Dose (rads/R)	C. of var. (%)	Dose (rads/R)	C. of var. (%)	Dose (rads/R)	C. of var. (%)
53	0.0	0.0	2.5E−02	9.8	3.4E−04	36.2	0.0	0.0	5.0E−02	0.6
54	0.0	0.0	5.7E−02	7.4	1.1E−03	27.0	0.0	0.0	3.0E−02	0.9
55	0.0	0.0	1.7E−02	12.1	1.2E−03	20.5	0.0	0.0	8.5E−03	1.5
56	0.0	0.0	6.6E−03	20.1	2.7E−03	15.7	0.0	0.0	6.1E−03	1.8
57	0.0	0.0	3.0E−03	26.4	6.9E−03	10.1	0.0	0.0	4.2E−03	2.1
58	0.0	0.0	7.4E−04	42.3	2.4E−02	5.8	0.0	0.0	2.7E−03	2.4
59	0.0	0.0	6.1E−04	48.1	1.0E−02	8.7	0.0	0.0	1.5E−03	2.6
60	0.0	0.0	7.0E−05	99.6	5.2E−03	11.3	0.0	0.0	1.1E−03	2.4
61	0.0	0.0	0.0	0.0	2.9E−03	16.4	0.0	0.0	9.6E−04	1.8
62	0.0	0.0	1.7E−05	100.0	2.2E−03	16.9	0.0	0.0	9.4E−04	1.6
63	0.0	0.0	0.0	0.0	5.2E−04	30.0	0.0	0.0	6.6E−04	1.7
64	0.0	0.0	0.0	0.0	5.4E−04	31.5	0.0	0.0	1.9E−04	3.2
65	0.0	0.0	0.0	0.0	4.1E−04	42.8	0.0	0.0	6.5E−05	5.4
66	0.0	0.0	0.0	0.0	2.0E−04	63.4	0.0	0.0	2.1E−05	10.5
67	0.0	0.0	0.0	0.0	7.1E−05	93.1	0.0	0.0	8.4E−06	10.6
68	5.3E−04	48.4	0.0	0.0	0.0	0.0	3.3E−03	13.9	5.2E−03	1.4
69	1.7E−03	24.6	0.0	0.0	0.0	0.0	4.1E−03	12.2	2.7E−03	2.0
70	3.7E−03	17.7	0.0	0.0	0.0	0.0	1.2E−03	19.6	1.1E−03	2.9
71	3.9E−03	19.3	0.0	0.0	0.0	0.0	4.9E−04	37.8	8.8E−04	3.3
72	4.3E−03	15.6	0.0	0.0	0.0	0.0	5.0E−04	31.1	2.4E−03	2.0
73	4.7E−03	17.0	0.0	0.0	0.0	0.0	3.0E−04	41.2	5.9E−03	1.1
74	2.1E−03	22.4	0.0	0.0	0.0	0.0	2.0E−04	65.7	6.5E−03	1.0
75	6.9E−04	31.1	0.0	0.0	0.0	0.0	6.3E−05	76.7	5.8E−03	1.1
76	3.9E−04	37.0	0.0	0.0	0.0	0.0	3.8E−05	79.1	6.5E−03	1.0
77	3.9E−05	60.6	0.0	0.0	0.0	0.0	3.5E−06	100.0	5.3E−03	1.1
78	8.6E−06	92.5	3.8E−05	71.5	0.0	0.0	1.5E−05	100.0	5.7E−03	1.1
79	1.5E−04	69.6	9.1E−06	99.8	0.0	0.0	4.6E−05	100.0	5.6E−03	1.1
80	3.2E−05	71.9	1.8E−04	62.6	1.8E−09	100.0	9.4E−05	71.5	5.7E−03	1.2
81	4.1E−05	94.9	5.3E−04	47.4	0.0	0.0	0.0	0.0	5.0E−03	1.6
82	0.0	0.0	2.1E−03	30.8	1.0E−05	75.9	0.0	0.0	4.8E−03	2.0
83	0.0	0.0	3.8E−03	21.9	9.0E−06	83.6	0.0	0.0	6.9E−03	1.7
84	0.0	0.0	8.1E−03	16.7	8.7E−05	49.1	0.0	0.0	2.5E−02	0.9
85	0.0	0.0	2.2E−02	10.7	2.3E−04	46.7	0.0	0.0	4.2E−02	0.7
86	0.0	0.0	6.7E−02	6.8	4.4E−04	29.0	0.0	0.0	3.3E−02	0.8
87	0.0	0.0	1.5E−02	11.9	8.3E−04	22.5	0.0	0.0	2.4E−02	1.0
88	0.0	0.0	4.8E−03	18.6	1.9E−03	16.6	0.0	0.0	2.2E−02	1.0
89	0.0	0.0	2.1E−03	29.3	3.3E−03	14.0	0.0	0.0	1.9E−02	1.1
90	0.0	0.0	5.5E−04	52.0	2.5E−03	13.6	0.0	0.0	4.5E−03	1.7
91	0.0	0.0	2.2E−04	57.5	2.8E−03	13.7	0.0	0.0	2.8E−03	1.5
92	0.0	0.0	6.5E−07	92.5	1.8E−03	17.8	0.0	0.0	2.3E−03	1.1
93	0.0	0.0	0.0	0.0	9.1E−04	23.1	0.0	0.0	2.3E−03	0.9
94	0.0	0.0	7.0E−06	100.0	2.7E−04	37.3	0.0	0.0	2.2E−03	0.8
95	0.0	0.0	0.0	0.0	2.7E−04	33.9	0.0	0.0	1.5E−03	0.9
96	0.0	0.0	0.0	0.0	2.1E−04	64.7	0.0	0.0	1.8E−04	2.9
97	0.0	0.0	0.0	0.0	1.5E−04	53.3	0.0	0.0	5.0E−05	5.9
98	0.0	0.0	0.0	0.0	3.4E−05	100.0	0.0	0.0	1.5E−05	9.5
99	0.0	0.0	0.0	0.0	2.0E−05	100.0	0.0	0.0	5.0E−06	13.6
100	1.4E−03	27.6	0.0	0.0	0.0	0.0	4.6E−04	33.3	2.2E−03	2.1
101	1.2E−03	24.6	0.0	0.0	0.0	0.0	5.2E−04	29.8	1.2E−02	0.7
102	1.4E−03	23.6	1.5E−06	100.0	0.0	0.0	1.8E−04	51.1	1.4E−02	0.7
103	6.8E−04	31.8	0.0	0.0	0.0	0.0	5.1E−05	57.3	1.4E−02	0.7
104	3.7E−04	40.8	0.0	0.0	0.0	0.0	6.8E−05	89.2	1.4E−02	0.7
105	5.2E−04	31.0	0.0	0.0	0.0	0.0	1.2E−04	72.1	7.1E−03	1.0
106	3.7E−04	48.5	0.0	0.0	0.0	0.0	0.0	0.0	5.3E−03	1.0
107	1.7E−04	84.9	1.6E−04	100.0	0.0	0.0	0.0	0.0	4.8E−03	1.1
108	9.4E−05	100.0	2.9E−05	100.0	0.0	0.0	0.0	0.0	4.4E−03	1.3
109	0.0	0.0	1.3E−04	82.2	1.1E−05	100.0	0.0	0.0	3.1E−03	1.8
110	1.3E−04	98.1	1.2E−03	43.0	3.7E−05	100.0	0.0	0.0	2.5E−03	2.6
111	0.0	0.0	1.2E−03	37.8	8.9E−05	72.4	0.0	0.0	4.0E−03	2.2

Table 11.2 (continued)

Run number	Thyroid		Ovaries		Testes		Lens of eye		Red bone marrow	
	Dose (rads/R)	C. of var. (%)	Dose (rads/R)	C. of var. (%)	Dose (rads/R)	C. of var. (%)	Dose (rads/R)	C. of var. (%)	Dose (rads/R)	C. of var. (%)
112	0.0	0.0	5.2E–03	20.5	1.6E–05	92.9	0.0	0.0	1.3E–02	1.4
113	0.0	0.0	9.1E–03	14.7	2.6E–04	38.7	0.0	0.0	2.1E–02	1.0
114	0.0	0.0	1.0E–02	15.3	1.9E–04	45.3	0.0	0.0	2.1E–02	1.0
115	0.0	0.0	6.1E–03	20.3	5.5E–04	32.2	0.0	0.0	2.0E–02	1.1
116	0.0	0.0	2.8E–03	22.8	1.2E–03	22.8	0.0	0.0	2.0E–02	1.1
117	0.0	0.0	1.3E–03	34.0	1.5E–03	19.2	0.0	0.0	1.7E–02	1.2
118	0.0	0.0	5.2E–04	77.1	1.3E–03	20.3	0.0	0.0	4.4E–03	1.8
119	0.0	0.0	8.6E–05	93.1	1.1E–03	20.3	0.0	0.0	2.2E–03	1.8
120	0.0	0.0	0.0	0.0	6.2E–04	31.1	0.0	0.0	1.6E–03	1.5
121	0.0	0.0	3.9E–07	100.0	4.7E–04	27.1	0.0	0.0	1.2E–03	1.3
122	0.0	0.0	0.0	0.0	2.4E–04	35.5	0.0	0.0	9.5E–04	1.3
123	0.0	0.0	0.0	0.0	5.0E–04	43.9	0.0	0.0	5.5E–04	1.6
124	1.6E–03	27.7	0.0	0.0	0.0	0.0	6.8E–04	25.7	1.8E–03	1.9
125	1.4E–03	30.3	0.0	0.0	0.0	0.0	4.3E–04	35.0	1.3E–02	0.7
126	1.4E–03	27.7	0.0	0.0	0.0	0.0	8.4E–05	60.6	1.6E–02	0.6
127	8.3E–04	33.7	0.0	0.0	0.0	0.0	8.1E–05	63.7	1.5E–02	0.7
128	2.8E–04	62.0	0.0	0.0	0.0	0.0	1.5E–04	53.0	1.5E–02	0.6
129	2.9E–04	61.7	0.0	0.0	0.0	0.0	1.8E–05	100.0	7.0E–03	1.0
130	2.1E–04	51.1	1.5E–08	100.0	0.0	0.0	4.4E–07	100.0	4.7E–03	1.1
131	1.0E–04	77.2	5.1E–06	100.0	0.0	0.0	0.0	0.0	4.1E–03	1.2
132	1.6E–04	74.0	4.7E–06	85.0	0.0	0.0	0.0	0.0	3.8E–03	1.2
133	1.1E–04	100.0	2.3E–04	62.9	0.0	0.0	0.0	0.0	2.3E–03	1.9
134	0.0	0.0	2.8E–04	78.2	1.3E–05	73.1	0.0	0.0	1.4E–03	3.4
135	0.0	0.0	8.5E–04	38.1	0.0	0.0	0.0	0.0	2.0E–03	3.1
136	0.0	0.0	2.1E–03	30.6	9.4E–06	76.9	0.0	0.0	3.5E–03	2.4
137	0.0	0.0	4.1E–03	21.3	7.1E–05	96.6	0.0	0.0	5.0E–03	2.1
138	0.0	0.0	2.7E–03	27.1	1.3E–04	58.5	0.0	0.0	5.7E–03	1.9
139	0.0	0.0	3.3E–03	28.9	4.4E–04	31.6	0.0	0.0	5.6E–03	1.9
140	0.0	0.0	2.2E–03	31.8	7.3E–04	33.1	0.0	0.0	5.1E–03	2.0
141	0.0	0.0	7.2E–04	42.5	7.3E–04	32.1	0.0	0.0	4.0E–03	2.3
142	0.0	0.0	7.6E–04	51.9	6.6E–04	23.8	0.0	0.0	2.0E–03	3.0
143	0.0	0.0	0.0	0.0	2.7E–04	43.9	0.0	0.0	1.0E–03	3.5
144	8.2E–04	46.4	0.0	0.0	0.0	0.0	3.4E–04	36.9	1.0E–03	2.1
145	5.6E–04	47.9	0.0	0.0	0.0	0.0	5.0E–05	59.6	3.4E–03	1.0
146	1.2E–04	57.4	0.0	0.0	0.0	0.0	1.0E–04	60.0	3.6E–03	1.0
147	5.6E–06	90.4	0.0	0.0	0.0	0.0	9.3E–05	81.3	3.5E–03	1.0
148	0.0	0.0	0.0	0.0	0.0	0.0	0.0	0.0	2.9E–03	1.1
149	0.0	0.0	0.0	0.0	0.0	0.0	0.0	0.0	6.4E–04	2.8
150	4.6E–08	100.0	0.0	0.0	0.0	0.0	5.3E–06	100.0	5.0E–04	3.2
151	0.0	0.0	1.4E–06	100.0	0.0	0.0	0.0	0.0	4.4E–04	3.6
152	0.0	0.0	0.0	0.0	0.0	0.0	0.0	0.0	4.2E–04	3.9
153	1.0E–08	100.0	0.0	0.0	0.0	0.0	0.0	0.0	3.1E–04	5.0
154	0.0	0.0	3.3E–04	73.6	0.0	0.0	8.0E–06	100.0	2.4E–04	7.1
155	0.0	0.0	1.2E–04	72.0	3.8E–05	83.3	0.0	0.0	3.6E–04	6.4
156	0.0	0.0	3.3E–05	95.7	0.0	0.0	0.0	0.0	5.6E–04	5.5
157	0.0	0.0	7.1E–04	45.5	1.2E–04	58.3	0.0	0.0	8.4E–04	4.7
158	0.0	0.0	6.1E–04	47.0	1.8E–04	60.0	0.0	0.0	9.7E–04	4.5
159	0.0	0.0	8.3E–04	45.2	2.4E–04	50.6	0.0	0.0	9.5E–04	4.6
160	0.0	0.0	3.3E–04	70.5	2.4E–04	41.3	0.0	0.0	8.2E–04	4.9
161	0.0	0.0	3.1E–04	68.3	3.9E–05	81.1	0.0	0.0	6.7E–04	5.3
162	5.9E–04	36.1	0.0	0.0	0.0	0.0	1.6E–02	6.3	2.0E–02	0.5
163	8.9E–04	33.3	0.0	0.0	0.0	0.0	1.9E–02	6.0	2.6E–02	0.4
164	1.6E–02	9.0	0.0	0.0	0.0	0.0	1.3E–03	19.5	6.9E–03	1.2
165	1.5E–02	9.5	0.0	0.0	0.0	0.0	3.6E–04	36.4	6.7E–03	1.2
166	0.0	0.0	3.2E–02	9.4	2.3E–04	41.8	0.0	0.0	5.0E–02	0.6
167	0.0	0.0	5.8E–02	7.3	8.8E–04	22.3	0.0	0.0	3.0E–02	0.9

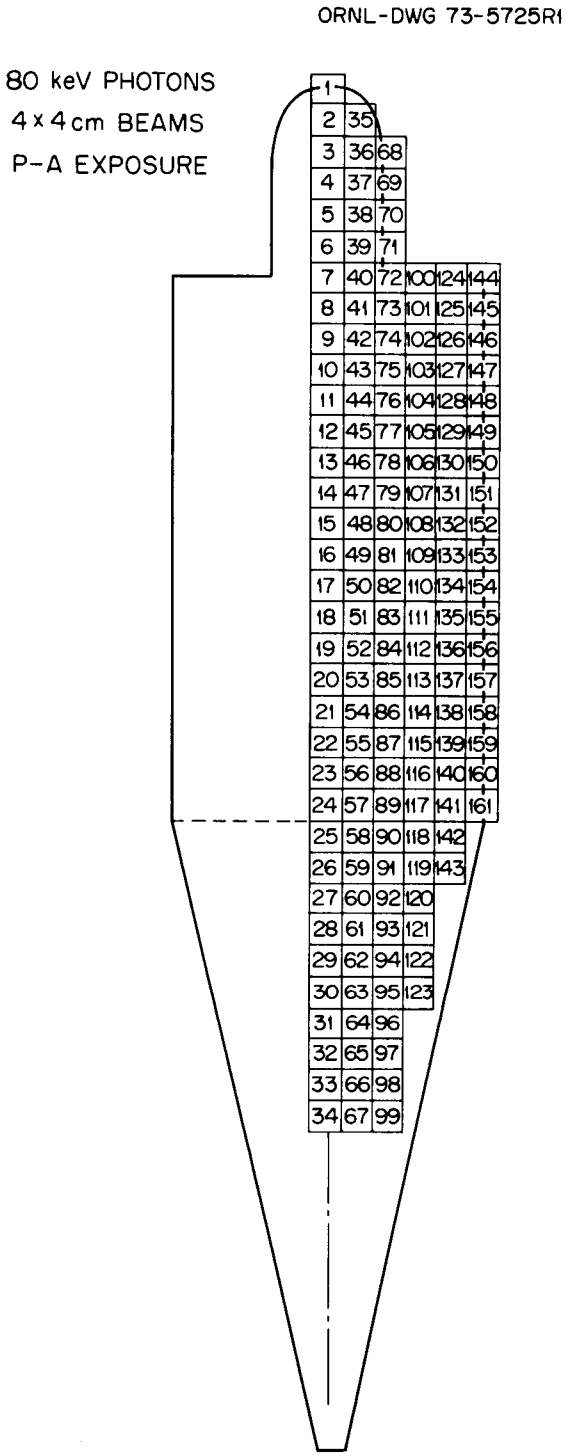

Fig. 11.3. Beam location diagram for calculations of absorbed dose due to 80-keV photons.

Table 11.3. Summary of calculated absorbed dose to organs of interest: 80-keV photons

Posterior/anterior exposure
4 × 4 cm beam
Note: 2.8E–05 read as 2.8×10^{-5} rads/R

Run number	Thyroid		Ovaries		Testes		Lens of eye		Red bone marrow	
	Dose (rads/R)	C. of var. (%)	Dose (rads/R)	C. of var. (%)	Dose (rads/R)	C. of var. (%)	Dose (rads/R)	C. of var. (%)	Dose (rads/R)	C. of var. (%)
1	9.2E–05	86.0	0.0	0.0	0.0	0.0	1.6E–03	18.0	8.6E–03	1.1
2	4.8E–04	38.6	0.0	0.0	0.0	0.0	7.6E–03	9.6	1.2E–02	0.8
3	9.8E–04	39.7	0.0	0.0	0.0	0.0	1.6E–02	7.2	1.5E–02	0.7
4	2.9E–03	19.5	0.0	0.0	0.0	0.0	1.9E–02	6.6	2.5E–02	0.6
5	8.5E–03	13.4	0.0	0.0	0.0	0.0	4.5E–03	12.1	2.9E–02	0.5
6	4.2E–02	7.2	0.0	0.0	0.0	0.0	1.6E–03	19.5	2.7E–02	0.6
7	3.6E–02	7.1	0.0	0.0	0.0	0.0	4.5E–04	30.3	2.7E–02	0.6
8	1.0E–02	12.6	0.0	0.0	0.0	0.0	5.3E–04	31.7	2.8E–02	0.6
9	3.6E–03	20.4	0.0	0.0	0.0	0.0	3.2E–04	50.1	2.8E–02	0.6
10	1.8E–03	24.4	0.0	0.0	0.0	0.0	2.8E–04	54.0	2.8E–02	0.6
11	1.2E–03	28.3	0.0	0.0	0.0	0.0	4.5E–05	78.8	2.8E–02	0.6
12	6.8E–04	41.4	0.0	0.0	0.0	0.0	4.2E–09	100.0	2.8E–02	0.6
13	3.7E–04	47.7	4.4E–05	98.7	0.0	0.0	3.3E–06	95.6	2.8E–02	0.6
14	1.9E–04	59.8	5.3E–04	70.7	3.4E–06	100.0	0.0	0.0	2.8E–02	0.6
15	1.7E–04	70.3	5.1E–07	94.2	4.1E–06	100.0	2.3E–08	100.0	3.0E–02	0.6
16	1.4E–04	82.4	9.5E–04	48.7	0.0	0.0	0.0	0.0	4.7E–02	0.6
17	0.0	0.0	2.0E–03	33.6	6.6E–06	100.0	0.0	0.0	5.3E–02	0.6
18	0.0	0.0	4.3E–03	23.6	1.1E–04	69.8	0.0	0.0	5.4E–02	0.6
19	0.0	0.0	1.3E–02	14.9	1.8E–04	38.6	0.0	0.0	5.1E–02	0.7
20	0.0	0.0	2.1E–02	12.1	5.2E–04	31.1	0.0	0.0	4.5E–02	0.7
21	0.0	0.0	2.7E–02	10.9	1.4E–03	21.1	0.0	0.0	2.7E–02	1.0
22	0.0	0.0	1.6E–02	13.6	2.6E–03	15.6	0.0	0.0	9.0E–03	1.7
23	0.0	0.0	8.5E–03	17.8	7.1E–03	11.0	0.0	0.0	6.2E–03	2.0
24	0.0	0.0	4.5E–03	23.0	1.4E–02	7.7	0.0	0.0	4.3E–03	2.3
25	0.0	0.0	2.9E–03	29.8	1.7E–01	2.6	0.0	0.0	3.0E–03	2.5
26	0.0	0.0	1.7E–03	39.1	2.7E–02	6.1	0.0	0.0	1.7E–03	3.1
27	0.0	0.0	3.5E–04	52.8	1.1E–02	9.4	0.0	0.0	1.0E–03	3.1
28	0.0	0.0	1.2E–04	94.3	4.4E–03	14.1	0.0	0.0	8.3E–04	2.9
29	0.0	0.0	3.1E–05	99.6	2.8E–03	15.6	0.0	0.0	6.3E–04	2.8
30	0.0	0.0	0.0	0.0	1.6E–03	23.8	0.0	0.0	4.2E–04	3.1
31	0.0	0.0	4.1E–08	100.0	1.2E–03	25.1	0.0	0.0	2.4E–04	5.0
32	0.0	0.0	0.0	0.0	6.5E–04	33.5	0.0	0.0	1.0E–04	6.4
33	0.0	0.0	0.0	0.0	9.0E–04	31.0	0.0	0.0	3.6E–05	9.0
34	0.0	0.0	0.0	0.0	1.8E–04	71.0	0.0	0.0	1.9E–05	19.4
35	3.8E–04	43.6	0.0	0.0	0.0	0.0	6.8E–03	9.6	1.4E–02	0.7
36	2.3E–03	25.6	0.0	0.0	0.0	0.0	3.3E–02	5.4	1.7E–02	0.7
37	4.0E–03	21.7	0.0	0.0	0.0	0.0	3.6E–02	5.2	2.5E–02	0.5
38	1.0E–02	12.7	0.0	0.0	0.0	0.0	6.2E–03	11.1	1.2E–02	1.0
39	1.9E–02	9.9	0.0	0.0	0.0	0.0	2.8E–03	17.0	7.8E–03	1.2
40	1.9E–02	9.7	0.0	0.0	0.0	0.0	9.9E–04	21.4	7.5E–03	1.3
41	8.9E–03	12.1	0.0	0.0	0.0	0.0	6.1E–04	26.4	9.3E–03	1.1
42	5.2E–03	17.6	1.0E–06	100.0	0.0	0.0	2.5E–04	39.8	9.8E–03	1.0
43	2.3E–03	25.4	0.0	0.0	0.0	0.0	2.3E–04	35.2	9.3E–03	1.0
44	1.2E–03	38.4	1.9E–04	100.0	0.0	0.0	1.0E–04	72.9	9.9E–03	1.0
45	5.5E–04	44.5	7.7E–06	100.0	0.0	0.0	1.5E–05	80.8	9.4E–03	1.1
46	6.8E–04	58.0	3.4E–05	99.3	0.0	0.0	5.3E–05	74.5	9.7E–03	1.1
47	2.3E–05	99.9	6.5E–04	46.5	0.0	0.0	0.0	0.0	1.0E–02	1.1
48	1.4E–05	100.0	3.0E–04	67.9	0.0	0.0	0.0	0.0	1.1E–02	1.2
49	1.5E–04	99.9	1.3E–03	42.3	2.4E–05	73.2	0.0	0.0	1.2E–02	1.3
50	3.4E–05	100.0	3.3E–03	25.7	1.2E–04	61.0	0.0	0.0	1.4E–02	1.4
51	0.0	0.0	6.3E–03	20.9	5.3E–04	46.9	0.0	0.0	1.6E–02	1.3
52	0.0	0.0	1.4E–02	14.5	4.8E–04	43.1	2.0E–06	100.0	3.1E–02	0.9

Table 11.3 (continued)

Run number	Thyroid		Ovaries		Testes		Lens of eye		Red bone marrow	
	Dose (rads/R)	C. of var. (%)	Dose (rads/R)	C. of var. (%)	Dose (rads/R)	C. of var. (%)	Dose (rads/R)	C. of var. (%)	Dose (rads/R)	C. of var. (%)
53	0.0	0.0	4.2E–02	8.9	4.6E–04	39.0	0.0	0.0	4.3E–02	0.7
54	0.0	0.0	8.0E–02	7.2	1.4E–03	20.7	0.0	0.0	2.8E–02	1.0
55	0.0	0.0	2.2E–02	12.1	2.4E–03	15.2	0.0	0.0	1.0E–02	1.5
56	0.0	0.0	1.0E–02	16.2	6.2E–03	10.9	0.0	0.0	7.8E–03	1.8
57	0.0	0.0	4.3E–03	24.6	1.1E–02	8.8	0.0	0.0	5.6E–03	2.0
58	0.0	0.0	1.7E–03	36.0	2.8E–02	6.1	0.0	0.0	3.8E–03	2.3
59	0.0	0.0	6.1E–04	46.5	1.5E–02	7.7	0.0	0.0	2.3E–03	2.5
60	0.0	0.0	6.5E–04	67.7	9.1E–03	9.3	0.0	0.0	1.7E–03	2.4
61	0.0	0.0	9.2E–05	100.0	4.2E–03	14.5	0.0	0.0	1.4E–03	2.2
62	0.0	0.0	0.0	0.0	3.0E–03	17.7	0.0	0.0	1.1E–03	1.8
63	0.0	0.0	0.0	0.0	1.4E–03	26.8	0.0	0.0	8.0E–04	1.9
64	0.0	0.0	0.0	0.0	1.2E–03	24.8	0.0	0.0	2.9E–04	2.9
65	0.0	0.0	0.0	0.0	4.7E–04	36.4	0.0	0.0	1.1E–04	4.2
66	0.0	0.0	0.0	0.0	3.3E–04	52.5	0.0	0.0	4.6E–05	7.7
67	0.0	0.0	0.0	0.0	2.4E–04	47.3	0.0	0.0	2.7E–05	19.1
68	1.1E–03	35.7	0.0	0.0	0.0	0.0	4.6E–03	12.7	4.4E–03	1.6
69	1.7E–03	28.7	0.0	0.0	0.0	0.0	4.4E–03	13.0	2.5E–03	2.3
70	3.4E–03	23.0	0.0	0.0	0.0	0.0	2.0E–03	19.0	1.2E–03	3.2
71	3.6E–03	21.4	0.0	0.0	0.0	0.0	1.1E–03	24.9	1.0E–03	3.4
72	5.8E–03	16.3	0.0	0.0	0.0	0.0	1.3E–03	23.4	2.9E–03	2.0
73	5.0E–03	16.5	0.0	0.0	0.0	0.0	4.2E–04	43.7	6.3E–03	1.2
74	2.6E–03	21.2	0.0	0.0	0.0	0.0	4.5E–04	44.6	6.5E–03	1.1
75	2.1E–03	24.7	0.0	0.0	0.0	0.0	1.3E–04	59.6	5.9E–03	1.2
76	4.1E–04	50.9	5.3E–06	100.0	0.0	0.0	4.4E–06	73.4	6.3E–03	1.1
77	9.3E–04	41.9	3.2E–04	97.7	0.0	0.0	4.6E–05	98.7	5.2E–03	1.3
78	2.5E–04	42.2	2.5E–04	93.0	0.0	0.0	6.6E–05	71.0	5.5E–03	1.3
79	2.2E–04	58.9	4.7E–05	100.0	0.0	0.0	1.6E–04	70.8	6.1E–03	1.3
80	2.5E–04	73.3	1.2E–03	53.1	8.0E–05	100.0	0.0	0.0	6.3E–03	1.5
81	0.0	0.0	1.2E–03	48.9	0.0	0.0	1.5E–05	100.0	6.2E–03	1.8
82	0.0	0.0	2.0E–03	31.3	1.1E–05	100.0	0.0	0.0	6.6E–03	1.9
83	0.0	0.0	3.3E–03	25.7	2.5E–04	43.7	0.0	0.0	9.1E–03	1.7
84	0.0	0.0	1.3E–02	14.3	2.3E–04	46.3	0.0	0.0	2.4E–02	1.0
85	0.0	0.0	3.6E–02	9.9	4.0E–04	40.8	0.0	0.0	3.9E–02	0.8
86	0.0	0.0	7.3E–02	7.5	8.0E–04	27.1	0.0	0.0	3.2E–02	0.9
87	0.0	0.0	1.9E–02	14.4	1.5E–03	17.1	0.0	0.0	2.3E–02	1.1
88	0.0	0.0	6.5E–03	18.8	3.3E–03	14.3	0.0	0.0	2.1E–02	1.1
89	0.0	0.0	2.6E–03	30.9	4.7E–03	12.5	0.0	0.0	1.8E–02	1.2
90	0.0	0.0	8.8E–04	40.5	5.7E–03	10.7	0.0	0.0	5.6E–03	1.7
91	0.0	0.0	7.3E–04	63.5	5.1E–03	11.9	0.0	0.0	3.5E–03	1.6
92	0.0	0.0	7.0E–04	75.9	3.0E–03	15.5	0.0	0.0	2.9E–03	1.4
93	0.0	0.0	7.0E–09	100.0	1.9E–03	20.5	0.0	0.0	2.6E–03	1.0
94	0.0	0.0	1.7E–04	99.5	1.6E–03	21.6	0.0	0.0	2.4E–03	0.9
95	0.0	0.0	0.0	0.0	8.3E–04	26.9	0.0	0.0	1.7E–03	1.1
96	0.0	0.0	0.0	0.0	2.8E–04	43.6	0.0	0.0	3.0E–04	3.0
97	0.0	0.0	0.0	0.0	3.0E–04	44.3	0.0	0.0	9.8E–05	6.0
98	0.0	0.0	0.0	0.0	4.4E–05	91.7	0.0	0.0	4.6E–05	13.7
99	0.0	0.0	0.0	0.0	0.0	0.0	0.0	0.0	1.5E–05	14.8
100	3.1E–03	22.7	0.0	0.0	0.0	0.0	1.2E–03	25.0	2.2E–03	2.2
101	3.2E–03	25.0	0.0	0.0	0.0	0.0	8.9E–04	26.0	1.0E–02	0.9
102	3.8E–03	19.7	0.0	0.0	0.0	0.0	2.8E–04	47.2	1.2E–02	0.8
103	2.3E–03	25.7	0.0	0.0	0.0	0.0	2.2E–04	40.8	1.1E–02	0.9
104	1.2E–03	31.1	8.3E–08	100.0	0.0	0.0	3.1E–04	47.1	1.2E–02	0.8
105	7.4E–04	38.4	0.0	0.0	0.0	0.0	0.0	0.0	6.4E–03	1.2
106	6.1E–04	45.9	6.9E–05	86.6	0.0	0.0	2.1E–05	100.0	4.7E–03	1.3
107	1.7E–04	76.1	1.4E–04	100.0	3.7E–06	100.0	1.5E–04	69.4	4.7E–03	1.4
108	5.3E–05	100.0	5.2E–04	68.8	0.0	0.0	0.0	0.0	4.7E–03	1.5

Table 11.3 (continued)

Run number	Thyroid		Ovaries		Testes		Lens of eye		Red bone marrow	
	Dose (rads/R)	C. of var. (%)	Dose (rads/R)	C. of var. (%)	Dose (rads/R)	C. of var. (%)	Dose (rads/R)	C. of var. (%)	Dose (rads/R)	C. of var. (%)
109	6.3E−05	100.0	1.2E−03	44.4	8.0E−08	100.0	0.0	0.0	4.0E−03	2.0
110	0.0	0.0	2.2E−03	33.5	1.3E−04	72.6	0.0	0.0	3.7E−03	2.5
111	0.0	0.0	5.8E−03	23.7	1.5E−04	65.3	0.0	0.0	5.4E−03	2.1
112	8.1E−06	100.0	6.3E−03	20.7	3.9E−04	55.1	0.0	0.0	1.3E−02	1.4
113	0.0	0.0	1.5E−02	15.6	4.1E−04	43.8	0.0	0.0	2.1E−02	1.1
114	0.0	0.0	1.2E−02	15.6	6.9E−04	31.0	0.0	0.0	2.2E−02	1.1
115	0.0	0.0	7.0E−03	18.7	1.2E−03	20.8	0.0	0.0	2.0E−02	1.2
116	0.0	0.0	3.5E−03	26.3	1.7E−03	22.3	0.0	0.0	1.9E−02	1.2
117	0.0	0.0	3.6E−03	34.0	2.5E−03	19.2	0.0	0.0	1.6E−02	1.3
118	0.0	0.0	9.4E−04	38.0	2.4E−03	17.0	0.0	0.0	5.2E−03	1.8
119	0.0	0.0	9.1E−04	51.5	2.2E−03	18.5	0.0	0.0	3.0E−03	1.9
120	0.0	0.0	9.2E−05	72.4	2.3E−03	17.1	0.0	0.0	2.0E−03	1.7
121	0.0	0.0	0.0	0.0	1.2E−03	21.9	0.0	0.0	1.5E−03	1.5
122	0.0	0.0	0.0	0.0	1.3E−03	24.7	0.0	0.0	1.1E−03	1.6
123	0.0	0.0	2.0E−04	100.0	3.1E−04	48.1	0.0	0.0	6.4E−04	1.9
124	1.7E−03	32.5	0.0	0.0	0.0	0.0	7.8E−04	31.9	1.9E−03	2.2
125	2.3E−03	23.7	0.0	0.0	0.0	0.0	8.5E−04	30.3	1.1E−02	0.8
126	6.9E−04	37.6	0.0	0.0	0.0	0.0	5.2E−04	31.9	1.3E−02	0.8
127	5.3E−04	36.5	0.0	0.0	0.0	0.0	2.8E−04	48.6	1.3E−02	0.8
128	3.6E−04	51.7	0.0	0.0	0.0	0.0	2.7E−05	100.0	1.3E−02	0.8
129	1.6E−04	64.0	0.0	0.0	0.0	0.0	5.8E−05	90.9	6.3E−03	1.1
130	3.3E−04	54.3	0.0	0.0	3.2E−05	100.0	0.0	0.0	4.5E−03	1.3
131	0.0	0.0	1.9E−04	80.8	8.9E−05	100.0	0.0	0.0	4.0E−03	1.4
132	7.3E−05	100.0	3.5E−04	100.0	0.0	0.0	8.3E−05	100.0	3.7E−03	1.5
133	1.2E−04	76.4	7.0E−04	46.0	4.6E−05	59.0	0.0	0.0	2.7E−03	2.2
134	0.0	0.0	1.3E−03	36.3	2.5E−05	100.0	0.0	0.0	1.9E−03	3.2
135	0.0	0.0	1.8E−03	38.2	1.4E−07	100.0	0.0	0.0	2.9E−03	2.9
136	0.0	0.0	3.3E−03	29.1	3.1E−05	94.4	0.0	0.0	4.1E−03	2.5
137	0.0	0.0	3.7E−03	28.1	3.8E−04	62.3	0.0	0.0	5.6E−03	2.2
138	0.0	0.0	4.3E−03	24.7	5.3E−04	32.3	0.0	0.0	6.2E−03	2.1
139	0.0	0.0	3.0E−03	23.1	9.9E−04	27.6	0.0	0.0	6.1E−03	2.1
140	0.0	0.0	3.2E−03	27.1	9.1E−04	25.8	0.0	0.0	5.4E−03	2.2
141	0.0	0.0	5.9E−04	45.9	1.4E−03	27.3	0.0	0.0	4.2E−03	2.4
142	0.0	0.0	1.2E−03	46.2	1.5E−03	21.0	0.0	0.0	2.6E−03	2.9
143	0.0	0.0	1.9E−04	98.7	1.1E−03	25.2	0.0	0.0	1.3E−03	3.4
144	1.3E−03	33.7	3.7E−05	100.0	0.0	0.0	5.5E−04	46.9	1.0E−03	2.5
145	8.0E−04	41.3	0.0	0.0	0.0	0.0	2.2E−04	53.8	3.2E−03	1.2
146	5.4E−05	100.0	0.0	0.0	0.0	0.0	0.0	0.0	3.2E−03	1.2
147	3.9E−04	50.7	6.9E−05	100.0	1.0E−08	100.0	1.3E−04	62.6	3.2E−03	1.2
148	1.0E−04	91.5	0.0	0.0	0.0	0.0	4.0E−05	100.0	2.7E−03	1.4
149	1.4E−06	100.0	0.0	0.0	0.0	0.0	1.9E−05	100.0	8.2E−04	3.1
150	2.6E−05	100.0	0.0	0.0	0.0	0.0	1.6E−08	100.0	6.4E−04	3.5
151	1.4E−05	87.5	9.1E−06	73.6	1.9E−05	100.0	0.0	0.0	5.4E−04	3.7
152	7.4E−06	100.0	4.3E−04	92.2	0.0	0.0	0.0	0.0	5.3E−04	4.1
153	0.0	0.0	4.0E−06	100.0	0.0	0.0	0.0	0.0	4.8E−04	5.3
154	0.0	0.0	2.8E−04	75.6	3.9E−05	100.0	0.0	0.0	4.1E−04	6.4
155	0.0	0.0	3.6E−04	65.5	0.0	0.0	0.0	0.0	5.5E−04	6.2
156	0.0	0.0	1.4E−03	42.3	2.1E−04	57.9	0.0	0.0	7.5E−04	5.5
157	0.0	0.0	4.8E−04	43.9	4.1E−05	100.0	0.0	0.0	9.7E−04	4.9
158	0.0	0.0	7.6E−04	48.0	2.0E−04	71.6	0.0	0.0	1.1E−03	4.6
159	0.0	0.0	8.4E−04	48.4	1.3E−04	62.5	0.0	0.0	1.1E−03	4.7
160	0.0	0.0	4.3E−04	68.5	1.4E−04	47.4	0.0	0.0	1.1E−03	4.7
161	0.0	0.0	1.1E−03	46.2	1.7E−04	60.1	0.0	0.0	7.7E−04	5.5

12. Absorbed Dose to Selected Internal Organs from Typical Diagnostic X-Ray Exposures

J. W. Poston G. G. Warner[1]

For these studies, two diagnostic x-ray procedures were simulated on a computer. The Monte Carlo technique and the phantom geometry developed by Snyder and his colleagues[2] were used in the calculations. Eight computer runs consisted of a set of exposures which simulated a chest x ray, and eight runs consisted of a set of exposures each of which simulated a gastrointestinal tract x ray.

Each of the 16 exposures consisted of a collimated 36 X 44 cm (14 X 17 in.) beam of 120,000 parallel photons incident on the rear of the phantom (posterior-anterior incidence, PA). In these calculations the source input was a set of eight measured x-ray energy spectra due to Epp and Weiss.[3] The spectra range from 45 kVp, 1 mm aluminum filtration to 105 kVp, 2 mm aluminum filtration. The energy of each photon was determined from a normalized distribution of relative photon fluences per unit energy interval between 10 and 102 keV. Monte Carlo methods were used to follow the transport of each photon through the phantom, determining the scattering angles, absorption sites, etc., and permitting the estimates of absorbed dose in units of absorbed dose per unit incident exposure (rads/R). Table 12.1 presents data for the simulated chest exposure; Table 12.2 presents data for the GI exposure.

The absorbed dose was calculated in the volume elements of the phantom as well as the internal organs mentioned in the tables. Typical depth-dose distributions in the trunk for the simulated chest x-ray exposures are shown in Fig. 12.1. These data are for 36 X 44 cm beams incident on the rear of the phantom. Illustrated are the effect on dose of the reduction in average energy of the beams and the attenuation of the beams as they pass through the phantom. Results for the simulated GI exposure are quite similar and will not be presented here.

The effect of various beam sizes on absorbed dose to selected organs was investigated for the two diagnostic examinations discussed above. Two spectra were selected as source input – 45 kVp, 1 mm aluminum and 105 kVp, 2 mm aluminum. Seven beam sizes were used, ranging from 4 X 4 cm to 36 X 44 cm. These data are presented in Tables 12.3–12.6.

This study represents only a beginning in that it demonstrates the versatility of Monte Carlo techniques in the simulation of diagnostic procedures. The computer programs used allow various source descriptions, such as point sources located at various source-to-skin distances, divergent beams, etc. In addition to beam size, the shape and angle of incidence on the phantom may also be specified.

---

1. Computer Sciences Division.
2. W. S. Snyder, M. R. Ford, G. G. Warner, and H. L. Fischer, Jr., "Estimates of Absorbed Fractions for Monoenergetic Photon Sources Uniformly Distributed in Various Organs of a Heterogeneous Phantom," MIRD Pamphlet No. 5, *J. Nucl. Med., Suppl. No. 3,* **10** (August 1969).
3. E. R. Epp and H. Weiss, "Experimental Study of the Photon Energy Spectrum of Primary Diagnostic X-Rays," *Phys. Med. Biol.* **11**(2), 225–38 (1965).

Table 12.1. Absorbed dose to selected organs from a simulated chest x ray

PA incidence (0, 48)

Organ	45 kVp, 1 mm Al		55 kVp, 1 mm Al		65 kVp, 2 mm Al		70 kVp, 2 mm Al		80 kVp, 2 mm Al		90 kVp, 2 mm Al		98 kVp, 2 mm Al		105 kVp, 2 mm Al	
	Dose (rad/R)	C. of var. (%)	Dose (rad/R)	C. of var. (%)	Dose (rad/R)	C. of var. (%)	Dose (rad/R)	C. of var. (%)	Dose (rad/R)	C. of var. (%)	Dose (rad/R)	C. of var. (%)	Dose (rad/R)	C. of var. (%)	Dose (rad/R)	C. of var. (%)
Bladder	0		3.22−7	100	7.70−4	88.4	3.21−3	49.5	4.79−3	37.6	3.14−3	39.2	2.02−3	55.5	6.01−3	33.9
Stomach	2.59−2*	8.7	6.59−2	6.3	1.28−1	5.0	1.58−1	4.6	2.02−1	4.1	2.64−1	3.7	2.66−2	3.9	3.27−1	3.5
ULI	1.22−2	11.3	1.90−2	9.2	4.20−2	7.0	5.80−2	6.1	7.96−2	5.5	9.11−2	5.2	1.23−1	4.8	1.14−1	4.9
LLI	5.50−4	38.7	2.62−3	24.8	5.17−3	17.6	7.57−3	18.0	1.09−2	14.8	1.17−2	15.2	1.36−1	14.4	2.07−2	12.5
Small int.	8.27−3	6.3	1.81−2	5.0	3.70−2	4.0	5.00−2	3.6	6.01−2	3.5	7.34−2	3.3	8.57−2	3.2	9.74−2	3.1
Kidneys	3.63−1	1.9	4.96−1	1.8	7.24−1	1.6	7.64−1	1.7	8.51−1	1.7	9.29−1	1.7	9.70−1	1.6	1.04	1.7
Liver	8.48−2	1.8	1.42−1	1.6	2.43−1	1.4	3.04−1	1.3	3.61−1	1.3	4.01−1	1.2	4.53−1	1.2	5.06−1	1.2
Lungs	1.79−1	1.4	2.75−1	1.3	4.21−1	1.1	5.00−1	1.1	5.69−1	1.1	6.41−1	1.0	6.92−1	1.0	7.50−1	1.0
R. marrow	2.42−1	0.48	3.43−1	0.49	5.03−1	0.49	5.73−1	0.50	6.57−1	0.51	6.96−1	0.51	7.54−1	0.52	8.05−1	0.53
Y. marrow	1.83−1	0.46	2.53−1	0.47	3.62−1	0.46	4.11−1	0.47	4.66−1	0.47	5.00−1	0.49	5.28−1	0.49	5.64−1	0.50
Ovaries	4.65−3	100	5.01−5	99.3	9.67−3	54.3	6.33−3	75.8	1.13−2	53.0	5.61−3	64.4	1.11−2	57.3	1.68−2	49.6
Trunk skin	2.45−1	0.77	2.63−1	0.82	2.91−1	0.91	3.09−1	0.93	3.29−1	0.95	3.45−1	0.96	3.49−1	1.0	3.63−1	1.0
Total skin	1.19−1	0.77	1.28−1	0.82	1.43−1	0.91	1.51−1	0.93	1.62−1	0.94	1.70−1	0.95	1.72−1	1.0	1.78−1	1.0
Testes	0		0		0		3.17−5	100	0		0		4.73−4	100	5.49−4	100
Thyroid	1.51−4	88.8	7.67−3	39.1	1.40−2	39.3	2.50−2	30.4	4.09−2	26.7	3.66−2	25.1	3.65−2	22.5	5.34−2	20.4
Uterus	9.91−5	60.0	1.92−3	48.1	2.41−3	48.6	6.66−3	32.1	7.09−3	28.3	9.51−3	24.3	1.05−1	25.6	1.72−2	21.6
Total body	8.15−2	0.08	1.12−1	0.1	1.62−1	0.1	1.87−1	0.1	2.15−1	0.1	2.34−1	0.1	2.52−1	0.2	2.75−1	0.2

*2.59−2 is read as 2.59×10^{-2} rad/R.

Table 12.2. Absorbed dose to selected organs from a simulated GI exposure

PA incidence (0, 35)

Organ	45 kVp, 1 mm Al		55 kVp, 1 mm Al		65 kVp, 2 mm Al		70 kVp, 2 mm Al		80 kVp, 2 mm Al		90 kVp, 2 mm Al		98 kVp, 2 mm Al		105 kVp, 2 mm Al	
	Dose (rad/R)	C. of var. (%)	Dose (rad/R)	C. of var. (%)	Dose (rad/R)	C. of var. (%)	Dose (rad/R)	C. of var. (%)	Dose (rad/R)	C. of var. (%)	Dose (rad/R)	C. of var. (%)	Dose (rad/R)	C. of var. (%)	Dose (rad/R)	C. of var. (%)
Bladder	1.90−3*	39.2	8.85−3	24.1	1.40−2	20.6	2.18−2	19.0	2.60−2	16.3	4.04−2	15.4	4.65−2	13.6	4.10−2	13.8
Stomach	3.13−2	8.1	6.14−2	6.6	0.136	4.6	0.175	4.3	0.220	4.0	0.272	3.8	0.284	3.8	0.348	3.5
ULI	3.04−2	7.1	6.44−2	5.2	0.129	4.1	0.173	3.7	0.223	3.4	0.298	3.1	0.299	3.2	0.380	2.9
LLI	1.26−2	12.8	2.37−2	9.8	6.34−2	6.6	7.81−2	6.0	0.102	5.5	0.123	5.6	0.140	5.1	0.157	4.8
Small int.	3.65−2	3.4	7.92−2	2.7	0.159	2.1	0.209	1.9	0.270	1.8	0.300	1.7	0.359	1.7	0.405	1.6
Kidneys	0.359	1.9	0.502	1.8	0.701	1.6	0.812	1.6	0.906	1.6	0.957	1.6	1.03	1.6	1.10	1.6
Liver	8.53−2	1.8	0.147	1.6	0.248	1.3	0.299	1.3	0.368	1.2	0.419	1.2	0.464	1.2	0.519	1.2
Lungs	0.143	1.6	0.212	1.5	0.329	1.3	0.381	1.3	0.435	1.2	0.476	1.2	0.508	1.2	0.553	1.2
R. marrow	0.301	0.6	0.445	0.6	0.653	0.6	0.770	0.6	0.881	0.6	0.950	0.6	1.02	0.6	1.09	0.6
Y. marrow	0.181	0.5	0.262	0.5	0.377	0.5	0.441	0.5	0.511	0.5	0.545	0.5	0.582	0.5	0.630	0.5
Ovaries	9.34−3	41.5	4.65−2	32.3	0.137	19.8	0.194	16.6	0.272	15.7	0.258	14.8	0.318	14.1	0.351	14.2
Trunk skin	0.234	0.8	0.252	0.8	0.287	0.9	0.298	0.9	0.312	1.0	0.323	1.0	0.339	1.0	0.352	1.0
Total skin	0.113	0.8	0.122	0.8	0.139	0.9	0.144	0.9	0.151	1.0	0.157	1.0	0.165	1.0	0.171	1.0
Testes	0		0		6.17−12	96.7	2.76−3	53.9	4.66−3	57.8	1.58−3	52.3	1.33−3	54.7	2.09−3	50.7
Thyroid	0		3.25−6	71.2	1.61−3	99.8	5.86−4	93.8	4.80−4	98.1	5.08−3	52.3	1.59−3	85.4	6.20−3	60.4
Uterus	2.03−2	16.0	4.96−2	12.3	9.04−2	10.0	0.144	8.5	0.178	7.6	0.221	7.1	0.226	6.85	0.259	6.5
Total body	8.12−2	0.08	0.112	0.1	0.161	0.1	0.188	0.1	0.218	0.1	0.237	0.1	0.256	0.2	0.279	0.2

*1.90−3 is read as 1.90×10^{-3} rad/R.

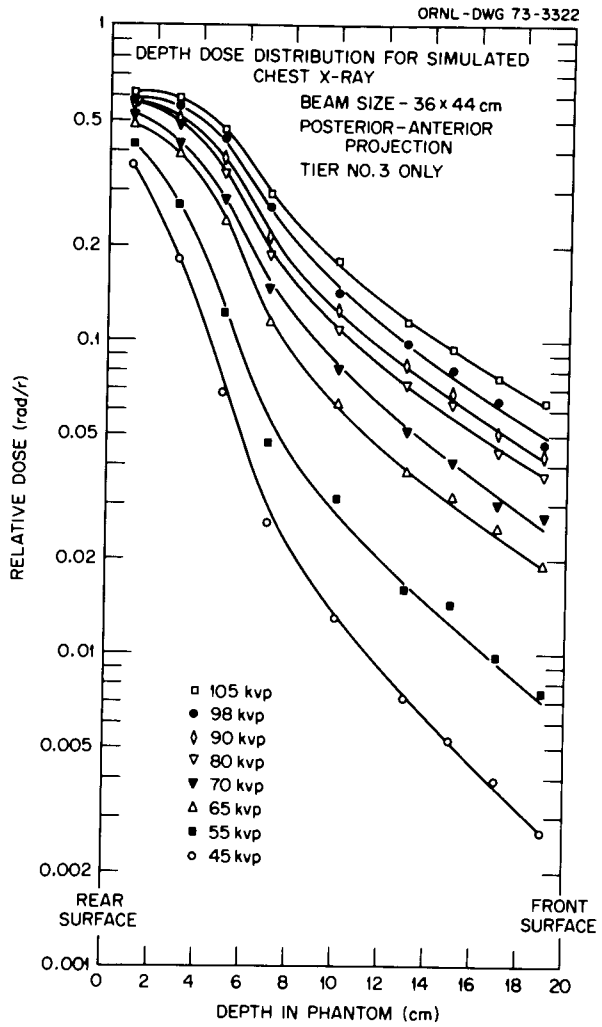

Fig. 12.1. Depth-dose distribution for simulated chest x ray.

Table 12.3. Effect of beam size on dose to selected organs

45 kVp, 1 mm Al @ (0, 35) PA incidence

Organ	4 × 4 cm		10 × 13 cm		13 × 20 cm		20 × 25 cm		25 × 30 cm		30 × 36 cm		36 × 44 cm	
	Dose (rad/R)	C. of var. (%)	Dose (rad/R)	C. of var. (%)	Dose (rad/R)	C. of var. (%)	Dose (rad/R)	C. of var. (%)	Dose (rad/R)	C. of var. (%)	Dose (rad/R)	C. of var. (%)	Dose (rad/R)	C. of var. (%)
Bladder	2.42−8*	98.2	1.35−5	100	1.74−6	100	1.71−5	62.4	4.86−4	68.7	6.10−4	63.8	1.90−3	39.2
Stomach	5.42−5	14.0	3.26−3	7.6	7.24−3	6.9	1.79−2	6.0	2.67−2	6.3	3.23−2	6.9	3.13−2	8.1
ULI	2.21−5	17.6	7.40−4	9.1	5.78−3	6.5	1.78−2	5.3	2.34−2	5.4	2.32−2	6.4	3.04−2	7.1
LLI	2.50−6	83.3	1.01−4	30.1	2.49−4	23.1	1.80−3	15.9	4.53−3	14.5	6.16−3	12.8	1.26−2	12.8
Small int.	1.68−5	11.3	7.91−4	5.2	5.44−3	3.4	1.98−2	2.6	2.82−2	2.7	3.41−2	3.0	3.65−2	3.4
Kidneys	1.71−3	2.0	8.86−2	1.1	1.83−1	1.0	3.45−1	1.1	3.75−1	1.2	3.66−1	1.5	3.59−1	1.9
Liver	9.03−5	4.6	3.24−3	2.6	9.57−3	2.1	2.82−2	1.7	5.05−2	1.6	7.47−2	1.6	8.53−2	1.8
Lungs	1.42−5	12.2	3.64−4	6.4	2.54−3	4.0	3.08−2	2.0	7.37−2	1.5	1.07−1	1.5	1.43−1	1.6
R. marrow	7.96−3	0.4	3.37−2	0.5	5.57−2	0.5	8.25−2	0.6	1.28−1	0.6	2.03−1	0.6	3.01−1	0.6
Y. marrow	3.63−3	0.3	1.77−2	0.4	3.17−2	0.5	5.23−2	0.5	7.83−2	0.5	1.19−1	0.5	1.81−1	0.5
Ovaries	1.44−6	100	2.34−6	80.5	3.18−4	91.5	2.01−4	69.3	1.81−3	62.5	3.30−3	73.3	9.34−3	41.5
Trunk skin	2.22−3	0.8	1.84−2	0.8	3.66−2	0.8	7.19−2	0.8	1.08−1	0.8	1.59−1	0.8	2.34−2	0.8
Total skin	1.08−3	0.8	8.89−3	0.8	1.77−2	0.8	3.48−2	0.8	5.21−2	0.8	7.72−2	0.8	1.13−1	0.8
Testes	0		0		0		0		0		0		0	
Thyroid	0		0		0		1.20−6	100	0		0		0	
Uterus	4.57−9	69.2	8.76−6	72.1	6.43−5	50.8	8.77−4	42.3	9.60−4	45.1	1.49−3	28.4	2.03−2	16.0
Total body	8.59−4	0.08	6.89−3	0.07	1.37−2	0.08	2.62−2	0.08	3.89−2	0.08	5.58−2	0.08	8.12−2	0.08

*2.42−8 is read as 2.42×10^{-8} rad/R.

Table 12.4. Effect of beam size on dose to selected organs

45 kVp, 1 mm Al @ (0.48) PA incidence

Organ	4 × 4 cm		10 × 13 cm		13 × 20 cm		20 × 25 cm		25 × 30 cm		30 × 36 cm		36 × 44 cm	
	Dose (rad/R)	C. of var. (%)	Dose (rad/R)	C. of var. (%)	Dose (rad/R)	C. of var. (%)	Dose (rad/R)	C. of var. (%)	Dose (rad/R)	C. of var. (%)	Dose (rad/R)	C. of var. (%)	Dose (rad/R)	C. of var. (%)
Bladder	0		0		0		0		0		0		0	
Stomach	1.24–5*	29.2	5.88–4	16.0	1.82–3	14.1	8.88–3	8.9	1.41–2	8.3	2.50–2	7.7	2.59–2	8.7
ULI	1.66–6	99.8	1.90–5	59.0	5.63–5	43.8	2.25–4	35.3	6.94–4	25.5	2.04–3	17.7	1.22–2	11.3
LLI	7.19–11	100	1.06–8	100	1.31–7	79.4	1.35–6	86.2	2.76–5	67.5	3.21–4	95.2	5.50–4	38.7
Small int.	4.37–7	69.2	6.48–6	37.5	3.04–5	37.5	1.61–4	21.8	3.49–4	19.8	1.30–3	10.8	8.27–3	6.3
Kidneys	1.64–5	18.9	5.75–4	10.9	3.80–3	5.8	4.59–2	2.9	1.48–1	2.0	2.76–1	1.8	3.63–1	1.9
Liver	3.58–5	6.5	2.10–3	3.1	7.03–3	2.5	2.43–2	1.9	4.47–2	1.7	6.84–2	1.6	8.48–2	1.8
Lungs	1.80–4	3.4	5.03–3	2.0	1.61–2	1.7	1.03–1	1.1	1.61–1	1.0	1.74–1	1.2	1.79–1	1.4
R. marrow	5.56–3	0.3	2.74–2	0.4	4.91–2	0.4	7.74–2	0.4	1.21–1	0.4	1.81–1	0.4	2.42–1	0.5
Y. marrow	3.45–3	0.2	2.04–2	0.3	4.06–2	0.4	7.03–2	0.4	1.00–1	0.4	1.36–1	0.4	1.83–1	0.5
Ovaries	0		0		0		0		0		7.98–6	100	4.65–3	100
Trunk skin	2.14–3	0.8	1.79–2	0.8	3.62–2	0.8	7.05–2	0.8	1.05–1	0.8	1.56–1	0.8	2.45–1	0.8
Total skin	1.05–3	0.8	8.80–3	0.8	1.78–2	0.8	3.47–2	0.8	5.18–2	0.8	7.68–2	0.8	1.19–1	0.8
Testes	0		0		0		0		0		0		0	
Thyroid	4.73–7	97.9	1.04–7	84.9	2.15–6	99.7	1.67–4	77.9	5.03–4	100	1.02–3	79.6	1.51–4	88.8
Uterus	0		0		0		1.11–7	100	1.53–4	100	1.53–7	77.4	9.91–5	60.0
Total body	8.68–4	0.1	6.96–3	0.1	1.39–2	0.1	2.62–2	0.1	3.94–2	0.1	5.63–2	0.1	8.15–2	0.1

*1.24–5 is read as 1.24×10^{-5} rad/R.

Table 12.5. Effect of beam size on dose to selected organs

105 kVp, 2 mm Al @ (0, 35) PA incidence

Organ	4 × 4 cm		10 × 13 cm		13 × 20 cm		20 × 25 cm		25 × 30 cm		30 × 36 cm		36 × 44 cm	
	Dose (rad/R)	C. of var. (%)	Dose (rad/R)	C. of var. (%)	Dose (rad/R)	C. of var. (%)	Dose (rad/R)	C. of var. (%)	Dose (rad/R)	C. of var. (%)	Dose (rad/R)	C. of var. (%)	Dose (rad/R)	C. of var. (%)
Bladder	2.07−5*	46.2	3.48−4	29.7	3.06−3	26.3	4.82−3	22.7	8.21−3	20.8	1.89−2	16.6	4.10−2	13.8
Stomach	3.14−3	3.4	4.51−2	2.8	9.29−2	2.7	2.04−1	2.6	2.73−1	2.8	3.19−1	3.1	3.48−1	3.5
ULI	1.44−3	4.2	2.04−2	3.3	7.29−2	2.6	1.72−1	2.4	2.44−1	2.5	3.15−1	2.6	3.80−1	2.9
LLI	2.10−4	11.8	2.64−3	9.2	8.63−3	7.7	3.11−2	6.3	6.27−2	5.4	9.74−2	5.3	1.57−1	4.8
Small int.	1.19−3	2.6	1.67−2	2.1	6.05−2	1.6	1.64−1	1.4	2.55−1	1.4	3.59−1	1.4	4.05−1	1.6
Kidneys	1.39−2	1.3	2.73−1	0.9	5.33−1	0.9	9.73−1	0.9	1.04	1.1	1.11	1.3	1.10	1.6
Liver	3.19−3	1.4	4.41−2	1.1	9.40−2	1.1	2.13−1	1.0	3.30−1	1.0	4.41−1	1.0	5.19−1	1.2
Lungs	6.87−4	2.9	9.27−3	2.4	2.94−2	1.9	1.25−1	1.4	2.62−1	1.2	3.95−1	1.2	5.53−1	1.2
R. marrow	3.22−2	0.3	1.47−1	0.5	2.47−1	0.5	3.59−1	0.6	5.25−1	0.6	7.67−1	0.6	1.09	0.6
Y. marrow	1.25−2	0.3	6.15−2	0.4	1.08−1	0.4	1.73−1	0.5	2.61−1	0.5	3.93−1	0.5	6.30−1	0.5
Ovaries	1.24−4	51.4	6.53−3	32.7	9.85−3	29.0	3.37−2	20.8	5.30−2	20.6	1.76−1	16.9	3.51−1	14.2
Trunk skin	3.09−3	1.1	2.59−2	1.1	5.41−2	1.0	1.06−1	1.0	1.60−1	1.0	2.35−1	1.0	3.52−1	1.0
Total skin	1.50−3	1.1	1.26−2	1.1	2.62−2	1.0	5.11−2	1.0	7.77−2	1.0	1.14−1	1.0	1.71−1	1.0
Testes	0		4.63−5	78.8	2.67−4	74.0	3.71−4	88.5	1.31−3	47.0	7.36−4	84.4	2.09−3	50.7
Thyroid	0		8.79−6	91.8	6.23−7	67.6	1.41−4	69.0	1.64−3	71.4	5.67−3	57.0	6.20−3	60.4
Uterus	1.82−4	20.2	2.85−3	14.6	9.30−3	12.0	2.67−2	10.3	4.71−2	9.6	8.54−2	9.4	2.59−1	6.5
Total body	3.34−3	0.1	2.59−2	0.1	5.10−2	0.1	9.44−2	0.2	1.38−1	0.2	1.95−1	0.2	2.79−1	0.2

*2.07−5 is read as 2.07×10^{-5} rad/R.

Table 12.6. Effect of beam size on dose to selected organs

105 kVp, 2 mm Al @ (0, 48) PA incidence

Organ	4 × 4 cm		10 × 13 cm		13 × 20 cm		20 × 25 cm		25 × 30 cm		30 × 36 cm		36 × 44 cm	
	Dose (rad/R)	C. of var. (%)	Dose (rad/R)	C. of var. (%)	Dose (rad/R)	C. of var. (%)	Dose (rad/R)	C. of var. (%)	Dose (rad/R)	C. of var. (%)	Dose (rad/R)	C. of var. (%)	Dose (rad/R)	C. of var. (%)
Bladder	3.02–6*	100	2.45–7	100	4.04–5	47.3	2.34–4	60.9	3.03–3	39.6	1.18–3	67.3	6.01–3	33.9
Stomach	9.54–4	5.9	1.22–2	4.9	3.58–2	4.3	1.10–1	3.6	1.93–1	3.4	2.67–1	3.4	3.27–1	3.5
ULI	1.06–4	14.2	1.21–3	13.1	3.78–3	10.2	9.17–3	9.1	2.38–2	7.2	4.76–2	6.2	1.14–1	4.9
LLI	1.15–5	43.7	1.49–4	29.6	5.46–4	29.1	2.14–3	22.8	2.83–3	18.4	6.68–3	18.0	2.07–2	12.5
Small int.	9.97–5	9.0	9.35–4	8.0	2.83–3	6.8	7.26–3	5.9	1.62–2	4.9	3.61–2	4.1	9.74–2	3.1
Kidneys	6.05–4	5.7	9.86–3	4.5	3.75–2	3.2	1.82–1	2.2	4.60–1	1.7	8.04–1	1.6	1.04	1.7
Liver	1.55–3	1.9	2.51–2	1.4	6.72–2	1.3	1.69–1	1.2	2.79–1	1.1	4.01–1	1.1	5.06–1	1.2
Lungs	3.72–3	1.3	4.74–2	1.1	1.11–1	1.0	3.86–1	0.8	5.87–1	0.8	6.89–1	0.9	7.50–1	1.0
R. marrow	2.17–2	0.3	1.06–1	0.4	1.85–1	0.4	2.81–1	0.5	4.01–1	0.5	5.81–1	0.5	8.05–1	0.5
Y. marrow	1.00–2	0.2	5.71–2	0.3	1.08–1	0.4	1.83–1	0.4	2.64–1	0.4	3.80–1	0.4	5.64–1	0.5
Ovaries	3.01–6	99.8	4.49–4	67.5	1.64–3	61.2	1.83–3	99.6	1.40–3	70.0	2.84–3	48.6	1.68–2	49.6
Trunk skin	2.98–3	1.1	2.56–2	1.1	5.32–2	1.0	1.06–1	1.0	1.61–1	1.0	2.29–1	1.0	3.63–1	1.0
Total skin	1.45–3	1.1	1.25–2	1.1	2.59–2	1.0	5.15–2	1.0	7.84–2	1.0	1.12–1	1.0	1.78–1	1.0
Testes	0		0		7.99–5	100	0		4.04–4	100	0		5.49–4	100
Thyroid	1.25–4	37.5	1.54–3	32.2	6.18–3	27.8	5.82–3	34.1	2.02–2	24.7	3.19–2	24.5	5.34–2	20.4
Uterus	1.04–5	81.4	1.99–4	49.4	7.18–4	37.4	1.52–3	40.9	2.45–3	27.8	6.88–3	30.6	1.72–2	21.6
Total body	3.31–3	0.1	2.55–2	0.1	5.04–2	0.1	9.13–2	0.2	1.34–1	0.2	1.93–1	0.2	2.75–1	0.2

*3.02–6 is read as 3.02×10^{-6} rad/R.

13. X-Ray Exposure Facility

P. S. Stansbury[1] J. W. Poston

To facilitate the experimental program of the Medical Physics and Internal Dosimetry Section, an x-ray facility has been designed and is under construction. The design criteria for the facility include suitable shielding for a 125-kVcp x-ray machine, space to perform experiments under conditions of good geometry, and provision for other incidental facilities (e.g., lab benches, storage space, water, gas, electric power, etc.). It was felt that a laboratory meeting these criteria was needed for various dosimetric experiments under way in the section. These include those experiments involving the physical mockup of the Snyder-Fisher phantom and both external and internal radiation sources. There is an immediate need for the facility in the experimental program to measure spectral fluence in the physical mockup of the Snyder-Fisher phantom exposed to x-ray fields representative of medical diagnostic radiology. Such an experiment requires an x-ray machine different from those commercially available. Since the spectral fluence will be measured at "in-beam" and "out-of-beam" locations in the phantom, large variations of fluence rate are anticipated. According to calculations, the rate at which photons are incident on the detector per unit exposure (or per unit x-ray tube current) will vary by as much as five orders of magnitude. To prevent saturation of the NaI(Tl) scintillator during "in-beam" exposures and to allow "out-of-beam" measurements to be made in a reasonable amount of time, the x-ray machine must be able to operate over the approximate range of 10 μA to 10 mA. Further, the relative spectral distribution of x rays produced must be constant over the operating range, and, obviously, the x-ray machine must be well regulated.

The design to meet the above criteria involves modifying a conventional orthovoltage therapy x-ray machine (a Siemens Stabillipan, 250 kVcp). The therapy-type tube, with tube shield, oil cooler, and tube stand, will be modified to conform to a cathode-grounded configuration. The anode will be powered by a 5 to 125 kV, 0 to 10 mA high-voltage supply with 0.01% ripple and no-load–full-load regulation of 0.1%. The filament will be powered by a conventional 10 V, 10 A power supply. The filament being at near ground potential will facilitate current sensing

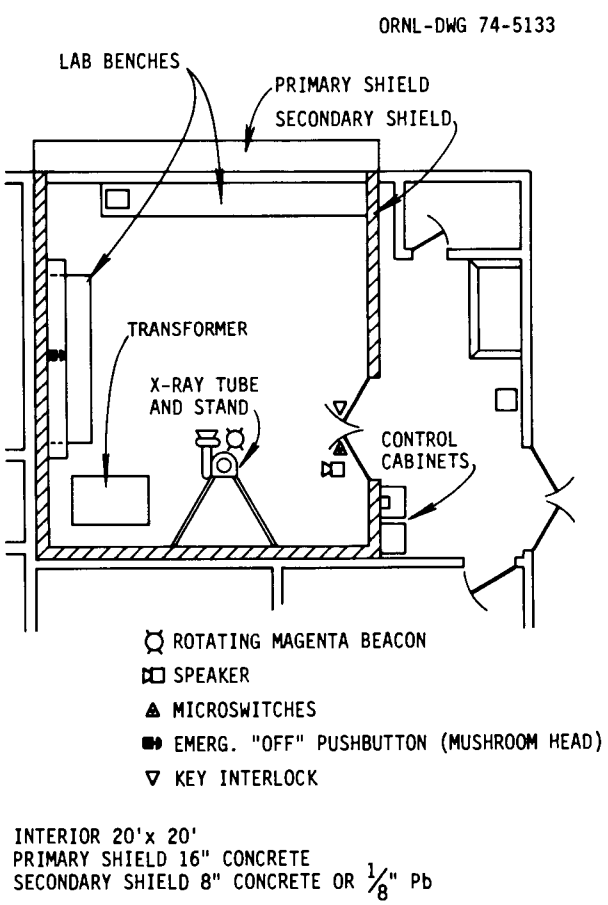

Fig. 13.1. Floor plan for x-ray facility.

1. ORAU Laboratory Graduate Participation Grant, School of Nuclear Engineering, Georgia Institute of Technology.

and interfacing of the filament and its power supply. The usual milliammeter and timer will be replaced with a current integrator.

The x-ray machine, power supply, and ancillary equipment will be installed in the laboratory in the east end of Building 2008. Figure 13.1 shows the primary shield (16 in. of concrete), the secondary shield (8 in. of concrete), and some of the features of the safety interlock system. The facility should be completely operational by December 1974.

14. An NaI(Tl) Scintillation Detector for Spectrometry and Dosimetry of Medical Diagnostic X Rays

P. S. Stansbury[1] J. W. Poston G. G. Warner[2]

The determination of absorbed dose and other dosimetric quantities in various tissues during medical diagnostic radiology is important in the assessment of genetic and somatic radiation risk. Although the interest in measuring dosimetric quantities in a phantom usually centers on in-beam measurements, the radiation field outside the useful beam is of interest also. Under most conditions the spectral and angular distributions of the radiation field inside the body are unknown. However, most of the ionization or solid-state dosimeters used in such measurements require that the spectral distribution and angular distribution of the radiation be known in order to properly "correct" the observations. Any dosimetric quantity of interest (e.g., absorbed dose in soft tissue, absorbed dose in bone or bone marrow, or exposure) can be determined from a knowledge of the spectral fluence at the location of interest.

An experimental program has been undertaken to measure the spectral fluence at locations within the MR. ADAM (Mockup of a Representative Analytical Description of an Adult Male) phantom when exposed to external beams of photons in the energy range 10 to 130 keV. This experiment will concentrate on exposure situations typical of medical diagnostic exposures.[3] In addition, the results will be compared with results from Monte Carlo calculations which match the exposure parameters of the experiment as closely as possible.

For such exposure situations, it is not expected that the photon fields inside the phantom could be considered in "good geometry" or isotropic. Therefore a detector system must be chosen which exhibits a directionally independent response. After considering several alternatives, a spherical NaI(Tl) scintillation detector was designed and procured. The detector (shown in Fig. 14.1) consists of a sphere of NaI(Tl) with a cross-sectional area of 0.3 cm^2. One hemisphere of the scintillator is embedded in a polyvinyl toluene light pipe. The light pipe is optically coupled

1. ORAU Laboratory Graduate Participation Grant, School of Nuclear Engineering, Georgia Institute of Technology.
2. Computer Sciences Division.

3. *Population Exposure to X-Rays, U.S. 1970,* DHEW Publication (FDA) 73-8047 (November 1973).

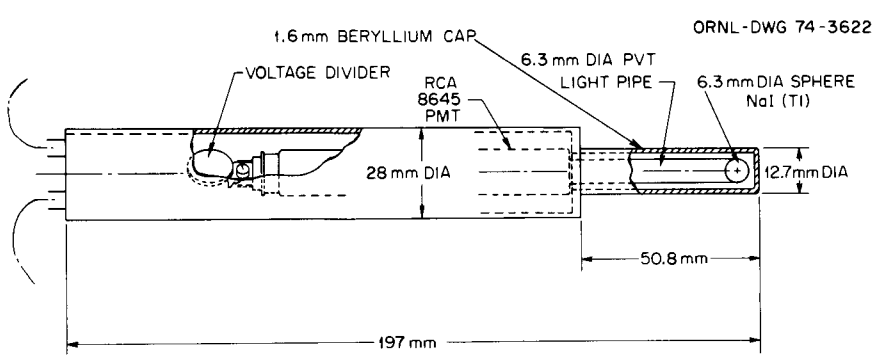

Fig. 14.1. NaI(Tl) scintillation detector.

Table 14.1. Summary of experimental plan for spectrometric study of exposure from diagnostic radiology

All measurements will be made for 60, 80, and 100 kVcp generating potential and will be normalized to tube current

Beam location[a]	Distance[b]	Field sizes [cm (in.)]	Location of measurements	Comments
1	1 m and less	36 × 44 (14 × 17), 10 × 44 (4 × 17), 10 × 10 (4 × 4)	L5 vertebra, right ovary, testes[c]	Data will be relevant to lumbar spine, barium enema (radiographic), and abdominal examinations. These examinations contribute heavily to the gonad doses.
2	1 m	36 × 44 (14 × 17)	Lens of eye, thyroid, thoracic spine, right ovary, heart, testes[c]	Data will be relevant to shoulder examination. Although this examination should not contribute high gonad doses, doses to lenses of eyes and thyroid should be significant.
3	1 m	36 × 44 (14 × 17)	L5 vertebra, right ovary, testes[c]	Data will be relevant to pyelogram. Pyelogram contributes heavily to the gonad dose.
4	1 m	36 × 22 (14 × 8.5)	L5 vertebra, right ovary, testes,[c] thoracic spine, heart	Data will be relevant to upper GI examination.
5	1 m and less	44 × 36 (17 × 14)	L5 vertebra, right ovary, testes	Data will be relevant to pelvic examination.
6[d]	2 m	36 × 44 (14 × 17)	Thyroid, thoracic spine, right ovary, testes,[c] heart	Data will be relevant to chest examination. Note that this beam is posterior-anterior.

[a]See Fig. 14.2 for beam location.
[b]Focus to "film" distance (i.e., to remote side of phantom).
[c]Measurements of spectra will be made at the testes with and without the detector shielded with a thickness of lead typical of a gonad shield.
[d]Posterior-anterior exposure.

to an RCA 8645 photomultiplier tube (the photocathode has an S-20 response). The scintillator and the light pipe are covered by a 0.16-cm beryllium cap, and the entire assembly is waterproof to a depth of 1 m. The probe should be suitable for use in the fluid-filled MR. ADAM phantom.

Measurements are planned for many locations in the phantom. Of particular interest are the spectra incident on the testes, ovaries, thyroid, and lenses of the eyes and inside skeletal structures containing red marrow. All exposure situations will be representative of diagnostic radiology (see Table 14.1 and Fig. 14.2).

During the experiment the pulse-height spectrum from the detector will be accumulated in a multichannel analyzer with a paper-tape-punching interface. Spectral distortions introduced by iodine K x-ray escape, energy nonlinearity, Gaussian broadening, and Compton scattering will be removed from the observed spectrum by use of a computer-coded iterative procedure similar to that of Turner et al.[4]

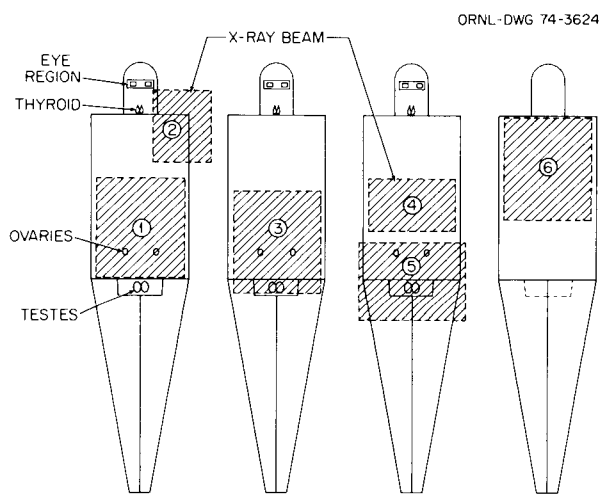

Fig. 14.2. Beam locations for spectrometric study of exposure from diagnostic radiology.

Response distributions have been calculated for the exposure of the detector to parallel beams of monoenergetic photons. These calculations excluded consideration of Gaussian broadening and nonlinearity and were for 61 monoenergies from 10 to 130 keV. A typical distribution for an initial energy of 110 keV is

4. J. E. Turner, V. E. Anderson, R. D. Birkhoff, and D. R. Johnson, "The Determination of LET Spectra from Energy-Porportional Pulse-Height Measurements – II. A Monte Carlo Unfolding Procedure," *Health Phys.* 18, 15 (1970).

shown in Fig. 14.3. These calculated distributions, along with the experimental determinations of nonlinearity and Gaussian broadening, are the necessary and sufficient information to unfold the observed spectral distributions. The corrected spectral fluence can be used to calculate many dosimetric quantities of interest, such as exposure, absorbed dose in tissue of varying composition, and electron spectrum.

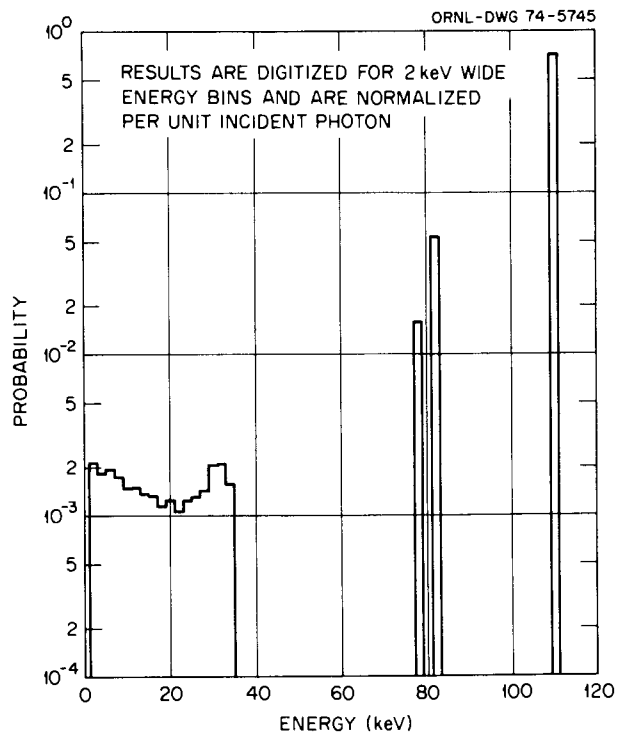

Fig. 14.3. Distribution of energy deposited in a NaI(Tl) sphere of 0.3 cm^2 cross section by a parallel beam of 110-keV photons.

15. Modifications to the MR. ADAM Phantom

P. S. Stansbury[1] J. W. Poston

As described elsewhere, modifications to the original Snyder-Fisher phantom include separation of the legs, rounding of the head, and incorporation of a pendent male genitalia region.[2] These modifications make the phantom more suitable for use in external beam exposure configurations. The MR. ADAM (Mockup of a Representative Analytical Description of an Adult Male) phantom has been changed to improve its resemblance to the newer mathematical model (see Fig. 15.1).

The lower section of MR. ADAM has been redesigned and remolded to have two separate leg regions and a male genitalia region. The head region has an ellipsoidal upper surface rather than the "flat-top" arrangement simulated by an elliptical cylinder. Both of these changes conform closely to the mathematical description. Also, the stand was redesigned to permit more realistic exposure of the phantom to external beams of radiation.

Dosimetric studies will be undertaken to provide experimentally determined estimates of absorbed dose to red bone marrow. The spine region has been modified to permit access to the skeletal-fluid-filled interior, and preliminary in-bone dosimetric studies will be possible in the near future.

The photon "equivalence" of constituent materials was another major improvement of the MR. ADAM phantom. An equivalent material (e.g., tissue-equivalent, bone-equivalent) has the same number and types of photon interactions over the energy range of interest as the material for which it is a substitute. In addition to the problems of finding a material (compound, mixture, aggregate, or solution) with suitable physical properties and convenient chemical properties,

Fig. 15.1. Photograph of MR. ADAM.

1. ORAU Laboratory Graduate Participation Grant, School of Nuclear Engineering, Georgia Institute of Technology.

2. W. S. Snyder, M. R. Ford, and G. G. Warner, "Estimates of Specific Absorbed Fractions for Monoenergetic Photon Sources Uniformly Distributed in Various Organs of a Heterogeneous Phantom," to be published as an MIRD Pamphlet, 1974.

finding equivalent materials for the photon energy range of 10 to 130 keV is further complicated by two of the characteristics of the interactions of radiation with matter. First, the partial mass attenuation coefficients, which determine number and type of interactions per unit mass, are sensitive functions of the elemental composition. Second, in the energy range of 10 to 130 keV, which includes most diagnostic medical x-ray fields, coherent-scattering partial mass attenuation coefficients are on the same order of magnitude as either photoelectric or Compton partial mass attenuation coefficients. To aid in the selection and evaluation of tissue-equivalent materials, a program, TECALC, was written.[3] TECALC was used to calculate the coherent, Compton, and photoelectric partial mass attenuation coefficients of materials of interest using the partial mass attenuation coefficients published by McMaster et al.[4] A comparison of the coefficients calculated at 17 logarithmically spaced intervals from 10 keV to 1 MeV was made in order to evaluate the equivalence of materials. Another feature of TECALC, one which allows the user to interactively adjust the composition of trial materials, was used to improve the soft-tissue-equivalent and lung-equivalent materials used previously in the phantom. A comparison between the Snyder-Fisher elemental descriptions and these two equivalent materials, along with the skeletal-equivalent material developed by Garry et al.,[5] is given in Tables 15.1–15.4.

The soft-tissue-equivalent material is 69% water, 25% isopropyl alcohol, 8% sucrose, and 1% sodium chloride and has a density of 0.99 ± 0.01 g/cm^3. The lung-equivalent material is 73.5% water, 25% dried cellulose sponge, and 1.5% sodium chloride with a density of 0.30 ± 0.01 g/cm^3.

Besides making the MR. ADAM phantom more suitable for external beam exposure studies, a method of polystyrene molding of the internal organs was developed. The use of polystyrene and the new molding techniques provides stronger, more durable organs and structures than were available previously. These developments should enhance the use of the phantom in future dosimetric studies.

3. P. S. Stansbury, *TECALC – a Program to Calculate Compton, Coherent, and Photoelectric Mass Attenuation Coefficients for Photons with Energies Less Than 1 MeV and to Assist in the Evaluation and Formulation of Photon-Equivalent Materials,* ORNL-TM-4451 (1974).

4. W. H. McMaster, N. K. Del Grande, J. H. Mallet, and J. H. Hubbell, *Compilation of X-Ray Cross Sections,* UCRL-50174, Sec. III, Rev. 1 (1969).

5. S. M. Garry, P. S. Stansbury, and J. W. Poston, *Measurement of Absorbed Fractions for Photon Sources Distributed Uniformly in Various Organs of a Heterogeneous Phantom,* ORNL-TM-4411 (1974).

Table 15.1. Description of Snyder-Fisher phantom subregions and their MR. ADAM phantom equivalents

	Soft tissue		Skeleton		Lung	
	Snyder-Fisher[a]	Equivalent[b]	Snyder-Fisher[a]	Equivalent[c]	Snyder-Fisher[a]	Equivalent[a]
Elemental composition, %						
H	10.474	11.26	7.036	6.47	10.208	9.78
C	23.020	18.36	22.793	19.15	10.008	11.11
N	2.339		3.865	3.94	2.802	
O	63.206	69.38	48.559	52.98	75.958	76.61
Na	0.128	0.393	0.315	0.17	0.190	0.59
Mg	0.016		0.111	0.18	0.008	
P	0.236		6.937	6.80	0.081	
S	0.221		0.169	0.01	0.230	
Cl	0.141	0.607	0.139		0.270	0.91
K	0.208		0.145		0.200	
Ca			9.914	10.30	0.007	
Fe	0.006		0.008		0.037	
Zn	0.005		0.010		0.002	
Density, g/cm^3	1.0	0.99 ± 0.01	1.5	1.50 ± 0.01	0.3	0.30 ± 0.01

[a]Composition given here is the same as given by Snyder et al. in MIRD Pamphlet No. 5 except that all elements with atomic number greater than zinc are considered zinc.

[b]Made from 66% H_2O, 25% isopropyl alcohol, 8% sucrose, and 1% NaCl.

[c]Made from bone flour, water, sucrose, and salts. See S. M. Garry, P. S. Stansbury, and J. W. Poston, *Measurement of Absorbed Fractions for Photon Sources Distributed Uniformly in Various Organs of a Heterogeneous Phantom,* ORNL-TM-4411 (1974).

[d]Made from 73.5% H_2O, 25.0% cellulose (sponge), and 1.5% NaCl.

Table 15.2. Calculated partial mass attenuation coefficients for Snyder-Fisher composition and comparison[a] of equivalent material used in MR. ADAM phantom – soft tissue

Energy (keV)	Photoelectric		Coherent		Compton	
	Coefficient (cm^2/g)	Comparison (%)	Coefficient (cm^2/g)	Comparison (%)	Coefficient (cm^2/g)	Comparison (%)
10	4.34	1.7	0.231	1.7	0.153	−0.7
15	1.18	1.5	0.132	1.6	0.176	−0.8
20	0.465	1.4	0.0862	1.6	0.186	−0.9
30	0.124	1.1	0.0513	1.6	0.192	−0.9
40	0.0485	1.0	0.0277	1.5	0.190	−0.9
50	0.0235	0.9	0.0187	1.5	0.185	−0.8
60	0.0130	0.8	0.0135	1.5	0.180	−0.8
80	5.12E−3	0.7	7.93E−3	1.5	0.169	−0.7
100	2.50E−3	0.6	5.20E−3	1.4	0.160	−0.7
150	6.96E−4	0.4	2.37E−3	1.4	0.141	−0.6
200	2.85E−4	0.3	1.34E−3	1.5	0.128	−0.6
300	8.40E−5	0.1	5.91E−4	1.5	0.111	−0.5
400	3.62E−5	0.1	3.30E−4	1.5	0.100	−0.6
500	1.92E−5	0.3	2.09E−4	1.6	0.0926	−0.6
600	1.15E−5	0.4	1.44E−4	1.6	0.0871	−0.6
800	5.36E−6	0.7	8.05E−5	1.7	0.0798	−0.8
1000	3.01E−6	0.9	5.13E−5	1.8	0.0751	−0.9

[a]Percent comparison of coefficients for equivalent material calculated as

$$100 \times \frac{(\mu/\rho)_{\text{equivalent}} - (\mu/\rho)_{\text{Snyder-Fisher}}}{(\mu/\rho)_{\text{Snyder-Fisher}}}$$

Table 15.3. Calculated partial mass attenuation coefficients for Snyder-Fisher composition and comparison[a] of equivalent material used in MR. ADAM phantom – skeleton

Energy (keV)	Photoelectric		Coherent		Compton	
	Coefficient (cm^2/g)	Comparison (%)	Coefficient (cm^2/g)	Comparison (%)	Coefficient (cm^2/g)	Comparison (%)
10	15.4	−1.2	0.327	1.5	0.143	−1.2
15	4.62	−0.9	0.192	1.4	0.164	−0.9
20	1.93	−0.8	0.126	1.4	0.174	−0.8
30	0.554	−0.6	0.0671	1.4	0.181	−0.6
40	0.267	−0.5	0.0416	1.4	0.179	−0.5
50	0.113	−0.5	0.0282	1.4	0.176	−0.5
60	0.0641	−0.5	0.0204	1.3	0.172	−0.5
80	0.0261	−0.5	0.0120	1.3	0.162	−0.5
100	0.0131	−0.5	7.90E−3	1.3	0.154	−0.5
150	3.76E−3	−0.6	3.61E−3	1.3	0.138	−0.6
200	1.57E−3	−0.6	2.04E−3	1.3	0.126	−0.6
300	4.73E−4	−0.6	9.02E−4	1.3	0.109	−0.6
400	2.06E−4	−0.6	5.02E−4	1.4	0.0981	−0.6
500	1.10E−4	−0.6	3.18E−4	1.4	0.0905	−0.6
600	6.66E−5	−0.5	2.19E−4	1.4	0.0848	−0.5
800	3.08E−5	−0.5	1.22E−4	1.4	0.0768	−0.5
1000	1.73E−5	−0.4	7.80E−5	1.5	0.0715	−0.4

[a]Percent comparison of coefficients for equivalent material calculated as

$$100 \times \frac{(\mu/\rho)_{\text{equivalent}} - (\mu/\rho)_{\text{Snyder-Fisher}}}{(\mu/\rho)_{\text{Snyder-Fisher}}}.$$

Table 15.4. Calculated partial mass attenuation coefficients for Snyder-Fisher composition and comparison[a] of equivalent material used in MR. ADAM phantom – lung

Energy (keV)	Photoelectric		Coherent		Compton	
	Coefficient (cm^2/g)	Comparison (%)	Coefficient (cm^2/g)	Comparison (%)	Coefficient (cm^2/g)	Comparison (%)
10	4.85	1.4	0.246	1.0	0.152	−0.8
15	1.33	1.3	0.141	1.0	0.176	−0.7
20	0.524	1.2	0.0918	1.0	0.186	−0.6
30	0.140	1.0	0.0480	1.0	0.192	−0.5
40	0.0549	0.8	0.0295	1.0	0.190	−0.5
50	0.0266	0.7	0.0199	1.0	0.185	−0.5
60	0.0147	0.6	0.0143	1.0	0.180	−0.5
80	5.81E−3	0.5	8.43E−3	1.0	0.169	−0.4
100	2.85E−3	0.4	5.52E−3	1.0	0.160	−0.4
150	7.91E−4	0.2	2.51E−3	1.1	0.140	−0.4
200	3.25E−4	0.1	1.42E−3	1.1	0.128	−0.4
300	9.57E−5	0.1	6.29E−4	1.1	0.111	−0.4
400	4.13E−5	0.2	3.51E−4	1.1	0.100	−0.4
500	2.19E−5	0.3	2.23E−4	1.1	0.0926	−0.4
600	1.32E−5	0.4	1.54E−4	1.1	0.0872	−0.4
800	6.10E−6	0.5	8.60E−5	1.1	0.0798	−0.4
1000	3.43E−6	0.6	5.49E−5	1.2	0.0751	−0.4

[a]Percent comparison of coefficients for equivalent material calculated as

$$100 \times \frac{(\mu/\rho)_{\text{equivalent}} - (\mu/\rho)_{\text{Snyder-Fisher}}}{(\mu/\rho)_{\text{Snyder-Fisher}}}$$

16. A Comparison of the GTC Cross Sections with ENDF/B III

J. J. Shonka[1] T. D. Jones

For nearly a decade, many of the neutron transport calculations of the Health Physics Division have been made using cross sections from the O5R library,[2] BNL 325,[3] and Brown.[4] Brown's analyses provided cross sections for most inelastic and nonelastic reactions inadequately described in the literature. In all, 33 reactions were allowed with the four primary components of tissue, consisting of hydrogen, carbon, nitrogen, and oxygen.[4] Many of the 33 reactions were actually "pseudoreactions," that is, a single reaction process used to replace two or more reactions having nearly equal energy thresholds and similar decay products. Brown's cross sections for many of the reactions are linearly extrapolated through experimental points to a maximum theorized value; however, documentation for these data is unavailable. There have been no efforts to update the Generalized Tissue Code (GTC) cross sections since Brown's initial endeavors.

A Monte Carlo code is being developed which will transport neutrons through the Snyder-Fisher phantom.[5] Cross sections for elements such as phosphorus, sulfur, potassium, etc., in addition to those for hydrogen, carbon, nitrogen, and oxygen, will be required for this code.[6] A comparison was made between the GTC cross sections and ENDF/B III (Evaluated Nuclear Data File)[7] cross sections which were developed for intralaboratory use. The objective was to determine the feasibility of using the ENDF library exclusively, as a self-consistent source of cross sections. Even though some of the detail of the GTC library will be lost, it is hoped that this loss will not be significant enough to affect the dose calculations. At the same time it was also desirable to reevaluate the GTC cross sections because of the additional experimental data published in the past ten years.

Several conclusions were drawn from that comparison. (1) Cross sections for the hydrogen (n,γ), the nitrogen (n,p), as well as the elastic reactions for all four elements, are substantially the same. For these six reactions, graphical information and tabulated values were in agreement at randomly checked points. Slight differences observed were probably due to the fact that ENDF/B III has more data points in resonance regions and uses nuclear modeling to interpolate between experimental points at high energy. This has the appearance of fitting a higher order polynomial to the curve in contrast to GTC's linear approach. (2) All GTC reactions had some corresponding ENDF/B III reaction. These agreed in terms of thresholds and approximate values. (3) ENDF/B III lists more possible reactions than GTC. This is not merely reactions that GTC had combined, as in the case of the pseudoreactions. One example is the $^{14}N(n,d)^{13}C$ reaction, listed by ENDF/B III but not considered by GTC. This cross section amounts to about 5% of the total nitrogen cross section in the 11-MeV region. (4) ENDF/B III is deficient for absorbed-dose calculations in that only prompt reaction products are emitted. Allowances are not made for radioactive end products. GTC considers some of the more important reactions

1. ORAU Laboratory Graduate Participation Grant, School of Nuclear Engineering, Georgia Institute of Technology.

2. D. C. Irving, R. M. Freestone, Jr., and F. B. K. Kam, *O5R, a General-Purpose Monte Carlo Neutron Transport Code,* ORNL-3622 (1965).

3. *Neutron Cross Sections,* BNL-325 (1955) and BNL-325, suppl. 2 (1966).

4. J. A. Auxier, W. S. Snyder, and T. D. Jones, "Neutron Interactions and Penetration in Tissue," *Radiation Dosimetry,* vol. I, Attix, Roesch, and Tochlin, eds., Academic Press, New York, 1968.

5. W. S. Snyder et al., *Health Phys. Div. Annu. Progr. Rep. July 31, 1967,* ORNL-4168, pp. 245–57.

6. J. J. Shonka, "Important Elements in the MIRD Phantom for Neutron Calculations," unpublished.

7. *Data Formats and Procedures for the ENDF Neutron Cross Section Library,* ed. by M. K. Drake, BNL-50274 (October 1970).

involving radioactive decay. An example is the $^{16}O(n,p)^{16}N$ reaction, where the nitrogen nucleus decays with a half-life of 7.14 sec, emitting a 6.1-MeV gamma ray. GTC generates a gamma ray for this reaction, whereas ENDF/B III does not. (5) Finally, ENDF/B III has no gamma rays produced from reactions with carbon. Future versions of ENDF/B should remove this deficiency.

A detailed comparison was impossible because GTC had pseudoreactions. This analysis can be summarized in two statements. First, the GTC library is still adequate for its purposes, which is testimony to the compilation done nearly ten years ago. Second, ENDF should be the library of choice for elements in the MIRD phantom. Elemental cross sections not described by ENDF should be derived from the Lawrence Livermore Laboratory's library (ENDL), which has been transformed to ENDF format.

Part II. Civil Defense Research

C. V. Chester

17. Effects of Electromagnetic Pulse (EMP) from High-Altitude Detonations

P. R. Barnes J. H. Marable D. B. Nelson G. L. Ragan

TRANSMISSION THROUGH UNDERGROUND CABLES

The calculation of transmission-line parameters, namely, the propagation constant Γ and the characteristic impedance Z_0, is not a trivial task, although many useful approximate formulas are known.

One well-known approximate formula for underground cables is given by Sunde.[1] Sunde's formula requires the use of an iterative technique for calculating Γ and Z_0. Calculations here at ORNL of EMP surges transmitted along underground cables give inconsistent results if Sunde's formula is used. Investigation has shown that Sunde's formula gives rise to a pole in the right half of the complex Laplace transform s plane. This pole gives rise to a complex propagation constant and a complex characteristic impedance, which are physically unacceptable. This occurs because, at some frequencies, the attenuation constant or the resistance may be negative. Thus it follows that Sunde's formula is not a useful approximation for methods that make use of analytic complex-variable transform methods.

Maxwell's equations have been solved directly for a three-media model of underground transmission lines. The result leads to an iterative procedure as simple as that of Sunde's formula. The resulting propagation constant and characteristic impedance have been shown to be physically acceptable at all values of the Laplace transform variable in the right half of the complex s plane.

This technique has been incorporated into a number of computer programs used for calculating EMP surges.

A VERSATILE PULSER FOR PROOF-TESTING EMP HARDNESS BY PULSE INJECTION

Equipment has been obtained for delivering electrical test pulses having a broad range of shapes (time variations) and amplitudes. These pulses are to be injected into selected circuits within an EMP-hardened communications center or other installation; the objective is to test the efficacy of the devices that have been installed to protect sensitive circuit components against damage by EMP-induced transients. A study was made of the shapes and amplitudes of typical transients induced on power lines, antenna cables, and telephone lines entering such installations. On the basis of these findings, equipment specifications were developed for the range of rise times, fall times, and amplitudes that are required if a pulse-injection system is to simulate these induced effects. Further requirements were (1) that the equipment be suitable for field tests – portable, reliable, and simple to operate – and (2) that the adjustments needed to select the desired pulse shape and amplitude be easily accomplished.

A very versatile and convenient pulser system was built to our specifications by Maxwell Laboratories of San Diego, California, at a cost of about $40,000. Principal characteristics of the system are shown in Table 17.1.

1. E. E. Sunde, *Earth Conduction Effects in Transmission Systems*, p. 270, Dover Publications, Inc., New York, 1967.

Table 17.1. Characteristics of pulser system

Pulse amplitude	1.6 to 150 kV
Pulse shape	Two-exponential
Selectable rise times (10 to 90%)	10, 20, 50, 100, 200, 500, 1000 nsec
Selectable fall times (to $1/e$)	0.5, 1, 2, 5, 10 μsec
Minimum pulse interval, sec	5, 10, 20, 50, 100 (respectively)
Maximum energy per pulse, J	225 times (fall time in μsec)
Output cable type	RG-220/U (50 Ω)
Output cable length	Up to 500 ft
Output pulse polarity	Selectably plus or minus
Operating temperature range	20°F to 110°F
Operating relative humidity range	10 to 90%
Power requirements	1 kW from 115 V at 60 Hz
Triggering	Manual or electrical pulse
Pulse jitter	< 100 nsec
High voltage insulating medium used	Transformer oil
Maximum weight, any unit	500 lb (without oil)
Mounts and lifts on units	Wheels and lifting eyes

The first field test using the equipment was conducted in June 1974 at the Federal Regional Center in Thomasville, Georgia. This test checked both the effectiveness of typical EMP-protective devices that had been installed at the Center and also the suitability of the pulser system for making such tests. For this test the pulser system was mounted in a large truck that served as a control point for the operation. Protective devices tested included (1) thyristors on a power distribution circuit, (2) metal oxide varistors on a fluorescent lighting circuit, (3) capacitors on a motor circuit, (4) gas gaps on an incoming antenna cable, and (5) gas gaps on circuits in an incoming telephone cable.

RESPONSE OF AN INFINITELY LONG PERFECTLY CONDUCTING CYLINDRICAL ANTENNA TO AN ELECTROMAGNETIC PLANE WAVE PULSE

In communications systems the antenna is an important means of coupling transient electromagnetic energy to some of the most vulnerable electronics components in the system. In order to specify surge protection requirements for communications equipment, knowledge of the early time response of the antenna to a transient electromagnetic source is desirable.

In this study,[2] the exact solution of the response of an infinitely long perfectly conducting cylindrical antenna to an electromagnetic plane wave pulse is considered. The antenna and incident wave are shown in Fig. 17.1. The response of the infinite antenna is the same as that of the finite antenna until the ends of the finite structure begin to have effect. Thus the solution of the infinite cylindrical antenna is an early-time solution for the cylindrical dipole antenna.

The solution of the infinite cylindrical antenna response can be written in terms of the Norton equivalent circuit parameters. The voltage across a load admittance Y_L is given by

$$V = \frac{I_a}{Y_a + Y_L}, \tag{1}$$

where the Laplace transform of the Norton equivalent current is

$$I_a = \frac{2\pi c\, E(s)}{Z \sin\theta\; sK_0\,(as \sin\theta/c)}, \tag{2}$$

s is the Laplace transform variable, and Y_a is the antenna admittance. $E(s)$ is the Laplace transform of the incident electric field, c is the speed of light in free space, Z is the free-space wave impedance, and θ and a are defined in Fig. 17.1.

The antenna admittance used in this study was that of an infinitely long cylindrical antenna excited by a finite uniform distributed source.[3] The finite source removed the unrealistic singularity found in many conventional antenna admittance expressions.

Early and late asymptotic forms of the infinite antenna response have been derived, and a parametric study of the antenna response has been performed. These results are documented in ref. 2.

2. P. R. Barnes, "On the Response of an Infinitely Long, Perfectly Conducting, Cylindrical Antenna to an Electromagnetic Plane Wave Pulse," *Interaction Notes*, Note 157, Air Force Weapons Laboratory, February 1974.

3. P. R. Barnes, "On the Input Admittance of an Infinitely Long Cylindrical Antenna Excited by a Finite Uniform Distributed Source," *Interaction Notes*, Note 154, Air Force Weapons Laboratory, February 1974.

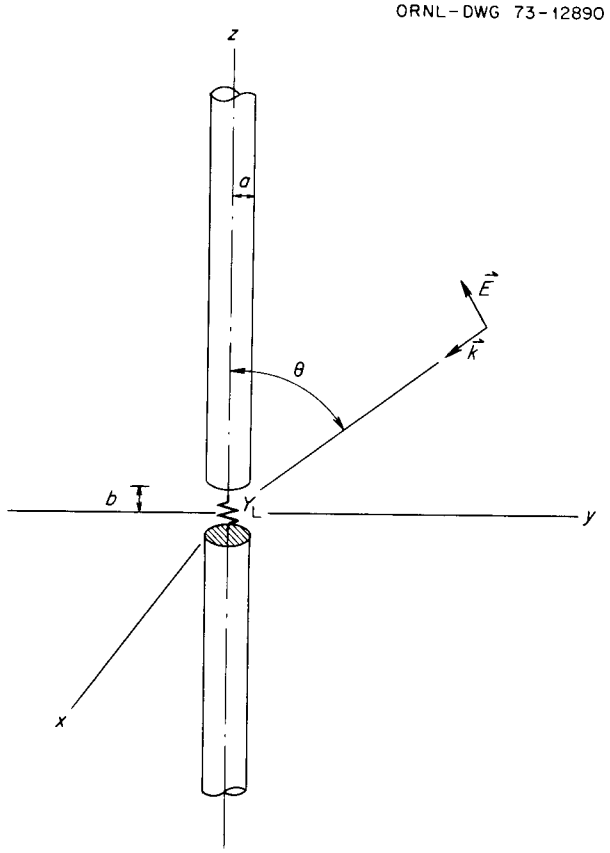

Fig. 17.1. Infinitely long, circular, cylindrical antenna and incident vector plane wave.

TRANSIENT RESPONSE OF LOW-FREQUENCY (LF) VERTICAL ANTENNAS TO HIGH-ALTITUDE NUCLEAR ELECTROMAGNETIC PULSE

As part of the EMP effects programs, several antenna models have been applied to the study of the response of top-loaded vertical low-frequency antennas. Among the models employed were the infinite antenna described in the preceding section, the singularity expansion method,[4] the quasi-first-order theory of King for the electrically short antenna,[5] and the theory of Wu for the electrically long antenna.[6] Top loading was introduced empirically by modifying the effective height and the impedance of the antenna. This method produces correct early- and late-time response but may introduce errors for times comparable with l/c, where l is the antenna length and c the speed of light.

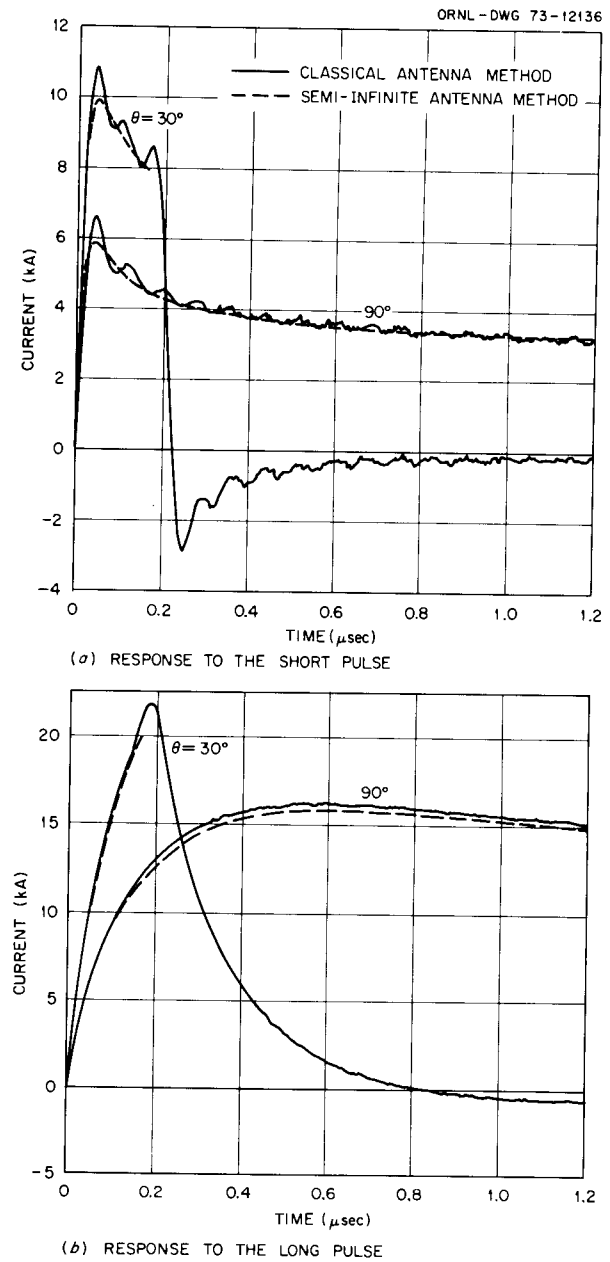

Fig. 17.2. Early-to-moderate time short-circuit current response.

4. C. E. Baum, "On the Singularity Expansion Method for the Solution of Electromagnetic Interaction Problems," *Interaction Notes,* Note 88, Air Force Weapons Laboratory, December 11, 1971.

5. R. W. P. King et al., "The Electrically Short Antenna as a Probe for Measuring Free Electron Densities and Collision Frequencies in an Ionized Region," *J. Res. Nat. Bu. Stand., Sect. D* **65**, 371 (1961).

6. T. T. Wu, "Theory of the Dipole Antenna and the Two Wire Transmission Line," *J. Math. Phys.* 4, 550 (1961).

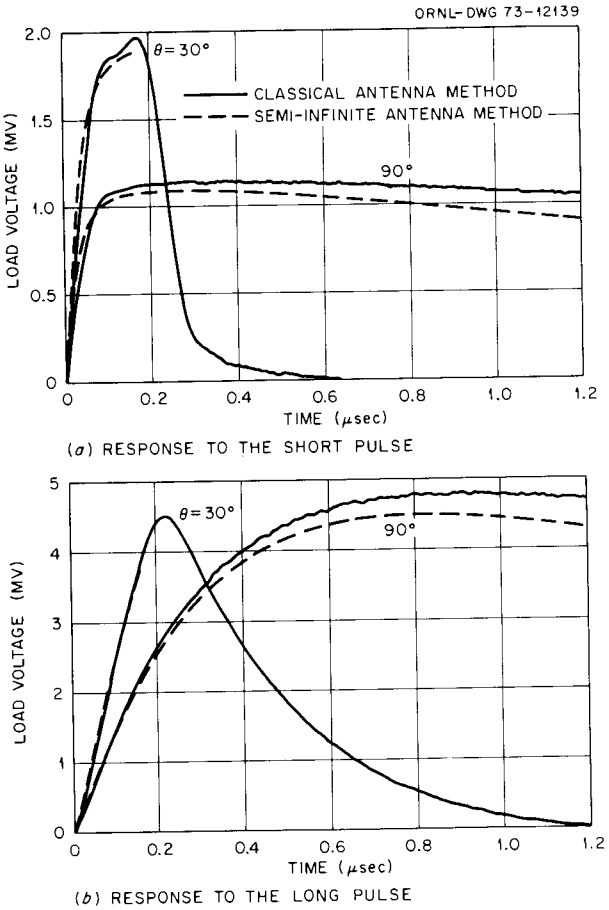

Fig. 17.3. Early-to-moderate time load voltage response.

Of particular importance in this study were the early-time behavior, including initial rate of rise of current and voltage and the peak value attained, the duration of the antenna response, and the variation in response for different EMP wave shapes and angles of incidence. Almost all computed curves were checked by comparing the results from at least two different antenna models. In every case the agreement was quite good. Further details may be found elsewhere.[7]

Low-frequency vertical radiators respond quite dramatically to EMP from high-altitude detonations. Calculated peak currents exceed 20 kA (Fig. 17.2), and peak load voltage is almost 5 MV (Fig. 17.3). Peak rates of rise are 500 kA/μsec and 30 MV/μsec. These values can be compared with average peak lightning currents of 10 to 20 kA and rate of rise of 5 to 20 kA/μsec. The duration of current surges from lightning strokes would generally be longer than those induced by EMP. For these calculations, we have not included any lightning arresters or other protective devices. Such devices would shorten the duration of EMP-induced surges.

The effect of the angle of incidence θ is quite pronounced. The early-time current and voltage at 30° is almost twice what it is at 90°, confirming the $\sin^{-1}\theta$ behavior. On the other hand, end effects occur sooner at 30°, reducing the low-frequency content. Thus the late-time behavior is greater for 90°. In general, it will be true for long antennas that effects depending on initial rate of rise will be maximized for small θ, whereas effects that depend on total surge energy will be maximized for broadside incidence.

7. P. R. Barnes and D. B. Nelson, *Transient Response of Low Frequency Vertical Antennas to High Altitude Nuclear Electromagnetic Pulse (EMP)*, ORNL-4960 (June 1974).

18. Strategic Defense

C. V. Chester C. H. Kearny
G. A. Cristy R. N. Thurmer

STRATEGIC IMPLICATIONS OF EXPEDIENT SHELTER

As part of the development of the technology of protecting citizens from the potential effects of nuclear weapons, we have been developing and field testing a family of expedient shelter designs (see section on Expedient Shelter Handbook). These are shelters that can be constructed by average citizens in less than 48 hr using their own resources of labor, tools, and materials. We believe the eventual wide availability of information on these shelter designs will have the potential to significantly alter the outcome of a nuclear war, and hence affect (by restoring somewhat) the strategic balance between the United States and the Soviet Union.

The very high protection factor of these shelters, over 500 for most below-grade versions, will permit not only survival, but freedom from even symptoms of radiation exposure in the most intense fallout fields likely to be encountered. Most below-grade versions provide very significant protection against blast. The log-covered trench has survived 13 psi and the small-pole shelter has survived 29 psi from a 500-ton TNT explosion.[1]

Repeated field experiments have demonstrated the ability of ordinary civilian families to construct these shelters by using only written instructions and available tools and materials. Arguments that white-collar families cannot construct these shelters, especially if the weather and digging conditions are unfavorable, were put in considerable doubt by an experiment run in Colorado in December 1973. A family with no adult male constructed a door-covered trench shelter in 36 hr (which included a sleep period) in very hard ground, under Colorado winter conditions. The attached photo set (Photos 1–6) shows the construction sequence. The last photo hints at the strength of the shelter in this type of soil, showing an 8-ton backhoe, hired to demolish the shelter, driven onto the roof.

Covered trench shelters can be constructed using a variety of widely available materials to support the roof. These include poles or logs, interior doors, hog wire, lumber, and even carpeting or canvas. The principal strength of the roof comes from earth arching and depends on soil properties and cannot be estimated from the strength of the roof support material.

Expedient shelter can greatly alleviate some difficult problems of the Defense Civil Preparedness Agency's current Crisis Relocation Planning. The present philosophy is to evacuate everyone out to the threat of 2 psi. Nationwide, this will require the movement and hosting of nearly 120 million people. If the criterion for evacuation is raised to a threat of 5 psi, the number to be moved drops to approximately 60 million. This has enormous advantages; not only is the refugee population decreased by 60 million, but the host population is *increased* by 60 million. There is a corresponding reduction in the problems of maintaining critical industries and services. A further increase to 15 psi of acceptable risk overpressure would reduce the population to be evacuated to 30 million. Although shelter designs to withstand this overpressure exist, uncertainties in target priorities, exact aiming points, weapon size, and delivery accuracy make remaining in these areas a risky proposition. Some idea of the areas involved by the different overpressures are shown in

1. C. H. Kearny and C. V. Chester, *Blast Test of Expedient Shelters,* ORNL-4905 (January 1974).

PHOTO 3022-73

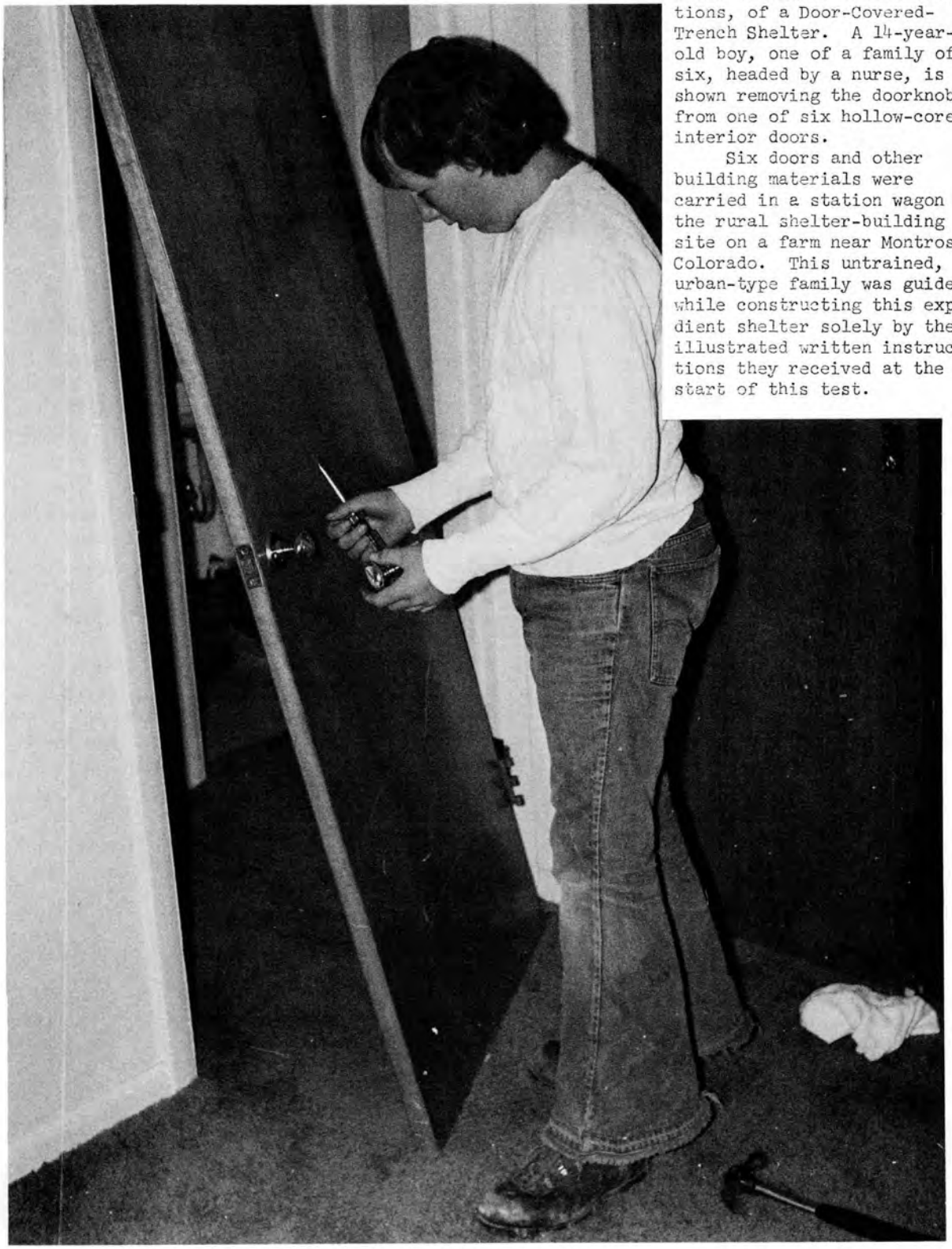

1. Start of the construction, under simulated crisis conditions, of a Door-Covered-Trench Shelter. A 14-year-old boy, one of a family of six, headed by a nurse, is shown removing the doorknobs from one of six hollow-core interior doors.

Six doors and other building materials were carried in a station wagon to the rural shelter-building site on a farm near Montrose, Colorado. This untrained, urban-type family was guided while constructing this expedient shelter solely by the illustrated written instructions they received at the start of this test.

2. Starting work shortly after dawn on the second day, Sunday, Nov. 25, 1973. The incentive motivating this man-less family to build a Door-Covered Trench Shelter under simulated crisis conditions was the hope of earning $400 by building it within 36 hours of receiving the building instructions.

Due to hard ground and inexperience, these soft-muscled people had succeeded in digging the trench only a couple of feet deep on the first day.

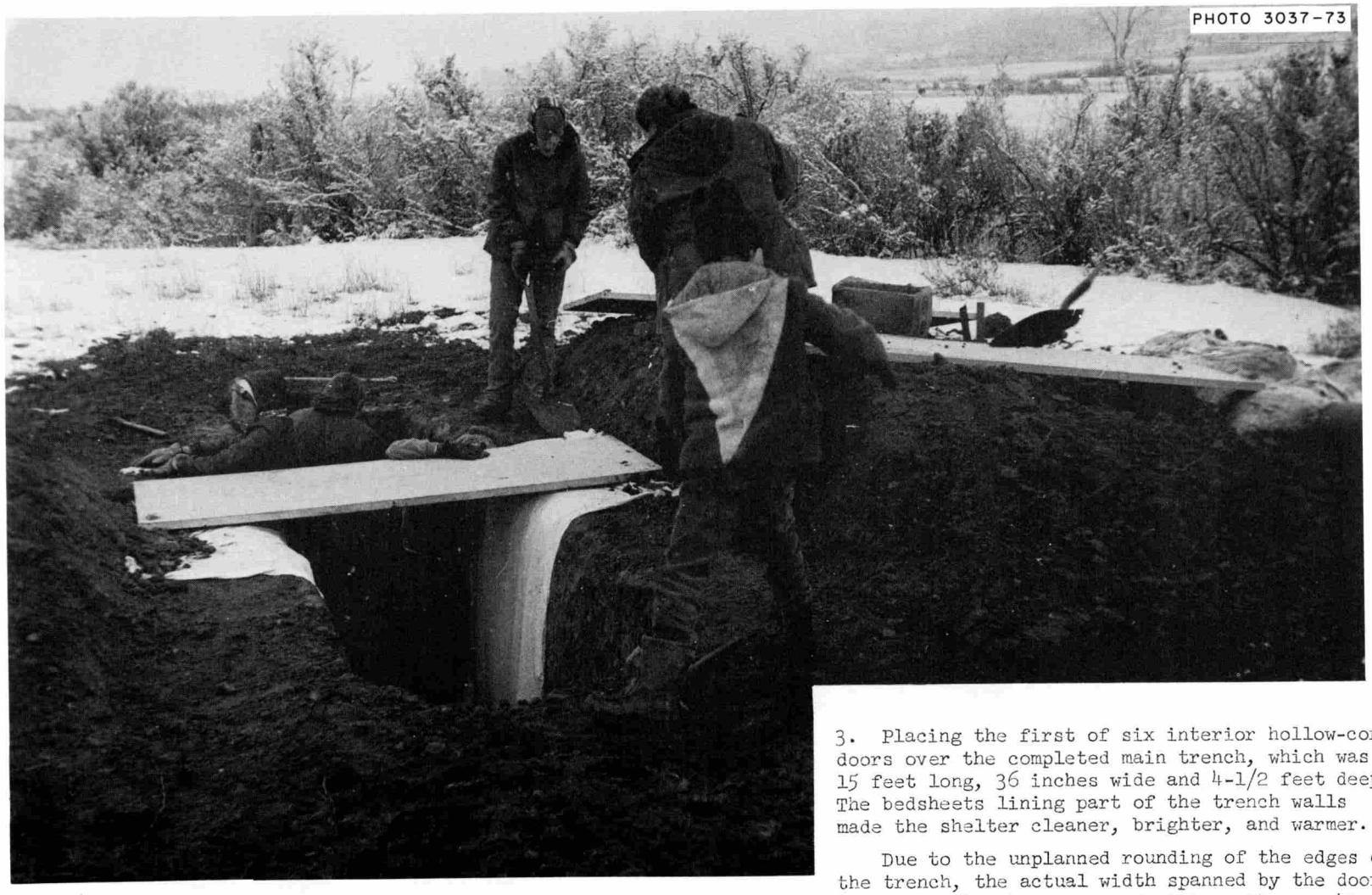

3. Placing the first of six interior hollow-core doors over the completed main trench, which was 15 feet long, 36 inches wide and 4-1/2 feet deep. The bedsheets lining part of the trench walls made the shelter cleaner, brighter, and warmer.

Due to the unplanned rounding of the edges of the trench, the actual width spanned by the doors, after they had been covered with earth, was 40 to 42 inches.

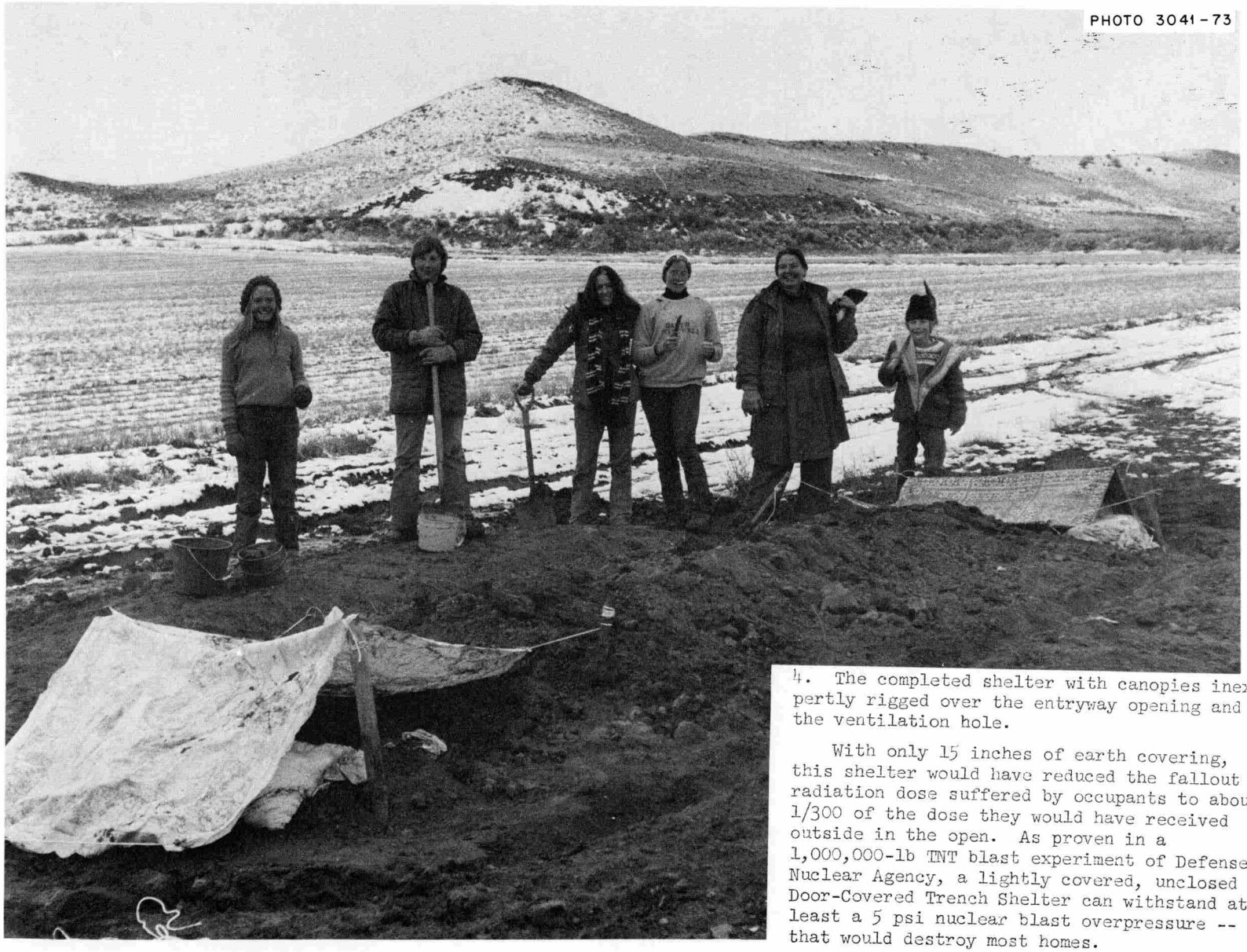

4. The completed shelter with canopies inexpertly rigged over the entryway opening and the ventilation hole.

With only 15 inches of earth covering, this shelter would have reduced the fallout radiation dose suffered by occupants to about 1/300 of the dose they would have received outside in the open. As proven in a 1,000,000-lb TNT blast experiment of Defense Nuclear Agency, a lightly covered, unclosed Door-Covered Trench Shelter can withstand at least a 5 psi nuclear blast overpressure -- that would destroy most homes.

Elizabeth, aged 11, asked the observers of this test a pertinent question: "But how [in a crisis] would people know how to build shelters?"

5. Inside their completed Door-Covered Trench Shelter, and all pepped up by their success in finishing an unexpectedly hard job. This family completed its shelter at 3:50 PM on November 25, 34 hours after first receiving the instructions on November 24.

CONCLUSION: Even most unskilled, untrained urban families could build blast-protective Door-Covered Trench Shelters, within two days, provided: (1) they have one door per person at a shelter site with suitable earth; (2) they have a pick and shovel; (3) they have as good, step-by-step, well illustrated instructions as guided this family.

6. An 8-ton backhoe was driven back and forth over this shelter with about 3-1/2 feet of earth over its roof made of 20-pound interior doors. Observers looking through the opened-up entryway noted no additional deflection of the undamaged doors.

Earth arching produced above the doors -- and not primarily the strength of the doors -- supported this heavy machine.

Subsequent experiments have indicated that a closed Door-Covered Trench Shelter of these dimensions, if built in the majority of the areas with stable earth and if covered properly with at least 3 feet of earth, would protect its occupants against blast overpressures capable of destroying most buildings.

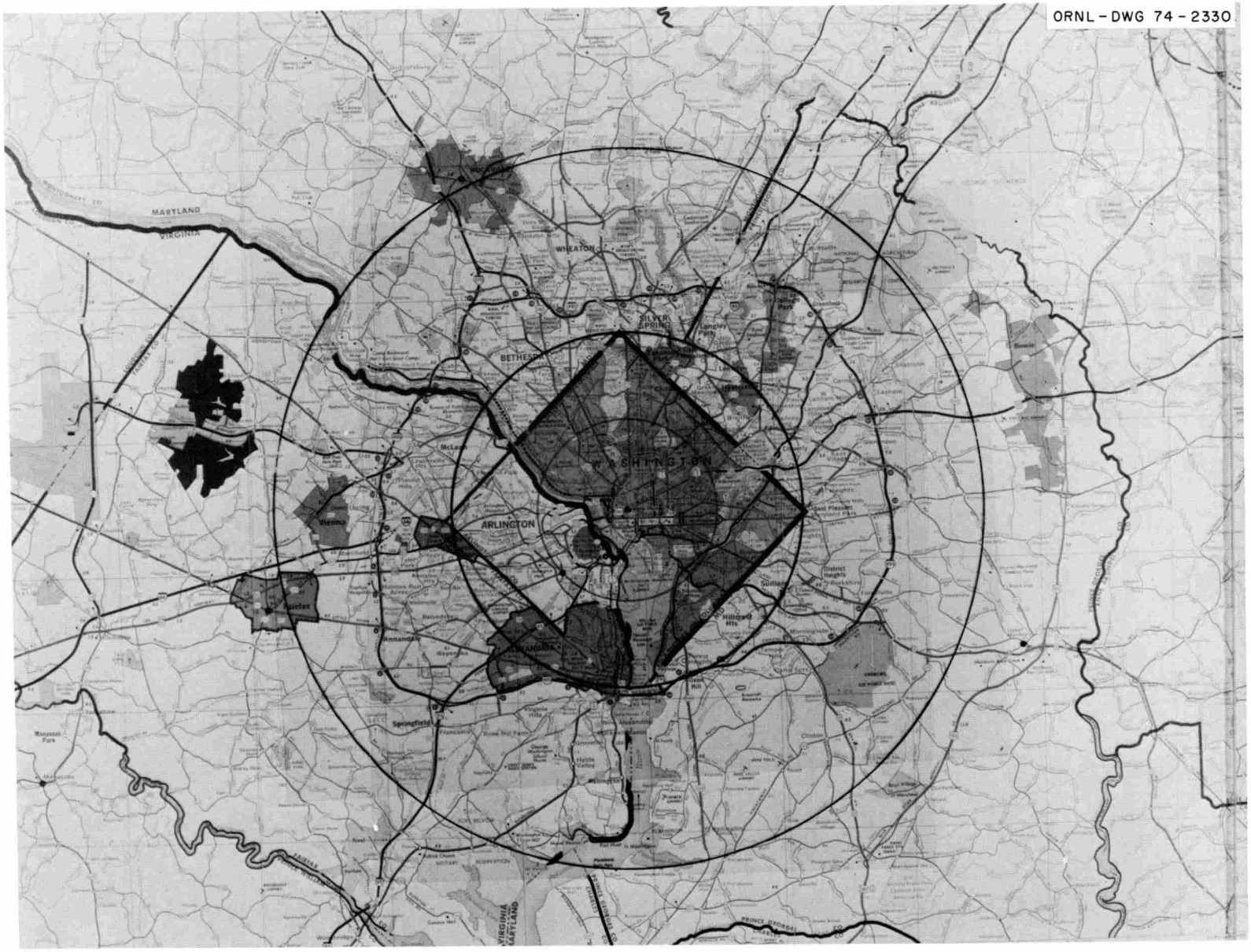

Fig. 18.1. The 2-, 5-, and 15-psi contours from a 5-megaton air burst over Washington, D.C.

Fig. 18.1 for Washington, D.C. In this example, the 2-, 5-, and 15-psi contours from a 5-megaton burst over the White House are shown. The advantage of sheltering in place rather than evacuating the population between 2 and 5 psi is obvious. The population in this area is almost equal to the population inside the 5-psi circle. Expedient shelter can make this area available for hosting the evacuees, with an enormous reduction of the pressure on the logistic infrastructure in the more rural areas.

Incorporation of expedient shelter in crisis relocation planning will require rethinking some widely held concepts of nuclear war. In conjunction with evacuation of population centers and high-overpressure areas around important military and industrial targets, expedient shelters offer the theoretical possibility of saving *everyone* from weapon effects in a nuclear attack. This is in marked contrast to rhetoric currently in vogue in high diplomatic and academic circles about a nuclear war being "the end of mankind" or "the end of civilization." Postattack reconstitution of vital logistic systems, such as food supply, and economic recovery are areas in which a great deal of work remains to be done, but these areas contain no theoretical barriers to the ultimate recovery of the nation.

EXPEDIENT SHELTER HANDBOOK (ORNL-4941)

An expedient shelter handbook was published which was designed to be of assistance to local civil defense organizations in the preparation of new plans necessary to meet the changing strategic conditions of the seventies. The Defense Civil Preparedness Agency is moving into a new program of "all-hazards, all-contingencies" planning that will include developing a crisis-oriented evacuation capability. Such planning should increase the survivability of the population in the event of a nuclear attack and should be a counter against certain "nuclear blackmail" threats. Planning for the development of shelter capabilities for either an in-place or evacuated posture will require an ability to build large numbers of new expedient shelters rapidly in addition to upgrading existing fallout shelters. (Expedient shelters are shelters that can be built under crisis conditions within 48 hr using only locally available materials, equipment, and labor.)

Detailed step-by-step instructions and pictorial design drawings of 15 expedient shelters are included in the appendixes of the Handbook. The instructions and drawings for one or more of these shelters can be preprinted by local civil defense organizations for rapid dissemination in a crisis. Most of the shelter designs are simple enough that they can be built by ordinary Americans, even ones who have had no previous building experience and who have no guidance other than the drawings and instructions included in the Handbook. Many of the designs have been proof-tested (i.e., built under simulated crisis conditions) by unskilled urban or rural people with no prior preparation other than reading these instructions for building one of these shelters. Typical design drawings are shown in Figs. 18.2–18.4. Figures 18.2 and 18.3 are photoreduced copies of the design drawings for the small-pole shelter, the most versatile shelter and the one which has been most thoroughly proof-tested. Figure 18.4 is a photoreduced copy of the design drawing for the door-over-trench shelter, which is one of the easiest of the shelters to build. Designs and instructions for building Kearny air pumps (KAP's) and an expedient, quick-closing blast door are also included in the appendixes.

It is recommended that all these shelters, especially the designs that have not yet been built by average citizens, be proof-tested under simulated crisis conditions by ordinary civilians and that the experiences so gained be used to refine and improve the designs and instructions.

DEVELOPMENT AND CONSTRUCTION OF ABOVEGROUND EXPEDIENT SHELTERS

The Need

If the United States adopts a damage-limiting nuclear defense strategy[2] similar to that of the Soviet Union[3] – a strategy that depends heavily on urban evacuation and the building of expedient shelters during a few days of an escalating crisis – then the millions of Americans in areas with high water tables or shallow soil above bedrock would need to know how to build good aboveground shelters. Furthermore, even if, during an escalating crisis, Americans did not evacuate probable target areas, millions of Americans living in areas where belowground expedient shelters are impractical would be able to improve their chances of surviving a nuclear attack if they knew how to build good aboveground expedient shelters.

---

2. See Secretary of Defense James R. Schlesinger's military posture report for 1974, which indicates progress toward such a prudent strategy; this report mentions ongoing preparations to relocate (i.e., evacuate during some types of crises) most Americans from 250 cities that are probably targeted.

3. See section on Soviet Civil Defense Studies in this report.

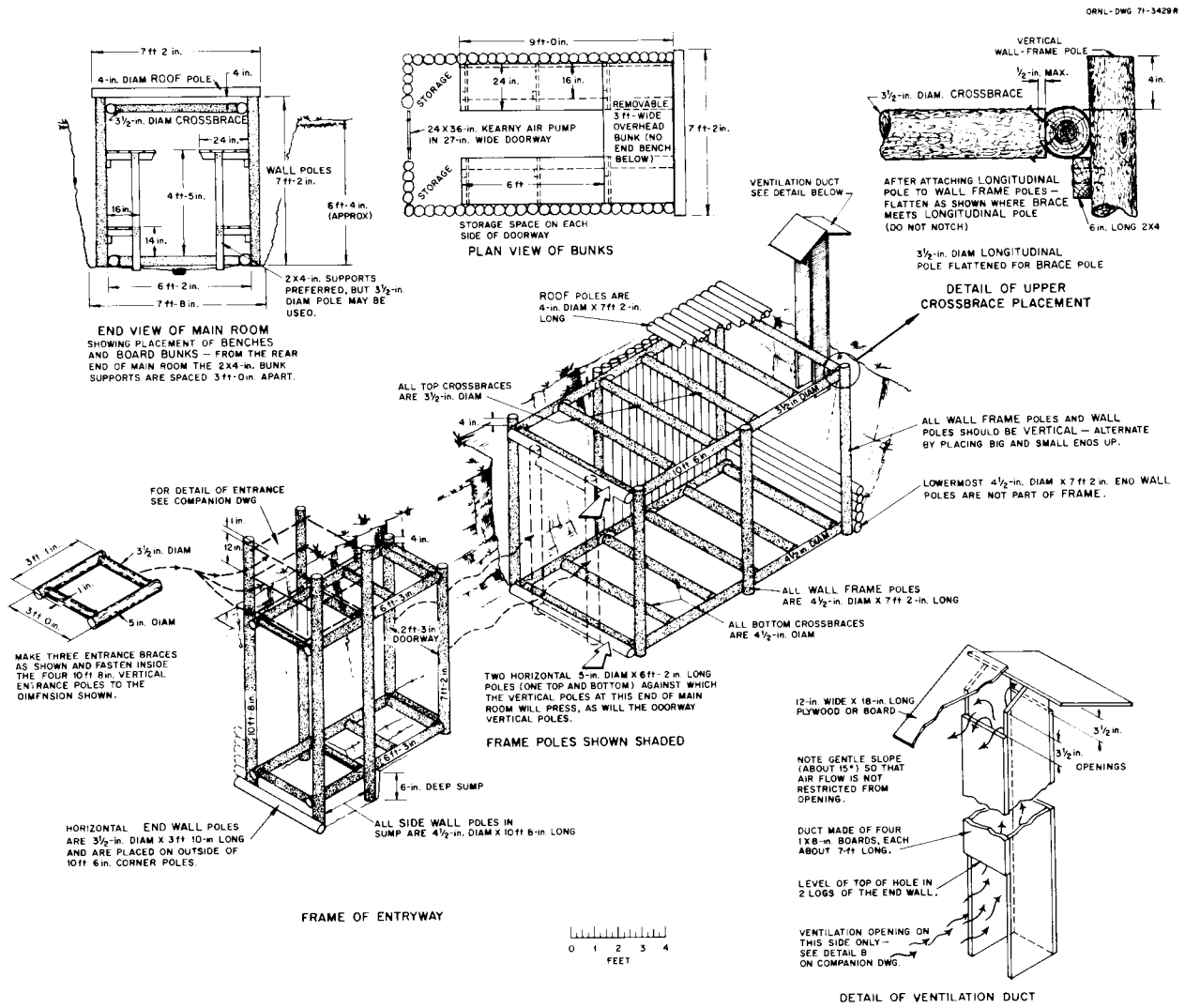

Fig. 18.2. Pictorial view of small-pole shelter.

One of the obvious weaknesses of U.S. and foreign civil defense preparations is that civil defense publications contain very few designs for *aboveground* expedient shelters, and the ones that are available are not widely applicable for use by untrained, unprepared Americans.

Experimental Procedures

The author followed the same procedures in developing and testing aboveground expedient shelters as he used in past years for developing belowground expedient shelters:[4]

1. Conceive, or select, the designs of shelters that appear most practical for average untrained Americans to build in the specified environment, using locally available materials.
2. Write step-by-step instructions and create illustrations to guide the builders of the shelters.
3. Have workmen build one or more prototypes of each of these promising shelter designs, and improve the designs.
4. Have untrained families build the shelters while guided only by the illustrated written instructions — both to determine the practicality of each design for average Americans to build and to improve the illustrated instructions.

4. C. H. Kearny, "Hasty Shelter Construction Studies," chap. 21 of *Civil Defense Research Project Annual Progress Report, March 1970–March 1971*, ORNL-4679.

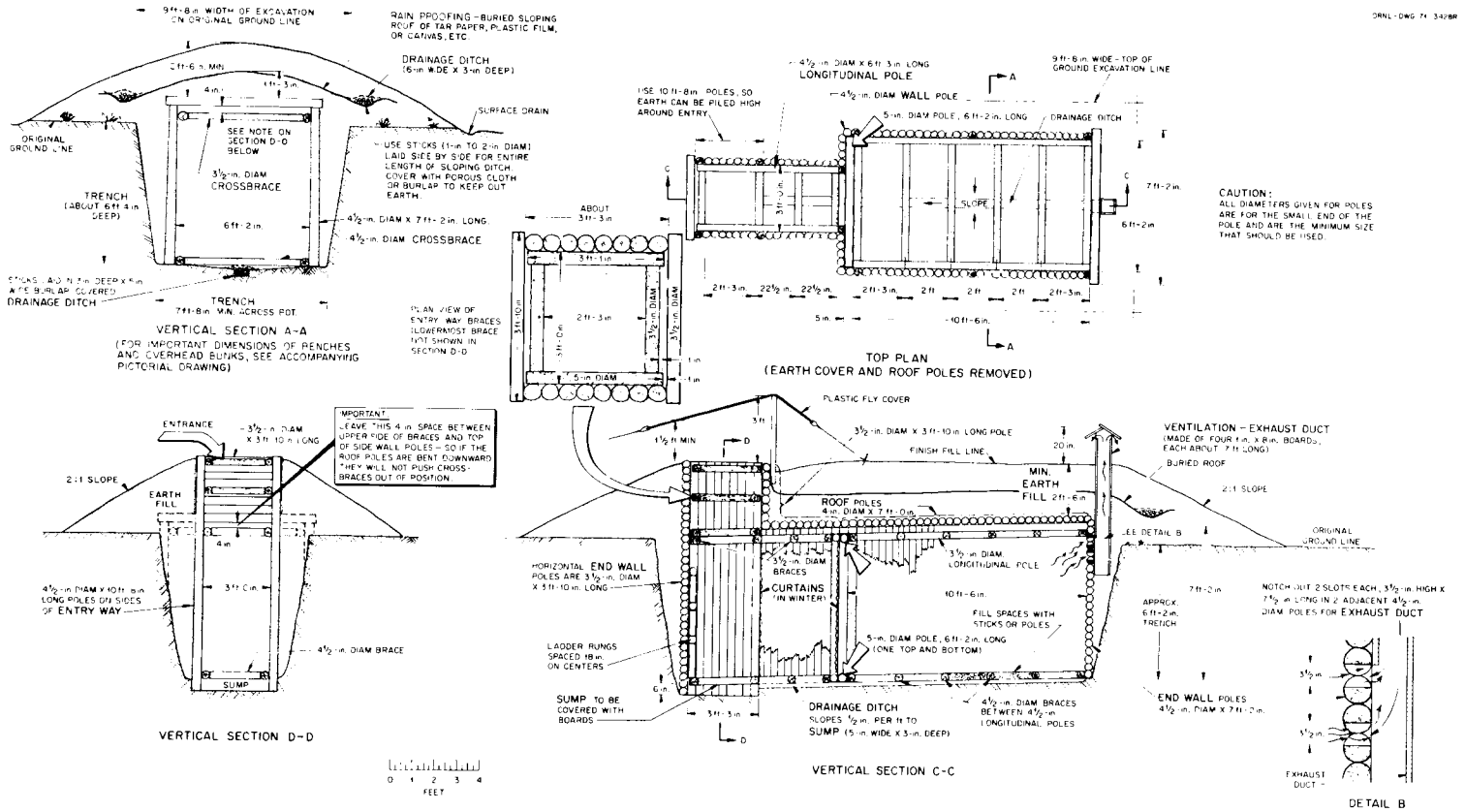

Fig. 18.3. Plan and elevation of small-pole shelter.

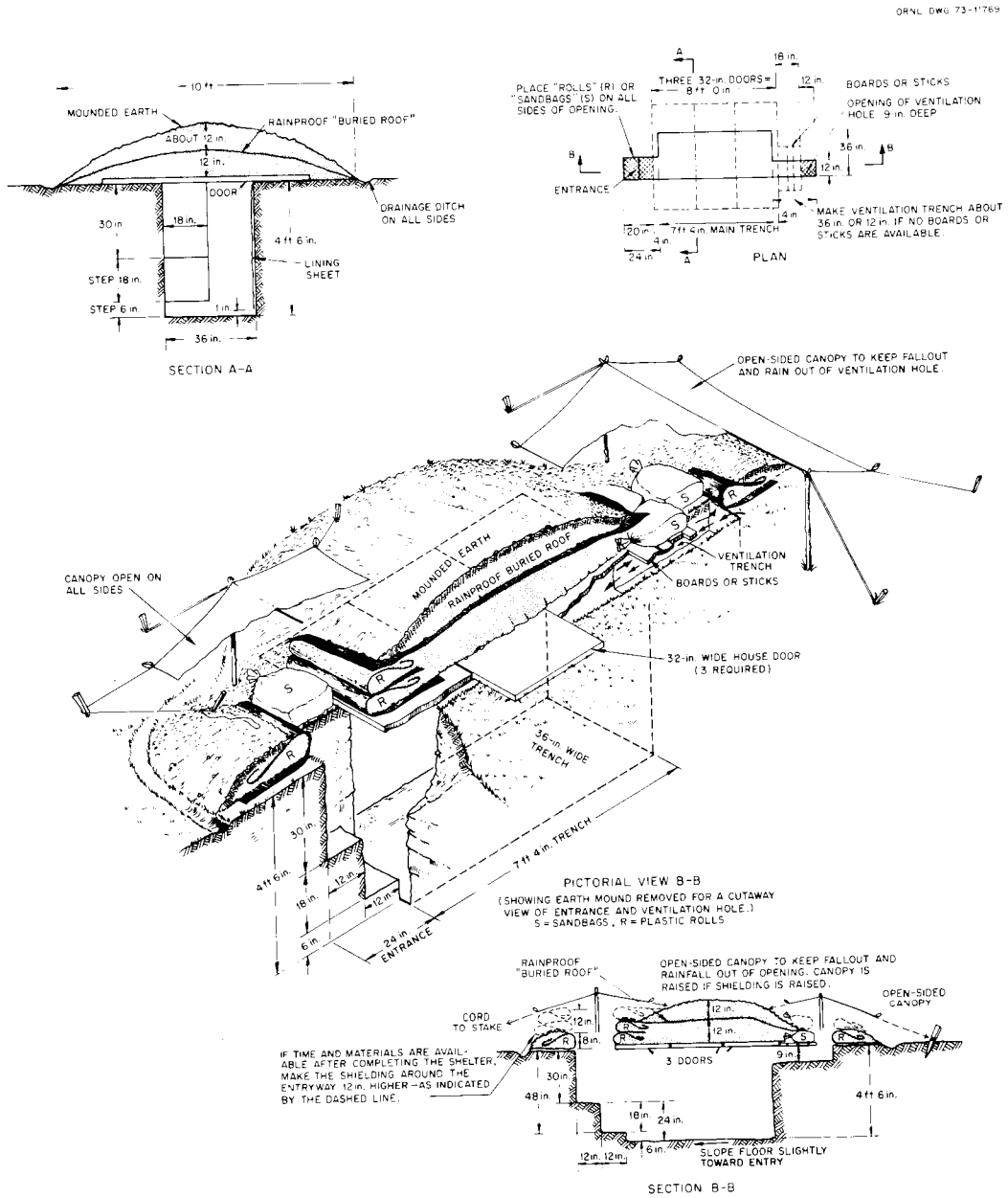

Fig. 18.4. Door-over-trench shelter.

Experiments in Florida

During February, March, and April of 1974, the author, following the procedures outlined above, developed and tested shelter components and had seven types of expedient shelters built in a typical part of Flagler County, Florida. In most parts of this well-wooded county, the water table is only a foot or two below the surface. Like areas where millions of Floridians live or could relocate themselves during a possible crisis, Flagler County offers very few existing structures that would afford good fallout protection.

Families were given sufficient monetary incentives to persuade them to build the four most promising types of expedient aboveground shelters while working under simulated crisis conditions necessitating rapid construction. These four types of shelters were (1) aboveground door-covered shelter, (2) crib-walled shelter, (3) ridgepole shelter, and (4) A-frame pole shelter.

Aboveground door-covered shelter. *Purpose.* This austere shelter is designed for unskilled families that have no materials with which to build expedient shelter except the hollow-core interior doors from their homes. It requires only doors, bed sheets, bedspreads, pillowcases, some waterproof household materials, and a shovel. It can be built on a home lawn; alternatively, if a pickup truck or station wagon is available, a family can carry from their home to the country all materials needed to build this new type of shelter, together with water containers, food, etc.

Construction. Figure 18.5 illustrates how interior doors were used by an untrained family to build walls of earth-filled "rolls" made of their bed sheets. This photograph also shows earth-filled pillowcases at the end of one of the two horizontal crawlway entrances. Two entryways were designed into all the Florida shelters. These two entryways were at opposite ends of the shelter and faced in opposite directions. This arrangement would provide adequate cooling ventilation except in warm, humid, *still* weather, when a homemade shelter-ventilating pump (a KAP[5]) would have been required.

The evening before the shelter-building day, this family received at their home only a list of the required materials and the instructions for building and using KAP's and were told the size of KAP to fit the entryways of the shelter they were to build. They built an excellent KAP, using only materials found in their house.

The white-collar family of six that built this seven-place shelter used nine interior doors – fewer interior doors than there are in their house in Bunnell, some 10 miles distant from the rural site. Each shelter space provided $7\frac{1}{2}$ ft^2 of floor space, not including space in the entryways. This family completed their shelter 13 hr 43 min after receiving the building instructions at 8:40 AM.

5. Kearny air pump. C. H. Kearny, *How to Make and Use a Home-Made Large Volume, Efficient Shelter Ventilation Pump: The Kearny Air Pump,* ORNL-TM-3916 (August 1972).

Fig. 18.5. Using lightweight hollow-core interior doors (without doorknobs) as temporary forms to build the walls of an aboveground door-covered shelter. The forms permit the construction of stable walls, vertical on their inner sides by building earth-filled "rolls" of bed sheets, one on top of the other. These same doors later were used for the gently sloped shelter roof, which was covered with waterproof materials and 15 in. of sandy earth.

Crib-walled shelter. *Purpose.* This shelter is designed for unskilled families who have tools with which to cut poles and shovel earth and who can bring their bed sheets, bedspreads, and some waterproof materials to the building site. This type of pole shelter requires no exactitude in cutting or fitting the poles.

Construction. As indicated by Fig. 18.6, a crib-walled shelter has several adjoining earth-filled wall sections. Each of these cribs is 2½ ft thick and is constructed quite like a frontiersman's corn crib or hog pen made of poles. The wide spaces between poles are covered on the inside of each crib with bed sheets or bedspreads and are then filled with earth. Under pressure, earth arching develops across the spaces between the poles and prevents the bed-sheet linings from being torn. Two feet of earth cover, with an intermediate rainproof "buried roof," are placed over the horizontal roof, made of 9-ft poles.

Ridge-pole shelter. *Purpose.* This shelter is designed to minimize the necessity for skilled workmanship and to halve the number of side-wall poles required, as compared with an A-frame pole shelter.[6] Figure 18.7 illustrates the wide spacing of the side-wall poles and their inexact lengths.

Construction. A group of related families (consisting of 16 persons, including 2 toddlers) completed this shelter 23 hr 40 min after receiving an evacuation checklist and the shelter-building instructions at their home 12 miles from the building site. They used only muscle-powered hand tools and carried or dragged the poles to the site. The earth cover had a minimum depth of 2 ft.

A-frame pole shelter. *Purpose.* For families planning to build an expedient aboveground shelter in an area that may be subjected to blast effects,[7] this shelter is

6. For previous work on the A-frame pole shelter, see *Civil Defense Research Project Annual Progress Report, March 1971–March 1972,* ORNL-4784, p. 81 (December 1972).

7. An aboveground A-frame pole shelter withstood 17-psi blast effects from a 1,000,000-lb TNT test explosion. C. H. Kearny and C. V. Chester, *Blast Tests of Expedient Shelters,* ORNL-4905, pp. 38–40 (January 1974).

Fig. 18.6. Crib-walled shelter built in four days by this family. Torrential rains on the first day of this period prevented these builders from reaching this rural site until almost sunset. With no hope of winning the bonus for completion within 48 hr, they worked at a pace necessary to win the basic offer for completion within four days.

Fig. 18.7. Partially completed frame for ridge-pole shelter. After pine branches had been laid horizontally across the spaces between the side-wall poles, they were covered with bed sheets before placing a 2-ft earth cover, containing a "buried roof," over the entire shelter frame. The ridge-pole was supported by four posts.

the best. However, it requires more poles and more skill to build than do the other Florida shelters and would be difficult to build without using a chain saw.

Construction. A group of families, all rural except one and consisting of 22 individuals, built an A-frame pole shelter with 273 ft^2 in its main room. Fifteen men, women, and larger children were able to work hard and efficiently to complete this shelter only 13 hr after receiving the instructions. Besides cutting and hauling the trees and poles, they excavated and moved with hand tools about 80 tons of earth in order to cover their shelter with earth to a minimum depth of 2 ft. Two pregnant wives worked only on building a shelter-ventilating KAP.

SOVIET CIVIL DEFENSE STUDIES

Our research in the area of Russian Civil Defense Planning has continued to reveal interesting details concerning this important department of the Soviet military organization. There is no doubt that the Soviets regard civil defense as an integral part of their defense strategy for the U.S.S.R.

During the past year we have published two translations of Russian civil defense documents. The first of these was published as ORNL-TR-2745, entitled *Civil Defense of the USSR – Antiradiation Shelters in Rural Areas,* and the second was *Civil Defense (Moscow 1970)*, published as ORNL-TR-2656 (see Fig. 18.8).

ORNL-TR-2656

CIVIL DEFENSE

ГРАЖДАНСКАЯ ОБОРОНА

MOSCOW 1970

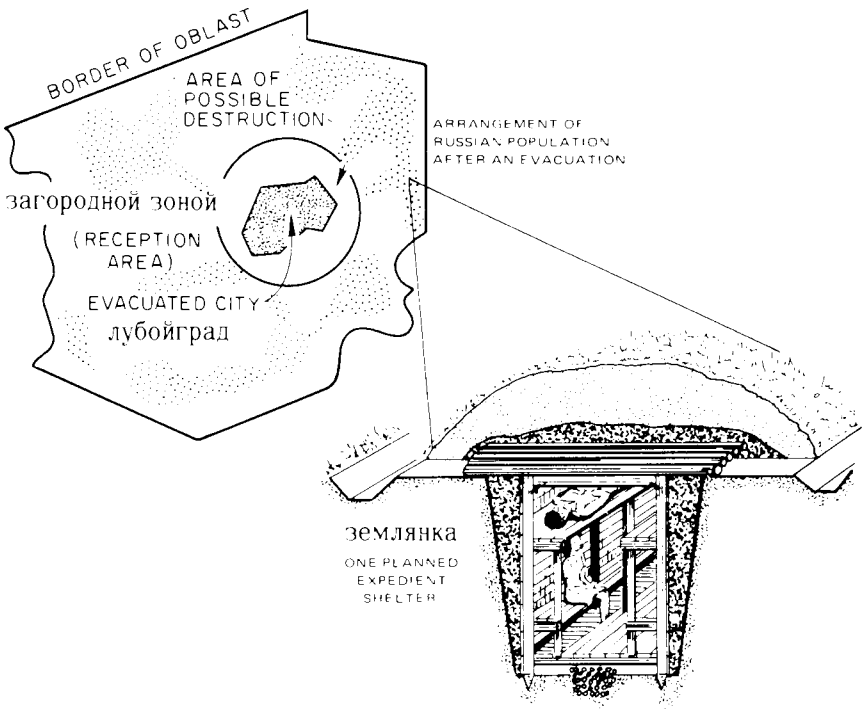

PREPARED BY OAK RIDGE NATIONAL LABORATORY

SUPPORTED BY UNITED STATES ATOMIC ENERGY COMMISSION

DEFENSE ADVANCED RESEARCH PROJECTS AGENCY

Fig. 18.8. A facsimile of the cover of our translation of the Russian Civil Defense Document, *Civil Defense (Moscow, 1970)*.

Both documents were extensively edited by members of the Section and have been widely distributed to Civil Defense officials, members of government, and the general public in order to publicize the work being done by the Soviets to ensure protection of their population and their essential industries in the event of nuclear war.

For an extended period in the later months of 1973, there was an apparent lull in the reports of civil defense activities coming out of Russia. It was most unusual in view of the prominent place ordinarily given it in the past. However, Col. Gen. A. Altunin, U.S.S.R. Deputy Minister for the Civil Defense, states in an article[8] entitled, "The Main Direction" (Moscow, *Voyennyye Znaniya,* Russian, No. 12, December 1973):

> Civil defense is an important part of our military power and our system of strategic state measures associated with defending the population and objects of the country's national economy. Its role has increased immeasurably under modern conditions. Following the instructions of the CPSU Central Committee and the Soviet Government, in 1973 an entire complex of organizational measures was implemented for restructuring and improving all areas of civil defense and investigating and introducing new forms of training of the population for defense from modern armament. Measures were taken for further improvement in administrative agencies, for organization of communications, for supplying the population, military subdivisions, and nonmilitary civil defense formations with modern means of protection, and for equipping them with authorized property and technical equipment.
>
> Last year, for a number of reasons, preparatory measures for the new training year were delayed. The necessary conditions now exist for the staffs and civil defense services to promptly plan the training process, to hold meetings about methods for management and command personnel in October and November, to bring the tasks to all units, and, in a number of places, to create the necessary training and material base and thus begin training in an organized way by 1 December.

We have noted that, since the issuance of Col. Gen. Altunin's article, there is a definite flurry of activity among all the civil defense officials to implement his directives. The practical aspect of civil defense training is now being stressed everywhere – farms, industries, and schools. It is compulsory in Russia at this time for every citizen to have a minimum 20-hr training course in the practical application of civil defense measures.

From a summary of a talk[9] by Col. Gen. Vladimir Filippovich Chizh, Chief of the Ukrainian Civil Defense Staff, aired by Kiev radio in Russian on January 31, 1974, we quote the following statement:

> At most places the new training year has begun auspiciously. All exercises are well attended and materially well provided. It is to be emphasized that the most essential thing for the training of all the population is to practically meet the minimum standards of the 20-hour general training program, which is compulsory for every citizen in the country.
>
> In the countryside, defense from radioactive fallout has top priority. The rural population must be taught how to build shelters and how to adapt cellars for this purpose. This is simple and absolutely indispensable for every home and family.

Civil defense is included in the regular school curriculum as early as the second grade, where these young children are taught to don and use gas masks and respirators.

The publication of numerous articles by members of the Section in the open literature has served to inform the U.S. public of some of the measures taken in Russia to protect their people. Close contact with the Department of Defense, members of the Congress, and other influential public officials is maintained, and briefings on Russian civil defense have been given on several occasions (see Theses, Papers, Publications, and Lectures section of this report).

Our following of Soviet civil defense brings us into contact with the major portion of the Russian news media, and as a result we constantly hear of the extremely poor faith displayed by the U.S. and China because of (1) the U.S. defense budget and (2) the Chinese tunnels under their cities. In view of this, the following very brief, recent news broadcast[10] raised a question regarding the future potential of the "underground construction" planned for Moscow.

UNDERGROUND CONSTRUCTION PLAN
APPROVED FOR MOSCOW

Moscow Domestic Service in Russian
0600 GMT 11 Apr 74 L

> (Text) The Moscow Gorispolkom has approved the main points of a plan for the use and organization of underground spaces in Moscow. The aim of the project is to put underground those structures which (? do not require daylight), such as garages, parking lots and transformer substations. It is also planned to house large shopping complexes in special underground approaches to such subway junction stations as Oktyabrskaya, Taganskaya and Paveletskaya.
>
> In those areas which are most valuable from the architectural viewpoint, such as historical monuments, it is proposed to

8. Quoted from *Translations on USSR Military Affairs, No. 1009,* Joint Publications Research Service, JPRS-61288, Feb. 21, 1974, pp. 45–47.

9. Quoted from *Translations on USSR Military Affairs, No. 1010,* Joint Publications Research Service, JPRS-61309, Feb. 25, 1974, p. 23.

10. Quoted from *Daily Report, Soviet Union,* FBIS-SOV-74-82, No. 82, vol. III, April 26, 1974, Foreign Broadcast Information Service.

construct underground streets. At the Belorussiky rail terminal and near the Komsomolskaya Ploshchad it is planned to construct large underground transfer points which will include bus links and taxi stands.

The new watchword of Russian foreign policy is "detente" (as defined by one prominent Communist, "the unstringing of a bow"). This condition is uppermost in all press and radio releases that we have read for many months. The "unstringing" is urged for all "imperialist" nations; however, the "state of readiness" of the Soviet military and civilian population is constantly being upgraded.

The primary purpose of our researching Russian civil defense is to keep abreast of new developments in their preparations for maintaining a system of protection of their population and to make every effort to bring this information to the attention of the U.S. public and the proper government authorities.

19. Nuclear Reactor Safety Studies

C. V. Chester R. O. Chester C. M. Haaland

EMERGENCY PLANNING FOR ACCIDENTAL RADIOACTIVITY RELEASES FROM A LICENSED NUCLEAR FACILITY

Two topics which determine the time available to institute emergency procedures after a water-cooled power-reactor core meltdown have been examined. First, a realistic calculation of fission product release as a function of time has been made.[1,2] The release time function can determine, in part, the speed and type of response that is necessary. Second, the time-dependent meteorological dispersion and deposition of the radioactive aerosol released to the environment have been calculated.[3] Inhalation dose as a function of time is also estimated because it is the immediate concern of emergency planning for the population surrounding a licensed nuclear facility.

Fission Product Release to the Environment

The objective of the fission product release calculation was to develop a realistic model of the effects of a core meltdown. The model relates the fission product release from a water-cooled power reactor to the reactor containment configuration and degree of damage to the containment.

Reactor description. A typical large 1000-MW(e) boiling water reactor (BWR), such as TVA's Browns Ferry Nuclear Power Plant or the Pennsylvania Power and Light's Susquehanna Steam Electric Station, is used as a model.[4] In the model the reactor core is inside the damaged pressure vessel. The pressure vessel is, in turn, inside the primary containment, and a reactor building then covers the entire structure.

The pressure vessel, containment, and reactor building are characterized by volumes, leakage rates, and average particle fall distances. Containment volumes and design-basis leak rates were obtained from the Final Safety Analysis Report of the Susquehanna plant. The leakage rate for a badly damaged containment was selected as ten volume changes per day. Fall distances were estimated from inspection of the Browns Ferry plant.

A similar large 1000-MW(e) pressurized water reactor (PWR) is also modeled.[5] The major difference is that the primary containment and the reactor building are the same structure. However, a filter-absorber is inside this structure and, when operating, decreases the release to the environment as much as an additional building.

Accident description. An improbable, catastrophic reactor accident is modeled in which the core and the fission products are vaporized by the fission product afterheating and by heat from the metal-water reaction. The vaporized core and fission products then diffuse through a sequence of containments to the environment.

It is assumed that there is a break in the coolant lines to the pressure vessel and that the emergency core cooling is totally disabled. After reactor shutdown, blowdown is assumed completed in 10 sec, and the core starts heating until the metal-water reaction is initiated at about 60 sec. The metal-water reaction proceeds until 20% of the zirconium has reacted. This takes about a half hour; then fission product afterheating dominates.[6,7]

---

1. J. A. Auxier and R. O. Chester, *Report of the Clinch Valley Study, May 15–June 2, 1972,* Appendix VI, ORNL-4835 (January 1973).
2. D. Y. Hsia, "A Study of the Fission Product Release from a Badly Damaged Water-Cooled Reactor," Thesis, University of Tennessee, Knoxville (June 1974).
3. R. O. Chester, *Dose and Deposition from a Nuclear Reactor Core Meltdown,* ORNL-4944 (1974).
4. Tennessee Valley Authority, *Final Safety Analysis Report, Browns Ferry Nuclear Power Plant, Units 1–3,* USAEC Docket Nos. 50-259/260/296 (1973).
5. USAEC, *The Safety of Nuclear Power Reactors (Light Water-Cooled) and Related Facilities,* USAEC report WASH-1250 (July 1973).
6. W. K. Ergen, Chairman, *Emergency Core Cooling Report of Advisory Task Force on Power Reactor Emergency Cooling,* USAEC report TID-24226 (1967).
7. L. Baker and R. O. Ivins, "Analyzing the Effects of a Zirconium-Water Reaction," *Nucleonics* 23(7), 70 (July 1965).

The resultant releases to the environment of fission products from a core meltdown for a 1000-MW(e) PWR and for a 1000-MW(e) BWR are given in Figs. 19.1 and 19.2 respectively. The curves labeled "undamaged" are the release calculated for a core meltdown with the primary containment and reactor building assumed intact and with the doors shut. In this case, the

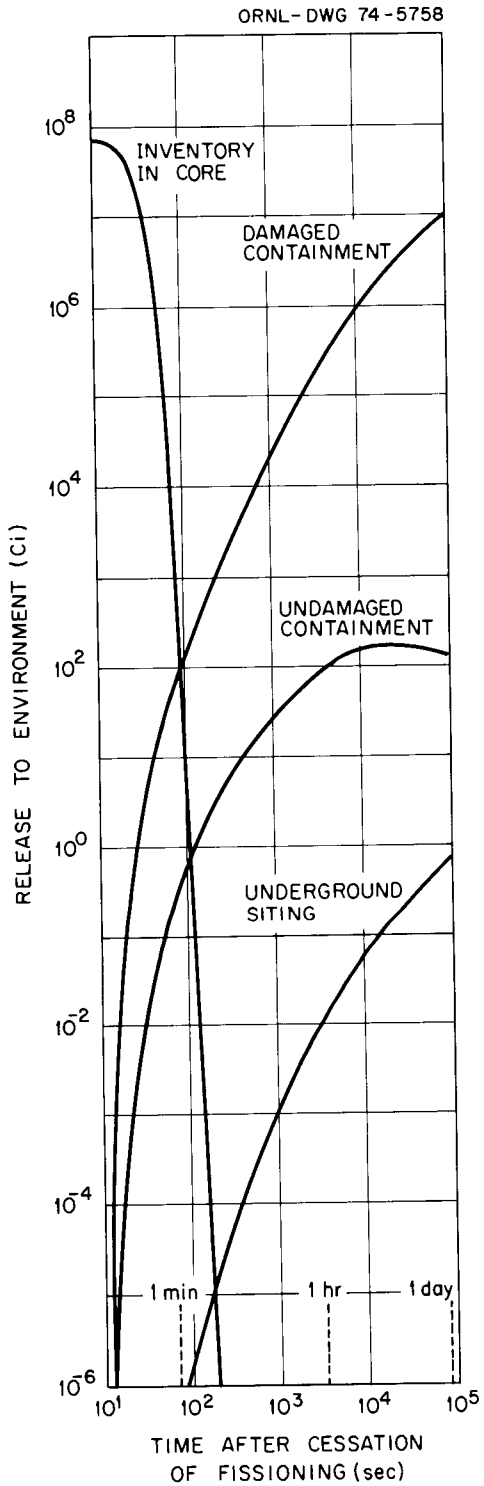

Fig. 19.1. Iodine release from a pressurized water reactor after a core meltdown.

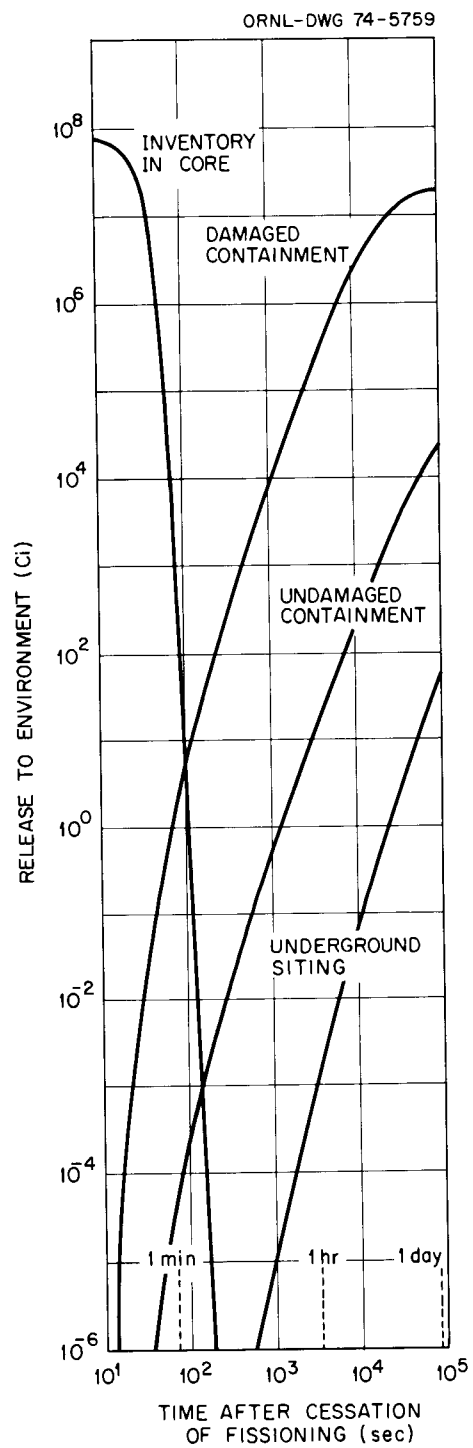

Fig. 19.2. Iodine release from a boiling water reactor after a core meltdown.

design-basis leakage rates of 0.5% of the volume per day for the containment and 100% of the volume per day for the reactor building are assumed. The PWR is also assumed to have an operational filter-absorber. The curves labeled "damaged" show the same reactors with both the primary containment and reactor building doors jammed open or blown off, either accidentally or intentionally. In this case, both containment and reactor building leakage rates are assumed equal to ten volume changes per day. The PWR filter is assumed inoperative. Under some conditions, this leakage rate is achieved if a door is jammed open or blown off its hinges. The curves labeled "underground siting" show the release of fission products from undamaged reactors that are sited underground with the access tunnel doors shut and leakage at the design rate of 6×10^{-8} volume/sec.

Comparison with Other Results

The AEC Regulatory Staff suggests typical values of the amount of radioactivity which leaves a PWR reactor core and reaches the reactor building.[8] The AEC values are essentially the total airborne release from the core. They include natural deposition processes but not the effects of washdown or filtering from protective safeguards. Next, leakage to the environment is assumed to occur at a constant rate of 0.1% per day.

In order to compare the calculated values in the present work with the AEC suggested values, three numerical values must be examined (see Table 19.1). First, the fission product inventories in the pressure vessel, containment, and reactor building and the releases into the environment are summed. By doing the summation this way, the deposition process was included, but the effect of leakage was excluded. The summed values can be compared directly with the AEC suggested values of percent inventory in the reactor building. Further, it should be noted that the calculated values are a nonlinear function of time. The time chosen for comparison is 10^4 sec after shutdown. This is approximately 3 hr, the longest time realistically estimated before backup emergency assistance will have arrived at the reactor site.[1] Also, in many circumstances, in 3 hr the pressure vessel will not yet have melted through. (This would require a basic geometry change in the calculation.) Second, the calculated airborne inventory in the reactor building at 10^4 sec is listed in the table. The third value listed is the calculated total release to the environment at 10^4 sec. Parker suggested values for cesium and ruthenium based on his experimental work.[9] These values are also included in the comparison shown in the table.

8. J. J. DiNunno, F. D. Anderson, R. E. Baker, and R. L. Waterfield, *Calculation of Distance Factor for Power and Test Reactor Sites,* USAEC report TID-14844 (1962).

9. G. W. Parker, G. E. Creek, C. J. Barton, W. J. Martin, and R. A. Lorenz, *Out-of-Pile Studies of Fission-Product Release from Overheated Reactor Fuels at ORNL – 1955–1965,* ORNL-3981 (July 1967).

Table 19.1. Comparison of the calculated fission product releases with estimated values

Fission product	Estimated percent of inventory		Calculated percent of inventory[b]		
	In building	To environment[a]	Sum	In building	To environment
Xe	100[a]	0.012	47	30	0.01
I	50[a]	0.003	46[c]	28[c]	0.0098[c]
Zr	1[a]	1.2×10^{-4}	2×10^{-3}	9×10^{-4}	2×10^{-7}
Nb	1[a]	1.2×10^{-4}	2×10^{-2}	7×10^{-3}	2×10^{-6}
Ba	1[a]	1.2×10^{-4}	36	22	7×10^{-3}
Sr	1[a]	1.2×10^{-4}	36	15	4×10^{-3}
Cs	50[d]	0.006	3.8	2.3	8×10^{-4}
Ru	5[d]	6×10^{-4}	2×10^{-3}	1×10^{-3}	2×10^{-7}
Gross activity	15[a]	1.8×10^{-3}	16	10	3.5×10^{-3}

[a]These values are estimated by J. J. DiNunno, F. D. Anderson, R. E. Baker, and R. L. Waterfield, *Calculation of Distance Factor for Power and Test Reactor Sites,* USAEC report TID-14844 (1962).

[b]The calculated values are obtained at 10^4 sec, and assume 10^{-3} of the decay heat available for the evaporization of UO_2. Radiological decay of all the isotopes is included in these values.[2]

[c]In this particular calculation, 50% of the core inventory of iodine is considered to have aerosol properties similar to the rare gases. As such, these numbers may be an overestimate of the release.

[d]These values are estimated by G. W. Parker, G. E. Creek, C. J. Barton, W. J. Martin, and R. A. Lorenz, *Out-of-Pile Studies of Fission-Product Release from Overheated Reactor Fuels at ORNL – 1955–1965,* ORNL-3981 (July 1967).

Table 19.1 shows that the other values compared to the currently calculated values of zirconium and niobium overestimated the release by at least a factor of 50, but the values for barium and strontium were underestimated by a factor of 36. The iodine release was slightly overestimated, whereas the xenon release was overestimated by a factor of 2. The higher calculated values of strontium and barium releases can be explained by the change from an oxidizing condition to a reducing condition by the zirconium-steam reaction. Hence the vapor pressure of strontium and barium increases by more than two orders of magnitude.

Dose and Deposition from Dispersion of the Release

Assume that a 1000-MW(e) BWR undergoes a core meltdown. Further assume that the reactor building and containment are damaged as discussed previously. The accident, for the purpose of this illustration, is assumed to have taken place at midnight, February 23, 1967, and the meteorological conditions for the next 12 hr are as follows:[10]

Time	Wind velocity (mph)	Wind (from compass point)
12 midnight to 1 AM	4	11
1 AM to 2 AM	5	13
2 AM to 3 AM	8	11
3 AM to 4 AM	7	11
4 AM to 5 AM	5	15
5 AM to 6 AM	2	12
6 AM to 7 AM	3	11
7 AM to 8 AM	1	12
8 AM to 9 AM	2	10
9 AM to 10 AM	3	13
10 AM to 11 AM	3	11
11 AM to 12 noon	7	10

These are meteorological data taken at an Oak Ridge station on February 23, 1967. Therefore the data given would apply to a BWR if it were sited in the Oak Ridge area and had an accident at midnight on that date. Release to the environment is assumed to proceed as indicated in Fig. 19.2 by the "damaged" curve until 2 hr have elapsed. At this time, it is assumed that the leakage rate is drastically reduced by appropriate emergency procedures.

10. The meteorological data were kindly supplied by W. Culkowski of the Atmospheric Diffusion and Turbulence Laboratory of the National Oceanic and Atmospheric Administration.

Release and transport. A cold ground release is assumed. The standard relations of turbulence types to weather conditions and of dispersion coefficient, release concentration, and cloud depletion to total path length from the release point are assumed.[11]

The calculation of this deposition differs from many others because the virtual source team and both horizontal and vertical dispersion coefficients are functions of time as well as total diffusion path length.

To facilitate calculations, the fission products were divided into classifications according to their dispersion characteristics. Different classifications include rare gases, halogens, volatiles such as strontium and cesium, and refractories such as yttrium and niobium.

Deposition. A settling velocity of 0.01 m/sec is assumed. This constant is roughly characteristic of halogens and uranium oxide to which many fission products have become attached. Deposition is assumed to have taken place on a smooth plane. Results are given in curies per square meter.

The contours are drawn for 1, 2, and 3 hr after reactor shutdown in Fig. 19.3. These are critical hours during which emergency procedures are put into effect. The contours after 6 hr are drawn in Fig. 19.4 because the 1×10^{-3} Ci/m^2 contour does not change shape after this time due to depletion of the plume by deposition and dilution of the plume due to meteorological dispersion.

Figure 19.5 shows the effect of radiological decay on the deposition after 15 years. Effects of rain, absorption, and groundwater transport are not included. Activity has decreased by about two orders of magnitude.

Dose calculations. For thyroid dose calculations, only iodine need be considered.[1] In this case, activity in curies is not sufficient because several isotopes of iodine are involved. The necessary quantity is the total energy absorption in a 20-g adult thyroid by all the iodine isotopes. The assumptions are that the breathing rate is 10 liters/min. Of the material inhaled, about one-third is retained in the lungs and absorbed immediately into the bloodstream. One-fifth of the iodine in the bloodstream collects within a half hour in the thyroid, where the biological half-life is roughly 140 days. One hundred percent of the beta-ray energy and that fraction of the gamma-ray energy absorbed in a 20-g sphere of tissue from each iodine decay are calculated. The lifetime dose contours for an unprotected population 6 hr after the accident are plotted in Fig. 19.6.

11. D. H. Slade, ed., *Meteorology and Atomic Energy 1968*, USAEC report TID-24190 (1968).

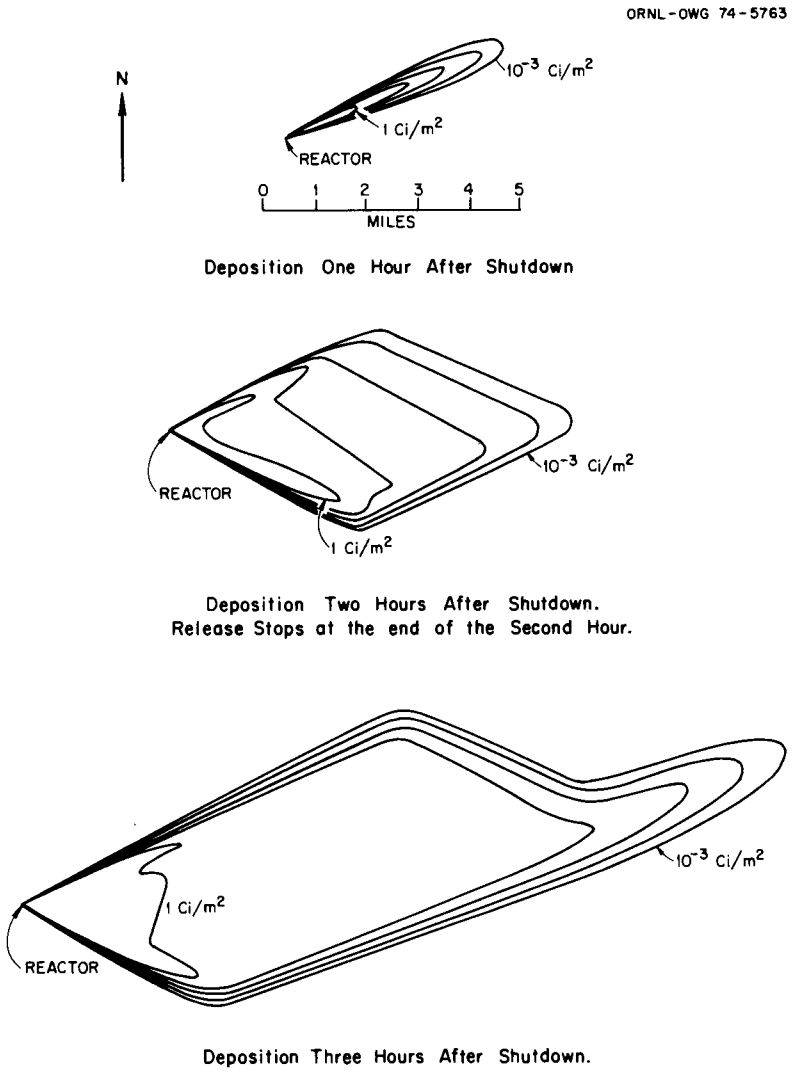

Fig. 19.3. Fission product deposition 1, 2, and 3 hr after a 1000-MW(e) BWR core meltdown starts. The containment is assumed badly damaged.

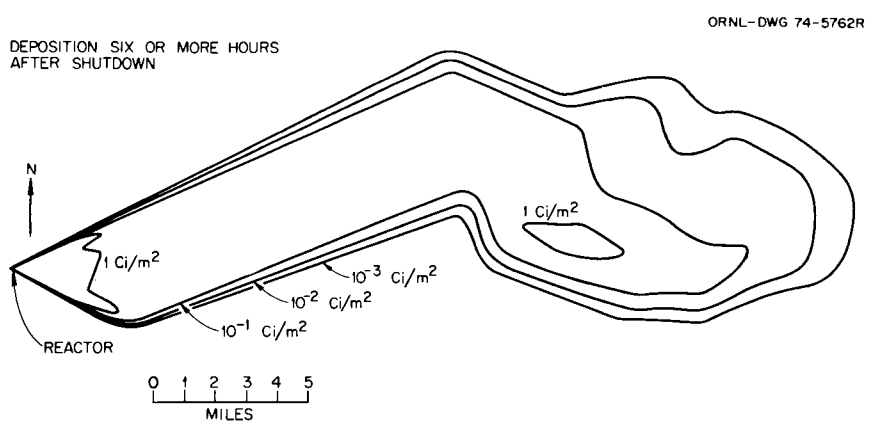

Fig. 19.4. Fission product deposition six or more hours after a 1000-MW(e) BWR core meltdown starts. The containment is assumed badly damaged.

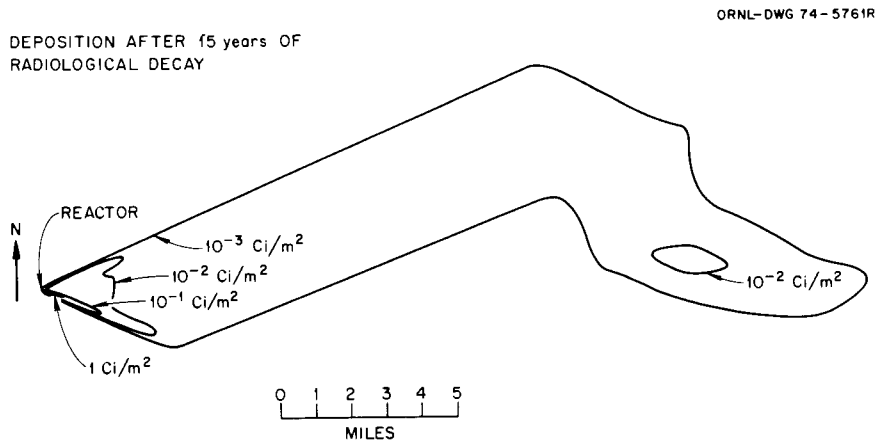

Fig. 19.5. Fission product deposition from a 1000-MW(e) BWR core meltdown after 15 years of radiological decay. No allowance has been made for weathering.

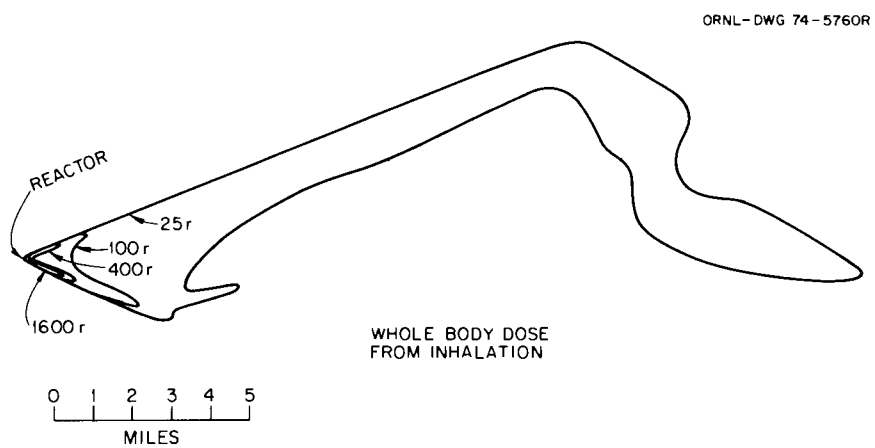

Fig. 19.6. Inhalation whole-body dose from a 1000-MW(e) BWR core meltdown. No protective measures were assumed.

To estimate the whole-body dose from inhalation, not only must the iodine dose be calculated, but appreciable dose is received from other isotope oxides that are soluble in lung fluids and hence enter the bloodstream immediately and have various biological half-lives. Insoluble isotope oxides are deposited in the lungs and contribute appreciably to the whole-body dose. Insoluble isotope oxides are expelled from the lungs via several mechanisms, the most important of which has a 500-day half-life. All the beta- and gamma-ray energy released per isotope decay is assumed to contribute to the whole-body dose. The 6-hr results are plotted in Fig. 19.7.

CALCULATION OF SITE POPULATION FACTOR (SPF)

The difficult task of locating sites for power reactors may possibly be simplified by maps which show isopleths of the site population factor. This factor is a number which indicates the suitability of a specific location relative to others in terms of population at risk from a potential nuclear reactor accident at the location. The actual or future populations within circular areas surrounding the specified location are summed and modified by a weighting factor. The resulting number is "normalized" by dividing by the

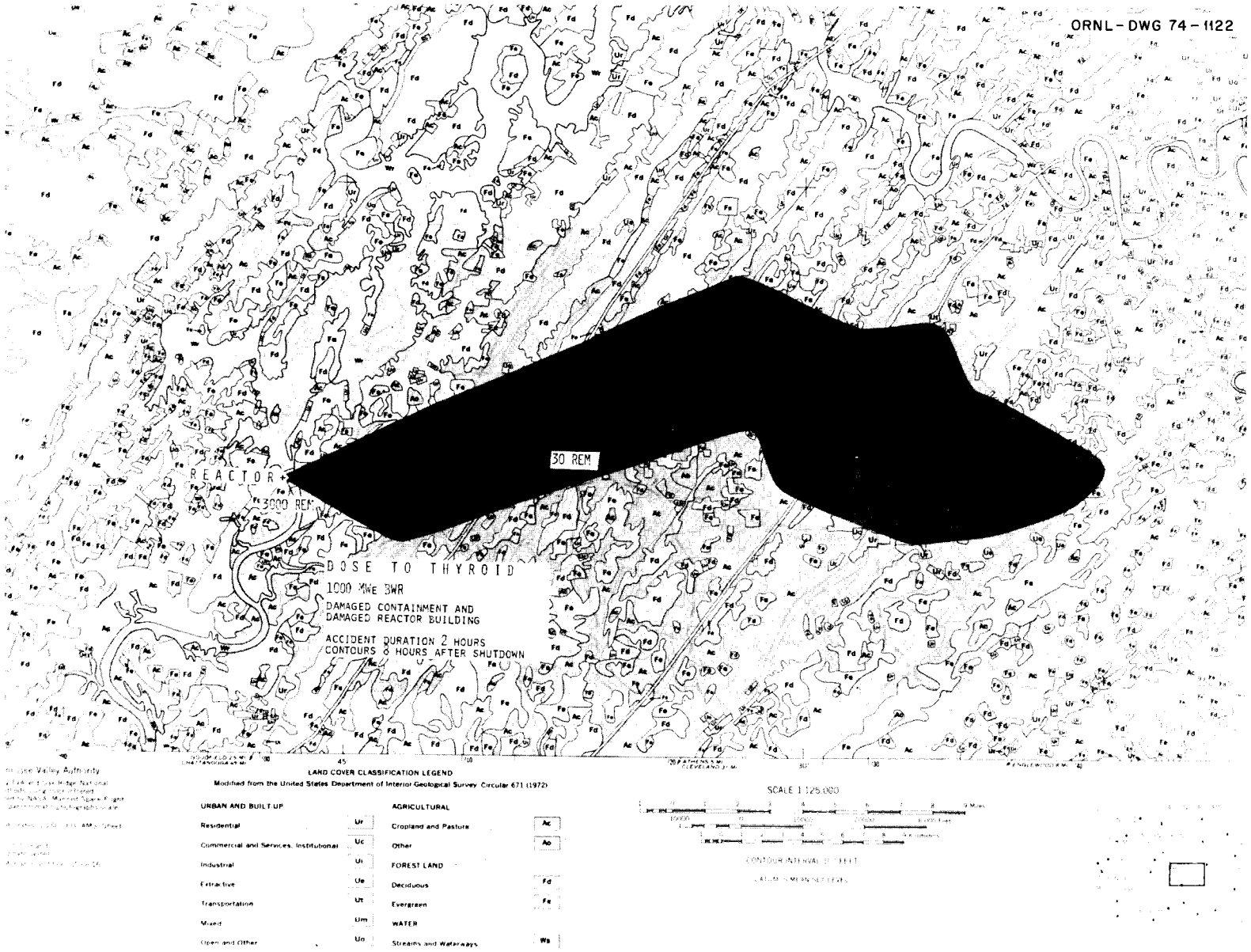

Fig. 19.7. Inhalation dose to thyroid from a 1000-MW(e) BWR core meltdown. No protective measures were assumed.

sum of a hypothetical population of uniform density in the same area, modified by the same weighting factor.

Implicit in the formula for calculating SPF is the conservative assumption that any direction is possible for wind movement at the time of an accident. Consequently, the formula treats the total population in concentric circular annuli without special weighting according to wind direction.

The weighting factor in the SPF formula is derived from the diffusion factor, which represents the deconcentration of contaminants in the downwind plume due to atmospheric diffusion. The diffusion factor, D, can be represented for many conditions by a simple function of the form

$$D = kr^{-\delta} , \qquad (1)$$

in which k and δ are constants and r is the distance downwind from a ground-level point source. From the model described in AEC Safety Guide 4, in which atmospheric diffusion factors are given for various times and distances from a source, it can be verified that the choice of $\delta = 3/2$ in Eq. (1) results in a fairly good representation of the diffusion factor in the range of 1 to 20 km downwind.

The formula that was used to calculate SPF contours for the entire United States is given by

$$\mathrm{SPF} = \frac{r_t^{-\delta} \sum_{r_i \leqslant r_t} P_{r_i} + \sum_{r_t < r_i \leqslant R} r_i^{-\delta} P_{r_i}}{[\pi\rho_0/(2-\delta)](2R^{2-\delta} - \delta r_t^{2-\delta})} , \qquad (2)$$

in which r_t is the truncation radius inside which the weighting factor is constant, δ is the diffusion factor exponential constant, P_{r_i} is the population in the subarea with centroid located at radius r_i from the specified site, R is the maximum radius from the site of the circular area through which the SPF is calculated, and ρ_0 is the hypothetical uniform population density within the circle of radius R.

The population P_{r_i} was computed from a data base we constructed from the MED-X list of the 1970 residential population as provided by the Bureau of the Census. In our data base, we divide the entire United States into subareas bounded by latitude and longitude lines 0.05° apart. These subareas have dimensions of 3.45 statute miles in the north-south direction and 2.68 statute miles in the east-west direction at 39° latitude. The population in each subarea is the sum of the population of all Enumeration Districts on the MED-X list which have centroids with geographical coordinates falling within the boundaries of the subarea. This step of processing the MED-X list into an orderly array of population cells reduces the SPF computation time by a factor of 5 to 10 compared with the direct use of centroids of Enumeration Districts.

The truncation radius is placed in Eq. (2) for two reasons: to reduce the weighting factor which would be given to population centroids located very close to the specified reactor site and to reduce error by making the truncation radius suitably larger than the characteristic dimension of the population subareas.

Calculations of SPF have been made for hypothetical reactor sites located at each intersection of 1/4 deg latitude and longitude lines for the entire coterminous United States, involving approximately 330,000 locations. The values of the maximum radius R in Eq. (2) were specified by the AEC to be 20, 30, 40, and 50 miles for each site. From this body of data, maps showing isopleths of SPF were prepared for values of SPF corresponding to 0.2, 0.4, 0.5, 0.7, and 1.0. In all cases the truncation radius, r_t, was 5 miles; the diffusion factor, δ, was 3/2; and the hypothetical uniform population density, ρ_0, was 1000 people per square mile. This value for the population density corresponds to the value defined by the Bureau of the Census in connection with their definition of "urban fringe."

A representative map showing SPF contours for the case where R = 40 miles is shown in Fig. 19.8 for the region stretching from Illinois through Pennsylvania. State boundaries have been plotted with the aid of a digitized data base for county and state boundaries obtained from the Federal Highway Administration.

For comparison, a map showing contours of population density is shown for the same area in Fig. 19.9. Two general effects of applying the SPF formula are immediately obvious: (1) Most of the areas of small cities (with a population of less than about 150,000), which make up the clutter in the population density maps, do not appear on these SPF maps. (2) The shapes of the metropolitan areas are smoothed out by the SPF formulation, and the contours extend further out from the centers of the cities than they do for population density.

These effects are caused by (1) the integrating effect of the SPF formula and (2) the smaller mesh size (1/20 deg compared with 1/4 deg) of the population density data base compared with the SPF data base used for generating the contours.

If future reactor sites were allowed only outside the areas enclosed by SPF contours, over 90% of the coterminous U.S. land area would be suitable for sites for SPF = 0.2, and over 95% for SPF = 0.4 or greater, for $R \geqslant 20$ miles. In the most densely populated multistate regions, these percentages decrease to 65 and 80% respectively.

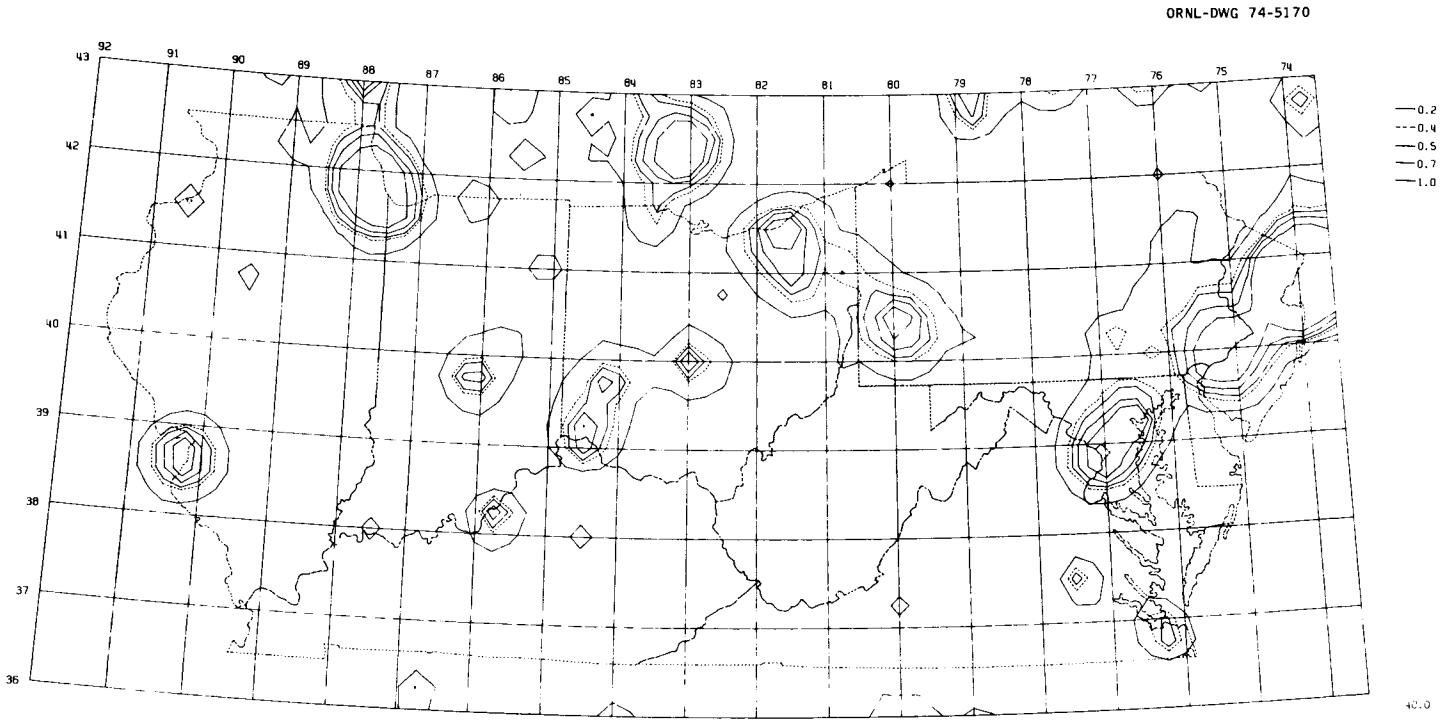

Fig. 19.8. Site population factor (SPF) contours for region 2, including Delaware, Maryland, Illinois, Indiana, Kentucky, New Jersey, Pennsylvania, Virginia, and West Virginia.

ORNL-DWG. 74-4538

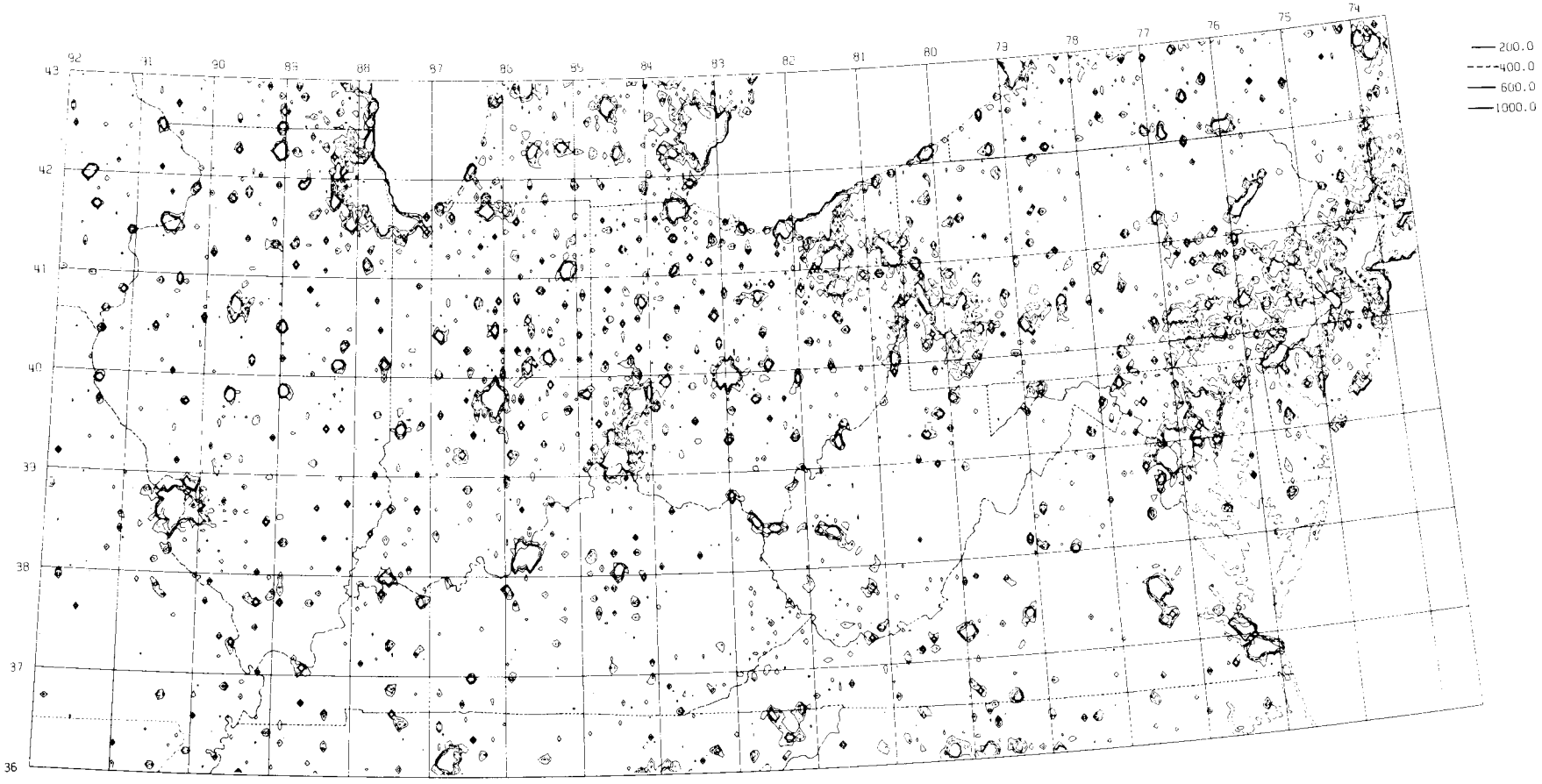

Fig. 19.9. Population density contours for region 2.

Part III. Fundamental Health Physics Research

R. D. Birkhoff W. R. Garrett R. H. Ritchie

20. Electron and Ion Collision Physics

R. N. Compton

V. E. Anderson[1]
Ada Carter
C. D. Cooper[2]
J. T. Cox
Liliana Deleanu[3]
C. E. Klots
G. Ostrom[3]
B. P. Pullen[4]
P. W. Reinhardt
J. A. D. Stockdale
J. F. Wilson[5]
J. M. Younkin[3]

COLLISIONAL IONIZATION OF CESIUM BY MOLECULES: DETERMINATION OF MOLECULAR ELECTRON AFFINITIES

Studies of the collision of "one-electron atoms," notably the alkali atoms, with neutral gas targets have received great attention in atomic and molecular physics. Well-controlled beams of ground-state cesium atoms with small energy spread (about 0.2 eV) can now be obtained by a variety of methods. Owing to its small ionization potential, electrons can be easily transferred from cesium to another atom or molecule. The distance (in angstroms) between the centers of the two colliding particles at which electron transfer is most likely to occur is approximately given by

$$R_c = \frac{14.2}{\Delta E},$$

where ΔE is the difference (in electron volts) between the ionization potential of cesium and the electron affinity of the molecule. In many cases ΔE is about 1 or 2 eV, and the distance over which the electron is transferred can be large (about 10 Å); therefore large cross sections are expected (about 100 Å^2).

Studies of chemi-ionizing collisions between fast cesium atoms and molecules are yielding important information as to the structure of molecular negative ions. For example, the electron affinities of many polyatomic molecules have been determined by measuring the threshold for the formation of ion pairs in collisions of cesium with O_2,[6] NO, NO_2, N_2O,[7] SF_6, TeF_6,[8] and a number of organic molecules.[9,10] This work has continued over the past year. The apparatus has been equipped for crossed-beam collision geometry, and provisions have been made for measurement of ion

1. On loan from Computer Sciences Division.
2. Consultant from the University of Georgia.
3. Graduate student, University of Tennessee.
4. University Research Participant, ORAU.
5. Radiological Health Physics Fellow, University of Tennessee.

6. S. J. Nalley and R. N. Compton, *Chem. Phys. Lett.* 9, 529 (1971).
7. S. J. Nalley, R. N. Compton, H. C. Schweinler, and V. E. Anderson, *J. Chem. Phys.* 59, 4125 (1973).
8. R. N. Compton and C. D. Cooper, *J. Chem. Phys.* 59, 4140 (1973).
9. C. D. Cooper and R. N. Compton, *J. Chem. Phys.* 60, 2424 (1974).
10. R. N. Compton, P. W. Reinhardt, and C. D. Cooper, *J. Chem. Phys.* 60, 2953 (1974).

kinetic energies. In the following, we briefly discuss these studies.

CESIUM COLLISIONS WITH CO_2

Carbon dioxide is a linear molecule with a C-O bond distance of 1.162 Å. According to the Walsh rules, CO_2^-, with 17 valence electrons, will be bent in its ground state. Experimental evidence from electron spin resonance and infrared studies of CO_2^- in solids shows that the bond angle is 134°, and the C-O bond distance of 1.25 Å is consistent with an analysis of the molecular infrared absorption bands. Previously, we reported[11] studies of CO_2^- from collisions of electrons and cesium atoms with organic molecules containing "bent" CO_2 subunits. We arrived at an estimated value of -0.4 ± 0.2 eV for the electron affinity of CO_2. Theoretical calculations[12] are consistent with the "bent" and extended geometry of CO_2^- and our electron affinity value.

Collisions of cesium atoms with carbon dioxide result in the following two ionic reactions:

$$Cs + CO_2 \rightarrow CO_2^{-*} + Cs^+$$
$$Cs + CO_2 \rightarrow O^- + CO + Cs^+$$

The reactions were studied in a crossed atom-molecular beam apparatus, shown schematically in Fig. 20.1. The relative cross sections for the formation of CO_2^- ions as a function of collision energy are shown in Fig. 20.2.

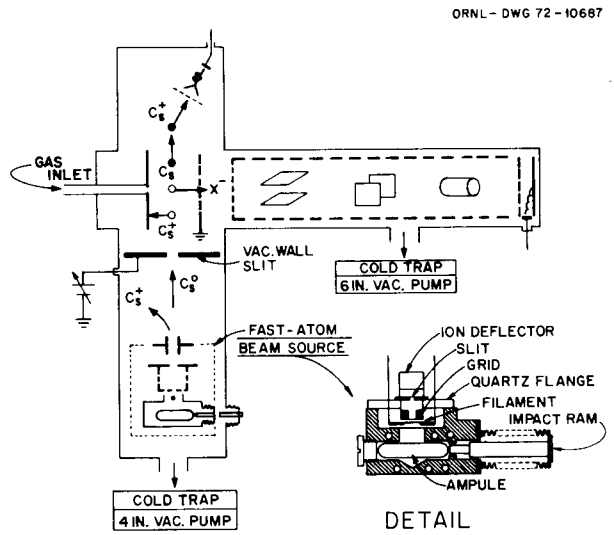

Fig. 20.1. Schematic diagram of the fast-atom collisional ionization experiment.

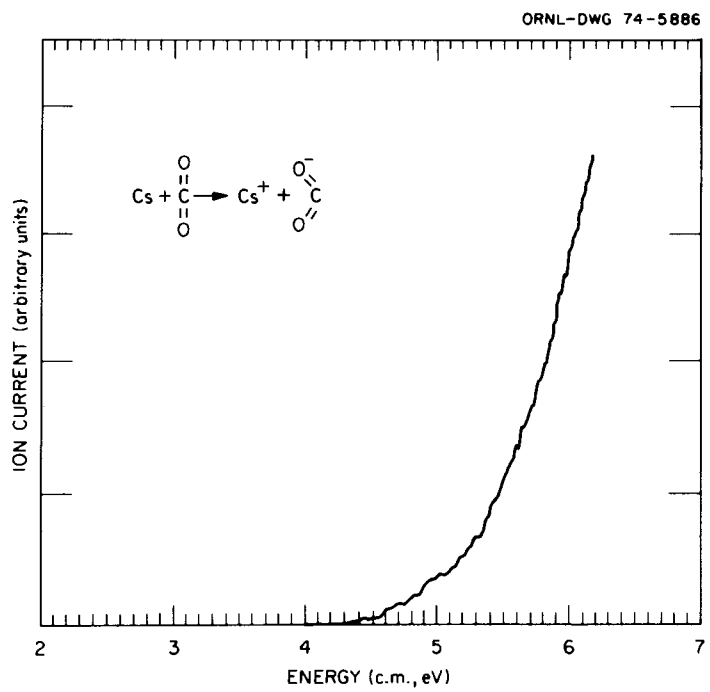

Fig. 20.2. Relative cross section for the production of CO_2^- ions from collisions with fast cesium atoms as a function of the center-of-mass collision energy.

11. C. D. Cooper and R. N. Compton, *Chem. Phys. Lett.* **14**, 29 (1973); *J. Chem. Phys.* **59**, 3550 (1973).
12. M. Krauss and D. Neumann, *Chem. Phys. Lett.* **14**, 26 (1972).

O^- ions are also observed to occur at 7.9 eV, which is approximately equal to the dissociation energy of the OC-O bond plus the ionization potential of cesium minus the electron affinity of the oxygen atom. The onset for the formation of CO_2^- is somewhat difficult to determine due to the slowly rising cross section; however, a value of 4.3 eV with an uncertainty of ±0.2 eV seems appropriate. This gives an electron affinity that is consistent with our earlier estimate, $EA(CO_2) = -0.4 \pm 0.2$ eV. It should also be noted that the CO_2^- ions were metastable with respect to electron ejection (autodetachment). The lifetime was determined to be 8 (±1) $\times 10^{-5}$ sec and was independent of collision energy from 5.5 to 10 eV(center of mass). Lifetime measurements are presently being carried out for energies closer to threshold.

Carbonyl sulfide is also a linear molecule, and the ion is expected to be bent. COS^- and S^- ions are observed as products of the reaction of cesium with COS. This series of studies will be completed by examining negative ion production in CS_2.

CESIUM COLLISIONS WITH SOME OCTAHEDRAL HEXAFLUORIDE MOLECULES

The polyatomic molecules SF_6, SeF_6, and TeF_6 belong to the highest symmetry point group (O_h). There is much interest in these molecules from the points of view of both theory and experiment. Previously, we had shown that these molecules exhibit unusual negative ion properties. For example, SF_6 captures slow electrons with an extremely large attachment rate, whereas attachment of thermal electrons to SeF_6 and TeF_6 produces only weak ion signals of SeF_5^- and TeF_5^-. The attachment rate as compared with SF_6 is down by more than a factor of 10^2 for SeF_6 and 10^4 for TeF_6. On the other hand, collisions of fast cesium atoms with SeF_6 and TeF_6 produce mainly SeF_6^- and TeF_6^-, whereas collisions with SF_6 yield mainly SF_5^-. The electron affinities of SeF_6 and TeF_6 are also considerably greater than that of SF_6 (see Table 20.1).

Figure 20.3 shows the relative cross sections for the formation of SeF_6^-, SeF_5^-, SeF_4^-, and F^- as a function

Table 20.1. Electron affinities for XF_n

In electron volts

XF_n	Energy	X = S	X = Se	X = Te	X = W	X = Re
XF_6	EA	0.54	3.0	3.34	≥3.89	≥3.89
XF_6	$D(XF_5-F)^a$	3.29	3.15	3.52	5.26	
XF_5	EA	2.8	4.9	4.0	1.4	

[a] J. L. Settle, F. M. Feder, and W. N. Hubbard, *J. Phys. Chem.* **65**, 1337 (1961); P. A. G. O'Hare and W. N. Hubbard, ibid. **70**, 3353 (1966); P. A. G. O'Hare, J. L. Settle, and W. N. Hubbard, *Trans. Faraday Soc.* **62**, 558 (1966).

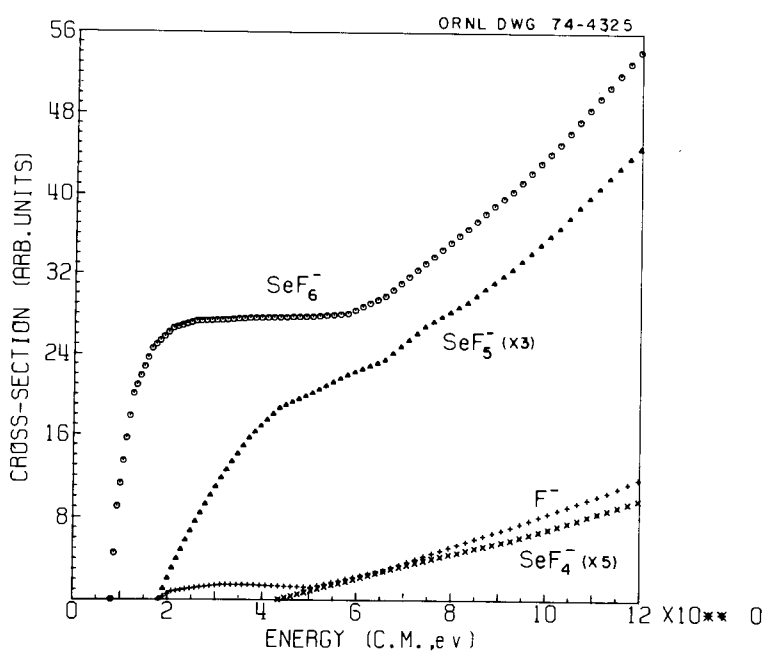

Fig. 20.3. Relative cross sections for the production of negative ions resulting from collisions between fast cesium atoms and SeF_6 as a function of the center-of-mass collision energy.

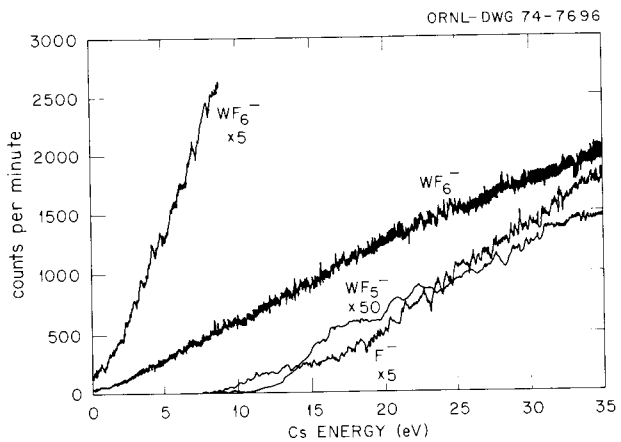

Fig. 20.4. Relative cross sections for the production of negative ions resulting from collisions between fast cesium atoms and WF_6 as a function of the center-of-mass collision energy.

of the collision energy (energy in the center-of-mass system).

Recently, Bartlett[13] examined the oxidizing properties of the third transition-metal series hexafluorides and estimated that the electron affinity increases about 0.9 eV with unit increase of the atomic number of the central heavy atom. The increase in the electron affinity was attributed to the need of the fluorine ligands to replace electron density lost to the central heavy atom. The electron affinities of many of the molecules were estimated to be greater than 5 eV. We have studied cesium atom collisions with two of these molecules (WF_6 and ReF_6) and observed a remarkable effect. Figure 20.4 shows the ion current yields of WF_6^-, WF_5^-, WF_4^-, and F^- as a function of collision energy. The cross section is seen to increase as the collision energy decreases. In fact, it appears that reactions from the collisions of thermal cesium atoms ($T \simeq 400°K$), which are always present with the fast-atom beam, also produce WF_6^-. A similar effect was observed for ReF_6. In order for WF_6 and ReF_6 to extract electrons from cesium, the binding energy of WF_6 and ReF_6 for an electron (electron affinity) must be greater than the energy required to ionize cesium (3.89 eV). We should caution that an alternative explanation of this thermal reaction is the possibility of surface ionization reactions, which have not been thoroughly studied. An in-depth study of these and related compounds is now being jointly pursued by H. F. Krause, B. K. Annis, and S. Datz of the ORNL Chemistry Division and our group.

13. N. Bartlett, *Angew. Chem. Int. Ed. Engl.* 7, 433 (1968).

In some cases the electron affinities of molecular fragments can be determined by measuring the minimum energy required to produce a fragment ion. Provided that the bond dissociation energy is known, the electron affinity of the fragment can be calculated. Table 20.1 also summarizes such data obtained for the hexafluorides.

ELECTRON ATTACHMENT AND CESIUM COLLISIONAL IONIZATION STUDIES OF ORGANIC MOLECULES (BENZOQUINONES)

A detailed study of the attachment of electrons and collision of fast cesium atoms with benzoquinone, chloranil, fluoranil, and TCNQ has been performed. The lifetimes for autodetachment as a function of electron energy to each of these have been examined, and many resonances with differing lifetimes are observed. The electron affinities of benzoquinone and TCNQ are determined to be 1.8 eV and 2.8 eV respectively. Figure 20.5 shows typical data for the onset of the formation of benzoquinone negative ions as a function of collision energy between cesium and benzoquinone.

An approximate energy-level diagram for the negative ion states of TCNQ determined from this work is shown in Fig. 20.6 along with calculated energy levels obtained

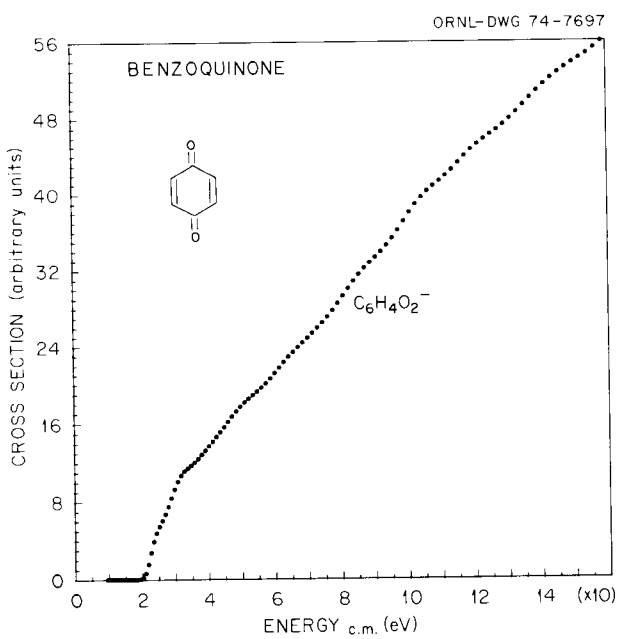

Fig. 20.5. Relative cross sections for the production of negative ions resulting from collisions between fast cesium atoms and benzoquinone as a function of the center-of-mass collision energy.

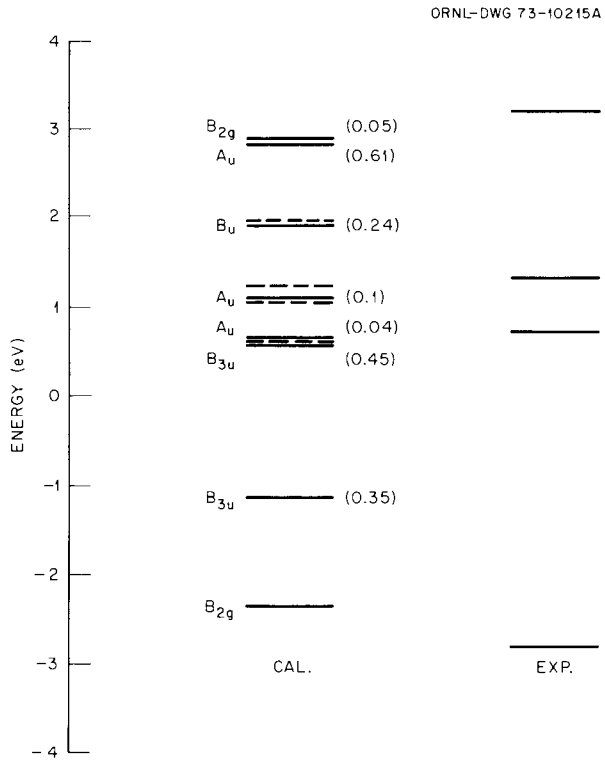

Fig. 20.6. Negative ion states of TCNQ as experimentally determined in the present work. Juxtaposed are those calculated by Hiroma et al. [S. Hiroma, K. Kuroda, and H. A. Kamatu, *Bull. Chem. Soc. Jap.* **44**, 9 (1971)]. The dashed lines indicate optically forbidden states, and the numbers in parentheses indicate the calculated oscillator strengths for the allowed transitions.

by Hiroma, Kuroda, and Akamatu.[14] The energy level of the ground $^2B_{2g}$ state (−2.35 eV) was also calculated by this method[15] and is in reasonable agreement with our electron affinity measurement. There is considerable interest in this compound since ionic crystals containing TCNQ display interesting electrical conductivity properties[16] and show some promise of affording superconductivity at much higher temperatures than hitherto achieved.[17]

Tentative values for the electron affinities of chloranil and fluoranil have been determined. The values obtained are considerably (about 2 eV) higher than those obtained from charge-transfer spectra. Chloranil is used as a standard charge-transfer acceptor molecule, and many electron affinity values are determined relative to chloranil. Because of the importance of establishing an accurate electron affinity for chloranil, independent measurements are being carried out at Wright Patterson Air Force Base by Dr. T. O. Tiernan.

ELECTRON ATTACHMENT AND CESIUM COLLISIONAL IONIZATION STUDIES OF TETRAFLUOROSUCCINIC AND HEXAFLUOROGLUTARIC ANHYDRIDES

The versatility of the cesium collisional ionization mass spectrometry technique can best be illustrated with data obtained on the completely fluorinated derivatives of succinic (**I**) and glutaric (**II**) anhydrides:

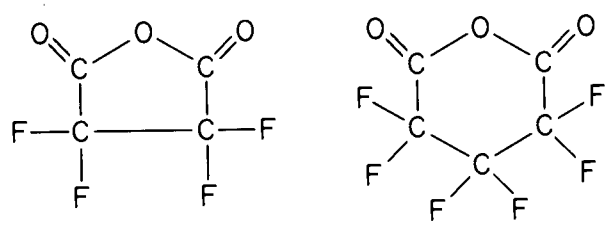

(I) (II)

Thermal electron attachment to either of these molecules produces instantaneous dissociation into various fragment negative ions. Cesium collision with both **I** and **II** produced ions with masses corresponding to molecules **I** and **II** (see, for example, Fig. 20.7). This study clearly shows the utility of the collisional ionization technique, namely, ions of the lowest energy possible are produced by cesium collisions, which may not be the case for electron collisions. The following is quoted from ref. 9, which describes this work in detail.

The electron affinities of tetrafluorosuccinic anhydride (I) and hexafluoroglutaric anhydride (II) were measured to be 0.5 ± 0.2 eV and 1.5 ± 0.2 eV, respectively, using a cesium collisional ionization technique. Dissociative electron attachment to I produced the negative ions: $C_2F_4CO_2^{-}$* (≥5 msec), $C_2F_4CO^{-}$* (124 μsec), $C_2F_4^{-}$* (14 μsec), and F^{-}; while $C_3F_6CO_2^{-}$* (≥1.2 msec), $C_3F_6CO^{-}$* (80 μsec), $C_3F_6^{-}$* (760 μsec), and F^{-} were observed from II. The asterisk indicates that the ion is metastable with respect to autodetachment, and the numbers in parentheses are the measured autodetachment lifetimes for incident electrons at the maximum in the cross section. Very large cross sections (~10^{-14} cm^2) for production of $C_2F_4CO_2^{-}$* and $C_3F_6CO_2^{-}$* were observed for dissociative attachment of thermal electrons to I and II, respectively. The parent negative ions $C_4F_4O_3^{-}$ and $C_5F_6O_3^{-}$, as well as all of the ions (with the exception of $C_2F_4^{-}$) which were observed for dissociative electron attachment, were observed from collisions between fast cesium atoms and I and II.

14. S. Hiroma, H. Kuroda, and H. Akamatu, *Bull. Chem. Soc. Jap.* **44**, 9 (1971).

15. H. Kuroda, private communication.

16. J. P. Ferraris, D. O. Cowan, V. V. Nalatka, and J. H. Pearlstein, *J. Amer. Chem. Soc.* **95**, 948 (1973).

17. L. B. Coleman, J. J. Cohen, D. J. Sandman, F. G. Yamagishi, A. F. Garito, and A. J. Heeger, *Solid State Commun.* **12**, 1125 (1973).

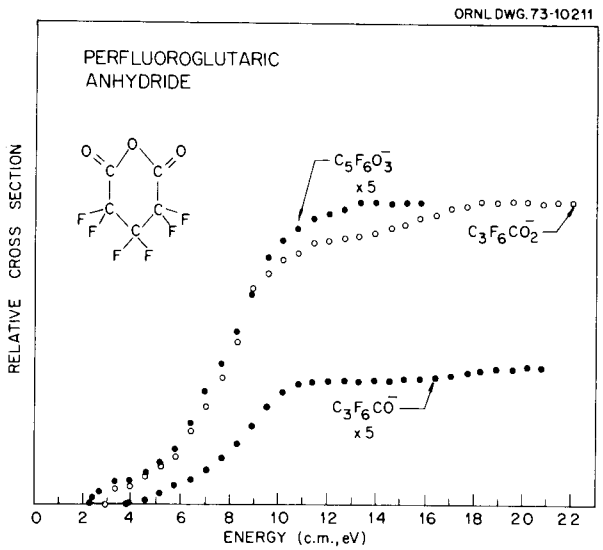

Fig. 20.7. Relative cross sections for the production of negative ions resulting from collisions between fast cesium atoms and perfluoroglutaric anhydride as a function of the center-of-mass collision energy.

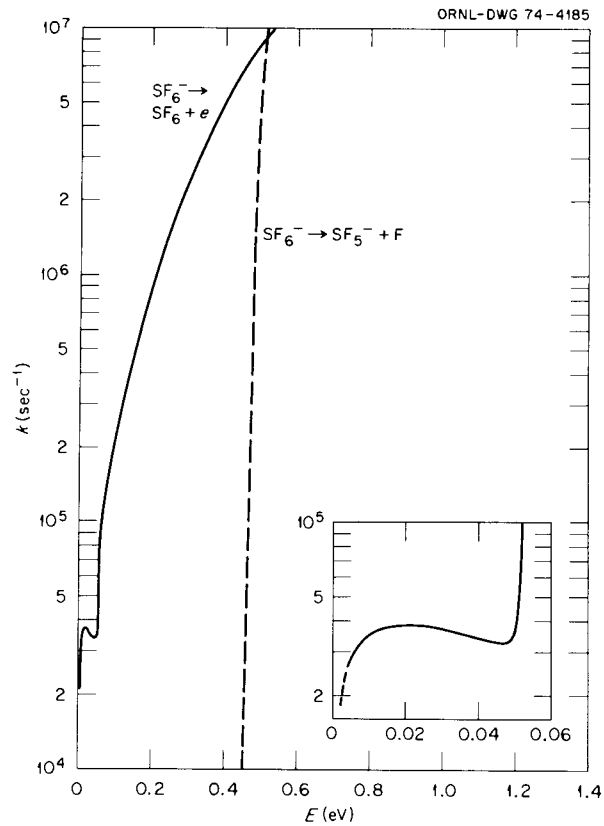

Fig. 20.8. Calculated autodetachment rate constant for SF_6^- as a function of internal energy.

DISSOCIATION AND AUTOIONIZATION LIFETIMES

Many experiments are now yielding information on the kinetic energy distribution of the fragments from unimolecular dissociations. The statistical theory for such reactions has been analyzed to predict these distributions. A unified treatment for species of low angular momentum, such as those produced by electron or photon impact, and those of high angular momentum, as in ion-molecule collision complexes, has been obtained. A quantum treatment of transmission coefficients for the polarization barrier has been included. It is found that these transmission coefficients play an important role in the attachment of electrons to molecules such as SF_6 and in their subsequent autodetachment. The magnitude of the room-temperature rate constant for electron capture by SF_6 is predicted, for example, to be about one-half that obtained by assuming perfect capture. The agreement with experiment is good. The predicted autodetachment rate constant of SF_6^-, as a function of internal energy, is displayed in Fig. 20.8. Again, the agreement with a variety of experiments is good.

ENERGY PATHWAYS IN THE RARE GASES

A rather complete review of energy dissipation mechanisms in irradiated rare gases has been prepared;[18] emphasis has been placed on the mechanisms of energy transfer to impurities. During the preparation of the review, three new mechanisms for energy dissipation were discovered. The collision-induced conversion of helium 2^1P atoms to the 2^1S state by a Born-Oppenheimer forbidden mechanism has been identified as the important "missing link" in the energy pathway scheme in helium.[19] The conditions under which imprisoned photons (as emitted, for example, by helium 2^1P atoms) will be directly intercepted and absorbed by impurity atoms have been delineated. Finally, direct mass spectrometric proof of the previously postulated "near-resonance" energy transfer from argon to xenon atoms, followed by formation of the Xe_2^+ ion, has been obtained.[20]

18. G. S. Hurst and C. E. Klots, "Elementary Process in Irradiated Noble Gases," in *Advances in Radiation Chemistry*, M. Burton and J. L. Magee, eds., Wiley, New York (in press).

19. M. G. Payne, C. E. Klots, and G. S. Hurst, to be published.

20. C. E. Klots and L. W. Sieck, *Chem. Phys. Lett.* (in press).

DISSOCIATIVE IONIZATION OF MOLECULES BY ELECTRON IMPACT

The dissociative ionization process

$$e + AB \rightarrow A^+ + B + e + e \qquad (1)$$

often contributes a large fraction of the total ionization produced by electron impact on molecules. Rapp, Englander-Golden, and Brigalia[21] have shown that for electron impact on H_2 and D_2 the fraction of positive ions with kinetic energies greater than 0.25 eV reaches 6% of the total ionization at its maximum, near an electron energy of 140 eV. Since very little momentum is transferred in a collision of the type

$$e + AB \rightarrow AB^+ + e + e\,, \qquad (2)$$

almost all of this 6% corresponds to dissociative ionization – process (1). For O_2, N_2, and many other molecules, this fraction becomes even greater, exceeding 25%. For photon impact, still higher ratios of dissociative to nondissociative ionization have been observed. Van Brunt, Hirsch, and Whitehead[22] showed in a study of x-ray-induced ionization of N_2, O_2, NO, CO, and CO_2 that dissociative ionization makes a dominant contribution to the total ionization, accounting for over 95% of the ions formed at x-ray energies above the K absorption edges of the atomic constituents and 50 to 80% below. Browning and Fryar[23] have studied dissociative photoionization of H_2 and D_2 through the $1s\sigma_g$ ionic state and report H^+/H_2^+ ratios roughly twice those seen in electron impact studies.

Though dissociative ionization is clearly an important part of the total ionization process, few measurements have been made of the nature and kinetic energies of the fragment ions and fewer still of their angular distributions. Such measurements are of fundamental importance to radiation chemistry and microdosimetry, since the nature and distribution of the final products of irradiation will be determined by the energies and angular distributions of the primary dissociation products. Such results are also basic to our knowledge of the symmetries and positions of the molecular states involved in the dissociation process.[24]

Figure 20.9 shows schematically an apparatus that has been constructed to study the kinematics of molecular dissociation. It is an improved version of the equipment described in the previous annual report.[25] Briefly, it consists of a pulsed horizontal electron beam which intersects a vertical molecular gas beam. The electron gun can be rotated in the horizontal plane about the molecular beam, and reaction products formed in the beam intersection region drift under field-free conditions to the entrance aperture of a quadrupole mass spectrometer, which can be located at various distances from the beam intersection region. Ions are mass-analyzed by the quadrupole and detected by an off-axis Channeltron electron multiplier. The apparatus has been used to study dissociative ionization in D_2 and N_2 in considerable detail. Some illustrative results follow.

DISSOCIATIVE IONIZATION OF D_2

Figure 20.10, taken from Dunn and Kieffer,[26] shows the known potential energy curves of the H_2^+ ion which would be expected to play a role in dissociative ionization of H_2 (or D_2). On the left is shown a reflection of the square of the ground H_2 vibrational state wave function in the lowest two H_2^+ states – the $^2\Sigma^+_g$ ionic state and its companion $^2\Sigma^+_u$ state. This reflection gives very nearly the expected H^+ energy distribution from dissociative ionization of H_2 if just these two states are involved. The procedure does not give the relative magnitudes of the two contributions. Figure 20.11 shows recent experimental results for this proton energy distribution obtained by Van Brunt and Kieffer[27] and Crowe and McConkey.[28] Both used equipment with a static gas target rather than the crossed-beam arrangement of the present experiment. The apparatus of Van Brunt and Kieffer discriminated against low-energy ions, and they did not present results much below 4 eV. Particular interest centers on two points: the observation of structure in the data of Crowe and McConkey which cannot be attributed to excitation of the $^2\Sigma^+_g$ and $^2\Sigma^+_u$ states of H_2^+, and the electron energies (appearance potentials) at which these

21. D. Rapp, P. Englander-Golden, and D. D. Briglia, *J. Chem. Phys.* 42, 4081 (1965).
22. R. J. Van Brunt, R. G. Hirsch, and W. D. Whitehead, *Bull. Amer. Phys. Soc.* 17, 1145 (1972).
23. R. Browning and J. Fryar, *J. Phys. B: At. Mol. Phys.* 6, 364 (1973).
24. G. H. Dunn, *Phys. Rev. Lett.* 8, 62 (1962).
25. *Health Phys. Div. Annu. Progr. Rep. July 31, 1973*, ORNL-4903, p. 93.
26. G. H. Dunn and L. J. Kieffer, *Phys. Rev.* 132, 2109 (1963).
27. R. J. Van Brunt and L. J. Kieffer, *Phys. Rev. A* 2, 1293 (1970).

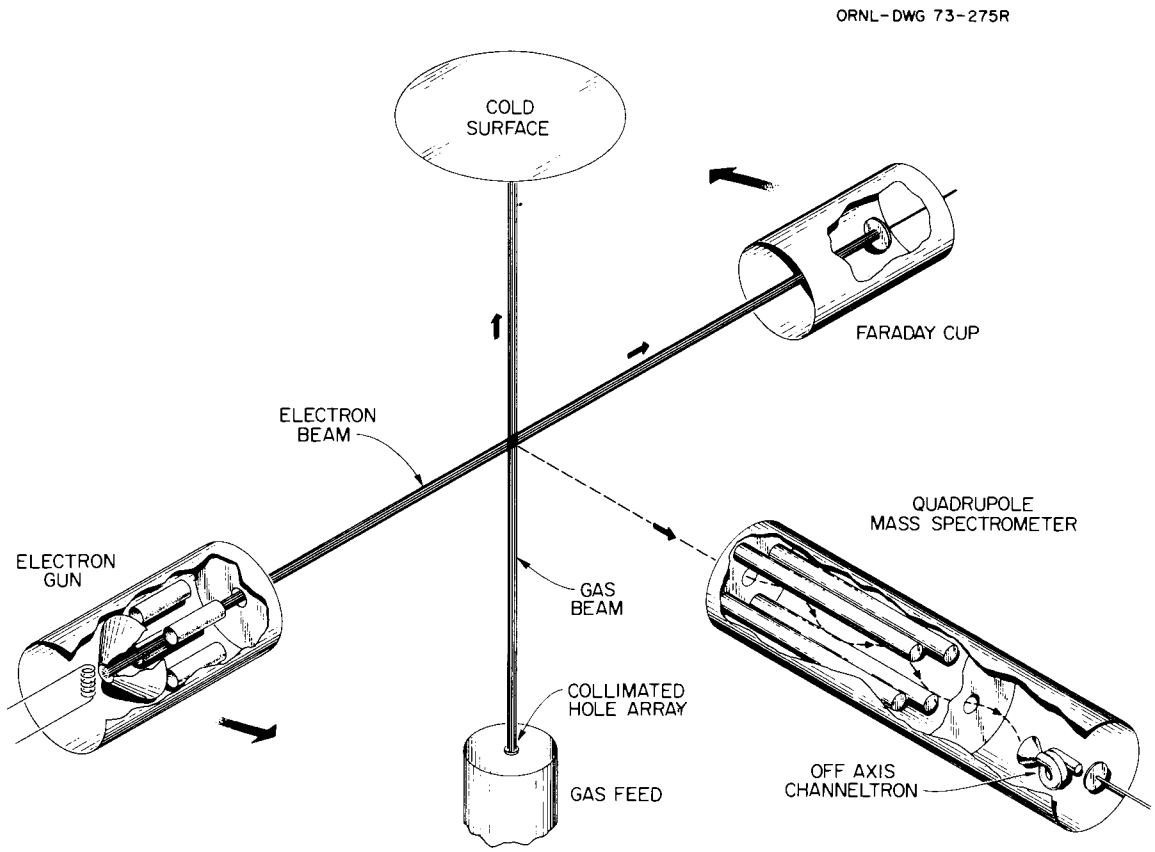

Fig. 20.9. Schematic diagram of equipment for the study of dissociative ionization. Approximate apparatus: beam pulse, 1.0 μsec repeated every 100 μsec; integrated beam current, 2×10^{-8} A; angular resolution, $\leq 1 \times 10^{-6}$ torr, angular range, 30° (forward direction) to 110°; ion time-of-flight distance, 28.7 cm.

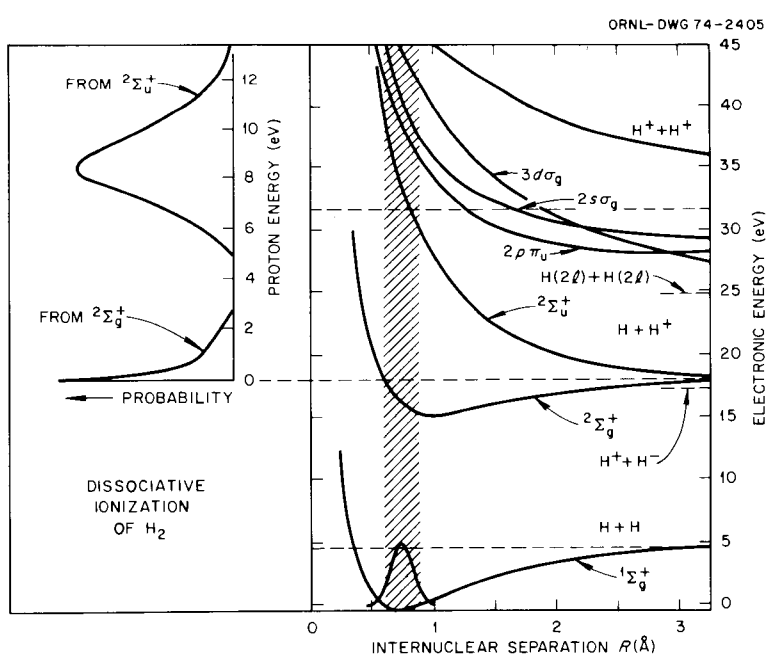

Fig. 20.10. Potential-energy diagram for the ground state of H_2, some of the states of H_2^+ and H_2^{2+}. The energy scale is relative to the ground vibrational level of H_2. On the left is indicated the expected energy distributions of protons from the $^2\Sigma_g^+$ and $^2\Sigma_u^+$ states of H_2^+. The relative heights of these two curves are not to be compared. Source: G. H. Dunn and L. J. Kieffer, *Phys. Rev.* **132**, 2109 (1963).

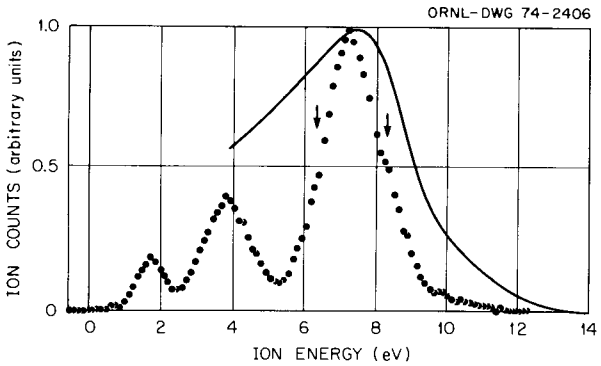

Fig. 20.11. Proton energy distributions obtained for impact of 50-eV electrons on H_2. Dots are data of Crowe and McConkey (ref. 28) taken at 27° to the incident electron beam; dashed line is data of Van Brunt and Kieffer (ref. 27) taken at 23°.

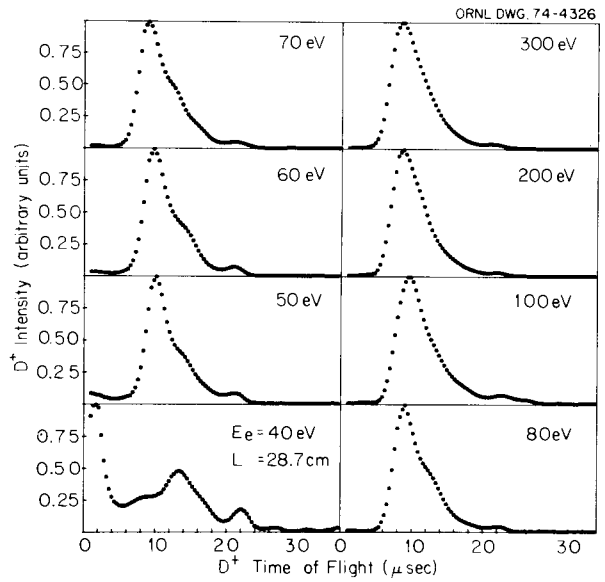

Fig. 20.12. Time-of-flight spectra for D^+ ions obtained by impact of electrons of the states' energies, E_e (eV), on D_2. Data taken at 90° to the incident electron beam with apparatus of Fig. 20.9. Electron-beam pulse width of 3.5 μsec has been unfolded, and data have been smoothed to reduce statistical fluctuations. All curves are normalized to unity at the maximum.

structural features first appear. Crowe and McConkey[28] reported appearance potentials of 26 eV for the 3.8-eV ion group and 23 and 26.5 to 27 eV for two separate components of the 1.7-eV group. It is thus difficult to account for these groups in terms of singly excited states, since their appearance potentials lie below the $^2\Sigma^+_u$ curve of H_2^+ in the Franck-Condon (shaded) region and since ions of these energies, peaking in this manner, cannot be obtained from the $^2\Sigma^+_g$ ionic curve of H_2^+.

Figure 20.12 shows time-of-flight spectra for D^+ ions obtained in the present experiment by impact of electrons of various fixed energies from 40 to 300 eV on D_2 for an electron-beam–detector angle of 90° Figure 20.13 shows the corresponding D^+ kinetic energy spectra derived from the data of Fig. 20.12. Due to the method used for correcting for the D^+ transit time through the quadrupole mass spectrometer, the results of Fig. 20.13 show an artificially large number of ions with kinetic energies above 8 eV; however, there clearly is structure in the D^+ kinetic energy spectrum below 8 eV, with peaks occurring at approximately the energies observed by Crowe and McConkey.[28] However, the present work[29] indicates that this structure arises very largely, if not completely, at electron energies above 30 eV (Fig. 20.14). In addition, no

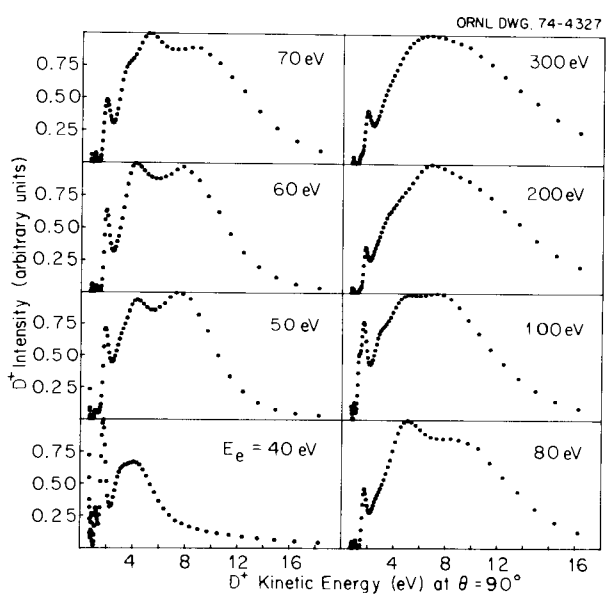

Fig. 20.13. D^+/D_2 kinetic energy spectra obtained by computer transformation of the data of Fig. 20.12.

evidence has been obtained for structure reported by Crowe and McConkey[28] in the wings of the "8-eV" ion peak, indicated by arrows in Fig. 20.11.

28. A. Crowe and J. W. McConkey, *J. Phys. B: At. Mol. Phys.* 6, 2088 (1973).

29. J. A. D. Stockdale, V. E. Anderson, A. E. Carter, R. N. Compton, and Liliana Deleanu, "Dissociative Ionization of Molecules by Electron Impact," to be published.

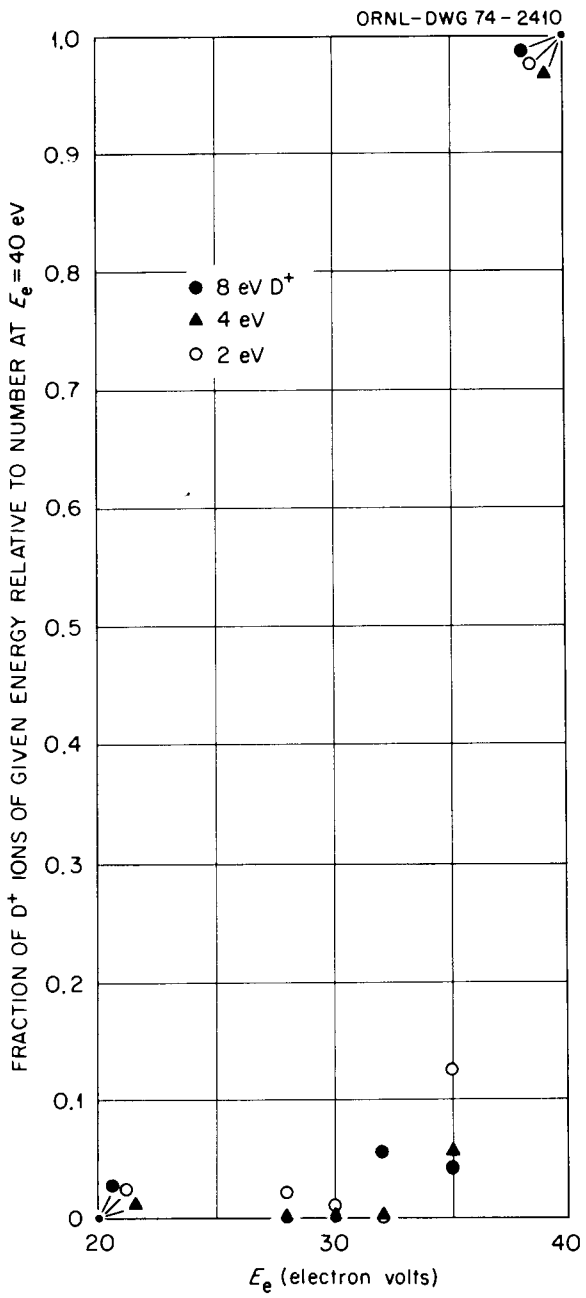

Fig. 20.14. Plot of the fractions of D^+ ions of kinetic energy 8, 4, and 2 eV (relative to an abundance of unity at 40-eV electron energy) as a function of incident electron energy between 20 and 40 eV. Data taken at 90° to incident electron beam.

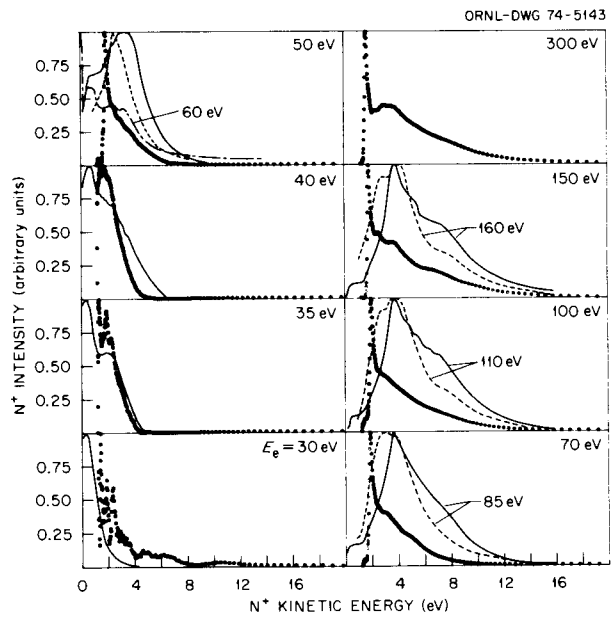

Fig. 20.15. Kinetic energy spectra of N^+ ions produced by electron impact on N_2. Solid line is high-Rydberg nitrogen atom data of Smyth, Schiavone, and Freund (ref. 30); dashed line, N^+ spectra of Kieffer and Van Brunt (ref. 31); –. –. –. , spectra of Locht and Schopman (ref. 32). All data are at an electron-beam detector angle of 90° except that of ref. 31, which is at 55°. All distributions are normalized to unity at the maximum except the curve of Locht and Schopman, which is normalized to unity at 2.0 eV.

DISSOCIATIVE IONIZATION OF N_2

Figure 20.15 shows kinetic energy spectra for N^+ ions produced by electron impact on N_2. Also shown are kinetic energy spectra of nitrogen atoms in high-Rydberg states – N** – obtained in an electron impact experiment by Smyth, Schiavone, and Freund[30] and N^+ spectra obtained by Kieffer and Van Brunt[31] and Locht and Schopman.[32] The high-Rydberg data are included since they have been successfully interpreted in terms of the dissociation of N_2^+ core ions with an attendant loosely bound Rydberg electron so that the same N_2^+ states are involved both in N^+ production in dissociative ionization and in N** production. Except for the data of Locht and Schopman,[32] the spectra display similar features. As in the case of D^+/D_2 the present results show an enhancement of the percentage of low-kinetic-energy ions and also show apparently better ion energy resolution than the previous electron impact measurements. A discussion of the possible N_2^+

30. K. C. Smyth, J. A. Schiavone, and R. S. Freund, *J. Chem. Phys.* **59**, 5225 (1973).

31. L. J. Kieffer and R. J. Van Brunt, *J. Chem. Phys.* **46**, 2728 (1967).

32. R. Locht and J. Schopman, *Proceedings of the VIII International Conference on the Physics of Electronic and Atomic Collisions, July 16–21, 1973, Belgrade, Yugoslavia.*

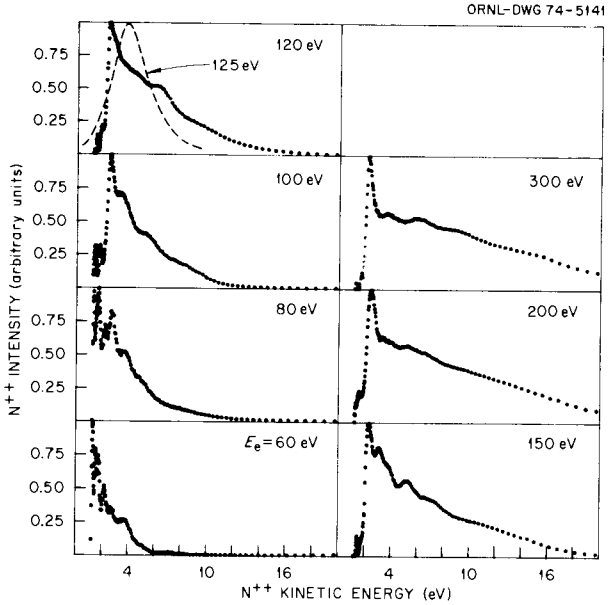

Fig. 20.16. N^{2+}/N_2 kinetic energy distributions. Dashed-line data of Kieffer and Van Brunt (ref. 31) taken at 55° to electron beam; present data, at 90°.

states giving rise to the various N^+ kinetic energy groups is given elsewhere.[33] Figure 20.16 shows N^{2+} kinetic energy spectra obtained for impact of various energy electrons on N_2. Considerable structure is apparent, in contrast to the one previously published result of Kieffer and Van Brunt.[31]

PREDISSOCIATION OF THE $B^2\Sigma^-_g$ STATE OF O_2^+

Predissociation can be an important process in molecular dissociation. It involves the excitation of a molecule to a bound excited state which will contain one or more vibrational levels. The wave functions of these vibrational levels overlap to a greater or lesser extent the free-state wave functions of a repulsive (unbound) molecular state. Hence, after a certain period of time the molecule crosses from the bound state to the repulsive state and then very rapidly dissociates. Evidence for predissociation of the $B^2\Sigma^-_g$ state of O_2^+ has been obtained from optical studies[34] and from energy analysis of electrons detected in coincidence with O^+

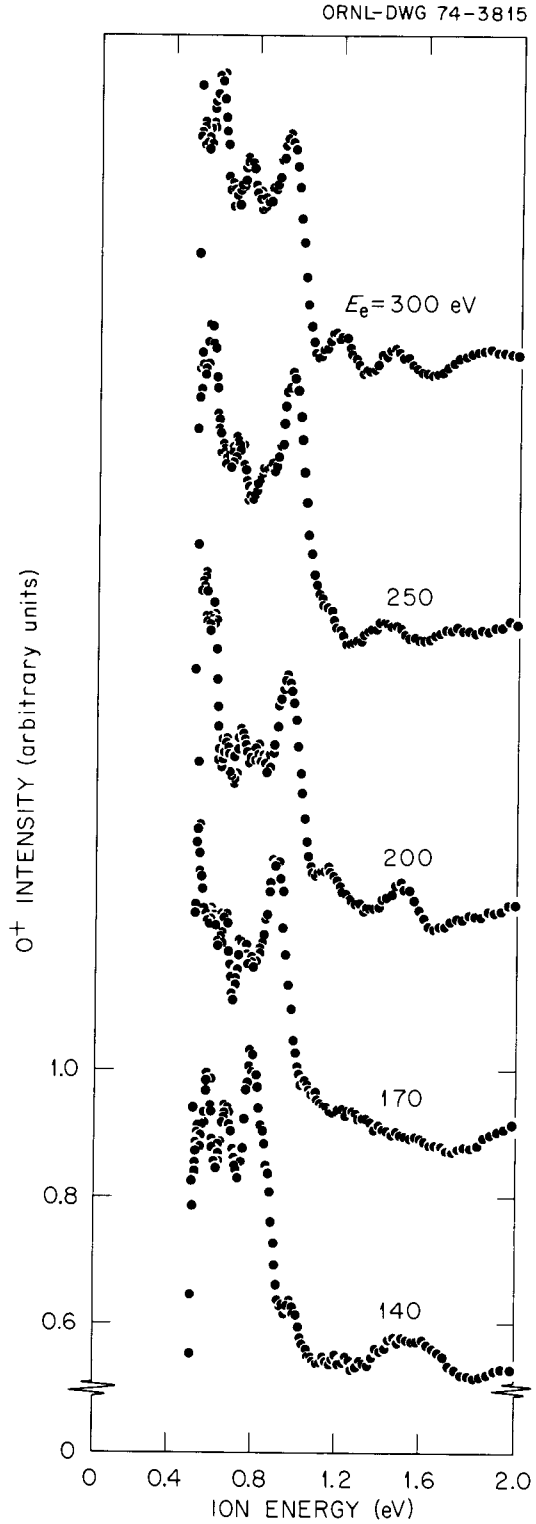

Fig. 20.17. Kinetic energy spectra of O^+ ions from impact of electrons of energies E_e (eV) on O_2. Data obtained at 90° to electron-beam direction without mass analysis. Electron beam pulse width, 1.0 μsec. Ion drift distance, 20.0 cm.

33. L. Deleanu and J. A. D. Stockdale, "Dissociative Ionization of Molecules by Electron Impact. II. Kinetic Energy and Angular Distributions of N^+ and N^{2+} Ions from N_2," to be published.

34. K. Yoshino and Y. Tanaka, *J. Chem. Phys.* 48, 4859 (1968).

ions produced by photon impact.[35] Appearance potential measurements[36–38] and angular distribution studies[36,39] of energy-analyzed O^+ ions produced by electron impact on O_2 are consistent with the suggestion that the lowest kinetic energy (about 1 eV) O^+ peak arises from a predissociation of the $B^2\Sigma^-_g$ state. If this is so, high-resolution studies of this peak might reveal structure with a spacing equivalent to one-half the vibrational spacing of the $B^2\Sigma^-_g$ state, namely, approximately 0.075 eV. This is because a dissociation of the type

$$e + O_2 \rightarrow O_2^+ + e + e \rightarrow O^+ + O + e + e \qquad (3)$$

results in the O^+ ion and O atom sharing the available dissociation energy equally. Figure 20.17 shows part of the results of some measurements made with the present apparatus. There is clearly structure in the "1-eV" peak, with spacing of approximately that required for the predissociation. The peaks in the region above 1.2 eV are associated with other O_2^+ states.[36]

MASS ANALYSIS OF NEGATIVE IONS PRODUCED IN SWARM EXPERIMENTS: ION CLUSTERING REACTIONS IN AMMONIA

In the preceding annual report,[40] we described studies of ion clustering reactions in pure water vapor at pressures up to 5 torr. These studies have been extended to include deuterated water vapor and ammonia. The dominant primary ions from NH_3 are H^- and NH_2^- at an electron energy of about 5.6 eV.[41] The negative ion yields from ammonia at a pressure of 1 torr are shown in Fig. 20.18. In addition to H^- and NH_2^-, the cluster ions $NH_2^-\cdot(NH_3)$ are observed, where $n = 1$ to 3. The cluster ion $NH_2^-\cdot(NH_3)_4$ was also observed but had an intensity much lower than the $NH_2^-\cdot(NH_3)_3$ signal. No evidence for a mass corresponding to $NH_2^-\cdot(NH_3)_5$ was found. Attempts are being made to relate these ion clustering studies to the radiation chemistry of gases.

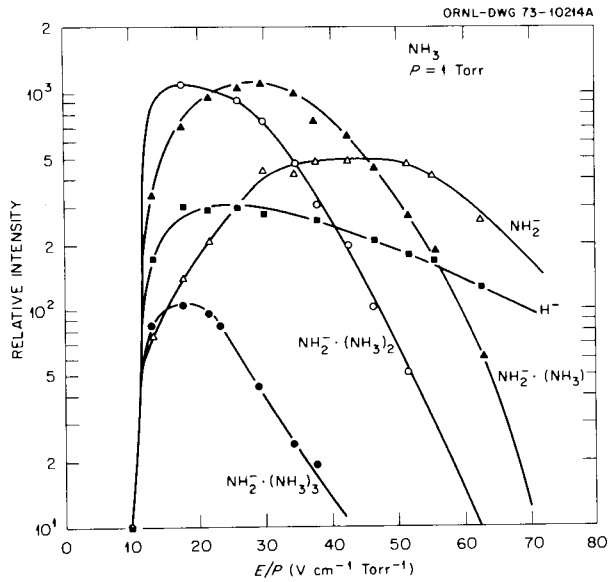

Fig. 20.18. Negative ion yields from electron swarm interactions with ammonia at a pressure of 1 torr as a function of the ratio of the electric field to pressure.

LOW-ENERGY-ELECTRON-INDUCED SPUTTERING OF ALKALI HALIDES

The irradiation of single crystals of alkali halides with low-energy electrons (100 to 2000 eV) results in the emission of atoms and molecules from the surface. The process is very efficient, sputtering yields of one particle released per electron impact being typical. The sputtering has been explained as a result of the formation of F centers according to the Pooley-Hersh model. The application of this mechanism to electron sputtering implies that the emitted atoms and molecules should possess kinetic energies of up to 5 eV.

The Health Physics Division is interested in evolution of chlorine gas from irradiated rock salt, with application to storage of radioactive wastes in salt mine repositories. Sheldon Datz of the Chemistry Division and Dr. F. Schmidt-Bleek of the Department of Chemistry, University of Tennessee, are interested in development of a fast halogen atom source. Since both interests could be satisfied by a common experiment, a joint venture was undertaken. The following paragraphs describe work for the Ph.D. thesis of Dr. G. L. Ostrom.

A series of experiments was performed in which alkali halide single crystals were bombarded with 100- to 2000-eV electrons and the sputtered neutral particles

35. C. J. Danby and J. H. D. Eland, *Int. J. Mass Spectrom. Ion Phys.* **8**, 153 (1972).
36. J. A. D. Stockdale and L. Deleanu, *Chem. Phys. Lett.* **22**, 204 (1973).
37. P. H. Doolittle, R. I. Schoen, and K. E. Schubert, *J. Chem. Phys.* **49**, 5108 (1968).
38. R. S. Freund, *J. Chem. Phys.* **54**, 3125 (1971).
39. R. J. Van Brunt, G. M. Lawrence, L. J. Kieffer, and J. M. Slater, to be published.
40. *Health Phys. Div. Annu. Progr. Rep. July 31, 1973*, ORNL-4903, p. 96.
41. R. N. Compton, J. A. D. Stockdale, and P. W. Reinhardt, *Phys. Rev.* **180**, 111 (1969).

were investigated under ultrahigh-vacuum conditions. The sputtered particles were ionized and analyzed with a quadrupole mass spectrometer as a function of electron energy, electron current, target temperature, and angle of ejection. In addition, by pulsing the electron beam, a time-of-flight spectrum of the sputtered particles was obtained. The time-of-flight spectrum was then converted to a kinetic energy distribution.

Halogen atoms, diatomic halogen molecules, and metal atoms were the only species found to be sputtered from the target. These species were emitted with a linear dependence upon bombarding electron current. The sputtering yield increased somewhat less than linearly with increasing bombarding energy. The peak in the time-of-flight spectrum was found to go through a broad maximum at a bombarding energy of approximately 600 eV and to decrease at higher bombarding energies. The sputtering yield increased with increasing temperatures. The angular distribution was found to be predominantly cosine, corresponding to particles emitted in random directions.

The time-of-flight spectra showed the particles to be emitted with a predominantly thermal energy distribution. This finding was interpreted as representing the production of interstitial halogen atoms (*H* centers) deep within the crystal by the Pooley-Hersh mechanism, followed by the diffusion of the *H* centers to the surface and subsequent emission with a thermal energy distribution. The *H* centers are also believed to react with halogen ions at the crystal surface to form diatomic halogen molecules and liberate metal atoms.

A halogen peak with energy of approximately 0.15 eV was found in the time-of-flight spectra of KI, KBr, KCl, and NaCl at low crystal temperatures. Figure 20.19 shows the predominant thermal peak at $T \geqslant 145°C$ and the relative increase in the peak at about 0.15 eV. This peak did not vary in energy with changes

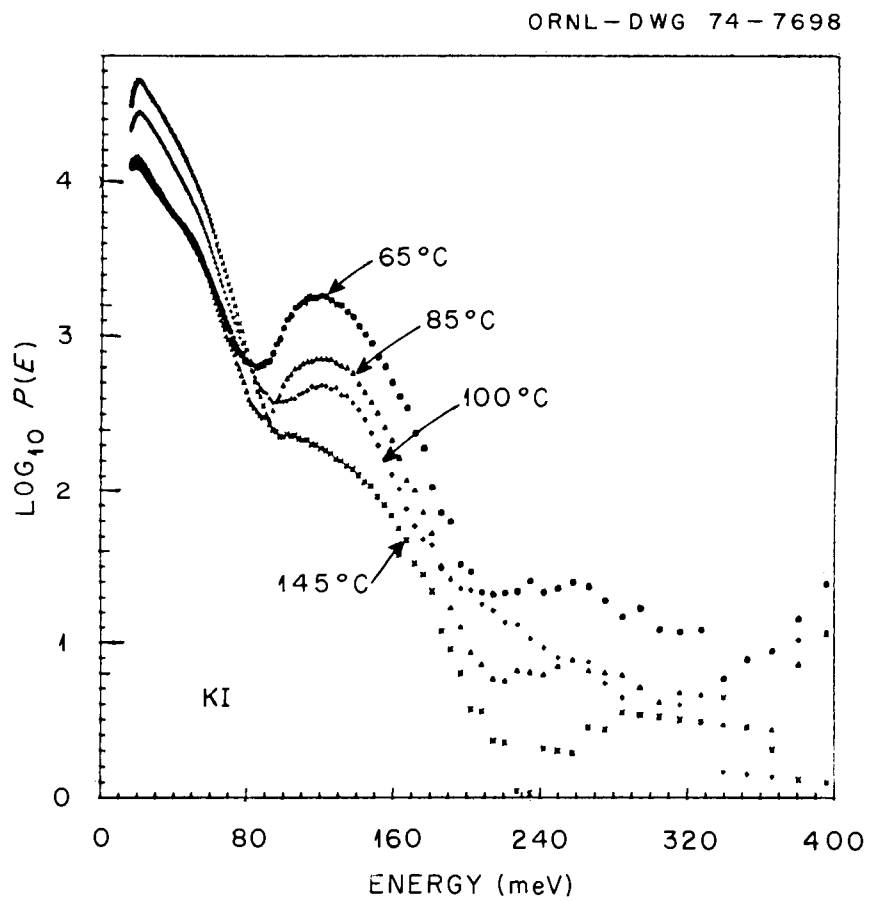

Fig. 20.19. Distribution in energy of the iodine atom peak from electron-irradiated potassium iodide for different temperatures.

in electron energy (Fig. 20.20), electron current, temperature, or angle of ejection. The angular distribution was sharply peaked toward the crystal normal. This "hot" peak decreased in magnitude with increasing temperature. At the present time, we have no satisfactory explanation for the physical origin of this peak. The most reasonable explanation for this peak is that it results from the reaction between the *H* center and a bombarding electron, upon the arrival of the *H* center at the surface.

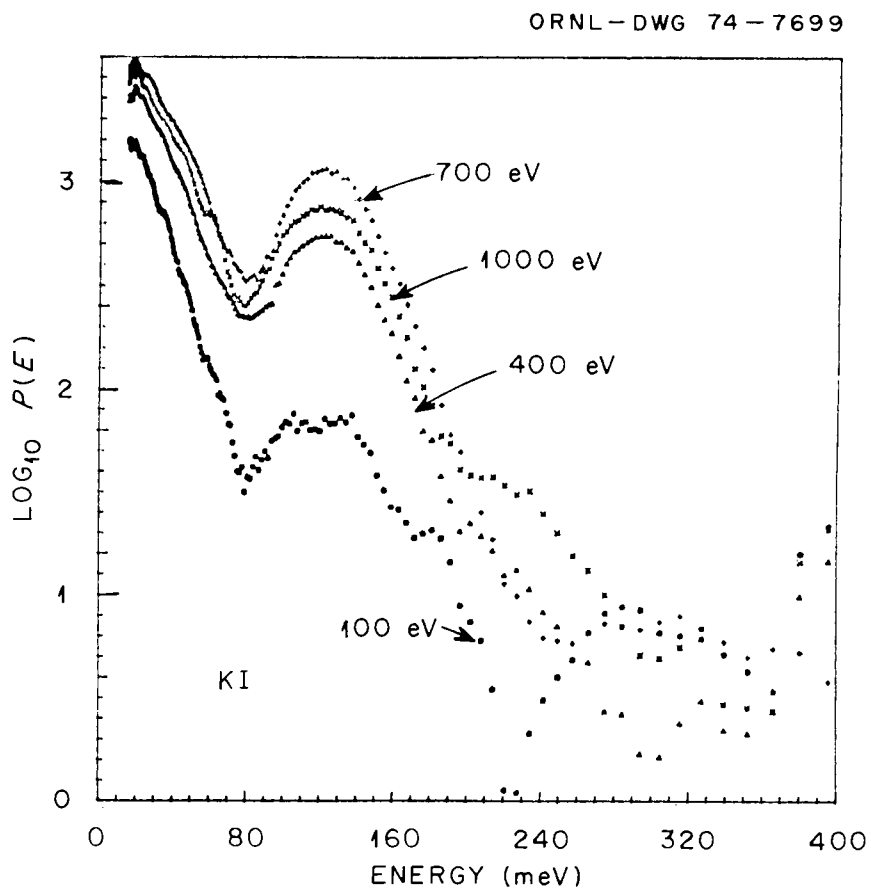

Fig. 20.20. Distribution in energy of the iodine atom peak from electron-irradiated potassium iodide for different electron energies.

21. Interaction of Radiation with Liquids and Solids

E. T. Arakawa
R. D. Birkhoff[1]
A. J. Braundmeier[2]
T. A. Callcott[2]
J. T. Cox
L. C. Emerson
D. G. Hall[3]
R. N. Hamm
T. Inagaki[4]
R. J. Warmack[3]
C. E. Wheeler[3]
Mary W. Williams

ULTRAVIOLET OPTICAL PROPERTIES OF LITHIUM

As a continuation of our studies on the alkali metals,[5] the reflectances $R(\theta)$ of evaporated films of lithium were measured as functions of angle of incidence, θ, for photon energies between 3 and 10.7 eV. These data were then analyzed, by a two-parameter least-squares fit to Fresnel's equations, to determine the real and imaginary parts n and k, respectively, of the complex refractive index for each energy. The lithium film under study was evaporated onto the flat surface of a semicylindrical substrate. A semicylinder was used so that, in measurements made with light incident through the substrate, the incident and reflected beams pass normally through the curved vacuum-substrate interface for all angles of incidence on the flat surface. Lithium was deposited on only one-half of the plane-substrate surface; the remaining half was used as a reference surface that had a substrate-vacuum interface. Angular reflectance curves made on the reference surface gave values of the total incident-beam flux and of the index of refraction of the substrate, which were used in the subsequent analysis of $R(\theta)$ data from lithium. Measurements were made at both substrate and vacuum interfaces on both thick and thin films. At energies greater than 6 eV, all measurements of thick films deposited on MgF_2 substrates gave the same values of optical and dielectric functions, within a few percent. These results may be confidently taken as the values appropriate to bulk lithium. At lower photon energies, the different measurements, when interpreted on the assumption of ideal film interfaces, gave widely differing values of n and k, depending on the surface on which measurements were made, on the thickness and structure of the films, and on the polarization of the incident light. Values of n and k calculated from values of $R(\theta)$ measured on several thick films of lithium deposited on an MgF_2 semicylinder are shown in Figs. 21.1 and 21.2.

Real film surfaces are rough and, in the case of the vacuum interface, have an oxide coating. Any imperfections of the reflecting surface can have a considerable effect on $R(\theta)$ below the plasma energy. Since the plasma energy for lithium is ~7 eV, an accurate interpretation of the lower-energy results requires the development of a structure-dependent model of the behavior of the reflectance as well as careful characterization of the surfaces. Studies of some of these surface and thickness effects in lithium films have been reported recently by Rasigni and Rasigni, who correlated film structure with abnormal optical properties in the low-energy region.[6] They found that typical films are granular and that absorption depends strongly on the film structure. They attributed anomalies to roughness-aided surface-plasmon excitations, with perhaps some contributions from diffuse scattering. It seems clear that optical data in the surface-plasmon region

1. Also Chief of Fundamental Health Physics Research Section.
2. Consultant.
3. Graduate student.
4. Postdoctoral fellow.
5. E. T. Arakawa et al., *Health Phys. Div. Annu. Progr. Rep. July 31, 1972*, ORNL-4811, pp. 13–15.
6. M. Rasigni and G. Rasigni, *J. Opt. Soc. Amer.* **62**, 1033 (1972); **63**, 775 (1973).

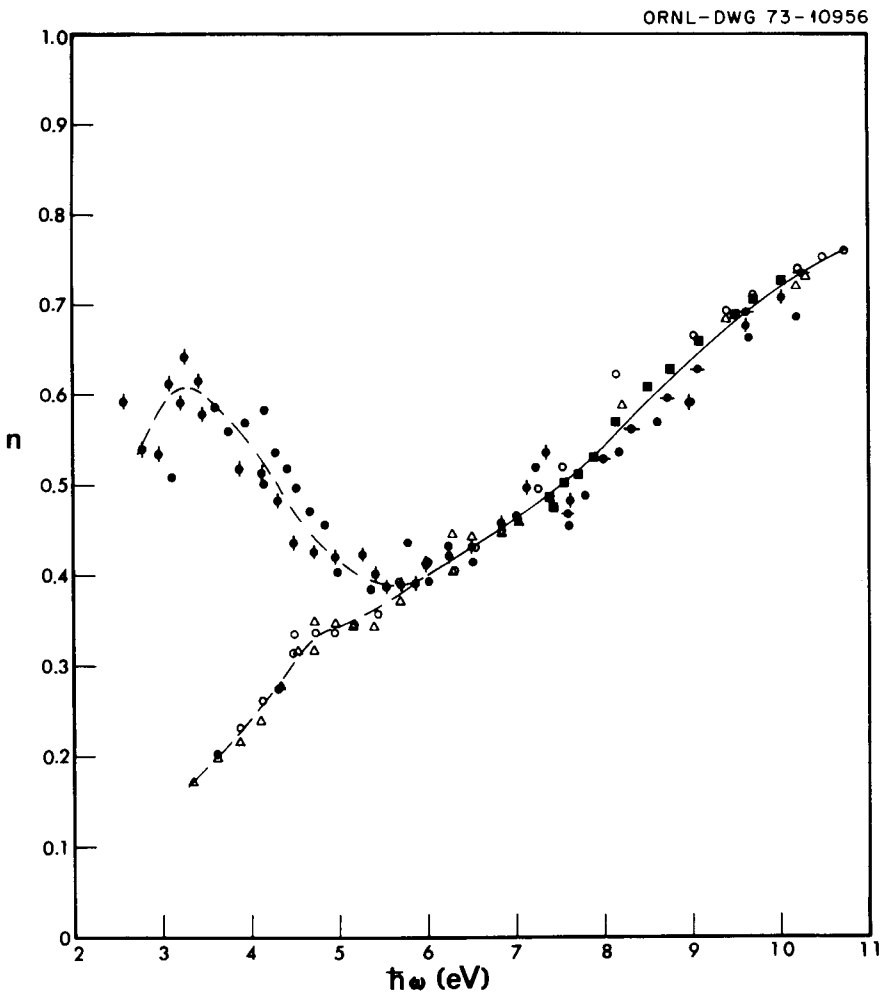

Fig. 21.1. Index of refraction vs photon energy for lithium films on MgF_2 substrate derived from $R(\theta)$ measurements. The symbols ●, ♦, -◆-, ■ are values for light incident through the substrate, and the symbols ○, △ are values for light incident from the vacuum.

must be treated with great care. In order to find bulk optical parameters from such data, either the anomalous effects must be eliminated by preparing smooth films, or the roughness must be accurately measured and its effects on the optical measurements must be accurately modeled and used to correct the observed data.

In the spectral region from 6 to 10.7 eV, where we consider our values of n and k to be reliable, we have calculated the real and imaginary parts of the dielectric function using the standard relations $\epsilon_1 = n^2 - k^2$ and $\epsilon_2 = 2nk$. Values of n and k were taken from the solid curves drawn through the data points in Figs. 21.1 and 21.2. The resulting values of ϵ_1, ϵ_2, and the energy loss function $-\mathrm{Im}(1/\epsilon)$ are shown in Fig. 21.3. The plasmon energy of lithium, defined as the photon energy for which $\epsilon_1(\omega) = 0$, is found to be (6.7 ± 0.3) eV, whereas the plasmon loss peak in $-\mathrm{Im}\,(1/\epsilon)$ is centered at 7.1 eV. Both the position and width of the peak are in excellent agreement with the experimental electron energy loss data of Kunz,[7] which show a peak centered at 7.12 eV.

For the heavier alkali metals potassium, rubidium, and cesium, strong absorption peaks in ϵ_2 occur at energies above the direct *s-p* interband absorption peak in these metals.[5,8] We suggested that the peaks might

7. C. Kunz, *Z. Phys.* **196**, 311 (1966).
8. U. S. Whang, E. T. Arakawa, and T. A. Callcott, *Phys. Rev. B* **5**, 2118 (1972).

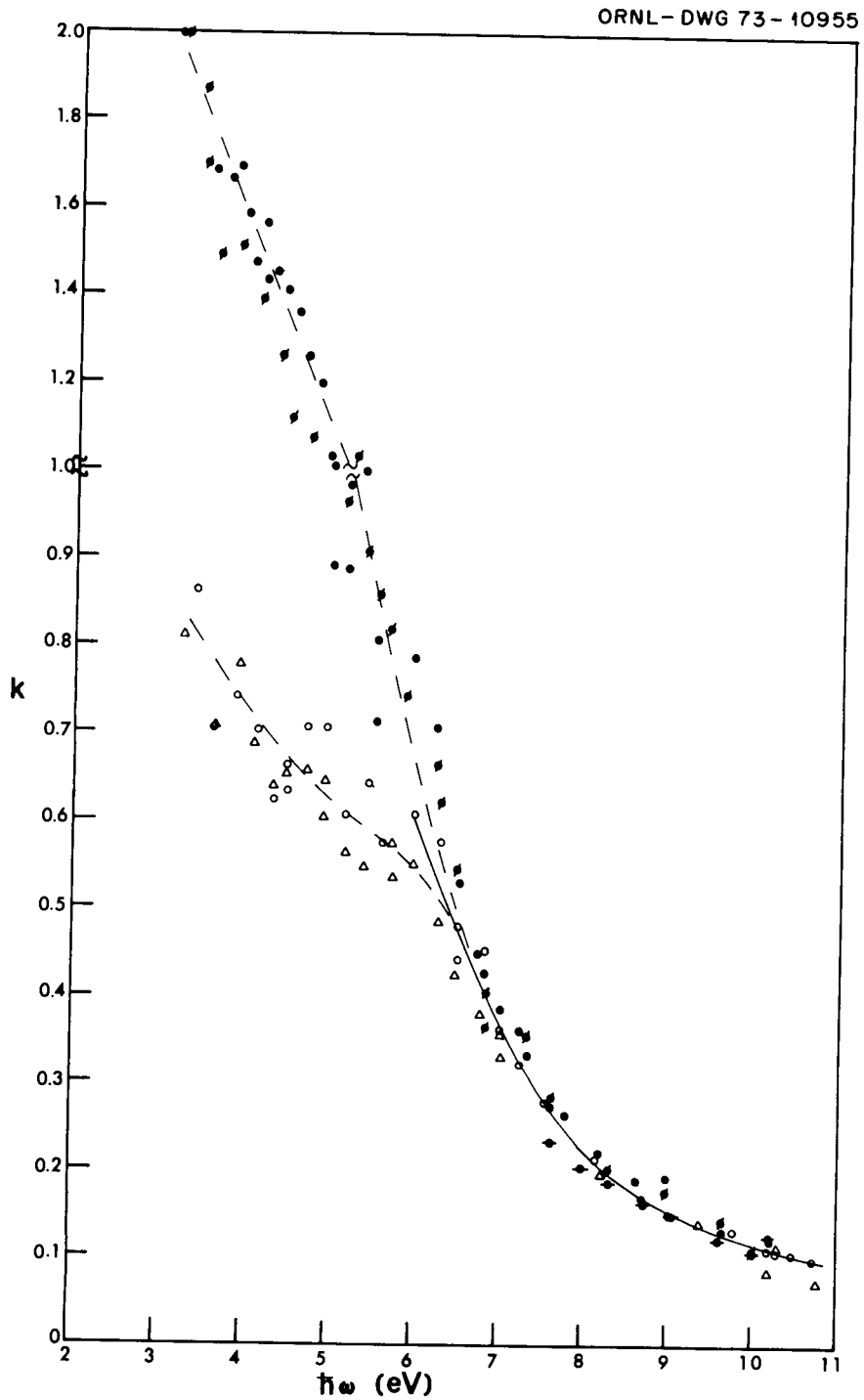

Fig. 21.2. Absorption coefficient vs photon energy for lithium films on MgF_2 substrate derived from $R(\Theta)$ measurements. The symbols •, ϕ, ⊕ are values for light incident through the substrate, and the symbols ○, △ are values for light incident from the vacuum.

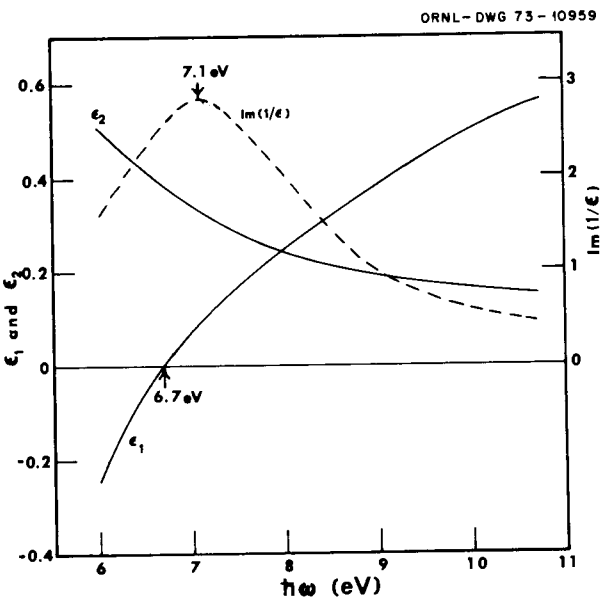

Fig. 21.3. Dielectric functions ϵ_1 and ϵ_2 and the energy loss function $-\mathrm{Im}\ (1/\epsilon)$ for photon energies from 6 to 10.7 eV. Plasma frequencies shown for condition where $\epsilon_1 = 0$ (6.7 eV) and for maximum in energy loss function (7.1 eV).

represent absorption by a collective effect. However, a calculation by Ching and Calloway showed that this peak was due to direct transitions from the conduction band to higher lying *d*-like bands.[9] Such transitions should not be present in lithium, and no extra absorption above the plasma frequency is observed for lithium, in agreement with the calculation.

ELECTRON ATTENUATION LENGTHS IN CARBON FILMS[10]

Electron attenuation lengths of photoexcited electrons in thick carbon films have been obtained from measurements of the total photoelectric yield as a function of photon angle of incidence, over the range of photon energies from 20 to 64 eV.

The basic apparatus for photoelectric measurements has been described previously. A grazing incidence scanning monochromator[11] was used to disperse the light, which then entered a stainless steel high-vacuum chamber[12] optically coupled to the monochromator. The essential features of this chamber are a sample holder at the center of a cylindrical electron collector. The sample holder can be rotated through 360°, so that the angle of incidence of the photons can be varied, and the cylindrical electron collector allows collection of virtually all photoelectrons emitted in any direction. The aluminum sample holder was designed to accept a standard microscope slide as a substrate. Thus, for the carbon films, vapor from a carbon arc was deposited, in vacuum, directly onto a clean glass slide. The sample was then exposed to the atmosphere on being transferred to the sample holder. Electrical contact was made directly to the carbon film, which was connected to ground through an electrometer. After insertion of a carbon film, the experimental chamber was pumped down to $\sim 2 \times 10^{-7}$ torr. The films were effectively infinitely thick as far as the incident radiation was concerned.

For a certain photon energy, defined by the setting on the monochromator, the total photoelectric yield was obtained in terms of the current going from the sample to the electron collector, as a function of photon angle of incidence, θ. This was repeated over the whole range of photon energies. For each energy, the yield at angle θ, $Y(\theta)$, relative to the yield for normal incidence, $Y(0)$, was analyzed as a function of θ as described previously.[13,14] For a given photon energy, the ratio $Y(\theta)/Y(0) = G(\theta)$ shows a single maximum when plotted vs θ if the film is infinitely thick and if its refractive index, n, is less than unity. For a small extinction coefficient, k (<0.1), of the film, these curves can be analyzed to yield n and either k or L, where L is the electron attenuation length for the photoexcited electrons. The position of the maximum of $G(\theta)$ vs θ is in the vicinity of θ_c, where $\theta_c \cong \sin^{-1} n$, and hence yields a value of n, while the magnitude of $G(\theta_c)$ is sensitive to k and L. In the present case, we obtained values of k independently from measurements of reflectance as a function of photon angle of incidence for thick evaporated carbon films similar to those used for the photoelectric yield measurements. We then used a two-parameter least-squares fitting

9. W. Y. Ching and J. Calloway, *Phys. Rev. Lett.* **30**, 441 (1973).

10. Research sponsored in part by the Defense Nuclear Agency, under subtask TA040, but does not reflect endorsement by the sponsor.

11. W. F. Hanson, E. T. Arakawa, and M. W. Williams, *J. Appl. Phys.* **43**, 1661 (1972).

12. T. F. Gesell and E. T. Arakawa, *Phys. Rev. Lett.* **26**, 377 (1971).

13. E. T. Arakawa et al., *Health Phys. Div. Annu. Progr. Rep. July 31, 1973*, ORNL-4903, pp. 88–90.

14. E. T. Arakawa, R. N. Hamm, and M. W. Williams, *J. Opt. Soc. Amer.* **63**, 1131 (1973).

procedure to obtain n and L from $G(\theta)$ vs θ. Figure 21.4 shows representative data points of $G(\theta)$ vs θ for a photon energy of 51.87 eV. Using $k = 0.04$, measured independently, a least-squares fit of this data to the theory gave $n = 0.89$ and $L = 2.4$ Å. The values obtained for the electron attentuation lengths of photoexcited electrons in evaporated carbon films are shown in Fig. 21.5 as a function of incident photon energy. Since the reflectance vs photon angle of incidence measurements yielded both n and k values, a consistency check could be made by comparing the values of n obtained, at a given photon energy, from the reflectance and from the photoelectric yield measurements. It was found that good agreement was obtained between the two n values over the whole energy range studied.

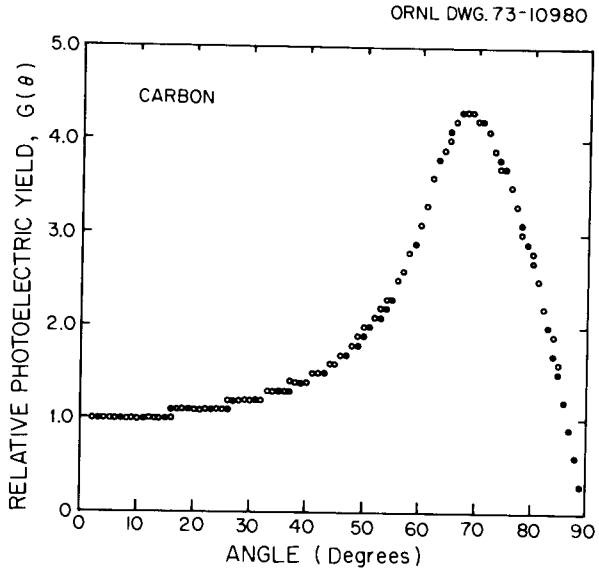

Fig. 21.4. Relative photoelectric yield vs angle of incidence for 51.87-eV photons (○ = experimental data points; • = least-squares fit to theory).

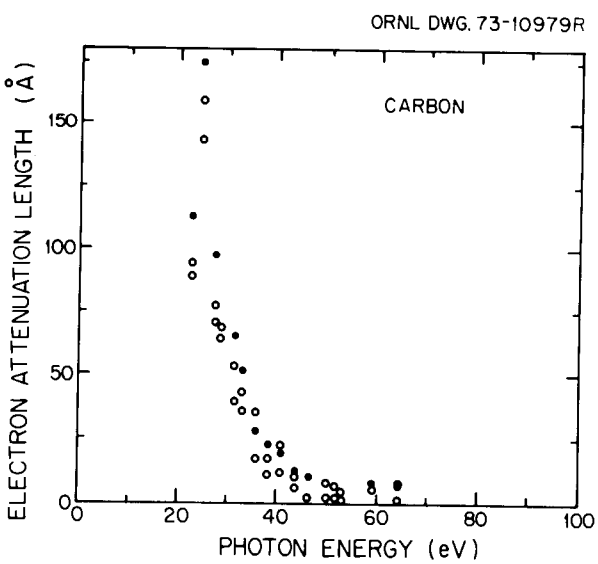

Fig. 21.5. Electron attenuation lengths of photoexcited electrons in carbon films vs incident photon energy.

PLASMON RESONANCE PHOTOEMISSION FROM ALUMINUM

Light of p polarization obliquely incident on a thin metal film through a transparent substrate of higher index of refraction may be used to generate a surface-plasma oscillation on the vacuum surface of the film. At the plasma resonance angle, there is a strong dip in reflectance and a large increase in the photoyield. The effects on reflectance have been described previously.[15] We discuss here measurements of photoyield as a function of incident light angle for light incident through an MgF_2 semicylinder onto thin (about 200 Å) films of aluminum. At photon energies near the threshold for photoemission, a plasmon resonance peak was observed at about 50° from normal incidence with yields more than 100 times that observed at normal incidence. These results are shown in Fig. 21.6 for several photon energies.

Volume and Surface Emission Processes in Resonance Photoemission

These data may be interpreted to determine what portion of the emission is due to each of two possible processes. Photoemission has sometimes been interpreted as a surface process in which electrons are excited from bulk states to vacuum with momentum being conserved by the surface potential barrier. It has usually been interpreted, however, as a volume process in which optical excitation in the bulk is followed by transport to and escape through the surface. A recent calculation by Endriz[16] indicates that the surface effect is dominant for fields associated with surface plasmons. We have been able to confirm this conclusion by analysis of the photoemissive yield curves.

On a smooth surface the surface process is excited only by electric fields normal to the surface. Thus photons at normal incidence produce electrons only by the volume emission process. Using Pepper's theory of photoemission from volume processes,[17] we calculated

15. E. T. Arakawa et al., *Health Phys. Div. Annu. Progr. Rep. July 31, 1973*, ORNL-4903, pp. 83–85.
16. J. G. Endriz, *Phys. Rev. B* **7**, 3464 (1973).
17. S. V. Pepper, *J. Opt. Soc. Amer.* **60**, 805 (1970).

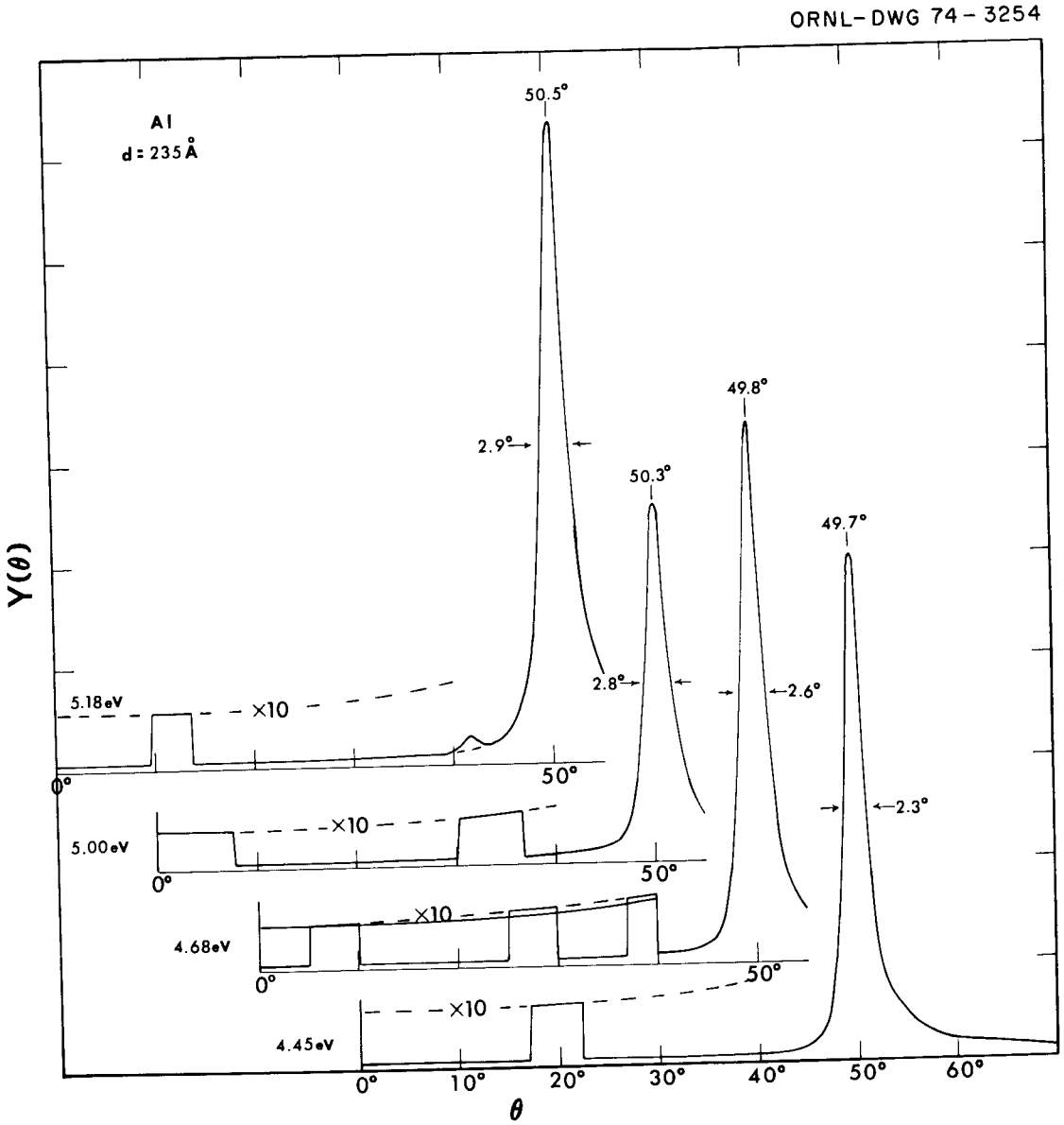

Fig. 21.6. Total photoyield vs incident angle of *p*-polarized light for photon energies near threshold. Solid curves are traces from raw data. Some portions of each curve taken at 10× magnification. Curves are labeled with photon energies.

the angular yield ratio $Y(\theta)/Y(0)$ for the volume process alone. The calculated yield ratio depends on the optical constants of the film and substrate, on the film thickness (d), and on the escape depth for electrons (L). The result of the calculation is shown in Fig. 21.7 for the measured film thickness and escape depth L ($L = 45 \pm 15$ Å). For all values of L and d within experimental limits, the calculation shows that only 35 ± 10% of the yield observed at the plasmon peak may be accounted for by the volume process. The remaining 65% of the yield is attributed to the surface emission process.

DETERMINATION OF ELECTRON SCATTERING LENGTHS IN ALUMINUM FROM MEASUREMENTS OF PHOTOEMISSION ESCAPE DEPTHS

An important parameter in models of the volume photoemission process is the escape depth, L, for photoexcited electrons. This quantity is of considerable interest because it is essentially a direct measure of the scattering length of hot electrons if the data are analyzed in terms of the partial yield of the most energetic electrons. Considerable ingenuity is required,

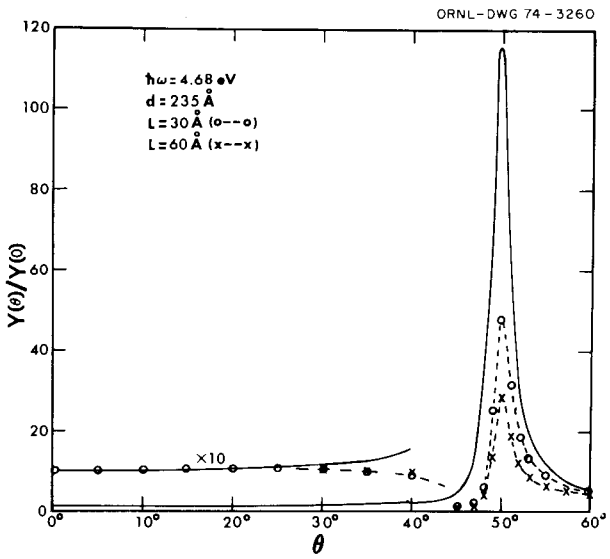

Fig. 21.7. Comparison of experimental values of the angular yield ratio to values calculated from the volume photoemission model. No plausible choice of film thickness (d) and escape depth (L) can account for the yield observed at the plasmon resonance peak.

however, to separate the effect of L on the photoyield from the effect of the many other parameters in the theory. We describe here a determination of the escape depth in aluminum that is unaffected by the poorly known parameters in the theory and depends only on independently measurable quantities.

Values of L were determined for electrons with energies between 5 and 10 eV from measurements of the ratio of the yield observed with light incident from the substrate onto a thin film of aluminum. Normal incidence light was used to suppress the surface photoemission process. By determining L from a ratio of yields, we eliminate uncertainties associated with poorly known excitation and escape probabilities.

Studies were made on films with thicknesses ranging from 100 to 200 Å, where the dependence of the yield ratio on L is strongest. The calculated yield with light incident from vacuum on the surface may be written

$$Y_V = C\,F(L, n_0, n_1, k_1, n_2, d)\,,$$

and with light incident through the substrate,

$$Y_s = C\,F'(-L, n_2, n_1, k_1, n_0, d)\,e^{-d/L}\,.$$

F is a function of the optical constants of vacuum (n_0), of aluminum (n_1 and k_1), and of the MgF_2 substrate (n_2) as well as of the escape depth (L) and film thickness (d). F' differs from F only in the interchange of n_0 and n_2 in the equations giving F. The full equations for F are available in the literature.[17] The constant C contains excitation and escape factors that are identical with either direction of incident light, so that the theoretical yield ratio is given by

$$(Y_s/Y_V)_{\text{theor}} = \frac{F'(-L)}{F(L)}\,e^{-d/L}\,.$$

In Fig. 21.8 this function is plotted vs escape depth for films with thicknesses between 75 and 250 Å and optical parameters appropriate to aluminum on MgF_2 at light wavelengths of 2400 Å. It is interesting that the ratio may exceed unity for thin films. This results because light incident through the substrate is internally reflected at the vacuum interface and thus makes two passes through the region near the emitting surface.

An additional term must be taken into account before the above equation can be compared with experiment. With light through the substrate, we must multiply the yield by a factor $(1 - R_{02})$ to account for reflection losses at the curved surface of the semicylinder and by a factor T_2 to account for transmission losses in the MgF_2, which become significant below about 2000 Å. Our analysis thus uses an equation of form

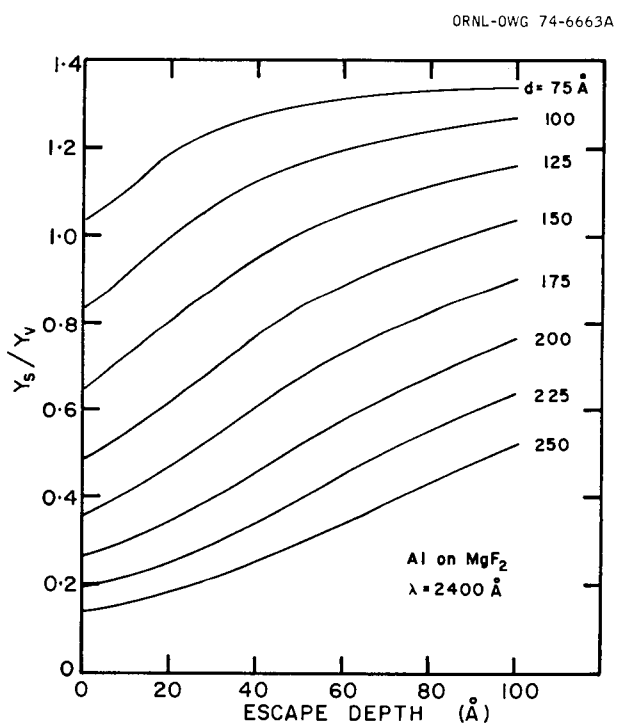

Fig. 21.8. Relative yield function vs escape depth for aluminum films with thicknesses between 75 and 250 Å.

$$(Y_S/Y_V)_{exp} = T_2(1 - R_{02})\frac{F'(-L)}{F(L)}e^{-d/L} .$$

Using measured values of Y_S/Y_V and of d, independently determined values of the optical constants of aluminum and MgF_2, and values of $T_2(1 - R_{02})$ determined from transmission measurements on an uncoated semicylinder, we found the values of L listed in Table 21.1 for several electron energies.

RADIATION-INDUCED CHANGES IN THE SOFT X-RAY EMISSION FROM LiF AND NaCl

A suggestion that salt mines might be used as radioactive waste repositories has increased the interest in radiation-induced effects in ionic crystals, particularly NaCl. We have demonstrated that LiF and NaCl show dramatic radiation-induced changes in structure, including evolution of the halogen and coagulation of the alkali metal on the surface of the crystal.

An electron beam of energy from 2 to 2.5 keV and a beam current from 0.7 to 3.0 mA was incident on cleaved single crystals of LiF and NaCl attached directly to the water-cooled copper anode of the x-ray source with conducting silver paste. The photons emitted were dispersed with a grazing-incidence (82°) scanning monochromator and detected with a channel electron multiplier from which the output current was read with a logarithmic electrometer.[18,19] The pressure was 3×10^{-7} to 5×10^{-7} torr, and the scanning speed was such that the resolution in the x-ray spectra was limited only by the slit width of 200 μ.

The soft x-ray emission spectra as a function of bombardment time are presented for both crystals in Fig. 21.9. For LiF, beam currents of 0.7 to 2.0 mA did not produce any noticeable difference in the sample during several minutes of bombardment, but a beam current of 3 mA resulted in a shiny metallic surface within about 5 min. For NaCl, a beam current of 0.7 mA gave a shiny metallic appearance to the sample within 1 to 2 min. The K_α emission spectrum from lithium in LiF is seen peaking at 47 eV in the first two spectra. After bombardment and exposure to the 3×10^{-7} to 5×10^{-7} torr vacuum, the K_α emission for lithium in Li_2O at 50 eV and for the pure lithium metal at 54 eV are also seen.[18,19] As has been noted previously in the literature,[20] the L_{23} emission for sodium in NaCl is not seen, but after bombardment the L_{23} emission for pure sodium peaking at 30.5 eV is seen. As had been noted earlier for the pure metal, no evidence of oxidation is seen.[19] The $L_1 - L_{23}$ emission is unshifted in going from the halide to the pure metal, indicating that the two core levels are equally shifted when sodium is incorporated in NaCl. Similar changes of the soft x-ray emission spectrum with time have been obtained for MgF_2, whereas the spectrum for MgO does not change with time.[11] Sputtering from cleaved NaCl crystals due to low-energy electron bombardment in vacuum has also been studied.[21] Both Cl^+ and Cl_2^+ ions were ejected from the NaCl surface and detected with a mass spectrometer. These observations show that irradiation results in coagulation of the metal in the crystal because of the evolution of the halogen.

ELECTRICAL CONDUCTIVITY AND OPTICAL PROPERTIES OF (TTF)(TCNQ)

Because of its extreme electrical anisotropy and its metallic-like conduction, the charge transfer complex (TTF) (TCNQ) (tetrathiofulvalene tetracyanoquinodimethan) offers unique possibilities for understanding

18. E. T. Arakawa et al., *Health Phys. Div. Annu. Progr. Rep. July 31, 1973*, ORNL-4903, pp. 90–91.
19. E. T. Arakawa and M. W. Williams, *Phys. Rev. B* 8, 4075 (1973).
20. V. A. Fomichev, T. M. Zimkina, and I. I. Zhukova, *Sov. Phys. – Solid State* **10**, 2421 (1969).
21. R. N. Compton et al., *Health Phys. Div. Annu. Progr. Rep. July 31, 1973*, ORNL-4903, p. 101.

Table 21.1. Parameters used in the calculations of escape depth from the front-to-back yield ratio

Wavelength (Å)	Electron energy (eV)	d (Å)	$(1 - R_{02})T_2$	n_1	k_1	n_2	Y_V/Y_S	L (Å)
2400	5.0 ± 0.2	130 ± 15	0.96	0.158	2.59	1.41	1.06	55 ± 15
1610	7.2 ± 0.5	130 ± 15	0.54	0.08	1.8	1.47	0.406	30 ± 10
1255	8.9 ± 1	130 ± 15	0.34	0.06	1.2	1.59	0.250	26 ± 10

ORNL-DWG 74-6869

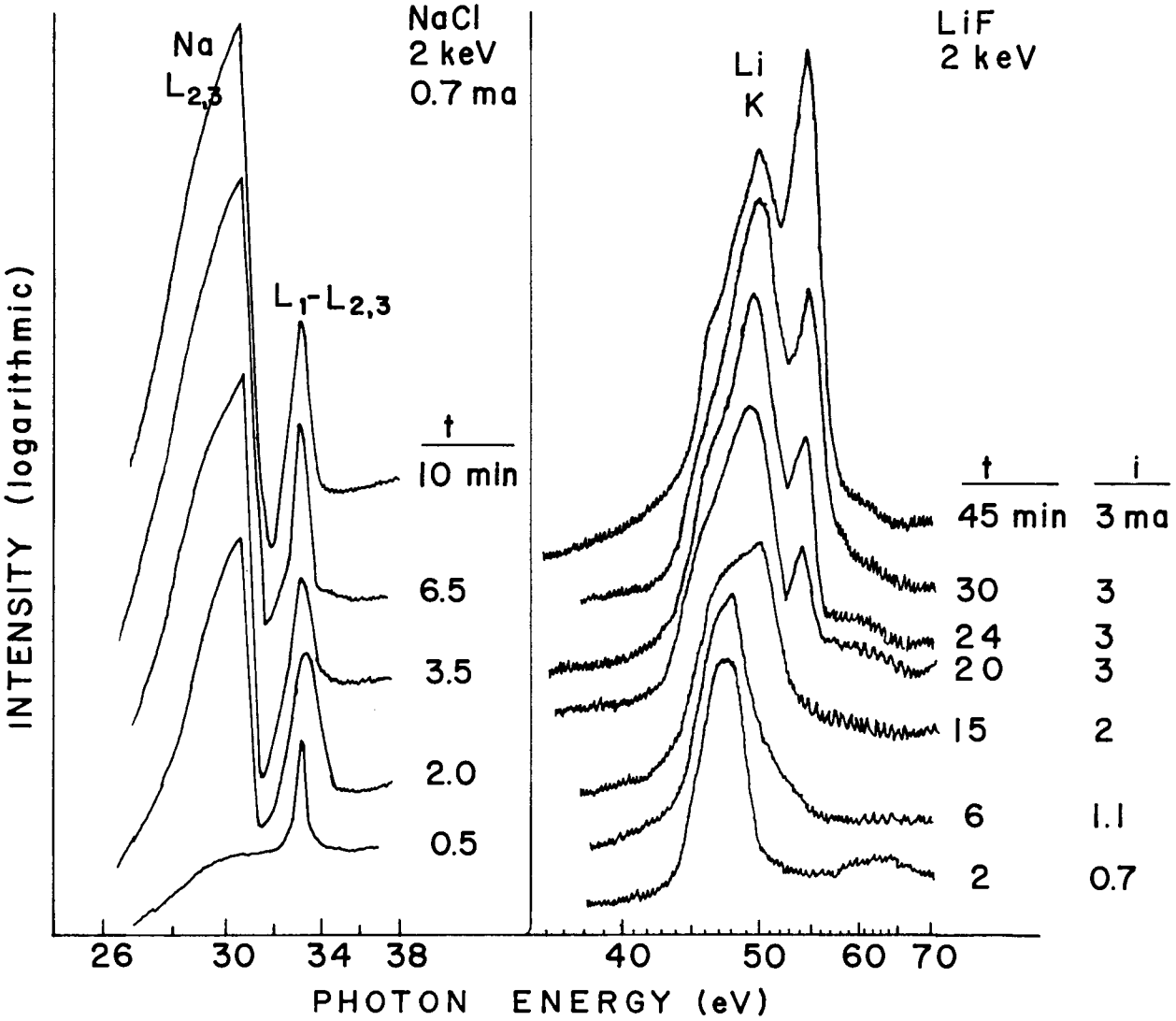

Fig. 21.9. Recorder traces of soft x-ray emission spectra of sodium chloride and lithium fluoride showing the dependence on electron-beam current and total bombardment time.

the nature of the metallic state in pseudo one-dimensional conductors. The fact that one group of observers has reported extraordinarily high conductivity peaks has led to an interpretation as a possible superconductive fluctuation.

Single crystals[22] of (TTF) (TCNQ) were prepared (larger than any other group has prepared), and the dc electrical conductivities were measured (Fig. 21.10). Although we did not observe any extraordinary conductivity peaks, it must be stressed that intrinsic measurements are difficult because of impurities, defects, and even the measurement procedure itself. The suggestion that a probe misalignment could generate false high peaks was investigated by computer modeling this situation. Although very high conductivity peaks can easily be generated by computer modeling (which fit experimentally misaligned probe data), the temperature dependence of the measured extraordinary peaks

22. Crystals of (TTF) (TCNQ) prepared by V. F. Raaen of the Chemistry Division, ORNL.

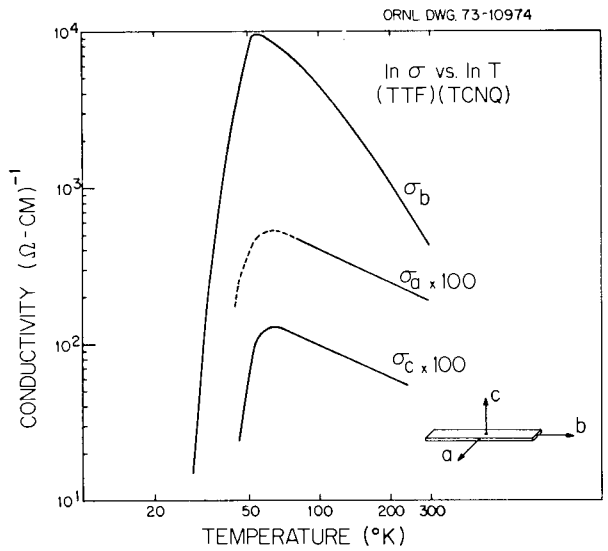

Fig. 21.10. Experimentally measured conductivities for the three principal directions of (TTF)(TCNQ).

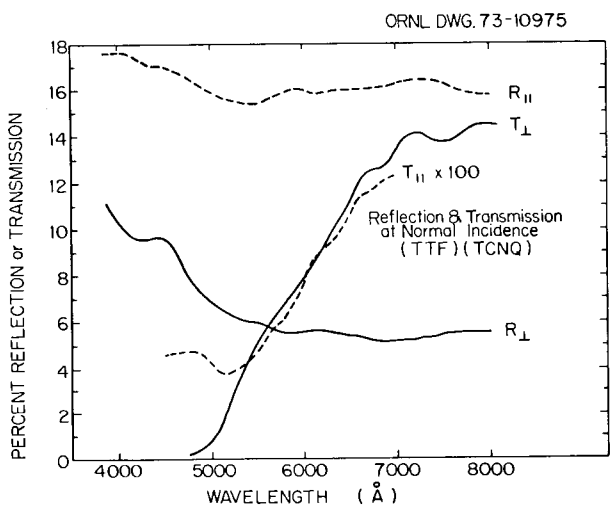

Fig. 21.11. Reflection and transmission of (TTF)(TCNQ) at room temperature. ∥refers to the electric solid vector E along the *b* axis (high conductivity direction), and ⊥ refers to E along the *a* axis (see Fig. 21.10).

can in no way be attributed to simple probe misalignment.[23]

The determination of the optical constants and their temperature dependence is being investigated for (TTF) (TCNQ) and related compounds in the energy region of the near infrared through the far ultraviolet. Figure 21.11 shows the reflection and transmission at room temperature in the visible region. The anisotropic behavior of this crystal is clearly seen in the transmittance curves.

EFFECT OF DAMPING ON SURFACE-PLASMON DISPERSION

It is conventional to represent the dispersion of surface plasmons on a semi-infinite dielectric bounded by vacuum by the equation

$$k_s = (\omega/c)[\epsilon/(\epsilon + 1)]^{1/2} , \qquad (1)$$

where k_s is the surface-plasmon wave vector along the surface, ω is the angular frequency, and $\epsilon = \epsilon_1(\omega) + i\epsilon_2(\omega)$ is the complex dielectric function of the medium. If ϵ_2 is set equal to zero, the surface-plasmon dispersion curve, that is, a plot of ω vs k_s for the wave, goes asymptotically to the characteristic surface-plasmon frequency ω_s for large wave vectors, that is, for $\epsilon_1 \to -1$. If damping is included, that is, $\epsilon_2 \neq 0$, the surface-plasmon dispersion curve as defined by Eq. (1) does not increase monotonically to ω_s as k_s increases but instead, at some finite k_s value, turns back toward the light line. This is shown for silver in Fig. 21.12, where the solid curve has been calculated from Eq. (1) using experimental values of ϵ_1 and ϵ_2 from the literature.[24,25] It was found that both sets of data from the literature and our own measurements of ϵ_1 and ϵ_2 for silver gave essentially the same curve.

We have obtained experimental data relating to the shape of the surface-plasmon dispersion curve, shown by the points in Fig. 21.12. Experimental determinations of the dispersion of surface plasmons from electron energy loss measurements and from previous attenuated-total-reflection techniques have shown no indication of a bending back in the dispersion curve in the vicinity of ω_s.

Our experimental arrangement, employing the method of attenuated total reflection, is shown in Fig. 21.13. A transparent semicylinder was cleaned and then a thin silver film deposited by vacuum evaporation on the plane surface. Monochromatic, *p*-polarized light, incident through the curved surface of the semicylinder, was reflected from the semicylinder-silver interface and the reflectance measured as a function of the angle of incidence θ. At an angle just greater than the critical

23. R. J. Warmack, T. A. Callcott, and H. C. Schweinler, *Appl. Phys. Lett.* **24**, 635 (1974).

24. M. M. Dujardin and M. L. Theye, *J. Phys. Chem. Solids* **32**, 2033 (1971).

25. H. Ehrenreich and B. H. Philipp, *Phys. Rev.* **128**, 1622 (1962).

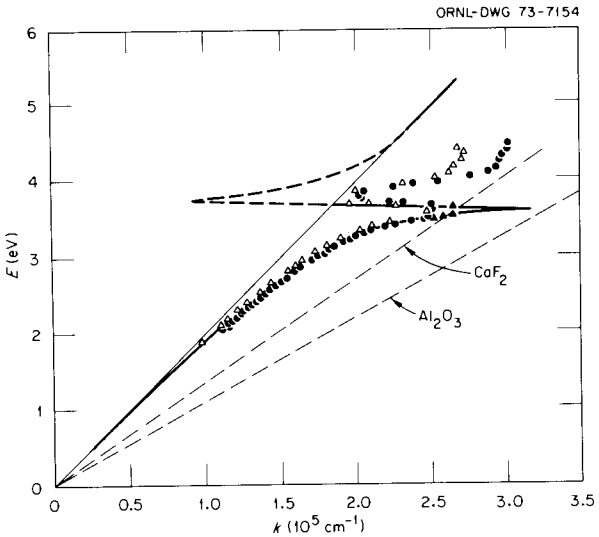

Fig. 21.12. Surface-plasmon dispersion curve. Solid line, calculated from Eq. (1); open triangles, 340-Å-thick silver film on CaF_2; circles, 290-Å-thick, and filled triangles, 500-Å-thick silver films on sapphire. The dashed portion of the theoretical curve to the left of the light line is predicted from Eq. (1) and is presented for completeness but does not correspond to the existence of surface plasmons in this region.

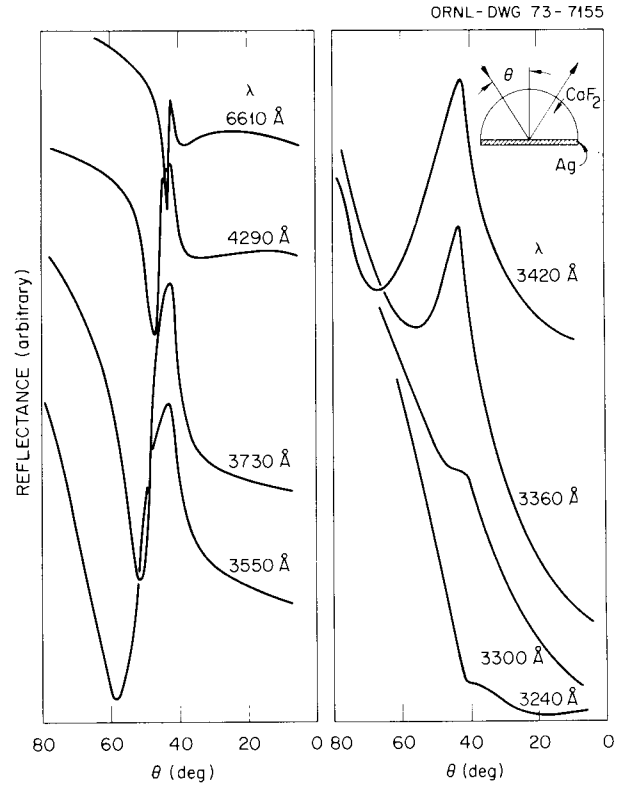

Fig. 21.13. Experimental curves of reflectance vs angle of incidence for 340 Å of silver on a CaF_2 semicylinder and for different wavelengths.

angle for total internal reflection of the material of the semicylinder, a sharp minimum occurs in the reflectance. At this angle photons refracted along the semicylinder-silver interface can excite surface plasmons associated with the silver-vacuum surface. The angular position of the minimum in reflectance is governed by the condition

$$k_s = k_{\parallel} = (\omega/c)n \sin\theta \ , \qquad (2)$$

where $k_{\parallel}$ is the component of the photon wave vector parallel to the semicylinder-silver interface and n is the index of refraction of the material of the semicylinder.

Figure 21.13 shows representative measurements of reflectance vs angle of incidence for photons of various wavelengths. The semicylinder was CaF_2 and the silver film was 340 Å thick. The silver film was vacuum evaporated, in situ, at 10^{-9} torr and was not exposed to the atmosphere during measurements. The thickness was calculated from a least-squares fit to the reflectance vs angle of incidence based on Fresnel's equations. The thickness of the silver film was chosen to be thin enough for the incident energy to be able to penetrate to the silver-vacuum interface and excite surface plasmons and thick enough that the dispersion curves are identical for the normal and tangential nonradiative surface plasmon modes in the silver film. The variation of $k_{\parallel}$ with ω, calculated from the positions of the minima shown in Fig. 21.13 and using Eq. (2), is shown in Fig. 21.12. It is seen that agreement is obtained with the ω-vs-k_s variation calculated from Eq. (1) for regions to the right of the light line and for energies below the volume plasmon energy for silver (3.75 eV), except for the regions with the largest k values. Also shown in Fig. 21.12 are two lines indicating the maximum $k_{\parallel}$ value which can be excited by this method, calculated from Eq. (2) with $\sin\theta = 1$ and the values of n for CaF_2 and sapphire in the vicinity of ω_s for the silver-vacuum interface. It is seen that using CaF_2 we cannot excite as high k values as are calculated from Eq. (1). The observations were thus repeated using a 290-Å-thick silver film on a sapphire semicylinder. The thickness of this film was monitored with a quartz-crystal thickness monitor, and then the optical data, shown in Fig. 21.12, were obtained at atmospheric pressure. It is seen that the results are substantially the same as with the CaF_2 semicylinder and that the higher k values predicted by Eq. (1) are not obtained, although with the sapphire semicylinder this should be possible experimentally. It was thought that possibly the silver film

thickness might influence these results. Solutions of Fresnel's equations for the angle at which the reflectance is a minimum as a function of the thickness of the silver film confirm the values obtained experimentally for both the CaF_2 and sapphire semicylinders. The maximum value of k which can be excited by this method is found to depend on the film thickness but never becomes as great as predicted by Eq. (1). As an illustration, results for a 500-Å silver film on sapphire are also shown in Fig. 21.12. Our calculations show that the data for this film represent approximately the largest k values which can be excited for a silver film of any thickness on sapphire by this method.

The discrepancy between results from electron-energy-loss experiments and attenuated-total-reflectance experiments arises because the surface-plasmon dispersion cannot be represented completely in terms of a single ω-vs-k relationship. Starting with the known optical constants of silver, interesting differences are found in the calculated dispersion relations based on electron energy losses and on attenuated total reflection (optical absorption). This difference has not been noted before, theoretically or experimentally, to our knowledge. The explanation of this difference seems to lie in the fact that the dispersion curves are inferrred from the respective experiments in different ways. In the usual electron-energy-loss experiment, a distribution of energy losses is measured at fixed momentum transfer $\hbar k$; the energy corresponding to the most probable energy loss to the surface plasmon field is determined and is plotted vs k to establish a single point on the surface-plasmon dispersion curve. This procedure is repeated for various values of k until an experimental ω-vs-k curve can be established. The procedure followed in the attenuated-total-reflection experiment as described here in essence corresponds to finding the direction of the incident photons for which the absorption is a maximum for a constant photon energy. A complete description of the surface plasmon, when damping is present, therefore requires a three-dimensional representation which gives some characteristic response of the surface plasmon in terms of k and ω, rather than a single ω-vs-k relation.

The results obtained for $k_{\parallel}$ vs ω above the volume plasmon energy, that is, the upper portions of the experimental curves in Fig. 21.12, are not fully understood in terms of a simple surface-plasmon model at this time. These values were calculated using Eq. (2) with θ determined as before from the minimum in the reflectance-vs-angle data. However, ϵ_1 is greater than -1 in this energy region, and the minimum in the R-vs-θ curve presumably does not represent the excitation of surface waves.

A CONCENTRIC ANGLE DOUBLER FOR VACUUM ULTRAVIOLET STUDIES

The reflectance of both solids and liquids as a function of the angle of incidence is used to extract the optical properties of the material by a number of techniques. Critical-angle methods, multiangle reflectance studies, and techniques based on Brewster's angle are among those used for this purpose. To maintain the detector in the beam reflected from a rotating sample, it is necessary that the detector rotate at twice the angular velocity of the sample. Previously this was accomplished by driving the separate shafts of the sample and the detector from a common shaft by means of toothed timing belts and pulleys of the appropriate diameters.[26]

A new angle doubler has been designed and constructed, as shown in Fig. 21.14, which eliminates some of the problems of the earlier design. The use of gear drives reduces the lateral force on the sample and detector shafts, whereas the concentric mounting from a single flange removes the possibility of mechanical misalignment of the two shafts. Desirable features of the earlier design were retained, for example, provisions for independently adjusting the sample position and a means of withdrawing the sample from the incident beam. Both of these may be accomplished with the chamber under vacuum.

The driving system consists of a fine angle stepping motor[27] which rotates the sample by integral multiples of 0.225° with a noncumulative error of ±0.05°. The motor control system consists of a variable-speed oscillator with a preset count to permit accurate and reproducible positioning of the detector and sample. Both a manual and an automatic mode are available. In the manual mode a Schmitt trigger circuit drives a series of pulse dividers to give a pulse train of variable frequency, synchronous with the recorder chart drive. In the automatic mode the motor control system is interfaced with an analog-to-digital converter and Teletype to provide output suitable for direct computer processing.

26. R. C. Vehse, J. C. Sutherland, and E. T. Arakawa, *Rev. Sci. Instrum.* 39, 268 (1968).

27. USM Corporation, Gear Systems Division, Wakefield, Mass.

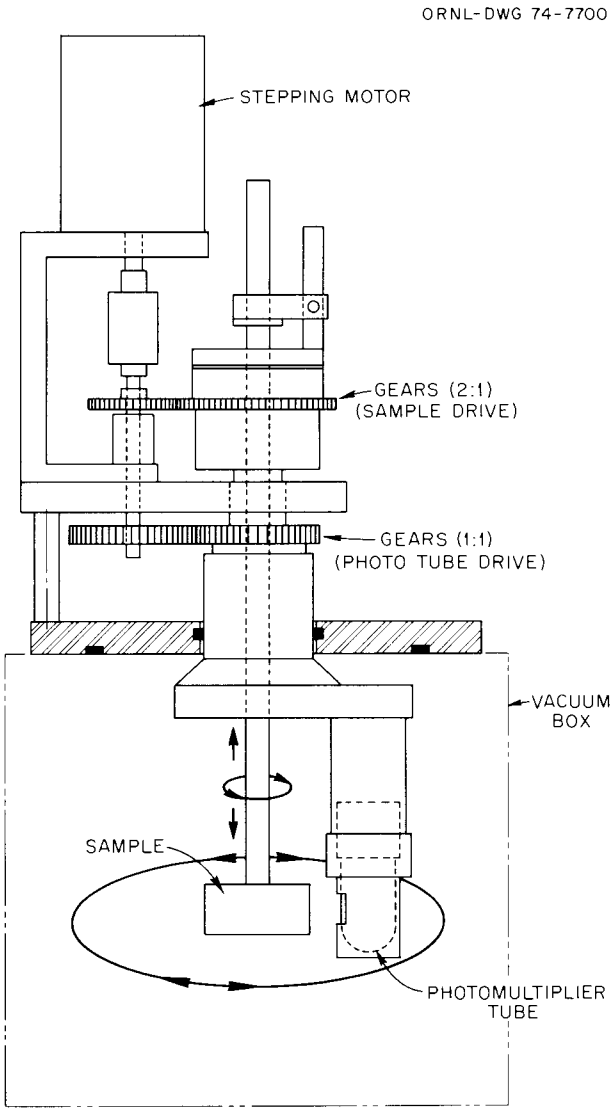

Fig. 21.14. A concentric angle doubler for vacuum uv studies.

PHOTON SCATTERING FROM CYLINDERS

It has been recently suggested[28] that the structure seen in the angular distribution of light reflected from thin metallic cylinders near grazing incidence is due to the excitation of surface plasmons. Our theoretical radiation physics group has initiated a comprehensive study of the scattering and absorption of electromagnetic radiation in cylindrical geometries. We have programmed a number of the equations resulting from this study in order to evaluate the various parameters required in an experimental study.

Miziumski suggested that only the higher-order guided waves are associated with radiative modes. Therefore the programming effort has concentrated on developing routines for $J_n(Z)$ and $Y_n(Z)$, Bessel functions of the first and second kinds, respectively, of high order n and argument Z as well as for $I_n(Z)$ and $K_n(Z)$, the modified Bessel functions of the first and second kinds respectively. In the most general case, Z may be a complex quantity.

The quantities calculated were the differential scattering efficiency $dS^{\parallel,\perp}/d\phi$ and the differential scattering probability $dP^{\parallel,\perp}/d\phi$ at azimuthal angle ϕ for photons of frequency ω incident on a cylinder with radius a at an angle θ with respect to the cylinder axis. These are given by

$$\frac{dS^{\parallel,\perp}}{d\theta} = \frac{1}{\pi(\epsilon_2)^{1/2}\,(a\omega/c)\sin\theta}\left[\left|A_0{}^s + 2\sum_{n=1}^{\infty}(-1)^n\cos(n\phi)\,A_n{}^s\right|^2 + \left|2\sum_{n=1}^{\infty}(-1)^n\sin(n\phi)\,B_n{}^s\right|^2\right],$$

$$\frac{dP^{\parallel,\perp}}{d\theta} = \frac{1}{2\pi}\,\frac{\left|A_0{}^s + 2\sum_{n=1}^{\infty}(-1)^n\cos(n\theta)\,A_n{}^s\right|^2 + \left|2\sum_{n=1}^{\infty}(-1)^n\sin(n\theta)\,B_n{}^s\right|^2}{\left|A_0{}^s\right|^2 + 2\sum_{n=1}^{\infty}\left|A_n{}^s\right|^2 + 2\sum_{n=1}^{\infty}\left|B_n{}^s\right|^2},$$

where

$$A_n{}^{s,\parallel} = \frac{J_n(\mathrm{v})}{H_n{}^{(2)}(\mathrm{v})} + i\,\frac{2\left[H_n{}^{(2)\prime}(\mathrm{v})/\mathrm{v}\,H_n{}^{(2)}(\mathrm{v}) - J_n{}'(u)/u\,J_n(u)\right]}{\pi\mathrm{v}^2\,[H_n{}^{(2)}(\mathrm{v})]^2\,D}$$

28. C. Miziumski, *Phys. Lett.* **40A**, 187 (1972).

and

$$B_n^{s,\parallel} = \frac{2}{\pi v^2}(1/v^2 - 1/u^2)\frac{n\cos\theta}{[H_n^{(2)'}(v)]^2 D}$$

are amplitudes[29] associated with the scattered electric and magnetic fields when the electric vector of the incident plane wave lies in the plane defined by the axis of the cylinder and the direction of the incident photons. For the case of the electric vector perpendicular to this plane the corresponding amplitudes are

$$A_n^{s,\perp} = \frac{J_n(v)}{H_n^{(2)}(v)} + i\,\frac{2\left[H_n^{(2)'}(v)/v\,H_n^{(2)}(v) - \frac{\epsilon_c}{\epsilon_m}\cdot J_n'(u)/u\,J_n(u)\right]}{\pi v^2\,[H_n^{(2)}(v)]^2 D}$$

and

$$B_n^{s,\perp} = \epsilon_m B_n^{s,\parallel}\,.$$

Here

$$D = \left[\frac{H_n^{(2)'}(v)}{v\,H_n^{(2)}(v)} - \frac{J_n'(u)}{u\,J_n(u)}\right] \times \left[\frac{H_n^{(2)'}(v)}{v\,H_n^{(2)}(v)} - \frac{\epsilon_c J_n'(u)}{\epsilon_m u\,J_n(u)}\right] - \left(\frac{1}{v^2} - \frac{1}{u^2}\right)^2 n^2\cos^2\theta\,.$$

The $H_n^{(2)}(v)$ are Hankel functions of the second kind of order n and argument v. All primes denote derivatives with respect to the argument. The arguments of the Bessel and Hankel functions are given by

$$u = \frac{a\omega}{c}(\epsilon_c - \epsilon_m\cos^2\theta)^{1/2}$$

and

$$v = \frac{a\omega}{c}(\epsilon_m)^{1/2}\sin\theta\,.$$

In these expressions c is the velocity of light in vacuum and ϵ_c and ϵ_m are the dielectric constants of the cylinder and the surrounding medium respectively. In all cases, nonmagnetic materials are assumed, so that the magnetic permeabilities are everywhere equal to 1.

In the special case of photons incident normally on the cylinder ($\theta = \pi/2$) and at $\phi = 0$ the scattering amplitudes agree with those previously published.[30] In this case, both $B_n^{s,\parallel}$ and $B_n^{s,\perp}$ are zero. Similar calculations for the more general case of nonnormally incident photons have not been published.

For the case of a cylinder with radius $a = 80$ Å and a dielectric constant of a free-electron gas immersed in vacuum, the differential scattering efficiency, $dS^{\perp}/d\phi$, for perpendicularly polarized photons of frequency $\omega = \omega_p$ is shown in Fig. 21.15 for several values of θ. The dipole character of the scattered fields is evident for the larger angles. These functions exhibit pronounced structure near the suface-plasma energy as shown in Fig. 21.16, which is drawn for a free-electron gas with $\hbar\omega_p = 14.98$ eV. In this case the parallel component,

29. J. R Wait, *Can. J. Phys.* **33**, 189 (1955).

30. B. K. Larkin and S. W. Churchill, *J. Opt. Soc. Amer.* **49**, 188 (1959).

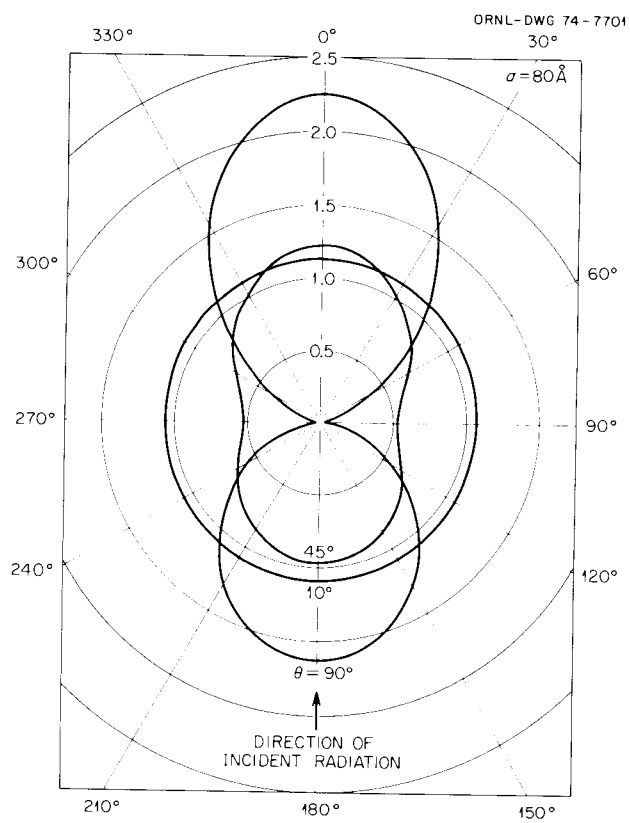

Fig. 21.15. The differential scattering efficiency, $dS^{\perp}/d\phi$, for perpendicular polarized photons of frequency $\omega = \omega_p$ as a function of azimuthal angle ϕ.

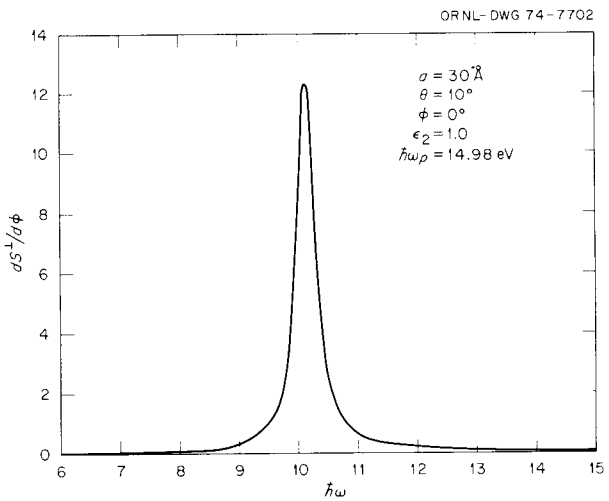

Fig. 21.16. The differential scattering efficiency for perpendicular polarized photons for a cylinder of free-electron gas of radius a = 30 Å as a function of photon energy.

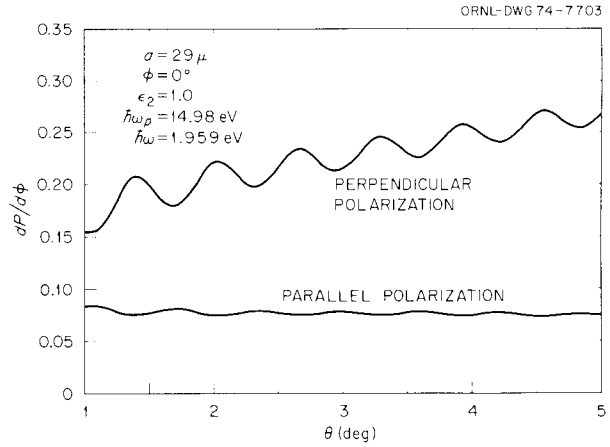

Fig. 21.17. The differential scattering probability for a 29-μ-radius cylinder of a free-electron gas with a plasma energy of 14.98 eV as a function of the grazing angle Θ.

$dS^{\parallel}/d\phi$, shows similar structure. The differential scattering probabilities $dP^{\parallel,\perp}/d\phi$ for the case studied experimentally by Miziumski[28] is shown in Fig. 21.17. Here, the structure in the perpendicular component is much more pronounced than that in the parallel component. Some features of these results are not in agreement with Miziumski's work, indicating that further study is required.

The use of cylindrical geometries may offer a convenient method of studying surface-plasma oscillations in a variety of materials. We anticipate that these calculations will suggest a number of experimental studies associated with the excitation of surface-plasma waves.

22. Physics of Tissue Damage

E. T. Arakawa
R. D. Birkhoff[1]
J. K. Baird
L. C. Emerson
R. N. Hamm
T. Inagaki[2]
Sung-I Juan[3]
R. A. MacRae[4]
Linda R. Painter[4]
R. H. Ritchie
Mary W. Williams

COLLECTIVE ELECTRON EFFECTS IN MOLECULAR LIQUIDS

A knowledge of the interactions of radiation with molecular liquids such as glycerol, water, and benzene has direct biological application in terms of understanding radiation damage to living material. The conditions necessary for the existence of collective electron effects in molecular liquids have been considered, and the collective behavior associated with a single oscillator and with a collection of oscillators has been compared with the behavior of a free-electron gas.

The response of a medium to an externally applied electric field of angular frequency ω can be described in terms of its complex dielectric function $\epsilon(\omega)$. In particular, it can be shown that $\epsilon(\omega) = 0$ defines a natural longitudinal resonance of the system which is physically observable as a collective electron oscillation.

The analytical form used to approximate $\epsilon(\omega)$ depends on the model of the medium used in its derivation. A simple representation for the complex dielectric constant of a condensed medium, if one assumes the field at each molecule to equal the externally applied field, is

$$\epsilon(\omega) = 1 + \alpha(\omega) , \tag{1}$$

where $\alpha(\omega)$ is proportional to the polarizability. We assume a random array of sites at each of which is an identical collection of classical oscillators. These oscillators are identified by resonant frequencies ω_i, corresponding damping γ_i, and oscillator strengths f_i. This leads to the Drude-Sellmeier formula for the complex dielectric constant, in which $\alpha(\omega)$ is given by

$$\alpha(\omega) = \sum_{i=0}^{q} \frac{f_i \omega_p{}^2}{\omega_i{}^2 - \omega^2 - i\gamma_i\omega} , \tag{2}$$

where ω_p, the plasma frequency, is given by $\omega_p = \sqrt{4\pi n e^2/m}$, where e is the electronic charge and m is the electron mass. Since for the liquids we have studied[5] the core electrons are not excited, it is convenient to limit the transitions included in Eq. (2) to those involving only the noncore electrons. The electron density n in the formula for the plasma frequency is then the density of noncore electrons. In this case the sum rule

$$\sum_{i=0}^{q} f_i = 1$$

is no longer exact; the sum may add up to a value slightly larger than one.[6] A useful expression for the plasma energy in molecular liquids is $\hbar\omega_p = 28.8(z\rho/M)^{1/2}$ eV, where z is the number of noncore electrons per molecule, M is the molecular weight, and ρ is the density in grams per cubic centimeter.

1. Also Chief of Fundamental Health Physics Research Section.
2. Postdoctoral fellow.
3. Graduate student.
4. Consultant.

5. E. T. Arakawa et al., *Health Phys. Div. Annu. Progr. Rep. July 31, 1973*, ORNL-4903, pp. 104–6, and previous reports in this series.
6. C. J. Powell, *J. Opt. Soc. Amer.* 59, 738 (1969).

Using the Drude-Sellmeier model for $\epsilon(\omega)$, we can show the essential conditions under which collective electron effects are seen in an insulator, although in the interpretation of actual data it may be necessary to assume a more complicated form of $\epsilon(\omega)$ to replace Eq. (1).

Combining Eqs. (1) and (2) gives

$$\epsilon_1 = 1 + \sum_{i=0}^{q} \frac{f_i \omega_p^2 (\omega_i^2 - \omega^2)}{(\omega_i^2 - \omega^2)^2 + \gamma_i^2 \omega^2} \tag{3}$$

and

$$\epsilon_2 = \sum_{i=0}^{q} \frac{f_i \omega_p^2 \gamma_i \omega}{(\omega_i^2 - \omega^2)^2 + \gamma_i^2 \omega^2} . \tag{4}$$

Metallic Behavior

For a metal where $f_0 = 1$, $\omega_0 = 0$, and $f_i = 0$ for $i \neq 0$, we obtain the well-known Drude equations

$$\epsilon_1 = 1 - \frac{\omega_p^2}{\omega^2 + \gamma_0^2} , \qquad \epsilon_2 = \frac{\omega_p^2 \gamma_0}{\omega(\omega^2 + \gamma_0^2)} , \tag{5}$$

where for $\gamma_0 \approx 0$ the resonance condition $\epsilon(\omega) \approx 0$ occurs at $\omega \approx \omega_p$. In a metal this resonance has been termed a collective oscillation or volume plasmon oscillation. The energy loss function, $-\mathrm{Im}[1/\epsilon(\omega)]$, describes the probability that high-energy charged particles traversing an isotropic medium will lose an amount of energy $\hbar\omega$, if one assumes that the energy losses are small compared with the initial particle energy and that the scattering angle is zero. For a metal with $\gamma_0 \approx 0$, $-\mathrm{Im}[1/\epsilon(\omega)]$ has a maximum at $\omega \approx \omega_p$, where $\epsilon(\omega) \approx 0$ and the conditions are those for a collective oscillation. Thus, for many metals which are free-electron-like, the experimentally observed peak in the characteristic electron energy loss spectrum at the plasma energy is correctly identified as being due to the excitation of a collective electron oscillation in the metal.

Nonmetallic Behavior with a Single Resonance

Now consider the behavior associated with just the transitions of frequency ω_1 without modifications caused by oscillators close in frequency to ω_1. That is, we set $f_0 = 0, f_1 = p$, so that

$$\sum_{i>1} f_i \approx 1 - p ,$$

and we assume $\omega_i \gg \omega_1$ for $i > 1$. At a frequency sufficiently above ω_1 the system behaves like a nearly free electron gas. This can be seen by assuming $\omega \gg \omega_1$ in Eqs. (3) and (4), which then have the same form as the Drude equations (5); that is,

$$\epsilon_1 = 1 - \frac{f_1 \omega_p^2}{\omega^2 + \gamma_1^2} , \qquad \epsilon_2 = \frac{f_1 \omega_p^2 \gamma_1}{\omega(\omega^2 + \gamma_1^2)} . \tag{6}$$

Although at a high enough frequency the dielectric functions always become those of a free-electron gas, the peak in the energy loss function may or may not occur in the free-electron-like region. It can be shown that there is only one peak in the calculated loss function, $-\mathrm{Im}[1/\epsilon(\omega)]$, associated with a single oscillator and that this peak occurs at

$$\omega \approx \sqrt{f_1 \omega_p^2 + \omega_1^2} \tag{7}$$

for small damping. Thus it is seen that the peak in $-\mathrm{Im}[1/\epsilon(\omega)]$ may fall below ω_p, at ω_p, or above ω_p depending on the values of f_1, ω_1, and ω_p for the system. For molecules in the vapor state, the electron density, n, is very small, and $\omega_p \approx 0$. The peak in the loss function then occurs at $\omega \approx \omega_1$, that is, at the same energy as the peak in ϵ_2. In this limit it is obvious that the peak in $-\mathrm{Im}[1/\epsilon(\omega)]$ corresponds to the single oscillator at ω_1, and a peak in the electron energy loss spectrum for that material would be identified as being due solely to single-electron excitations of energy $\hbar\omega_1$. However, as one condenses the vapor, the electron density increases; so ω_p increases. In the limit that

$$f_1 \omega_p^2 \gg \omega_1^2 \tag{8}$$

the peak in $-\mathrm{Im}[1/\epsilon(\omega)]$ occurs at $\omega \approx \sqrt{f_1}\,\omega_p$ and corresponds to a longitudinal free-electron resonance. Between these two limits the peak in $-\mathrm{Im}[1/\epsilon(\omega)]$ corresponds to a combination of effects and cannot be

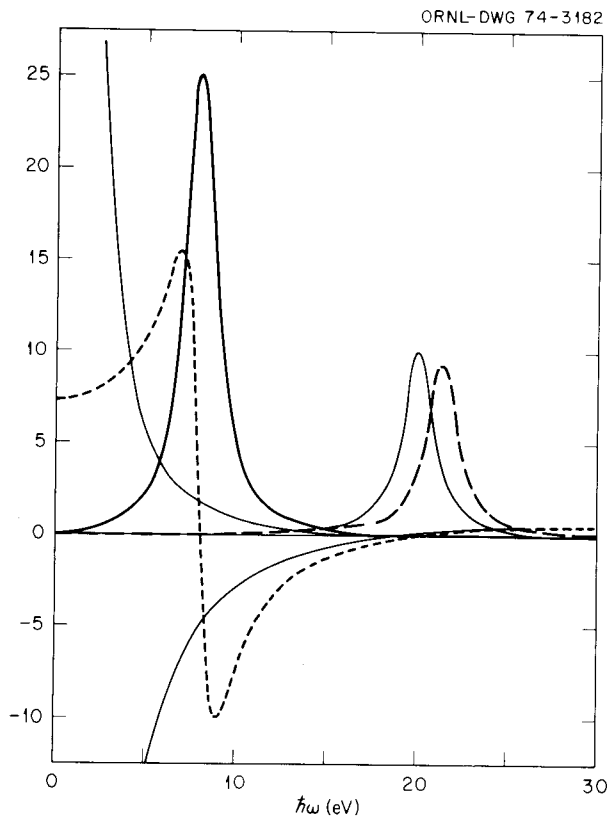

Fig. 22.1. Dielectric functions ϵ_1 (- - - - - - - -) and ϵ_2 (————) and energy loss function $-\mathrm{Im}\,(1/\epsilon)$ (– – – – –) for one oscillator having $\hbar\omega_1$ = 8 eV, $\hbar\omega_p$ = 20 eV, $\hbar\gamma_1$ = 2 eV, and f_1 = 1 compared with those for a free-electron gas (————) with the same values of $\hbar\omega_p$ and $\hbar\gamma_1$.

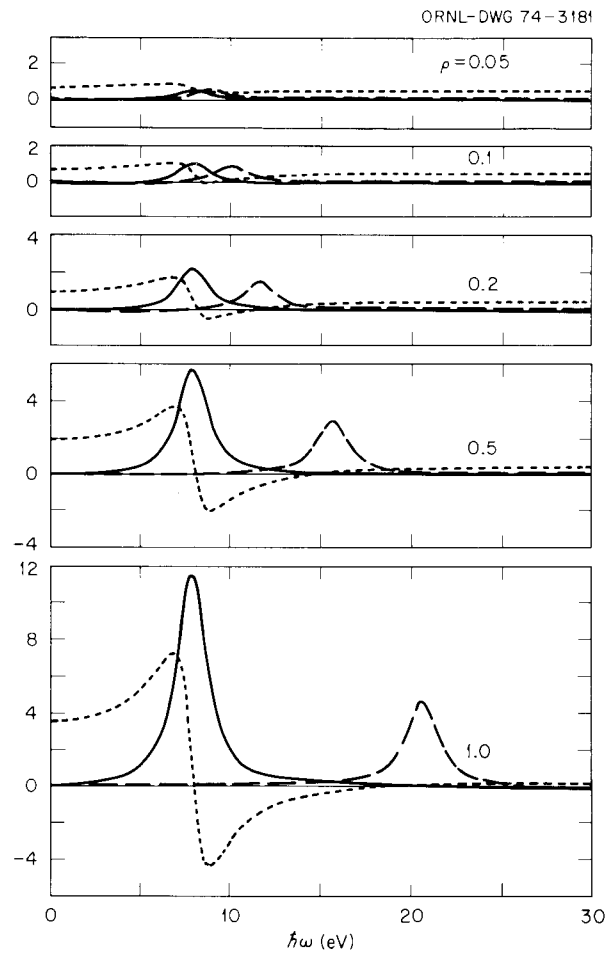

Fig. 22.2. Dielectric function ϵ_1 (- - - - - - - -) and ϵ_2 (————) and energy loss function $-\mathrm{Im}\,(1/\epsilon)$ (– – – – –) for a single oscillator having $\hbar\omega_1$ = 8 eV, $\hbar\gamma_1$ = 2 eV, and f_1 = 1.0 for a condensed medium with densities 0.05, 0.1, 0.2, 0.5, and 1.0 g/cm^3. ($\hbar\omega_p$ = 4.3, 6.1, 8.6, 13.6, and 19.2 eV respectively.)

attributed completely either to single-electron or to collective effects. Figure 22.1 shows an example of conditions under which collective electron oscillations can occur in a condensed system of identical single oscillators. In the particular case shown, $\hbar\omega_1$ = 8 eV, $\hbar\omega_p$ = 20 eV, f_1 = 1, and $\hbar\gamma_1$ = 2 eV, and the condition given by inequality (8) is satisfied. It can be seen by examination that the conditions for a collective oscillation given by Ehrenreich and Philipp[7] are also satisfied. Although the values of $\hbar\omega_1$, $\hbar\omega_p$, and $\hbar\gamma_1$ chosen for Fig. 22.1 are typical values for molecular liquids, real liquids do not behave according to Fig. 22.1 because, in practice, the whole strength f = 1 is not located in a single oscillator but is distributed over a range of energies. In general, as $f_1\omega_p^2$ is increased in a system, the energy of the peak $-\mathrm{Im}[1/\epsilon(\omega)]$ moves upward from $\hbar\omega_1$. In many systems, $f_1\omega_p^2$ is of the same order of magnitude as ω_1^2, and Eq. (7) must be used to find the energy of the peak, which may exceed $\hbar\omega_p$. This is illustrated in Fig. 22.2, where $\hbar\omega_1$ = 8 eV, $\hbar\gamma_1$ = 2 eV, and $\hbar\omega_p$ has values calculated for densities of the medium of 0.05, 0.1, 0.2, 0.5, and 1.0 g/cm^3 and for the molecular weight and number of loosely bound electrons appropriate for water. Figure 22.2 shows that the separation in energy between the peak in ϵ_2 at $\hbar\omega_1$ and the calculated peak in $-\mathrm{Im}[1/\epsilon(\omega)]$ is a measure of the degree of collective behavior that the system exhibits. Except in the free-electron-like limit, this collective behavior should not rightly be termed a plasma resonance.

7. H. Ehrenreich and H. R. Philipp, pp. 367–74 in *Proc. Int. Conf. Phys. Semiconductors*, ed. by A. C. Strickland, Bartholomew Press, Dorking, England, 1962.

Nonmetallic Behavior with Two Resonances

For two single oscillators at $\hbar\omega_1$ and $\hbar\omega_2$, where $\omega_2 > \omega_1$, several cases can be considered. If $\omega_1 \approx \omega_2$, the two oscillators can, for $\omega \gg \omega_2$, be considered as a single oscillator at an energy between $\hbar\omega_1$ and $\hbar\omega_2$. As the energy separation between the two oscillators becomes greater, the modification of the dielectric functions of each oscillator by the other becomes less. In general the magnitude of a peak in $-\mathrm{Im}(1/\epsilon)$ in the frequency interval between the oscillators is depressed, and it is shifted down in frequency because of the presence of the higher energy oscillator, while the peak in $-\mathrm{Im}(1/\epsilon)$ above ω_2 is enhanced and shifted up in frequency. These features are illustrated in Fig. 22.3, where $\hbar\omega_p = 20$ eV, $\hbar\omega_1 = 8$ eV, $\hbar\omega_2 = 22$ eV, $\hbar\gamma_1 = \hbar\gamma_2 = 2$ eV, and $f_1 = f_2 = 0.5$.

Fano[8] has considered the possibility of collective effects occurring in a nonmetallic medium containing a collection of oscillators. He has presented several approaches to the problem, arriving at results in general agreement with each other and with those presented in this report. In particular, he has treated the case of a cubic array of coupled dipole oscillators and has found that the condition

$$\frac{\omega_p^2 f_i}{|\omega_i^2 - \omega_{i\pm 1}^2|} \gg 1 , \qquad (9a)$$

for oscillators with discrete frequencies, or

$$\omega_p^2 \left| \frac{df}{d(\omega^2)} \right| \gg 1 , \qquad (9b)$$

for a continuum, leads to the presence of a collective oscillation in the system. This condition is a requirement for the concentration of oscillator strength in space and in spectrum and is similar to our condition (8) for the existence of a free-electron collective oscillation.

The Fano condition, (9*b*), was used by Platzman[9] to evaluate the importance of collective effects in molecular liquids. His conclusion was that collective effects should be unimportant in such liquids, since the Fano condition for a free-electron-like resonance was not expected to be satisfied. Our treatment differs in that we recognize that collective effects can be quite important in a system even though the conditions for a completely free electron resonance are not met.

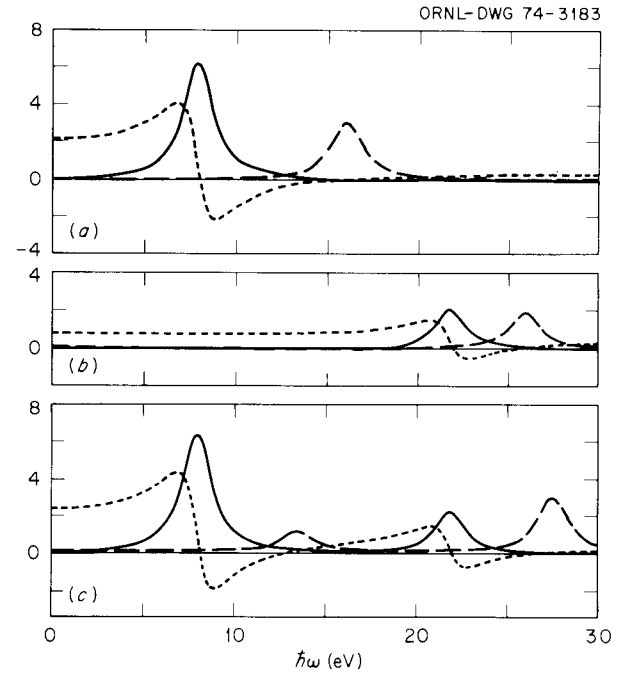

Fig. 22.3. Dielectric functions ϵ_1 (- - - - - - - -) and ϵ_2 (————) and energy loss function $-\mathrm{Im}\,(1/\epsilon)$ (– – – – –) for (*a*) $\hbar\omega_1 = 8$ eV, $\hbar\omega_p = 20$ eV, $\hbar\gamma = 2$ eV, and $f_1 = 0.5$; (*b*) $\hbar\omega_2 = 22$ eV, $\hbar\omega_p = 20$ eV, $\hbar\gamma_2 = 2$ eV, and $f_2 = 0.5$; and (*c*) a combination of the oscillators shown in (*a*) and (*b*).

COLLECTIVE OSCILLATION IN LIQUID WATER

All biological materials absorb energy most strongly in the vacuum-ultraviolet region of the spectrum. Thus, since water is present in all living matter, an understanding of the properties of water in the vacuum ultraviolet is of utmost importance.

A collaborative effort with Dr. L. R. Painter of the Physics Department at the University of Tennessee has resulted in the measurement and interpretation of the optical properties of liquid water for the range of photon energies from 7.6 to 25.6 eV. This is a continuation of work started at ORNL.[5] The reflectance of water at a temperature of 1°C has been measured from 7.6 to 25.6 eV, utilizing an open dish in

8. U. Fano, *Phys. Rev.* **118**, 451 (1960); "Comments on 'Collective' Effects in Atoms and in Extended Media," *Nat. Acad. Sci.–Nat. Res. Counc., Nucl. Sci. Ser*, Rep. No. 29, pp. 163–68 (1958).

9. R. L. Platzman, "Energy Spectrum of Primary Activations in the Action of Ionizing Radiation," p. 20 in *Radiation Research*, ed. by G. Silini, North-Holland Publishing Co., Amsterdam, Holland, 1967.

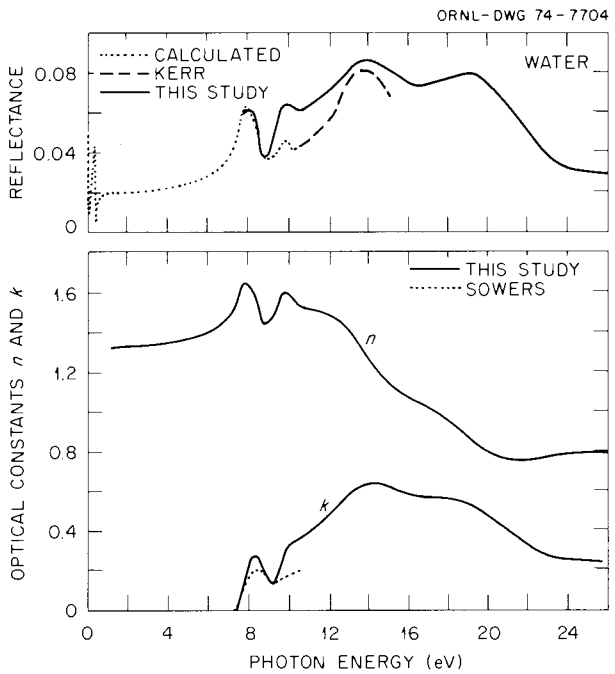

Fig. 22.4. Normal incidence reflectance of water calculated from the literature, 15° reflectances calculated by Kerr et al. (ref. 10), 15° reflectances measured in this study, and optical constants n and k as a function of photon energy.

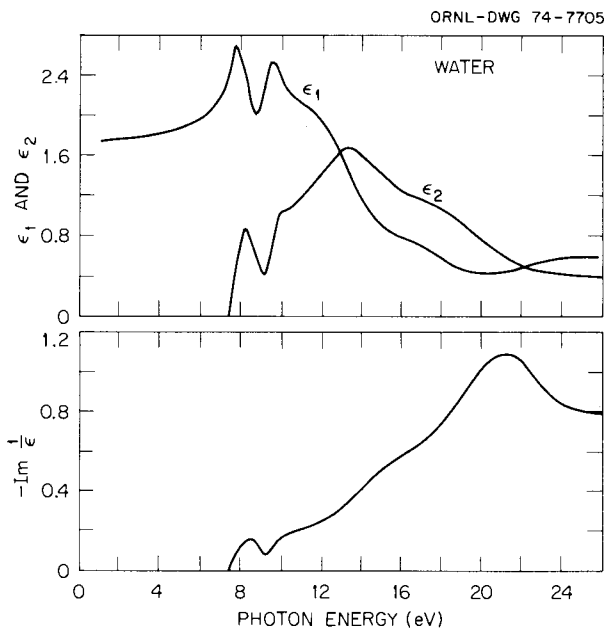

Fig. 22.5. Dielectric constants and energy loss function of water vs photon energy.

a variable-angle reflectometer[10] set at a fixed angle of incidence of 15°. By using a 700-Å blazed grating, the reflectance from the free water surface was measured relative to that from a gold reference surface in the same reflectance chamber under the same conditions of temperature and pressure. Since for both the water and gold the optical path lengths were equal, the strong optical absorption in the vapor above the dish was the same for both the liquid and gold surfaces and canceled out in the ratio of the two reflectances. The reflectance of water for photons incident at 15° is shown in Fig. 22.4. Also shown are the normal-incidence reflectance calculated from values of n and k found in the literature[11-14] and the reflectance determined by Kerr et al.[10] The measured reflectance above 7.6 eV and the calculated reflectance below 7.6 eV were used in a normal-incidence Kramers-Kronig analysis[15] to calculate the real and imaginary parts of the index of refraction n and k. The values obtained for n and k shown in Fig. 22.4 were used to calculate the real and imaginary parts (ϵ_1 and ϵ_2) of the dielectric function (where $\epsilon_1 = n^2 - k^2$ and $\epsilon_2 = 2nk$) and the energy loss function, $-\mathrm{Im}(1/\epsilon) = \epsilon_2/(\epsilon_1{}^2 + \epsilon_2{}^2)$. These are shown in Fig. 22.5.

Structure is seen in ϵ_2 at $\hbar\omega_1 = 8.2$, $\hbar\omega_2 = 9.8$, and $\hbar\omega_3 = 13.5$ eV. The absorption at 8.2 eV has been attributed to $n \rightarrow \sigma^*$ and that at 9.8 eV to $\sigma \rightarrow \sigma^*$ excitations.[10] Structure in the energy loss function $-\mathrm{Im}(1/\epsilon)$ at 8.8 and at about 10.0 eV has been interpreted[10] as being due to the corresponding molecular excitations at 8.2 and 9.8 eV respectively, while structure in $-\mathrm{Im}(1/\epsilon)$ at 21 eV can be associated with a collective electron oscillation. The behavior of water is clearly not free-electron-like. Water has eight loosely bound electrons, yielding a plasma energy of $\hbar\omega_p = 19.2$ eV from Eq. (2). A sum-rule analysis[10] gives an oscillator strength for the 8.2-eV transition of 0.018. The strongest transition is at 13.5 eV with an oscillator strength of 0.43. Our inequality (8) shows that the conditions associated with the transition at 8.2 eV are

10. G. D. Kerr, R. N. Hamm, M. W. Williams, R. D. Birkhoff, and L. R. Painter, *Phys. Rev. B* **5**, 2523 (1972).

11. L. R. Painter, R. D. Birkhoff, and E. T. Arakawa, *J. Chem. Phys.* **51**, 243 (1969).

12. M. W. Irvine and J. B. Pollark, *Icarus* **8**, 324 (1968).

13. L. Pointier and C. Dechambenoy, *Ann. Geophys.* **22**, 633 (1966).

14. M. R. Querry, B. Curnutte, and D. Williams, *J. Opt. Soc. Amer.* **59**, 1299 (1969).

15. F. Stern, pp. 327–40 in *Solid State Physics, Advances in Research and Applications*, vol. 15, ed. by F. Seitz and D. Turnbull, Academic Press, New York, 1963.

clearly not free-electron-like since $f_1(\hbar\omega_p)^2 = 6.6$ and $(\hbar\omega_1)^2 = 67$. Also, the peak in $-\mathrm{Im}(1/\epsilon)$ at 8.8 eV is even closer to 8.2 eV than it would be for the single oscillator because of presence of higher energy transitions. For the peak at 13.5 eV, $f_3(\hbar\omega_p)^2 = 159$ and $(\hbar\omega_3)^2 = 182$, which again does not satisfy the conditions for a free-electron oscillation. However, the peak in $-\mathrm{Im}(1/\epsilon)$ at 21 eV is shifted appreciably from the corresponding peak in ϵ_2 at 13.5 eV, indicating that some collective effects are associated with this peak in $-\mathrm{Im}(1/\epsilon)$.

The energy loss function is proportional to the probability that a high-energy charged particle will lose energy to the medium. Ionizing radiation produces delta rays in matter, and essentially all the energy of the primary is ultimately found as secondary electrons. To determine the importance of the peak in the loss function at 21 eV to the absorption of radiation in water, we performed a calculation similar to that reported by McConnell et al.[16] for ^{64}Cu beta rays slowing down in aluminum. In the present study the energy loss function for water was converted to an excitation cross section, and the slowing-down flux of electrons in water was approximated from that measured for ^{64}Cu beta rays in aluminum by taking account of the densities and stopping powers of aluminum and water. The cross section was integrated over the electron slowing-down spectrum, and it was found that essentially all the primary energy eventually goes into the excitation of the collective oscillation at 21 eV. This is similar to the result reported by McConnell[16] for aluminum. Thus this loss represents an extremely important energy absorption mechanism in water.

OPTICAL PROPERTIES OF ORGANIC LIQUIDS

As a continuation of our study of the optical properties of biologically related liquids,[5] we have studied 1,2,3,5-tetramethylbenzene and pentafluorobenzene. These liquids were chosen to investigate the effects of substitutions in the benzene molecule on the optical properties. Transmission measurements were made using our recently developed transmission cell over the range of photon energies from 4 to 10.5 eV, and the values of the extinction coefficient, k, obtained for these two liquids are shown in Figs. 22.6 and 22.7.

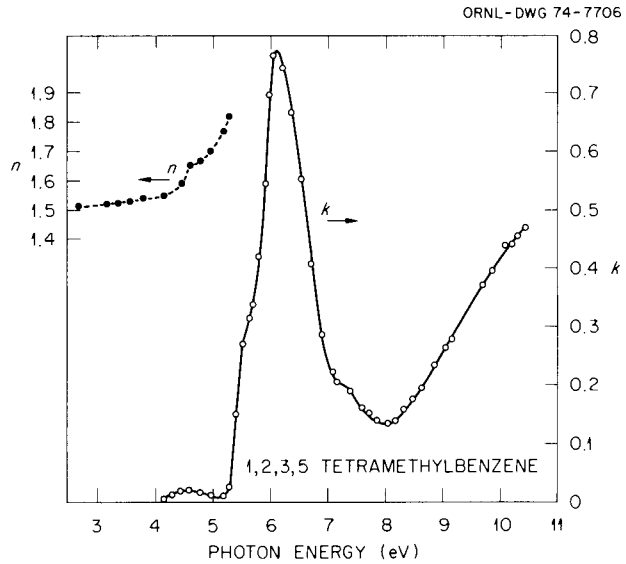

Fig. 22.6. Optical constants of liquid 1,2,3,5 tetramethylbenzene vs incident photon energy.

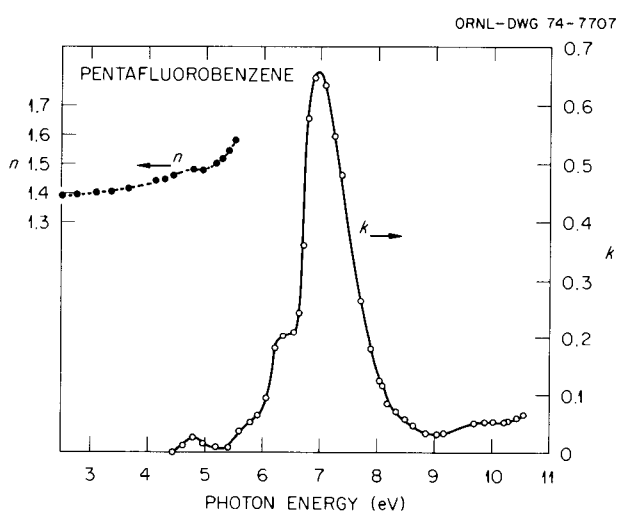

Fig. 22.7. Optical constants of liquid pentafluorobenzene vs incident photon energy.

The real part, n, of the refractive index was determined in the transparent region from critical-angle measurements. For these measurements a closed cell with a semicylindrical window was used, the reflectance being obtained as a function of photon angle of incidence at

16. W. J. McConnell, R. D. Birkhoff, R. N. Hamm, and R. H. Ritchie, *Radiat. Res.* 33, 216 (1968).

the semicylinder-liquid interface. The values obtained for n are also shown in Figs. 22.6 and 22.7. The analysis of these data is not complete. However, it can be seen that the absorption spectrum of 1,2,3,5-tetramethylbenzene is similar to that of benzene[17] with increased $\sigma \rightarrow \sigma^*$ absorption above 8 eV due to the extra σ electrons in the $-CH_3$ groups. The absorption spectrum of pentafluorobenzene shows structure below the main $\pi \rightarrow \pi^*$ transition at 7 eV which is not seen in the absorption spectrum of benzene. This is presumably due to the nonbonding electrons associated with the fluorine. In addition, the $\sigma \rightarrow \sigma^*$ absorption seen in benzene is suppressed, presumably because the $\sigma \rightarrow \sigma^*$ transition associated with the C-F bond is of higher energy (>10.5 eV) than that associated with the C-H bond.

INDEX OF REFRACTION OF AQUEOUS SOLUTIONS OF ALKALI HALIDES IN THE ULTRAVIOLET[18]

The indices of refraction of the alkali halides LiCl, NaCl, NaI, and KCl have been measured in aqueous solution throughout a range of wavelengths in the near ultraviolet. The data are summarized in Figs. 22.8–22.11. For comparison, the index of refraction of pure water has been plotted as a function of wavelength in each figure. The indices of refraction were measured by critical-angle reflectance following the method described by Painter et al.[11]

17. E. T. Arakawa et al., *Health Phys. Div. Annu. Progr. Rep. July 31, 1971*, ORNL-4720, pp. 52–55.

18. Also involved in this study were J. M. Donohue, P. E. Koppee, and R. P. Leemhius, students of the Massachusetts Institute of Technology Practice School of Chemical Engineering, fall 1973.

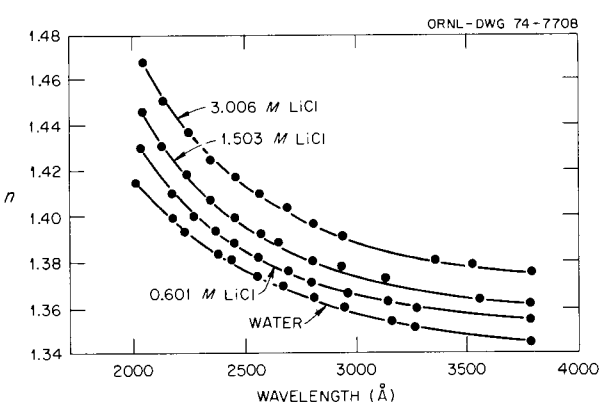

Fig. 22.8. Index of refraction vs wavelength for lithium chloride solutions.

Through the Clausius-Mossotti formula,

$$\frac{n^2 - 1}{n^2 + 2} = \frac{4\pi}{3} N_i(\alpha_+ + \alpha_-) + \frac{4\pi}{3} N_w \alpha_w \ , \qquad (10)$$

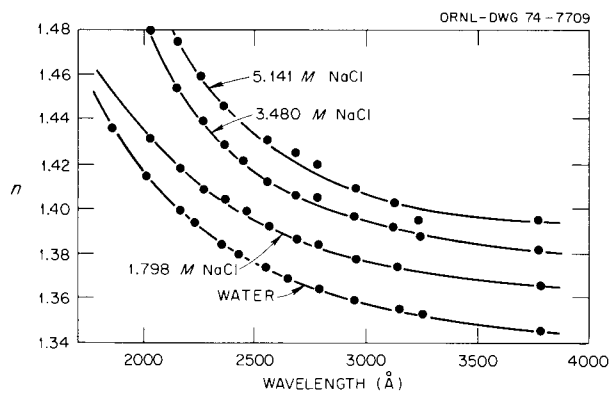

Fig. 22.9. Index of refraction vs wavelength for sodium chloride solutions.

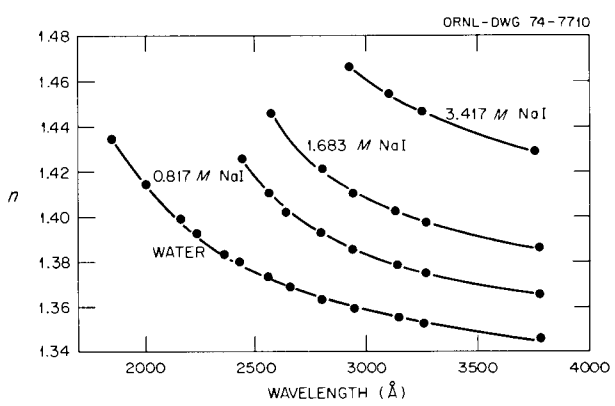

Fig. 22.10. Index of refraction vs wavelength for sodium iodide solutions.

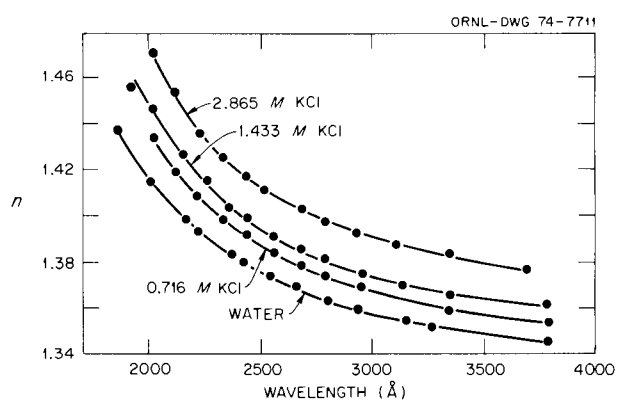

Fig. 22.11. Index of refraction vs wavelength for potassium chloride solutions.

the index of refraction n of a solution can be related to the polarizabilities α_+ and α_-, respectively, of the positive ion and negative ion and α_w of the solvent, where N_i and N_w are the concentrations in molecules per cubic centimeter of the univalent ions and the water solvent respectively. If the Clausius-Mossotti formula is used to obtain the polarizability of the water molecule from a measurement of the index of refraction of pure water, then the term $(4\pi/3)N_w\alpha_w$ may be subtracted from Eq. (10), allowing the sum $\alpha_+ + \alpha_-$ to be determined. Values of this sum are listed in Table 22.1.

Table 22.1. Molecular polarizability for aqueous salt solutions

Salt	λ (Å)	α (Å^3)	α_{solid} (Å^3)
NaCl	2798	4.28 ± 0.40	3.96
	3779	3.93 ± 0.27	3.54
KCl	2798	5.24 ± 0.23	4.84
	3350	5.01 ± 0.36	4.60
LiCl	2798	4.02 ± 0.22	
	3779	3.75 ± 0.30	
NaI	2798	11.29 ± 0.39	
	3779	9.16 ± 0.20	

For comparison, the table includes a list of this sum as determined from measurements on the indices of refraction[19] of the solid alkali halides. In the case of the solids, the Clausius-Mossotti formula was also used to obtain $\alpha_+ + \alpha_-$. The values of $\alpha_+ + \alpha_-$ are comparable but systematically about 8% higher in the aqueous solutions than in the solids. Lack of agreement may be due to hydration of the ions by surrounding water molecules in aqueous solution. However, the agreement may be improved if the index of refraction data are analyzed using the corrected Clausius-Mossotti formula recommended by Bottcher.[20]

ELECTRON SLOWING-DOWN STUDIES

Last year we reported[21] measurements of the electron slowing-down flux in polished aluminum oxide and assumed that the differences in flux values between

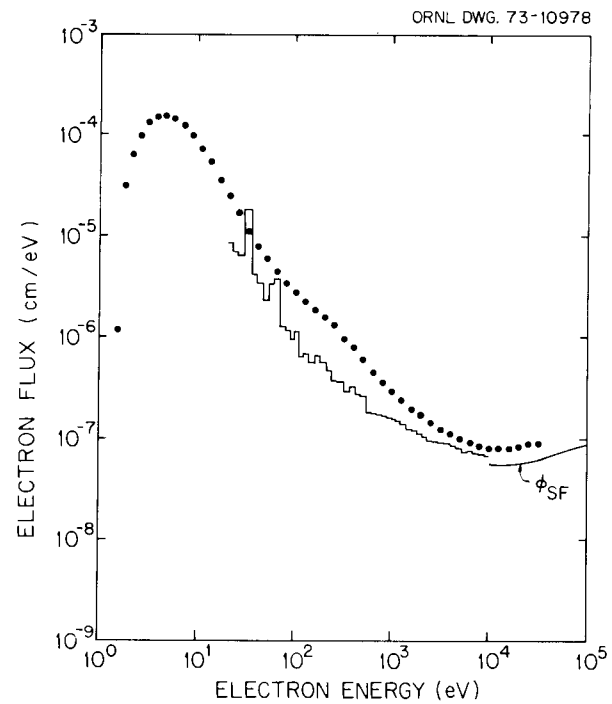

Fig. 22.12. Electron-slowing-down spectrum of aluminum oxide.

these results and those obtained from our earlier studies using unpolished sources resulted from uncertainties in the thermal neutron flux at the time of irradiation rather than in the electron flux itself. We have now eliminated this uncertainty through an analysis of a set of flux monitors that were irradiated along with the set of polished source disks. An accurate value for the thermal flux was obtained from a cobalt-aluminum monitor, while corrections for the epithermal flux were obtained from simultaneous measurements using silver-aluminum monitors. Uncertainty in the ^{164}Dy cross section of (2700 ± 200) × 10^{-24} cm^2 represents the largest uncertainty in the determination of the absolute secondary electron flux.

The electron slowing-down flux in aluminum oxide on the basis of this new neutron flux determination is shown in Fig. 22.12 over an energy range extending from 1.5 eV to 32 keV. The flux is slightly higher than that reported previously and reflects the more careful determination of the 2200-m/sec thermal neutron flux. Also shown in the figure is the spectrum calculated by using Monte Carlo techniques and employing inelastic cross sections obtained from a sum-rule-constrained classical binary collision model. Details of this calculation are discussed in the General Radiation Physics Section.

19. J. Bartels, H. Borchers, K.-H. Hellwege, K. Schäfer, and E. Schmidt, eds., *Landolt-Börnstein Zahlenwerte und Funktionen aus Physik, Chemie, Astronomie, Geophysik, und Technik,* 6th ed., vol. 2, part 8, *Optische Konstanten,* ed. K.-H. Hellwege and A. M. Hellwege, Springer-Verlag, Berlin, 1962.

20. C. J. F. Bottcher, *Theory of Electric Polarization,* p. 276, Elsevier Publishing Co., New York, 1952.

21. E. T. Arakawa et al., *Health Phys. Div. Annu. Progr. Rep. July 31, 1973,* ORNL-4903, pp. 103–4.

RADIATION INTERACTIONS WITH NUCLEIC ACID BASES

We have continued our studies of the optical and electronic properties of the nucleic acid bases by extending the experimental data for guanine down to 1.9 eV. In the region of transparency (1.9 to 3.8 eV), the index of refraction n was measured directly using a method due to Abelès.[22] In this method, n is obtained from the relation $n = \tan \phi$, where ϕ is the angle at which the reflectance of the film-covered substrate for p-polarized light matches that for the bare substrate.

The data previously reported[23] showed a pronounced peak in the energy loss function, $-\mathrm{Im}(\epsilon^{-1})$, near 22 eV which was compared with the peak[24] observed at 20.7 eV in $-\mathrm{Im}(\epsilon^{-1})$ calculated from electron energy loss measurements. We have repeated the reflectance measurements in this energy region using guanine films that exhibit reflectances significantly higher than those found earlier. In general, higher reflectance values are associated with better-quality film. A Kramers-Kronig analysis of the latest data was performed which showed that the peak in the loss function was shifted to 25.5 eV.

Data on adenine films have been obtained over the energy region between 2.1 and 84 eV using techniques similar to those employed for guanine. At low energies, n was measured directly using Abelès' method, while at high energies the complex index of refraction, $\tilde{n} = n + ik$, was obtained from multiangle reflectance data. The normal-incidence reflectance R_n was calculated from these quantities and used, together with measured values of R_n in the intermediate energy region, in a Kramers-Kronig analysis to obtain n, k, the complex dielectric function $\tilde{\epsilon} = \epsilon_1 + i\epsilon_2$, and the energy loss function over the full energy range from 0 to 84 eV. Values of the real and imaginary parts of the dielectric constant are shown in Fig. 22.13. These results are similar to those found earlier for guanine and show fair agreement with the dielectric constant obtained from electron energy loss measurements.[25] The structure exhibited by ϵ_2 below about 8 eV has been attributed to a $\pi \rightarrow \pi^*$ transition, whereas that at higher energies is associated with $\sigma \rightarrow \sigma^*$ transitions. A recent ab initio calculation[26] has shown that the π and σ levels are intermixed to a large extent in the intermediate energy region.

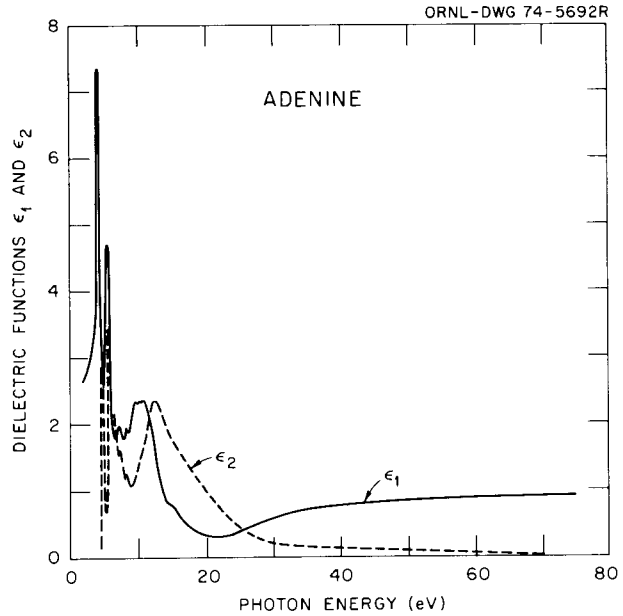

Fig. 22.13. The dielectric functions of adenine vs incident photon energy.

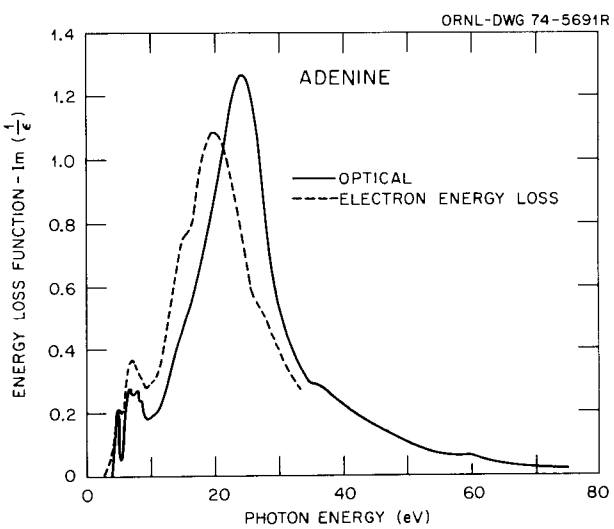

Fig. 22.14. Energy loss function for adenine vs incident photon energy.

Figure 22.14 shows the energy loss function vs photon energy calculated from the dielectric constant. The pronounced peak at 24.4 eV is shifted from the corresponding peak in ϵ_2 at 15 eV, indicating a degree of collective behavior of the loosely bound electrons. The corresponding peak in the electron energy loss measurements occurs near 20 eV.

22. F. Abelès, *J. Phys. Radium* **11**, 310 (1950).
23. E. T. Arakawa et al., *Health Phys. Div. Annu. Progr. Rep. July 31, 1973*, ORNL-4903, pp. 106–8.
24. D. E. Johnson, *Radiat. Res.* **49**, 63 (1972).
25. M. Isaacson, *J. Chem. Phys.* **56**, 1803 (1972).
26. B. Mely and A. Pullman, *Theor. Chim. Acta* **13**, 278 (1969).

The reason for the discrepancy between our results and those obtained in the electron energy loss experiments cannot be explained on the basis of experimental error in the measurements. We have noted that the position of the high-energy peak in the loss function is dependent upon the optical quality of the film and that the peak occurs at lower energies for the poorer films (i.e., lower reflectance). We are continuing these studies with the pyrimidine bases cytosine, thymine, and uracil.

OPTICAL AND DIELECTRIC PROPERTIES OF DNA IN THE EXTREME ULTRAVIOLET

The optical and dielectric properties of dry films of deoxyribonucleic acid (DNA) have been determined for incident photon energies from 2 to 82 eV.

To prepare thin films of DNA for transmission measurements, sodium salt of calf thymus DNA was dissolved in distilled water. Several drops of this solution were placed on a fine-mesh nickel screen, and the water was allowed to evaporate at room temperature. Solid films produced in this manner were ascertained to be uniform in thickness over a sufficiently large region at the center of the film compared with the cross section of the incident light flux by measuring the transmittance at different portions of the film. Transmission measurements were made on these films at room temperature in the region 2 to 82 eV, that is, 6200 to 150 Å. A Seya-Namioka vacuum ultraviolet monochromator was used for the wavelength region 6200 to 600 Å, and a grazing-incidence monochromator was used from 1200 to 150 Å. In the nonabsorbing region between 6200 and 3100 Å, some films showed interference patterns. These patterns not only indicated thickness uniformity of the films but also were used to calculate the thickness with an accuracy of ±50 Å. Refractive indices n in the transparent region were obtained by critical-angle measurements made with the films deposited on a sapphire semicylinder. All the above measurements were carried out in a vacuum chamber maintained at about 10^{-5} torr. However, in restricted energy regions, additional measurements of absorbance (4 to 6 eV) and critical angle (2 to 4 eV) were made at various levels of relative humidity to check the effect of humidity on the optical properties. The density of our dry film was determined from the thickness measured in vacuum and the absorbance of the 260-nm band measured at 92% relative humidity, assuming that the molar extinction coefficient of this band at this humidity is the same as that in solution under the condition where DNA molecules have the native conformation. This estimate gave the value of 1.35 g/cm^3 for our dry DNA film, which is considerably smaller than the value of 1.62 to 1.63 g/cm^3 reported for solid strands of DNA measured by gravimetry.[27,28]

The transmittance, T, of a free-standing film in vacuum may be expressed by[29]

$$T = \exp(-4\pi kd/\lambda)\, F(n, k)\,, \tag{11}$$

where $F(n, k)$ is a known function of n and k, the real and imaginary parts of the complex refractive index of the film, and d is the thickness of the film. The measured transmittance and film thickness were used in Eq. (11) with $F(n, k) = 1$ to give a first-order approximation to k over the region 2 to 82 eV. The resulting k values were then used in the Kramers-Kronig equation,

$$n(E) = 1 + \frac{1}{2\pi} \int_0^\infty \frac{E'\, k(E')}{E'^2 - E^2}\, dE' \tag{12}$$

to obtain n over the same energy region. For this purpose it was assumed that k is zero in the region below 2 eV, and, for the region above 82 eV, values of k at 72 and 82 eV were linearly extrapolated. The resulting n values as well as the first-order k values were used to calculate values of $F(n, k)$, which were used in Eq. (11) to give second-order approximations to k, which, in turn, were used in Eq. (12) to obtain a better approximation of n. This procedure was repeated until the n and k values converged. Since the values of n obtained by critical-angle measurements were considered more reliable than the thickness determined from interference, d was changed in Eq. (11) so that n obtained from transmission measurements would agree with n from critical-angle measurements in the region of overlap. The iterative procedure described above was repeated until we obtained a self-consistent set of n and k values for which there was agreement with the critical angle n in the region 2 to 4 eV. Using the final set of n and k values, we calculated the dielectric constants $\epsilon_1 = n^2 - k^2$ and $\epsilon_2 = 2nk$ and the energy loss function

$$-\mathrm{Im}(1/\epsilon) = \epsilon_2/(\epsilon_1{}^2 + \epsilon_2{}^2)\,.$$

27. W. T. Astbury, *Symp. Soc. Exp. Biol.* 1, 66 (1947).
28. R. E. Franklin and R. G. Gosling, *Acta Crystallogr.* 6, 678 (1953).
29. W. L. Buck, B. R. Thomas, and A. Weinreb, *J. Chem. Phys.* 48, 549 (1968).

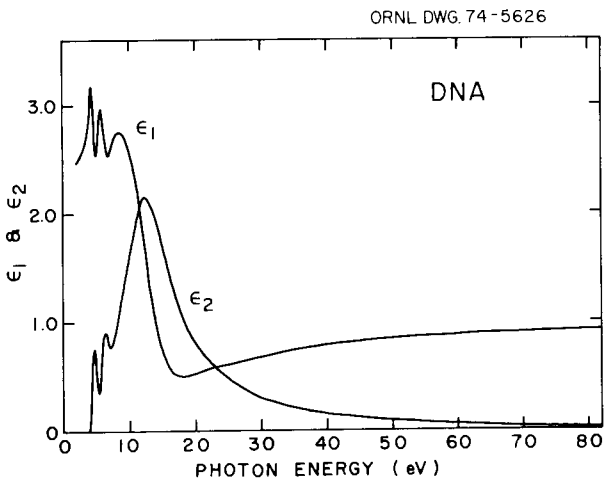

Fig. 22.15. Real and imaginary parts of dielectric constant $\epsilon(=\epsilon_1 + i\epsilon_2)$ of dry film of DNA as functions of photon energy.

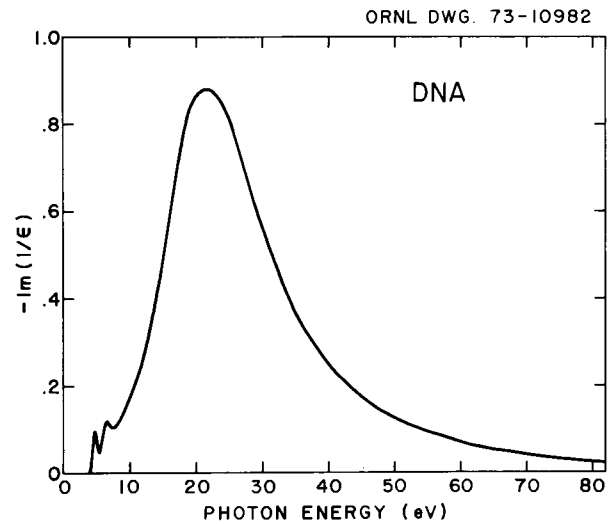

Fig. 22.16. Energy loss function of dry film of DNA vs incident photon energy.

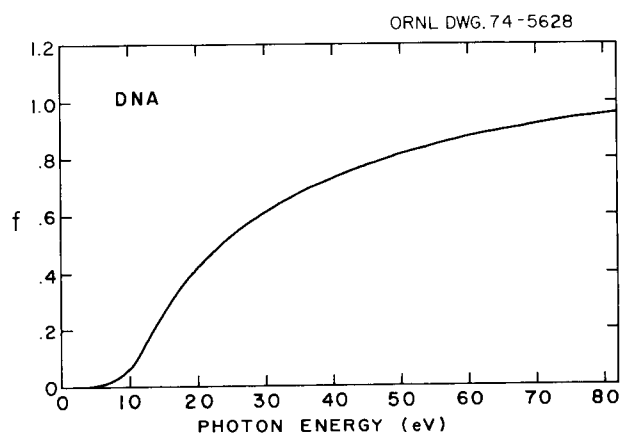

Fig. 22.17. Oscillator strength f of dry film of DNA as a function of photon energy.

The dielectric constants and the energy loss function obtained for a 715-Å film are shown as functions of incident photon energy in Figs. 22.15 and 22.16 respectively. The imaginary part, ϵ_2, of the dielectric function shows maxima at 4.8, 6.6, and 13.8 eV. The first peak corresponds to the well-known 260-nm band, and the second corresponds to the so-called Y band. Both these bands have been found for the DNA bases[30,31] and have been attributed to single-electron excitations of π electrons in the bases. The third peak, around 13.8 eV, with much greater intensity than those at low energy, possibly arises from σ-electron excitations mainly associated with the ribose-phosphate chain. In fact, available data on the ribose-phosphate monomer[30,32] show a steep rise in the absorption starting from around 7 eV toward the higher-energy region, whereas those of the DNA bases do not show such behavior. The energy loss function $-\mathrm{Im}(1/\epsilon)$ describes the probability that a high-energy charged particle will lose energy in the medium by exciting single-electron transitions or collective excitations of electrons. Peaks are seen in this quantity at 4.8, 6.6, and 21.6 eV. The first two peaks occur at the same energies as peaks in ϵ_2 and thus correspond to the excitation of these $\pi \rightarrow \pi^*$ transitions. The peak in $-\mathrm{Im}(1/\epsilon)$ at 21.6 eV is shifted from the peak in ϵ_2 at 13.8 eV, indicating a considerable degree of collective electron behavior.[33]

The oscillator strength

$$f(E) = (m_{\mathrm{eff}}/2\hbar^2\pi^2 N n_0 e^2) \int_0^E E' \, \epsilon_2(E') \, dE'$$

was calculated, assuming an effective mass of the electron, m_{eff}, equal to the free-electron mass. N, the number of nucleotide-pair units per unit volume, was estimated from the measured density (1.35 g/cm^3) of our film. The number of electrons per nucleotide-pair unit, n_0, was 238, counting all the loosely bound electrons whose atomic energy levels are lower than 82 eV. The result is plotted as a function of photon energy in Fig. 22.17. The f value becomes close to unity at high energies, implying that most of the loosely bound

30. H. DeVoe and I. Tinoco, Jr., *J. Mol. Biol.* **4**, 518 (1962).
31. T. Yamada and H. Fukutome, *Biopolymers* **6**, 43 (1968).
32. S. Onari, *J. Phys. Soc. Jap.* **26**, 214 (1969).
33. See "Collective Electron Effects in Molecular Liquids," this section.

electrons participate in the optical transitions observed below 82 eV. Observations in the present study at different humidities and comparison with published data in that energy range indicated that our dry films were, in fact, completely dehydrated.

It should be pointed out that it is difficult to derive biological implications directly from the present data. While they describe the optical and dielectric properties of film material of DNA, they may apply to isolated molecules. Biologically meaningful responses of DNA to radiation must be represented by microscopic quantities associated with single molecules in which biological phenomena take place.

OPTICAL PROPERTIES OF CHLOROPLASTS AND RED BLOOD CELLS IN THE VACUUM ULTRAVIOLET

The real and imaginary parts, ϵ_1 and ϵ_2, of the complex dielectric constant ϵ were presented last year[34] for chloroplasts (the chlorophyll-containing bodies in plant cells in which photosynthesis takes place) over the range of photon energies from 2 to 22 eV. These data have now been analyzed in terms of the absorption processes occurring in the main constituents of chloroplasts. The extinction coefficient, k, has been measured for packed red blood cells from 2 to 10.6 eV using a transmission cell of known thickness, d.

Despite their different appearance in the visible region, chloroplasts and red blood cells have many similarities, and it is of interest to compare their absorption spectra, shown in Fig. 22.18. The dry weight of chloroplasts that have lost their water-soluble components consists of about 50% proteins, about 34% lipids, about 8% chlorophyll, about 1% carotenoids, and about 7% other components, including carbohydrates. The dry weight of complete chloroplasts consists of about 69% proteins, about 21% lipids, about 5% chlorophyll, $\lesssim$1% carotenoids, and $\gtrsim$4% other components, including salts, enzymes, RNA, DNA, and carbohydrates. Presumably our chloroplast films have an average chemical composition between that of broken and that of unbroken chloroplasts, with from 5 to 8% chlorophyll, where the chlorophylls of importance are chlorophyll *a* ($C_{55}H_{72}N_4O_5Mg$) and chlorophyll *b* ($C_{55}H_{70}N_4O_6Mg$). These are basically porphin ($C_{20}H_{14}N_4$) with an Mg^{2+} ion in the center, an extra five-member carbon ring, and a "tail" consisting of a 20-carbon phytyl side chain. The packed red blood cells

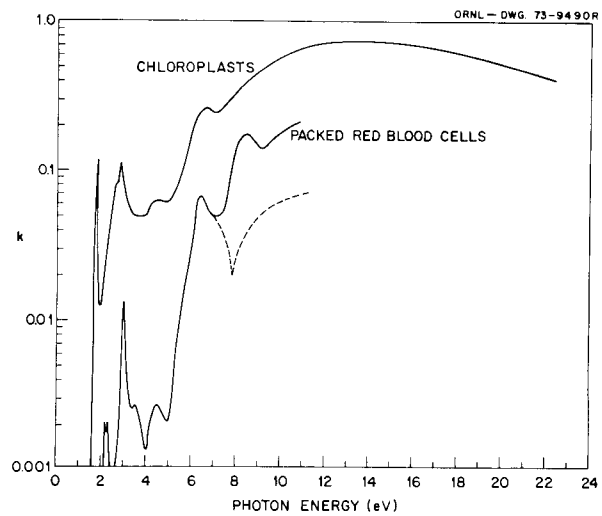

Fig. 22.18. Absorption spectra for chloroplasts and packed red blood cells. The dotted curve is the absorption spectrum for packed red blood cells with the water contribution subtracted.

used in this study were associated with less than 5% intercellular fluid. The composition of packed red blood cell samples is about 65% water, about 32% hemoglobin, and about 3% other constituents, including other proteins, lipids (including cholesterol), carbohydrates, vitamins, enzymes, and nucleotides. Neither RNA nor DNA has been found in mature red blood cells. Heme ($C_{34}H_{32}O_4N_4Fe$) is essentially porphin with an Fe^{2+} ion in the center and some short side chains. Heme constitutes about 4% of the mass of hemoglobin, or about 1% of the red blood cell.

The characteristic absorption of chlorophyll and of heme occurs in the visible. In this region the spectrum for chlorophyll[35] given in Fig. 22.18 shows the well-known Soret $\pi \rightarrow \pi^*$ excitation at 2.85 eV associated with the whole porphin ring. The extra five-member ring in chlorophyll results in removal of the degeneracy associated with the Soret band in a simple porphin structure and the appearance of an absorption band at 1.78 eV. Also seen is structure due to carotenoids[36] in the region of 2.5 to 3.1 eV. The spectrum for the packed red blood cells in the visible is that of oxyhemoglobin,[37] with absorption peaks at 2.14, 2.29, and 2.99 eV, where the sharp structure at 2.99 eV is the Soret band in heme.

34. E. T. Arakawa et al., *Health Phys. Div. Annu. Progr. Rep. July 31, 1973,* ORNL-4903, pp. 108–9.

35. P. Latimer and E. Rabinowitch, *J. Chem. Phys.* **24,** 480 (1956).

36. J. T. O. Kirk and R. A. E. Tilney-Bassett, *The Plastids,* W. H. Freeman and Co., London and San Francisco, 1967.

37. J. F. Seitz, *The Biochemistry of the Cells of Blood and Bone Marrow,* Charles C. Thomas, Springfield, Ill., 1969.

To our knowledge the spectrum of chloroplasts has not been measured previously above 4.2 eV. For red blood cells the spectrum has been obtained to about 6 eV, and the ultraviolet part has been attributed to tyrosine and tryptophan. In the energy region above 4 eV, the constituents contributing significantly to the spectra are proteins and lipids in the chloroplasts and water and protein (globin) in the red blood cells. Absolute extinction coefficients for liquid water have been reported from the absorption edge at 7.2 eV to 10.65 eV.[38] Since the packed red blood cell samples were about 65% water, this percentage of the k values given by Sowers et al. for water was subtracted correspondingly from the measured k values for red blood cells. The result is shown as the dotted curve in Fig. 22.18. It can be seen that the structure at about 8.2 eV can be attributed to the water in the red blood cells.

Proteins are made up of some 20 important amino acids; in tyrosine, tryptophan, and phenylalanine the side group is aromatic, whereas in the rest it is aliphatic. The aromatic amino acids tyrosine and tryptophan[39] show absorption starting in the region of 4 eV and peaking at about 4.5 eV. The absorption for phenylalanine is less intense and is shifted to a slightly higher energy.[39] For all three aromatic amino acids the absorption increases with increasing energy after the first characteristic absorption band. The aliphatic amino acids[40] show characteristic absorption starting at about 6.5 eV, peaking in the region of $7 \rightarrow 7.5$ eV, and then increasing with increasing energy up to the limit of the available data at 10.6 eV. Lipids are built up from glycerol or spingosine and fatty acids. Glycerol[41] starts to absorb at about 7.5 eV, showing a maximum at about 12.6 eV. Saturated fatty acids can be typified by acetic acid and trifluoroacetic acid (CF_3COOH), which start to absorb at about 7 eV and peak at about 8.4 eV.[42] Thus the structure in the spectra for both chloroplasts and red blood cells at about 4.5 eV is due mainly to the aromatic amino acids tyrosine and tryptophan present in the proteins, whereas the structure at about 6.5 eV is presumably due mainly to a combination of the amino acids, both aromatic and aliphatic. The rising absorption at energies above 7 eV is due mainly to proteins and lipids in chloroplasts and to protein in red blood cells. The nucleic acid bases start to absorb at about 4 eV, showing peaks in absorption at about 4.5 eV. Thus if our chloroplasts contain any DNA, its absorption is included in the spectrum above 4 eV.

Finally, our analysis for chloroplasts[34] yielded both the real and imaginary parts, ϵ_1 and ϵ_2, of the complex dielectric constant. A calculation of the energy loss function, $-\mathrm{Im}(1/\epsilon)$, shows a maximum in the region of 20 eV consistent with the possibility of electronic collective oscillations, or plasmons, in chloroplasts at this energy. Similar results are expected for red blood cells. Although irradiation with photons in the near ultraviolet is known to inhibit photosynthesis, the excitation of collective oscillations, or plasmons, might provide an efficient energy transfer mechanism. Thus the existence of plasmons, either in the bulk material or in the constituent macromolecules, may be important when considering energy transfer mechanisms associated with the interaction of radiation with matter.

38. B. L. Sowers, R. D. Birkhoff, and E. T. Arakawa, *J. Chem. Phys.* **57**, 583 (1972).
39. D. B. Wetlaufer, *Advan. Protein Chem.* **17**, 303 (1962).
40. T. Inagaki, *Biopolymers* **12**, 1353 (1973).
41. J. M. Heller, Jr., R. D. Birkhoff, M. W. Williams, and L. R. Painter, *Radiat. Res.* **52**, 25 (1972).
42. H. Basch, M. B. Robin, and N. A. Kuebler, *J. Chem. Phys.* **49**, 5007 (1968).

23. Atomic and Molecular Radiation Physics

L. G. Christophorou

C. H. Abner[1]
V. E. Anderson[2]
J. K. Baird
R. P. Blaunstein[3]
Ada E. Carter
J. G. Carter
C. E. Easterly[1]
Kathy S. Gant[4]
R. E. Goans[4]
J. P. Johnson[4]
E. T. Loy[1]
D. L. McCorkle[3]
D. Pittman
J. Rademacher[4]

ATTACHMENT OF SLOW (<1 eV) ELECTRONS TO O_2 IN VERY HIGH PRESSURES OF NITROGEN, ETHYLENE, AND ETHANE[5]

Our study on the capture of slow (<1 eV) electrons by O_2 to form O_2^- embedded in very high pressures of nitrogen (up to about 40 atm), ethylene (up to about 22 atm), and ethane (up to about 23 atm) has been completed. Large changes have been observed in both the magnitude and the energy dependence of the attachment rate (and cross section) with increasing density of these three media. Figure 23.1 shows an example of the dependence of the attachment rate on the density and the nature of the medium. At sufficiently low pressures ($\lesssim$1500 torr for N_2; $\lesssim$2500 torr for C_2H_4; $\lesssim$3500 torr for C_2H_6), low-energy electron attachment to O_2 can be treated approximately as a three-body process. However, as the density of each medium increases, each affects the capture process differently, demonstrating the profound effect and importance of the environment on the electron attachment process. Electron capture mechanisms and reaction schemes, consistent with the observed dependences of the attachment rates on the density of each medium, have been developed.[6]

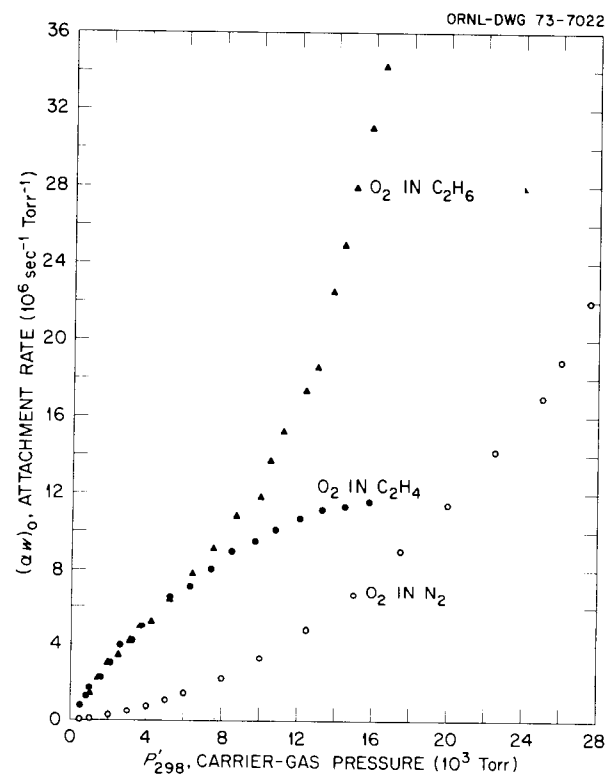

Fig. 23.1. Attachment rate $(\alpha w)_0$ for O_2 in N_2 (○), in C_2H_4 (●), and in C_2H_6 (▲) as a function of the carrier-gas pressure. The data plotted are for E/P'_{298} values equal to 0.03 V cm^{-1} torr^{-1} for N_2 and 0.1 V cm^{-1} torr^{-1} for C_2H_4 and C_2H_6. These E/P values correspond to a mean electron energy of ~0.05 eV.

Of special interest is the analysis of our data on O_2 in C_2H_4, where the simple reaction scheme

1. Dual assignment.
2. On loan from the Computer Sciences Division.
3. Consultant.
4. Graduate student.
5. R. E. Goans and L. G. Christophorou, *J. Chem. Phys.* **60**, 1036 (1974).
6. L. G. Christophorou, *J. Phys. Chem.* **76**, 3730 (1972).

$$e + O_2 \xrightarrow{k_1} O_2^{-*} ,$$

$$O_2^{-*} \xrightarrow{k_2} O_2 + e,$$

$$O_2^{-*} + C_2H_4 \xrightarrow{k_3} O_2^- + C_2H_4 + \text{energy}$$

has been shown to describe the experimental results very adequately. On the basis of this reaction mechanism,

$$(\alpha w)_0^{-1} = A + B(P'_{C_2H_4})^{-1} , \qquad (1)$$

where $A = 1/k_1$ and $B = k_2/k_1k_3$. The experimental data on $(\alpha w)_0$ vs $P'_{C_2H_4}$ are plotted, in the manner suggested by Eq. (1), in Fig. 23.2 for $E/P'_{298} = 0.1$ V cm^{-1} torr^{-1} and are seen to be consistent with Eq. (1).

The high-pressure data on O_2 in C_2H_4 gave for the lifetime $\tau(O_2^{-*})$ of O_2^{-*}

$$\tau(O_2^{-*}) = (k_2)^{-1} = 1.9 \times 10^{-12} \text{ sec} .$$

This value is in agreement with our earlier estimate[6] and with a value deduced recently[7] from electron scattering experiments.

We were also successful in relating the high-pressure data on O_2 in C_2H_4 and N_2 to "liquid-state" behavior. Thus we predicted that the O_2 molecule will capture thermal electrons in liquid ethylene at the rate of 3.3×10^{11} sec^{-1} M^{-1}. Although there is no measurement of the electron capture rate for O_2 in liquid ethylene, Bakale and Schmidt[8] reported a rate equal to 5×10^{11} sec^{-1} M^{-1} for O_2 in neopentane and a rate equal to 5.2×10^{11} sec^{-1} M^{-1} for O_2 in neohexane, both at 296°K. Similarly, Richards and Thomas[9] reported a rate equal to 1.5×10^{11} M^{-1} sec^{-1} for O_2 in *n*-hexane at 193°K. These values are in good agreement with the one we determined from the gaseous data. This agreement may be taken to suggest that the process of thermal electron capture by O_2 in C_2H_4 is well understood for the entire density range from the low-pressure gas to the liquid (see further discussion in ref. 5).

7. F. Linder and H. Schmidt, p. 95, paper W1, in *Abstracts of the 24th Annual Gaseous Electronics Conference,* Gainesville, Fla., 1971.

8. G. Bakale and W. F. Schmidt, private communication, 1973.

9. J. T. Richards and J. K. Thomas, *Chem. Phys. Lett.* **10,** 317 (1971).

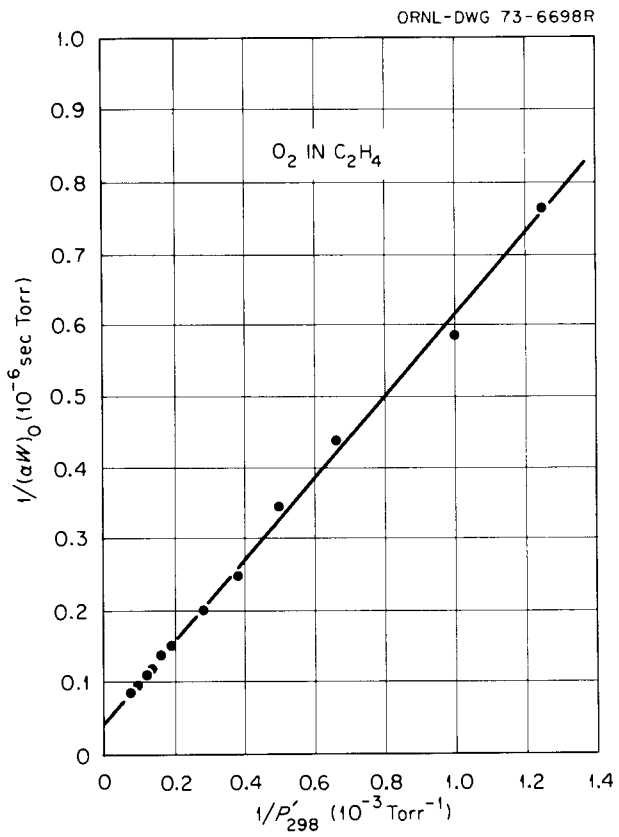

Fig. 23.2. $1/(\alpha w)_0$ as a function of $1/P'_{298}$ for O_2 in C_2H_4. The data plotted are for $E/P'_{298} = 0.1$ V cm^{-1} torr^{-1}.

LOW-ENERGY (<1 eV) ELECTRON ATTACHMENT TO MOLECULES IN VERY-HIGH-PRESSURE GASES: C_6H_6[10]

Benzene has been found to capture slow ($\lesssim$0.3 eV) electrons in high densities of N_2 (and argon) with a rate that increases with increasing N_2 density and decreasing electron energy at near-thermal energies. The dependence of the attachment rate, $(\alpha w)_0$, on the pressure-reduced electric field, E/P_{298}, and the mean electron energy, $\langle\epsilon\rangle$, is shown in Fig. 23.3 for the indicated N_2 pressures, P_{N_2}.

In Fig. 23.4, $(\alpha w)_0$ is plotted as a function of P_{N_2} for a number of values of $\langle\epsilon\rangle$. It is seen that initially, $(\alpha w)_0$ increases linearly with P_{N_2}, but as P_{N_2} increases further, $(\alpha w)_0$ shows a less than linear dependence on P_{N_2}. The higher the $\langle\epsilon\rangle$, the higher the N_2 pressure range over which $(\alpha w)_0$ varies linearly with P_{N_2}; this is a consequence of the fact that the lifetime of $C_6H_6^{-*}$ decreases with increasing mean electron energy.

10. L. G. Christophorou and R. E. Goans, *J. Chem. Phys.,* **60,** 4244 (1974).

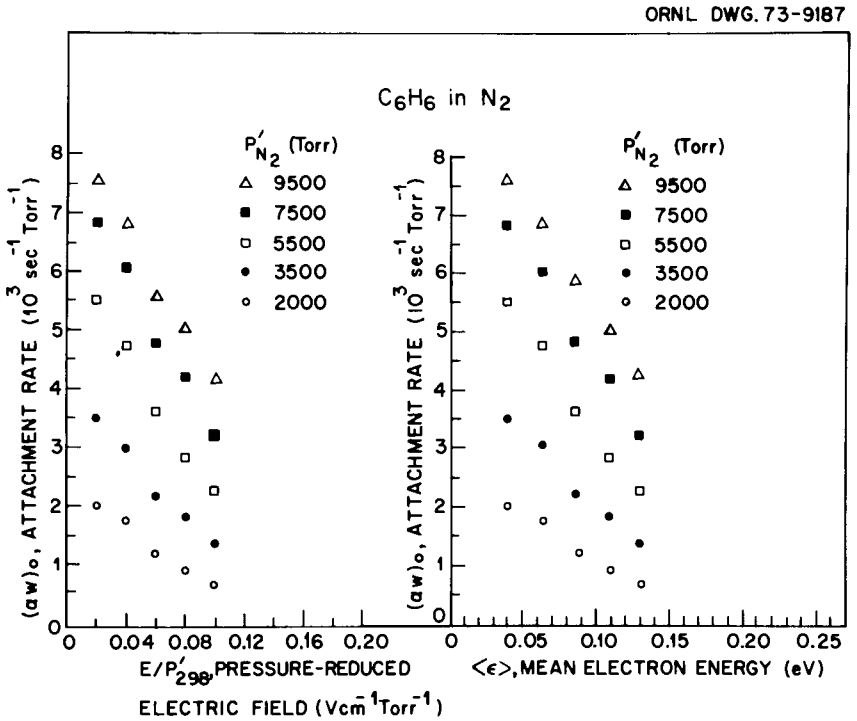

Fig. 23.3. Attachment rate $(\alpha w)_0$ for C_6H_6 in N_2 as a function of E/P_{298} and $\langle\epsilon\rangle$ at the indicated N_2 pressures.

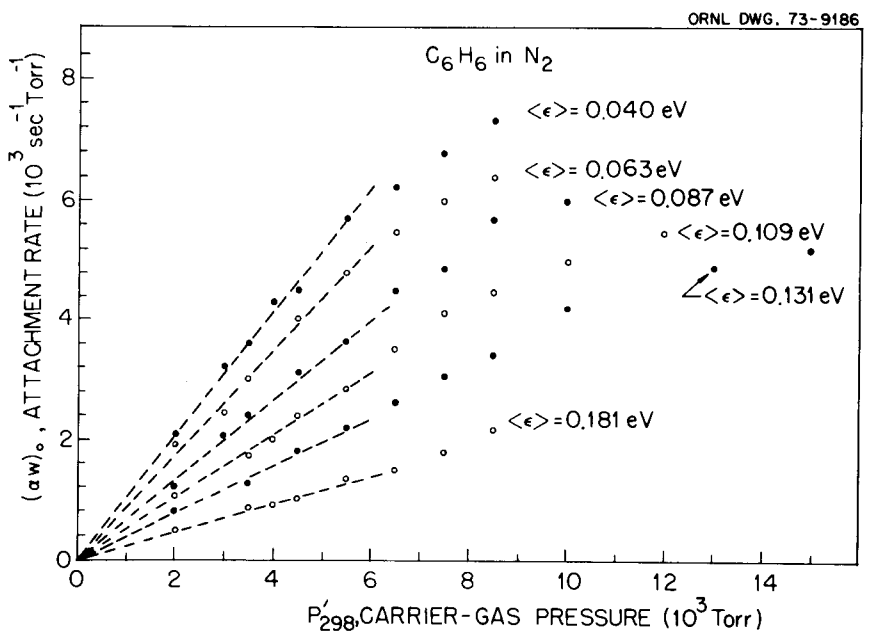

Fig. 23.4. Attachment rate $(\alpha w)_0$ for C_6H_6 as a function of the carrier-gas pressure at the indicated mean electron energies. The broken lines are a linear least-squares fit to the data for $P_{N_2} \leqslant 6000$ torr.

The data in Figs. 23.3 and 23.4 were analyzed on the basis of the following reaction scheme:

$$e + C_6H_6 \xrightarrow{k_1} C_6H_6^{-*} ,$$

$$C_6H_6^{-*} \xrightarrow{k_2} C_6H_6 + e ,$$

$$C_6H_6^{-*} + N_2 \xrightarrow{k_3} C_6H_6^{-} + N_2 + \text{energy} .$$

This predicts

$$\frac{1}{(\alpha w)_0} = A + B\frac{1}{P_{N_2}} , \qquad (2)$$

where $A = 1/k_1$ and $B = k_2/k_1k_3$. The experimental data on $(\alpha w)_0$ vs P_{N_2} are plotted, in the manner suggested by Eq. (2), in Fig. 23.5 for six mean electron energies in the range 0.04 to 0.181 eV, and they are seen to be consistent with Eq. (2). From a linear least-squares fit to the data in Fig. 23.5, k_1^{-1} and k_2/k_3 were obtained. The value of k_1 seems to be independent of $\langle\epsilon\rangle$ and equal to about 5×10^4 sec^{-1} torr^{-1}, although, in view of the spreading in the experimental data, it would be more appropriate to write $k_1 \gtrsim 5 \times 10^4$ sec^{-1} torr^{-1}. If we take for k_1 the value of 5×10^4 sec^{-1} torr^{-1}, we determine for k_2/k_3 the values listed in Table 23.1. The ratio k_2/k_3 is equal to the critical pressure P_{cr}, that is, the pressure at which the rate of autoionization of $C_6H_6^{-*}$ is equal to the rate of stabilization of $C_6H_6^{-*}$ via collisions.

To estimate the autodetachment lifetime, τ_a, of $C_6H_6^{-*}$, we first calculated the average time, τ_c, between collisions of $C_6H_6^{-*}$ and N_2 for the values of P_{cr} in Table 23.1 from[5]

$$\tau_c = \nu_c^{-1} = \frac{1}{2\pi n_{N_2}}\left(\frac{M_r}{e^2\alpha}\right)^{1/2} . \qquad (3)$$

Table 23.1. Values of k_2/k_3 ($\equiv P_{cr}$) and $\tau_a(C_6H_6^{-*})$ at various mean electron energies, $\langle\epsilon\rangle$

$\langle\epsilon\rangle$ (eV)	k_2/k_3 ($\equiv P_{cr}$) (torr)	$\tau_a(C_6H_6^{-*})$ (sec)
		$\times 10^{-13}$
0.040	4.4×10^4	10.4
0.063	5.5×10^4	8.3
0.087	7.0×10^4	6.5
0.109	9.2×10^4	5.0
0.131	1.25×10^5	3.6
0.181	2.0×10^5	2.3

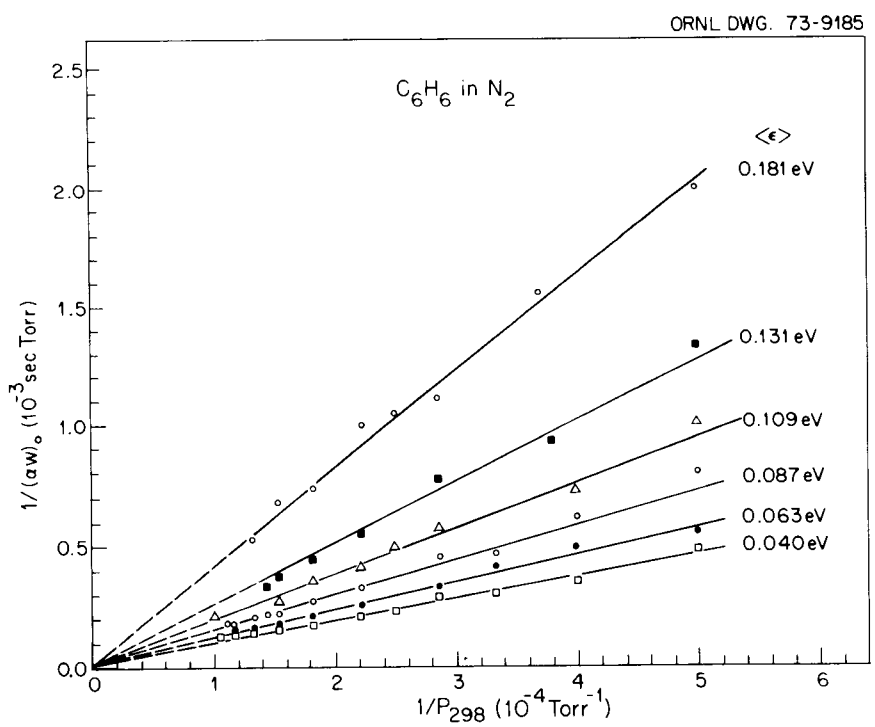

Fig. 23.5. $1/(\alpha w)_0$ as a function of $1/P_{N_2}$ for C_6H_6 in N_2 for the indicated values of $\langle\epsilon\rangle$. For each $\langle\epsilon\rangle$ the solid lines are Eq. (2) with the corresponding values for A ($\equiv 1/k_1$) and B($\equiv k_2/k_1k_3$) given in the text and in Table 23.1.

In Eq. (3), $\nu_c = v\sigma_L n_{N_2}$ is the collision frequency, v is the relative velocity of $C_6H_6^{-*}$ and N_2, n_{N_2} is the number density of N_2 at the corresponding value of the critical pressure, σ_L is the Langevin expression for the cross section for spiraling collisions between $C_6H_6^{-*}$ and N_2, α is the static polarizability of N_2, e is the electronic charge, and M_r is the reduced mass. Using Eq. (3) and the values of P_{cr} in Table 23.1, and assuming that the probability of stabilization, p, of $C_6H_6^{-*}$ at each collision with N_2 is unity, we obtained for the autodetachment lifetime of $C_6H_6^{-*}$ the values listed in column 3 of Table 23.1. These values are seen to lie in the picosecond and subpicosecond region. The dependence of $\tau_a(C_6H_6^{-*})$ on $\langle\epsilon\rangle$ is shown in Fig. 23.6. If $p < 1$, the average time for stabilizing $C_6H_6^{-*}$ in collisions with N_2 will be greater than τ_c; hence

$$\tau_a(C_6H_6^{-*})_{p<1} > \tau_a(C_6H_6^{-*})_{p=1} \cdot$$

Thus the present estimates of $\tau_a(C_6H_6^{-*})$ represent lower limits.

The plots $(\alpha w)_0^{-1}$ vs $P_{N_2}^{-1}$ in Fig. 23.5 represent an excellent method for relating the present information on C_6H_6 in N_2 gas to "liquid-state" behavior. Assuming that the linear relationship found between $(\alpha w)_0^{-1}$ and $P_{N_2}^{-1}$ over the P_{N_2} range covered in this study holds up to the liquid nitrogen density, the value of $(\alpha w)_0$ for $P_{N_2} \to \infty$ can be obtained. From the data in Fig. 23.5,

$$[(\alpha w)_0]_{\text{intercept}} \gtrsim 5 \times 10^4 \text{ sec}^{-1} \text{ torr}^{-1}$$
$$\simeq 1 \times 10^9 \text{ sec}^{-1} M^{-1}$$

For liquid N_2 and $\langle\epsilon\rangle = 0.04$ eV,

$$[(\alpha w)_0]_{\text{liquid}} \simeq [(\alpha w)_0]_{\text{intercept}} \cdot$$

Although no measurement has been made of the rate of attachment of thermal electrons to C_6H_6 in liquid N_2, an upper limit of 1×10^9 sec$^{-1}M^{-1}$ has been placed by Bakale et al.[11] on the rate of attachment of thermal electrons to C_6H_6 in liquid *n*-hexane.

Many theoretical calculations have been made of the electron affinity, $(EA)_B$, of benzene.[12] From the results of these calculations, one can justify the commonly assumed value of −1.4 eV for $(EA)_B$.

11. G. Bakale, E. C. Gregg, and R. D. McCreary, *J. Chem. Phys.* 57, 4246 (1972).

12. See L. G. Christophorou, *Atomic and Molecular Radiation Physics*, Wiley-Interscience, New York, 1971.

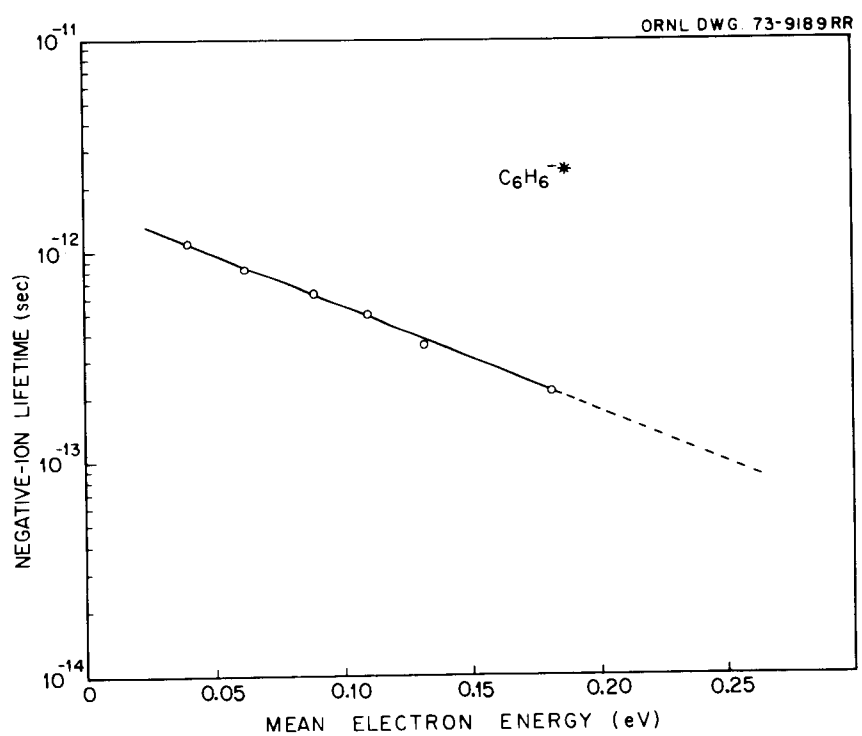

Fig. 23.6. Variation of the autodetachment lifetime of $C_6H_6^{-*}$ with mean electron energy.

Additionally, low-energy electron scattering experiments[12] revealed the existence of a compound negative ion resonance (CNIR) state in benzene, with a maximum at about 1.4 eV. Actually, this value is the "vertical attachment energy."[12] The finding of the present work that $C_6H_6^-$ exists in the gaseous phase requires $(EA)_B$ to be positive (>0 eV). However, in view of the very short autodetachment lifetime of $C_6H_6^{-*}$ (and the small cross section for its formation), $(EA)_B$ must be small. It is finally noted that, since electron scattering experiments and most of the theoretical calculations are concerned with the vertical transition between B (plus an electron at rest at infinity) and B^- and since in the present work we are concerned with the adiabatic value of $(EA)_B$, the requirement of our findings that $(EA)_B > 0$ eV may indicate that the potential energy surface of B^- has its minimum below that of B in a different geometry from that of B.

Finally, benzene was also studied in mixtures with C_2H_4 and with C_2H_4 and N_2. The results of these latter experiments strongly indicated that the probability of electron detachment in collisions between $C_6H_6^{-*}$ and C_2H_4 is large.

LOW-ENERGY (<3 eV) ELECTRON ATTACHMENT TO MOLECULES IN VERY-HIGH-PRESSURE GASES: C_2H_5Br

Significant changes have been observed in both the magnitude and the energy dependence of the rate of attachment of slow (<3 eV) electrons to bromoethane (C_2H_5Br) embedded in the gaseous media N_2 and argon with increasing density of these media from 500 to 25,000 torr for N_2 and from 500 to 42,500 torr for argon. These are illustrated in Figs. 23.7–23.10. Two plausible models – a one-state and a two-state model – have been considered to account for the observed density and energy dependences of the attachment rate. On the basis of the one-state model, determinations were made of the relative magnitudes of the rates for dissociation, autoionization, and collisional stabilization of the metastable $C_2H_5Br^{-*}$ ion as a function of the mean electron energy $\langle\epsilon\rangle$. On the basis of the same model the lifetime of $C_2H_5Br^{-*}$ was estimated and found to decrease from about 6 psec at $\langle\epsilon\rangle = 0.2$ eV to about 0.8 psec at $\langle\epsilon\rangle = 1.1$ eV. This decrease reflects the increase with $\langle\epsilon\rangle$ of the rate of dissociation of $C_2H_5Br^{-*}$. Additionally, an estimate of 0.4×10^{12} sec^{-1} M^{-1} was obtained for the attachment of slow electrons to C_2H_5Br in liquid argon. This study also requires that the adiabatic electron affinity of the C_2H_5Br molecule be positive (>0 eV).

MOBILITIES OF SLOW ELECTRONS IN LOW- AND HIGH-PRESSURE GASES AND IN LIQUIDS[13]

The mobility, μ, of thermal electrons in molecular gases decreases with increasing magnitude of the permanent electric dipole moment D. This is shown in Fig. 23.11, where μ_{torr} (defined as the value of S/P_T for $P_T = 1$ torr, where S is the slope of w vs E/P_T curves in the region where the drift velocity w varies linearly with the pressure-reduced electric field E/P_T) is plotted as a function of D. From a linear least-squares fit to the experimental data (the solid line in Fig. 23.11), we obtained the relationship

$$\mu_{torr} = 2.74 \times 10^5 \times D^{-1.48} . \quad (4)$$

The broken line in Fig. 23.11 is a theoretical estimate of the dependence of μ_{torr} on D based on a calculation by Altshuler,[14] who considered the problem of electron scattering by a point dipole in the Born approximation. Although this theoretical prediction,

$$\mu_{torr} = 4.51 \times 10^5 \times D^{-2} , \quad (5)$$

13. L. G. Christophorou, *Int. J. Radiat. Phys. Chem.*, in press.
14. S. Altshuler, *Phys. Rev.* **107**, 114 (1957).

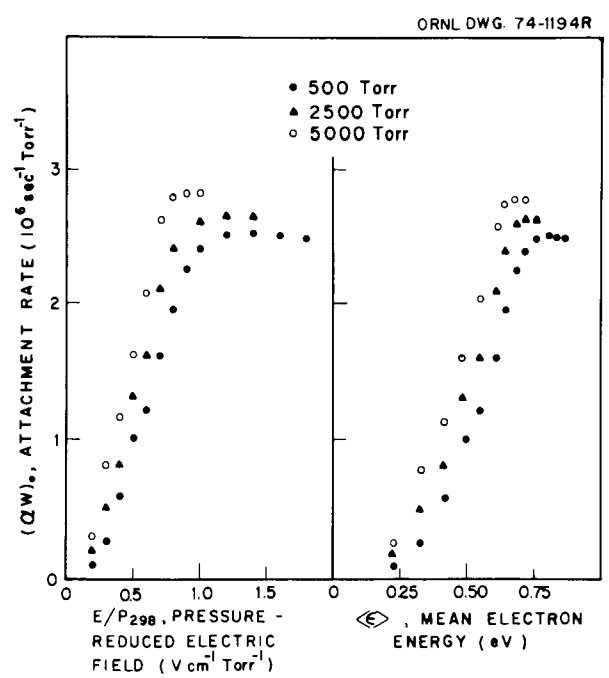

Fig. 23.7. Attachment rate, $(\alpha w)_0$, as a function of E/P_{298} and $\langle\epsilon\rangle$ for C_2H_5Br in N_2 for the indicated N_2 pressures.

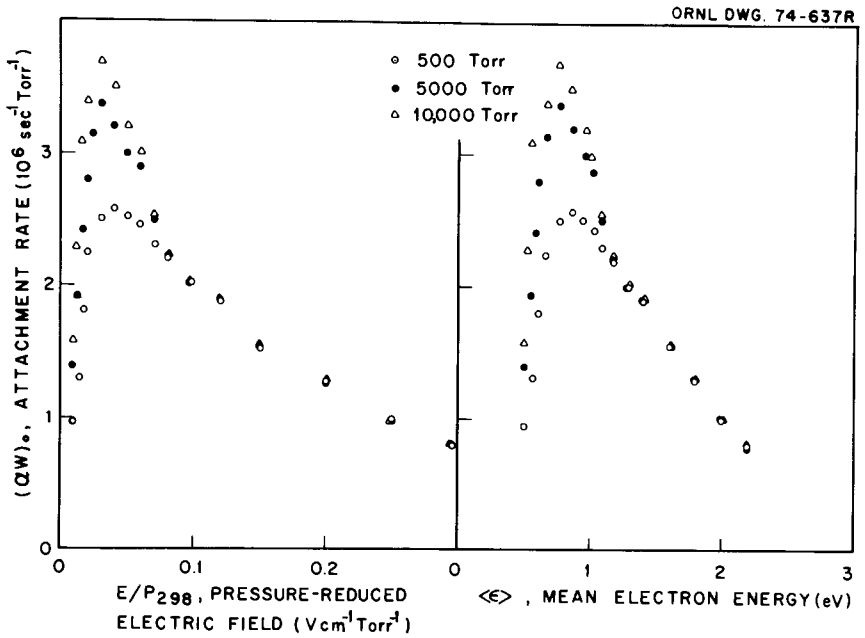

Fig. 23.8. Attachment rate, $(\alpha w)_0$, as a function of E/P_{298} and $\langle\epsilon\rangle$ for C_2H_5Br in argon.

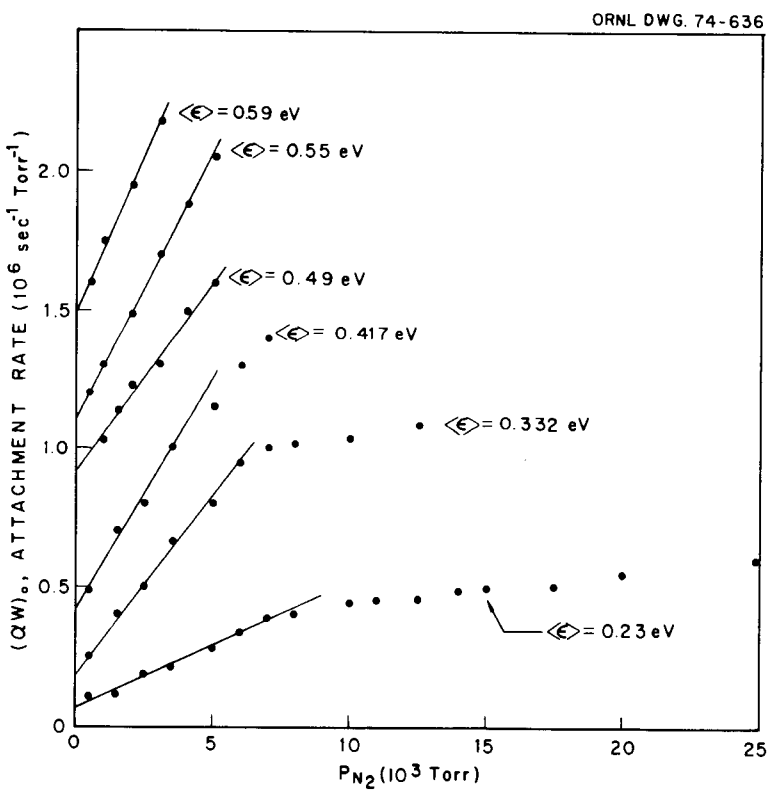

Fig. 23.9. Attachment rate, $(\alpha w)_0$, for C_2H_5Br in N_2 as a function of N_2 pressure for several $\langle\epsilon\rangle$.

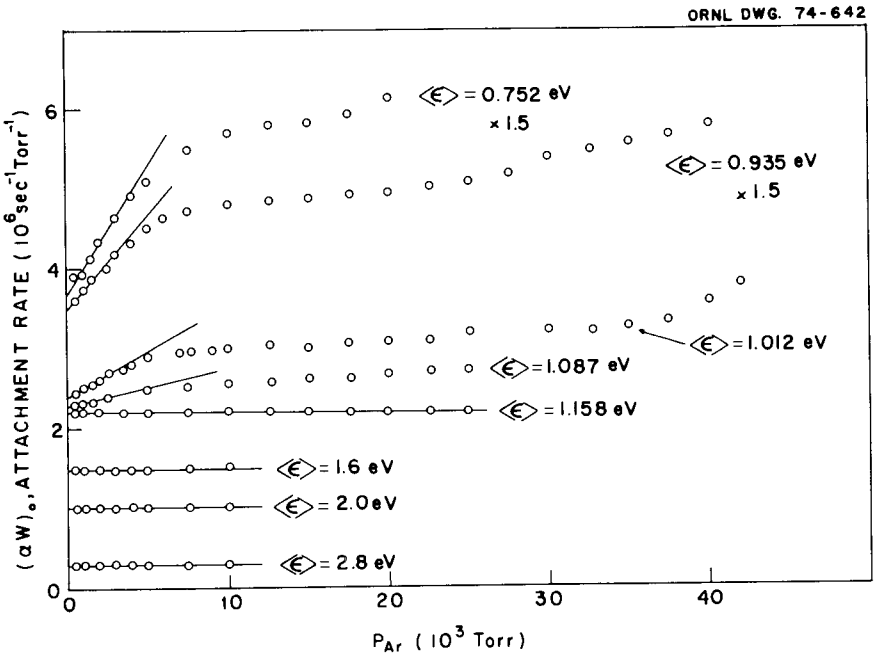

Fig. 23.10. Attachment rate, $(\alpha w)_0$, for C_2H_5Br in argon as a function of argon pressure for several $\langle\epsilon\rangle$. Note that the y axis for $\langle\epsilon\rangle$ = 0.752 and 0.935 eV has been multiplied by a factor of 1.5 for convenience of display.

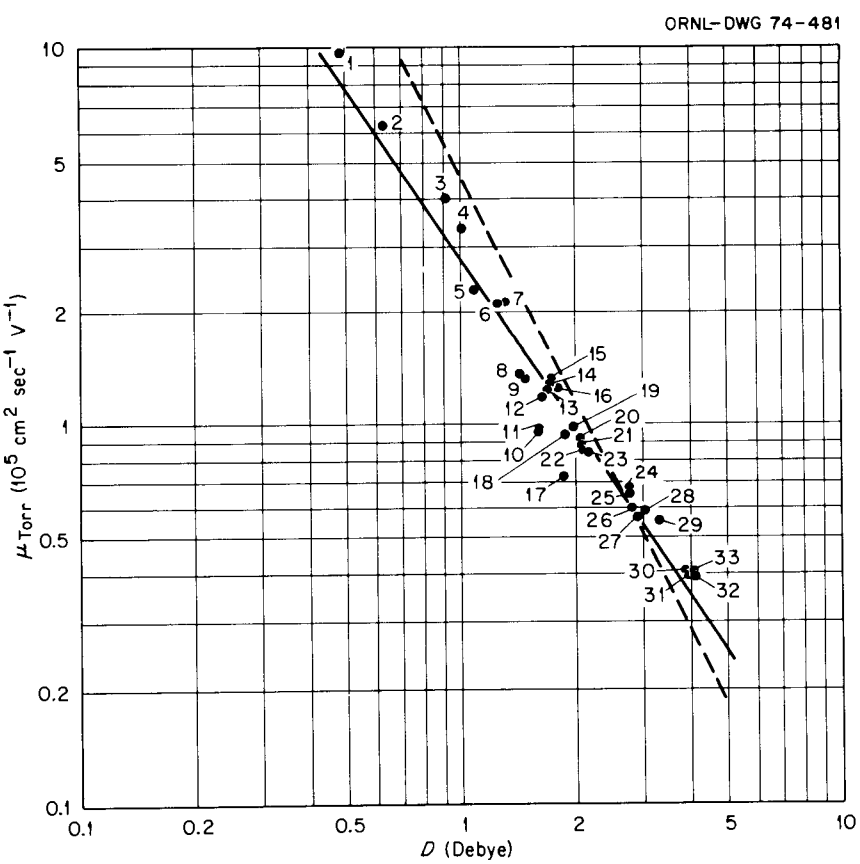

Fig. 23.11. μ_{torr} vs D.

differs from experiment (Eq. 4), the differences are not drastic, and the magnitude of μ_{torr} is seen to be determined primarily by the electron–electric-dipole scattering potential. For $D \gtrsim 0.5$ D, Eq. (4) can be used to predict μ_{torr} from a knowledge of D. For small values of D ($\rightarrow 0$), μ decreases with increasing static polarizability (see Fig. 23.12).

In addition to these molecular parameters, distinct submolecular characteristics of the molecular structure affect μ. Thus μ has been found to decrease with increasing number of doubly occupied π-electron orbitals for a number of linear, cyclic, and aromatic hydrocarbons. For linear hydrocarbons with two doubly occupied π-electron orbitals, μ increases with increasing separation of the two π orbitals. The dependence of μ on the mean electron energy for a number of organic molecules has been determined also.[13]

The recently discovered large and varying effects of pressure on the electron mobility in high-pressure gases have been summarized and discussed.[13] In Fig. 23.13 we show the three distinct types of pressure dependence of the electron mobility as exemplified by the behavior of CH_4, C_2H_6, and CO_2. These, as well as the thermal electron mobilities in low-pressure gases, have been related to the molecular structure and have been compared with the electron mobilities in the liquid phase. The importance of an electron capture-and-loss process in delaying the electron drift has been elaborated on.

For a number of relatively spherical hydrocarbons and for the heavier rare-gas atoms, thermal electrons seem to be more mobile in the liquid than in the gaseous phase.[13,15] The experimental evidence indicates that this behavior is due to scattering potentials in the liquid state reminiscent of those giving rise to the Ramsauer-Townsend effect in the heavier rare gases. The importance of an integrated approach, encompassing low-pressure, high-pressure, and liquid-state information, in understanding this and similar problems has been clearly demonstrated.

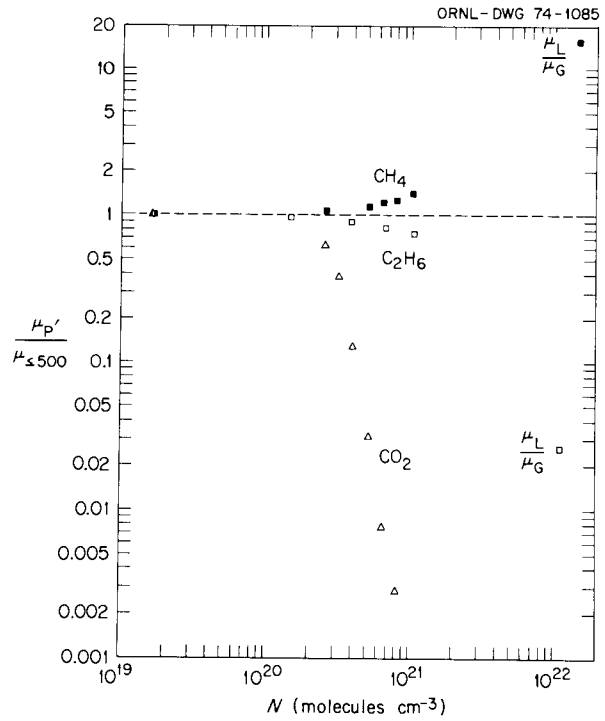

Fig. 23.13. $\mu_{P'}/\mu_{\leq 500}$ vs N, the number density, for CH_4, C_2H_6, and CO_2. The quantity $\mu_{P'}$ denotes the electron mobility at a pressure P', and $\mu_{\leq 500}$ is equal to the low-pressure mobility μ. The symbol P' (rather than P) is now used for the pressure to indicate that the measured pressures have been corrected for compressibility; so the number density N is proportional to P'. μ_L/μ_G gives[13,15] the value of the ordinate for densities corresponding to those of the respective liquids.

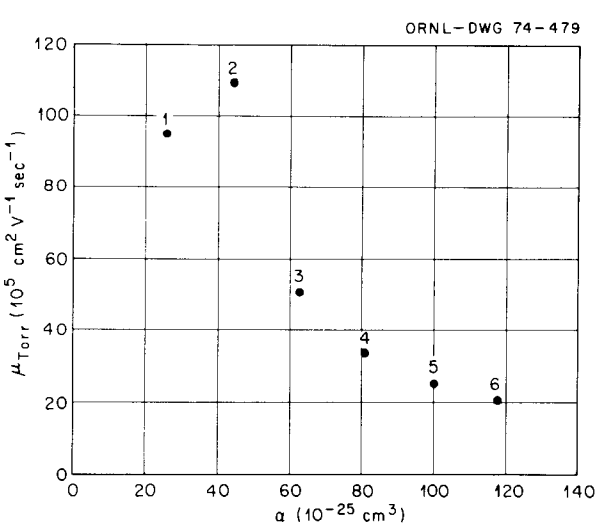

Fig. 23.12. μ_{torr} vs α for the linear hydrocarbons: (1) CH_4, (2) C_2H_6, (3) C_3H_8, (4) C_4H_{10}, (5) C_5H_{12}, (6) C_6H_{14}.

MOBILITIES OF THERMAL ELECTRONS IN LOW-PRESSURE ORGANIC VAPORS

We continued the measurement of electron mobilities in low-pressure gases for several organic molecules for which the mobility, μ_L, in the corresponding liquids has been measured. Thus mobility values have been determined for butene-1, 1.31×10^6 cm^2 V^{-1} sec^{-1}; *cis*-butene-2, 1.32×10^6 cm^2 V^{-1} sec^{-1}; *trans*-

15. L. G. Christophorou, R. P. Blaunstein, and D. Pittman, *Chem. Phys. Lett.* **22**, 41 (1973).

butene-2, 3.71×10^6 cm^2 V^{-1} sec^{-1}; and 2-methylpropene (isobutene), 6.56×10^5 cm^2 V^{-1} sec^{-1}. These data show differences in electron mobilities in the trans and cis forms of the butene-2 molecule; the mobility of the trans form is about 2.8 times larger than that of the cis form. These findings have been compared with those on μ_L.[13]

ELECTRON MOBILITIES IN HIGH-PRESSURE GASES ("QUASI LIQUIDS")

Over the last few years we have been engaged in an intense effort to link our knowledge on electron transport and drift in dilute (low-pressure) gases with knowledge on electron transport in liquids, through the high-pressure ("quasi-liquid") regime.[13,15] In this effort, although we have been successful in measuring the mobility of thermal electrons at low pressures ($\lesssim$1 atm) for a number of branched hydrocarbons and in establishing that the electron mobility for $C(CH_3)_4$ (neopentane) increases rather than decreases with increasing gas density, our efforts to apply our existing method for gas pressure $\gtrsim$2 atm proved fruitless. For this reason, we have designed and are presently building a high-pressure drift apparatus with which we shall be able to measure electron mobilities at pressures up to about 80 atm and at temperatures up to about 450°C. The method is similar to that developed by Raether.[16] A short-duration (10-nsec) high-density light source will be used to produce photoelectrons from one of the plates of a parallel-plate capacitor. The electrons traversing the drift space produce in a series resistor a voltage drop which is amplified and displayed on a fast oscilloscope. The drift velocity is determined directly from a measurement of the drift time (i.e., the start and stop of the voltage pulse from the series resistor) and the drift distance.

DIRECT MEASUREMENT OF THE MOBILITY OF EXCESS ELECTRONS IN LIQUIDS

The apparatus for an experiment to measure the mobility of excess electrons in liquids is under construction. When completed, this apparatus should permit the measurement of mobilities to an accuracy of about 2%. In the experiment, excess electrons are created in the liquid by the ionization produced by a radioactive source. The electrons are repelled from the source by a strong electric field, which drags them through the liquid to be collected by a metal plate at ground potential. The current drawn by this collector plate is measured by an electrometer. The time taken by the electrons to travel from the source to the collector is established as follows. At the start, a pair of grids next to the source is biased so as to collect "all" the electrons produced by the source. The pair of grids acts as an electron shutter. When the biasing voltage on the grids is removed, the electrons move toward the collector. Before reaching the collector, the electrons must pass through another pair of grids, which forms a second shutter. The biasing voltage on this pair of grids is operated in synchronization with that on the first so that the electrons pass this second shutter if their drift time is commensurable with the period of oscillation of the shutter voltages. A measurement of the drift time, the spacing between the shutters, and the electric field applied between the source and the collector suffices to determine the electron mobility as a function of field strength.

The design of the apparatus is similar to that reported by Schnyders, Rice, and Meyer.[17] In their experiment the excess electrons in the liquid were produced by a ^{210}Po alpha-particle source in physical contact with the liquid. In the present experiment the ionization will be produced by an encapsulated ^{204}Tl beta-particle source, which greatly reduces the hazard of contamination. Thallium-204 has a half-life of 3.8 years and produces a beta spectrum with an average energy of 243 keV. This source is nearly a pure beta emitter and is contaminated relatively little by electromagnetic radiation from electron bremsstrahlung and from mercury x rays produced by electron capture by thallium.

The electron drift region is about 1 cm long. The electric field applied between the source and collector is adjustable from 0 to 10 kV with a spatial homogeneity over the electron drift region of the order of 1%. The grids forming the shutters have been chosen so that they will have a transmission of 85% and will distort the electric field applied between the source and the collector by an average of no more than 0.25%.

Care is being taken to assure the chemical purity of the liquid. The apparatus is designed so that it may be evacuated under heating. The source has been prepared so that it can withstand these conditions without rupturing. After many cycles of "freeze-pump-thaw," the liquid will be transferred to the evacuated mobility apparatus by condensation from a vapor.

16. H. Raether, *Electron Avalanches and Breakdown in Gases*, Butterworths, London, England, 1964.

17. H. Schnyders, S. A. Rice, and L. Meyer, *Phys. Rev.* **150**, 127 (1966).

POTENTIAL ENERGY FUNCTION FOR AN EXCESS ELECTRON IN A NONPOLAR LIQUID

The polarization potential for an excess electron in a nonpolar liquid has been calculated by Springett, Jortner, and Cohen.[18] They have shown that the polarization potential function can be expressed as the potential energy of interaction of an electron with a molecule in free space times a screening factor that takes into account the screening of the field of the electron by the liquid as a whole. In their formulation the screening factor is derived from the Lorenz-Lorentz formula for a nonpolar dielectric. Implicit in the use of the Lorenz-Lorentz formula is the assumption that the electric field of the electron is uniform, made up of parallel lines of force. This is, of course, an oversimplification. We considered the radial nature of the field of the electron, and an outline of our approach is given below.

A single molecule in a liquid is represented by a spherical cavity in a uniform medium of dielectric constant ϵ. At the center of the cavity, there is a point dipole representing the dipole moment induced in the molecule by the field of the electron. Neglecting the point dipole for a moment, consider first the cavity in the field of the electron alone. If Laplace's equation is solved for the electrostatic potential with the condition that the potential and the electric displacement are continuous at the surface of the cavity, one finds for the electric field at the center of the cavity

$$E_q = \frac{3}{2\epsilon + 1}\frac{q}{b^2}, \tag{6}$$

where b is the distance of the electron from the center of the cavity and q is the charge of the electron. Neglecting the presence of the electron, consider the cavity with the point dipole at the center. Again Laplace's equation is solved under the same boundary conditions.[19] The electric field at the center of the cavity is

$$E_m = \frac{2m}{a^3}\frac{\epsilon - 1}{2\epsilon + 1}, \tag{7}$$

where m is the magnitude of the dipole moment and a is the radius of the cavity. The total electric field E_t at the center of the cavity is the sum of Eqs. (6) and (7). However, the dipole moment m is proportional to the total field:

$$m = \alpha E_t ,$$

where α is the polarizability of the molecule. Hence, for the total electric field, we have

$$E_t = \frac{3}{2\epsilon + 1}\frac{q}{b^2} + \frac{2}{a^3}\frac{\epsilon - 1}{2\epsilon + 1}\alpha E_t$$

and, for the dipole moment,

$$m = -\frac{\alpha[3/(2\epsilon + 1)](q/b^2)}{1 - (2\alpha/a^3)[(\epsilon - 1)/(2\epsilon + 1)]} .$$

With this result for m, the potential energy $V(r)$ for the electron in the nonpolar liquid is

$$V(r) = \frac{1}{2}\frac{q^2}{a\epsilon}\frac{\epsilon - 1}{2\epsilon + 1} \times \frac{1 - (\alpha/a^3)[(\epsilon + 2)(4\epsilon - 1)/(\epsilon - 1)(2\epsilon + 1)]}{1 - 2(\alpha/a^3)[(\epsilon - 1)/(2\epsilon + 1)]} + \sum_{l=2}^{\infty}\frac{1}{2}\frac{q^2}{a\epsilon}\frac{l(\epsilon - 1)}{\epsilon(l + 1) + l}\left(\frac{a}{r}\right)^{2(l+1)} .$$

The first term in this sum represents the interaction of the electron with the induced dipole moment in the liquid, and the remaining terms represent the interaction of the electron with higher moments. If we allow ϵ to approach unity, which corresponds to allowing the density of the liquid to go to zero, we find

$$\lim_{\epsilon \to 1} V(r) = -\frac{1}{2}\frac{\alpha e^2}{r^4},$$

thereby recovering the expression for the potential energy of interaction of an electron with a nonpolar molecule in vacuum.

COMPOUND NEGATIVE ION RESONANT STATES AND THRESHOLD ELECTRON EXCITATION SPECTRA OF MONOSUBSTITUTED BENZENE DERIVATIVES[20]

Threshold electron excitation (TEE) spectra for fluorobenzene, benzaldehyde, and benzoic acid have been

18. B. E. Springett, J. Jortner, and M H. Cohen, *J. Chem. Phys.* **48**, 2720 (1968).
19. L. Onsager, *J. Amer. Chem. Soc.* **58**, 1486 (1936).
20. L. G. Christophorou, J. G. Carter, and D. L. McCorkle, *J. Chem. Phys.*, **60**, 3779 (1974).

obtained and compared with photoabsorption spectra. Figures 23.14 and 23.15 show representative TEE spectra for benzoic acid and fluorobenzene. The solid arrows above the spectrum indicate the positions of the maxima in the TEE spectrum, and the broken arrows indicate the positions of the onsets. The numbers that accompany each arrow give the position (in electron volts) of a peak or an onset, and they have been

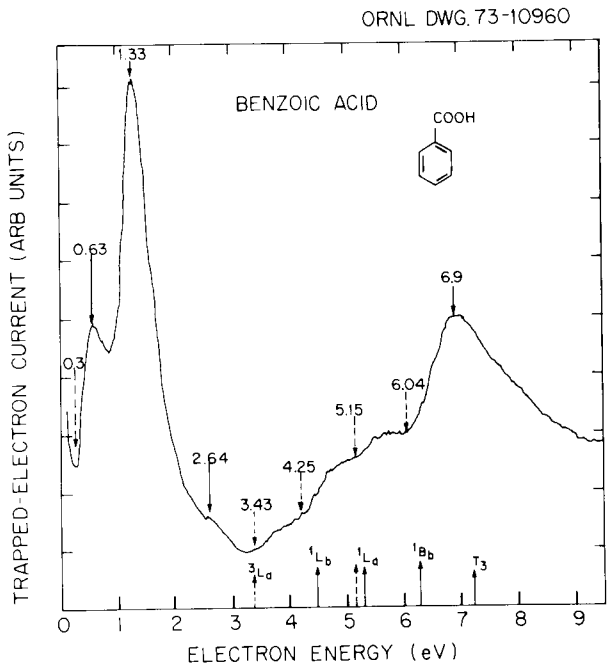

Fig. 23.14. Threshold electron excitation (TEE) spectrum of benzoic acid.

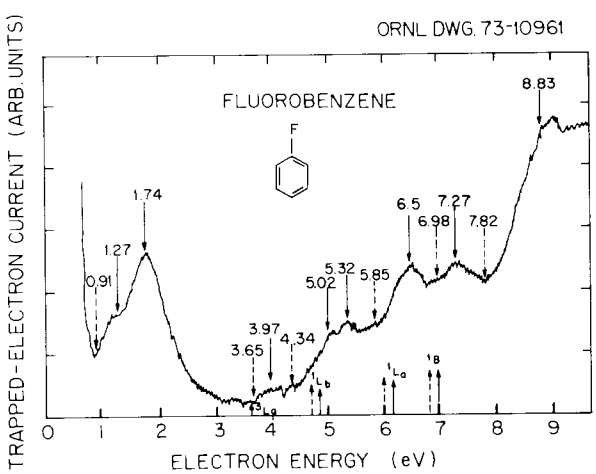

Fig. 23.15. Threshold electron excitation (TEE) spectrum of fluorobenzene.

obtained by an averaging of the data for a large number of spectra similar to the one presented. The solid and broken arrows perpendicular to the energy axis give, respectively, the positions of the band onsets ($0 \rightarrow 0$ transitions) and band maxima obtained with photophysical methods. The excitation of optically forbidden states is clearly evident in the TEE spectra.

The two distinct peaks at 1.27 and 1.74 eV for fluorobenzene and at 0.63 and 1.33 eV for benzoic acid are due to excitation of two compound negative ion resonant (CNIR) states. Actually, two CNIR states were observed below the first excited electronic state, as opposed to only one for benzene, for all nine monosubstituted benzene derivatives studied. The positions of the maxima of these double resonances are shown in Fig. 23.16. The bracketed numbers accompanying the formula for each compound are the photoionization or photoabsorption values (in electron volts) of the ionization potentials of the parent molecules. The numbers below each level give (in electron volts) the positions of the maxima of the observed CNIR's. The maxima of the $C_6H_5NO_2$ resonances were determined on the basis of an earlier study[21] on dissociative attachment to $C_6H_5NO_2$, where the lowest-lying resonance above thermal energies peaked at 1.06 eV and led to the production of NO_2^-.

The number and positions of these double CNIR's have been understood[20] in terms of the net π-electron charge transfer between the substituent and the benzene ring. For the benzene molecule the two lowest unfilled π orbitals of benzene, $e_{2u,1}$ and $e_{2u,2}$, are degenerate; this accounts for the observation of only one CNIR for benzene since electron capture in either orbital will yield a resonance at exactly the same energy. For the benzene-derivative molecules, however, the two lowest unoccupied π orbitals are no longer degenerate, due to the perturbation introduced by the substituent; thus two CNIR's arise from the quasi trapping of slow electrons in the $e_{2u,1}$ and $e_{2u,2}$ orbitals. The present results distinctly show the effects of intramolecular charge transfer between the substituent and the benzene ring on the energies of the lowest unoccupied π orbitals involved in the quasi trapping of slow electrons responsible for the observed CNIR's. A full discussion of this and a detailed exposition of the results can be found in ref. 20.

21. L. G. Christophorou, R. N. Compton, G. S. Hurst, and P. W. Reinhardt, *J. Chem. Phys.* **45**, 536 (1966).

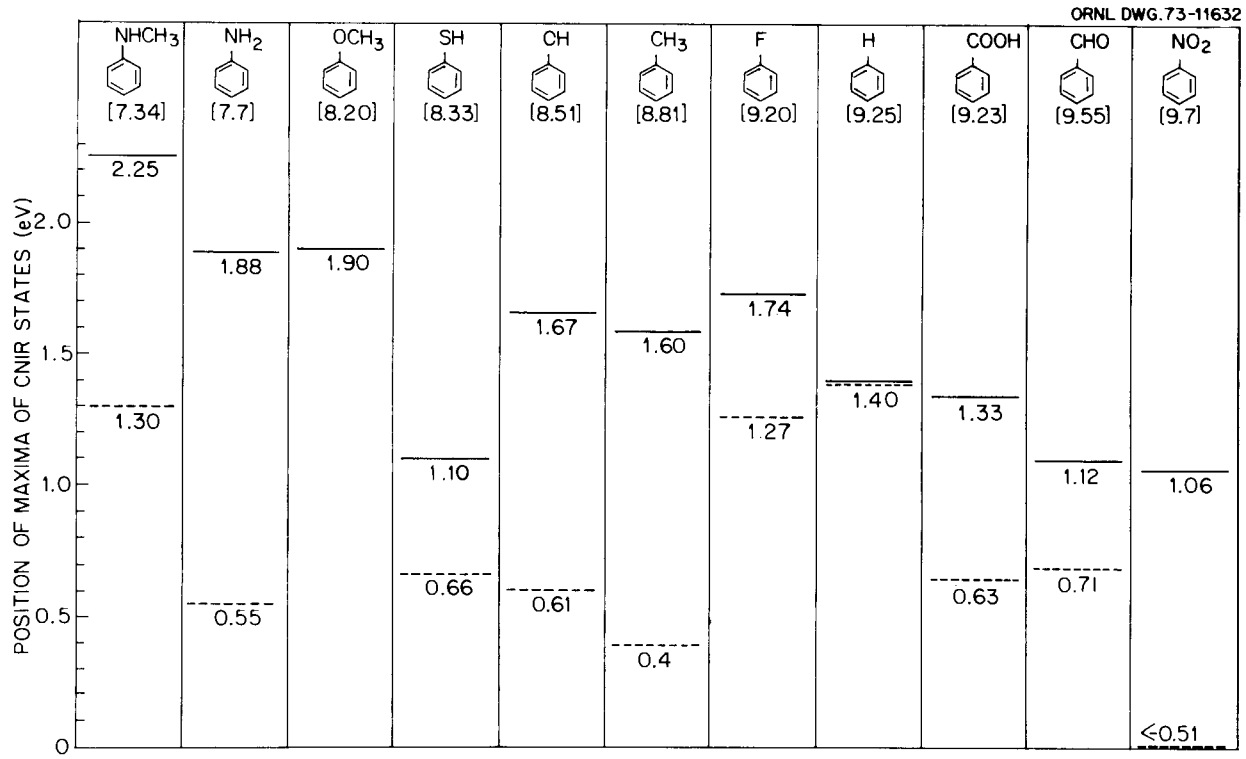

Fig. 23.16. Position of maxima of the double compound negative ion resonant (CNIR) states for benzene and seven monosubstituted benzene derivatives in descending order of the ionization potential of the neutral molecule.

LIFETIMES OF LONG-LIVED MONO-SUBSTITUTED NITROBENZENES

The mass spectrometric studies of key groups of organic molecules directly involved in biological reactions have continued with a focusing on the mono-substituted nitrobenzenes. The lifetimes of ten such molecules in their ortho, meta, and para forms have been determined and have been related to the respective molecular structures and the donor-acceptor properties of the substituents. In this regard, valence-shell calculations using the complete neglect of differential overlap approximation are being performed for both the neutral molecules and the negative ions. It has been found that for π-electron-donating substituents the extra electron is located primarily on the NO_2 group, whereas for π-electron-accepting substituents the attached electron is more evenly shared between the NO_2 group and the benzene ring. Efforts are presently directed toward relating the measured autodetachment lifetimes to the π-electron migration between the ring and the substituents for para monosubstituted nitrobenzenes.

Previous studies in this program[22,23] first demonstrated that the autodetachment lifetime of some molecular negative ions decreases with increasing incident electron energy. This important phenomenon has again been demonstrated by us, and Fig. 23.17 shows an example of the results obtained. The solid points represent the observed dependence of the parent negative-ion lifetime for nitro-α,α,α-trifluorotoluene on the incident electron energy, ϵ, and the open circles represent the yield of the parent negative ion as a function of ϵ. The lifetime measurements were made utilizing the retarding potential difference capacity of the electron gun. Figure 23.18 shows the way in which the lifetimes were determined at the various electron energies. At each electron energy the lifetime τ was obtained from the slope of the $-\ln(N^-/N^T)$ vs t lines by a least-squares fit to the experimental data, including the origin [N^- is the number of negative ions that have

22. P. M. Collins, L. G. Christophorou, E. L. Chaney, and J. G. Carter, *Chem. Phys. Lett.* **4**, 646 (1970).

23. L. G. Christophorou, A. Hadjiantoniou, and J. G. Carter, *J. Chem. Soc., Faraday Trans. 2* **69**, *1713* (1973).

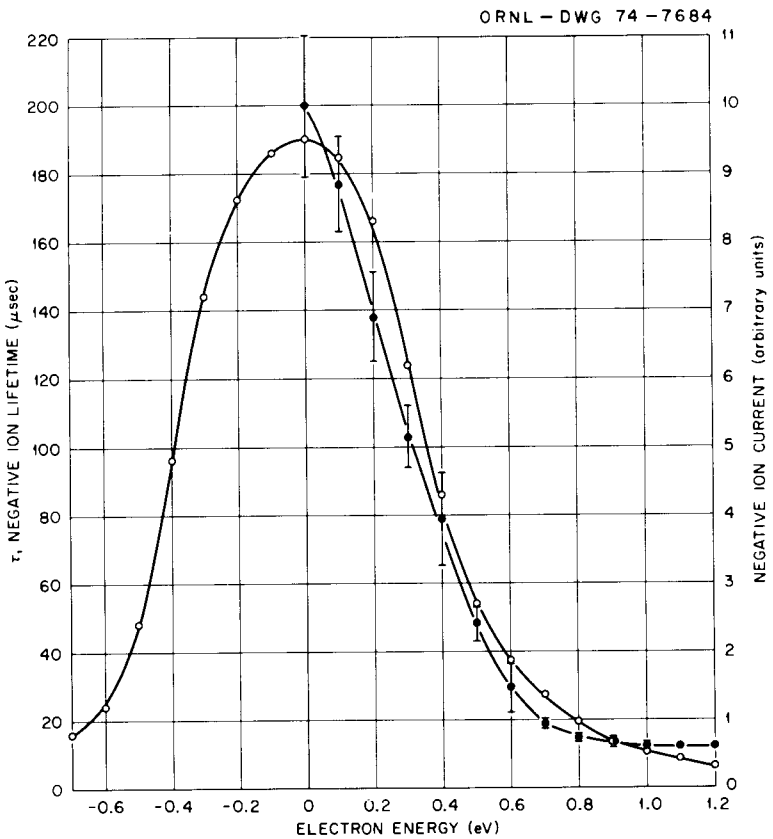

Fig. 23.17. Negative-ion lifetime (•) and negative-ion yield (○) (without the retarding-potential difference method) for m-nitro-α,α,α-trifluorotoluene.

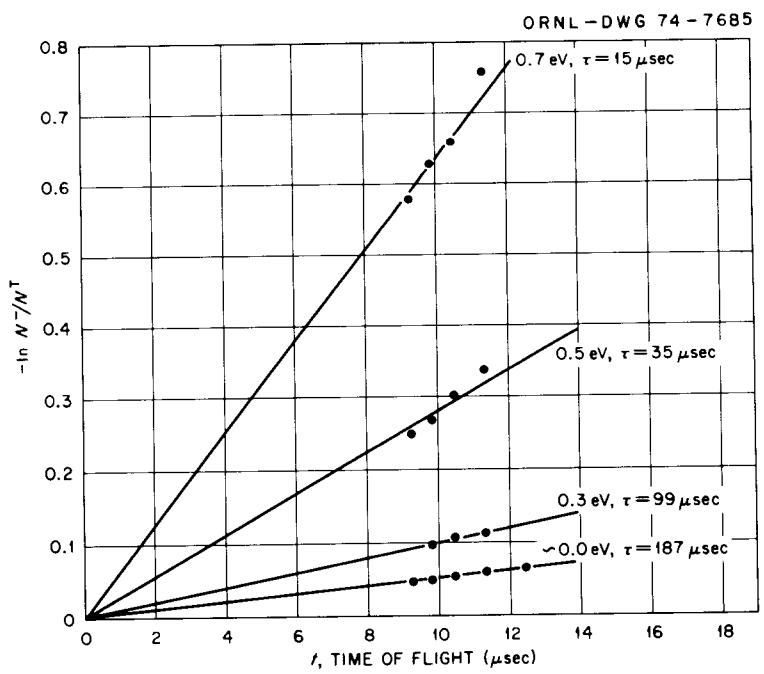

Fig. 23.18. $-\ln N^{-}/N^{T}$ vs the time-of-flight t for about 0.0, 0.3, 0.5, and 0.7 eV incident electron energy for m-nitro-α,α,α-trifluorotoluene.

survived autodetachment after they have traveled for a time t (time of flight) along the flight tube of a time-of-flight mass spectrometer, and N^T is the total number of ions at time $t = 0$]. The sharp decrease in τ with ϵ has been discussed by us in some detail recently.[23]

DUAL FLUORESCENCE OF AROMATIC HYDROCARBONS IN SOLUTION

The results of our investigation of dual fluorescence of aromatic hydrocarbons in solution have been summarized and discussed in two recent publications.[24,25] Our work in this area continued in an effort to describe the physical mechanisms associated with dual fluorescence of aromatic molecules in solution more quantitatively and to separate the emission from the second excited π singlet state from any possible "hot" emission from the first excited π singlet state. In this regard the dual fluorescence of 1,12-benzperylene has been studied in various solvents, including heptane, benzene, chloroform, acetone, and triethylene glycol.

---

24. C. E. Easterly, L. G. Christophorou, and J. G. Carter, *J. Chem. Soc., Faraday Trans. 2* **69**, 471 (1973).
25. C. E. Easterly and L. G. Christophorou, *J. Chem. Soc., Faraday Trans. 2* **70**, 267 (1974).

24. Theoretical Radiation Physics

R. H. Ritchie

V. E. Anderson[1] R. N. Hamm
J. C. Ashley V. N. Neelavathi[3]
W. Brandt[2] J. Neufeld[2]
T. L. Ferrell[2] H. C. Schweinler
W. R. Garrett J. E. Turner[4]
H. A. Wright

PION BEAM DOSIMETRY

The computer code PION-1, which was discussed in last year's annual report, has been further improved and used for several calculations related to the use of pions for cancer radiotherapy and also for calculations related to radiation protection.

Calculations have been made to estimate dose equivalent and average quality factors[5] for both π^+ and π^- beams typical of those currently being used in radiobiological experiments. For a π^- beam of Gaussian momentum distribution with a mean of 175 MeV/c and a spread such that one-half of the particles have momentum within 2% of the mean, it was found that the average quality factor is approximately 1.5 between the surface and a depth of 15 cm; thereafter it rises to a maximum of near 6 in the stopping region around 21 cm depth.

In planning for cancer therapy treatments using pion beams, multiple Coulomb scattering must be considered. A study has been made of different ways of treating this scattering in calculations of dose distributions due to pion beams. These calculations will give some guidance as to ways of treating multiple Coulomb scattering in simulation codes to be used for day-to-day treatment planning.

Calculations have been made of the distributions of absorbed dose in a soft-tissue phantom containing regions of bone and air. Examples of the kind of results obtained are shown in Figs. 24.1–24.4. These figures were calculated for a uniform circular beam of pions of radius 2 cm, having a Gaussian momentum distribution with a mean momentum of 153 MeV/c (corresponding to a mean range of 15 cm in soft tissue) and a 2% spread (so that one-half of the pions have momentum within 2% of the mean). Figure 24.1 shows the isodose contours that result for a homogeneous soft-tissue phantom. Figure 24.2 shows contours that result when a cylindrical region of bone (density 2 g/cm^3) of radius 0.5 cm is located on the beam axis between 1 and 6 cm in the phantom. Pions that penetrate the bone have a shorter range in the phantom. In the absence of multiple Coulomb scattering a pion would either penetrate the entire 5-cm length of bone or miss it completely. In reality, edge effects occur because some pions are scattered into or out of the region of bone. This scattering results in a complicated change of the isodose contours when Fig. 24.2 is compared with Fig. 24.1. Figure 24.3 shows isodose contours for the case of a cylindrical bone region of 1 cm radius. Figure 24.4 shows results for a 0.5-cm-radius cylindrical region of air embedded in the phantom. Inhomogeneities are very important in planning radiotherapy treatments for cancer.

The computer code PION-1 has been modified to include the cell-survival model of Katz.[6] Calculations have been made[7] of the survival of T-1 kidney cells as a

1. On loan from Mathematics Division, ORNL.
2. Consultant.
3. Graduate student.
4. Also Associate Director, Health Physics Division, ORNL.
5. H. A. Wright, R. N. Hamm, and J. E. Turner, to be published in *Health Physics*.
6. R. Katz, B. Ackerman, M. Homayoonfar, and S. C. Sharma, *Radiat. Res.* 47, 402 (1971).
7. H. A. Wright, R. N. Hamm, and J. E. Turner, "Dose, Dose Equivalent, Effected Dose and Cell Survival from Negative Pions," to be published in *Proceedings of Third International Congress of IRPA, Washington, D.C., Sept. 9–14, 1973.*

ORNL-DWG 74-6668

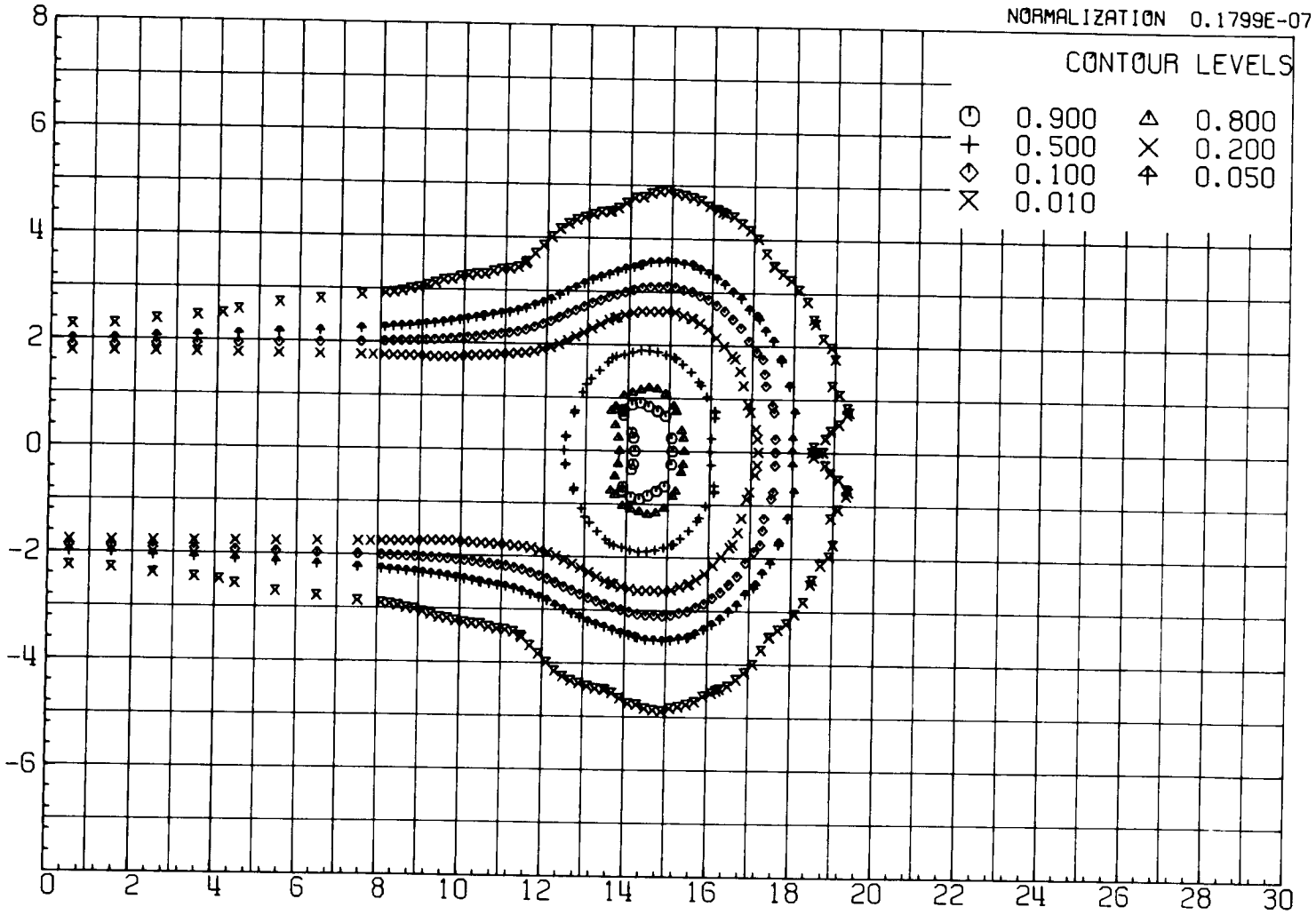

Fig. 24.1. Isodose contours in a homogeneous soft-tissue phantom irradiated by a uniform circular negative pion beam of radius 2 cm. Mean momentum is 153 MeV/c, and the momentum spread is 2%.

ORNL-DWG 74-6434

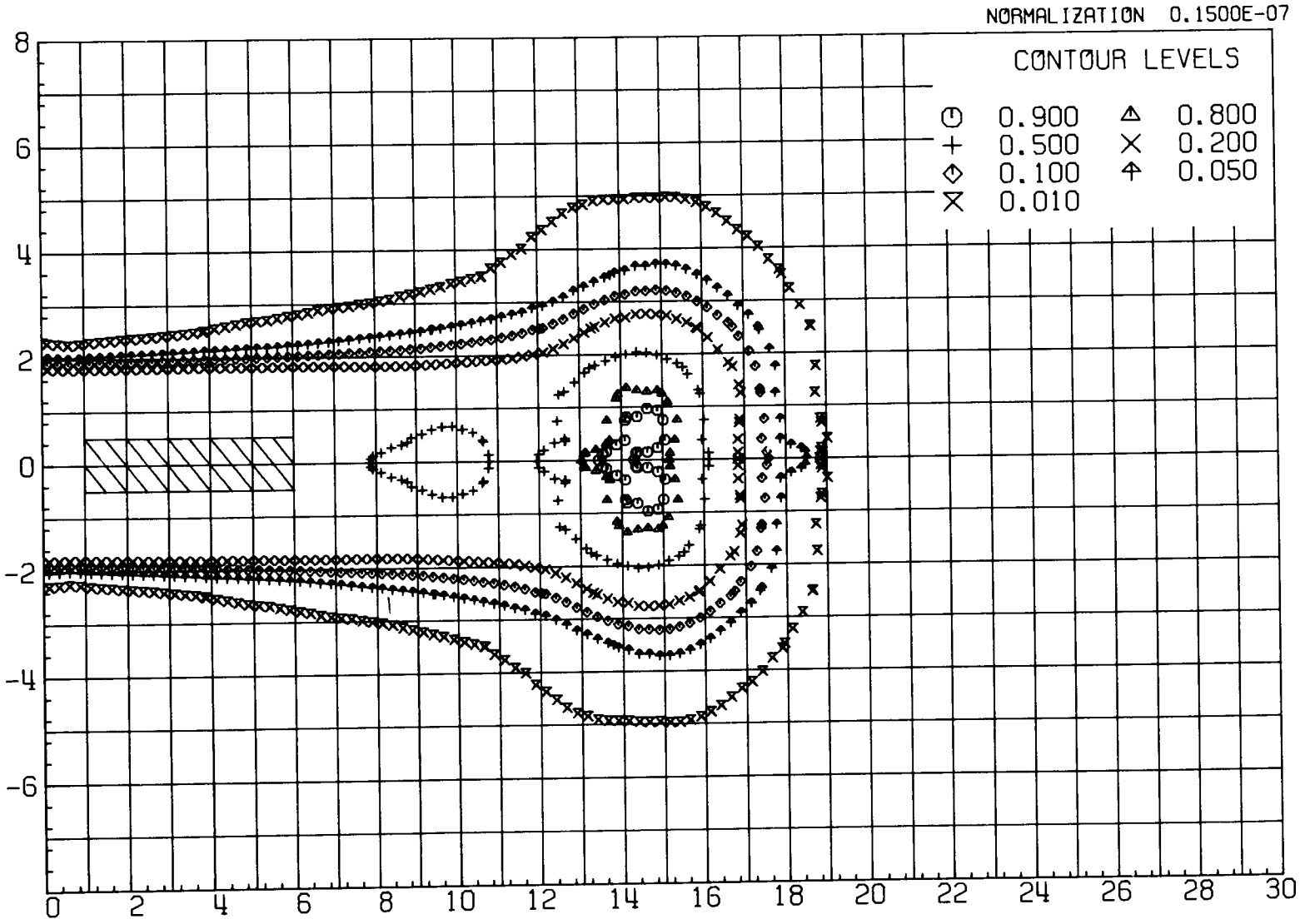

Fig. 24.2. Isodose contours in a tissue phantom containing a cylindrical region of bone (density, 2.0 g/cm^3) of radius 0.5 cm and length 5 cm along the axis of the beam. The beam is the same as in Fig. 24.1.

ORNL-DWG 74-6432

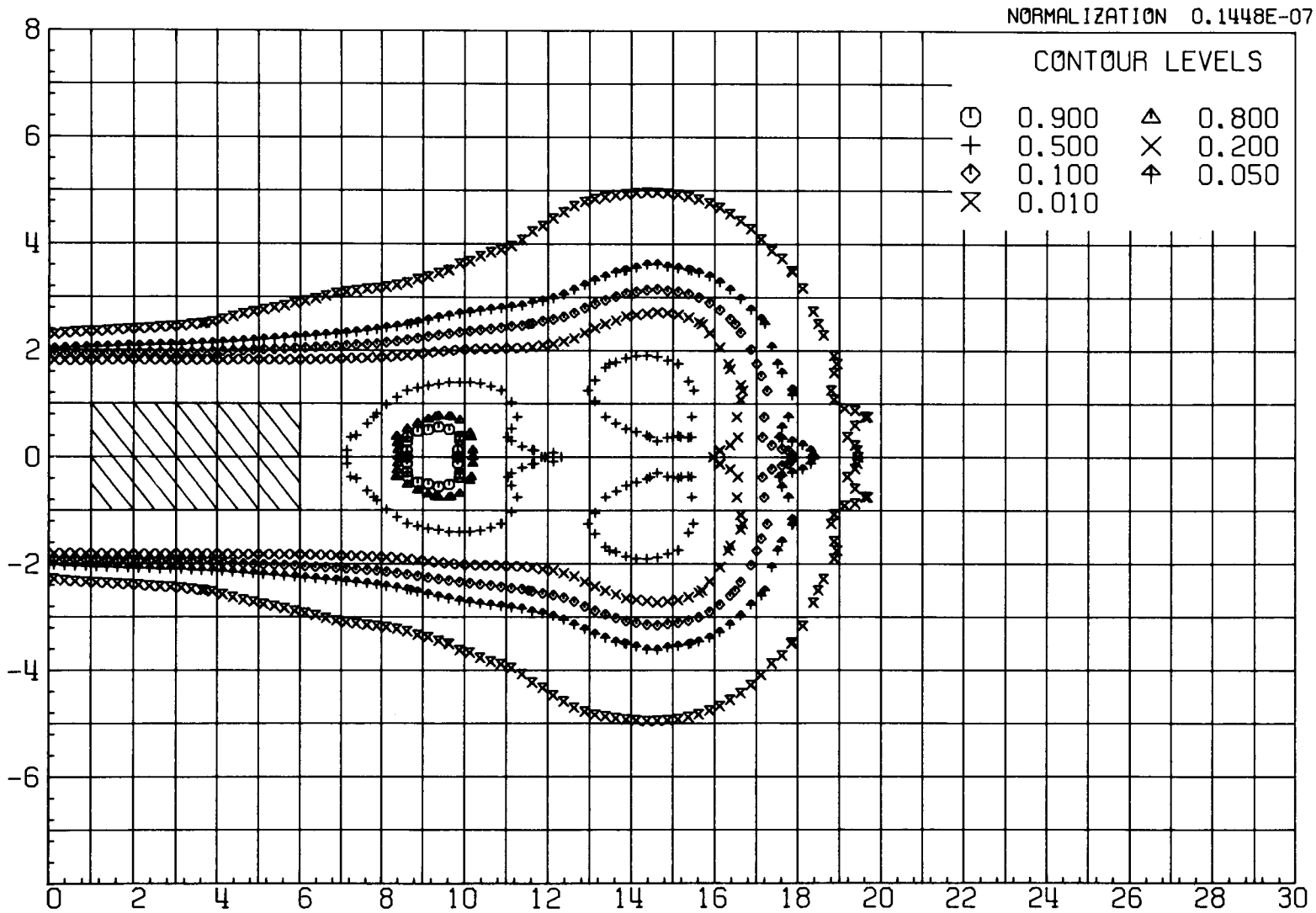

Fig. 24.3. Isodose contours similar to Fig. 24.2 but with the region of bone having radius of 1 cm.

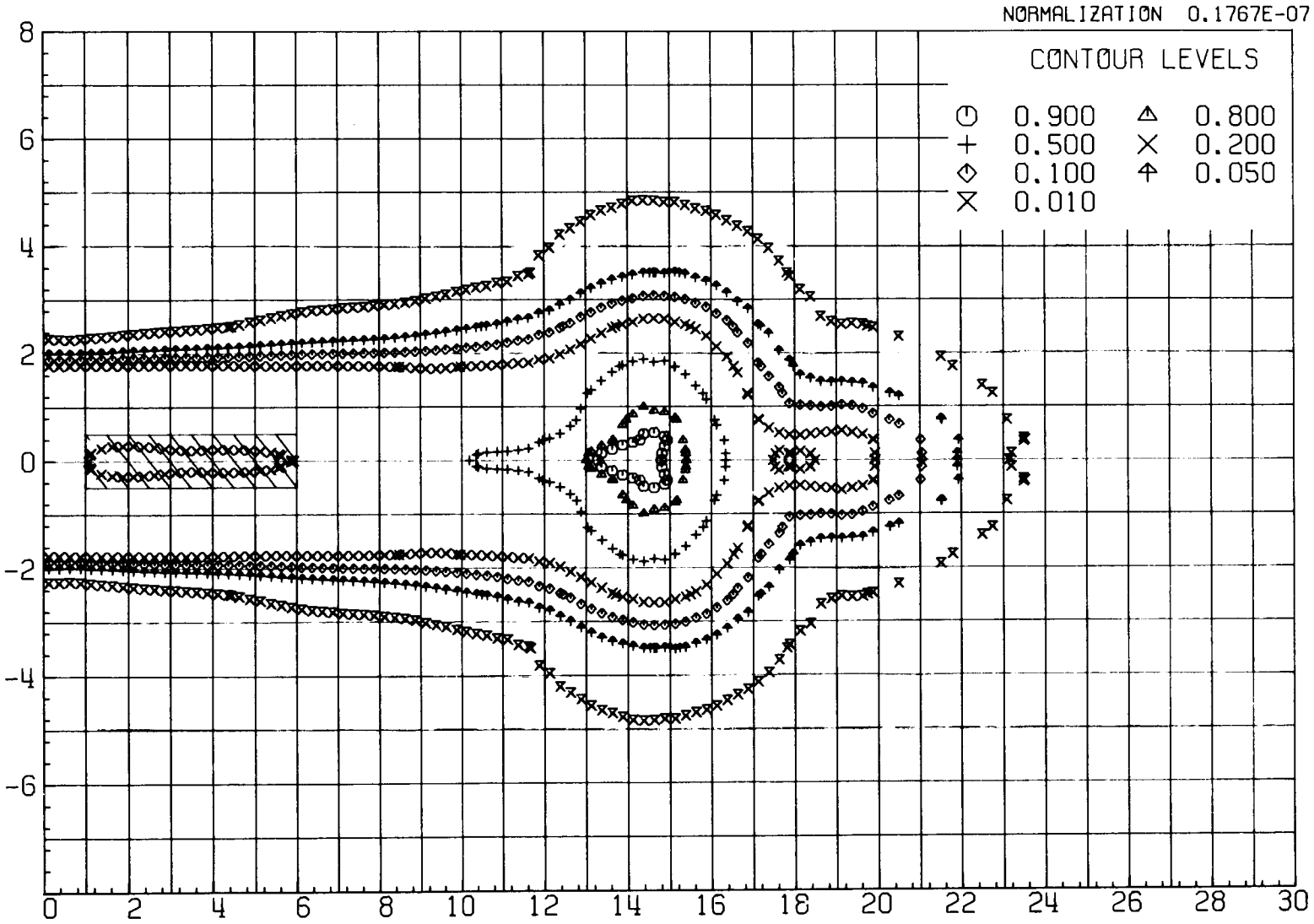

Fig. 24.4. Isodose contours similar to Fig. 24.2 but with the bone replaced by air of the same volume and dimensions.

function of position in a tissue phantom irradiated by a pion beam. The cell survival estimated by using the model of Katz is compared with that obtained by weighting the dose contributions of various secondary particles by experimentally determined values of relative biological effectiveness (RBE) as a function of linear energy transfer (LET).

CONVERSION FACTORS FOR ESTIMATING DOSE AND DOSE EQUIVALENT FROM ^{11}C ACTIVATION

Monitoring of areas for high-energy radiation can be accomplished by using plastic scintillators and subsequently counting the resulting ^{11}C activity. However, the conversion factors necessary to estimate absorbed dose and dose equivalent from the ^{11}C activity are not well known. Some preliminary calculations have been made of the ^{11}C activity in plastic scintillator disks placed at various depths in a water phantom irradiated by a beam of neutrons having an energy spectrum (maximum energy 400 MeV) similar to that used in an experiment at CERN. Figure 24.5 shows the calculated (absolute) and experimentally measured (relative) ^{11}C activity as a function of depth. There appears to be good agreement between the shape of the theoretical and experimental curves. Some preliminary conversion factors have been obtained for estimating dose and dose equivalent from ^{11}C activity. For a plastic cylinder of mass 1250 g irradiated by neutrons of energies 100, 250, and 400 MeV, the conversion factors in rems per ^{11}C activation per gram were found to be 5.2×10^{-5}, 5.5×10^{-5}, and 5.8×10^{-5} respectively.

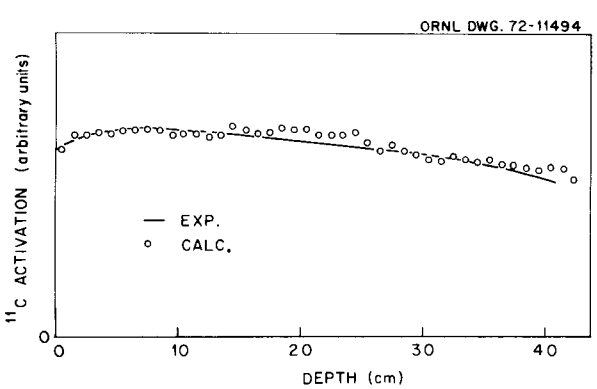

Fig. 24.5. Carbon-11 activation in a plastic scintillator disk as a function of depth in a water phantom irradiated with a beam of neutrons having an energy spectrum between 50 and 400 MeV. The solid line is the experimental result obtained at CERN, and the circles are calculated values.

COMMENTS ON THE THEORY OF RADIATION RISK

A systematic outline of a theory of radiation risk has been presented.[8] The most basic ideas of the theory can be expressed by two quantities that represent the administrative approach to radiation risk. These quantities are "specific dose," D_s, which relates to individual organs or tissues, and "overall dose," D_o, which relates to the entire human body. By taking D_s and D_o as a starting point and by using postulational methods, two auxiliary quantities, "dose equivalent," $D_e(\mathbf{r})$, and quality factor, Q, have been derived. Dose equivalent, $D_e(\mathbf{r})$, is a macroscopic field quantity and is therefore different from the ICRP-defined dose equivalent H, which is microscopic. An experimental program and a computational program have been outlined for obtaining a relationship between Q and linear energy transfer L. It has been shown that, by applying Monte Carlo procedures, one can determine distributions of L in critical organs of animals exposed to ionizing radiations. Then, by using biological data for critical effects (extrapolated from high radiation levels to presumed effects at low levels), sets of linear equations can be obtained in which the coefficients are the doses delivered in intervals of L and the unknowns are "biological weighting factors," λ. From these equations one can derive λ's for various L's as they relate to critical effects in animals. Then, using value judgment and combining the calculated results with data observed on men, one can obtain a Q-L relationship which is more directly based on experimental evidence than that which is currently used.

TWO-COMPONENT MODELS OF CELLULAR SURVIVAL

The "two-component" models for estimating the survival of irradiated mammalian cells in proliferating cell cultures have been critically examined.[9] These models approximate cellular survival empirically in terms of two mechanisms: (1) an irreversible mechanism in which a single event produces a fatal lesion, excluding any possibility of recovery, and (2) a reversible mechanism in which sublethal damage results from a single event but the cumulative effect of more than one such event can produce cell death. Three separate

8. Jacob Neufeld, *Health Phys.* **26**, 229 (1974).

9. Jacob Neufeld, H. A. Wright, and R. N. Hamm, "A Comparison of Two-Component Models of Cellular Survival," to be published in *Proceedings of Fourth Symposium on Microdosimetry, Verbania, Italy, Sept. 24–28, 1973.*

two-component models, independently formulated, have been examined from the point of view of their prognostic ability in determining cell survival after irradiation.

MATHEMATICAL ANALYSES OF CELL SURVIVAL MECHANISMS

A research effort between members of the Fundamental Health Physics Research and the Radiation Research and Development Sections of the Health Physics Division is continuing in the area of theoretical studies of radiation-stimulated biological effects. Some of the results of this effort are described in Part IV, Chap. 27.

MOLECULAR SCATTERING: CONVERGENCE OF CLOSE-COUPLING EXPANSIONS IN THE PRESENCE OF MANY OPEN CHANNELS

In low-energy atomic scattering theory, it is well known that the accuracy of the familiar target-eigenstate-expansion or "close-coupling" methods cannot be relied upon unless all open channels of the target system are included in the expansion. We show that the same methods, as applied to low-energy scattering by a molecular target, converge even though all open channels above a certain energy level may be truncated in the target eigenstate expansion.

The convergence properties of certain expressions for total molecular scattering cross sections were discussed recently[10] in the limit of an infinite number of open rotational channels (infinite moment of inertia). It was shown that the limiting case yields an infinite cross section for molecules possessing a long-range electric dipole potential. In molecular scattering problems, one is almost always forced to deal with situations in which a number of inelastic channels are open, since the thresholds for rotational excitation are so extremely low in energy. With increasing molecular size the number of open channels at a given energy and, often, the number which are effectively coupled to a given channel increase. For low-energy collisions in atomic and molecular scattering phenomena, one of the most powerful and useful theoretical methods for obtaining detailed cross-section information is the target-eigenstate-expansion or close-coupling method.[11] It is well established that, in the application of the usual close-coupling method to low-energy atomic scattering, one cannot show that the inclusion of a few more open channels in the resulting coupled equations will make a contribution less than an arbitrary epsilon in the cross sections for the other open channels to which they are coupled.[12] We show that the opposite is true for low-energy molecular scattering below the thresholds for vibrational and electronic excitation channels, even in the presence of long-range dipolar fields.

For simplicity, consider the scattering of a structureless particle by a diatomic[13] molecule. We ignore vibrational and electronic degrees of freedom in the closed channels and write the Hamiltonian of the system as

$$\underline{H} = T_R - \frac{\hbar^2}{2M} \nabla_r^2 + V(\mathbf{r}, \mathbf{s}) . \tag{1}$$

The target rotational Hamiltonian, T_R, has eigenfunctions

$$T_R \; Y_j^{m_j}(\hat{s}) = \frac{\hbar^2}{2I} j(j+1) \, Y_j^{m_j}(\hat{s}) , \tag{2}$$

where $\hat{s} \equiv (\theta', \varphi')$ specifies the orientation of the internuclear axis with respect to space-fixed axes and $j\hbar$ is the rotational angular momentum of the molecule. $V(\mathbf{r}, \mathbf{s})$ is the interaction between the target and the projectile at (r, θ, φ), and M is the reduced mass of the system. The target-eigenstate-expansion method for low-energy molecular collisions was thoroughly treated by Arthurs and Dalgarno[14] and has been used in many studies of such phenomena. Briefly, the total wave function, $\Psi_j^{JM}(\mathbf{r}, \hat{s})$, for the system which has initial rotational quantum number j and angular momentum l of the incident particle coupled to give total angular momentum J is expanded in the form

$$\Psi_{jl}^{JM}(\mathbf{r}, \mathbf{s}) = \sum_{j'} \sum_{l'} Y_{j'l'}^{JM}(\hat{r}, \hat{s}) \, U_{j'l'}^{Jjl}(r)/r . \tag{3}$$

The use of this expression in the time-independent Schroedinger equation,

$$\left[T_R - \frac{\hbar^2}{2M} \nabla_r^2 + V(\mathbf{r}, \mathbf{s}) \right] \Psi_{jl}^{JM}(\mathbf{r}, \hat{s}) = E_j \, \Psi_{jl}^{JM}(\mathbf{r}, \hat{s}) , \tag{4}$$

10. W. R. Garrett, *Phys. Rev. A* **4**, 2229 (1971).

11. See, for example, Kenneth Smith, *The Calculations of Atomic Collision Processes*, Wiley-Interscience, New York, 1971, Chap. 2.

12. P. G. Burke, *Proc. Phys. Soc.* (London) **82**, 443 (1963).

13. The results may easily be generalized to include symmetric top molecules.

14. A. M. Arthurs and A. Dalgarno, *Prof. Roy. Soc. London*, Ser. A **256**, 540 (1960).

gives the familiar set of close-coupling equations:

$$\frac{\hbar^2}{2M}\left[-\frac{d^2}{dr^2}+\frac{l'(l'+1)}{r^2}-k_{j'j}{}^2\right]U_{j'l'}{}^{Jjl}(r)$$

$$+\sum_{j''l''}\langle j''l'';J|V|j'l':J\rangle\, U_{j''l''}{}^{Jjl}(r)=0\,. \qquad (5)$$

The channel wave number $k_{j'j}$ is given by

$$k_{j'j}{}^2=\frac{2M}{\hbar^2}\left[E_j-\frac{\hbar^2}{2I}j'(j'+1)\right] \qquad E_j>\hbar^2 j'(j'+1)/2I\,,$$

$$k_{j'j}{}^2=\frac{2M}{\hbar^2}\left[\frac{\hbar^2}{2I}j'(j''+1)-E_j\right] \qquad E_j<\hbar^2 j'(j'+1)/2I\,,$$

and

$$\langle j''l'';J|V|j'l':J\rangle=\iint Y_{j''l''}{}^{JM*}\,V\,Y_{j'l'}{}^{JM}\,d\hat{r}\,d\hat{s}\,. \qquad (6)$$

The functions $Y_{jl}{}^{JM}(\hat{r},\hat{s})$ are coupled spherical harmonics[15] which are eigenfunctions of J^2 and J_z.

Now consider the partial cross section for scattering in a particular open channel j (and all other open channels j' of lower energy). We wish to establish the effect of higher-energy *open* channels, $j''>j$, on the cross sections in channels of energy $E_{j'}\leqslant E_j$.

Consider the elastic and the first few inelastic channels above the ground state, say up to channel n. We write the $n+1$ channel wave functions $U_0{}^J, U_1{}^J, \ldots, U_n{}^J$ as a column matrix

$$\underline{\Phi}_0{}^J=\begin{pmatrix}U_0{}^J\\ U_1{}^J\\ \vdots\\ U_n{}^J\end{pmatrix} \qquad (7)$$

and all remaining components as

$$\underline{\Phi}_c{}^J=\begin{pmatrix}U^J{}_{n+1}\\ U^J{}_{n+2}\\ \vdots\end{pmatrix}\,. \qquad (8)$$

15. A. R. Edwards, *Angular Momentum in Quantum Mechanics*, Princeton University Press, Princeton, N.J., 1960.

We then define the matrix operator $\underline{H}$ as

$$(\underline{H}_0)_{pq}=\frac{\hbar^2}{2M}\left[-\frac{d^2}{dr^2}+\frac{l'(l'+1)}{r^2}-k^2{}_{j'j}\right]\delta_{pq}+V_{pq}\quad p,q\leqslant n\,, \qquad (9)$$

$$(\underline{H}_c)_{pq}=\frac{\hbar^2}{2M}\left[-\frac{d^2}{dr^2}+\frac{l'(l'+1)}{r^2}-k^2{}_{j'j}\right]\delta_{pq}+V_{pq}\quad p,q>n \qquad (10)$$

and the potential matrices:

$$\underline{V}(0,0)=\begin{pmatrix}V_{00} & V_{01} & \cdots & V_{0n}\\ V_{10} & V_{11} & \cdots & \cdot\\ \vdots & & & \\ V_{n0} & V_{n1} & \cdots & V_{nn}\end{pmatrix}\,, \qquad (11)$$

$$\underline{V}(0,c)=\begin{pmatrix}V_{0,n+1} & V_{0,n+2} & \cdots\\ V_{1,n+1} & V_{1,n+2} & \cdots\\ \vdots & \vdots & \\ V_{n,n+1} & V_{n,n+2} & \end{pmatrix}\,. \qquad (12)$$

With this new notation the coupled equations (5) become

$$[\underline{H}_0-\underline{E}]\,\underline{\Phi}_0{}^J=-\underline{V}(0,c)\,\underline{\Phi}_c{}^J\,, \qquad (13)$$

$$[\underline{H}_c-\underline{E}]\,\underline{\Phi}_c{}^J=-\underline{V}_c{}^\dagger(c,0)\,\underline{\Phi}_0{}^J\,. \qquad (14)$$

Our objective now is to determine the convergence properties of the coupled equations as the number of open-channel terms in $\underline{\Phi}_c{}^J$ is increased (j_m increased). For this purpose, we first solve Eq. (14) formally for $\underline{\Phi}_c{}^J$ and eliminate $\underline{\Phi}_c{}^J$ from Eq. (13). Thus

$$\underline{\Phi}_c{}^J=\frac{1}{\underline{E}-\underline{H}}\,\underline{V}^\dagger(c,0)\,\underline{\Phi}_0{}^J\,. \qquad (15)$$

The set of equations (5) for the channels of interest, $i=0,\ldots,n$, thus becomes

$$\left[\underline{H}_0+\underline{V}(0,c)\frac{1}{\underline{E}-\underline{H}_c}\,\underline{V}^\dagger(c,0)-\underline{E}\right]\underline{\Phi}_0{}^J=0\,. \qquad (16)$$

The middle term in Eq. (16) is of the form of the optical potential expression of Feshbach.[16] It is convenient to evaluate this expression in terms of the eigenvalues of $\underline{H}_c$. Thus we define

$$\underline{H}_c \underline{\gamma}_m{}^J = \epsilon_m \underline{\gamma}_m{}^J \tag{17}$$

for the discrete states and

$$\underline{H}_c \underline{\gamma}_\epsilon{}^J = \epsilon \underline{\gamma}_\epsilon{}^J \tag{18}$$

for the continuum part of the spectrum of $\underline{H}_c$. The column matrices $\underline{\gamma}_m{}^J$ have radial components $g_i^m(r)$ as defined above for $\underline{\Phi}$:

$$\underline{\gamma}_m{}^J = \begin{pmatrix} g^m{}_{n+1} \\ g^m{}_{n+2} \\ \vdots \end{pmatrix} . \tag{19}$$

In this representation the expression for the optical potential becomes:

$$\begin{aligned} V_{\text{opt}} &= \underline{V}(0, c) \frac{1}{\underline{E} - \underline{H}_c} \underline{V}^\dagger(c, 0) \\ &= \sum_i \frac{\underline{V}(0, c)\, \underline{\gamma}_j{}^J \rangle \langle \underline{\gamma}_j{}^J\, \underline{V}^\dagger(c, 0)}{E - \epsilon_i} \\ &\quad + \int_{\epsilon_n} \frac{d\epsilon\, \underline{V}(0, c)\, \underline{\gamma}_\epsilon{}^J \rangle \langle \underline{\gamma}_\epsilon{}^J\, \underline{V}^\dagger(c, 0)}{E - \epsilon} . \end{aligned} \tag{20}$$

In the absence of the optical potential term in Eq. (16), the coupled equations for the lowest n components of the expansion coefficient U_j^J, represented by the n-dimensional column matrix $\underline{\Phi}_c{}^J$, are just the familiar close-coupling equations that are encountered when the eigenstate expansion is truncated to n terms. The optical potential represents the contribution to the total scattering interaction which is contributed by all the additional open and closed channels not included in the set n.

From the defining equations for $\underline{\gamma}_\epsilon$ and $\underline{V}(0, c)$, one can show that contributions to the optical potential from higher excited states of the target system converge rapidly due to the fact that each rotationally excited state is defined by a higher angular momentum, j, which implies higher orbital angular momentum, l, since $j + l = J$. This is in contrast to electronic excitations, where an infinite series of states exist for $l = 0, 1, \ldots$, etc. Thus, for low-energy molecular collision phenomena where vibrational and electronic excitation channels are closed, the powerful close-coupling method can give reliable results even in the presence of open channels that are truncated in the eigenstate expansion.

SCATTERING OF ELECTROMAGNETIC WAVES BY A CYLINDER

The theoretical treatment of the scattering of electromagnetic waves normally incident on a cylinder of infinite length has a long history, but it is only relatively recently that the case of nonnormal angles of incidence has been developed.[17] Our interest was drawn to this problem by the results of an experiment by Miziumski[18] on the reflection of a laser beam (6328 Å) from an aluminum cylinder at small angles from the cylinder axis. The reflected intensity, measured as a function of the angle of incidence, exhibited dips which were attributed, on the basis of a very simple theory, to the excitation of surface plasmons on the cylinder.

We are exploring this question of surface-plasmon excitation in some detail using the full treatment for scattering of electromagnetic waves at oblique angles of incidence from a cylinder. The rather complicated expressions in ref. 17 for the scattering coefficients have been programmed for machine computation. The program is designed to calculate the differential scattering efficiency, differential scattering probability, total scattering efficiency, and the extinction coefficient for an arbitrary angle of incidence of either s- or p-polarized electromagnetic waves. These quantities are functions of the angle of incidence, position of the observation point, polarization and frequency of the incident field, dielectric functions of the cylinder and the surrounding medium, and the cylinder radius. Partial checks on the correctness of the computational program have been made with available normal-incidence calculations. The routines for calculating the required Bessel functions limit the calculations to real dielectric functions for the cylinder and the surrounding medium; the extension to complex dielectric functions is needed. Further work is aimed at including routines to calculate certain Bessel functions of large order and large argument in order to perform calculations for comparison with the experimental work of

16. H. Feshbach, *Ann. Phys.* (New York) **5**, 357 (1958).

17. J. R. Wait, *Can. J. Phys.* **33**, 189 (1955).

18. C. Miziumski, *Phys. Lett. A* **40**, 187 (1972).

Miziumski. In addition, this work should help in a theoretical understanding of the properties of radiative surface plasmons for a cylindrical surface.

X-RAY EXCITATION OF SURFACE PLASMONS ON SPHERES AND CYLINDERS

Our interest in the properties of surface plasmons and their manifestation in the interaction of charged particles and photons with matter has continued. We have been particularly interested during the last year in the process of surface-plasmon excitation in x-ray inelastic scattering on spherical and cylindrical particles.

The theoretical calculations for small spherical particles were prompted by the experimental work of Koumelis et al.[19] on the inelastic scattering of x rays from colloidal graphite particles, where the energy loss of the photon was attributed to surface-plasmon excitation. We consider a system composed of small spheres distributed at random in a dielectric medium. The number of spheres per unit volume is assumed to be so small that the scattering from each sphere is not influenced by the presence of the other spheres. The theoretical calculation then reduces to the calculation of the cross section for x-ray inelastic scattering from a single spherical particle.

The model chosen to represent the response of the sphere to perturbations is the classical free-electron gas treated in the hydrodynamical approximation.[20] For the case of x-ray photons with frequency much greater than the plasma frequency, the interaction Hamiltonian is given by

$$V' = \frac{e^2}{2mc^2} \int d^3r\, n(\mathbf{r})\, \mathbf{A}(\mathbf{r}) \cdot \mathbf{A}(\mathbf{r}) \,, \tag{21}$$

where $\mathbf{A}(\mathbf{r})$ is the vector potential of the photon field and $n(\mathbf{r})$ is the hydrodynamic density fluctuation operator for the electron gas in the sphere. For a sphere of radius r_0 embedded in a medium with dielectric constant ϵ_0, we find that

$$n(\mathbf{r}) = -\frac{\delta(r - r_0)}{4\pi e} \sum_{l,m,p} \left\{ \frac{2\pi\hbar\omega_l}{[\epsilon_0(l+1)+l]\, r_0^{\,3}} \right\}^{1/2} \times (2l+1)\, Y_{lmp}(\theta, \varphi)\, (b_{lmp} + b^{\dagger}_{lmp}) \tag{22}$$

in a spherical coordinate system with origin at the center of the sphere. The delta function $\delta(r - r_0)$ indicates that density fluctuations occur only on the surface of the sphere. The Y_{lmp}'s are real spherical harmonics; b_{lmp} ($b^{\dagger}_{lmp}$) is the annihilation (creation) operator for the l, m, p surface-plasmon state with a frequency ω_l which depends only on the integer l ($\geqslant 1$) through the equation

$$\omega_l^{\,2} = l\omega_p^{\,2} / [\epsilon_0(l+1) + l] \,, \tag{23}$$

with ω_p the plasma frequency for the electron gas.

The cross section can now be calculated by using standard methods of quantum mechanics. We find the differential cross section $d\sigma_l/d\Omega$ for exciting a surface plasmon of energy $\hbar\omega_l$ by scattering photons into the solid angle $d\Omega$ about the direction of the incident photon beam, for an unpolarized incident beam, to be given by

$$\frac{d\sigma_l}{d\Omega} = \frac{1}{4}\alpha^3 a_0^{\,2} \frac{r_0\omega_l}{c} \frac{(2l+1)^3}{\epsilon_0(l+1)+l} \times j_l^{\,2}(kr_0)\,(1 + \cos^2\theta) \,. \tag{24}$$

Here k is the momentum transfer to the sphere (in units of $\hbar$), $\alpha \equiv e^2/\hbar c$, $a_0 \equiv \hbar^2/me^2$, and j_l is the spherical Bessel function of order l. For a target composed of spheres of radius r_0 distributed at random, with a small average number density N, in a dielectric medium of thickness a along the incident beam direction, the differential scattering probability is given by

$$\frac{dP_l}{d\Omega} = Na\frac{d\sigma_l}{d\Omega} \,. \tag{25}$$

There seem to be no experimental data available in the literature from which cross sections comparable with those derived here may be inferred. It is hoped that further experimental work will be done so that x-ray inelastic scattering with surface-plasmon excitation may be studied in detail. A complete description of the theoretical work outlined here is to be published in *The Physical Review*.[21]

The calculation of surface-plasmon excitation on a cylinder in x-ray inelastic scattering proceeds with the same general scheme as outlined above for the case of a sphere. The details of this calculation are being prepared for publication.

19. C. Koumelis, D. Leventouri, and K. Alexopoulos, *Phys. Status Solidi B* **46**, K89 (1971); C. Koumelis and D. Leventouri, *Phys. Rev. B* **7**, 181 (1973).

20. See, for example, R. H. Ritchie and R. E. Wilems, *Phys. Rev.* **178**, 372 (1969).

21. J. C. Ashley, T. L. Ferrell, and R. H. Ritchie, *Phys. Rev.*, in press.

DISPERSION RELATIONS OF COLLECTIVE STATES WHEN DAMPING IS PRESENT

The topic entitled "Effect of Damping on Surface Plasmon Dispersion" is treated in Chap. 21 of this report. A discussion is given there of experimental work which demonstrates that the dispersion relation of the surface plasmon, when inferred from certain optical measurements, may be radically different from that deduced from electron energy loss determinations. The reason for this difference is discussed briefly there; the effect of damping on dispersion of a general collective state is considered here.

The term "dispersion relation" in electromagnetic theory, in solid-state physics, and in the physics of plasmas has come to signify a relation specifying the dependence of ω, the eigenfrequency (or energy) of a wave, a particle, or an elementary excitation, on k, its wave vector (or momentum).

Quite generally, the dispersion relation of, for example, an elementary excitation in a solid may be obtained by studying the poles of the propagator, or Green function, of the excitation in energy-momentum representation. Such a procedure is quite straightforward in case the elementary excitation is only weakly damped and thus is a well-defined "particle" rather than a "resonance," to use a term from elementary particle physics.

When damping is appreciable, a dispersion relation $\omega = \omega(k)$ for real k may have complex solutions in which the imaginary part is comparable in magnitude with the real part. Conversely, if ω is taken to be real, k may be complex. Although straightforward in a theoretical framework, there may be some ambiguity about the significance of complex values of ω or of k in the interpretation of experiment.

Requiring k to be real and allowing ω to be complex is appropriate to a situation where the spatial dependence of a field is specified but its amplitude is allowed to decay as time increases. Conversely, requiring ω to be real and allowing k to be complex is appropriate to a situation where a system is perturbed at a fixed frequency and consequently can decay in space.

In experimental situations, it may be difficult to observe temporal or spatial decay of a resonance due to the rapidity of its temporal decay or due to the smallness of the region over which spatial decay occurs respectively. Then it may be necessary to infer the properties of such excitations from experiments involving the use of probes which impart energy and momentum to the system and involve, then, both real ω and real k. Such inference may be difficult when damping is large.

Zeros of the $D(k, \omega)$ Relation

Suppose that the denominator of the Green function for a given excitation contains a factor $D(k, \omega)$, the zeros of which correspond to the energy-momentum (dispersion) relation for this excitation.

In general, the relation $D(k, \omega) = 0$ describes a connection between complex $\omega = \omega_1 + i\omega_2$ and a complex $k = k_1 + ik_2$. To illustrate the qualitative difference between the ω vs k relationships obtained (1) when ω is chosen real and (2) when k is real, we display, in Fig. 24.6, curves calculated for the different assumptions 1 and 2. We have taken $D(k, \omega) = \eta\epsilon + \nu$, where $\eta = (k^2 - \omega^2/c^2)^{1/2}$, $\nu = (k^2 - \epsilon\omega^2/c^2)^{1/2}$. The free-electron model for the dielectric function $\epsilon = 1 - \omega_p{}^2/[\omega(\omega + ig)]$ with $\hbar\omega_p = 15$ eV and $g/\omega_p = 0.0514$ is used. This is the condition for the existence of surface plasmons at a plane interface between an electron gas and a medium of unit dielectric permittivity. The curves labeled k_1 and k_2 correspond to real ω (case 1), while those labeled ω_1 and ω_2 were computed for real k.

Response Functions

To illustrate how dispersion relations manifest themselves in different experiments, we have displayed two different response functions in Figs. 24.7 and 24.9.

Figure 24.7 shows a representation of $g(k, \omega) \equiv \mathrm{Im}[-1/(\epsilon\eta + \nu)]$ in the ω-k plane. This is the important factor in the function describing energy loss to surface plasmons by normally incident fast electrons. The solid

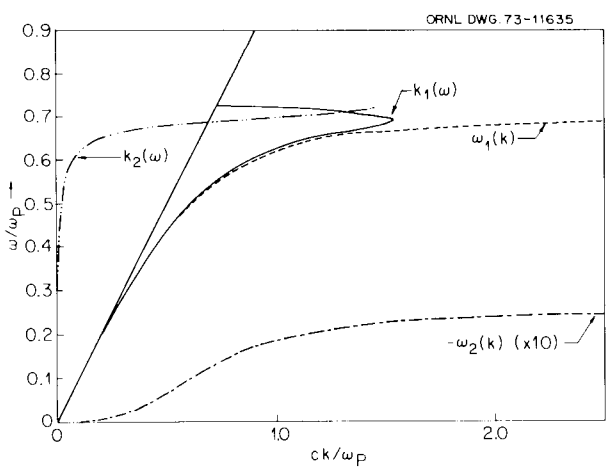

Fig. 24.6. Dispersion curves relating to the surface plasmon on a plane surface of aluminum metal. $\omega(k) = \omega_1(k) + i\omega_2(k)$ is the complex frequency which satisfies the relation $D(k, \omega) = \epsilon\eta + \nu = 0$ when k is constrained to be real. The quantities η, ν, and ϵ are defined in text. $k(\omega) = k_1(\omega) + ik_2(\omega)$ is a complex solution of the same equation when ω is real.

ORNL DWG. 73-10965

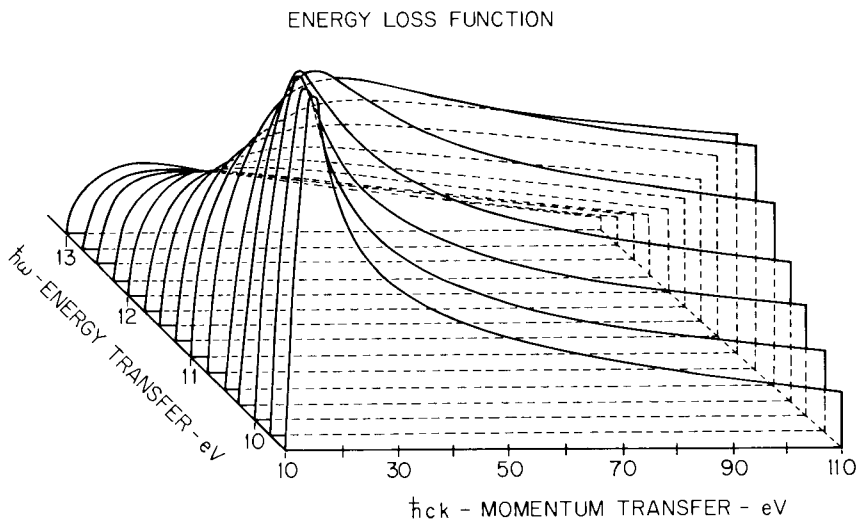

Fig. 24.7. Representation of a function $g(k, \omega) = \mathrm{Im}\ [-1/(\epsilon\eta + \nu)]$ related to the probability that a fast electron shall lose energy $\hbar\omega$ and momentum $\hbar ck$ to the surface-plasmon field.

curves show $g(k, \omega)$ vs $\hbar ck$ for various values of $\hbar\omega$, again calculated using the electron gas model. A logarithmic scale is used to display values of $g(k, \omega)$ on the vertical axis for easy visibility. Consider the points at which $g(k, \omega)$ has maximum values as k is varied and ω is kept fixed. If the locus of these points is plotted in the ω-k plane, as in Fig. 24.8, curve A, one sees that the resulting "energy-fixed" ω-vs-k curve is similar to the dispersion curve $k_1(\omega)$ of Fig. 24.6 for the case where ω is assumed to be real and k is allowed to be complex.

On the other hand, if in Fig. 24.7 one looks for maxima in $g(k, \omega)$ as ω is varied while k is kept constant, one finds that the locus of maximum points (the "momentum fixed" curve) is quite different from the locus of maxima when k is varied while ω is fixed but is not dissimilar to the dispersion curve $\omega_1(k)$ displayed in Fig. 24.6. The momentum-fixed ω-vs-k curve is plotted in Fig. 24.8, curve B.

Figure 24.9 shows an isometric representation of a response function surface $\tilde{R}(k, \omega)$ for the case where photons are incident from a transparent dielectric medium with dielectric permittivity $\epsilon_0 > 1$ on a thin metallic film with thickness d in contact with the dielectric. The film is assumed to be bounded on the other side by a medium having unit dielectric permittivity. We have taken $\tilde{R}(k, \omega) = 1 - R(\vartheta_0, \omega)$, where R is the reflectance of this system for photons incident from the dielectric but plotted against the angle ϑ_0.

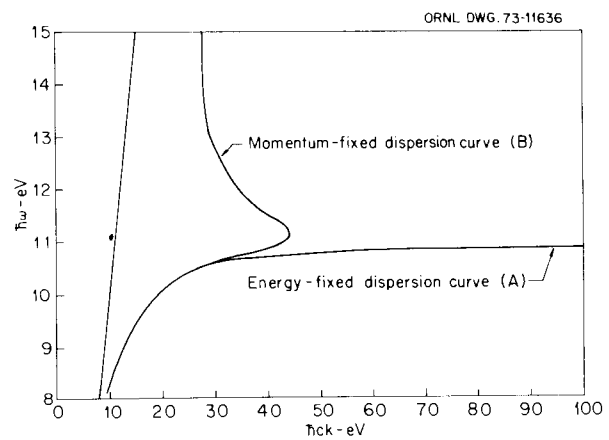

Fig. 24.8. Dispersion curves inferred from the data shown in Fig. 24.7. Curve A is the locus of maxima in the function $g(k, \omega)$ as k is varied with ω held constant. Curve B is the locus of maxima in $g(k, \omega)$ as ω is varied with k held constant.

The wave number, k, for photons incident at an angle ϑ_0 relative to the film normal is equal to $(\epsilon_0{}^{1/2}\ \omega \sin \vartheta_0)/c$, where ϵ_0 is taken to be that for sapphire.

As in the case of the response function displayed in Fig. 24.7, different dispersion relations may be derived from these data depending on which variable is held constant while the maximum is found. Figure 24.10 shows both the energy-fixed dispersion curve (curve A)

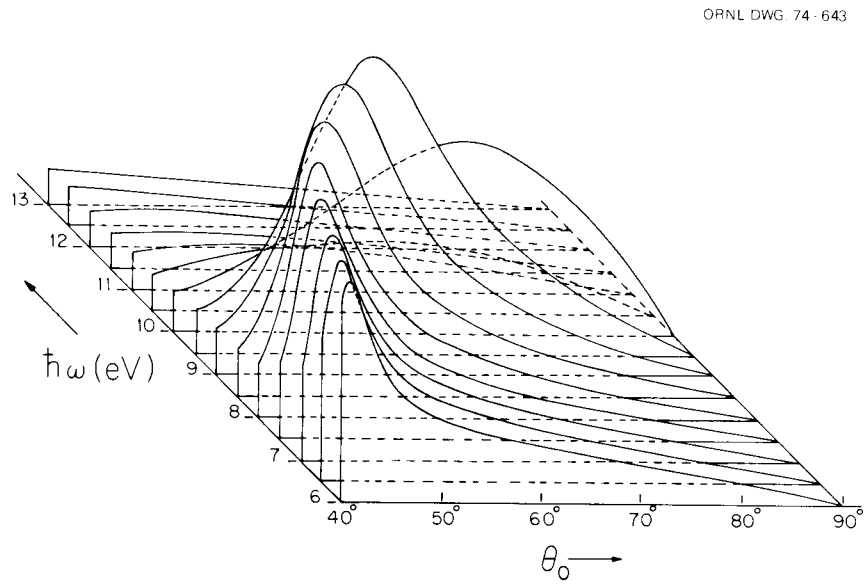

Fig. 24.9. Representation of the reflectance $\tilde{R}(\theta_0, \omega)$ of a thin aluminum foil deposited on a sapphire substrate for p-polarized light incident from the dielectric. The angle of incidence is θ_0 relative to the foil normal. The photon energy $\hbar\omega$ is held constant as θ_0 is varied.

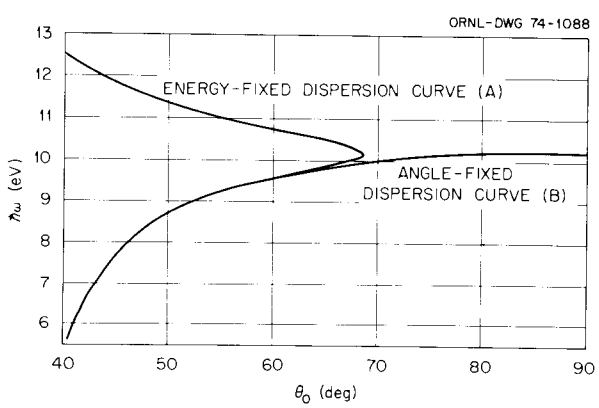

Fig. 24.10. Dispersion curves inferred from the data shown in Fig. 24.9. Curve A is the locus of maximum points in the function $\tilde{R}$ as θ_0 is varied while ω is held contant. Curve B is the locus of maximum points in $\tilde{R}$ as ω is varied while θ_0 is held fixed.

and the angle-fixed dispersion curve (curve B). Note that curve B is slightly different from the curve that would be obtained if the momentum $\hbar\omega\sqrt{\epsilon_0}\sin\theta_0/c$ were held fixed while the maximum in the response function $\tilde{R}$ is located.

In general, an elementary excitation may be characterized by a relation like

$$D(k, \omega) = 0 ,$$

where the complex wave number, k, of the excitation may be regarded as a function of the complex frequency ω, or vice versa. $D(k, \omega)$ may be a multiple-valued function. It may be necessary to specify it on a number of Riemann sheets, depending on the nature of any branch points that may occur. The quantity $D(k, \omega)$ occurs in the denominator of the Green function describing propagation of the elementary excitation in question and in the response function of a system in which the elementary excitation may be created.

Determination of a dispersion relation from an experiment in which real k and real ω are involved generally involves a response function that depends on $D(k, \omega)$ but which, in general, contains other functions of k and ω. Thus the response function plotted in the k-ω plane may be a locus (or loci) of maxima quite different from that of, for example, Im $D(k, \omega)$ itself or from the locus of zeros of $D(k, \omega)$.

ENERGY GAIN FROM SURFACE PLASMONS IN ELECTRON ENERGY LOSS EXPERIMENTS

Schilling and Raether[22] have recently measured energy spectra of fast electrons reflected at a very smooth surface of liquid indium. For electrons incident at grazing angles, a small fraction (about 10^{-9}) were

22. J. Schilling and H. Raether, *J. Phys. C.* **6**, L358 (1973).

observed to gain the surface-plasmon energy $\hbar\omega_s$. This intriguing result is the first success in many attempts to observe energy gain through a plasmon field. A theoretical treatment[23] of a similar energy gain process has prompted attempts to observe it experimentally.[24] The large level of energy deposition in a thin foil in such experiments gives rise to the rapid deterioration of the foil and has, so far, prevented a successful experimental verification of the theory.

We have estimated the probability of electron energy gain in a grazing-incidence configuration corresponding to the experiments of Schilling and Raether, assuming that fast electrons may be represented adequately in terms of plane-wave eigenfunctions. These electrons are assumed to interact pairwise through the surface-plasmon field; a given electron may thus gain a quantum of the surface-plasmon field at the expense of another electron, which experiences a decrease in kinetic energy in the same amount.

Figure 24.11 shows a diagrammatic representation of the interactions that were considered. It is possible to obtain a compact analytical representation for the probability, P_g, of this energy-gain scattering process if one assumes that the electrons have nearly the same momentum initially, that the surface-plasmon field is only weakly damped, and that the surface-plasmon eigenfrequency is nearly independent of its momentum.

We find that

$$P_g = \frac{10\pi}{3} n \frac{e^4 \mathrm{v}}{\hbar^2 \omega_s{}^2 \gamma_s} (\cos\theta)^{-3} , \qquad (26)$$

where v is the speed of an incident electron, θ is its angle measured from the surface normal, ω_s and γ_s are the frequency and damping rate of a surface plasmon, and n is the density of electrons in the incident beam.

The experiments of Schilling and Raether were done with 10-keV electrons incident at angles of about 88.5°. Using currents and beam sizes appropriate to their experiments, we find that Eq. (26) predicts that P_g should be about 5×10^{-9}. This is somewhat larger than the measured value of P_g, possibly because we have neglected higher-order processes in obtaining Eq. (26). A detailed paper describing the present theory, including the effect of multiple surface-plasmon emission and absorption, will be submitted for publication soon.

23. R. H. Ritchie, *Phys. Lett. A* **24**, 348 (1967).

24. Private communication from A. Metherell and H. Raether.

ORNL-DWG 74-7690

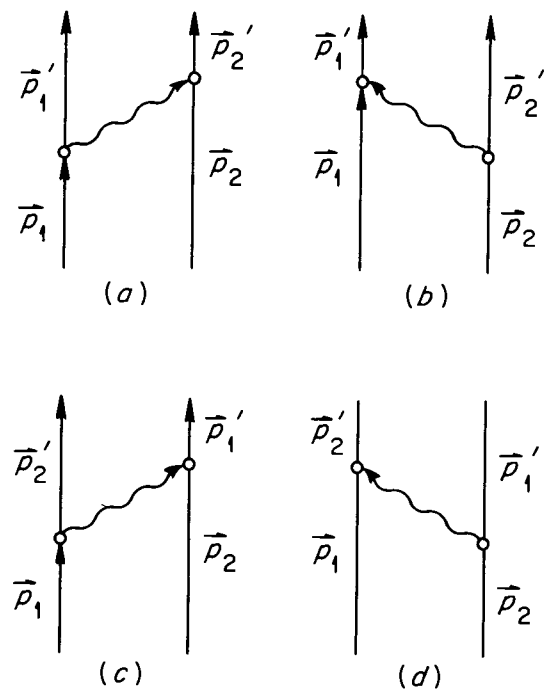

Fig. 24.11. Diagrammatic representation of processes in which two electrons exchange a surface plasmon (SP). Diagrams (*a*) and (*b*) represent, respectively, the two alternatives in which an electron with initial momentum $\mathbf{p}_1$ imparts the energy of the SP field to another electron with momentum $\mathbf{p}_2$ and the loss by the electron with momentum $\mathbf{p}_2$ to the other electron. Diagrams (*c*) and (*d*) represent exchange processes which are necessary for the total matrix element for the process to be antisymmetric.

THE IMPACT PARAMETER REPRESENTATION OF CHARGED-PARTICLE ENERGY LOSSES IN CONDENSED MEDIA

The impact parameter dependence of stopping power has received attention over many years in connection with the structure of charged-particle tracks in condensed media. All published theoretical treatments[25–27] model inelastic losses to electrons in terms of interactions with an assembly of weakly interacting

25. E. J. Williams, *Proc. Roy. Soc. London*, Ser. A **139**, 163 (1933); P.M.S. Blackett and J. G. Wilson, *Proc. Roy. Soc. London*, Ser. A **160**, 304 (1937).

26. J. Neufeld, *Proc. Phys. Soc.* (London), Sect. A **66**, 590 (1953).

27. U. Fano, in *Charged Particle Tracks in Solids and Liquids*, Institute of Physics, London, 1970.

atoms or molecules. We have recently studied the impact parameter representation (IPR) of energy loss in terms of the general dielectric response function of a medium.

For simplicity, we consider the case in which the dielectric function of the medium depends only on energy transfer $\hbar\omega$ and on the magnitude of the momentum transfer $\hbar\mathbf{k}$. A heavy particle with charge $Z_1 e$ and constant velocity $\mathbf{v}$ interacts with a medium according to

$$\frac{d^3\tau}{d\omega\, d^2\kappa} = \frac{Z_1{}^2}{\pi^2 \mathrm{v}} \frac{1}{k^2} \operatorname{Im}(-1/\epsilon_{k,\omega}) , \tag{27}$$

where τ is the inverse mean free path for inelastic encounters in the medium. Here $k^2 = \kappa^2 + \omega^2/\mathrm{v}^2$, ω is the energy loss to the medium, and $\boldsymbol{\kappa}$ is the momentum transfer in a direction perpendicular to $\mathbf{v}$. Atomic units are used throughout this and succeeding equations.

Equation (27) is well known.[28] We have found the IPR of this expression, in which the variable $\boldsymbol{\kappa}$ is replaced by $\mathbf{b}$. The latter may be interpreted as the impact parameter specifying the position of a volume element at which energy absorption occurs in the medium. The vector $\mathbf{b}$ is actually the projection on a plane perpendicular to $\mathbf{v}$ of a vector connecting the particle and a particular volume element.

The differential interaction probability in the IPR is given by

$$\frac{d^3\tau}{d\omega\, db^2} = \frac{Z^2\omega}{\pi^2 \mathrm{v}^3} \times \left[\frac{\omega}{\mathrm{v}} K_0\left(\frac{b\omega}{\mathrm{v}}\right) \int_0^\infty \frac{\kappa\, d\kappa\, J_0(\kappa b)}{\kappa^2 + \omega^2/\mathrm{v}^2} \operatorname{Im}\left(\frac{-1}{\epsilon_{k,\omega}}\right) + K_1\left(\frac{b\omega}{\mathrm{v}}\right) \int_0^\infty \frac{\kappa^2\, d\kappa\, J_1(\kappa b)}{\kappa^2 + \omega^2/\mathrm{v}^2} \operatorname{Im}\left(\frac{-1}{\epsilon_{k,\omega}}\right) \right] , \tag{28}$$

where $k^2 = \kappa^2 + \omega^2/\mathrm{v}^2$. J_n and K_n are Bessel functions of the nth order. It may be shown that

$$\int \frac{d^3\tau}{d\omega\, d^2 b} d^2 b = \int \frac{d^3\tau}{d\omega\, d^2\kappa} d^2\kappa$$

and that

$$-\frac{dE}{dR} = \int_0^\infty \omega\, d\omega \int \frac{d^3\tau}{d\omega\, d^2 b} d^2 b = \int_0^\infty \omega\, d\omega \int \frac{d^3\tau}{d\omega\, d^2\kappa} d^2\kappa ,$$

where $-dE/dR$ is just the standard expression for the stopping power of the medium for the particle.

It is interesting to consider the limiting case in which ϵ depends only on ω and not at all upon k. Then Eq. (28) reduces to

$$\frac{d^3\tau}{d\omega\, d^2 b} = \frac{Z^2\omega^2}{\pi^2 \mathrm{v}^4} \left(K_0{}^2 \frac{\omega b}{\mathrm{v}} + K_1{}^2 \frac{\omega b}{\mathrm{v}} \right) \operatorname{Im}\left(\frac{-1}{\epsilon_\omega}\right) , \tag{29}$$

which is a generalization of a result given by Fano, among others [Eq. (15) of ref. 27]. Suppose one takes $\epsilon_\omega \approx 1$, corresponding to a dilute assembly of atoms. Standard dielectric theory gives

$$\operatorname{Im}\left(\frac{-1}{\epsilon_\omega}\right) \approx 2\pi^2 N \Sigma (f_n/\omega_n)\, \delta(\omega - \omega_n) ,$$

where f_n and ω_n are the oscillator strength and transition frequency for the nth transition of one of the atoms of the medium, respectively, and N is the density of atoms. We work in the dipole approximation here. Then we find

$$\frac{d^3\tau_n}{d\omega\, d^2 b} = \frac{2Z^2 N}{\mathrm{v}^4} f_n \omega_n \left[K_0{}^2\left(\frac{\omega_n b}{\mathrm{v}}\right) + K_1{}^2\left(\frac{\omega_n b}{\mathrm{v}}\right) \right] \tag{30}$$

corresponding to the nth transition. This agrees with Fano's Eq. (15) if one sets

$$d^3\tau_n/d\omega\, d^2 b = N\, d^3\sigma_n/d\omega\, d^2 b .$$

Note that Eq. (30) is valid only for values of b that are not too small. The dipole approximation does not suffice in this limit; its use leads to a divergent interaction cross section as $b \to 0$.

A convenient case that may be studied to illustrate the dependence of $d^3\tau/d\omega\, d^2 b$ on b over the whole range of impact parameter is that of an assembly of free electrons at rest. Lindhard has given a compact analytical expression for $\epsilon(k, \omega)$ appropriate to such a system.

Figure 24.12 illustrates the IPR dependence of $d^3\tau/d\omega\, d^2 b$ [abbreviated $p(\omega, b)$ here] on b for a few

28. D. Pines and P. Nozieres, *Theory of Quantum Liquids*, W. A. Benjamin, New York, 1966.

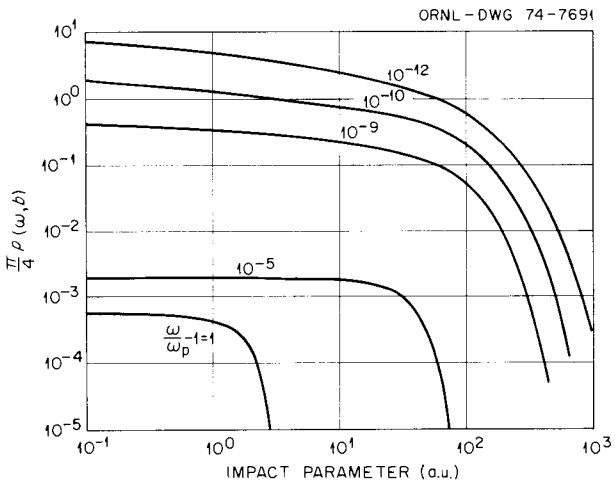

Fig. 24.12. Representation of the variation in the differential inverse mean free path $p(\omega, b)$ as a function of impact parameter b for various values of ω, the energy transferred to the medium by a 200-MeV proton. The impact parameter b is measured perpendicular to the track of the fast proton.

values of ω in the case of a charged particle passing through a cold electron gas. The quantity $\omega_p = \sqrt{4\pi n_0}$ is the plasma frequency, and n_0 is the density of electrons in the undisturbed system. The calculations were carried out assuming the fast particle to be a 200-MeV proton. A clear division between collective and single-particle properties is displayed in these results. For energy loss ω only slightly greater than ω_p (the minimum possible in this model), $p(\omega, b)$ declines slowly with increasing b until, when $b \sim v/\omega_p$, it becomes small. The value $b_c = v/\omega_p$ is Bohr's adiabatic cutoff distance for this system. For losses appreciably larger than ω_p, p tends to become small when $b \sim \omega^{-1/2}$, the wavelength of an electron with kinetic energy ω. One sees that a very high density of energy deposition must exist for such values of b; however, this energy is rapidly transported to larger distances via energetic delta rays. The description furnished by our model applies to the primary energy deposition events, rather than to later stages.

An intriguing aspect of $p(\omega, b)$ as given in Eq. (28) is that, in general, it becomes alternately negative and positive as b increases after a range of smaller b in which p is positive. The negative values of $p(\omega, b)$ reflect the essentially quantum mechanical nature of the collision process. It may be shown that $p(\omega, b)$ is related to van Hove's pair distribution function expressing the correlation between density fluctuations at different space-time points. This function is known to assume negative values for some space-time separations, even though its energy-momentum representation is positive definite.

We will apply Eq. (28) to more realistic cases for which approximate $\epsilon(k, \omega)$ functions are available. Generalization will also be made to the case of a real solid crystal for which the dielectric function becomes a matrix function of k and ω.

RADIATIVE CAPTURE OF ELECTRONS BY SWIFT IONS IN SOLIDS

Recent experiments[29-31] have established the surprising fact that photons resulting from the capture of electrons by swift ions traversing solids can now be measured. The experiments of Appleton, Datz, and co-workers[31] are sufficiently precise that both the cross sections for the radiative transitions and the distribution of the resulting photons in energy may be determined. Since this work was done with channeled ions, it seems possible that the impact parameter dependence of these quantities can be established in future experiments.

It is known that the theory of electron capture by swift ions is not highly accurate. However, one expects radiative capture cross sections obtained with the use of state-of-the-art theoretical techniques to have roughly the correct dependence on energy and charge of the ion and the electron states of the medium and to give reasonably accurate predictions of photon distribution. We have used standard radiation theory together with a statistical model of electron states in a single-crystal lattice of atoms in order to analyze the results of Appleton et al.[31]

Consider a system of nearly free electrons through which a swift heavy ion of charge $Z_1 e$ passes. Let $\mathbf{R}$ be the coordinate of an electron relative to the ion and r_c be the coordinate of the center of mass of the electron-ion system. Then we may write the Hamiltonian of the electron-ion-radiation system as $H = H_0 + H_{\text{rad}} + H'$, where

29. H. W. Schnapper, H. D. Betz, J. P. Delvalte, K. Kalata, and A. R. Shoval, *Phys. Rev. Lett.* **29**, 898 (1972).
30. P. Kleinle et al., *Phys. Rev. Lett.* **31**, 1099 (1973).
31. B. R. Appleton, J. A. Biggerstaff, T. S. Noggle, S. Datz, C. D. Moak, M. D. Brown, H. F. Krause, V. N. Neelavathi, and R. H. Ritchie, Fifth International Conference on Atomic Collisions in Solids, Gatlinburg, Tennessee, Sept. 24–28, 1973.

$$H_0 = -\frac{1}{2}\frac{1+M}{M}\nabla_R{}^2 - \frac{1}{2(1+M)}\nabla_{\mathbf{r}_c}{}^2 - \frac{Z_1}{R},$$

$$H_{\text{rad}} = \sum_{\mathbf{k},\lambda} \omega_k\, a^\dagger{}_{\mathbf{k}\lambda}\, a_{\mathbf{k}\lambda}\,,$$

$$H' = -i\sum_{\mathbf{k},\lambda}\left(\frac{2\pi}{\omega_k \Omega}\right)^{1/2} \hat{e}_{\mathbf{k}\lambda}\, \mathbf{O}(a^\dagger{}_{\mathbf{k}\lambda} + a_{-\mathbf{k}\lambda})$$

are the Hamiltonians, respectively, of the electron-ion system, the noninteracting radiation field, and the field-matter system, in first order. The operator $\mathbf{O}$ is given by

$$\mathbf{O} = \exp\left[i\mathbf{k}\cdot\left(\mathbf{r}_c + \frac{M}{1+M}\mathbf{R}\right)\right]\left(\nabla_{\mathbf{R}} + \frac{1}{1+M}\nabla_{\mathbf{r}_c}\right)$$

$$-\frac{Z_1}{M}\exp\left[i\mathbf{k}\cdot\left(\mathbf{r}_c - \frac{1}{1+M}\mathbf{R}\right)\right]\left(-\nabla_{\mathbf{R}} + \frac{M}{1+M}\nabla_{\mathbf{r}_c}\right),$$

and all quantities are expressed in atomic units. M is the ion mass, and ω_k is the frequency of a photon with wave vector $\mathbf{k}$. To find the probability of photon emission accompanied by capture of the electron into a bound state $u_f(\mathbf{k})$ on the ion one may use standard Golden Rule theory for transition between the initial state

$$|i\rangle = \frac{1}{\sqrt{\Omega}} e^{i\mathbf{P}_0\cdot\mathbf{r}_0}\, u_0(R)|0\rangle$$

and the final state

$$|f\rangle = \frac{1}{\sqrt{\Omega}} e^{i\mathbf{P}\cdot\mathbf{r}_c}\, u_f(R)\, a^\dagger{}_{\mathbf{k}\lambda}|0\rangle\,.$$

In the above, $a^\dagger{}_{\mathbf{k}\lambda}$ is a creation operator for a photon with wave vector $\mathbf{k}$ and polarization λ, Ω is the normalization volume, and $|0\rangle$ represents the vacuum state of the radiation field.

We have adopted a plane-wave basis set to describe electrons in initial states and have assumed a distribution of initial states corresponding to an electron gas characterized by maximum energy ϵ_F. We find that the probability per unit length of travel of the ion in the gas per unit photon energy may be written

$$\frac{dP}{d\epsilon} = \frac{16 Z_1{}^5}{3\pi c^3 \mathrm{v}^2}\,\frac{\epsilon - \epsilon_B}{\epsilon^3}\,[\epsilon_F - (\sqrt{\epsilon_1} - \sqrt{\epsilon - \epsilon_B})^2]\,,$$

where v is the speed of the ion, ϵ_B is the binding energy of the captured electron in its ground state on the ion, and $\epsilon_1 = \mathrm{v}^2/2$. The energy of the photon emitted in the capture process is ϵ. The factor in the square brackets is set equal to zero when it would otherwise assume negative values.

We wish to obtain cross sections for radiative capture as a function of impact parameter in a crystal in which the spatial density of electrons may vary greatly along the projectile path. To do this, we have adopted a statistical model for the capture process in which each volume element of the crystal is characterized by a density $n(\mathbf{r})$ of crystal electrons: with a given density we associate an electron gas with Fermi energy

$$\epsilon_F = \frac{1}{2}[3\pi^2\, n(\mathbf{r})]^{2/3}.$$

Capture radiation from the space-varying density $n(\mathbf{r})$ is computed by averaging over an appropriate distribution of impact parameters. The "binding energy" of electrons having energy ϵ_F is assumed to be equal to $K\epsilon_F$, where the constant K is taken to be about 1.

The data of Appleton et al.[31] were obtained for channeled O^{8+} ions in a single-crystal silver target. Figure 24.13 shows typical measured photon distributions corresponding to nonchanneled conditions (lower curve) and channeled conditions (upper curve). The difference between these sets of data is taken to be the contribution from radiative capture of electrons on the oxygen ion. The ion energy was 27.8 MeV in these experiments.

The points of Fig. 24.14 show the difference between data values shown in the upper curve of Fig. 24.13 and the averaged lower curve of Fig. 24.13, plotted as a function of photon energy. Two theoretical estimates of the photon distribution are shown also.

The theoretical distributions were evaluated using $n(\mathbf{r})$ data obtained from a relativistic Hartree-Fock calculation for silver at a normal density of 10.5 g/cm^3 (ref. 32). The Wigner-Seitz boundary condition was used so that the electron density distribution is appropriate to the silver metal lattice. It is seen that reasonable agreement between theory and experiment is obtained; there is some indication that capture to both the O^{8+} and O^{7+} ions may be occurring in these experiments.

32. We are indebted to C. W. Nestor, Jr., for furnishing us with these data from his relativistic Hartree-Fock program.

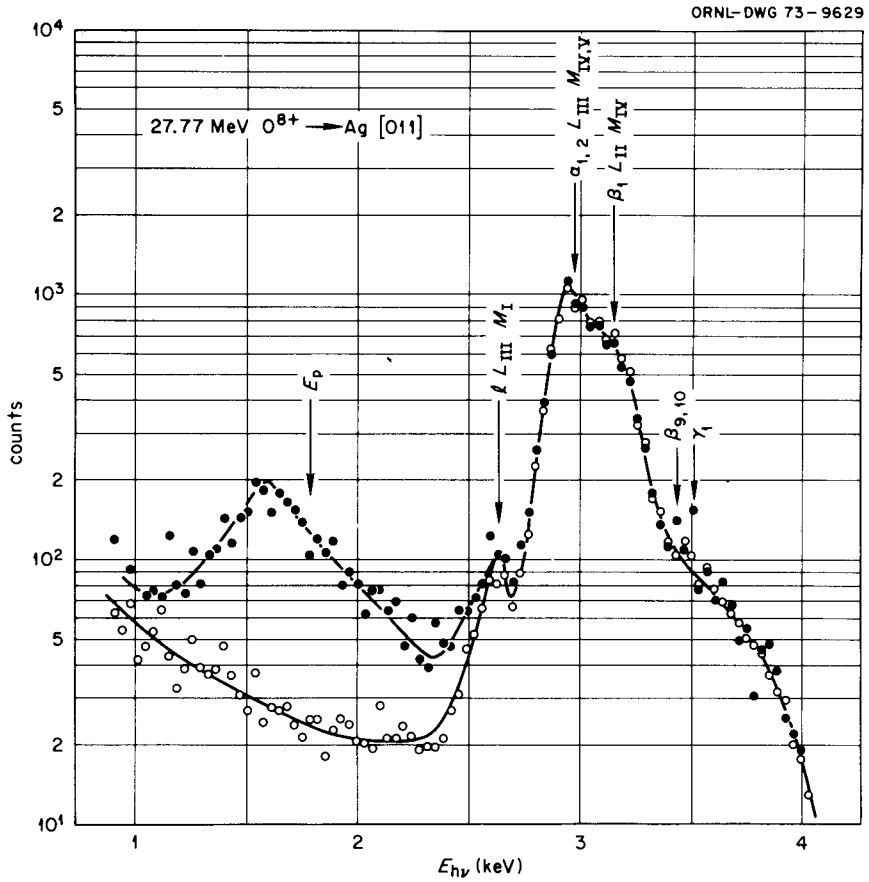

Fig. 24.13. Experimental data obtained by Appleton et al.[31] on the yield of photons as a function of photon energy ($E_{h\nu}$) resulting from the interaction of 27.77-MeV O^{8+} ions with a thin single crystal of silver. The upper curve shows the photon distribution obtained when the ions are channeled in the [011] direction, and the lower curve shows that found when the ions are not channeled. The arrows indicate energies associated with the filling of various inner shell vacancies in the silver cores caused by the swift-ion bombardment.

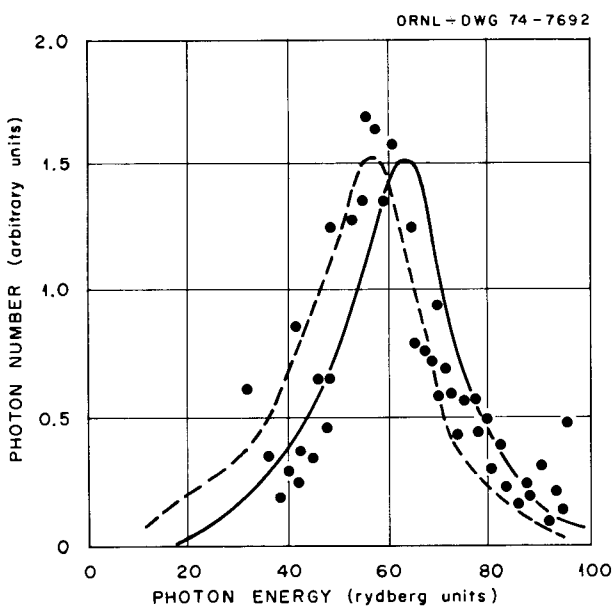

Fig. 24.14. A plot of the number distribution of photons emitted per unit energy as a function of photon energy $\hbar\omega$ in the radiative capture of electrons by highly stripped O^+ ions channeled in a silver crystal. The points show the experimental values obtained by Appleton et al.[31] The curves were computed by the method described in text. The solid curve was computed assuming the ion to be completely stripped, while the dashed curve shows the distribution computed assuming the ion to have a charge of 7+ when capture occurs.

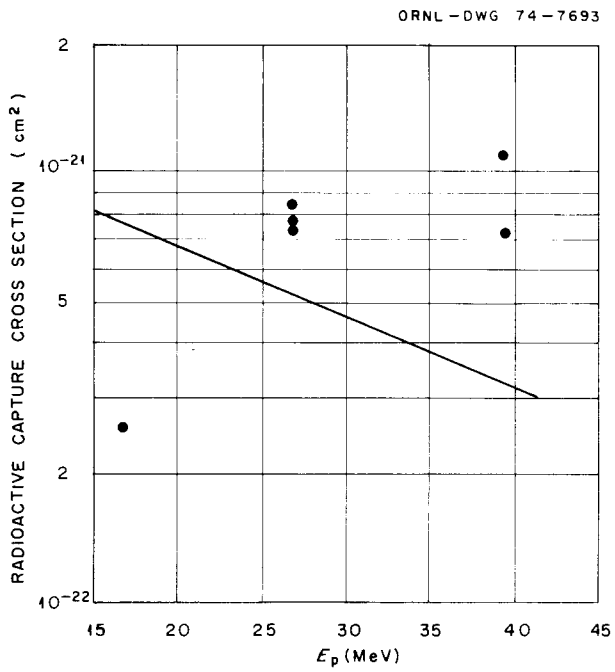

Fig. 24.15. The cross section for radiative capture of electrons on a completely stripped O^{8+} ion as a function of projectile energy. The points were found experimentally as described in ref. 31. The curve shows values computed as described in ref. 31.

Figure 24.15 shows a comparison between the measured and calculated cross sections for radiative capture as a function of projectile energy E_p. The ions are assumed to be completely O^{8+} in these calculations. Although the agreement between theory and experiment is only fair, it is expected that more complete data will soon be obtained by Appleton et al. and that the theory will be refined to account for the distortion of initial-state electron wave functions due to the presence of the swift ion.

SURF-RIDING ELECTRON STATES TRAILING SWIFT IONS IN CONDENSED MATTER

The energy loss of a fast charged particle moving in condensed matter can be described in terms of the complex dielectric function of the medium. Physically, the target response manifests itself as a cylindrically symmetric wake of electron density fluctuations behind the particle. Its axis defines the particle track. The wake consists of a series of domains, at distinct distances behind the projectile, in which the electron density is alternately enhanced and depleted relative to the mean density n_0 in the medium. Domains of density enhancement create regions of negative electron potential, and domains of depletion create regions of positive potential. If sufficiently deep, these potential troughs can trap, respectively, positive or negative particles and sweep them along in states we define as "surf-riding states," which trail behind the projectile. Experimental verification of surf-riding states would contribute significantly to the understanding of the dynamic many-body response of condensed matter to moving charged particles. Moreover, projectile trailing by surf-riding particles may contribute to several important phenomena associated with the penetration of charged particles through dense matter.

We may approximate the shape of the potential in the wake of a swift charged particle with velocity **v** and charge Ze to obtain quite a simple result. Figure 24.16 is a schematic representation of the oscillatory portion of the potential energy function of an electron moving with the ion. The variable ρ is the polar coordinate of the electron measured from the center of the track, and the coordinate z is measured parallel with **v**. We have assumed that the medium in which the charged particle travels can sustain well-defined plasmons of energy

$$\hbar\omega_p = \hbar(4\pi n_0 e^2/m_0)^{1/2} ,$$

in the sense that the plasmon decay rate, γ, is so small that $\gamma/\omega_p \ll 1$. In a metal the density of the participating electrons, n_0, would correspond to the density of valence electrons. In condensed matter the potential can persist over many wavelengths behind the projectile. It is important to note that, in the limit $\gamma \rightarrow$

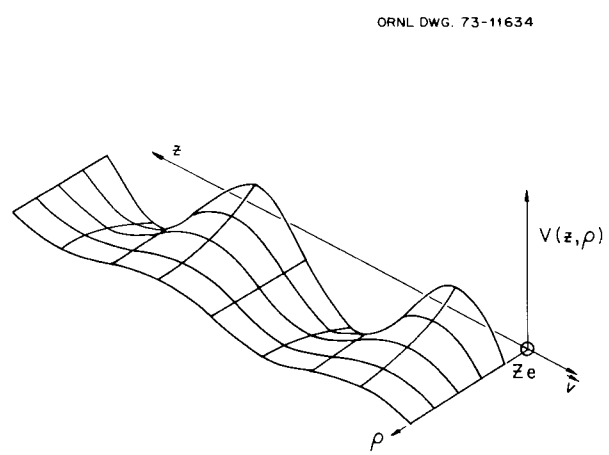

Fig. 24.16. Schematic representation of the oscillatory portion of the potential energy of an electron as a function of position behind a projectile of charge Ze. The charge is assumed to be moving with velocity **v** in the direction of the negative z axis of a coordinate system with origin placed at the projectile.

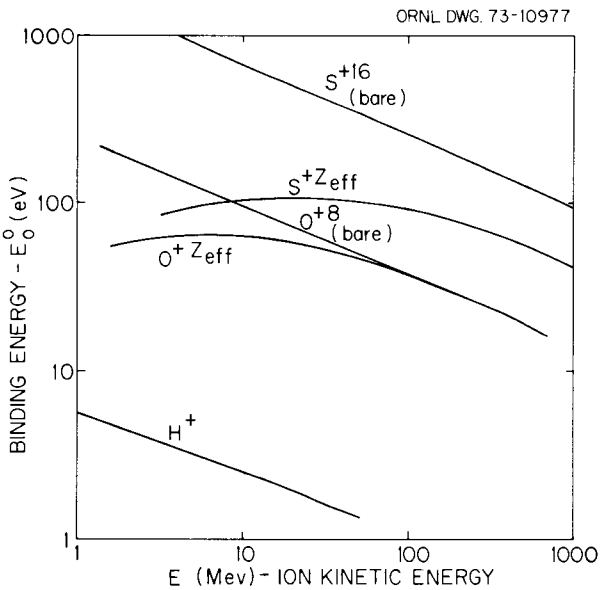

Fig. 24.17. Ground-state binding energies (in electron volts) of an electron in the first ($m = 0$) trough of the polarization potential created in a medium like aluminum by ions of hydrogen, oxygen, and sulfur as a function of their kinetic energies. The curves labeled $O^{+Z_{eff}}$ and $S^{+Z_{eff}}$ were calculated for effective ion charges $Z_{eff}(v)$ as described in text.

0, the spatial integral over the electron density fluctuation from the origin to the first zero at the distance $z = \pi v/\omega_p$ is just equal to Ze, the charge of the moving ion.

The depth of the first trough increases linearly with Z and is about $Ze\,\omega_p/v$. If this quantity is sufficiently large, bound quasi-stationary states of particles in the oscillating tail of $\Phi(r)$ may exist. In a medium with given ω_p, the number of bound states in a trough depends upon Z/v.

We have made variational estimates of the binding energy of electrons in surf-riding states. Figure 24.17 displays the variation of the ground-state binding energy $E_0{}^0$ for an electron surf-riding in the first potential through ($m = 0$) behind hydrogen, oxygen, and sulfur ions as a function of their kinetic energy. The ions are assumed to move in a medium like aluminum metal for which $\hbar\omega_p = 15.4$ eV and $\gamma/\omega_p = 4.6 \times 10^{-2}$. The curves labeled O^{+8} (bare) and S^{+16} (bare) were computed assuming that the ions remain stripped during their passage through the medium. Such high charge states may be selected in experiments with channeled ions, where the low probability of small impact parameter collisions between a channeled ion and crystal ion cores makes electron capture from the solid unlikely, compared to the situation in random media. The curves labeled $O^{+Z_{eff}}$ and $S^{+Z_{eff}}$ were computed assuming a velocity-dependent effective charge number of the form

$$Z_{eff}(v) = Z[1 - \exp(v/Z^{2/3}v_0)] .$$

Auger-type capture into surf-riding states should be efficient. Assuming that the binding energy of the states is dissipated through particle-hole pair production in the conduction band of the metal, one estimates. for example, a mean free path of about 300 Å for capture into a surf-riding state behind a 2-MeV O^{8+} ion in aluminum. It may be possible to detect electron capture into surf-riding states by observing the associated Auger electrons or the soft x rays generated in the capture loss.

When an ion trailed by a surf-riding electron emerges from a metal into a vacuum, the potential trough seen by the electron vanishes. Then, in first approximation, we expect surf-riding electrons to appear outside the metal as a group of electrons with velocities centered about v and with a spread determined by the momentum transform of the surf-riding wave packet. These electrons should contribute a component to the electron distribution associated with the emergence of positive ions from metals which so far have been explained only in terms of capture into continuum states on the positive ions in vacuo.

Other possible consequences of surf-riding states in solids are:

1. The amount of charge separation in solid-state detectors of ionizing radiation may be affected by the existence of spatially coherent surf-riding electron states of moving particles. Such states would be expected not only to reduce particle-hole recombination in solid-state detectors but also to diminish the recombination of electrons with their geminate ions in insulators such as organic liquids.
2. Correlated capture and loss through surf-riding may determine the velocity dependence of the neutral beam fraction in experiments with charged particles emerging from solid surfaces. The binding energy of an electron trailing an energetic proton is expected to be about 10 eV ~ 1 Ry in a typical metal. Thus the interesting picture of a dynamically stabilized solid-state hydrogen atom emerges, in which the proton rides ahead, trailed by the wave packet of the electron at a distance of about $3\pi v/2\omega_p$. An antimorph of the entity that might exist by virtue of the wake phenomenon is the *dielectron.* Two electrons might experience strong spatial correlation due to density fluctuations. Energy lost by a dielectron

or by the solid-state hydrogen atom in distant collisions should be altered relative to that by a single electron; its mean free path in condensed matter should be longer than that of either electron separately, enhancing the likelihood that it will produce observable effects.

3. Experiments on the transmission probability of channeled H_2^+ ions through gold foils show that a significant fraction emerges from the foils as molecules. H^+-H^+ pairs locked in spatial correlation may contribute significantly to this transmission probability. It would be interesting to ascertain the importance of surf-riding states of protons behind heavier ions, for example, in transmission experiments with incident fast molecules such as LiH, CH, OH, or hydrogen halides.

Part IV. Radiation Research and Development

F. F. Haywood

25. Dosimetry for Human Exposures and Radiological Impact

G. D. Kerr

S. A. Abdullah W. F. Fox
J. A. Auxier T. D. Jones
J. S. Cheka S. B. Lupica
H. W. Dickson J. J. Shonka[1]
D. G. Wilhoit[2]

STUDY OF RADIATION EXPOSURE TO ATOMIC BOMB SURVIVORS RESIDING IN THE UNITED STATES

At the request of the U.S. Atomic Energy Commission, a study of the radiation exposure to atomic bomb survivors of Hiroshima and Nagasaki, Japan, who are now residing in the United States was started in 1973.

In preliminary work, recent survey information from several sources in Los Angeles on 69 survivors was analyzed in cooperation with the Atomic Bomb Casualty Commission (ABCC) in Hiroshima and Nagasaki. In all but one of 22 cases where this information could be compared with information in the Master Files of the ABCC obtained at a much earlier date, the agreement on location and shielding was excellent. With additional information found in the files of the ABCC, it was possible to make tentative estimates of 44 individual's radiation exposure. Estimates of radiation exposure in the other 25 cases were not considered usable either because an exact identification of the individual could not be made or because sufficient data could not be obtained. Without an exact identity, such as a maiden name, it was not possible to search the files of the ABCC for additional information.

Because of uncertainties in some of the 44 tentative estimates resulting from the use of average or typical shielding factors, a distribution was constructed with large increments at the higher exposure levels, where detailed shielding data are necessary to make more accurate estimates. This distribution was found to be skewed toward higher exposures than distributions previously determined by the ABCC for the Japanese populations of Hiroshima and Nagasaki. Some bias shown in information from one source in Los Angeles may account for this because attempts were made to include (in the sample of interviews to date) individuals likely to have greater radiation exposures. There may, however, be other contributing factors, such as an inordinate migration of persons who were exposed closer to the hypocenter and who suffered large losses of family members.

It is felt that these preliminary results indicate the feasibility of and the need for a more complete study. A distribution of radiation exposures based on more accurate individual estimates and a larger sample is desirable as supporting information in making budget estimates for funding a bill such as H.R. 17112. If passed, this bill will provide financial support toward the medical care of some survivors now living in the United States.

1. Graduate student.
2. Consultant.

At present, the sample is being enlarged by including additional survivors in the Los Angeles area and by extending the study to San Francisco. The survivors in these two areas constitute approximately one-half of the estimated 500 survivors residing in the United States. Forms have been prepared for use by voluntary bilingual interviewers who are familiar with Hiroshima and Nagasaki. These forms are useful in collecting data on location and shielding and provide for searching the files of the ABCC for additional pertinent information on each person. Efforts of these voluntary interviewers are being coordinated by the staffs of the Office of the Chief Medical Examiner-Coroner for the County of Los Angeles and the Department of Public Health of the City and County of San Francisco. Staff members of the ORNL Health Physics Division, the USAEC Division of Biomedical and Environmental Research, and the ABCC have consulted with these agencies in California concerning the collection of data on survivors.

IN-VIVO DOSE ESTIMATES FOR ATOMIC BOMB SURVIVORS IN HIROSHIMA AND NAGASAKI

The ABCC has radiation dose estimates for most of the 117,000 atomic bomb survivors in the Master Sample. However, these estimates, denoted T65D,[3-5] actually predict dose or kerma to infinitesimal amounts of human tissue under exact analog exposure conditions, except for the absence of the specific survivor. Because attenuation and multiple scattering by the body are neglected in these estimates, they are inadequate to assess the dose to some internal organs of survivors and to survivors exposed in utero.

A complete transport calculation of dose inside the body of each survivor is impractical due to the large amount of modeling necessary to describe the body and all the shielding in close proximity to the survivor. Hence the current objective is to establish generalized techniques that can be used easily to estimate in-vivo doses from the T65D estimates in specific cases of interest.

Because the sample population exposed inside Japanese residential structures (about 10,000 in Hiroshima and 4000 in Nagasaki) constituted the most important group of survivors and because their T65D assignments based on the "9-parameter" method[4] are quite good, this group influenced most of the assumptions and approximations concerning the energy and angular distributions of radiation incident on a survivor's body. The wide variation of parameters required to describe the internal organs in a heterogeneous population encouraged the use of depth-dose curves instead of the more realistic organ approximations.[6] A Monte Carlo transport analog[7] was used to calculate the depth-dose distributions in several different sizes of cylindrical phantoms chosen to approximate regions of a survivor's body.

An incident gamma-ray spectrum was computed, using discrete-ordinates transport techniques,[8] for a fission-source-to-survivor distance of about three interaction path lengths (900 m in air). Spectral calculations for an infinite air medium were used because, for a fission source height of 500 m or more (the estimated height of burst was 500 m in Nagasaki and 570 m in Hiroshima), only the magnitude of the kerma from neutrons seemed to change near the air-ground interface.[8] A distance of 900 m of air was selected because the energy spectrum has reached equilibrium after rapid initial variation with distance.

The angular distribution for gamma rays is difficult to predict, even for the light shielding provided by Japanese residential structures, but past experience[4] indicates that it is approximately correct to assume that the incident gamma rays come isotropically from a hemisphere above the ground. Because the largest uncertainties in these calculations are the energy and angular distributions of the incident neutrons, it is considered advantageous that the T65D gamma component in Nagasaki completely overwhelmed the corresponding neutron component and that, even in Hiroshima, the dose from the gamma component usually dominated when considering the total dose to an internal organ. Also, those Hiroshima survivors who were shielded by

3. H. H. Hubbell, *Health Physics Division of Oak Ridge National Laboratory and Atomic Bomb Casualty Commission Liaison Pool Activities Report for Period from May 1 to August 31, 1960* (Nov. 25, 1960).

4. J. S. Cheka, F. W. Sanders, T. D. Jones, and W. H. Shinpaugh, *Distribution of Weapons Radiation in Japanese Residential Structures,* AEC report CEX-62.11 (1965).

5. J. A. Auxier, J. S. Cheka, F. F. Haywood, T. D. Jones, and J. H. Thorngate, "Free Field Radiation Dose Distributions from the Hiroshima and Nagasaki Bombings," *Health Phys.* 12, 425–29 (1966).

6. W. S. Snyder, M. R. Ford, G. G. Warner, and H. L. Fisher, Jr., "Estimates of Absorbed Fractions for Monoenergetic Photon Sources Uniformly Distributed in Various Organs of a Heterogeneous Phantom," MIRD Pamphlet No. 5, *J. Nucl. Med., Suppl. No. 3* **10** (August 1969).

7. J. A. Auxier, W. S. Snyder, and T. D. Jones, *Radiation Dosimetry,* vol. 1, Academic Press, New York, 1968.

8. E. A. Straker and M. L. Gritzner, *Neutron and Secondary Gamma-Ray Transport in Infinite Homogeneous Air,* ORNL-4464 (1969).

reinforced concrete structures, terrain, etc., usually received several times more dose from gamma rays than from neutrons.

Because neutrons in Hiroshima and at the Health Physics Research Reactor (HPRR) are produced by fission of the same type of material (mostly ^{235}U) in similar critical assemblies having minimal moderation, the leakage spectrum of the HPRR should be quite similar to that in Hiroshima.[9] Due to the thick metal shroud about the Hiroshima weapon, the leakage spectrum contained more low-energy neutrons, but the low-energy neutrons are moderated and absorbed faster than the neutrons of higher energies; so the transported spectrum at several hundred meters could be approximated by the leakage spectrum from the unshielded critical assembly of the HPRR. The neutron spectrum in Nagasaki (critical assembly of ^{239}Pu surrounded by a high explosive) was different from the leakage spectrum of the HPRR but does not need to be treated differently due to the overwhelming domination of total dose, especially to internal organs, by the external gamma rays.

The angular distribution of neutrons inside a typical Japanese house has not been measured for a transported fission spectrum; however, some measurements have been made in a test house for a degraded $^{3}H(d, n)^{4}He$ spectrum denoted as a D-T spectrum.[10] The leakage spectrum from the D-T source is sharply peaked at about 14 MeV; but, when an essentially monoenergetic spectrum is transported through several interaction path lengths of air, there is a softening effect, and the average energy is degraded very quickly. Because the angular distribution is not sensitive to the spectral distribution, no serious errors should result from using the angular distribution from the D-T source.

Values of depth dose and their corresponding coefficients of variation are given in Tables 25.1–25.3 for each of the three phantoms used to approximate regions of the survivor's body. Techniques used in selecting direction cosines to represent the angular distributions of the incident neutrons and gamma rays and in normalizing dose to fluence in the Monte Carlo transport calculations are discussed in ORNL-4903.[11] Values of kerma per unit fluence for the gamma-ray and neutron fission spectra used in the depth-dose calculations, which are needed to convert the T65D dose assignments to in-vivo dose estimates using the above tables, are 0.454×10^{-7} erg/g (0.454×10^{-9} rad) per fluence gamma ray and 2.3×10^{-7} erg/g (2.3×10^{-9} rad) per fluence neutron respectively.

In estimating in-vivo doses, most internal organs can be approximated by regions inside simple quadratic surfaces.[6] Organs other than those described by Snyder et al.[6] can often be modeled from *Grant's Atlas of Anatomy,*[12] which views many organs of the anatomy through sagittal planes. Sagittal views, common in *Grant's Atlas,* seem to be fairly uncommon in most other books on anatomy.

In Fig. 25.1, part of the shielding information is shown for a survivor having T65D gamma-ray and neutron dose assignments of 85 and 15 rads respectively. Let us assume that this survivor is a female carrying a six-week-old fetus and that we wish to estimate a dose to the fetus and to the isthmus of the thyroid because of a malignant nodule formation there. The T65D neutron dose ratio (D_γ/D_n) is 5.67, which establishes the ratio of gamma fluence to neutron fluence (ϕ_γ/ϕ_n) at about 28, by use of Fig. 25.2.

To estimate a dose to the fetus, let us use the phantom analog having a radius of 12 cm, based on the mother's body size, and assume the small fetus still has a central location in a sagittal plane through the lower part of the mother's torso, as illustrated in ORNL-4584.[13] The isthmus of the thyroid gland, as illustrated in Fig. 25.3, lies in the outer ring of the 6-cm-radius phantom analog at a penetration depth of 0.4 to 1.0 cm. These in-vivo dose estimates from the 6-cm-radius phantom analog in Table 25.1 with $24 \leqslant Z \leqslant 36$ and the 12-cm-radius phantom analog in Table 25.2 with $12 \leqslant Z \leqslant 24$ are shown in Table 25.4. For an organ or a fetus in a later stage of development (whose dimensions are not small compared with the geometrical divisions of the phantom analogs), an integration of dose at a given depth weighted by the mass of the organ or fetus would be necessary.

In order to normalize the gamma dose contribution to the incident neutron fluence, it is necessary to use $\phi_\gamma/\phi_n = 28$ for this specific example, in which case the total doses to the fetus and the isthmus of the thyroid are 4.79×10^{-9} and 12.7×10^{-9} rad/ϕ_n respectively.

9. F. W. Sanders, F. F. Haywood, M. I. Lundin, L. W. Gilley, J. S. Cheka, and D. R. Ward, *Operation Plan and Hazards Report – Operation BREN,* AEC report CEX-62.02 (1962).

10. J. S. Cheka, *Distribution of Radiation from a 14 MeV Neutron Source in and near Structures,* AEC report CEX-65.13 (1969).

11. *Health Phys. Div. Annu. Progr. Rep. July 31, 1973,* ORNL-4903, pp. 1–18.

12. J. C. B. Grant, *Grant's Atlas of Anatomy,* The Williams & Wilkins Co., Baltimore, Md., 1962.

13. *Health Phys. Div. Annu. Progr. Rep. July 31, 1970,* ORNL-4584, pp. 131–33.

From the T65D neutron dose of 15 rads and the kerma per fluence neutron value of 2.3×10^{-7} erg·g^{-1}·ϕ_n^{-1} (2.3×10^{-9} rad/ϕ_n), the neutron fluence becomes 6.5×10^9 neutrons/cm^2, giving total dose estimates of 31 rads to the fetus and 82 rads to the thyroid, as shown in Table 25.5.

From the example given in Table 25.5, the importance of correlating radiation effects observed in atomic bomb survivors with in-vivo dose estimates rather than T65D assignments is clearly demonstrated by the decrease in dose, especially that from neutrons, in the body.

Table 25.1. Analogical depth-dose distributions for primary application to thyroid-carcinoma and nodule-formation studies of the Hiroshima and Nagasaki atomic bomb survivors

Penetration depth (cm)	Dose from recoil ions		Dose from photons produced in phantom[a]		Dose from photons produced in radiation field[b]	
	Rads per fluence neutron	Coefficient of variation (%)	Rads per fluence neutron	Coefficient of variation (%)	Rads per fluence neutron	Coefficient of variation (%)
	$\times 10^{-9}$		$\times 10^{-9}$		$\times 10^{-9}$	
			$48 \leqslant Z \leqslant 60$ cm[c]			
0–1.2	1.56	2	0.044	5	0.377	2
1.2–2.4	1.17	3	0.064	5	0.284	3
2.4–3.6	1.06	4	0.084	5	0.266	3
3.6–4.8	1.17	5	0.104	5	0.265	4
4.8–7.2	1.17	8	0.113	8	0.244	7
			$36 \leqslant Z \leqslant 48$ cm[c]			
0–1.2	1.54	2	0.056	4	0.398	2
1.2–2.4	1.01	3	0.080	4	0.274	3
2.4–3.6	0.790	4	0.114	4	0.247	3
3.6–4.8	0.720	6	0.136	4	0.280	4
4.8–7.2	0.481	10	0.136	8	0.201	8
			$24 \leqslant Z \leqslant 36$ cm[c]			
0–1.2	1.50	2	0.057	4	0.397	2
1.2–2.4	0.911	4	0.086	4	0.300	3
2.4–3.6	0.746	5	0.115	4	0.252	3
3.6–4.8	0.589	6	0.121	5	0.258	4
4.8–7.2	0.664	9	0.144	7	0.260	8
			$12 \leqslant Z \leqslant 24$ cm[c]			
0–1.2	1.49	2	0.056	4	0.402	2
1.2–2.4	0.973	3	0.084	4	0.299	3
2.4–3.6	0.783	4	0.116	4	0.254	3
3.6–4.8	0.648	7	0.130	5	0.239	4
4.8–7.2	0.597	11	0.154	7	0.266	8
			$0 \leqslant Z \leqslant 12$ cm[c]			
0–1.2	1.45	2	0.041	5	0.392	2
1.2–2.4	0.843	4	0.054	5	0.287	3
2.4–3.6	0.689	5	0.067	5	0.256	3
3.6–4.8	0.561	6	0.081	6	0.226	4
4.8–7.2	0.543	12	0.094	9	0.239	8

[a]These photons were produced by neutron interactions in the phantom (rads per fluence photon).
[b]These photons were produced in the radiation field encompassing the phantom (rads per fluence photon).
[c]Z is the distance measured along the axis of the phantom from the bottom toward the top.

Tab 25.2. Analogical depth-dose distributions for primary application to studies of in-utero survivors of Hiroshima and Nagasaki (small torso)

Penetration depth (cm)	Dose from recoil ions		Dose from photons produced in phantom[a]		Dose from photons produced in radiation field[b]	
	Rads per fluence neutron	Coefficient of variation (%)	Rads per fluence neutron	Coefficient of variation (%)	Rads per fluence neutron	Coefficient of variation (%)
	$\times 10^{-9}$		$\times 10^{-9}$		$\times 10^{-9}$	
			$48 \leqslant Z \leqslant 60$ cm[c]			
0–2.4	1.24	2	0.078	3	0.355	2
2.4–4.8	0.860	3	0.123	2	0.284	3
4.8–7.2	0.905	3	0.160	2	0.285	3
7.2–9.6	0.885	4	0.164	3	0.288	4
9.6–14.4	1.01	7	0.180	5	0.254	7
			$36 \leqslant Z \leqslant 48$ cm[c]			
0–2.4	1.14	2	0.103	2	0.333	2
2.4–4.8	0.527	4	0.162	2	0.240	3
4.8–7.2	0.358	5	0.191	2	0.197	4
7.2–9.6	0.302	7	0.194	3	0.170	5
9.6–14.4	0.270	15	0.192	4	0.160	9
			$24 \leqslant Z \leqslant 36$ cm[c]			
0–2.4	1.09	2	0.103	2	0.337	2
2.4–4.8	0.506	4	0.160	2	0.230	3
4.8–7.2	0.334	5	0.188	2	0.196	4
7.2–9.6	0.260	8	0.191	3	0.194	5
9.6–14.4	0.177	14	0.192	4	0.149	9
			$12 \leqslant Z \leqslant 24$ cm[c]			
0–2.4	1.09	2	0.092	2	0.342	2
2.4–4.8	0.521	4	0.146	2	0.226	3
4.8–7.2	0.356	5	0.167	2	0.190	4
7.2–9.6	0.246	8	0.180	3	0.190	5
9.6–14.4	0.254	14	0.168	4	0.156	10
			$0 \leqslant Z \leqslant 12$ cm[c]			
0–2.4	1.03	2	0.062	3	0.344	2
2.4–4.8	0.432	4	0.095	3	0.218	3
4.8–7.2	0.262	6	0.107	3	0.182	4
7.2–9.6	0.202	9	0.108	4	0.175	5
9.6–14.4	0.172	15	0.102	6	0.157	9

[a]These photons were produced by neutron interactions in the phantom (rads per fluence neutron).
[b]These photons were produced in the radiation field encompassing the phantom (rads per fluence photon).
[c]Z is the distance measured along the axis of the phantom from the bottom toward the top.

Table 25.3. Analogical depth-dose distributions for primary application to studies of in-utero survivors of Hiroshima and Nagasaki (larger torso)

Penetration depth (cm)	Dose from recoil ions		Dose from photons produced in phantom[a]		Dose from photons produced in radiation field[b]	
	Rads per fluence neutron	Coefficient of variation (%)	Rads per fluence neutron	Coefficient of variation (%)	Rads per fluence neutron	Coefficient of variation (%)
	$\times 10^{-9}$		$\times 10^{-9}$		$\times 10^{-9}$	
			$48 \leqslant Z \leqslant 60$ cm[c]			
0–3	1.120	2	0.086	2	0.352	2
3–6	0.796	3	0.138	2	0.291	2
6–9	0.796	3	0.162	4	0.284	3
9–12	0.838	4	0.167	3	0.278	4
12–18	0.970	6	0.180	4	0.320	6
			$36 \leqslant Z \leqslant 48$ cm[c]			
0–3	0.995	2	0.110	2	0.300	2
3–6	0.412	4	0.163	2	0.212	3
6–9	0.246	6	0.190	4	0.178	4
9–12	0.226	8	0.184	3	0.162	5
12–18	0.124	14	0.189	4	0.132	9
			$24 \leqslant Z \leqslant 36$ cm[c]			
0–3	0.990	2	0.114	2	0.314	2
3–6	0.377	4	0.166	2	0.206	3
6–9	0.228	6	0.177	2	0.162	4
9–12	0.159	10	0.176	2	0.171	5
12–18	0.171	19	0.159	4	0.136	9
			$12 \leqslant Z \leqslant 24$ cm[c]			
0–3	0.975	2	0.101	2	0.316	2
3–6	0.384	4	0.151	2	0.208	3
6–9	0.234	6	0.155	2	0.186	4
9–12	0.132	10	0.149	3	0.172	5
12–18	0.114	17	0.141	5	0.148	9
			$0 \leqslant Z \leqslant 12$ cm[c]			
0–3	0.907	2	0.071	2	0.303	2
3–6	0.332	4	0.103	2	0.202	3
6–9	0.202	7	0.108	3	0.176	4
9–12	0.122	11	0.092	3	0.160	5
12–18	0.093	20	0.094	6	0.166	8

[a]These photons were produced by neutron interactions in the phantom (rads per fluence neutron).
[b]These photons were produced in the radiation field encompassing the phantom (rads per fluence photon).
[c]Z is the distance measured along the axis of the phantom from the bottom toward the top.

ORNL-DWG 74-1908

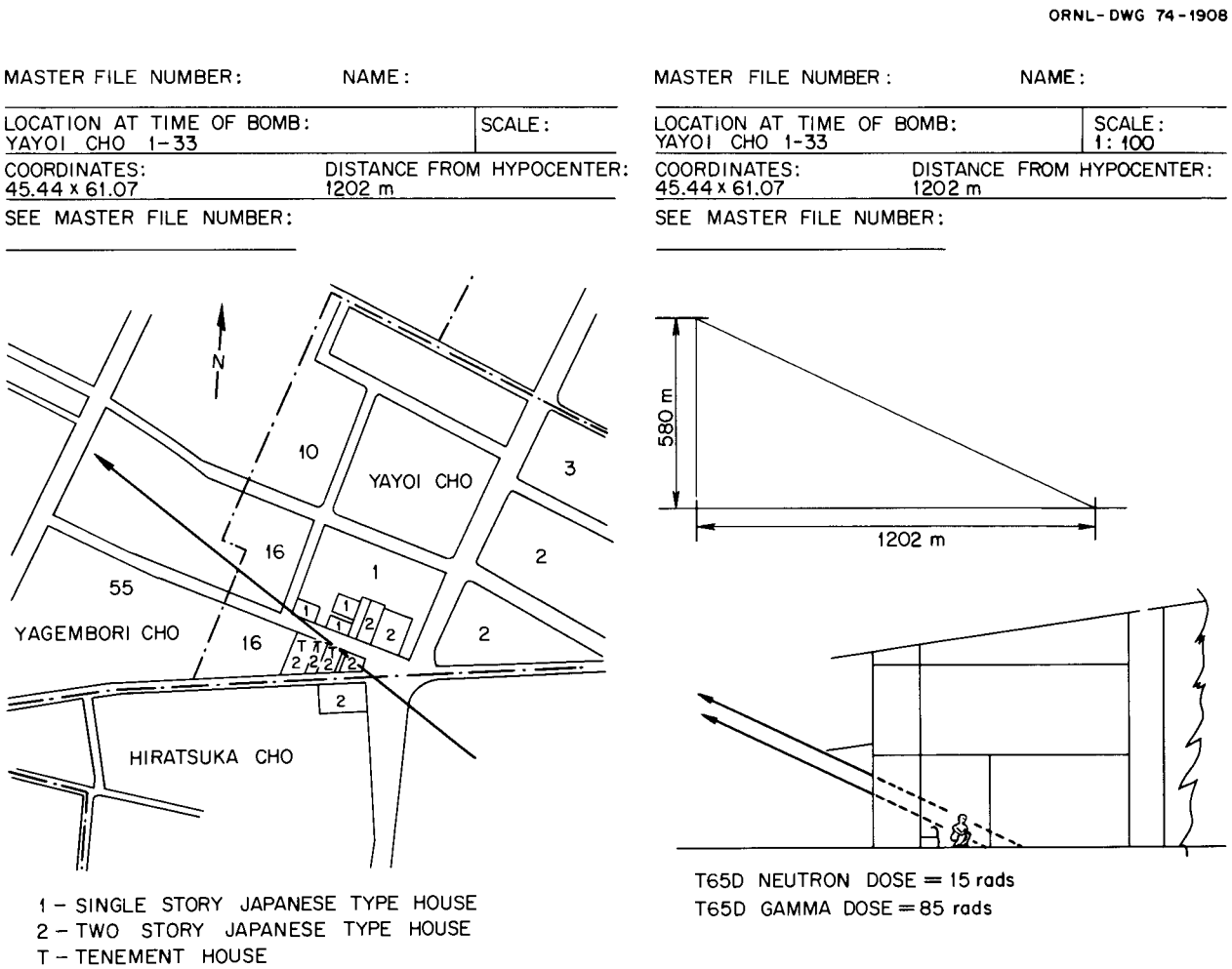

Fig. 25.1. Extracts from shielding information on a typical Hiroshima atomic bomb survivor.

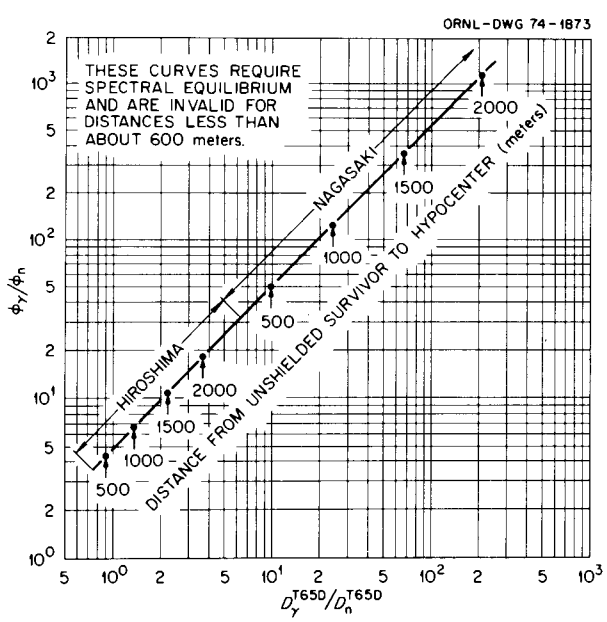

Fig. 25.2. Ratio of gamma-ray fluence to neutron fluence as a function of T65D gamma-ray dose per unit T65D neutron dose.

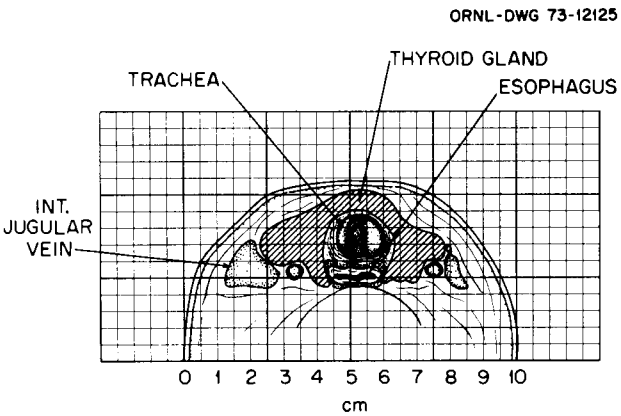

Fig. 25.3. Neck on cross section at the level of the thyroid gland.

Table 25.4. Dose estimates to representative organs of a typical survivor

	Fetus (penetration = 12 cm)	Thyroid isthmus (penetration = 0.7 cm)
	$\times 10^{-9}$	$\times 10^{-9}$
D_n, rads per fluence neutron	0.254	1.50
$D_{n,\gamma}$, rads per fluence neutron	0.168	0.057
D_γ, rads per fluence gamma	0.156	0.397

Table 25.5. Radiation dose to the fetus and the isthmus of the thyroid gland for a typical survivor

In rads

	Neutron	Gamma	Autogamma	Total
T65 dose	15	85	0	100
Dose to thyroid isthmus	9.8	72	0.37	82
Dose to fetus	1.6	28	1.1	31

CESIUM DISTRIBUTION IN SOIL OF THE OAK RIDGE AREA

In order to use in-situ gamma spectrometry for the determination of concentrations of radioactivity in the soil, a model for the distribution of activity as a function of depth in the soil must be assumed. For natural emitters, one generally assumes uniform distribution in the soil. However, for fallout emitters this assumption obviously cannot be made. Studies[14,15] have been done on the actual distribution of fallout emitters in the soil, and the general agreement is that emitters such as ^{137}Cs are distributed exponentially with depth. Since disagreement existed on the best exponential parameters to use, it was decided to make measurements of ^{137}Cs distributions in the Oak Ridge area.

A soil sampling and analysis program was established which could yield information on soil density, soil moisture, and concentration of radionuclides in the soil, including, but not restricted to, ^{137}Cs. Several sites were selected in the Oak Ridge area where in-situ gamma measurements would be made.

Samples were obtained by cutting away the surface vegetation and then taking a core sample to a depth of approximately 10 cm. Several cores were taken at each site and were sliced into 1-cm-thick sections. All sections taken at the same depth were combined for analysis. A total sample size of 200 to 400 g was used.

The soil was returned to the laboratory wrapped in plastic bags. It was then weighed, dried in an oven at 85°C for 24 hr, and reweighed to determine the moisture content. The dry soil was pulverized and passed through a No. 14 mesh screen. The larger particles were discarded, and the meshed soil was placed in a specially prepared sample holder to a specified volume and reweighed. The density determination was made based on this volume and weight.

Moisture content of the soils sampled ranged from 16.2 to 46.2%, depending on the site and the depth at a given site. Moisture content was always greatest in the first centimeter and continued to decrease until about the fourth or fifth centimeter, after which it remained nearly constant to the maximum depth sampled. Soil densities were all remarkably similar. Below 2 cm the dry density was found to be about 1.3 g/cm^3 at all sites. Above that depth the density was less and was somewhat variable from site to site. If moisture content is included, soil densities average nearly 1.6 g/cm^3. This density has been proposed as a good approximation for general use in calculations involving in-situ gamma-ray measurements,[15] and we are able to verify this as a reasonable average value.

Counting of the samples was accomplished using a 5 X 4 in. NaI crystal in a graded shield. The output of the

14. H. L. Beck, *Health Phys.* **12**, 313 (1966).
15. H. L. Beck, J. DeCampo, and C. Gogolak, *In Situ Ge(Li) and NaI(Tl) Gamma-Ray Spectrometry*, HASL-258 (September 1972).

Table 25.6. Distribution of ^{137}Cs measured in soils of the Oak Ridge area

Depth (cm)	Activity (nCi/m^2)					
	Gallaher Bridge[a]	Golf Course[a]	White Oak Dam[a]	EGCR[b]	CARL[a]	Kerr Hollow[a]
0–1	34.7	11	195	9.9	16.8	6.8
1–2	13.2	12	146	5.8	18.0	5.8
2–3	4.2	12	95	4.5	14.7	6.5
3–4	0.23	12	61	3.6	8.4	5.6
4–5		10.8	41		2.5	4.6
5–6		7.3	22	2.9	1.8	
6–7		6.4	12.2			0.93
7–8		2.8	9.9			0.94
8–9		2.5				0.60
9–10		2.2				0.26

[a]All of these were grass-covered sites that probably had not been disturbed for several years.

[b]This was an eroded site where the soil had probably been disturbed during the construction phase at EGCR.

detector was connected through an amplifier to a 512-channel analyzer which recorded the gamma spectrum up to 3 MeV. In order to produce a sufficient number of counts, the counting time was set for 24 hr. Background (including the sample container) was measured for the same length of time and subtracted from the sample count, channel for channel. The net spectrum was used for subsequent analysis. Detector efficiency was measured by counting a standard prepared by tagging typical soil with ^{137}Cs.

The ^{137}Cs analysis was complicated by interference from the 609-keV line of ^{214}Bi, which is a natural radionuclide. The 10% resolution of the NaI detector produced an overlap of the 662- and 609-keV lines. A simple gamma spectrum stripping routine was written. Using a Gaussian fit to the peaks, the computer was able to separate cleanly these two interfering peaks in all samples except those with extremely low ^{137}Cs activity.

Having determined the integral under the ^{137}Cs peak, the soil activity was calculated using the measured efficiency of the detector. The activity has been expressed in nanocuries per square meter for comparison with measurements done by Ritchie et al.[16] Results of the present study are given in Table 25.6.

An attempt was made to define the ^{137}Cs distribution in terms of an exponential function,

$$s = s_0 e^{-\alpha t} ,$$

where s is the activity at depth t (cm), s_0 is the surface activity (photons cm^{-3} sec^{-1}), and α is the reciprocal of the relaxation length (cm^{-1}) of the assumed exponentially distributed source activity with depth.

Values of α ranging from 0.05 to 0.5 have been found to describe some fallout distributions. The value of α best describing the distribution depends on the type of soil, soil density, and moisture content. Since these varied for the local sites, it is not surprising that the fitting parameter varied for the sites. Values of α ranging from 0.1 to 0.5 were found to give the best fit for the various sites. It was also noted in at least two cases that the maximum activity was not on the surface but rather 2 to 3 cm deep. In these cases the activity was nearly uniform through the first 3 cm.

In conclusion, while it was hoped that we could clearly establish the fallout distribution with depth in soil in the Oak Ridge area, it became apparent that the distribution varies enough from site to site that it is prudent to establish the distribution for each site. This is especially wise if the site will be a routine sampling point. Otherwise, the error one must accept on the calculation of ^{137}Cs photon flux above the ground using in-situ gamma measurements is ±25% from this approximation alone.

IN-SITU GAMMA-RAY MEASUREMENTS

Gamma-ray spectroscopy using a lithium-drifted germanium [Ge(Li)] detector has been applied to the determination of radionuclide concentrations in soil and the associated gamma dose rates above the earth

16. J. C. Ritchie, J. R. McHenry, and A. C. Gill, *Health Phys.* **22**, 197 (1972).

ORNL-DWG 72-12137

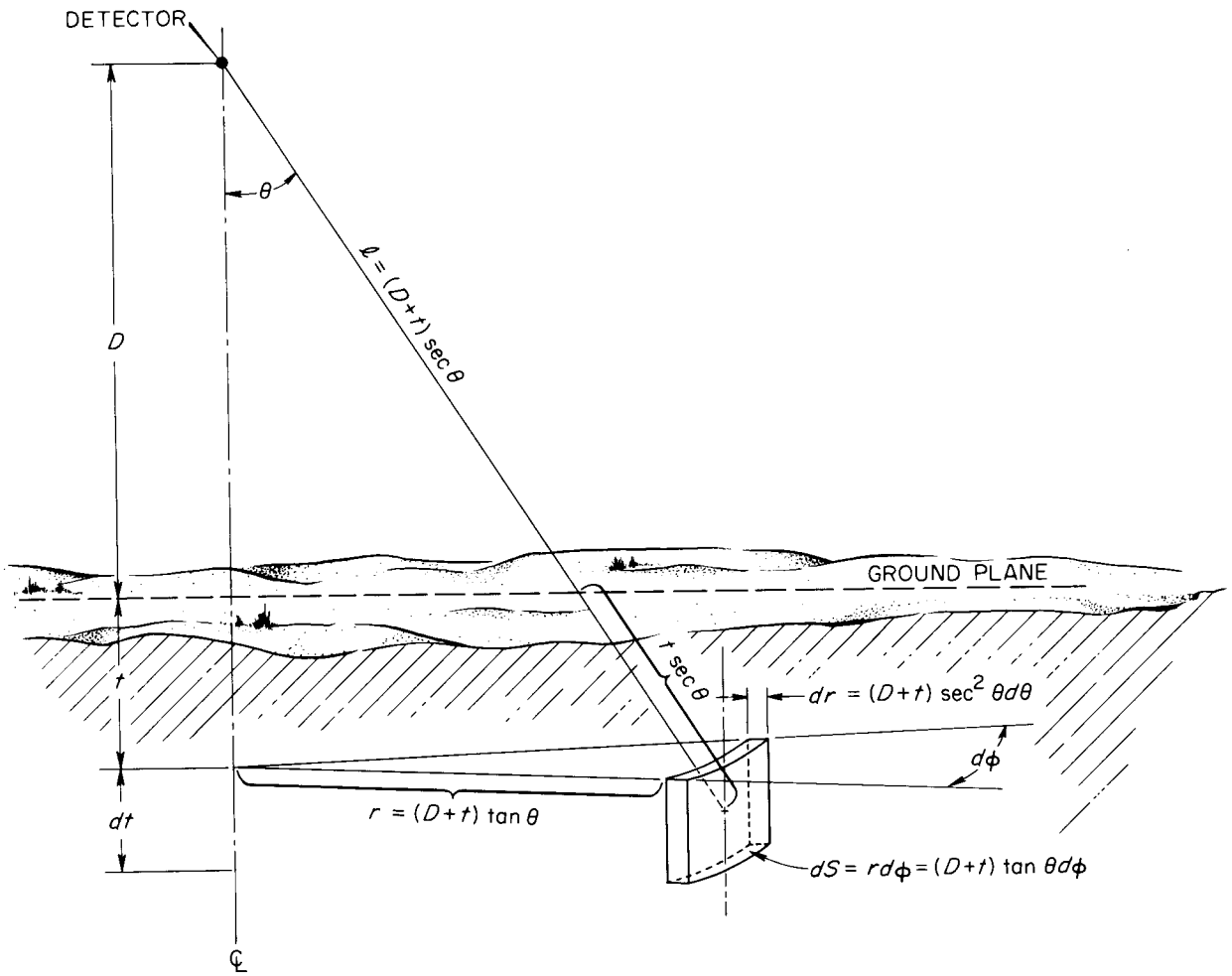

Fig. 25.4. Diagram showing geometrical parameters used in computing gamma-ray fluences from the ground.

plane.[15,17,18] In-situ measurements of soil radioactivity are more sensitive and more representative of the area under consideration than are laboratory analyses of core samples taken from the soil of the area. An unshielded Ge(Li) detector placed about 1 m above the earth detects gamma radiation from an area of about 100 m^2. This represents a large volume of soil compared with the size of a sample usually taken for laboratory analysis.

In order to relate the counts recorded in the total energy peak of the gamma-ray spectrum to the concentration of radionuclides in the soil, a number of parameters must be taken into account. The primary factors are the efficiency of the detector as a function of energy, the absorption of gamma rays by the soil and air, and the solid angle at the detector subtended by the source. The radioactivity distribution with soil depth and the soil density, moisture content, and chemical composition must either be assumed or else determined by time-consuming measurements. The usual practice is to assume some average soil characteristics which apply closely to most soils encountered.

Upon determining the effective center of the detector as a function of energy, the detector was assumed to be a point detector, since the largest error in making this assumption was only 1.2% for the distance of 66.3 cm used between the earth and the center of the detector.

In Fig. 25.4, geometrical terms are defined. The counts recorded by the spectrometer in the total energy

17. J. A. Auxier, D. J. Christian, T. D. Jones, G. D. Kerr, P. T. Perdue, W. H. Shinpaugh, and J. H. Thorngate, *Contribution of Natural Terrestrial Sources to the Total Radiation Dose to Man,* ORNL-TM-4323 (September 1973).

18. L. R. Anspaugh, P. L. Phelps, G. W. Huckabay, P. H. Gudiksen, and C. L. Lindeken, *Methods for the In Situ Measurements of Radionuclides in Soil,* UCRL-74061 (1972).

peak are given for a specified volume of emitter:

$$dn_e(E_\gamma) = n(t, E_\gamma)\, k(E_\gamma)$$
$$\exp\left[-\sec\theta\,(\mu_s t + \mu_a D)\right] \tan\theta\, d\theta\, dt\, d\phi\,, \quad (1)$$

where $k(E_\gamma)$ is the efficiency of the detector in counts per gamma ray multiplied by the distance squared. Photon attenuation in air and soil is given by the exponential factor, where μ_s and μ_a are the attenuation coefficients of the soil and air respectively. The concentration of emitters in the soil as a function of energy, E_γ, and depth, t, is $n(t, E_\gamma)$.

This expression may be integrated for a semi-infinite monoenergetic source of uniform distribution to give

$$n_e(E_\gamma) = \frac{2\phi n\, k(E_\gamma)}{\mu_s} E_2(\mu_a D)\,, \quad (2)$$

where ϕ is the azimuthal angle subtended at the detector by the source and E_2 is the second-order exponential integral defined by

$$E_2(x) = x \int_x^\infty \frac{e^{-z}}{z}\, dz\,. \quad (3)$$

In these calculations the air density was taken to be 1.15 mg/cm^3, and the soil density was taken to be 1.6 g/cm^3. The linear attenuation coefficient was assumed to be that for a soil composition of 11.25% Al_2O_3, 3.75% Fe_2O_3, 56.25% SiO_2, and 25% H_2O. While soil composition and density change from site to site, it was felt that these values represent characteristics that apply to most soils encountered. To allow for attenuation by the dewar, a solid angle was obtained by integrating over the polar angle, θ, from 0 to $\pi/2$ radians, and over the azimuthal angle, ϕ, from 0 to 5.2 radians.

The spectrometer system used incorporated a Ge(Li) detector (10% efficiency)[19] with a multichannel analyzer and paper-tape punch for recording the data. (see Fig. 25.5). This equipment was transported in a mobile laboratory assembled in a 1½-ton van truck complete with a gasoline auxiliary generator for providing electrical power at remote sites. The mobile laboratory and Ge(Li) spectrometer are shown in Fig. 25.6.

The formula used for fission product contamination based on an exponential source model was

19. Efficiency is defined in terms of the relative counting rate of a Ge(Li) detector compared with 3 × 3 in. NaI scintillation detector.

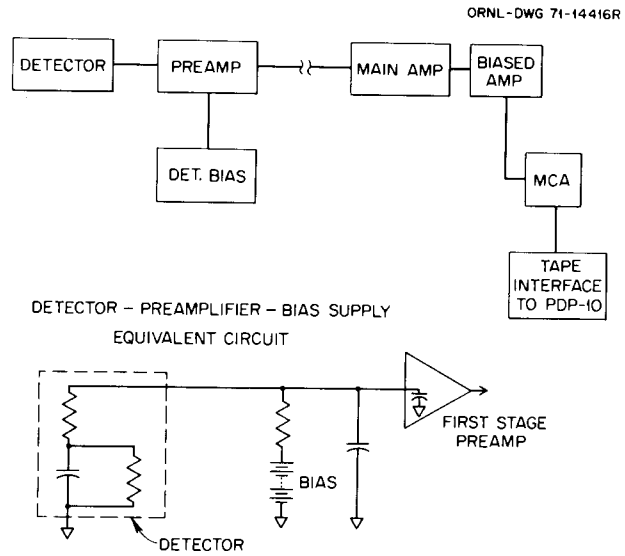

Fig. 25.5. Block diagram of Ge(Li) spectrometer system and diagram of input circuitry.

$$n_e(E_\gamma) = \frac{k(E_\gamma)\, s_0}{\alpha + \mu_s}\, E_2(\mu_a D)\,, \quad (4)$$

where s_0 is the surface activity (photons cm^{-3} sec^{-1}) and α is the reciprocal of the relaxation length (cm^{-1}) of the assumed exponentially distributed source activity with depth.

The detector was calibrated using several gamma sources covering the energy range from 121.9 keV to 2.754 MeV. Values of k were determined for all these sources, and a power function was fitted to the data to give $k(E_\gamma)$ for all energies from 100 to 2700 keV, which covers all the naturally occurring gamma radiation from the earth. Since uniform deposition of radionuclides in the soil was assumed for natural emitters, the factor

$$R = \frac{2\phi k}{\mu_s} E_2(\mu_a D) \quad (5)$$

was calculated for a number of energies from 100 to 3000 keV (see Table 25.7). Values of R for the energies in the data were found above 200 keV by a Guassian backward interpolation technique. The resulting factors were used to determine the gamma rays emitted per cubic centimeter of soil for each observed energy. By including the gamma abundance, a concentration in picocuries per cubic centimeter could be found.

Fig. 25.6. View of mobile laboratory and Ge(Li) spectrometer.

Table 25.7. Ratio R of counts in photopeak to gamma rays emitted per cubic centimeter of soil

E_γ (keV)	$\mu_a D$	$E_2(\mu_a D)$	μ_s	k (counts cm^2/photons)	R (counts cm^3/photons)
	$\times 10^{-3}$				
100	1.72	0.9883	0.2672	0.7940	15.27
150	1.89	0.9873	0.2256	0.5596	12.73
200	2.04	0.9865	0.2032	0.4365	11.02
300	2.20	0.9856	0.1744	0.3076	9.039
400	2.26	0.9853	0.156	0.2400	7.882
500	2.27	0.9852	0.143	0.1980	7.093
600	2.26	0.9853	0.132	0.1691	6.564
800	2.21	0.9856	0.116	0.1320	5.832
1000	2.14	0.9859	0.104	0.1088	5.363
1500	1.96	0.9869	0.0848	0.0767	4.642
2000	1.82	0.9877	0.0730	0.0598	4.207
3000	1.61	0.9890	0.0594	0.0422	3.654

For fission product contamination, notably ^{137}Cs, the source was assumed to be exponentially distributed, and the factor

$$R = \frac{2\phi k}{\alpha + \mu_s} E_2(\mu_a D) \tag{6}$$

was used for calculating the gamma rays emitted per cubic centimeter.

In-situ gamma spectra have been made at sites near the Oak Ridge National Laboratory. Some of these measurements, which were made in conjunction with an aerial survey of the Oak Ridge area by EG&G using the ARMS system,[20] are given in Tables 25.8–25.10. A typical detector spectrum is shown in Fig. 25.7. The majority of the lines in this spectrum can be accounted for by natural and fallout radionuclides. Gamma dose rates were obtained by using conversion factors determined by HASL.[15] These conversion factors allow direct computation of gamma dose rates based on a knowledge of the average soil concentration of the radionuclide under consideration. In order to facilitate

20. C. N. Anderson, D. H. Bundy, J. R. Cleland, and V. F. Weissman, *Aerial Radiological Measuring Systems (ARMS), EG&G Technical Report 1183-1457* (Dec. 5, 1969).

Table 25.8. Results of in-situ soil measurement at Y-12 site

Series	Radionuclide	Soil concentration (pCi/cm^3)	Dose rate (microrads/hr)
Uranium	^{214}Pb	2.14 ± 0.22	
	^{214}Bi	1.69 ± 0.16	
		Average 1.84 ± 0.13	1.99 ± 0.14
Thorium	^{208}Tl	1.12 ± 0.14	
	^{212}Pb	1.92 ± 0.27	
	^{228}Ac	1.12 ± 0.16	
		Average 1.22 ± 0.13	2.06 ± 0.22
Potassium	^{40}K	4.46 ± 0.62	0.47 ± 0.07
Cesium	^{137}Cs	5.98 ± 0.38[a]	0.28 ± 0.02
			Total 4.80 ± 0.27

[a]The ^{137}Cs concentrations are in terms of pCi/cm^3 at the surface.

Table 25.9. Results of in-situ soil measurements of Golf Course site

Series	Radionuclide	Soil concentration (pCi/cm^3)	Dose rate (microrads/hr)
Uranium	^{214}Pb	2.20 ± 0.52	
	^{214}Bi	1.56 ± 0.11	
		Average 1.74 ± 0.10	1.88 ± 0.11
Thorium	^{208}Tl	1.42 ± 0.13	
	^{212}Pb	1.93 ± 0.20	
	^{228}Ac	1.49 ± 0.14	
		Average 1.54 ± 0.09	2.60 ± 0.15
Potassium	^{40}K	8.87 ± 0.68	0.94 ± 0.07
Cesium	^{137}Cs	5.41 ± 0.35[a]	0.25 ± 0.02
			Total 5.67 ± 0.20

[a]The ^{137}Cs concentrations are in terms of pCi/cm^3 at the surface.

Table 25.10. Results of in-situ soil measurements at CARL site

Series	Radionuclide	Soil concentration (pCi/cm^3)	Dose rate (microrads/hr)
Uranium	^{214}Pb	2.10 ± 0.21	
	^{214}Bi	1.57 ± 0.09	
		Average 1.65 ± 0.09	1.78 ± 0.10
Thorium	^{208}Tl	1.06 ± 0.10	
	^{212}Pb	1.79 ± 0.19	
	^{228}Ac	1.13 ± 0.13	
		Average 1.19 ± 0.07	2.01 ± 0.12
Potassium	^{40}K	5.63 ± 0.51	0.60 ± 0.05
Cesium	^{137}Cs	3.11 ± 0.26[a]	0.15 ± 0.01
			Total 4.54 ± 0.16

[a]The ^{137}Cs concentrations are in terms of pCi/cm^3 at the surface.

the analysis of the large amount of data generated, a computer program was prepared with the assistance of the Spectrometric Dosimetry Group. Data from the multichannel analyzer on the mobile laboratory are punched onto paper tape. Upon return to ORNL the paper tape is read onto magnetic tape at the computer center. The magnetic tape is recalled at a remote terminal, and a FORTRAN file is written. The FORTRAN program BGAPE.F4 operates on this data file to find peaks, to integrate under the peaks, to assign energies based on calibration information, and to calculate soil concentrations using predetermined detector parameters.

In conclusion, we have developed an in-situ gamma measurement system which can be used conveniently in the field to obtain concentrations and dose rates from radionuclides in the soil. With slight modification, this system can be used for routine measurements in the environmental monitoring program at ORNL.

MEASUREMENTS OF RADON DAUGHTER CONCENTRATIONS IN AIR

An alpha-particle spectrometer developed at ORNL[21] and a spectrometry technique reported by Martz et al.[22] have been used in measurements of the effects of sealants on the emanation of radon from concrete.[23] In the spectrometry technique of Martz et al., the concentrations of the short-lived radon daughters RaA, RaB, and RaC attached to aerosols are calculated from one count rate of the RaA and two count rates of the RaC′ alpha-particle activity collected on a filter with an air-sampling device. Because the RaA alpha particles collected on the filter are counted separately, this technique offers more accuracy in the calculated concentrations, especially those of RaA, than other methods of taking three counts of the combined alpha-particle activity of RaA and RaC′ collected on the filter.[24,25]

In the spectrometer developed at this laboratory, helium is flowed between a silicon diode detector and a filter which are separated by a distance of about 0.5 cm. By using helium, the counter can be operated at atmospheric pressure, with considerable gain in filter-handling simplicity and little loss of resolution compared with measurements of the alpha-particle spectrum of RaA and RaC′ on the filter made in a vacuum. The resolution of the spectrometer for air samples collected at a flow velocity of about 50 cm/sec with a membrane (Metricel, Gelman GN-6) and glass-fiber (Acropor, Gelman AN-450) filter having a 0.45-μ pore size is compared with a more porous filter (Whatman grade 4) in Fig. 25.8. Either of these membrane or glass-fiber filters with a medium pore size of 0.45 to 0.80 μ allows easy resolution of the RaA and RaC′ alpha-particle activity on the filter. At flow velocities of up to 100

21. P. T. Perdue, W. H. Shinpaugh, J. H. Thorngate, and J. A. Auxier, *Health Phys.* **26**, 114 (1974).
22. D. E. Martz, D. F. Holleman, D. E. McCurdy, and K. J. Schiager, *Health Phys.* **17**, 131 (1969).
23. J. A. Auxier, W. H. Shinpaugh, G. D. Kerr, and D. J. Christian, to be published in *Health Physics.*
24. E. G. Tsivoglou, H. E. Ayer, and D. A. Holaday, *Nucleonics,* **11**(9), 40 (1953).
25. J. W. Thomas, *Health Phys.* **23**, 783 (1972).

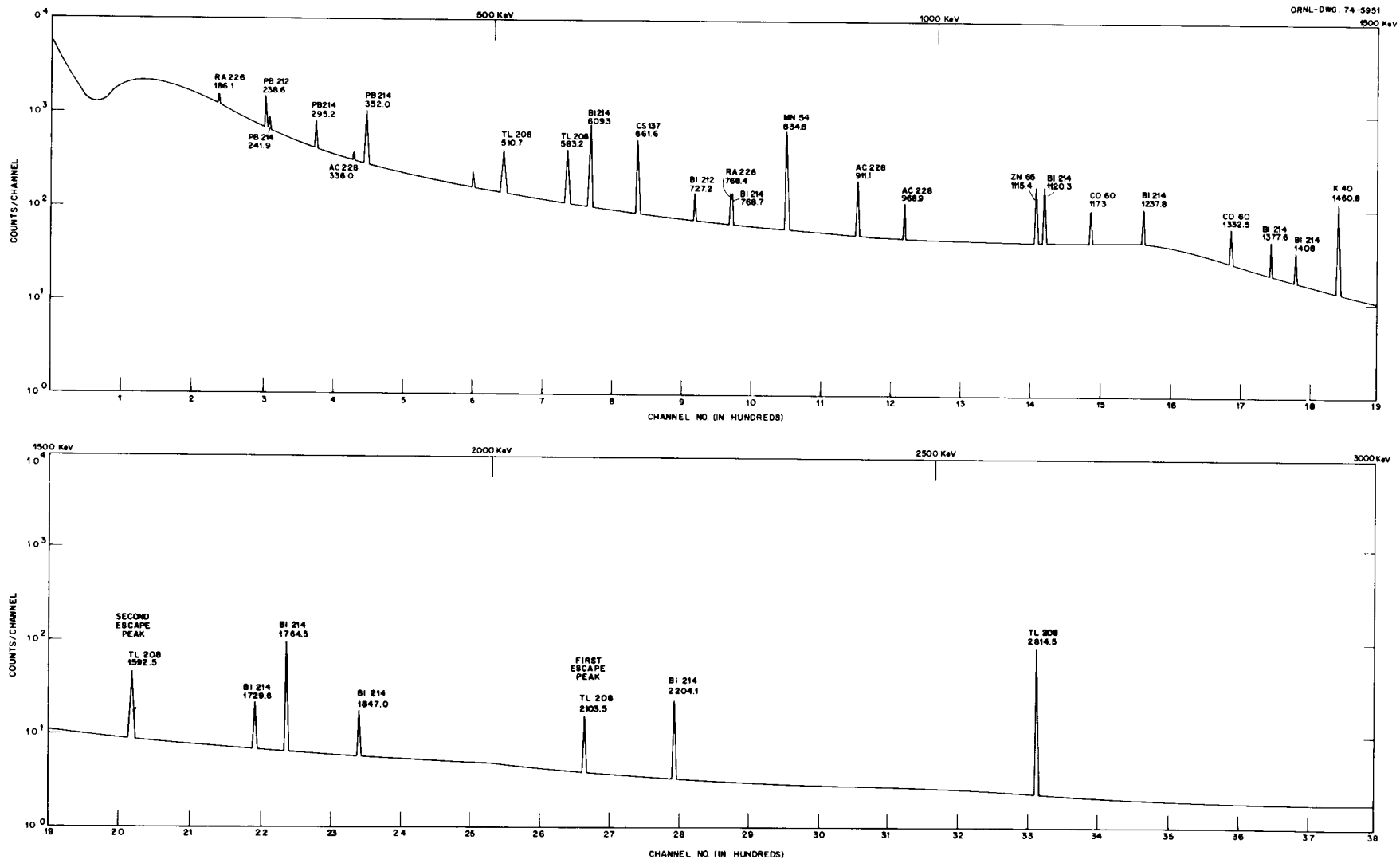

Fig. 25.7. Typical Ge(Li) detector spectrum of gamma rays from natural and fallout radionuclides in soil.

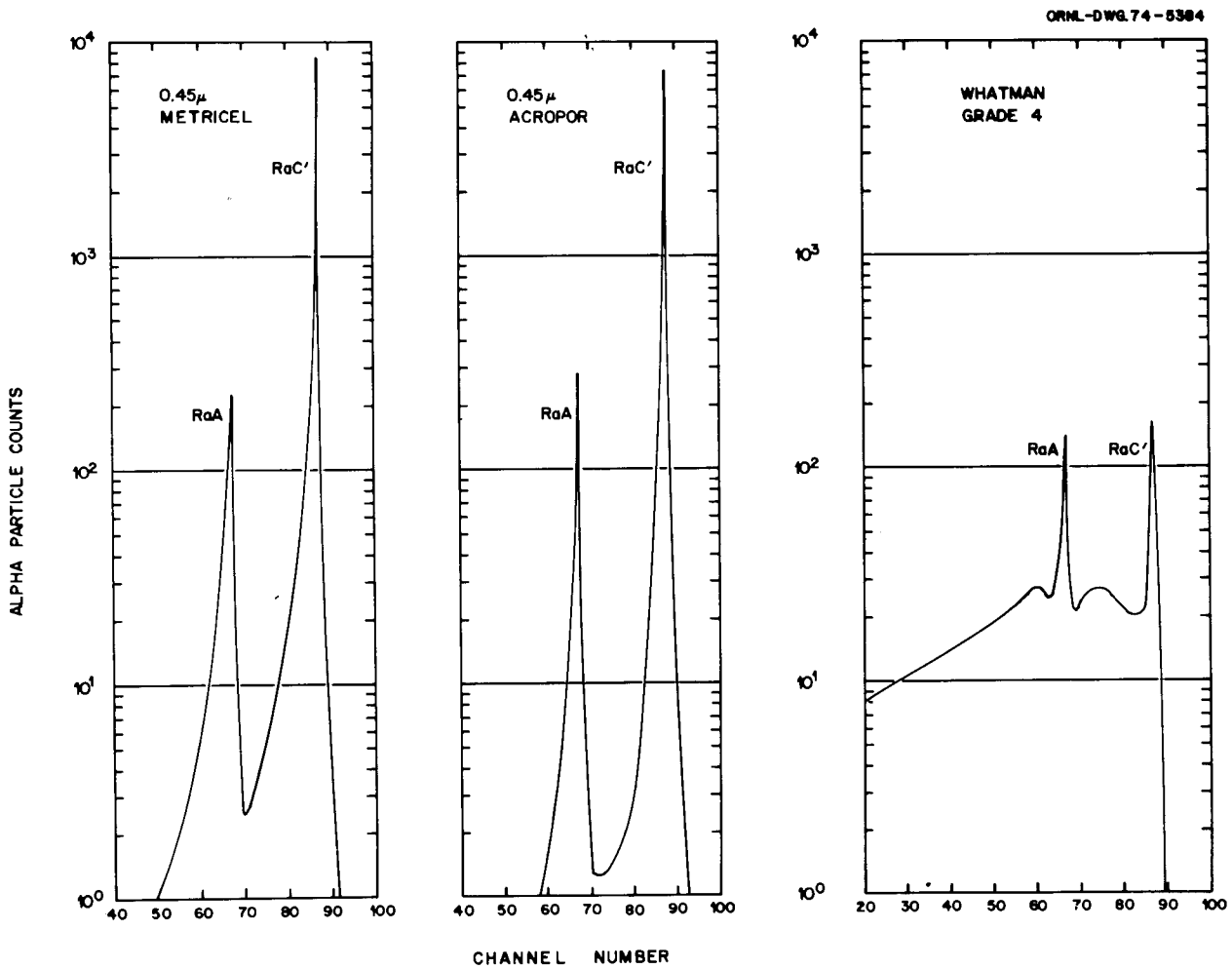

Fig. 25.8. Comparison of the spectra of radon daughter radionuclides collected on various filters and counted with alpha-particle spectrometer described in refs. 17 and 21.

cm/sec, these filters are normally more than 99% efficient in collecting aerosols.[26]

A modification of the spectrometry technique has also been developed at this laboratory[27] to improve the accuracy and sensitivity of radon daughter measurements. In this modification, radon daughter concentrations are calculated from one integral count of the RaA and two integral counts of the RaC′ alpha-particle activity collected on a filter. A computer program, RPCON4, has been written which will calculate the air concentrations and estimate the accuracy in the calculated concentrations of RaA, RaB, and RaC. This program is available in the BASIC language.

For sampling times in the range of 5 to 15 min, one RaA counting interval from 2 to 12 min and two RaC′ counting intervals from 2 to 12 min and from 15 to 30 min after the termination of the air sample collection have been found to give a good overall accuracy in the calculated concentrations for a wide range of RaB/RaA and RaC/RaA activity ratios. The starting time of 2 min for the first is the shortest practicable time for transferring the filter from the air sampling device to the spectrometer, and an ending time of 30 min is standard for techniques of this type.[22,24,25] Air sampling time intervals greater than 15 min were also investigated but were not found to offer any great improvement in the accuracy of the calculated concentrations.

In late October and early November of 1973, the alpha-particle spectrometer and modified spectrometry

26. American National Standards Institute, *Guide to Sampling Airborne Radioactive Materials in Nuclear Facilities*, ANSI-N13.1 (1969).

27. G. D. Kerr, *Trans. Amer. Nucl. Soc.* **17**, 541 (1973).

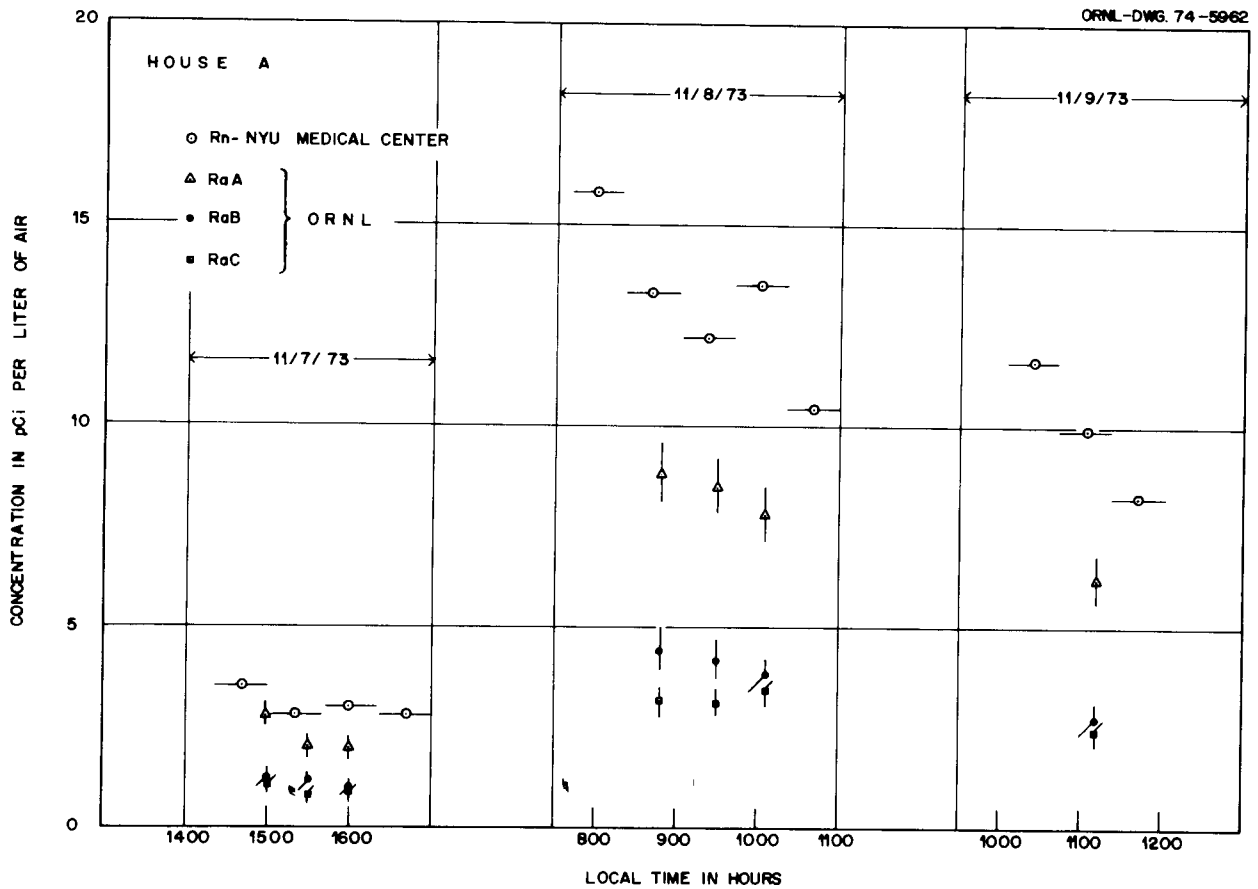

Fig. 25.9. Results of radon and radon daughter measurements in a house at Grand Junction, Colorado, showing variation in concentrations with time.

technique were used to measure radon daughter levels in nine structures in Grand Junction, Colorado, at the request of the AEC. Tailings from uranium mines had been used in their construction, but two had been reconstructed to remove most of the tailings. Because most of the tailings had been used as a fill, the measurements were made in either the basements of the structures or the first floor of slab-type structures. With one exception, the measurements were made in the living areas of the houses. Examples of the radon daughter measurements in one of the structures are shown in Fig. 25.9. Also shown in the figure are measurements of radon levels made by the Institute of Environmental Medicine of the New York University Medical Center.[28] The radon concentrations from their measurements are plotted at the center of 40-min measuring intervals, indicated by the horizontal bars. Radon daughter concentrations from our measurements are plotted at the midpoint of air sampling times of 5 to 15 min.

The vertical bars on the radon daughter concentrations are an estimate of the probable error in the measurements. These are based on a statistical uncertainty of one standard deviation in each of the three counts of activity on the filter and on systematic uncertainties of ±5% in both the detection efficiency of the alpha-particle spectrometer and the air sampling rate. Air sampling rates were measured with a flowmeter that had been calibrated with a wet test meter, using standard procedures.[29,30] Concentrations of

28. H. Spitz and McD. E. Wrenn, personal communications (1974).

29. American National Standards Institute, *Radiation Protection in Uranium Mines and Mills,* ANSI-N7.1a (1969).

30. R. L. Rock, R. W. Dalzell, and E. J. Harris, *Controlling Employee Exposure to Alpha Radiation in Underground Uranium Mines,* U.S. Department of the Interior, Bureau of Mines (1971).

Table 25.11. Average and standard deviation of radon daughter concentrations measured in structures at Grand Junction, Colorado

Structure	Period	Number of measurements	Average concentration (pCi/liter)			Trend in radon concentration
			RaA	RaB	RaC	
House A	Afternoon	3	23 ± 0.5	1.1 ± 0.2	1.0 ± 0.2	Falling slowly
	Morning	4	7.9 ± 1.2	3.8 ± 0.8	3.0 ± 0.4	Falling
House B	Morning	2	40 ± 5	25 ± 6	19 ± 6	Falling
	Afternoon	2	25 ± 5	19 ± 4	18 ± 3	Falling slowly
House C	Afternoon	3	0.8 ± 0.3	0.2 ± 0.04	0.4 ± 0.08	
	Morning	2	1.4 ± 0.4	0.6 ± 0.2	0.5 ± 0.08	
House D	Afternoon	3	28 ± 3	11 ± 0.9	8.4 ± 1.2	
	Morning	2	21 ± 11	9.1 ± 2.6	4.6 ± 1.8	Falling
House E	Morning	2	10 ± 4	5.5 ± 2.0	4.6 ± 1.2	Falling
House F	Afternoon	5	232 ± 22	172 ± 17	145 ± 14	Steady
House G						
Location 1	Afternoon	2	28 ± 5	13.2 ± 0.2	8.2 ± 0.1	Falling slowly
	Morning	1	38	15	11	Rising
Location 2	Afternoon	2	23 ± 7	13 ± 2	6.8 ± 0.4	Falling slowly
	Morning	1	42	14	9.2	Rising
House H	Afternoon	4	5.3 ± 0.4	3.1 ± 0.2	2.0 ± 0.3	Steady
	Morning	2	6.0 ± 0.7	3.4 ± 0.4	2.0 ± 0.6	Steady
School	Afternoon	3	0.8 ± 0.4	0.2 ± 0.09	0.2 ± 0.1	Rising slowly

RaA, RaB, and RaC measured in these structures varied from highs of 255 (±7%), 187 (±8%), and 156 (±7%) pCi/liter, respectively, in a nonreconstructed house to lows of 0.50 (±20%), 0.17 (±35%), and 0.15 (±30%) pCi/liter, respectively, in a school.

Because the general pattern of our measurements was to move from one structure in the forenoon and to set up at the next structure in the afternoon, the late afternoon and early morning measurements, which showed considerable variation in some structures, were averaged separately. The average and the standard deviation of the measured radon daughter concentrations for each set of afternoon or morning measurements are given in Table 25.11. Based on the NYU Medical Center measurements, trends in the radon levels spanning the time interval of our measurements in the structures were determined and are shown in Tables 25.11 and 25.12. In Table 25.12 the averages and standard deviations of the RaB/RaA and RaC/RaA activity ratios are given for each set of corresponding measurements in Table 25.11. The average activity ratios in Table 25.12 show that the closest approaches to an equilibrium condition (i.e., RaB/RaA = RaC/RaA = 1) were in the afternoon measurements at house B (RaB/RaA = 0.76 and RaC/RaA = 0.74) and house F (RaB/RaA = 0.74 and RaC/RaA = 0.63).

Large fractional standard deviations in the concentrations or the activity ratios of Tables 25.11 and 25.12, respectively, are mainly associated with either rapid changes in the radon levels or large uncertainties in the alpha-particle counts at the lower radon daughter levels. At higher and either steady or slowly changing radon daughter levels, very good estimates of the ventilation rate of a structure could be made from the average activity ratios and the steady-state solutions to the ventilation equations of Hultiqvist.[31] In five structures where estimates could be made within one standard deviation of the activity ratios, the ventilation rates ranged from 0.4 to 1.6 air exchanges per hour.

The ventilation rates of structures are, of course, affected by the type of heating system used, the opening of doors, etc., and therefore do not remain constant, as shown by the varying radon and radon daughter levels in Fig. 25.9. However, the range of ventilation rates estimated from the radon activity ratios in these structures compares very well with the range of ventilation rates measured in houses under similar conditions by other methods.[32] During our measurements, most of the houses were closed, and the heating systems were in operation.

31. B. Hultiqvist, *Studies on Naturally Occurring Ionizing Radiations*, Almqvist and Wiksells Boktryskeri AB, Stockholm, 1956.

32. T. H. Handley and C. J. Barton, *Home Ventilation Rates: A Literature Study*, ORNL-TM-4318 (September 1973).

Table 25.12. Average and standard deviation of the activity ratios of radon daughters measured in structures at Grand Junction, Colorado

Ventilation rates are based on activity ratios and steady-state solution to Hultqvist's ventilation equations

Structure	Period	Number of measurements	Average activity ratio		Ventilation rate (air exchanges/hr)	Trend in radon concentration
			RaB/RaA	RaC/RaA		
House A	Afternoon	3	0.48 ± 0.08	0.44 ± 0.06	1.2	Falling slowly
	Morning	4	0.48 ± 0.03	0.38 ± 0.03		Falling
House B	Morning	2	0.62 ± 0.06	0.46 ± 0.10		Falling
	Afternoon	2	0.76 ± 0.01	0.74 ± 0.02	0.4	Falling slowly
House C	Afternoon	3	0.31 ± 0.06	0.52 ± 0.01		
	Morning	2	0.42 ± 0.11	0.33 ± 0.01		
House D	Afternoon	3	0.40 ± 0.01	0.30 ± 0.02		
	Morning	2	0.46 ± 0.11	0.22 ± 0.03		Falling
House E	Morning	2	0.55 ± 0.03	0.47 ± 0.04		Falling
House F	Afternoon	5	0.74 ± 0.03	0.63 ± 0.04	0.5	Steady
House G						
Location 1	Afternoon	2	0.47 ± 0.07	0.30 ± 0.05	1.6	Falling slowly
	Morning	1	0.41	0.29		Rising
Location 2	Afternoon	2	0.59 ± 0.24	0.30 ± 0.10		Falling
	Morning	1	0.35	0.22		Rising
House H	Afternoon	4	0.60 ± 0.08	0.39 ± 0.04	1.3	Steady
	Morning	2	0.57 ± 0.04	0.32 ± 0.06	1.1	Steady
School	Afternoon	3	0.30 ± 0.05	0.32 ± 0.02		Rising slowly

Our laboratory finding that epoxy paint was effective in reducing radon emanation from concrete surfaces has also been verified by the NYU Medical Center[28] measurements of radon levels in some houses at Grand Junction where this technique was used. In our laboratory study, radon emanation from concrete was found to be reduced by a factor of 4 after the application of a heavy coat of epoxy paint.

SHIELDING MATERIALS FOR HIGH-YIELD NEUTRON SOURCE CARRIERS

Several materials have been investigated as suitable replacements for paraffin and fiberboard in source carriers for sealed isotopic neutron sources. Paraffin is, of course, an effective shielding material but does not meet newer impact and fire-resistance requirements of source carriers. Fiberboard meets these requirements, but it is one of the poorer shielding materials for high-yield neutron sources.

Machinable composition materials that are fire and impact resistant and that are suitable shielding materials are Bakelite and Transite. For transporting sources, Bakelite is more suitable as a replacement for paraffin because of its lower density. One disadvantage is, of course, the cost of machining slabs of either material to fit into the steel outer drum of a source carrier or other containers.

A search for a conventional formable material failed to produce any of sufficiently low density that were both fire and impact resistant. One has, however, been developed that appears to be promising as a replacement for paraffin. This material uses polyethylene and boric acid as the primary shielding material with a fire-resistant mineral binder containing fibrous strengthening agents. The material was prepared from a mixture of 20 lb of granulated polyethylene (Hifax type 1900), 4 lb of boric acid (anhydride), 8 lb of barium sulfate (anhydrous), 5 lb of sodium silicate (water glass), 2 lb of asbestos fibers, 1 lb of glass-wool fibers, 90 cm^3 of a surfactant (Du Pont Triton X-100), and 6500 cm^3 of water. This mixture was cast in a 14-in.-diam steel drum with a 2-in.-diam central bore for accepting a neutron source and was slowly cured in a stepwise manner to a final temperature of 140°C.

In Table 25.13, maximum dose-equivalent rates in millirems per hour from an americium-beryllium neutron source in a source carrier made from this material are compared with those from the bare source and from the source in identical source carriers made with several conventional shielding materials. All measurements were made perpendicular to the axis of the drum along

Table 25.13. Maximum dose-equivalent rates perpendicular to axis of drum at height of americium-beryllium neutron source in drum

Type of shielding material in drum	Distance between center of source and center of detector (cm)	Maximum dose equivalent (millirems/hr)				Weight of drum and shielding material (lb)
		Fast neutron	Thermal neutron	Gamma ray	Total	
Bare Am-Be source[a]	50	65	0.17	20	85	
	100	17	0.11	5	22	
Fiberboard	22[b]	350	0.60	24	375	46
	50	60	0.36	6	66	
	100	15	0.21	2	17	
Polyethylene mixture	22[b]	130	0.34	14	144	64
	50	30	0.23	4	34	
	100	10	0.15	2	12	
Paraffin	22[b]	90	2.6	15	108	63
	50	15	0.45	4	20	
	100	5	0.30	2	7	
Bakelite	22[b]	120	4.5	15	140	86
	50	20	1.0	4	25	
	100	6	0.30	2	8	

[a]Source strength was 1.27×10^7 neutrons/sec.
[b]Distance from center of drum to surface of drum plus 4 cm to center of detector.

a line through the center of an americium-beryllium neutron source where the thickness of the shielding material was about 6 in. The values of dose equivalent given in the table are for americium-beryllium source with a strength of 1.27×10^7 neutrons/sec. From this table, it can be seen that the weight and shielding properties of this mixture compare favorably with those of paraffin.

Source carriers made with this shielding material have not been subjected to standard impact and fire testing, but the material appears able to withstand these tests. For example, the material will scorch on the surface when exposed to an open flame from a torch, but it will not support combustion. The corrosive nature of the water glass in the uncured casting mixture could require the use of stainless steel shipping containers. This appears to be the only drawback in comparison with other conventional shielding materials.

26. Solid-State Dosimetry Research

Klaus Becker

M. Abdel Razek[1]
J. S. Cheka[2]
R. B. Gammage
F. F. Haywood[2]
J. S. Jun[1]
A. Moreno y Moreno[1]
N. Saheli[1]

OBJECTIVES

The solid-state dosimetry research work has as a major objective the development of improved detectors and techniques for the quantitative characterization of man's natural and artificial radiation environment. Emphasis is on integrating dosimeters with better sensitivity, accuracy, storage stability, linear energy transfer, and energy response, or other properties which make them superior to widely used photographic film, ionization chambers, or TLD systems for personnel dosimetry, environmental radiation monitoring, clinical dosimetry, etc. Of particular interest has been and is the development of new approaches and a better understanding of the principles involved. Another important aspect of the work is the collection and distribution of relevant information, training of specialists, intercomparison of systems, organization of meetings, and consultation with those who want to apply advanced dosimetric techniques. As in previous years, the main emphasis of the experimental work has been on track etching, TL, and TSEE dosimetry.

SPARK COUNTING OF NEUTRON-INDUCED RECOIL PARTICLES

The value of conventional techniques (photographic emulsions, TLD albedo methods) in fast-neutron personnel monitoring is known to be rather limited. Among the more promising alternatives are track-etching dosimeters. There have been essentially two approaches with different advantages and disadvantages. One possibility is to record fission fragments from ^{237}Np, ^{232}Th, etc., preferably in thin polycarbonate foils. This permits fast automatic evaluation of the resulting perforations in the foils by spark counting but also requires the use of fairly large quantities of radioactive materials, which may restrict large-scale use in personnel dosimetry. The other possibility is based on the detection of the tracks of the recoil nuclei which the neutrons produce by interaction with foil (or foil cover) constituents such as carbon and oxygen. (It is more difficult to record recoil proton tracks.) So far, however, the recoil tracks could not be counted efficiently with the spark counter due to their short range.

As can be seen in Fig. 26.1, the background spark count of an overetched unexposed foil is increased by exposure of a commercial cellulose nitrate foil (Kodak-Pathé LR 115 strippable) to fission neutrons. There is no well-defined plateau in the spark-count vs voltage diagram, and the count increases during repeated sparkings of the same foil. Optimum etching conditions have to be established separately for each foil by determining the signal-to-background ratio as a function of sparking voltage and etching time. The sensitivity increases with increasing foil sensitivity and neutron energy, but even in less sensitive Kimfol polycarbonate foils, 3 rads of fission neutrons produce a count substantially higher than background (Fig. 26.2). The count was consistently higher in Teflon-covered foils than in polyethylene-covered ones for different foil materials and neutron energies, indicating that no recoil proton tracks are sparked. A similar acceleration in electric breakdown is produced only by very high (about 10^4 to 10^6 R) gamma-radiation doses. It has thus been demonstrated that the efficient automatic spark counting of fast-neutron-induced recoil particle tracks in thin polymer foils such as cellulose nitrate and polycarbonate is possible if the foils undergo extended

1. Alien guest.
2. Dual capacity.

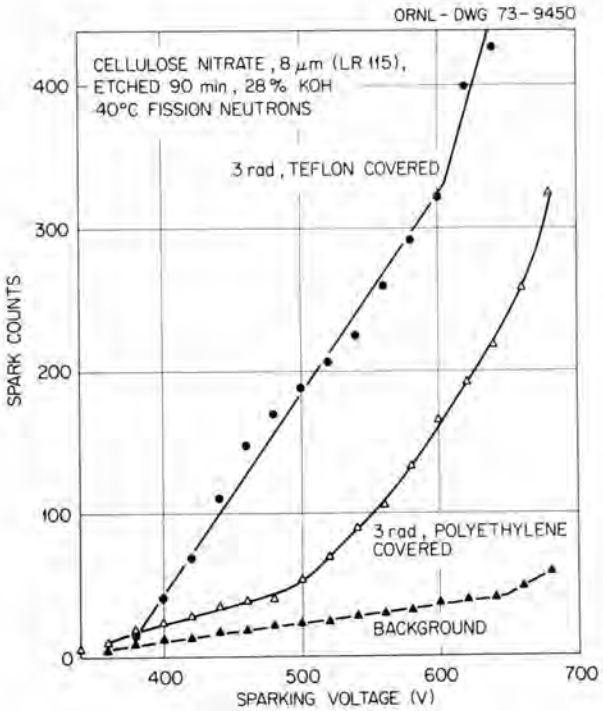

Fig. 26.1. Spark counting of neutron-induced heavy recoil nuclei tracks in ~1 cm^2 of "over-etched" cellulose nitrate in foils covered with either Teflon or polyethylene.

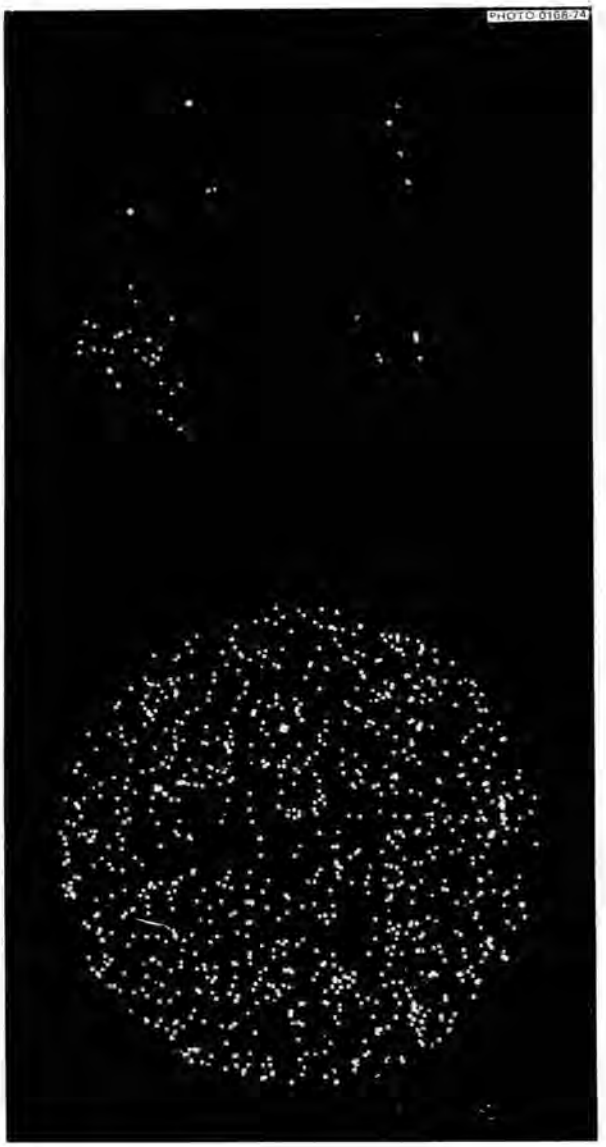

Fig. 26.2. Replica of spark-counted polycarbonate foils without exposure and after exposure to 5 rads of 14-MeV neutrons and extended etching in KOH.

etching to the point where electric breakdown begins to occur even in unexposed foils.[3] The neutron energy response, reproducibility, and threshold of measurability with regard to neutron dose and energy are being established.

PRECISION OF FAST-NEUTRON DOSIMETRY BY TRACK ETCHING

In past years, the emphasis of our track-etching fast-neutron dosimetry work has been on detector sensitivity, with the measurability of the low doses encountered in personnel dosimetry being the most important goal and the precision of secondary importance. As it later became apparent, there is frequently a need for accurate measurements of fairly high doses in the 50 to 500 rad range, for example, in accident dosimetry, in radiobiological or radiotherapeutical work, or for the intercomparison of neutron sources by mail. The latter application is the subject of a Research Agreement between ORNL and IAEA. It has to be determined if accuracies consistently better than ±5% can be obtained in neutron flux (or dose) measurements by track etching.

So far, three methods have been studied, using mostly exposures of about 100 rads of fast fission neutrons from the HPRR:

1. Lexan disks in direct contact with a thin (0.05-mm) thorium metal foil, evaluated after etching for 5 hr at 43 ± 0.5°C in KOH (density 1.239 at 20°C) by microscopic track counting at 100X magnification.

3. K. Becker and M. Abdel Razek, *Automatic Spark Counting of Fast Neutron Induced Recoil Particle Tracks in Polymer Foil*, ORNL-TM-4460 (1974).

2. Lexan disks in direct contact with a foil consisting of 2 mg/cm^2 of a mixture of 5% ^{237}Np and 95% gold (by weight) on a 0.16-mm silver backing and covered by a protective gold film 0.45 mg/cm^2 in thickness,[4] evaluated also by microscopic counting.
3. Thin (10-μm) Kimfol foils exposed in contact with a material consisting of 2% ThO_2 and 98% tungsten. This material is uniform and inexpensive. The foils are evaluated by spark counting (presparking at 760 V, counting by three sparkings at 500 V) after 3 hr of etching at 43 ± 0.5°C in KOH (1.239 g/cm^3).

With repeated exposures and etchings of ten foils each, standard deviations of 2 to 3.5% have been obtained for both spark counting and visual counting by different persons. It has been found that the time required for equally precise measurements was less for visual than for spark counting at the relatively high track densities (about 10^2 to 10^3 tracks/mm^2) encountered in high dose measurements (about 50 to 500 rads) and that the visual counting is much less dependent on small differences in etching conditions, etc. Calibrations of various track detectors at other neutron energies between 0.4 and 15 MeV are presently being carried out in cooperation with BNL.

Studies concerning the influence of environmental parameters on the characteristics of spark counters have also been carried out using a specially designed counter that permits exact definition of counting gas, gas pressure, etc. Apparently, normal fluctuations in ambient temperature, air pressure, and humidity have only little effect, and less influence of the counting polarity on the sparking plateau has been found than what has been reported by other investigators.[5]

THERMOLUMINESCENCE OF ANCIENT CERAMICS

It is well known that the environmental dose rate is subject to daily, seasonal, and other long-term fluctuations due to variations in temperature, soil humidity, snow cover, wind direction, etc. It would be desirable to obtain values that have been averaged over very long periods of time as a baseline for studies of such fluctuations and/or recent increases. It has been the goal of an experimental study to provide such an averaging measurement over the past hundreds or thousands of years by evaluating the TL signal in ancient ceramics such as potsherds, tiles, bricks, or terra-cotta statues of known age based on the relationship

$$\text{average dose rate} = \frac{\text{TL signal}}{\text{age} \times \text{sensitivity}} .$$

Large (100 to 200 μm) quartz grains, which are known to contain almost no radioactivity and may therefore be employed as a reliable detector for the long-range gamma radiation, have been isolated from the interior of Mesoamerican potsherds (provided by the National Museum in Mexico City). The alpha-radiation effect at their surface had to be eliminated by etching away most of the alpha-exposed surface layer with hydrofluoric acid. The "internal" beta-radiation dose, which can be measured by exposing thin layers of $CaSO_4$:Dy shielded by 30 mg/cm^2 of plastic between the potsherds, had to be subtracted for precise measurements. The details of these techniques are discussed in ref. 6. A typical ancient TL signal and the known modern calibration glow curve are given in Fig. 26.3.

The accumulated radiation dose can be estimated from the peak height as well as from the area under the peak. Some of the results from Mexican samples are compiled in Table 26.1 (samples from Egypt and Central Asia are presently being studied). The dose rates obtained are consistent with the results reported by other authors after the internal beta dose (mostly due to ^{40}K) has been subtracted. Also studied were the linearity of response; the effects of light, heat treatment, etc., on the sample characteristics; and methods of minimizing spurious signals.

As a side product of these studies in which scientists in several countries expressed a strong interest, a commercial TL reader has been used for authenticating art objects based on ceramics (vases, statues). As a typical example, the glow curves of unirradiated and of preirradiated quartz grains from a supposedly pre-Columbian object from Ecuador have been compared with the background signal in Fig. 26.4. Obviously, the object is a fake. If a faker should try to simulate old age by external irradiation, this can be detected by etching of the large quartz grains. In an old sample, removal of the surface layers, which were exposed to high alpha-radiation doses because of the thorium and uranium content of the clay matrix, results in a reduction of the TL output which does not occur if the sample has been uniformly irradiated.

4. Nuclear Radiation Development, North Grand Island, N.Y.
5. W. G. Cross and L. Tommasino, *Proc. Symp. Neutron Dosimetry*, EUR-4896, vol. I, p. 283 (1972).
6. K. Becker and A. Moreno y Moreno; *Applications of TL in Ancient Ceramics for Authenticity Tests and Environmental Monitoring*, ORNL-TM-4572 (1974).

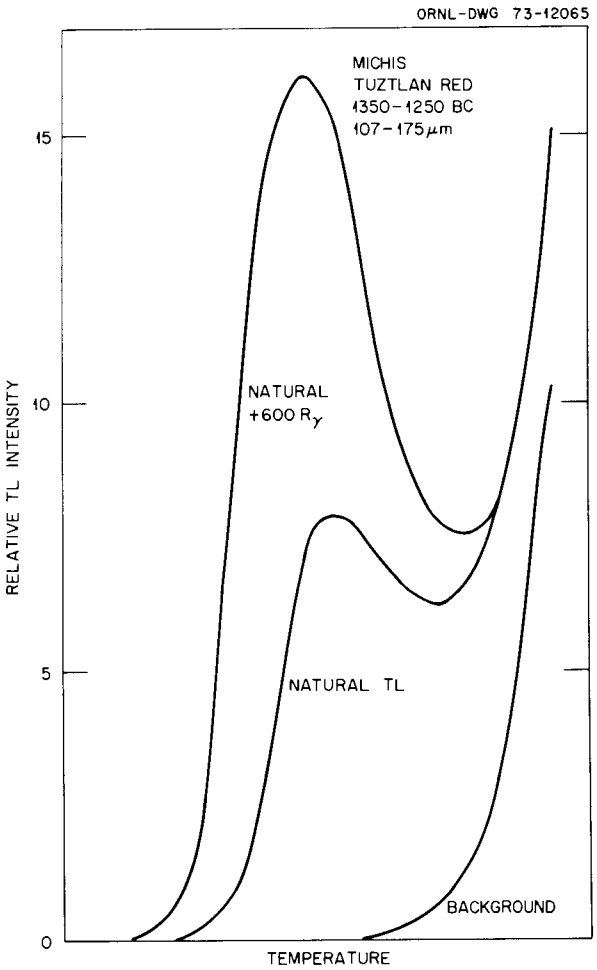

Fig. 26.3. Accumulated TL signal caused by natural radiation in large quartz grains from the interior of a pre-Columbian potsherd, with and without an additional exposure to 600 R of gamma radiation.

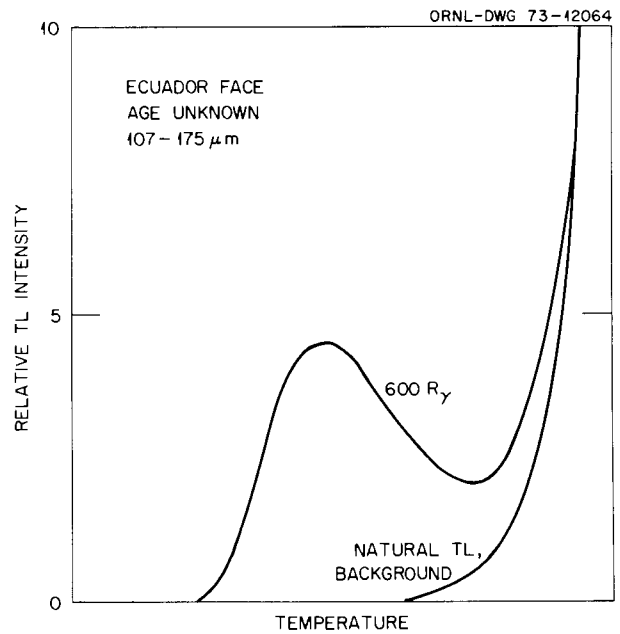

Fig. 26.4. Curves showing absence of natural TL in the large quartz grains from a faked, recently made "pre-Columbian" artifact.

Table 26.1. Doses and dose rates in various Mesoamerican potsherds

Sample	Method[a]	Dose (R)	Estimated age (years)	Environmental dose rate (mR/year)[b]
Guamuchal blanco diferenciado	a	385	3070	125
	b	380		
Xquic	a	653	3070	213
Michis Tuztlan red	a	565	3270	175
	b	580		
Burnished brown	a	133	1470	120
	b	220		
Burnished red on buff	b	324	1300	250

[a]a, peak height; b, peak area with a maximum temperature of about 400°C.
[b]Uncorrected for "internal" beta radiation dose.

ENVIRONMENTAL DOSIMETRY INTERCOMPARISONS

Perhaps not surprisingly, the results obtained in environmental monitoring by different investigators using different types of integrating detectors rarely agree within the accuracy limits that are claimed for each method. In order to compare and, if necessary, standardize the techniques, a workshop on this subject was organized and conducted in August 1973 as part of the Annual Dosimetry Intercomparison Study at ORNL. Six groups from three countries exposed their detectors under identical conditions for nine days at a location with increased background, accumulating a total of about 10 mR, and were asked to give their estimate of the local dose rate. The results of five groups (the results from Sweden have not yet been received), as compiled in Table 26.2, varied by more than a factor of 2. Although the situation was somewhat unusual because there was a strong low-energy (<100 keV) contribution to total dose which is not normally observed in environmental monitoring, this result clearly demonstrates the need for further intercomparisons. Based on extensive discussions, a more comprehensive study of this type is being organized in cooperation with the USAEC Health and Safety Laboratory and the University of Texas.

Table 26.2. Environmental monitoring intercomparison at ORNL, August 1973

Institution	Detector	Dose rate (μR/hr)
GFK Karlsruhe	CaF_2:Dy[a]	31.3
	LiF	34.5
Savannah River	CaF_2:Dy[a]	38.0
Harshaw Co.	CaF_2:Dy[a]	25.5
	CaF_2:Mn[a]	27.5
ORNL	BeO (TSEE)	20.5
	BeO (TSEE)	20.1
	BeO (TSEE)	18.2
	$CaSO_4$:Dy[b]	59.0
	$CaSO_4$:Dy[a]	40.3

[a]Behind energy compensation filter.
[b]Overestimate due to lack of filter.

TLD MEASUREMENTS WITH TERBIUM-ACTIVATED MAGNESIUM ORTHOSILICATE

Terbium-activated magnesium orthosilicate has been prepared by heating finely powdered mixtures of MgO and SiO_2 impregnated with a dilute solution of a Tb^{3+} salt to temperatures around 1800°C in a platinum crucible. Optimized preparation resulted in a material that is about 30 times as sensitive as the widely used LiF:Mg,Ti (TLD-100), exhibits less fading at elevated temperatures, and does not require a complicated multistep annealing cycle prior to reuse. Some supralinearity of response is observed at low-LET radiation doses exceeding 50 to 100 R (Fig. 26.5). The photon energy dependence (oversensitivity by a factor of about 4.5 for ~40-keV x rays) can be substantially reduced by

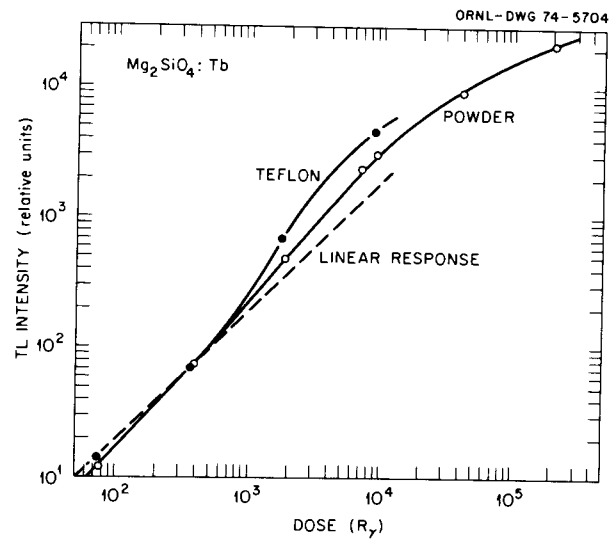

Fig. 26.5. TL of Mg_2SiO_4:Tb powder and of Mg_2SiO_4:Tb embedded in Teflon as a function of the gamma-radiation dose.

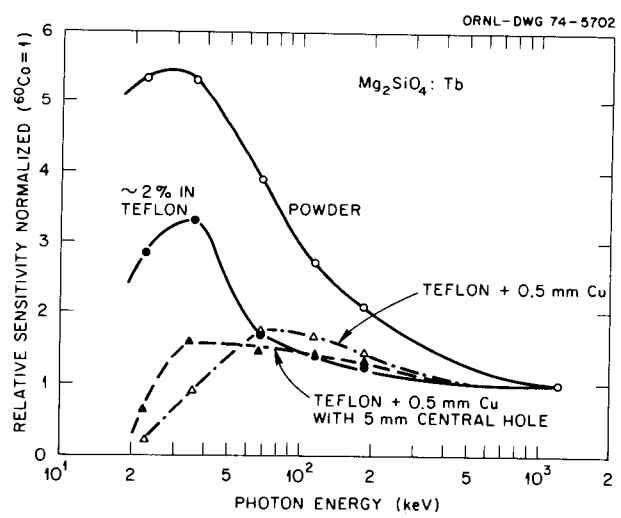

Fig. 26.6. Photon energy dependence of Mg_2SiO_4:Tb as powder in a polyethylene envelope, embedded in Teflon, and embedded in Teflon with additional metal compensation filters.

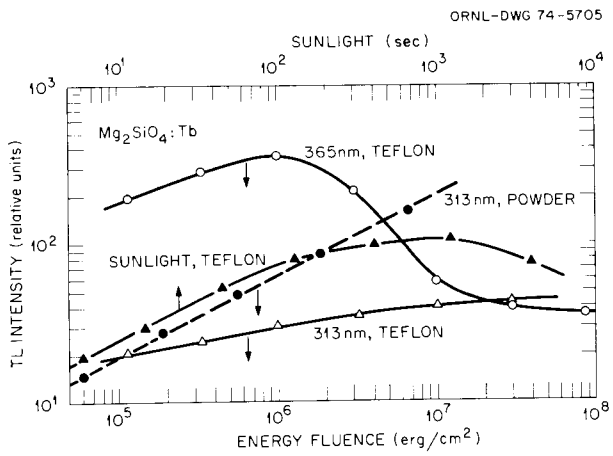

Fig. 26.7. Response of Mg_2SiO_4:Tb as a function of exposure to direct sunlight and monoenergetic uv radiation.

embedding the finely powdered phosphor into Teflon and/or optimized metal compensation filters (Fig. 26.6).

The pronounced uv sensitivity of Mg_2SiO_4:Tb depends on the wavelength of the uv and on whether it is embedded in Teflon or exposed as a thin powder layer (Fig. 26.7). As can also be seen in Fig. 26.7, for the exposure of the Teflon-embedded material to 365-nm uv and sunlight, the uv-induced signal decreases again after extended exposure. Further studies of the uv response of various partially or fully preannealed and/or preirradiated phosphors, using a Hilger uv monochromator with a 1-kW water-cooled high-pressure mercury lamp, are currently in progress.

TL DOSIMETRY WITH CERAMIC BeO

Beryllium oxide is a potentially useful TLD material of near tissue equivalence. Ceramic BeO disks (Brush Thermalox 995) are being used extensively in our TSEE work. Several of the treatments affecting the TSEE response have been examined for their possible influence on the TL, and the TLD characteristics of BeO 995 and other types of ceramic BeO have been investigated. For example, heating of the disks to 1400°C, which increases the TSEE sensitivity severalfold and reduces the intragroup standard deviation, does not increase the TL response but improves the reproducibility of the response, it being constant within a σ of 3% for individual detectors and 10% for the intragroup σ value of a batch of disks.

The TSEE is destroyed by heating at 1600°C or higher. Such heating is also detrimental for TLD; the detectors become very light sensitive, building up a response equivalent to several hundred roentgens. Also, erratic bursts of light occur during readout. Heating at 1400°C does not induce a significant light sensitivity, but etching with HF renders the detectors more light sensitive. It thus appears that a surface layer rich in phenacite (Be_2SiO_4), which is produced at 1400°C and promotes the exoelectron emission, also confers stability on the TL response.

Principal impurities in the ceramic BeO (Thermalox) are aluminum, silicon, and magnesium. Disks dosed with either of these impurities at the 0.5% weight level had the following TL sensitivities on a unit weight basis: Al, 1.00; Si, 0.75; and Mg, 0.20. The EPR of Thermalox 995 also points to participation of aluminum in the TL process. Another type of ceramic BeO (Consolidated Beryllium Ltd., England) contains substitutional fluorine in addition to aluminum. It was found not suitable for dosimetry because of its pronounced light sensitivity.

Thermalox BeO 995 shows promise as a dosimeter for measuring penetrating radiation. Its properties include good reproducibility of response, uncomplicated annealing at 500 to 600°C, a lower exposure limit of <1 mR, supralinearity of response starting at 20 R, and <5% fading after two months at 30°C and 80% relative humidity. The energy dependence of the response down to a photon energy of 20 keV has been determined for disks in a badge holder both on and off a thorax phantom (discussed later).

Both the TL and TSEE glow curves from Thermalox BeO 995 exhibit a predominant single peak. The peak temperatures, however, occur at surface temperatures of 167 and 276°C for the TL and TSEE respectively. This fact can be used to obtain both the TL and TSEE from a single detector; after the TL signal is read, the detector is evaluated in a TSEE reader, without significantly affecting the TSEE signal by the TL readout. Thus TSEE provides a backup for the TLD measurement. The technique can also be used to differentiate the doses from penetrating and nonpenetrating radiations with a single detector (e.g., recoil protons produced in a hydrogenous cover by fast neutrons, or tritium beta).

The ability to detect 10^4 beta particles from a ^{14}C source with and without prior reading of the TL is shown in Fig. 26.8. The beta radiation produced no detectable TL signal, whereas 1.9×10^4 exoelectrons were recorded. With more-penetrating beta particles from a ^{210}Bi source (average energy, 0.39 MeV), a TL

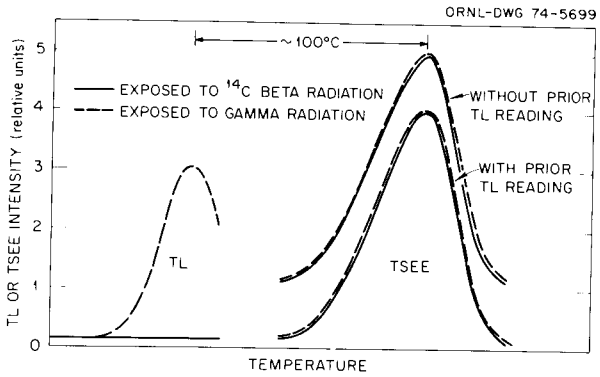

Fig. 26.8. TL and TSEE read separately from the same detector after exposure to ^{14}C beta radiation. TSEE is shown with and without a prior reading of the TL. The TL and TSEE responses to an equivalent TSEE exposure of ^{60}Co gamma radiation are also indicated.

response was registered which amounted to about 10% of the TSEE because the range of the electrons from ^{210}Bi is much larger.

COMPUTATIONAL EXTENSION OF THE DYNAMIC RANGE OF TL AND TSEE READERS

The measurement of high radiation doses with TL or TSEE readers is frequently limited, not by the response characteristics of the detector (saturation), but by the maximum light intensity or count rate which the readout instrument is designed to handle. This limit in instrument performance was encountered, for example, in measurements of the response characteristics of very sensitive TL phosphors with commercial TL readers or in TSEE readouts in a routinely used gas-flow G-M or proportional counter using the sensitized ceramic BeO disks. Dead-time losses rapidly increase in the peak region even at fairly low dose levels, and counter breakdown (which is indicated in G-M counters by an apparent multipeak structure in the main peak region at 320°C) begins to occur (Fig. 26.9). It is possible, however, to "reconstruct" the full peak and to determine the area under it as if it were recorded in full by using the following method.

During the first step the simplifying assumption was made that the TL or TSEE peak can be approximated by a Gaussian distribution $y(x)$, which has the property

$$y(x-1)/y(x+1) = \exp\,[2(x-x_0)/\sigma^2] = Q(x)\,.$$

A plot of ln $Q(x)$ as a function of x on a linear scale will consequently become a straight line with a slope of

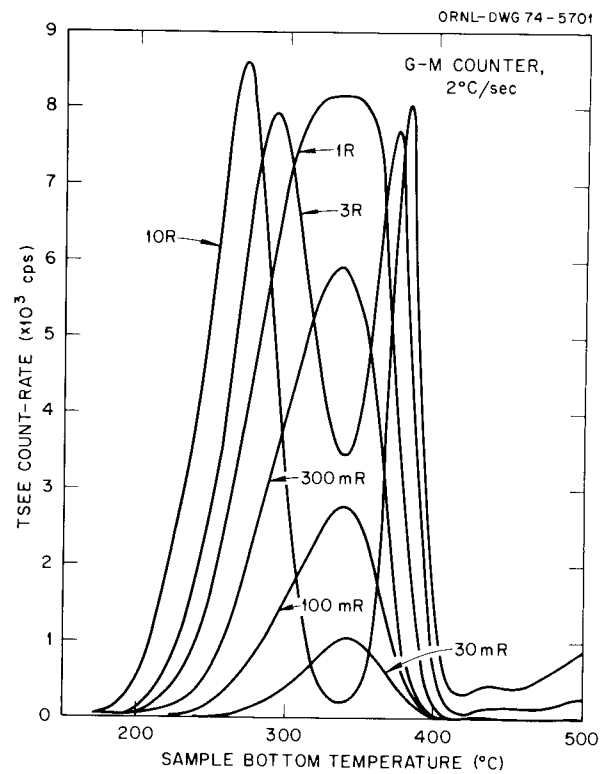

Fig. 26.9. Appearance of TSEE curves of sensitized ceramic BeO after exposure to different doses of gamma radiation, as measured with the standard ORNL G-M counter.

$2/\sigma^2$. The area under the Gaussian curve covering the 2σ interval is given by

$$A = 1.033 \times 2\sigma H\,.$$

H is the height of a triangle consisting of the baseline and the extension of the initial, almost linear, slopes of the curve. The value ln $Q(x)$ can be determined from the lower fragments of the incomplete curve. By linear interpolation on a plot of these values as a function of temperature, the value of σ is determined graphically. From H and σ, the total area is estimated with reasonable accuracy. It is thus possible to extend the useful range of G-M-type or proportional TSEE counters and TLD readers by about two orders of magnitude (Fig. 26.10).

An alternate approach (made in cooperation with J. E. Talmage, Elographics, Inc., Oak Ridge, Tennessee) is to assume that the glow curves scale approximately linearly in both X and Y coordinates. A standard curve is adopted and its area determined; then the scaling factors required to transform an arbitrary TSEE curve

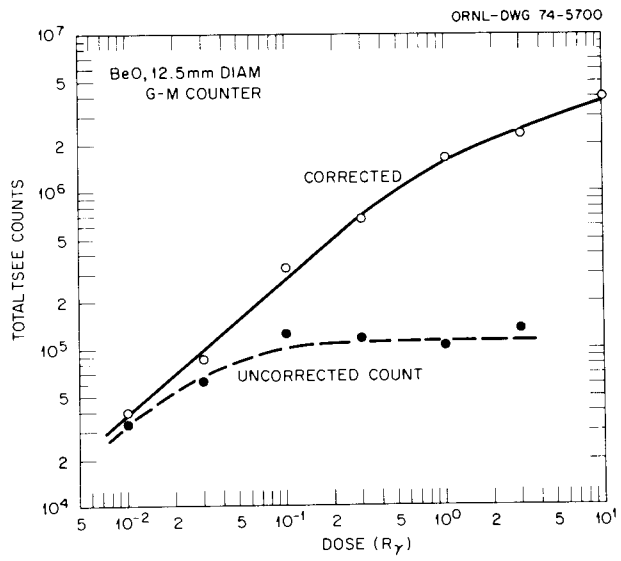

Fig. 26.10. Gamma-radiation response of sensitized Thermalox 995 disk in G-M-type TSEE counter saturating at ~100 mR before correction and not yet saturating at 10 R after computational correction by first step method.

to the standard curve can be used to find the area under the former curve from

$$\text{area} = (X \text{ scale factor}) \times (Y \text{ scale factor}) \times \text{standard area.}$$

To determine the appropriate scale factors when the values near the peak are unreliable, a digitizer–programmable-calculator system is used to determine a fit to the two wings of the curve, using simple functions to describe the two wings. For example, using a parabola $Y = a(x - x_0)^2$ to describe the low-temperature side and a straight line $Y = a_1(x - x_1)$ to describe the approximately linear region of the high-temperature side, one obtains:

$$X \text{ scale factor} = (x_1 - x_0)/(x'_1 - x'_0)$$

and

$$Y \text{ scale factor} = a/a' \; [(x_1 - x_0)/(x'_1 - x'_0)]^2 \; ,$$

where unprimed values refer to the standard curve and primed values refer to the arbitrary curve under examination.

PROPORTIONAL COUNTING OF TSEE DOSIMETERS

In recent years, about 10,000 readings of the standard TSEE detectors (BeO ceramic disks, Brush Thermalox 995, 12.5 mm in diameter) have been carried out with a gas-flow G-M counter. Although this reader is sufficiently reliable for many applications, it cannot be used to read the most sensitive detectors directly if they are exposed to gamma-radiation doses exceeding about 100 mR because of dead-time losses and counter breakdown (see previous section). Therefore a TSEE reader has been modified to be operated in the proportional mode. The reproducibility of response was constant within one standard deviation of 3%, and there was unit proportionality between the response and the exposure between 10 mR and 10 R (for comparison, the G-M-mode reader gives near unit proportionality only for doses below 10 mR). Both the apparent counting efficiency for exoelectrons and the background counts from an unirradiated detector are increased sevenfold by switching from G-M to proportional counting.

RELATIONSHIPS BETWEEN EPR, TL, AND TSEE IN CERAMIC BeO

A BeO ceramic produced by Consolidated Beryllium Ltd. in Britain is distinguishable from our standard Brush Beryllium specimens in that the normal and nuclear-grade BeO contain fluorine. They also have a set of different hole-type centers indicating that they are impurity related. These disks, however, are not very suitable for dosimetry because they are too thin and have unstable TL characteristics.

For the different grades of Brush Beryllium BeO, the intensity of the spin resonance due to hole centers varies by a factor of $^2/_3$. The specimen doped with 0.5 wt % Al_2O_3 gives the most intense resonance (this ceramic also produces the most intense TL). In Thermalox 995 exposed to a saturation dose in a tritium atmosphere, there was no Al^{2+} signal, and the central resonance was reduced by a factor of 30 compared with ^{60}Co radiation. Apparently there is no (or very little) substitutional aluminum within the range of the tritium beta particles. Also, the ceramic was completely free of tritium after exposure to a hard vacuum and washing in alcohol.

The rates of fading of hole and Al^{2+} centers, TL, and TSEE are shown in Fig. 26.11 for Thermalox 995. The principal hole center seems to contribute to the TL, although there is not a one-to-one correspondence between the hole-center and Al^{2+} annihilation. None of the hole centers and few of the Al^{2+} centers contribute to the TSEE. The annealing rate of the hole centers reflects the appearance of a high-temperature hole center. The activation energies are 0.3 and 1.5 eV for

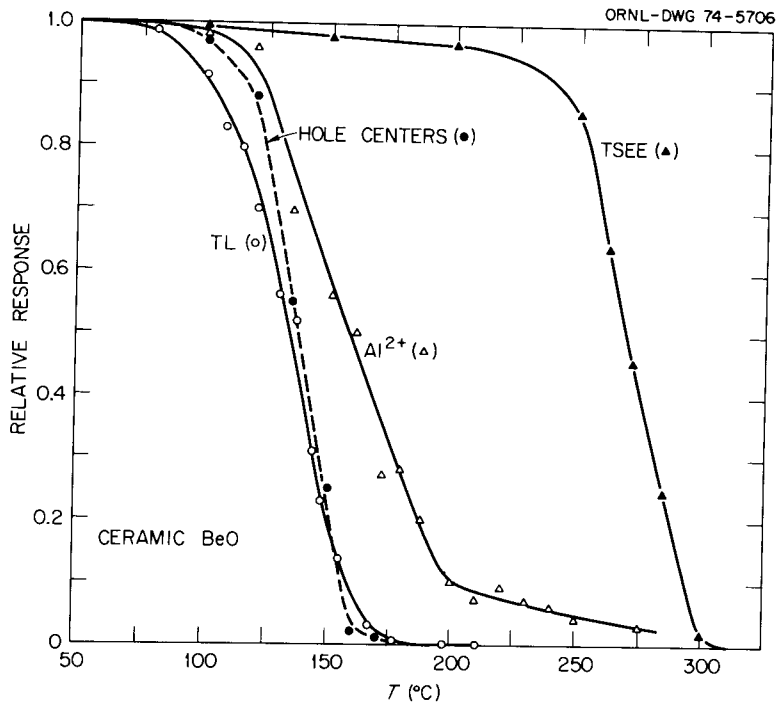

Fig. 26.11. Fading and annealing of TL, TSEE, and EPR signals in Thermalox 995 ceramic BeO heated at 1400°C; the disks were heated for 30 min at the indicated temperatures following gamma irradiation.

the liberation of holes and 0.5 eV for the trapped electron (Al^{2+}). The TL and TSEE fading curves highlight the large temperature separation of the TL and TSEE peaks.

DOSIMETRIC PROPERTIES OF BeO TSEE DOSIMETERS

In the continuing attempts to improve TSEE detector stability, an important and potentially disturbing annealing phenomenon has been observed. Detectors immersed in water and then dehydrated at increasing temperatures to 800°C show a continuously changing sensitivity (Fig. 26.12). The sensitivity change differs, not only from detector to detector, but also for a given detector hydrated and then dehydrated a second time. No set annealing temperature offers a definite advantage for all detectors. This result indicates that, when an annealing needs to be carried out, a much closer control of the temperature and time has to be exercised than has been assumed.

The sensitivity of TSEE dosimeters to ultraviolet light is of interest, not only as an undesirable interference with measurements of ionizing radiation, but also as a potential method of measuring biologically active uv radiation. Basically, as in TL phosphors, three uv-induced effects are observed either separately or superimposed:

1. buildup of a TSEE signal in carefully preannealed detectors followed by a uv-induced bleaching (Fig. 26.13),
2. optical annealing of detectors preexposed to a high gamma-radiation dose, and
3. trap transfer in detectors preexposed to a high gamma-radiation dose and then partially annealed at temperatures below 600°C.

The latter effect has been found to be particularly sensitive even to very low uv exposures (Fig. 26.13). Consequently, in practical dosimetric work, detectors that have previously received high radiation doses should not be used for low-dose measurements without annealing at about 800°C. Otherwise, even exposure to laboratory fluorescent lighting will generate a large "spurious" uv-induced signal.

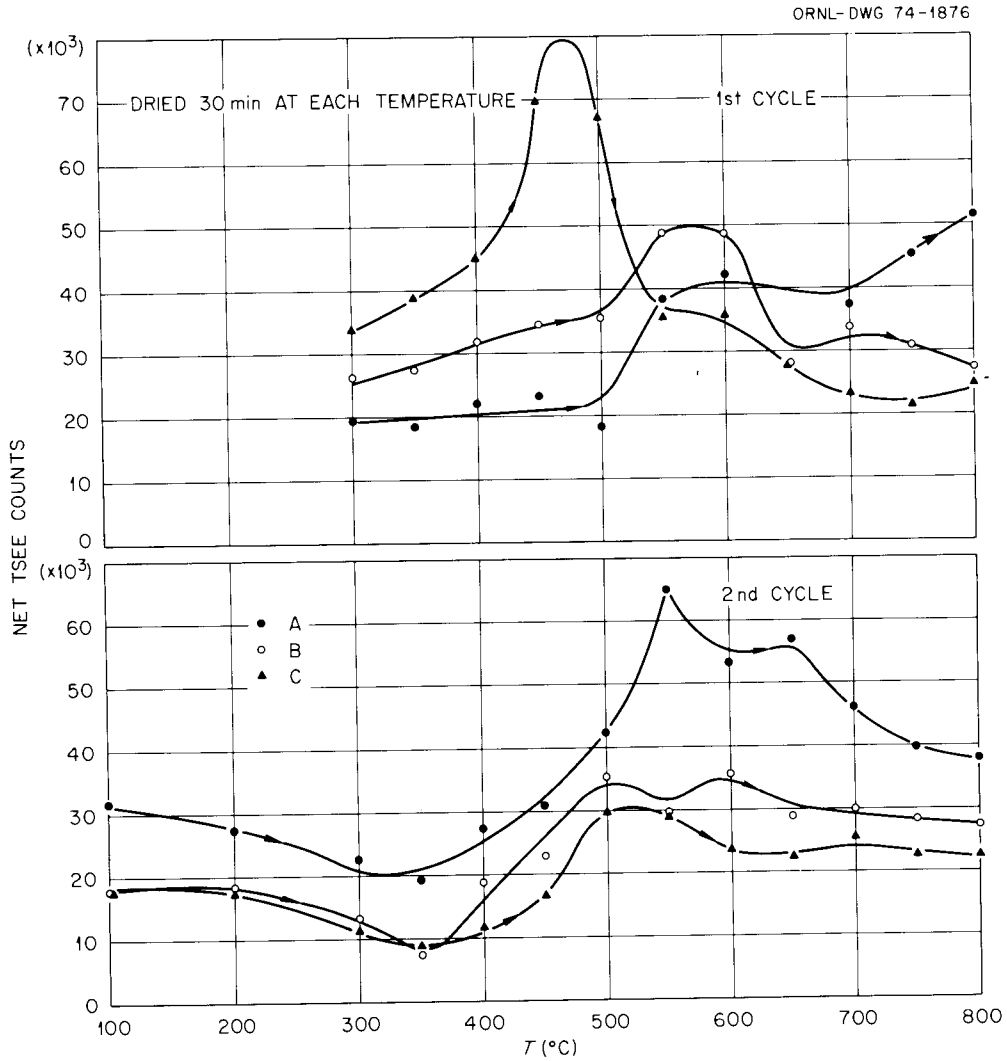

Fig. 26.12. Sensitivity changes in three detectors taken through two immersions in water and dehydration cycles.

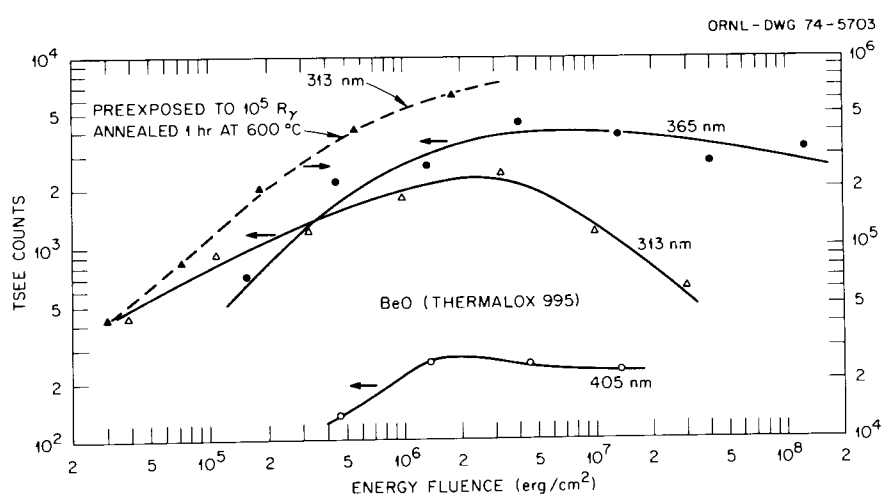

Fig. 26.13. Ultraviolet-induced TSEE signal as a function of exposure for preannealed ceramic BeO samples and for samples that had been preexposed to 10^5 R gamma radiation and annealed for 1 hr at 600°C.

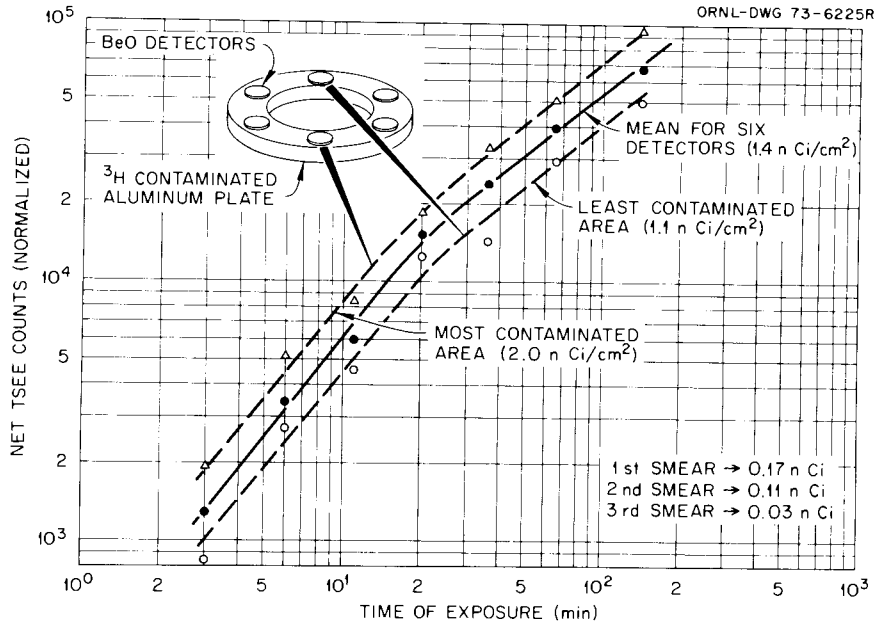

Fig. 26.14. Spatial monitoring for tritium contamination in an aluminum plate; the BeO disks were exposed face down in direct contact with the plate whose mean activity was 1.4 nCi/cm^2.

TSEE MONITORING OF BETA EMITTERS

Contaminated surfaces have been mapped for tritium contamination, an example being shown in Fig. 26.14. The detectors were first calibrated with a pure beta emitter (^{241}Pu, mean energy 6 keV). Activities of 1 nCi/cm^2 produce signal-to-noise ratios of 10 after a contact time of about 1 min. By placing the detectors in tritium-helium gas at 50 torr and at 50% of the MPC (40-hr occupational exposure), similar TSEE signal strengths were obtained in a few minutes (Fig. 26.15). Tritiated water has also been monitored, but its detection is complicated by fading of the latent exoelectrons and changes in detector sensitivity.

A characteristic of the detectors is of potential interest for tritium identification. The peak temperature is reduced by about 25°C and the shape of the curve is changed compared with higher-energy beta emitters and photon radiations of low (5.6 keV) as well as high (1.25 MeV) energy. The dependence of the TSEE peak temperature on electron energy in the range 0.26 to 18 keV is shown in Fig. 26.16. A sharp drop of about −60°C occurs at 1.5 keV, at which energy the exoelectron sensitivity is maximized.

The TSEE response has also been checked for higher-energy beta emitters embedded in metal surfaces.

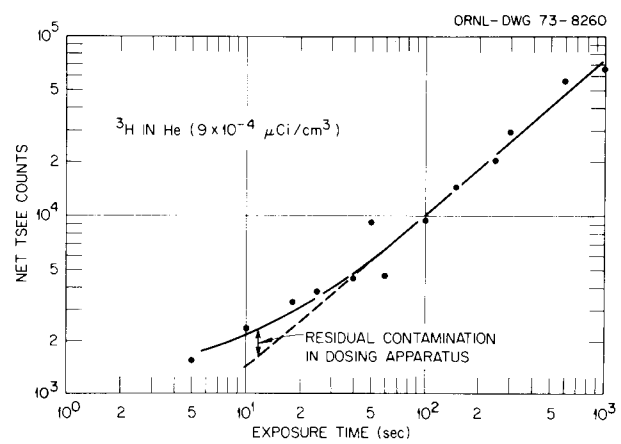

Fig. 26.15. TSEE counts from 0.7 cm^2 of a ceramic BeO after exposure to gaseous tritium (the scattering of the data points mainly reflects timing errors and residual tritium contamination of the containers).

The sensitivities (as exoelectrons per disintegration) are:

Nuclide	E_β max (MeV)	Relative TSEE sensitivity
^{241}Pu	0.21	0.23
^{14}C	0.15	2.0
^{204}Tl	0.76	0.76
^{210}Bi	1.15	0.78

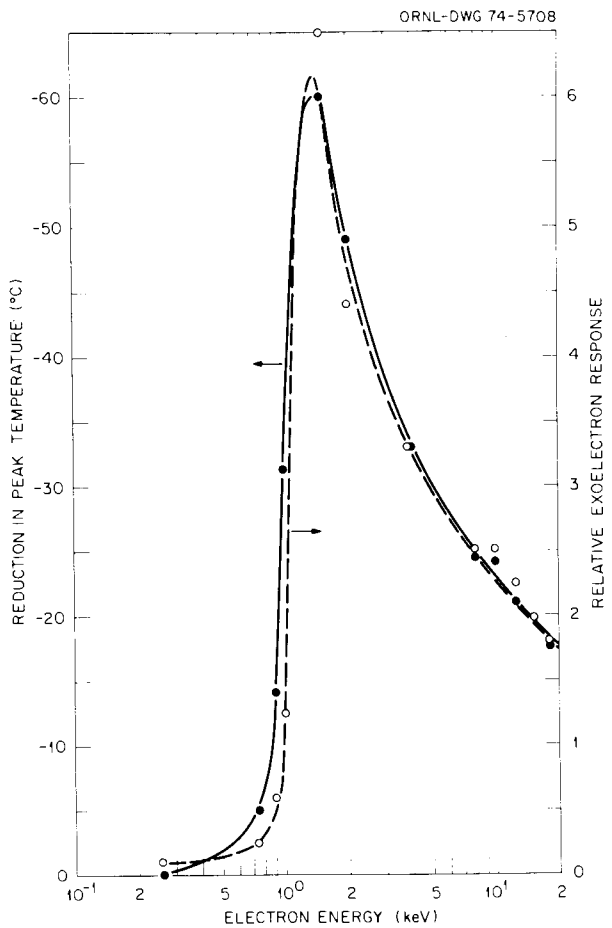

Fig. 26.16. Change in the TSEE peak temperature in ceramic BeO (compared to gamma radiation) and the relative exoelectron response as a function of incident electron energy.

TSEE IN PERSONNEL MONITORING

Ceramic BeO TSEE dosimeters have been worn by six members of the Applied Health Physics Section for one year. The primary objective was to gage the reliability of the detectors under real operating conditions for exposure times of one and three months. Readings from another badge containing film and TLD (LiF) provided comparative data. The dose range for a three-month period was 20 to 90 mR as measured by the TSEE dosimeter behind a plastic and paper window of 100 mg/cm^2. The TLD was included only for three quarters, and the film, TL, and TSEE data for this length of time are shown in Table 26.3 for one individual whose data were typical.

Of the five TSEE dosimeters in each badge, two were read at the end of each month, and the other three were read at the end of the quarter. The agreement between

Table 26.3. Dose readings (in milliroentgens) for one radiation worker during nine months of the personnel monitoring test

Quarter	TSEE		TLD	Film	
	Quarter reading	Sum of three One-Month readings		Depth	Surface
1	67	72	70	60	90
2	87	85	70	60	90
3	55	57	20	40	70

the sum of all the monthly readings and all the quarterly readings for all six individuals was within 1%. Because of the filters used, the TSEE data are closer to the skin dose than to the TL and film depth doses. Tribo signals occurred only rarely when a detector became scratched. Spurious signals were noted at high readout temperatures and tended to interfere with the radiation-induced signal. Washing the detectors in methanol prior to reading eliminated this problem.

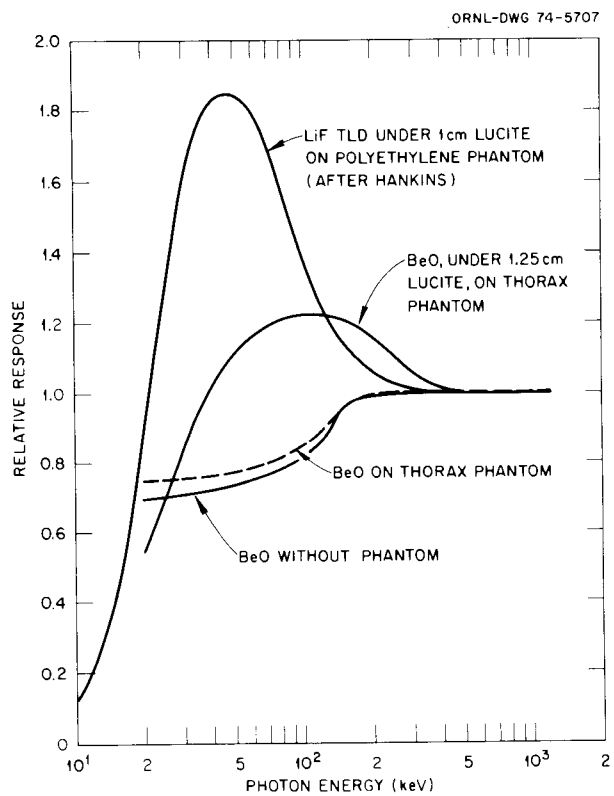

Fig. 26.17. Photon energy dependence characteristics of BeO dosimeters mounted in a personnel dosimetry badge: (*A*) with no phantom, (*B*) with the badge on a thorax phantom, (*C*) under 1.25 cm of Lucite and on a thorax phantom, and (*D*) LiF TLD's under 1 cm of Lucite and on a 10-cm-thick polyethylene phantom (LiF data from D. Hankins, LASL, personal communication).

Some fading of the TSEE apparently occurred during the hottest and most humid summer months. Additional field testing will be done during the summer months of 1974.

The x-ray energy dependence of the BeO disks has been measured between 22 and 159 keV (see Fig. 26.17). The detectors were in a personnel badge suspended on and off a thorax phantom, or they were covered by 12.5 mm of Lucite while resting against the phantom. The energy dependence is less pronounced than for LiF TLD. The angular dependence of the exoelectron-emitting detectors was also measured at two photon energies (36 and 159 keV) and was found to be invariant within ±10%.

MISCELLANEOUS

Work has also proceeded in other areas. In the field of education and information dissemination, for example:

1. graduate students and guest scientists from Egypt, Iran, Korea, and Mexico received advanced training;
2. one member of the group was instrumental in the organization of an International Symposium on Exoelectrons and Dosimetry (October 1973) and of the Fourth International Conference on Luminescence Dosimetry (August 1974); and
3. a comprehensive monograph on solid-state dosimetry has been completed and published.[7]

A batch of 500 TSEE BeO disks, each with the same pretreatment, have been standardized and are being distributed to research and dosimetry groups in various countries. The objective is to bring the studies on ceramic BeO into closer coincidence and dispel some of the confusion surrounding the exoelectron-emitting and dosimetric properties of this material.

In the field of TSEE fast-neutron dosimetry, activities have been concentrated on practical applications such as participation in the ORNL Tenth Intercomparison of Nuclear Accident Dosimetry. The TSEE dosimeters have also been used to determine the spatial distribution of fast-neutron and gamma doses (Fig. 26.18) at the base of a laminated polyethylene–borated-paraffin shield intended for the partial body irradiation of mice. By use of a combined TL-TSEE technique, it is hoped to improve accuracy and develop a small cylindrical pocket meter for measuring the orientation of the wearer in a neutron beam, as well as the neutron and gamma doses. One of the group's scientists also participated for about two months in a study concerning the surface structure of lunar materials within the framework of a NASA contract.

7. K. Becker, *Solid-State Dosimetry*, C R C Press, Cleveland, Ohio, 1973.

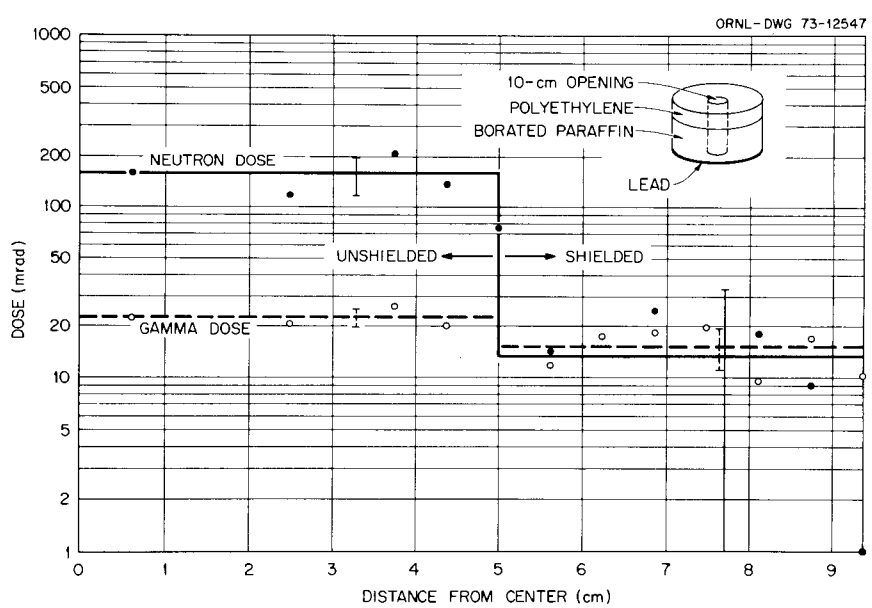

Fig. 26.18. Fast-neutron and gamma-dose profile inside a shield designed for the partial body irradiation of mice, measured with TSEE dosimeters.

27. Atomic Physics

G. S. Hurst
W. R. Garrett[1] J. R. McNeely[3]
J. P. Judish[2] M. G. Payne
C. E. Klots[1] E. B. Wagner

SYMPOSIUM ON THE JESSE EFFECT AND RELATED PHENOMENA

The U.S. Atomic Energy Commission, Argonne National Laboratory, and the ORNL Atomic Physics Group organized a symposium on the Jesse Effect and Related Phenomena which was held at Gatlinburg, Tennessee, on November 9–10, 1973. It was a highly successful symposium which presented excellent opportunities for investigators to summarize the status of their fields of research. All the material which was presented will be published in the August 1974 issue of *Radiation Research.* The following abstracts represent contributions from the Atomic Physics Group and are presented in this annual report because they describe the status of our work on energy pathways.

Transport of Resonance Radiation

It has long been recognized[4–6] that resonance states play an important role in determining the fate of energy deposited in inert gases by fast charged particles. Resonance states compete effectively in importance with metastable states because of their large oscillator strengths (and, hence, large populations) and because of the imprisonment of resonance photons, which leads to an effective lifetime for these states which may be thousands of times larger than their natural lifetime. A proper analysis of the intensity and time dependence of escaping resonance radiation gives much information[4,7,8] about processes that may convert the energy stored in the resonance states to other excited species. Some of these processes are (1) three-body collisions involving a resonance-state atom and two ground-state atoms which lead to electronically excited diatomic molecules,[4,7] (2) inelastic two-body collisions between a resonance-state atom and a ground-state atom which may lead to another resonance-state atom or to a metastable-state atom,[9] and (3) two-body collisional transfer to impurity gases[8,10,11] which may lead to ionization or dissociation of the impurity or to a fairly selective excitation of atomic or molecular states. A proper analysis of intensity and time dependence of resonance radiation also gives considerable information about the validity of spectral-line-broadening theories in the wings of the line. It is the wings of the line that must be described correctly if spectral-line formation and radiation transfer are to be calculated accurately.

The interpretation of the intensity of escaping resonance radiation is complicated by the fact that the time behavior depends not only on the geometry of the gas container but also on the point of exit and the direction of propagation of the photons observed in the experiment. In general, the observed time dependence is not exponential. Also, the widely used Holstein theory[12] has limitations related to the lifetime of the state, the range of pressures, and the container dimensions.

1. Fundamental Health Physics Research Section.
2. Physics Division, ORNL.
3. Graduate student, University of Tennessee.
4. N. Thonnard and G. S. Hurst, *Phys. Rev. A* **5**, 1110 (1972).
5. G. S. Hurst, T. E. Bortner, and R. E. Glick, *J. Chem. Phys.* **42**, 713 (1965).
6. G. S. Hurst, T. E. Stewart, and J. E. Parks, *Phys. Rev. A* **2**, 1717 (1970).
7. D. M. Bartell, G. S. Hurst, and E. B. Wagner *Phys. Rev. A* **7**, 1068 (1973).
8. G. S. Hurst, E. B. Wagner, and M. G. Payne, accepted for publication in the *Journal of Chemical Physics.*
9. R. T. Ku, J. T. Verdeyen, B. E. Cherrington, and J. G. Eden, submitted to the *Physical Review A.*
10. C. E. Klots, *J. Chem. Phys.* **56**, 124 (1972).
11. T. Watanabe and K. Katsuura, *J. Chem. Phys.* **47**, 800 (1967).
12. T. Holstein, *Phys. Rev.* **72**, 1212 (1947); *Phys. Rev.* **83**, 1159 (1951).

Investigations of the following problems associated with the transport of resonance radiation in laboratory situations have been carried out:

1. When the transition to the ground state is the preferred mode of deexcitation and the natural lifetime is short, we have shown that there are often regions of pressure (depending on the dimensions of the container and the lifetime of the excited state) where correlations between the frequency of absorbed and reemitted photons[13,14] are extremely important in determining the transport of the emitted radiation. A transport equation that includes such correlations has been derived, and its solution has been compared with an experiment on the transport of 1048-Å resonance photons in argon.[15] In the latter situation, correlations between the frequencies of absorbed and reemitted photons are very important in the frequency range 0.02 torr $< P <$ 2 torr for a long cylindrical container of radius 1.0 cm. At all pressures below 2 torr, a theory which neglects such correlations and assumes the emission profile to be equal to the absorption profile is in serious error in calculating the rate of detection of the 1048-Å photons from argon. The agreement between the above theory and a closely correlated experiment due to Talmage et al.[16] is good.

2. The effect of initial conditions and the geometrical effects associated with the method of detecting the escaping resonance photons have been incorporated into the theory[17] for the case where (1) at $t = 0$ all the excited atoms are along the axis of a long cylinder and (2) only those photons which exit normally through a window in the otherwise "black" wall of the cylindrical container are detected. Both the initial conditions and the method of observation have profound effects on the rate of detection of escaping photons.

3. The photoabsorption of resonance photons by an impurity has been incorporated into the Holstein-Biberman equation.[12] Analytic formulas have been derived for the effect of photoabsorption on the rate of detection of escaping photons for several limiting cases.[18] The simultaneous inclusion of collisional quenching is, of course, trivial, and the latter effect is included in all the work described above.

13. D. L. Huber, *Phys. Rev.* 178, 93 (1969).
14. A. Omont, E. W. Smith, and J. Cooper, *Astrophys. J.* 175, 185 (1972).
15. M. G. Payne, J. E. Talmage, G. S. Hurst, and E. B. Wagner, *Phys. Rev. A* 9, 1050 (1974).
16. J. E. Talmage, Jr., G. S. Hurst, M. G. Payne, and E. B. Wagner, ORNL-TM-4368 (1973); also, see ref. 17.
17. M. G. Payne, to be published; M. G. Payne and J. D. Cook, *Phys. Rev. A* 2, 1238 (1970).
18. M. G. Payne, to be published.

Energy Pathways, Including the Jesse Effect, in Noble Gases

The discovery of the Jesse effect in 1952[19] has led to intensive studies aimed mainly at determining the nature of the precursors or long-lived excited states which could lead to the ionization of minute concentrations of foreign species. As early as 1954, it was shown[20] that the Jesse effect in argon is not likely to be due solely to metastable states, and it was pointed out in 1965 that it is likely that resonance states play a major role.[5] The effort to learn the nature of the long-lived precursors soon led to a generalization of the study. Clearly, what is needed to understand the Jesse effect is the entire energy-pathways scheme involved after charged particles excite atomic states in a noble gas. The questions can be resolved in two categories: (1) What are the pathways followed by the atomic precursors as the pure system returns to thermodynamic and chemical equilibrium? (2) How are the pathways modified by the introduction of foreign species, and, in particular, which of the additional reactions lead to the increased ionization known as the Jesse effect?

To answer these questions, an increasingly long list of studies has been initiated over the past several years.

***W* values and Jesse effect.** In addition to the very excellent data obtained by Dr. Jesse and his colleagues, it was felt that more detailed studies were needed on *W* values and Jesse effect over a wide range of gas pressure. Accordingly, Parks et al.,[21] following some ideas presented in a paper by Larson,[22] developed a method for measuring *W* values where the *W* at a particular proton energy could be determined. This technique enabled him to study the Jesse effect for various concentrations of impurities in argon over a wide range of total pressure. The studies were also done for mixtures of helium with certain foreign species. A suggestion made earlier by Jesse that for a fixed concentration of the impurity the increase in ionization can depend on the total gas pressure was amply demonstrated by Parks et al. These data serve as a critical test of energy-pathways models.

Emission of vacuum ultraviolet (vuv) radiation. For the pure noble gases, study of the emission of radiation in the vuv region can provide information on the atomic

19. W. P. Jesse and John Sadauskis, *Phys. Rev.* **88**, 417 (1952).
20. C. E. Melton, G. S. Hurst, and T. E. Bortner, *Phys. Rev.* **96**, 643 (1951).
21. J. E. Parks, G. S. Hurst, T. E. Stewart, and H. L. Weidner, *J. Chem. Phys.* 57, 5467 (1972).
22. H. V. Larson, *Phys. Rev.* **112**, 1927 (1958).

species and other species that may be created by the collision of excited atoms with ground-state atoms. Therefore a program was carried out in which protons from a 6-MeV Van de Graaff accelerator at the University of Kentucky were used to excite noble gases for emission spectroscopic studies. These studies[23] showed that, not only is the emission observed from the resonance atomic states, but also continuum radiation characteristic of emission from diatomic molecules is observed. Similar results had already been observed in gas discharges, but it was recognized that in the case of gas discharges, metastable states are formed as a result of the impact of low-energy electrons. These metastable states play a more important role in the case of gas discharges than they do in the Jesse effect, where excitation is with swift particles.

Absolute measurement of vuv energy. Following the qualitative observations described in the preceding paragraph, it became evident that some quantitative measurements were needed on the amount of energy radiated in the vuv region. Hence Stewart et al.[24] defined a quantity $d\epsilon/dx$, which is the amount of energy radiated from 1 cm of a charged-particle track, and they measured this quantity for all the noble gases. It was found that this quantity is an appreciable fraction of the stopping power dE/dx and is, in fact, large enough to explain the amount of energy observed to be associated with the Jesse effect.[6]

Time dependence of the vuv emission. Radiation continua can result from the conversion of atomic states to molecules that radiate into a repulsive ground state. Strongly repulsive ground states of the noble gases can account for the wide continuous spectra observed merely by assuming Franck-Condon (vertical) transitions from an attractive upper state to a repulsive ground state. The work of Thonnard and Hurst[4] was aimed at obtaining the rate of decay of atomic resonance states and the buildup and subsequent decay of the continuum radiation. Their time-dependence work led to a model which made use of the conversion of various atomic states to bound molecules, both metastable and radiative. Bartell et al.[7] studied the time behavior of vuv emission from helium and suggested an energy-pathways model for pure helium which is consistent with much detailed information on the structure of helium molecules. Time-dependence studies have now been carried out for neon[25] and for krypton.[26]

Quenching of vuv radiation. When foreign species are added to a noble gas and produce ionization through the Jesse effect, it is expected that the vuv radiation would be quenched. Hence, Weidner[27] studied the quenching by foreign species of radiation from argon at wavelengths corresponding to resonance states and to the continuum radiation. Weidner's results show that the intensity of the vuv radiations rapidly decreases with the introduction of a foreign species which causes a Jesse effect. However, a direct correlation of quenching coefficients with the Jesse effect is not straightforward. This, in fact, is shown dramatically by looking at the energy-pathways model in pure argon which was based on the time-dependence studies of Thonnard and Hurst.[4] In the model it is shown that atomic resonance states are converted to metastable states, which have to be further converted to radiative molecules before vuv emission can occur. Therefore, quenching of vuv continuum radiation can occur because of (1) collisions of foreign species with the resonance states, (2) collisions of foreign species with the metastable molecules, and (3) collisions of the foreign species with the radiating molecule. On the other hand, in the case of molecular impurities added to argon, the Jesse effect will occur only from process 1, because invoking the Franck-Condon principle in processes 2 and 3 shows that insufficient energy is available to ionize the foreign species. This example serves to illustrate the need for quenching experiments that are done under time-resolved conditions. An example of this kind of investigation has been prepared for publication.[8] This work shows that the rate of transfer of energy from the resonance states to an impurity can be obtained very accurately from time-resolved studies and that these rate coefficients agree with calculations that can be made using the theory of Watanabe and Katsuura.[11]

Transport of resonance radiation. Because of the role played by resonance states, it becomes important to understand the transport of resonance radiation in an enclosure filled with a noble gas. It has been known for a long time[28] that resonance photons can be captured and reemitted many thousands of times before they escape from the container. This imprisonment process is

23. G. S. Hurst, T. E. Bortner, and T. D. Strickler, *Phys. Rev.* **178**, 4 (1969).

24. T. E. Stewart, G. S. Hurst, T. E. Bortner, J. E. Parks, F. W. Martin, and H. L. Weidner, *J. Opt. Soc. Amer.* **60**, 1290 (1970).

25. P. K. Leichner, *Phys. Rev. A* **8**, 815 (1973).

26. P. K. Leichner and R. J. Ericson, *Phys. Rev. A* **9**, 251 (1974).

27. H. L. Weidner, Ph.D. dissertation, University of Kentucky (1973).

28. A. C. G. Mitchell and M. W. Zemansky, *Resonance Radiation and Excited Atoms*, Cambridge University Press, London, 1934.

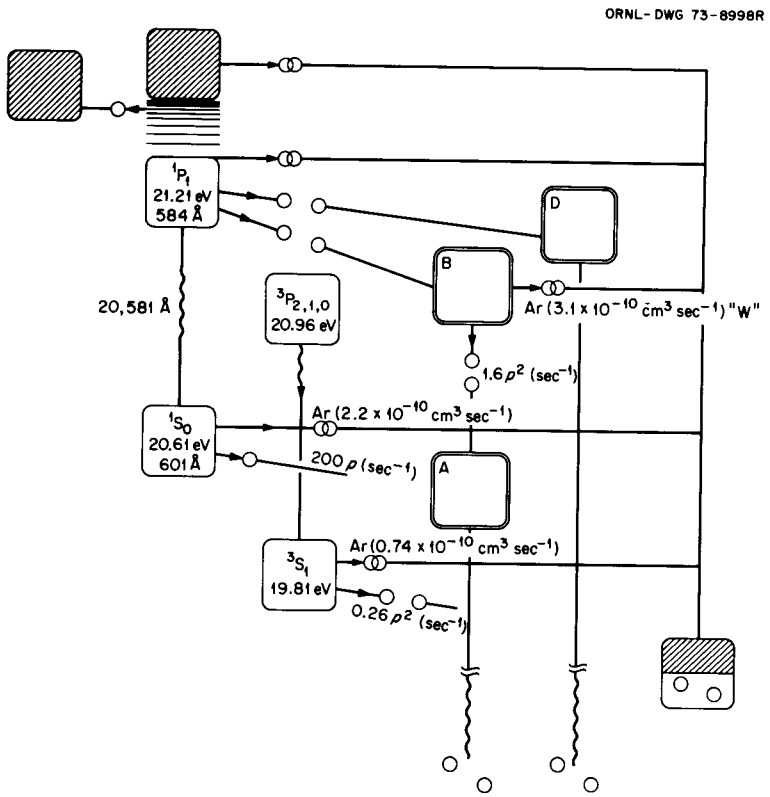

Fig. 27.1. Some energy pathways in helium. The atomic states shown in the single squares are produced by charged particles and by cascade from more highly excited atomic states. Molecules (double squares) are formed by three-body collisions involving an excited atomic state and two helium atoms (each shown as a small circle) in their ground states. Ionization is shown as hatched squares, and the Hornbeck-Molnar process, in which an excited Rydberg state can be converted to a molecular ion at reduced ionization potential, is included. The Jesse effect is interpreted as due to processes in which excited atomic or molecular states ionize impurities (overlapping circles) or produce neutral dissociation if the impurity is a molecule (lower right-hand square). Rate constants for the pathways involving pure helium and for additional pathways involving argon as an impurity are summarized in ref. 7.

very significant to the Jesse effect. From theory, it is well known that a swift charged particle will lose more energy to those states that have considerable oscillator strength; therefore resonance states should be populated in larger numbers than the metastable states. Hence, because of imprisonment of resonance radiation, large numbers of long-lived atomic species can be created by a swift charged particle. Detailed studies of the transport of resonance radiation have been very important to the interpretation of the Jesse effect and have been due largely to the excellent theoretical and experimental work of Payne et al.[15] and Talmage et al.[16] respectively.

Investigations of the types discussed in the preceding sections have been carried out to obtain the energy pathways, including the Jesse effect, for the noble-gas systems. It suffices here to note that we believe that the Jesse effect in helium (Fig. 27.1) is due mainly to metastable molecules of helium that are created by the three-body destruction of a resonance atomic state. On the other hand, the Jesse effect in argon mixtures (Fig. 27.2) appears to be due to collisions of resonance atomic states with the foreign molecules. A more complete summary of some of these energy pathways, particularly for helium and argon, is contained in a recent review article.[29] As our knowledge on the energy pathways in the noble gases increases, so will our understanding of the Jesse effect. Furthermore, the understanding of energy pathways has other interesting applications, as basic science always does. These applications include such varied fields as the determination of atmospheric pollution and the design of vuv lasers to produce energy by the fusion process.

29. G. S. Hurst and C. E. Klots, in *Advances in Radiation Chemistry*, vol. 4, ed. by M. Burton and J. L. Magee, Wiley-Interscience, New York (to be published).

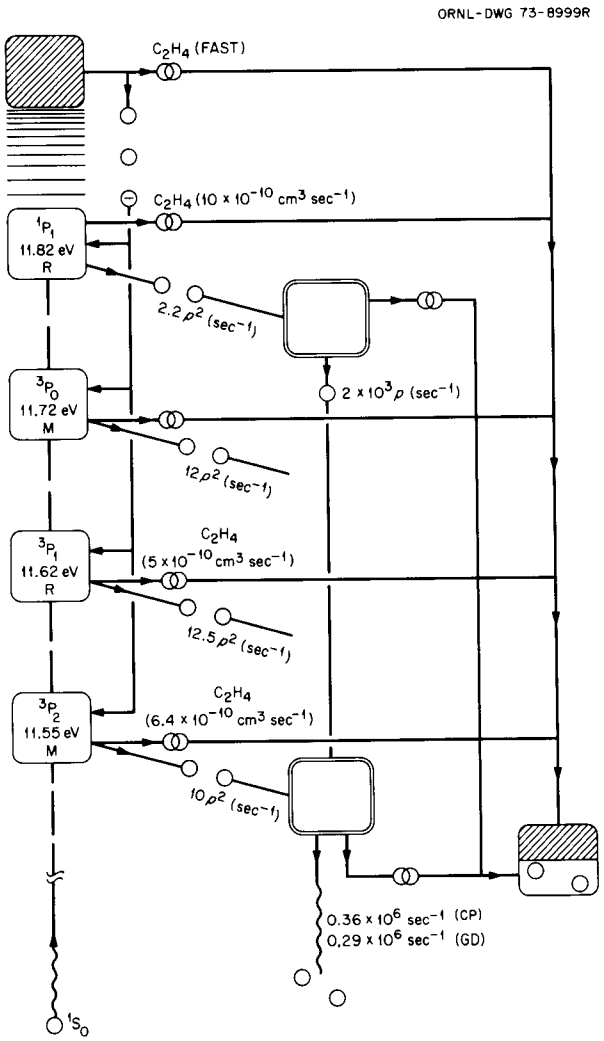

Fig. 27.2. Some energy pathways in argon. The atomic states shown in the single squares are produced by charged particles and by cascade from more highly excited states. Diatomic molecules of argon (double squares) are formed by three-body collisions involving an excited state and two ground-state atoms (each shown as a small circle). A recombination process, which does not occur under normal total ionization measurements of W values, is shown out of the ionization continuum (hatched box). The Jesse effect is interpreted as energy transfer from resonance ($^1P_1$ and $^3P_1$) and metastable ($^3P_0$ and $^3P_2$) atomic states and is illustrated here with C_2H_4 as an additive. Energy pathways and various rate constants for pure argon are contained in ref. 4. For the case of energy transfer from resonance states to C_2H_4 (overlapping circles), experimental (ref. 8) and theoretical (ref. 11) values are in excellent agreement. The rate constant for the transfer of energy from the $^3P_2$ metastable state to C_2H_4 is reported by M. Bourène and J. LeCalvé, *J. Chem. Phys.* **58**, 1452 (1973).

JESSE EFFECT IN HELIUM

Introduction

In a recent paper, Bartell, Hurst, and Wagner[7] reported an experiment in which pure helium was excited by a pulsed beam of 2.0-MeV protons and the time dependence of all radiation with 584 Å $\leqslant \lambda \leqslant$ 900 Å was measured as a function of pressure. The observed intensity of 584-Å resonance radiation was found to decay exponentially with a decay constant β_R given approximately by

$$\beta_R \simeq 3.0 \times 10^6 \text{ sec}^{-1} + 6.0 \times 10^4 P + 80.0 P^2 ,$$

where β_R has units of sec^{-1} and P is in torr.

The 3.0×10^6 sec^{-1} term was shown[7] to be consistent with radiation-trapping theory plus depletion of the resonance level by the alternate decay route to the 2^1S metastable level. The $80.0P^2$ term is poorly known due to the dominance of the other terms at $P <$ 150 torr, where the 584-Å line was strong enough for easy study. However, a P^2 term does seem to exist and was suggested[7] to represent the formation of the $^1\Sigma^+_u$ and $^1\Pi_g$ molecules. The formation of the $^1\Sigma^+_u$ molecule is consistent with the observation of a small portion of the continuum radiation having what appears to be the time dependence of the 584-Å line. The 584-Å resonance line was observed[7] to decrease rapidly in intensity as the linear pressure term became larger than 3.0×10^6 sec^{-1}. However, the question of origin of the linear term was left unanswered in ref. 7. It is the purpose of the present work to suggest an origin for the linear pressure terms and to provide several suggestions about the detailed energy pathways and the origin of Jesse effects in helium excited by fast charged particles. Suggestions concerning mechanisms determining the time dependence of the continuum radiation will also be made.

Cross Section for He(2^1P) + He(1^1S) → He(2^1S) + He(1^1S)

There are six almost degenerate stationary states corresponding to He(2^1P) + He(1^1S) with fixed nuclei and large internuclear separation. The number 6 comes from symmetric and antisymmetric linear combinations of product wave functions corresponding to 1^1S and the three magnetic substates of 2^1P. Correspondingly, there are two almost degenerate stationary states for 2^1S and 1^1S helium atoms separated by a large but fixed nuclear separation. In the latter case the states are $^1\Sigma^+_g$ and $^1\Sigma^+_u$, and in the former, the states are $^1\Sigma^+_g$,

$^1\Sigma^+_u$, $^1\Pi_g$, and $^1\Pi_u$. The Π states are, of course, doubly degenerate.

The effect of nuclear motion is to induce transitions between the adiabatic molecular states whose symmetry allows the transitions to occur. The nonadiabatic coupling is of two basic types. First, there is coupling due to change in nuclear separation (i.e., radial coupling), and second, there is coupling between states due to rotation of the internuclear axis. Radial coupling would cause coupling between $^1\Sigma^+_g(1^1S + 2^1P)$ and $^1\Sigma^+_g(1^1S + 2^1S)$ but cannot link states of different symmetry.[30] The latter type of effect has been estimated for transitions between $^3\Sigma^+_g(1^1S + 2^3S)$ and $^3\Sigma^+_g(1^1S + 2^3P)$ in helium by Evans, Cohen, and Lane.[31] In the latter situation [i.e., the collision $He(2^3S) + He(1^1S) \rightarrow He(2^3P) + He(1^1S)$], radial coupling was shown by Lenamon, Browne, and Olson[32] to be of much less importance than rotational coupling, which links states such that $+ \rightarrow +$, $- \rightarrow -$, $u \rightarrow u$, $g \rightarrow g$, and $\Delta\Lambda = \pm 1$.

Again, in the case of the reaction $He(2^1P) + He(1^1S) \rightarrow He(2^1S) + He(1^1S)$, we expect that the change in nuclear kinetic energy required in the transition $^1\Sigma^+_g(1^1S + 2^1P) \rightarrow {}^1\Sigma^+_g(1^1S + 2^1S)$ by radial coupling is prohibitive, as it is in transitions between $^1\Sigma^+_u(1^1S + 2^1P) \rightarrow {}^1\Sigma^+_u(1^1S + 2^1S)$. On the other hand, $^1\Pi_g(1^1S + 2^1P)$ has a potential curve which crosses that of $^1\Sigma^+_g(1^1S + 2^1S)$ at internuclear separation $R_x = 2.06$ Å. The adiabatic states in question are coupled by rotational effects, and, for internuclear separations near $R = 2.06$ Å, little or no change in nuclear motion is required. Since helium has a light nucleus, we expect that rotational coupling between the latter pair of states might lead to considerable quenching of 2^1P even at room temperature. The two-body rate of destruction of 2^1P at $T = 293°K$ was observed[7] to be $k = 1.8 \times 10^{-12}$ cm^3/sec. The latter rate is sufficiently large to play a dominant part in determining the time dependence of the 2^1P population of helium excited by a short burst of 2-MeV protons, providing the pressure is between 100 and 1000 torr.

We will now estimate the cross section for our process within the classical path approximation. In order to arrive at the total cross section, we first calculate $\sigma(i, j, \mathrm{v})$, the cross section for starting in adiabatic molecular state i [corresponding to $He(2^1P) + He(1^1S)$ at large R] and ending up in adiabatic molecular state j [corresponding to $He(2^1S) + He(1^1S)$ at large R] given that the infinite separation relative speed was v. Once $\sigma(i, j, \mathrm{v})$ is determined, we must carry out an ensemble average over all six possible initial molecular states that were degenerate at large R. Since we have estimated that, at thermal (i.e., room temperature in our case) energies, transitions between $^1\Pi_g(2^1P + 1^1S)$ and $^1\Sigma_g(2^1P + 1^1S)$ have little effect on the calculated value of $\sigma(^1\Pi_g, {}^1\Sigma^+_g, \mathrm{v})$, we will estimate the latter cross section within a two-state approximation. In the approximation that only $^1\Pi_g(2^1P + 1^1S)$ is coupled strongly with any of the j states, we obtain

$$\begin{aligned}\sigma(\mathrm{v}) &\simeq 2\sigma(^1\Pi_g, {}^1\Sigma^+_g, \mathrm{v})/6 \\ &= \tfrac{1}{3}\sigma(^1\Pi_g, {}^1\Sigma^+_g, \mathrm{v}) \qquad (1)\end{aligned}$$

= cross section for converting $He(2^1P)$ to $He(2^1S)$ by two-body collisions with $He(1^1S)$ if the relative speed is v.

The factor of 2 arises because $^1\Pi_g$ is doubly degenerate.

Since the rate measured by Bartell, Hurst, and Wagner[7] corresponds to a cross section at the mean thermal relative velocity of $\sim 10^{-17}$ cm^2, while $\pi R_x{}^2/2 \simeq 6 \times 10^{-16}$ cm^2, we expect that the probability of a transition on any crossing of the region with $R \simeq 2 \times 10^{-8}$ cm is much less than unity. Thus to a good approximation we can look at the relative nuclear motion as occurring in the potential $V(^1\Pi_g, R) - V(^1\Pi_g, \infty)$ and the amplitude for being in the $^1\Pi_g$ at any stage of the classical motion as being near unity in absolute value. $V(^1\Pi_g, R)$ is, of course, the energy of the system in the $^1\Pi_g$ state at fixed internuclear separation R. $V(^1\Pi_g, R)$ serves as a potential energy for nuclear motion, providing that the motion produces little probability of a transition to another adiabatic molecular state. It is thus appropriate to investigate the effect of $V(^1\Pi_g, R) - V(^1\Pi_g, \infty)$ on trajectories with initial relative speed v and impact parameter P. By conservation of angular momentum, we have

$$\mu R^2\dot{\theta} = \mu \mathrm{v} P\,, \qquad (2)$$

where μ is reduced mass and $\dot{\theta}$ is angular velocity. Further,

$$\frac{\mu\dot{R}^2}{2} + \frac{\mu}{2}\mathrm{v}^2(P/R)^2 + V(^1\Pi_g, R) - V(^1\Pi_g, \infty) = \frac{\mu \mathrm{v}^2}{2}\,. \qquad (3)$$

At internuclear separation such that $R > 4$ Å, we have

30. A. Russek, *Phys. Rev. A* **4**, 1918 (1971).

31. S. A. Evans, J. S. Cohen, and N. F. Lane, *Phys. Rev. A* **4**, 2235 (1971).

32. L. Lenamon, J. C. Browne, and R. E. Olson, *Phys. Rev. A* **8**, 2380 (1973).

$$V(^1\Pi_g, R) - V(^1\Pi_g, \infty) \simeq -\frac{3c^3\gamma\hbar}{4\omega^3 R^3} , \quad (4)$$

where $\hbar\omega$ = energy of 2^1P state above the ground state, γ = decay rate from 2^1P to the ground state, and c = speed of light. Equation (4) is reasonably good when there is no overlap of the atomic wave functions. We choose a function form of $V(^1\Pi_g, R) - V(^1\Pi_g, \infty) \equiv u(R)$ which joins smoothly with the Ginter and Battino[33] potential curves at $R < 2.3$ Å. In such a potential, it is found that for a given v an impact parameter $P_{max}(v)$ exists such that for $P > P_{max}(v)$ the internuclear separation never becomes as small as R_x = 2.06 Å. However, for any $P < P_{max}$, R does become smaller than 2.06 Å, and two crossings occur (inner crossings are ignored at the relevant low energies). Since the energy and angular momentum conservation relations enable one to calculate radial and angular velocities near R_x = 2.06 Å, we can calculate the probability of a transition to $^1\Sigma_g(2^1S + 1^1S)$ in such a crossing, and we find

$$\sigma(v) = \frac{16\pi^2}{9} |M/\hbar|^2 \times v\{\hbar/[\partial V(R_x)/\partial R]\} [1 + |u(R_x)|/E]^{3/2} \times [1 - (1-\gamma)^{3/2} - \tfrac{3}{2}\gamma(1-\gamma)^{1/2}] , \quad (5)$$

where

$$\gamma = [P_{max}(v)/R_x]^2 [1 + |u(R_x)|/E]^{-1} . \quad (6)$$

After averaging over a Maxwell distribution of speeds for the collision partners, we find for the rate constant at t = 298°K

$$k \approx 2.2 \times 10^{-12} \text{ cm}^2/\text{sec} . \quad (7)$$

We have examined the effect of changing the method of extrapolating $u(R)$ for 2.3 Å $< R <$ 4 Å and find that changes in k larger than 30% are unlikely unless relatively strange behavior occurs in the region in question. Since the agreement between theory and experiment is good, we expect that indeed the large He(2^1P) population is very rapidly converted to He(2^1S) by two-body collisions. Thus, for $P < 300$ torr, a very large fraction (~80%) of the energy available for the Jesse effect will be funneled into the 2^1S population (unless the amount of impurity is so large that quenching occurs from the 2^1P state).

Conclusions

In ref. 7 it was observed that the pressure dependence of the Jesse effect was such as to suggest competition between quenching by the impurity and a three-body collision process with ground-state atoms. The three-body rate was β_3 (sec^{-1}) = 1.6[P (torr)]^2, and the quenching rate for argon in helium was very near the observed value for Penning ionization of argon by He(2^1S).[34] This is again suggestive that the Jesse effect comes largely from He(2^1S) and that this excited atom also forms a molecule by way of three-body collisions. Some evidence for the 1.6 P^2 type of destruction of the He(2^1S) state comes from observing the collisionally induced radiation at 601 Å. The decay of this line following irradiation by a pulse of protons should follow that of the He(2^1S) population. It is indeed found that this line decays exponentially with a decay constant $\beta(2^1S) = 150P + 1.3P^2$ or, at higher pressures, $\beta(2^1S) = 1.6P^2$. It is likely that the molecule being formed is $A\ ^1\Sigma^+_u$, which has an allowed transition to the $X\ ^1\Sigma^+_g$ ground state. Thus, with our assumption, a large portion of the very strong continuum between λ = 601 Å and $\lambda \simeq$ 900 Å should have the same time dependence. This is observed to be the case.

Another puzzle concerning helium is the fate of the He(2^3S) and He(2^3P) states after irradiation. A logical guess is that He(2^3P) goes quickly to He(2^3S) (by radiative decay and two-body collisions) and that, in the pure gas, He(2^3S) forms the $a\ ^3\Sigma^+_u$ molecule, which is long-lived. He(2^3S) and $He_2(a\ ^3\Sigma^+_u)$ may live so long that Penning ionization of small amounts of impurities may be the principal mode of decay of the population at pressures above 100 torr and with low ionization densities. That helium is more sensitive to impurities than indicated by the conventional Jesse-effect measurements is evidenced by the fact that the neon resonance lines are among the strongest features in the emission spectrum of 99.9999%-pure helium at a pressure of 100 torr (see ref. 7). It is tempting to speculate that the W value for the purest helium commercially available may be somewhat lower than that of really pure helium due to ionization by the triplet population. If this is the case, the addition of a few parts per million of neon should destroy the triplet

33. M. L. Ginter and R. Battino, *J. Chem. Phys.* **52**, 4469 (1970).

34. A. L. Schmeltekopf and F. C. Fehsenfeld, *J. Chem. Phys.* **53**, 3173 (1970).

population before the minute population of impurities undergoes appreciable ionization and thus increases W (neon quenches the long-lived molecules by having its resonance levels populated). The latter "negative Jesse effect" has been observed by Parks et al.[21]

Experiments are being planned which will test some of the speculations described above.

ENERGY TRANSFER FROM THE RESONANCE STATES $Ar(^1P_1)$ AND $Ar(^3P_1)$ TO ETHYLENE

Energy transfer from resonance atomic states to molecules is an important subject for the understanding of energy pathways in the noble gases. We have examined this process experimentally for the $^1P_1$ (1048-Å) and the $^3P_1$ (1067-Å) states of argon and have made a comparison with the energy transfer theory of Watanabe and Katsuura.[11] The technique involves measuring the rate of decay of resonance photons escaping from a cylindrical cell in which excited states are created by a pulsed beam of 2-MeV protons traveling down the axis of the cylinder. We find, for example, with C_2H_4 that the rate constants are 10.3×10^{-10} cm^3/sec and 5.6×10^{-10} cm^3/sec for the $^1P_1$ and $^3P_1$ states of argon, respectively, compared with theory, which gives 10.3×10^{-10} cm^3/sec and 5.4×10^{-10} cm^3/sec for these two rate constants, respectively.

In Fig. 27.3 we show that the late decay is much more sensitive to C_2H_4 than is the early decay. Therefore, for this wavelength (1067 Å) the time-resolved quenching technique becomes an important tool. To within a crude approximation, a small amount

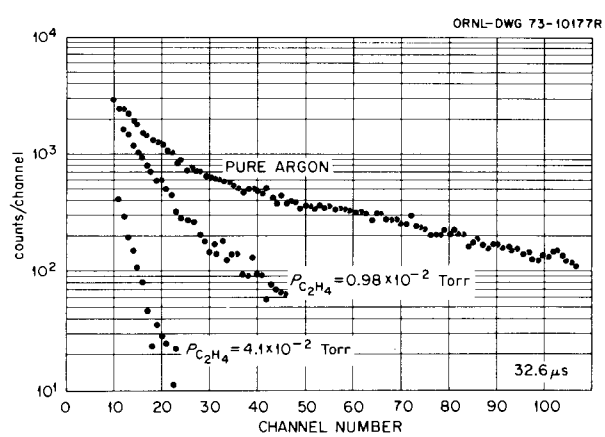

Fig. 27.3. Time decay of 1067-Å radiation from mixtures of argon with C_2H_4 at a total pressure of 100 torr. Time scale is 0.326 μsec/channel.

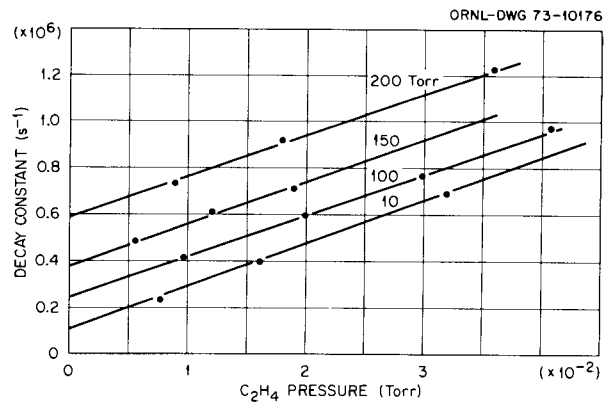

Fig. 27.4. Decay constants for 1067-Å radiation from argon as a function of C_2H_4 pressure for several mixture pressures.

of C_2H_4 will remove the late decay but will leave the early decay clearly visible. Of course the slope of the early decay has been increased, but this increase can be measured as a function of C_2H_4 pressure, and the data can be treated to obtain the rate constant for the process

$$Ar^*(^3P_1) + C_2H_4 \rightarrow C_2H_4^* + Ar(^1S_0) , \qquad (8)$$

as well as the rate of escape of the $^3P_1$ resonance photons in pure argon. This method of data treatment is shown in Fig. 27.4, where the total decay constant is plotted as a function of C_2H_4 pressure and as a function of the total pressure. The slopes of the rates plotted against the partial pressure of C_2H_4 are independent of the total pressure and give 5.6×10^{-10} cm^3 sec^{-1} for the rate constant for process (8). The decay constants of the 1067-Å resonance radiation in pure argon can be obtained by extrapolation of the data in Fig. 27.4 to zero pressure of C_2H_4. These results, which fit closely to the equation

$$\beta_e = 10^5 + 12.5P^2 , \qquad (9)$$

where β_e is in sec^{-1} when P is in torr, are shown in Fig. 27.5. A comparison of the decay constants for the $^1P_1$ and $^3P_1$ resonance radiation in argon for the cell geometry of Fig. 27.6 is shown in Fig. 27.7.

The Holstein theory[12] yields

$$\beta_e = \frac{2\sqrt{2}}{3}\gamma(k_p \pi y_0)^{-1/2} + A$$

$$= 0.165\gamma(\lambda_0/y_0)^{1/2} + A , \qquad (10)$$

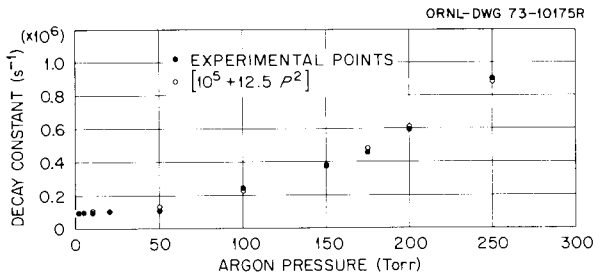

Fig. 27.5. Decay constant for 1067-Å radiation in pure argon obtained by extrapolation to zero C_2H_4 pressure.

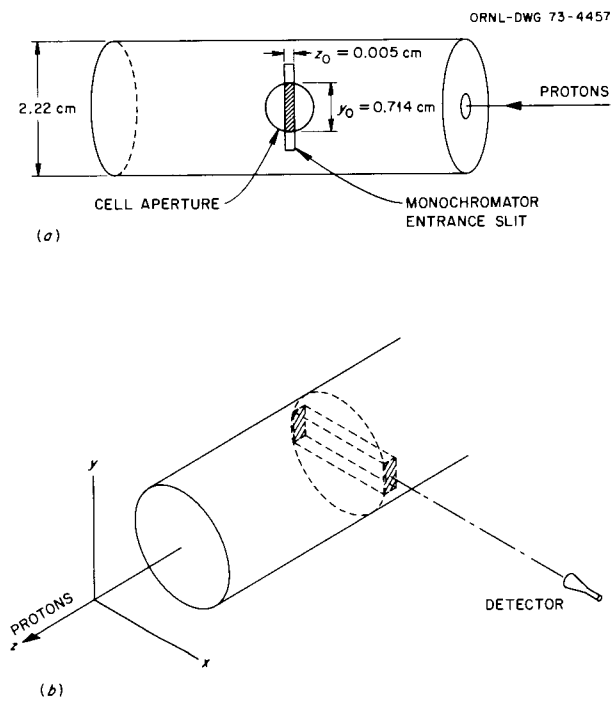

Fig. 27.6. The reaction cell as viewed by the photon detector. (*a*) Shaded area is in view at SEM detector. (*b*) Cross section of slab used in early-time analysis.

where A is the volume rate of depletion of the state and k_p is as defined by Holstein. At lower pressures, where $A = 0$, we find in argon $\beta_e \approx 0.33 \times 10^6$ sec^{-1} for 1048 Å and $\beta_e \approx 0.078 \times 10^6$ sec^{-1} for 1067 Å, if $\gamma = 5.1 \times 10^8$ sec^{-1} and 1.19×10^8 sec^{-1} respectively.[35] Figure 27.7 shows that the agreement between theory and experiment is fairly good for 2 torr $< P <$ 15 torr for the $^1P_1 \leftrightarrow {}^1S_0$ transition and for 2 torr $< P <$ 50 torr for the $^3P_1 \leftrightarrow {}^1S_0$ transition.

35. B. M. Miles, *Atomic Transition Probabilities,* vol. II, *Sodium through Cesium,* NSRDS-NBS 22 (Nat. Stand. Ref. Data Ser., Nat. Bur. Stand., No. 22), U.S. Government Printing Office, Washington, D.C., 1969.

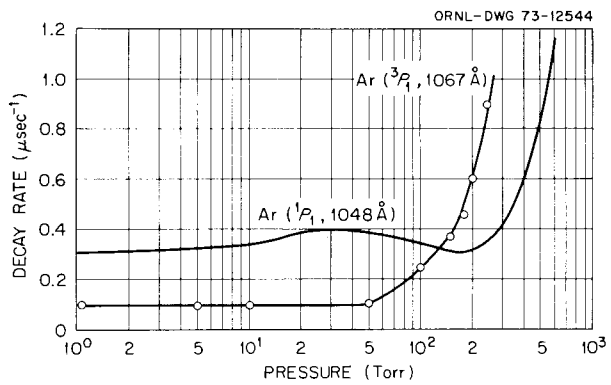

Fig. 27.7. Comparison of the decay constants for 1048-Å ($^1P_1$) and 1067-Å ($^3P_1$) resonance radiations from argon as a function of argon pressure.

ENERGY TRANSFER FROM THE RESONANCE STATES Ar($^1P_1$) AND Ar($^3P_1$) TO NITROGEN

Rate constants and average cross sections for the discrete-discrete transfer of electronic energy from argon resonance states, Ar($^1P_1$) and Ar($^3P_1$), to the nitrogen molecule, N_2, have been measured using the time-resolved quenching technique. This technique involved measurement of the time-dependent emission intensities of the argon resonance lines initially excited by 1.8-MeV protons. Experiments were carried out at intermediate argon pressure (30 to 200 torr), at 300°K, with small quantities of N_2 mixed with the argon. The early time dependence was nearly exponential, and the decay constant increased linearly with N_2 partial pressure. We found for the reaction

$$\mathrm{Ar}^*(^1P_1) + \mathrm{N}_2 \xrightarrow{K_Q} \mathrm{Ar}(^1S_0) + \mathrm{N}_2^*$$

that $K_Q = 5.9 \times 10^{-11}$ molecule^{-1} cm^3 sec^{-1} at 30 torr and for the reaction

$$\mathrm{Ar}^*(^3P_1) + \mathrm{N}_2 \xrightarrow{K_Q} \mathrm{Ar}(^1S_0) + \mathrm{N}_2^*$$

that $K_Q = 0.9 \times 10^{-11}$ molecule^{-1} cm^3 sec^{-1} at 30 torr.

RESONANCE IONIZATION SPECTROSCOPY

The theory of a direct method for determining the absolute number of excited states in a gas is reported. Use is made of a laser that is tuned to a resonance

transition between the desired excited state and some higher excited state. Photons in the same pulse photoionize the higher excited state; thus the ionization current vs photon wavelength has a resonance structure. Absolute yields of selected excited states can be obtained whenever the photon fluence per pulse is large enough to saturate the ionization current.

We initially considered a direct process in which enough photons would be available in one laser pulse to photoionize all excited states lying above a given energy. However, to obtain photons in this energy region requires frequency doubling of the output of a pulsed dye laser.[36] With frequency doubling, the energy per pulse is reduced by more than a factor of 10, and, as a consequence, the product of photon fluence and photoionization cross section is of the order of unity. Under this condition the conversion of excited states to ions is not complete. In the following, we discuss a technique that does not require frequency doubling but instead takes advantage of a two-step process for the conversion of excited atoms to ions. This avoids the ion yield difficulty, and it provides another very important feature – namely, resonance structure in the ionization yield. Thus a single laser beam can be tuned to promote transitions between an excited state and an intermediate state, and a second photon from the same laser pulse can photoionize the intermediate state. Such a process involving two photons in discrete steps to produce ionization has been utilized by Stebbings[37] to obtain cross sections for photoionization of the intermediate state. We are not discussing what is usually referred to as multiphoton ionization processes, which require very high peak power.[38]

We will observe true resonances in the ionization current at several wavelengths for each excited state. Furthermore, these resonances will occur in a region of wavelength more favorable for the pulsed dye laser. Frequency doubling will not be required, and an adequate fluence per pulse is available so that nearly all the atoms excited to a given state will be photoionized. Finally, any one of the states can be removed while the other states will not be disturbed, since what is resonance wavelength for promotion of a selected excited state will not be a resonance wavelength for the states not selected.

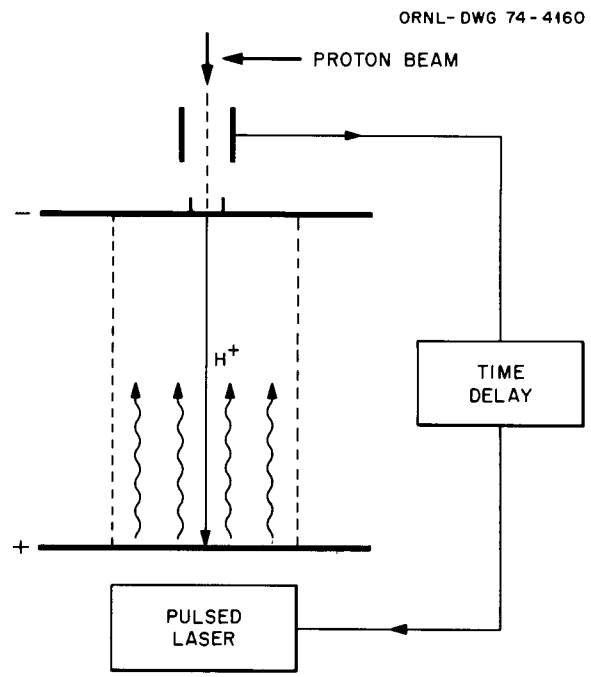

Fig. 27.8. Schematic of a method for the study of excited states in a gas. A pulsed proton beam creates ionization and excited states. At an arbitrary time after the proton pulse, a photon pulse is generated of sufficient fluence per pulse to convert all the states of certain species to ion pairs in a time that is short compared with the system lifetime.

In the present section, we will give a quantitative discussion of resonance ionization spectroscopy. It will be helpful to discuss the process first in a rather definite context. Thus we consider the situation illustrated in Fig. 27.8. Suppose that a noble gas has been excited by a pulse of protons which is short in duration and suppose that this excitation occurred at time $t = 0$. After a time delay t, a broad beam of photons is fired antiparallel to the proton beam. (This arrangement is convenient, and it allows measurement of the spatial profile of the species if the optics is such that the laser beam radius can be adjusted.) If the laser beam is tuned to a transition from a selected excited state (level 1) to an intermediate state (level 2), that is, it contains photons of frequency $h\nu_{12}$, and if $h\nu_{12} \geqslant h\nu_{1c}/2$, where ν_{1c} is the frequency of a photon that will ionize just level 1, some photoionization will be produced as a consequence of the two-step process.

36. The following information has been furnished by S. Edward Neister, President of Phase-R Corporation, New Durham, N.H. 03855: A pulsed dye laser is available which provides more than 1 J per pulse over the frequency range 4250 to 7400 Å. The pulse width is 300 nsec, the beam diameter is 15 mm, and the spectral width is 4 Å.

37. R. F. Stebbings, private communication.

38. M. Mohan and S. N. Hague, *Phys. Rev. A* **9**, 725 (1974).

Rate equations for levels 1 and 2 having populations of N_1 and N_2 respectively are

$$\frac{dN_1}{dt} = -\frac{\lambda_0{}^2}{8\pi}\gamma_{21}\frac{g_2}{g_1}F(\nu_{12})\,g(t)\,N_1 + \frac{\lambda_0{}^2}{8\pi}\gamma_{21}\,F(\nu_{12})\,g(t)\,N_2 - \beta_1 N_1 + \gamma_{21}N_2 \quad (11a)$$

and

$$\frac{dN_2}{dt} = \frac{\lambda_0{}^2}{8\pi}\gamma_{21}\frac{g_2}{g_1}F(\nu_{12})\,g(t)\,N_1 - \frac{\lambda_0{}^2}{8\pi}\gamma_{21}\,F(\nu_{12})\,g(t)\,N_2 - \sigma_{2c}(\nu_{12})\,g(t)\,N_2 - \gamma_{2T}N_2\,, \quad (11b)$$

in which λ_0 = photon wavelength corresponding to frequency ν_{12}; γ_{21} = rate of spontaneous decay from state 2 to state 1; γ_{2T} = total rate of spontaneous decay from state 2 to all lower states; g_1, g_2 = degeneracies of states 1 and 2 respectively; β_1 = total rate of decay of state 1 due to all processes occurring when the system is returning to thermodynamic equilibrium without interference from the laser beam; $F(\nu)\,d\nu$ = fraction of laser photons in frequency interval between ν and $\nu + d\nu$ (assumed to be nearly constant over the spectral line); $g(t)$ = frequency-integrated number of laser photons crossing a unit area per unit time, that is, the photon flux; and $\sigma_{2c}(\nu)$ = cross section for photoionization of state 2 by a photon of frequency ν.

We are interested in the number N_c of the selected excited states that are promoted to the continuum; this is obtained from

$$N_c = \sigma_{2c}(\nu_{12})\int_t^\infty g(t')\,N_2(t')\,dt'\,, \quad (12)$$

and we shall be comparing it with $N_1(t)$, the number of selected states as a function of time following excitation. Specifically, if $N_2 = 0$ when the laser pulse is fired, the number N_c represents some fraction of the states $N_1(t)$.

For the pulsed laser source under consideration, $g(t)$ is on the order of 10^{24} photons cm^{-2} sec^{-1}; therefore the first two terms in either Eq. (11*a*) or (11*b*) dominate the other terms. Quasi equilibrium [i.e., $g_2\,N_1(t) \approx g_1\,N_2(t)$] is reached very early, a condition in which the number of photons in the stimulated emission process is nearly equal to the rate of absorption. We find in quasi equilibrium:

$$\frac{N_c(t+\tau)}{N_1(t)} = \sigma_{2c}(\nu_{12})\left(1+\frac{g_1}{g_2}\right)^{-1}\int_0^\tau \frac{d\mathsf{F}}{d\tau'}(\tau')\,d\tau' \times \exp\left\{-[(\gamma_{2T}-\gamma_{21})\tau' + (g_1/g_2)\beta_1\tau' + \sigma_{2c}(\nu_{12})\,\mathsf{F}(\tau')]\right\}\,, \quad (13)$$

where

$$\mathsf{F}(\tau') = \int_t^{t+\tau} g(t')\,dt'\,.$$

We conclude by evaluating Eq. (13) for two low-lying states of helium as an illustration of the use of the technique for noble gases and show that under some typical pressures of interest to energy-pathways analysis the technique should work in practice. In the examples below, we assume that the laser beam has an area of 1 cm^2, that the flux is constant during the time τ_0 (0.3×10^{-6} sec), and that $F(\nu)$ is a square pulse of 4 Å width.

To evaluate the fraction $N_c(t+\tau_0)/N_1(t) \equiv f_c$ for He(2^1S), we make use of the diagram of Fig. 27.9. When the photon flux is applied, the 2^1S and 3^1P states come into quasi equilibrium. The 3^1P state radiates to the ground state (537 Å) at a rate of 5.7×10^8 sec^{-1} and to the 3^1S state at a rate of 2.5×10^5 sec^{-1}. The 537-Å radiation is trapped at moderate pressure; according to the Holstein theory,[12] the lowest eigenmode estimate of the rate of escape from a cylinder of 1-cm radius is 2.6×10^5 sec^{-1}. Thus the effective value of $(\gamma_{2T} - \gamma_{21})$ is just $(2.6 \times 10^5 + 2.5 \times 10^5)$ sec^{-1}, or 5.1×10^5 sec^{-1}. There is some uncertainty[29] in the value of β_1 for the He(2^1S) state at high pressures; up to pressure of a few hundred torr, it is not expected that it will exceed about 10^6 sec^{-1}. Assuming a laser pulse of 2.5 J at 5015 Å with $\tau_0 = 0.3 \times 10^{-6}$ sec and $\sigma_{2c} = 4.3 \times 10^{-18}$ cm^2, we find $\mathsf{F}(\tau_0)\,\sigma_{2c} = 35$ and $f_c = 0.99$.

The analysis of a lower state that emits resonance radiation proceeds in a similar way. Consider the He(2^1P) state, which emits the 584-Å resonance line to the ground state (Fig. 27.10). We utilize 3^1S as an intermediate state by tuning the laser to 7281 Å. Here $(\gamma_{2T} - \gamma_{21}) = 0$, and we can use measured values for the total rate of destruction, β_1, of the 2^1P state. With $\sigma_{2c} = 1.8 \times 10^{-17}$ cm^2 and assuming a laser pulse of 1.5 J, we find $\sigma_{2c}\,\mathsf{F}(\tau_0) = 97$. At 20 torr, β_1 is 4×10^6 sec^{-1} and f_c is 0.96. Consideration of the low-lying

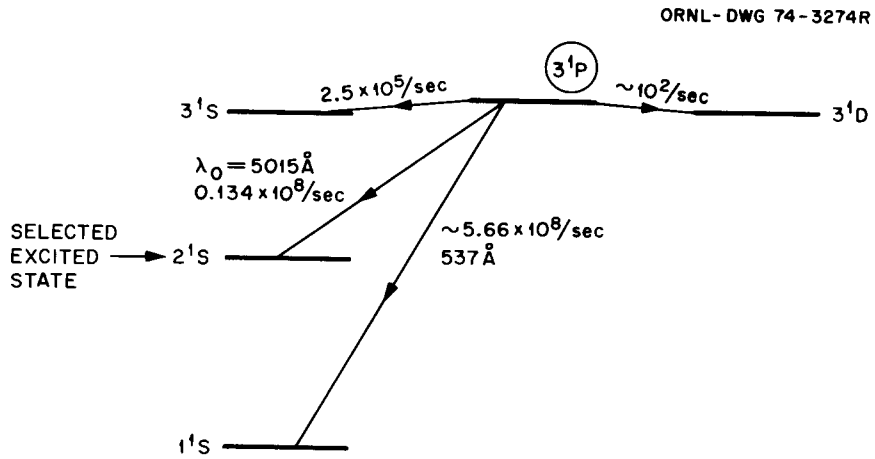

Fig. 27.9. Some transitions in helium relative to the consideration of resonance ionization of the 2^1S metastable state via the absorption of 5015-Å radiation to the 3^1P intermediate state.

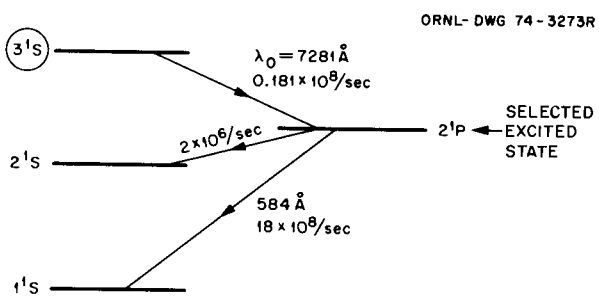

Fig. 27.10. Some transitions in helium relative to the consideration of resonance ionization of the 2^1P resonance state via the absorption of 7281-Å radiation to the 3^1S intermediate state.

triplet states shows that resonance ionization measurements of the 2^3P state through the transition ($2^3P \rightarrow 3^3S$), 7065 Å, and of the 2^3S state through the transition ($2^3S \rightarrow 3^3P$), 3888 Å, are also feasible. We believe that the long-lived resonance and metastable states for each of the noble gases can be studied with the RIS technique.

MICRODOSIMETRY

In recent years, several theories[39,40] have been developed which attempt to relate the probability of biological effects due to radiation to the amount of energy deposited in a "sensitive volume" having dimensions of the order of magnitude of a cell nucleus. One argument for such an approach is that, when a cell is irradiated, the average density of ionization occurring in any region of the cell is roughly proportional to the local absorbed dose, with the proportionality constant being nearly independent of the type of radiation. If the biological effect comes largely from ionization products and the large number of low-energy electrons produced in the slowing-down process, the chance of progress by applying such an approach to restricted types of radiation is substantial. For these reasons, we have started to develop a capability in the area of microdosimetry.

Katz[40] has pointed out the important role which radial dose distribution plays in determining the effect of radiation. The most general information about radial energy distribution around a track is contained in $\mathsf{F}(E_1, R)$, where $\mathsf{F}(E_1, R)\, dE_1$ is the probability of a single primary track with distance of closest approach R to the center of mass of a "sensitive volume" causing an amount of energy between E_1 and $E_1 + dE_1$ to be deposited in the sensitive volume. We find a spherical sensitive volume

$$\mathsf{F}(E_1, R_c) = \frac{1}{2\pi} \int_{-\infty}^{\infty} e^{i\omega E_1}$$

$$\times \exp\left[-\int dE'\, N(E', R_c)(1 - e^{-i\omega E'})\right] d\omega\,, \qquad (14)$$

with

$$N(E', R_c) = \int d\epsilon \int d\Omega\, \mathsf{P}(\epsilon, \theta)\, M(\epsilon, \theta, E', R_c)$$

$$+ Z(R_c)\, P_T(E')\,, \qquad (15)$$

39. A. M. Kellerer and H. H. Rossi, *Radiat. Res.* 47, 15 (1971); *Curr. Top. Radiat. Res. Quart.* 8, 85–158 (1972).

40. R. Katz, B. Ackerson, M. Homayoonfor, and S. C. Sharma, *Radiat. Res.* 47, 402 (1971).

$$M(\epsilon, \theta, E', R_c) = \int_{V_c} dV\, L(\epsilon, \theta, E', R) \,. \qquad (16)$$

In Eq. (16) the integral is over the volume elements of a sensitive site having its center of mass at distance R_c from the particle track, and $2\pi R\, dR\, dE'\, L(\epsilon, \theta, E', R)$ is the probability that an electron with energy ϵ ejected at angle θ relative to the primary-particle velocity will result in the deposition of energy between E' and $E' + dE'$ in the cylindrical shell between R and $R + dR$. $\mathsf{P}(\epsilon, \theta)\, d\epsilon\, dZ\, d\Omega$ is the probability that, in traversing dZ, an electron will be produced with energy in the interval $d\epsilon$ at ϵ and into solid angle $d\Omega$ at θ relative to the primary-particle velocity. $\mathsf{P}(\epsilon, \theta)$ has the ϵ and θ dependence of the differential cross section for the primary particles to produce electrons with the particular energy and angular dependence. $P_T(E)\, dE\, dx$ is the probability that energy between E and $E + dE$ will be deposited along the track in dx in the form of binding energy of ejected electrons or excitation of atomic or molecular states. $Z(R_c)$ is the track length in the sensitive volume if the track comes within R_c of the sphere's center. We have

$$-\frac{dE}{dx} = \int d\epsilon\, \epsilon \int d\Omega\, \mathsf{P}(\epsilon, \theta) + \int E\, P_T(E)\, dE \,. \qquad (17)$$

The approximation involved is that we treat energy deposition along the track and electron ejection as statistically independent.

If we define M_n by

$$M_n = \int E_1{}^n\, \mathsf{F}(E_1, R_c)\, dE_1 \,, \qquad (18)$$

we find from Eq. (14):

$$M_n = i^n \frac{d^n}{dx^n}$$

$$\{\exp[-\int dE'\, N(E', R_c)(1 - e^{-ixE'})]\}_{x=0} \,, \qquad (19)$$

so that

$$M_1 = \bar{E}_1(R_c) = \int dE'\, N(E', R_c)\, E' \qquad (20)$$

and

$$\sigma^2 = \int \mathsf{F}(E_1, R_c)\, (E_1 - M_1)^2\, dE_1$$

$$= M_2 - [M_1]^2$$

$$= \int dE'\, N(E', R_c)\, E'^2 \,. \qquad (21)$$

We have applied microdosimetry to several models of cell survival. We report one of these here. The model in question is very similar to one that has been studied extensively for low-LET radiation by Roesch.[41] It assumes that two types of biologically important damage sites can occur due to deposition of energy in the "sensitive volume" of the cell. If energy E_1 is deposited, there is a probability $(n_1!)^{-1}(\lambda E_1)^{n_1}\, e^{-\lambda E_1}$ that n_1 of the first-type sites will be formed and a probability $(n_2!)^{-1}\, (\beta E_1)^{n_2}\, e^{-\beta E_1}$ that n_2 of the second type will be formed. The first type of site is much rarer than the second, but it leads to reproductive death with certainty. The second is not lethal by itself, but it can combine by way of second-order kinetics with another of its type to yield a lethal lesion. In the case of the second type of event, which we will subsequently refer to as formation of a "pre-lesion," the second-order kinetic process competes with a "repair" process which depletes the number of pre-lesions present after their production. We take $A\, dt$ to be the probability that a pre-lesion will be repaired during dt and assume that $2\pi R_c\, dR_c\, F(t)\, dt$ gives the probability that a primary-particle track will come within R_c and $R_c + dR_c$ of the sensitive volume center of mass in time dt [$F(t)$ = primary-particle flux]. If either the combining of two pre-lesions or the formation of a lethal lesion (i.e., the first type of damage site) leads to reproductive death with certainty, we find for the survival probability F_s:

$$F_s = \exp\left[-(\pi R_B{}^2 + Q) \int_0^\infty F(t)\, dt - k \int_0^\infty \overline{n^2}(t)\, dt\right] , \qquad (22)$$

where k is the rate constant for combining of pre-lesions, R_B is defined by (inside R_B we assume that a lethal effect is certain) $(k/A)[\beta \bar{E}_1(R_B)]^2 = 5$,

$$Q = \int_{R_B}^\infty 2\pi R_c\, dR_c \times \int dE_1\, \mathsf{F}(E_1, R_c)\, (1 - e^{-\lambda E_1}) \,, \qquad (23)$$

$$\int_0^\infty \overline{n^2}(t)\, dt = A^{-1}(\beta\mu_1)^2 \int_0^\infty F(t)$$

41. W. C. Roesch, Hit Theory for Low-LET Radiation, BNWL-SA-4172 (1972).

$$\times \int_0^t e^{-A(t-t')} F(t')\, dt'$$

$$+ (2A)^{-1} (\beta^2 \mu_2) \int_0^\infty F(t)\, dt\,, \qquad (24)$$

and

$$\mu_n = \int_{R_B}^\infty 2\pi R_c\, dR_c \int_0^\infty E_1{}^n\, \mathsf{F}(E_1, R_c)\, dE_1\,. \qquad (25)$$

In all the above, we have followed Roesch in assuming $k/A \ll 1$.

If the LET of the primary particles is sufficiently low, a solution to $(k/A)[\beta\, E_1(R_B)]^2 = 5$ will not exist, and R_B is to be taken as zero. In the latter case, μ_1 becomes

$$\mu_1 = \int_0^\infty 2\pi R_c\, dR_c \int_0^\infty E_1\, \mathsf{F}(E_1, R_c)\, dE_1$$

$$= -V_c \frac{dE}{dx} \quad (V_c = \text{volume of "sensitive volume"})\,, \qquad (26)$$

and

$$\mu_2 = \int_0^\infty 2\pi R_c\, dR_c \int \mathsf{F}(E_1, R_c)\, E_1{}^2\, dE_1$$

$$= \int_0^\infty 2\pi R_c\, dR_c\, [\bar{E}_1(R_c)]^2$$

$$+ V_c \int d\epsilon \int d\Omega\, \mathsf{P}(\epsilon, \theta)\, \epsilon^2 \int 2\pi R\, dR$$

$$\times \int E_1{}^2\, L(\epsilon, \theta, E_1, R) \times dE_1 + V_c \int E^2\, P_T(E)\, dE\,. \qquad (27)$$

In the latter situation, Eq. (24) becomes

$$\int_0^\infty \overline{n^2}(t)\, dt = A^{-1}(\beta V_c P)^2$$

$$\times \int_0^\infty \dot{D}(t) \int_0^t e^{-A(t-t')}\, \dot{D}(t')\, dt'\, dt$$

$$+ (2A^{-1})(\beta^2 V_c P \mu_2/\mu_1)\, D(\infty)\,, \qquad (28)$$

where $D(\infty)$ is the total absorbed dose, $\dot{D}(t)$ is the dose rate at time t, and P is the density of the medium. In this same limit, λ is probably small enough so that

$$Q \cong \int_0^\infty 2\pi R_c\, dR_c \int dE_1\, \mathsf{F}(E_1, R_c)\, \lambda E_1$$

$$= -\lambda V_c \frac{dE}{dx}\,. \qquad (29)$$

Thus, letting

$$\alpha = (V_c P)^{-1} \mu_2/\mu_1$$

$$= (V_c P)^{-1} \int_0^\infty 2\pi R_c\, dR_c \int E_1{}^2\, \mathsf{F}(E_1, R_c)\, dE_1$$

$$\times \left[\int_0^\infty 2\pi R_c\, dR_c\, dR_c \int E_1\, \mathsf{F}(E_1, R_c)\, dE_1\right]^{-1}, \qquad (30)$$

we find

$$F_s = \exp\left\{-(\lambda V_c P)\, D(\infty) - (k/A)(\beta V_c P)^2 \left[(\alpha/2)\, D(\infty) + \int_0^\infty dt\, \dot{D}(t) \int_0^t e^{-A(t-t')}\, \dot{D}(t')\, dt'\right]\right\}. \qquad (31)$$

For constant dose rate over a finite time interval and for very-low-LET radiation so that $\alpha \ll D(\infty)$, we get the low-LET version of the Roesch model. At small doses the percent incidence of death is very similar to the Kellerer-Rossi theory of RBE. The fact that the present theory only agrees with the Kellerer-Rossi theory for sufficiently low LET indicates that it is quite likely that their theory neglects very substantial overkill (or lost dose) effects when a heavy ion comes sufficiently close to the cell nucleus. The importance of dealing with radial dose distribution in accounting for this problem has been emphasized by Katz.[40]

THEORETICAL MODELS FOR LOW-LET CELL-SURVIVAL STUDIES

Assumptions

During the last two decades a large amount of information has been obtained concerning the nature of cell survival under various conditions of irradiation. Much attention has been given to the design and execution of experiments that yield information on the

mechanisms governing radiobiological response.[42-55] While our understanding of cell survival is far from complete, there is considerable evidence that any model which hopes to explain most of the experimental facts must include as a minimum the following features:

1. Statistical fluctuations associated with both direct and indirect effects of radiation must be included for an arbitrary time history of the radiation field.[42,50] In connection with indirect effects, it must be possible to allow for the chemical kinetics which lead to the oxygen effect or to the action of protective chemicals.[44,45,48,52]
2. The phenomenon of repair must be included, along with the action of the radiation on the repair mechanism.[43,47-51] The repair mechanism should be capable of recovering from the effects of radiation under the proper conditions.[43,47,50,53]
3. Allowance should be made for the possibility of both repairable and irreparable damage.
4. It should be possible to allow for the action of chemicals that are believed to stop repair.[49]
5. The idea of a "fixation time" and other cell-cycle effects must be included.[42,49,54]

The detailed processes through which biological systems are affected by radiation are extremely complex and poorly understood, even in the simplest systems. Thus theoretical models must, of necessity, be rather schematic in their descriptions of the mechanisms that are involved in cell survival. However, in spite of the degree of oversimplification which must be invoked in constructing any tractable biological model, such efforts still offer the best possibility of achieving insight into the important mechanisms involved in biological response to radiation.

We have formulated a model that includes in an approximate way all of the above features (and others). The kinetics involved in indirect effects and in the effect of radiation on repair enzymes is not specified in the solution to the related problem in probability theory. The latter property should be useful to the biologist since he is, in effect, supplied with a very general solution from which predictions can be obtained with a wide range of assumptions concerning the indirect effect and the effects of recovery and of radiation on the repair mechanism. Further generality is obtained by determining a rather general probability function.

As examples of how the general solution can be used, we have shown how the models of Dienes,[56] Kappos and Pohlit,[57] Kapul'tsevich and Korogodin,[58] and Lea[59] follow as special cases. We have also analyzed the results of Calkins[49] on the effect of caffeine added at different times after irradiation and have shown how the idea of a "fixation time" after which no repair is possible can be incorporated.

We proceed by taking account of every energy loss event that occurs in a cell, regardless of whether it leads eventually to a potentially lethal lesion, and treating the number of these events as an additional stochastic variable in the formulation of the statistics problem. Thus there is a clear relation between the present formalism and models in which the number of energy loss events, n, occurs explicitly in the expression for the survival probability. For instance, an exact solution of the Roesch model[41] has been shown to follow as a special case.

Taking account of the fact that not all energy loss events play an important part in cell survival, we define $\mu(t)$ to be the probability that, in an energy loss event in the cell, a repairable lesion is formed, and we define

42. M. M. Elkind and G. F. Whitemore, *The Radiobiology of Cultured Mammalian Cells,* Gordon and Breach Science Publishers, Inc., New York and London, 1967.
43. V. I. Korogodin, Yu. G. Kapul'tsevich, M. N. Myasnik, A. F. Mosin, and V. V. Gridnev, *Advan. Biol. Med. Phys.* **12**, 255 (1968).
44. T. Alper and P. Howard-Flaners, *Nature* **178**, 978 (1956).
45. T. Alper, *Cellular Radiation Biology,* Williams and Wilkins Co., Baltimore, Md., 1965, p. 272.
46. R. H. Haynes, *Radiat. Res. Suppl.* **6**, 1 (1966).
47. R. B. Setlow and W. L. Carrier, *Proc. Nat. Acad. Sci. USA* **51**, 226 (1964).
48. P. Todd, *Radiat. Res. Suppl.* **1**, 196 (1967).
49. J. Calkins, *Radiat. Res.* **45**, 50 (1971).
50. W. Pohlit, *Advan. Biol. Med. Phys.* **12**, 275 (1968).
51. W. Szybalski, *Radiat. Res. Suppl.* 1, 147 (1967).
52. H. Loman, S. Voogd, and J. Blok, *Radiat. Res.* **42**, 437 (1970).
53. V. J. Korogodin, M. N. Meissel, and T. S. Remesova, in *Proceedings of Third International Congress on Radiation Research,* North-Holland Publishing Co., Amsterdam, 1967, pp. 538–57.
54. E. Nunes de Langguth and C. A. Beam, *Radiat. Res.* **53**, 226 (1973).
55. M. H. Patrick, R. H. Haynes, and R. B. Uretz, *Radiat. Res.* **21**, 144 (1964).
56. G. J. Dienes, *Radiat. Res.* **28**, 183 (1966).
57. A. Kappos and W. Pohlit, *Int. J. Radiat. Biol.* **22**, 51 (1972).
58. Yu. G. Kapul'tsevich and V. I. Korogodin, *Radiobiologiya* **4**, 349 (1964); *Radiobiology (USSR)* **4**, 18 (1964).
59. D. E. Lea, *Actions of Radiations on Living Cells,* Cambridge University Press, London, 1956.

$\lambda(t)$ to be the probability that the event causes an irreparable lesion to occur. Let $\gamma(t)$ be the probability that an energy loss event will cause a coexisting repairable lesion to be converted into an irreparable one, possibly of a different type. Further, let the probability of an energy loss event in the cell between times t and $t + dt$ be $dt\ \beta_0\ \dot{D}(t)$, where $\dot{D}(t)$ is the dose rate at time t, and finally assume that the probability that a coexisting repairable lesion will be repaired in this time interval is $R(t)\ dt$. We have derived differential equations based on these assumptions for $P(n, n_1, n_2, n_3, t)$ = probability that at time t a cell will have n_1 repairable lesions, n_2 irreparable lesions of the type formed by a further hit on a repairable lesion, and n_3 irreparable lesions of the type formed directly and that exactly n energy loss events have occurred in the cell. The stochastic variable n is superfluous to most reasonable cell-survival models and can be summed over in the differential equations to yield equations for the probability of having n_1, n_2, and n_3 lesions formed due to all possible values of n. The latter equations are readily solvable.

The Statistical Problem

Consider a very large number of identical cells N_p ($N_p \to \infty$) and let $N(n, n_1, n_2, n_3, t)$ be the number of these cells which after time t have suffered n energy loss events, have n_1 repairable lesions, have n_2 irreparable lesions of the type that arise due to added damage to a repairable lesion, and have n_3 irreparable lesions of a second type, each of which arises from a single energy loss event. Using the definitions and assumptions of the previous section, we derive a differential equation for the change in $N(n, n_1, n_2, n_3, t)$ in the time interval between t and $t + dt$. Since $P(n, n_1, n_2, n_3, t) = N(n, n_1, n_2, n_3, t)/N_p$, where N_p is the number of identical cells in the ensemble, the equation is also an equation for $P(n, n_1, n_2, n_3, t)$.

The complications that arise when one writes a survival probability as a sum of terms corresponding to survival after different numbers, n, of energy loss events is apparent in the Roesch model of cell survival.[41] However, n is superfluous since (by assumption) the significant hit events are those which correspond to the formation of lesions. Thus the index n may be summed over in the defining equation for $P(n, n_1, n_2, n_3, t)$ to give a much simpler equation for the total probability $\bar{P}(n_1, n_2, n_3, t)$ of having n_1, n_2, and n_3 lesions at time t due to all possible numbers of energy loss events.

If we define

$$\bar{P}(n_1, n_2, n_3, t) = \sum_{n=0}^{\infty} P(n, n_1, n_2, n_3, t)\ , \tag{32}$$

where $P(n, n_1, n_2, n_3, t)$ is zero unless $n_1 + n_2 + n_3 < n$, then the sum over n may be carried out with the result (k being the probability that the repair process aborts and results in a lesion of type 2):

$$\begin{aligned}\frac{d\bar{P}(n_1, n_2, n_3, t)}{dt} = &-\{\beta_0\ \dot{D}(t)\ [n_1\ \gamma(t) + \lambda(t) \\ &+ \mu(t)] + n_1\ R(t)\}\ \bar{P}(n_1, n_2, n_3, t) \\ &+ (1-k)(n_1+1)\ R(t)\ \bar{P}(n_1+1, n_2, n_3, t) \\ &+ \beta_0\ \dot{D}(t)\ \mu(t)\ \bar{P}(n_1-1, n_2, n_3, t) \\ &+ \beta_0\ \dot{D}(t)\ \lambda(t)\ \bar{P}(n_1, n_2, n_3-1, t) \\ &+ [\beta_0\ \dot{D}(t)\ \gamma(t)\ (n_1+1) \\ &+ (n_1+1)k\ R(t)]\bar{P}(n_1+1, n_2-1, n_3, t)\ .\end{aligned} \tag{33}$$

It can be shown by direct substitution that the solutions to Eq. (33) corresponding to no lesions at $t = 0$ (before irradiation) are

$$\bar{P}(n_1, n_2, n_3, t) = \prod_{i=1}^{3} [h_i(t)]^{n_i}\ [n_i!]^{-1}\ \exp[-h_i(t)]\ , \tag{34}$$

where

$$h_1(t) = \int_0^t \frac{d\Gamma_1(t')}{dt'}\, dt'\ \exp[\rho(t) + \Gamma_2(t') - \Gamma_2(t)]\ , \tag{35a}$$

$$h_2(t) = \int_0^t \left[\frac{d\Gamma_1(t')}{dt'} + k\ R(t)\right] dt' \times \int_0^{t'} \frac{d\Gamma_1(t'')}{dt''}\, dt''\ \exp[\rho(t'') - \rho(t') + \Gamma_2(t'') - \Gamma_2(t')]\ , \tag{35b}$$

$$h_3(t) = \int_0^t \beta_0\ \dot{D}(t')\ \lambda(t')\ dt'\ , \tag{35c}$$

with

$$\Gamma_1(t) = \int_0^t \beta_0\, \mu(t')\, \dot{D}(t')\, dt'$$

and

$$\Gamma_2(t) = \int_0^t \beta_0\, \gamma(t')\, \dot{D}(t')\, dt' .$$

Special Cases

Model for Calkins's data. The present analysis has been applied to Calkins's[49] data on survival of stationary-phase *Tetrahymena* irradiated with x rays and subjected to caffeine at different times, t_c, after irradiation.

We adopt a picture similar to that of Calkins and assume that all lesions are repairable, but if even one lesion remains unrepaired after the "fixation time," t_f, reproductive death occurs. Caffeine is assumed to stop repair, so that the survival probability P_s is given by

P_s = probability of zero repairable lesions after a time t_D ,

where t_D is the smaller of t_c and t_f. The relevant time is t_D because, if $t_c < t_f$, no further change in the number of lesions occurs after t_c. The repair function $R(t)$ is taken to be constant after irradiation and is equal to

$$R(t) = R_0 \exp[-\sigma_0 D] , \tag{36}$$

where D is the mean absorbed dose. The assumption that irradiation inactivates or impedes repair enzymes at doses of the order of 100,000 rads seems plausible.

The solution of the statistics problem outlined above is obtained by choosing $\lambda(t) = \gamma(t) = 0$ and $\dot{D}(t) = 0$ for $t > \tau$, with $R_0\tau \ll 1$. With these choices, $h_2(t) = h_3(t) = 0$, and $\bar{P}(n_1, n_2, n_3, t)$ is only nonzero for $n_2 = n_3 = 0$. Further, if $\mu(t) = \mu_0$ and $\mu_0\beta_0 = \beta$,

$$h_1(t) = \exp[-R_0 t \exp(-\sigma_0 D)]\, \beta D \tag{37}$$

and

$$\bar{P}(n_1, 0, 0, t) = [h_1(t)]^{n_1} [n_1!]^{-1} \exp[-h_1(t)] . \tag{38}$$

Thus, with our assumptions, the survival probability is

$$P_s = \bar{P}(0, 0, 0, t_D)$$
$$= \exp[-\beta D \exp(-R_0 t_D\, e^{-\sigma_0 D})] . \tag{39}$$

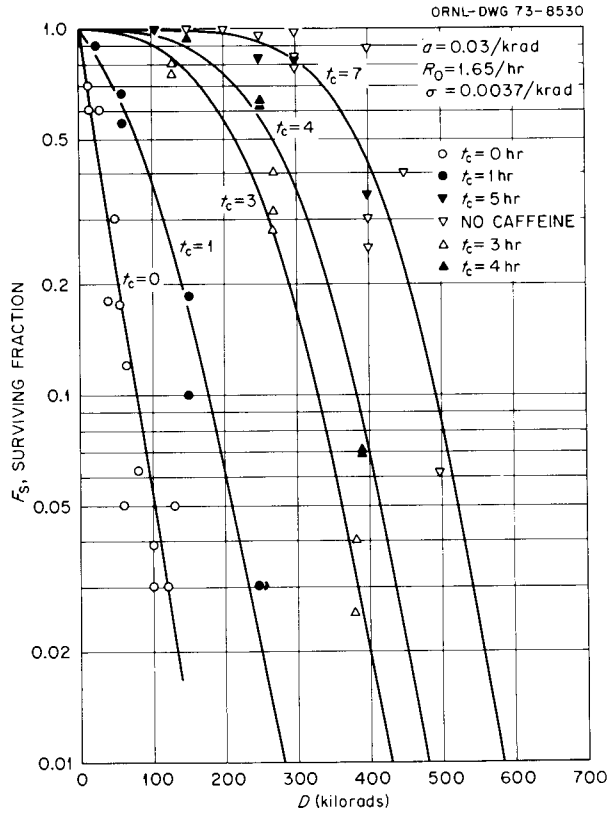

Fig. 27.11. Survival curves for stationary phase Tetrahymena Pyriformis irradiated by x rays with caffeine added at various times, t_c, after irradiation. The solid curves were calculated from the result $F_s = \exp\{-aD \exp[-R_0 t_d \exp(-\sigma D)]\}$, where t_d is the smaller of the fixation time t_f and the time t_c at which caffeine is added. a = 0.03/kilorad; R_0 = 1.65/hr; σ = 0.0037/kilorad. The experimental points are those of Calkins.[49]

In Fig. 27.11 we have compared the present simple theory with the data of Calkins.[49] In Calkins's experimental data, the agreement is particularly pleasing because t_D was effectively given five different values, and the theory reproduced the experimental data in each case with only three adjustable parameters: β, σ_0, and R_0.

Model of liquid holding recovery for yeast. The experiments of Korogodin et al.[53] and others[55] on liquid holding recovery for diploid yeast have shown that the surviving fraction F_s is given by $F_s = F[\bar{D}(t)]$, where $F(D)$ is the surviving fraction with immediate plating and $\bar{D}(t)$ is given by the empirical relation $\bar{D}(t) = [k + (1 - k)e^{-\beta t}]D$, where t is the time of liquid holding and k and β are constants. The irreversible fraction k has been shown to be almost independent of LET.

We have used the present formalism to describe a model for liquid-holding recovery in yeast. Unlike a somewhat similar model of Kapul'tsevich and Korogodin,[58] the present model includes a mechanism for the irreversible part of the radiation damage and yields the observed dependence of F_s on the liquid holding time t.[53,60]

Very briefly, we assume the following conditions in the general statistical formalism: (1) $\Gamma_2(t) = 0$; (2) $\gamma(t) = 0$; (3) $R(t) = R_0$ = constant; and (4) $\Gamma_1(t) = \alpha D(t)$, where α is a constant. We further adopt the view that liquid holding stops movement of the cell through the cell cycle but permits repair processes to continue. Thereby the fixation time, that is, the time available before all lesions become irreparable, can be lengthened by an arbitrary amount by holding in water. Thus the fixation time is almost equal to the time of liquid holding. Finally, we assume that the condition which causes reproductive death is the presence of at least N lesions after the fixation time t_0.

With this specific biological model of liquid holding processes, we get the result that the surviving fraction F_s after dose D and liquid holding time t_0 is

$$F_s = \sum_{n_1=0}^{N-1} \bar{P}(n_1, 0, 0, t_0)$$

$$= \sum_{n=0}^{N-1} [\alpha \bar{D}(t_0)]^n (M!)^{-1} e^{-\alpha \bar{D}(t_0)} , \qquad (40)$$

where

$$\bar{D}(t) = [k + (1-k)e^{-R_0 t_0}]D . \qquad (41)$$

With no liquid holding, the survival probability is given by setting $t = 0$. With $t = 0$, we get $\bar{D}(0) = D$. Thus liquid holding has the effect of decreasing the effective dose by the factor $k + (1-k)e^{-R_0 t}$. This prediction is in agreement with experiments[53,61] and with the conclusions of Kapul'tsevich.[62]

Model of Roesch. One of the more complicated cell-survival models is that of Roesch.[41] The latter model has several appealing characteristics, the most important being that it is one of the first[55] to have incorporated, simultaneously, repair and the formation of lethal lesions due to the accumulation of nonlethal repairable damage. Roesch's model is closely related to earlier work by Kellerer and Hug.[63]

Roesch took his picture to be similar to the one used here. Each energy loss event from low-LET radiation is classified as a hit. Thus, if the dose rate at time t is $\dot{D}(t)$, a given cell has a probability $\beta_0 \dot{D}(t)\, dt$ of undergoing a hit between t and $t + dt$. There is a probability λ that a hit will lead to irreparable damage and eventually to cell death. In addition, there is a probability $\mu(t)$ that a hit will lead to a sublethal lesion which is repaired in such a way that the probability that an existing repairable lesion will be deleted between t and $t + dt$ is $R(t)\, dt$. After a hit, there is a probability γ that a type 1 lesion will combine with another to form a type 2 lesion if they are not repaired before combining. The survival probability is taken by Roesch to be equal to the probability that a given cell will have no lethal lesions after irradiation, regardless of how many hits were sustained. Thus, in his model, repairable lesions are never lethal, and no allowance is made for fixation-time effects. The reader should note that in the Roesch approach, allowance for fixation-time effects would be very difficult indeed.

We now outline very briefly Roesch's own derivation of the survival probability P_s. From the assumptions of the last paragraph but by treating the formation of type 3 lesions as statistically independent of other events:

$$P_s = \sum_{n=0}^{\infty} \{\text{probability of } n \text{ hits}\} \{\text{probability of no direct lethal lesions after } n \text{ hits}\} \{\text{probability that no sublethal lesion is converted to a lethal if } n \text{ hits occur}\} .$$

The probability of n hits is $(\beta_0 D)^n (n!)^{-1} \exp(-\beta_0 D)$; the probability of no direct lethal lesions after n hits is $(1-\lambda)^n$. Thus

$$P_s = \sum_{n=0}^{\infty} (\beta_0 D)^n (n!)^{-1} \exp(-\beta_0 D)\, (1-\lambda)^n R_n , \qquad (42)$$

where R_n is the probability that no sublethal lesion is converted to a lethal one if n hits occur. Then, if we assume that all repairable lesions that can be converted to lethal ones with a further properly positioned hit are

60. M. H. Patrick and R. H. Haynes, *Radiat. Res.* **23**, 564 (1964).

61. Yu. G. Kapul'tsevich and V. G. Petin, *Radiobiology (USSR)* 1(2), 161–69 (1967).

62. Yu. G. Kapul'tsevich, *Radiobiology (USSR)* 1(6), 191–96 (1967).

63. O. Hug and A. Kellerer, *Biophysik* **1**, 20 (1963).

repaired at the same rate and that only a small fraction of the repairable lesions are converted to lethal ones, we get

$$R_n = (n!/D^n) \int_0^T \dot{D}(t_n)\, dt_n \times \int_0^{t_n} dt_{n-1}\, \dot{D}(t_{n-1}) \cdots \int_0^{t_2} dt_1\, \dot{D}(t_1) \times \prod_{j=i+1}^{n} \prod_{i=1}^{n-1} \{1 - \mu(t_i)\,\gamma(t_j) \times \exp[\rho(t_i) - \rho(t_j)]\}\,, \qquad (43)$$

where

$$\rho(t) = \int_0^t R(t')\, dt'$$

and T is the time of irradiation. If we take $\dot{D}(t)$, $\mu(t)$, $\gamma(t)$, and $R(t)$ to be constants for $0 < t < T$ and note that $\dot{D}(t)/D = 1/T$, Eq. (42) is the survival probability given by Roesch with his $a = \mu\gamma$ and his $b = R(t) =$ constant. Equation (43) is mathematically equivalent to a relation we shall derive except for the assumption of statistical independence of different types of lesion formation. We take a different (but mathematically equivalent) picture of the cell dying if either a type 3 or a type 2 lesion is formed. Thus

$$P_s = \sum_{n_1=0}^{\infty} \bar{P}(n_1, 0, 0, T) = \exp[-h_2(T) - h_3(T)]\,,$$

where the functions $h_2(T)$ and $h_3(T)$ are given by Eqs. (35). It is virtually certain that even at large D only a small fraction of the repairable lesions will be converted to lethal ones. Thus

$$h_2(T) = \int_0^t \frac{d\Gamma_2(t')}{dt'}\, dt' \times \int_0^t \frac{d\Gamma_1(t'')}{dt''}\, dt'' \exp[\rho(t'') - \rho(t')]\,, \qquad (44)$$

$$h_3(T) = \int_0^t \beta_0\, \dot{D}(t')\, \lambda(t')\, dt'\,. \qquad (45)$$

Letting $\dot{D}(t)$, $\mu(t)$, $\gamma(t)$, and $R(t)$ be constant and $a = \mu\gamma$, $b = R(t) =$ constant, and $m =$ mean number of hits $= \beta D$, we obtain

$$P_s = \exp[-\lambda m - am^2(bT - 1 + e^{-bT})/(bT)^2]\,. \qquad (46)$$

The latter formula was proven by Roesch to follow directly from his version of Eq. (42) in the limit where the mean number of hits is large.

Even though it is likely that the idea of a fixation time will be necessary to interpret many cell-survival experiments, the Roesch model, for which we obtain an exact solution, still offers an interesting alternative to many other cell-survival models. In addition, Roesch has shown that the experiments of Sinclair and Morton[64] on survival of mammalian cells with split doses can be accounted for with his model.

Comments

Our basic understanding of radiation biology is still far too rudimentary to make possible a formulation of even the simplest processes in sufficiently fundamental ways as to allow reliable predictive deductions to be made from mathematical equations. However, phenomenological models of biological response to radiation can be invaluable in providing a mathematical framework within which the presumed kinetics of various processes may be tested. In the present context a rather general mathematical model has been solved within the limitations set by the self-imposed requirement that analytical solutions be attainable. This should enable those who desire to model biological mechanisms to solve a variety of problems involving different assumptions about the rate functions that describe the kinetics of each type of damage.

64. W. K. Sinclair and R. A. Morton, *Biophys. J.* 5, 1 (1965).

28. Spectrometric Dosimetry

J. H. Thorngate
D. J. Christian
W. J. McDowell[1]
P. T. Perdue
W. H. Shinpaugh
G. K. Sumner[2]

APPLICATION OF PULSE-SHAPE DISCRIMINATION TO LIQUID SCINTILLATION ALPHA SPECTROSCOPY

Increases in sensitivity for the measurement of low levels of alpha activity in bioassay and environmental samples can be made by improving the efficiency of the counter or reducing the background. Although an alpha sample measurement contains both number and energy information, many measuring techniques do not utilize the energy information, and those that are energy specific often require difficult sample preparation procedures and have a limited counting geometry. However, a major advantage of spectroscopy is that only the background in the region of the peak being studied need be considered. Recently, a system of alpha analysis was developed that uses liquid scintillation techniques and combines ease of sample preparation with an energy resolution of 0.3 MeV.[3]

In a liquid scintillator, backgrounds of 1 count/min are typical for the region of the peak produced by the alpha particles from ^{239}Pu. These background events originate from three major sources: (1) the beta and gamma activity of the sample itself, which is accentuated by the greater light output that is produced per unit of energy deposited for electrons than for alpha particles in an organic scintillator; (2) the beta and gamma activity of the tube used to hold the sample; and (3) cosmic rays and externally produced gamma rays, including those from the glass of the photomultiplier tube. Interest in pulse-shape discrimination occurred when no other background reduction techniques were found that would reduce the background in the region of the ^{239}Pu alpha peak below 0.3 count/min. Further reduction was desired because many environmental samples were known to produce count rates of about 0.2 count/min.

A pulse-shape discrimination system was set up with an existing counter. The technique chosen measures the shape of the output of the linear amplifier by measuring the time from the start of the pulse to some point on its fall. Discrimination is obtained by having a multichannel analyzer record the pulse-height spectrum of only those pulses with lengths that correspond to alpha interactions with the scintillator.

The effect of such selection can be seen by comparing Figs. 28.1 and 28.2, both of which are 15-hr measurements of ^{232}Th and its daughters dissolved in a carefully outgassed liquid scintillator. The required pulse-shape information resides in the long-time components of the signals from the scintillator, so careful deoxygenation procedures must be used to prevent quenching. Figure 28.1 is the pulse-height spectrum recorded without pulse-shape discrimination, and Fig. 28.2 is that recorded with it. The major difference in the two spectra is in the lower channels, where the pulses due to the beta particles and gamma rays emitted by the source and the pulses produced by background gamma rays occur. The advantages of using pulse-shape discrimination are evident. A small number (<1%) of the alpha-produced pulses will be rejected by the circuit because the pulse-length discrimination cannot be perfect. This small loss can be compensated for by proper calibration of the detector system. An evaluation with a sample tube containing only an outgassed scintillator solution showed that the background occurring in the pulse-height region of the ^{239}Pu peak was on the order of 0.01 count/min.

1. Chemical Technology Division.
2. Consultant.
3. W. J. McDowell and L. C. Henley, ORNL-TM-3676 (1972), W. J. McDowell, D. T. Farrar, and M. R. Billings, to be published in *Talanta*.

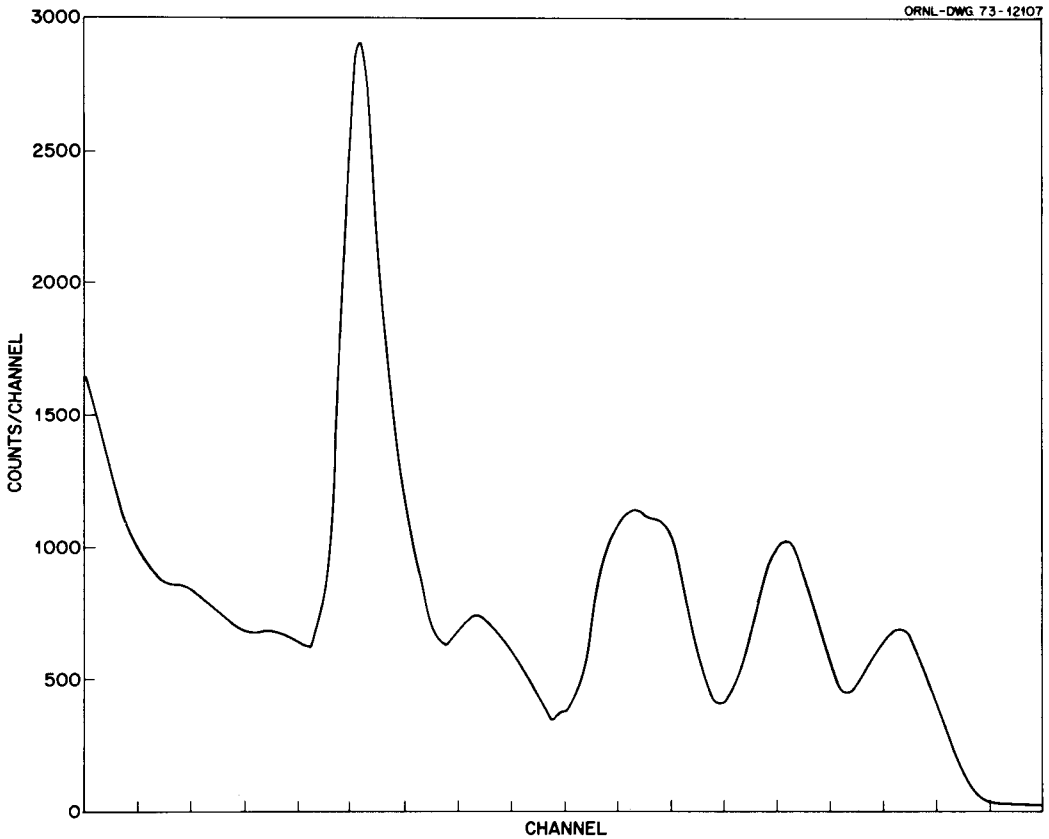

Fig. 28.1. Pulse-height distribution produced in a liquid scintillator by a ^{232}Th source.

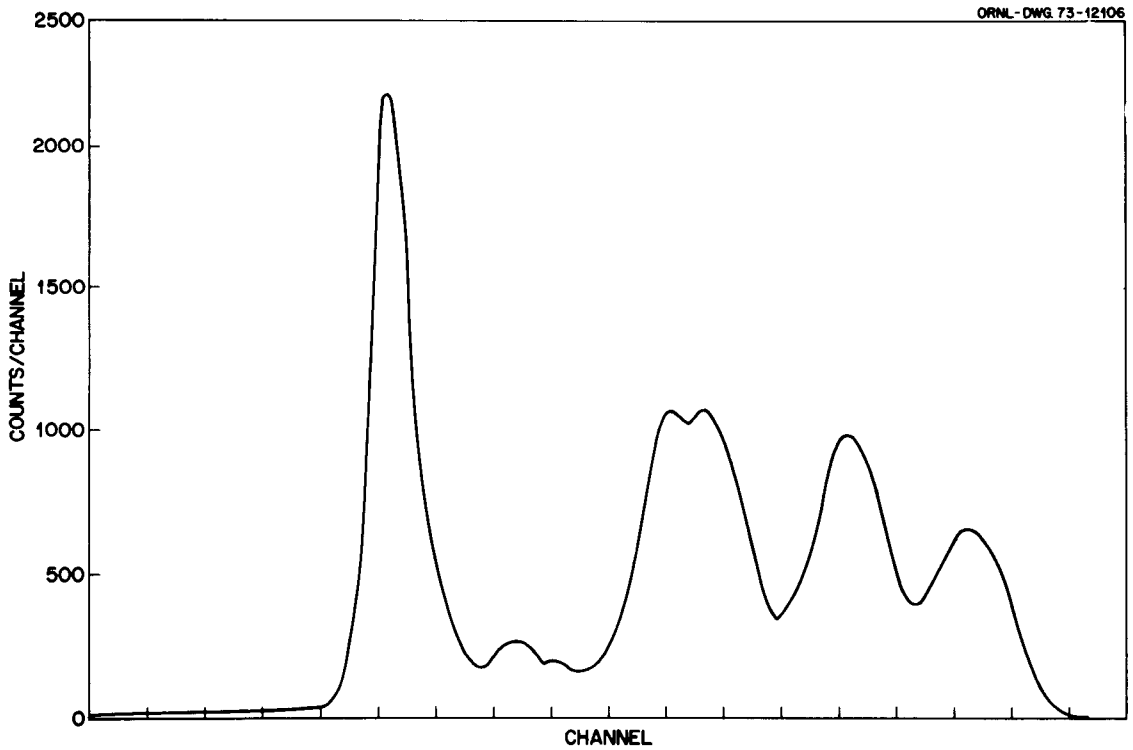

Fig 28.2. Pulse-height distribution produced in a liquid scintillator by a ^{232}Th source when the electron-produced pulses are rejected.

SPECTRA OF UNSCATTERED GAMMA RAYS WITH ENERGIES GREATER THAN 1.8 MeV THAT COME FROM THE HEALTH PHYSICS RESEARCH REACTOR DURING ITS OPERATION

An important parameter of an irradiation facility is the energy spectrum. The spectrum may be used directly for dosimetry purposes, or it may be used to omplete the evaluation of dosimetry information obtained by other means.

For a number of years a program of nuclear accident dosimetry intercomparisons has been conducted at the DOSAR, using pulses from the Health Physics Research Reactor (HPRR) as the radiation source. Besides direct irradiations, sets of steel and of Lucite shields are used during these experiments to modify the spectrum of neutrons and gamma rays. A program of neutron and gamma-ray spectrometry has been started to determine the direct spectra at 3 m from the reactor and the spectra behind the steel and Lucite shields when they are located at 2 m between the reactor and the detector.

That part of the gamma-ray spectrum with energies above 1.8 MeV that comes directly from the HPRR during its operation was measured with a scintillation spectrometer that records only the pulses produced when pair production occurs and both annihilation quanta escape the detector. This constraint was chosen to eliminate pulses produced by direct neutron interactions with the detector. The elaborate electronic system required is shown in Fig. 28.3. A large collimator-shield was required for the detector. It is diagrammed in Fig. 28.4.

Simple gamma-ray spectra were obtained which decreased exponentially with increasing energy. They are shown in Fig. 28.5. These shapes no doubt are the result of the large number of gamma rays produced by the fission process and by short-lived fission products coupled with the many scatters the gamma rays can undergo in leaving the high-density core of the reactor.

ORGANIC SCINTILLATOR RESEARCH

Work was completed on the synthesis and purification of parasexiphenyl (PSP) and similar organic materials. In cooperation with the ORNL Chemistry Division, the methods employed by Kovacic and Lange[4] were modified to produce a purer product from the synthesis of PSP from paraterphenyl. Fractional sublimation was chosen as the best means for purifying the PSP. This technique involves putting the impure material in one end of a glass tube that goes into a furnace that maintains a decreasing temperature gradient along the length of the tube. The hot end of the tube is kept below the melting point of PSP, but it sublimes below its melting point. A constant flow of dry nitrogen is run through the tube from the hot end to the cool end so

4. P. Kovacic and R. M. Lange, *J. Org. Chem.* **29**, 2416 (1964).

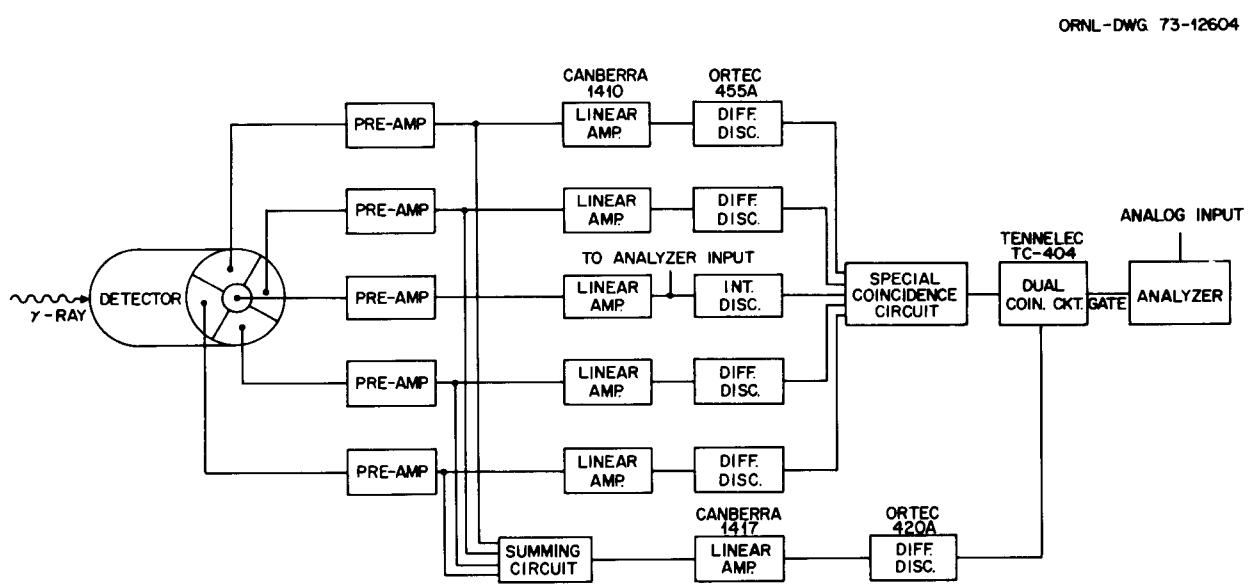

Fig. 28.3. Block diagram of the pair spectrometer system.

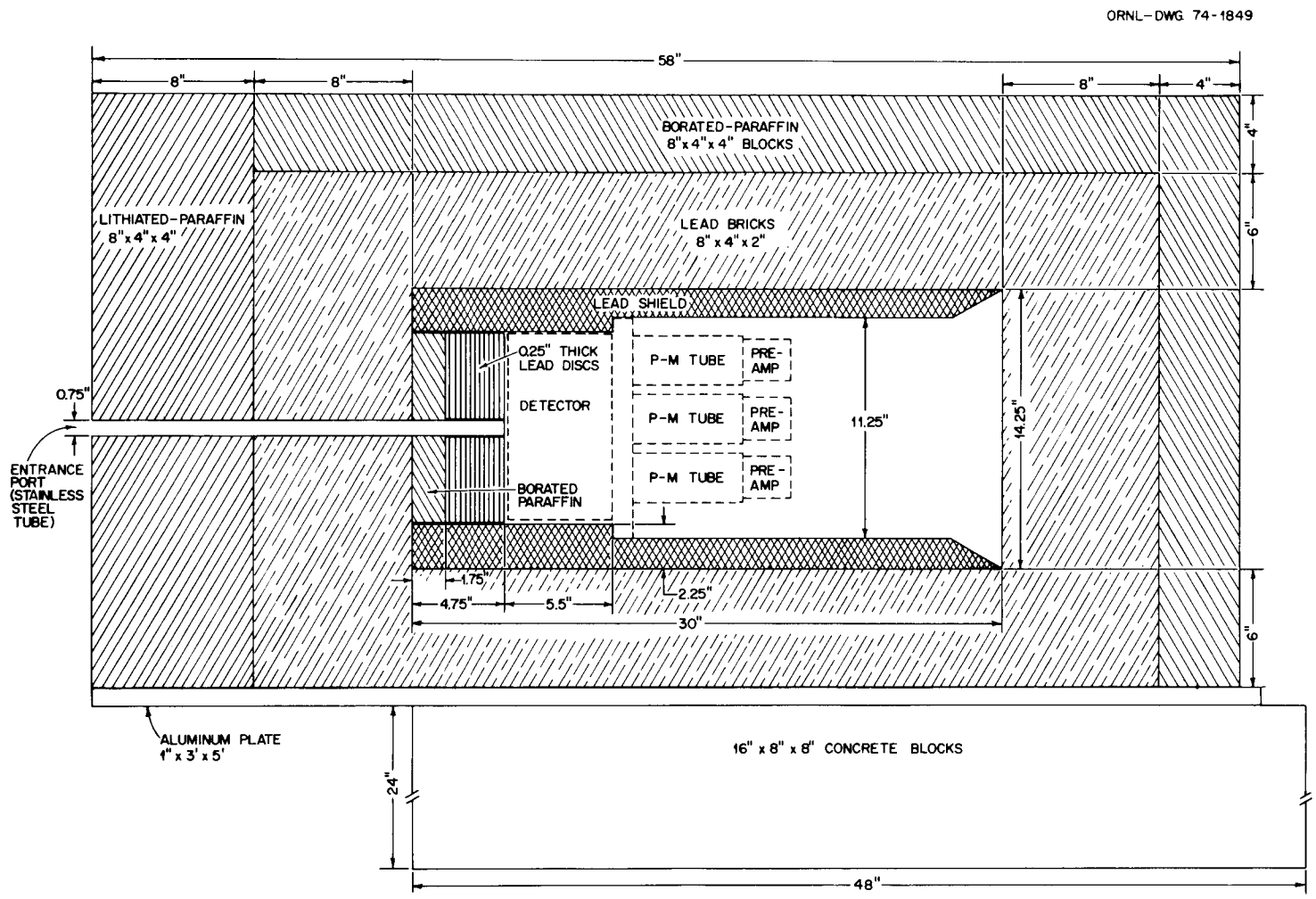

Fig. 28.4. Collimator-shield used with the pair spectrometer for reactor measurements.

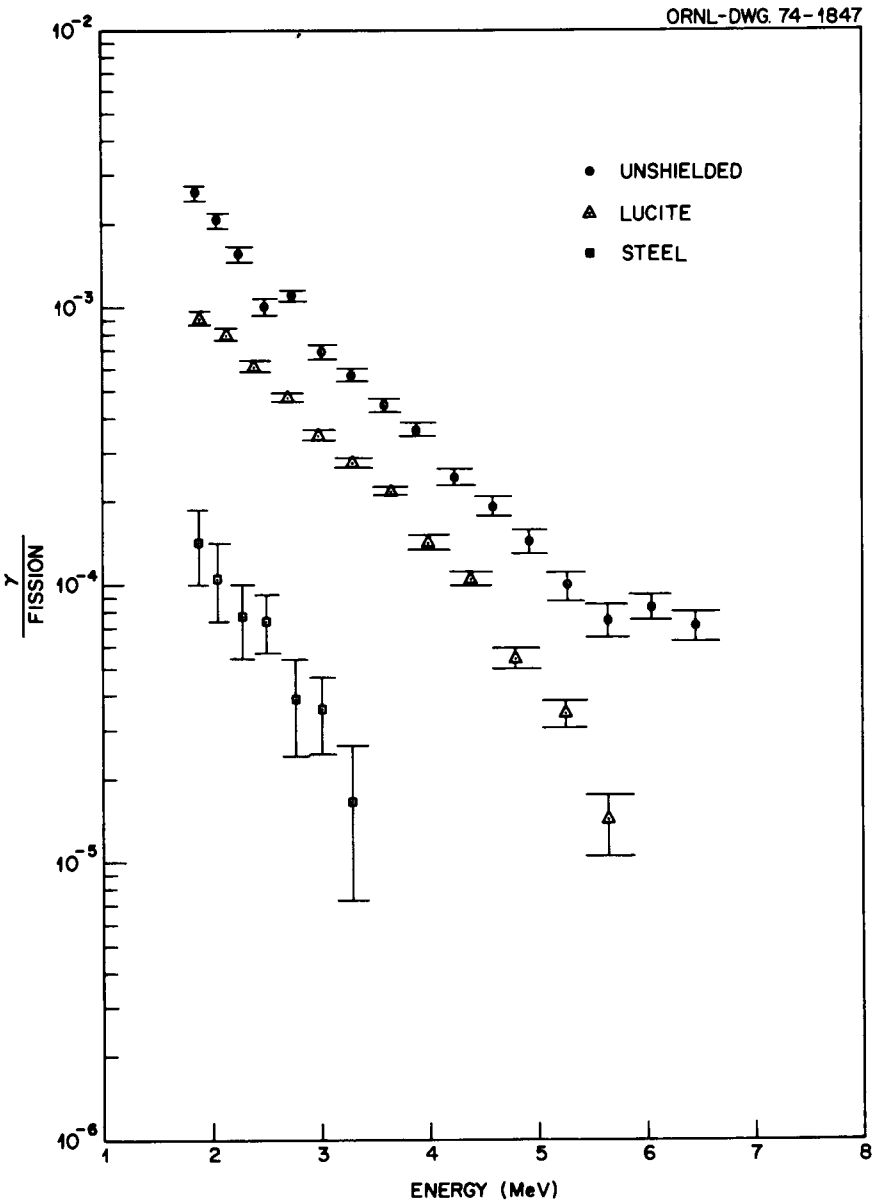

Fig. 28.5. The spectra of gamma rays which come directly from the reactor and which come through the steel and Lucite shields.

that the material that sublimes at the lowest temperature goes the farthest down the tube before it recrystallizes.

Crystals of zone-refined anthracene, stilbene, and paraquaterphenyl were grown which are suitable for measurement of light output as a function of incident-charged-particle energy. These data will also be obtained for PSP crystals. The experiment will provide a consistent set of data on the light output of the most commonly used solid organic scintillators as well as those being developed in this program.

A number of vacuum depositions of PSP on glass and sapphire were made to measure the optical characteristics. The refractive index of PSP vacuum-deposited on sapphire was found to be 1.55 at the fluorescence peak of 450 nm. Although PSP has a refractive index near glass when vacuum-deposited, microcrystals dispersed in a solution yield an index close to 1.68. Two

plastics were found which match this index closely: polyurethane and N-vinylcarbazole. This allows a neutron LET dosimeter to be built by dispersing micron-sized PSP cyrstals in these plastics. This combination could be superior to the Hornyak button, because the optical characteristics of the scintillator and plastic will be better matched.

Since PSP has a vapor pressure of 10^{-6} torr at room temperature and a prompt fluorescence decay of about 2 nsec, it should also be applicable as a wave shifter in the vacuum ultraviolet portion of the optical spectrum (60 to 300 nm).

29. HPRR and Accelerator Operations

D. R. Ward[1]
F. F. Haywood[2]
H. W. Dickson[2] C. P. Littleton[3]
W. F. Fox[2] E. B. Wagner[2]
J. Judish[4]

INTRODUCTION

The principal objective of the HPRR and Accelerator Operations Group is to operate and maintain a small network of irradiation facilities utilized in programs in which the ultimate goal is to gain a better understanding of the effects of ionizing radiation on biological systems. These facilities include the Health Physics Research Reactor (HPRR), the DOSAR Low Energy Accelerator, and the ORNL 3-MV Van de Graaff accelerator. These machines are capable of producing monoenergetic neutrons, photons, and charged particles, as well as a series of moderated fission spectra. These radiation fields are used on a routine basis by all four of the section's research groups. Members of other sections of the Health Physics Division, as well as scientists from colleges and universities, national laboratories, and foreign institutions, also use these facilities. In addition to operating the facilities, the HPRR and Accelerator Operations Group is responsible for conducting the neutron and gamma-ray standards and intercomparison activities for the section.

HEALTH PHYSICS RESEARCH REACTOR (HPRR)

The HPRR is a powerful tool for research in the dosimetry of coexistent neutron and gamma radiation fields, and it has been utilized in the development of a wide range of dosimeters and spectrometers for both routine and research applications (e.g., the development of photoluminescent, thermoluminescent, and exoelectron detectors for gamma rays and improved threshold detector systems for neutrons, both of which may be used for depth-dose studies in animals and phantoms). Depth-dose studies are known to be important in large-animal irradiations, including man, but only at the HPRR and its associated facilities (DOSAR facility) is there a concentrated effort in depth-dose studies (experiments and calculations) at both the microscopic and macroscopic levels, including the problem of tissue-bone and marrow-bone interfaces. Ultimately, the data developed will be used in the general correlation of the biological response functions and the radiation environment.

Use of the HPRR as an international testing and standardizing facility continues. In this respect, many items such as criticality alarm systems, nuclear accident dosimeters, and numerous other passive dosimetry systems related directly to radiobiology studies are subjected to irradiations. Most of these studies are directed toward the correlation of biological response with absorbed dose. Some of the important continuing radiobiology experiments in which the HPRR was utilized this year are: determination of relative biological effectiveness (RBE) for intestinal crypt cell survival, M-2 generation grain plant mutation studies, lens opacities in mice exposed to fission neutrons, effects of neutrons on poinsettias and sweet potatoes, and the effects of small doses of neutrons on one-day-old mouse embryos. For the third successive year, the reactor has been used by the University of Tennessee Nuclear Engineering Department (in the graduate engineering program). The principal users of the HPRR are given in Table 29.1.

1. Neutron Physics Division.
2. Dual capacity.
3. Instrumentation and Controls Division.
4. Physics Division.

Table 29.1. Principal users of the HPRR during 1973

Organization	Percent of total time
Radiation Research and Development	48.1
Biology Division	20.0
University of Tennessee Nuclear Engineering	9.6
University of Louisville	7.1
Comparative Animal Research Laboratory	6.7
Civil Aeromedical Institute	2.8
Dosimetry intercomparisons	1.6
Others	4.1

Table 29.2. Tenth Nuclear Accident Dosimetry Intercomparison Study: summary of results

Group	Pulse 1		Pulse 2		Pulse 3		Pulse 4	
	D_n	D_γ	D_n	D_γ	D_n	D_γ	D_n	D_γ
	Tissue kerma (rads)							
K-25	310	45	105	21	46	55		
SRL	331	60	131	21	100	60		
USNOL	319	95	54	4.4	62	65		
Dow					44.5	74	262	85
Karlsruhe	327	45	154	16.5	49	46		
Y-12	327	55	128	17	51	49		
ORNL 1	333	51	158	15.8	47	48	419	62.8
ORNL 2	380	75	221	41	52.2	110	415	
ORNL 3	324	30	137	16	54	37	236	51
Studsvik 1	377		77		80		444	
Studsvik 2	330		145		150		359	
BNWL	386		180		58		609	
Mean	340	57	135	24	66	60	392	66
	Yield (number of fissions) $\times 10^{-16}$							
	8.20		9.45		7.20		10.0	

Perhaps the most important single application of the HPRR is in connection with the dosimetry standardization and intercomparison activities. This program has enjoyed a high degree of success over the period of its operation, and a program patterned after the ORNL Intercomparison Studies was started by the International Atomic Energy Agency in 1970. The Tenth ORNL Dosimetry Intercomparison Study was conducted. In order to provide an opportunity for participation by representatives from foreign laboratories, this experiment was scheduled for August 27–September 7, 1973, which was the two weeks preceding the Third International Congress of the International Radiation Protection Association meeting in Washington, D.C. Participating in this study were representatives from several U.S. laboratories and two foreign institutions – Studsvik, Sweden, and Karlsruhe, West Germany. Some average values for neutron and gamma-ray doses are shown in Table 29.2; complete results are given in ref. 5. The principal purpose of this program is to provide facilities for dosimetrists to strengthen their ability to act at once in their home laboratories in the event of an accident. It has been shown that the ability of a team to provide dosimetry to within ±25% in 48 hr is directly related to the state of preparedness of the team. It is seen by the results of the ORNL Intercomparison Studies that the majority of first-time participants find it difficult to provide estimates of dose or fluence within the required accuracy or within the required time; actually, the uncertainty of results for first-time participants is frequently greater than a factor of 2. One fact seems to be clear: most licensees use personnel monitoring systems from companies providing commercial film-badge services. To date, results that have been reported by these companies have ranged from no data reported to values that were off by a factor of 4. In an effort to provide as much information as possible about the radiation field, extensive measurements were made of the gamma-ray spectrum for each of the three radiation fields used in the intercomparison program.[6]

The intercomparison program has been expanded to include periodic evaluations of the response of personnel monitoring devices when exposed to "standard" radiation fields similar in nature to those encountered in routine operations involving materials that emit both neutrons and gamma rays. The first in this series of experiments was held at the HPRR in May 1974. All participation was handled through the postal service. Results of the program are not available at this time.

Some of the routine services provided to users of the HPRR included:

1. Measuring and reporting the dose delivered at experimental stations used in experiments, as well as experiment planning.
2. Maintaining complete exposure records for all experiments.
3. Assistance to members of the Biology Division in the design of a partial body shield for mice. Measurements of the dose distribution inside the shield were also made at the HPRR.

5. H. W. Dickson and F. F. Haywood, *1973 Intercomparison of Nuclear Accident Dosimetry Systems at the Oak Ridge National Laboratory*, ORNL-TM-4566 (in preparation).

6. J. H. Thorngate, D. J. Christian, and G. K. Sumner, *The Spectrum of Gamma Rays with Energies Greater Than 1.8 MeV Coming Directly from the Health Physics Research Reactor during Its Operation*, ORNL-TM-4636 (in press).

An in-depth review was made of existing reactor instrumentation to determine whether the system was adequate to meet reactor safety requirements and to evaluate the need to update the system to state-of-the-art electronics. It was concluded that reactor safety requirements were met and that an overall updating of electronics at this time should not be done due to expected high costs. Improvements have been made in the reactor pickup mechanism of the positioning device. The purpose of this work is to assure more positive control of the remote handling of the reactor. A significant effort was put forth to update records of the reactor facility. Included in this updating are electrical and mechanical drawings, operating procedures, training and retraining of operators, and programmed maintenance. Also of major importance this year was the preparation of a complete set of Technical Specifications[7] for the HPRR. In addition, the HPRR Procedures Manual was revised and updated.

USE OF HPRR IN NUCLEAR ENGINEERING EXPERIMENTS

For three years the HPRR has been used for experiments in laboratory course work for senior students in the University of Tennessee Nuclear Engineering Department. This has been a successful arrangement and may prove to be the forerunner of a more comprehensive program.

There are three individual experiments[8] with the HPRR, which are designed to demonstrate the kinetic behavior of reactors and one inherent shutdown mechanism of a reactor, namely, thermal expansion and the negative temperature coefficient of reactivity. Since this reactor has no moderator or reflector, the mean energy of neutrons causing fission is about 1 MeV rather than thermal energy (about 0.025 eV). The HPRR control rods are neutron-producing rods rather than the neutron-absorbing-type rods of thermal reactors. The first experiment with the HPRR is critical loading and control-rod calibration.

In the second experiment the power level is raised to 5 kW. As the temperature increases, the densities of the reactor materials decrease, thereby reducing the neutron cross sections and increasing the leakage of neutrons from the core. Control rods are inserted to maintain the power level as the temperature increases to 500°F, and at 500°F the control-rod positions are fixed for the remainder of the experiment. Since appreciable power is being produced within the first 10 min, the temperature continues to increase to about 550°F. When increased expansion increases the leakage of neutrons, the power drops. As the power decreases (to about 4 W), the reactor is cooled by natural convection and radiation to the surrounding air. When the reactor cools sufficiently, the power rises to about 2 kW, and the cycling, which is a damped oscillation, continues. The results of this experiment (Fig. 29.1) show how a negative temperature coefficient of power affects the reactor stability.

The third experiment requires operation of the reactor above prompt criticality. A rapid power excursion is used to demonstrate the limiting effects of the negative temperature coefficient. This is an inherent

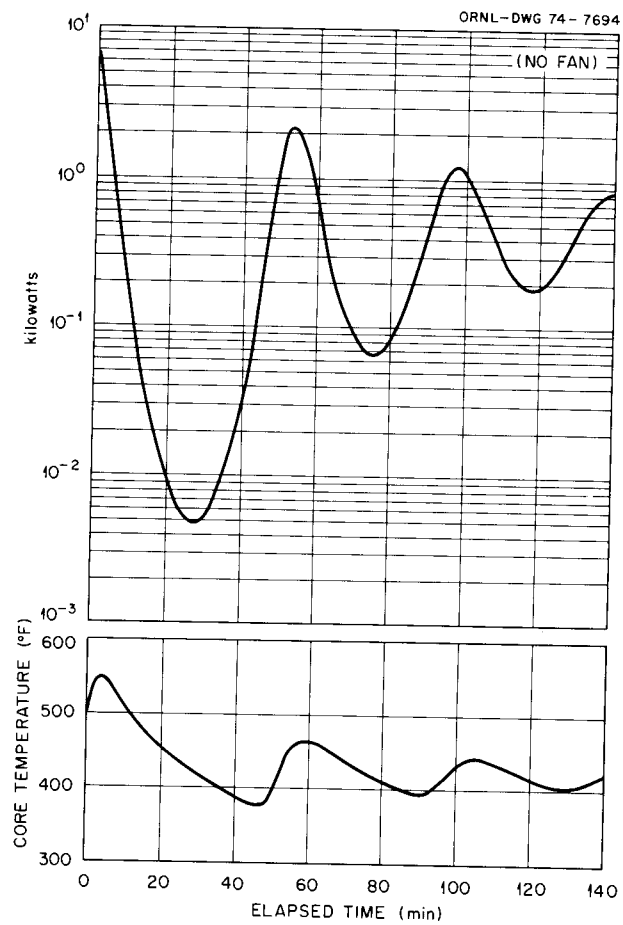

Fig. 29.1. Demonstration of the effect of the negative temperature coefficient of reactivity. A heavily damped oscillation is observed when the HPRR core temperature changes with a fixed fuel loading and initial power level of 5 kW.

8. J. T. Mihalczo, personal communication.

7. L. B. Holland, *Technical Specifications for the Health Physics Research Reactor,* ORNL-TM-4637 (in preparation).

shutdown mechanism in the reactor that terminates rapid excursions before the core is damaged. Typical results from this experiment show that the power rises a factor of *e* every 24 μsec until it attains 20,000 to 50,000 MW. By this time the reactor has expanded due to the temperature rise, and the excursion is terminated by the negative temperature coefficient of reactivity.

During the thermal cycling experiment, the irradiation effect of fast neutrons on barley seeds is demonstrated. By placing groups of these seeds at different distances from the reactor, the effect is studied for doses up to 1600 rads. The growth of subsequent seedlings is compared with that of a control group that has not been irradiated and with other groups that have been exposed to high levels of gamma rays (up to 80,000 rads) in cooperation with the UT-AEC Comparative Animal Research Laboratory. The seedling survival and growth (height and dry weight) are the observed variables. By comparing the results for equal doses of neutrons and gamma rays, the students can determine the RBE for neutrons for this effect.

DOSAR LOW ENERGY ACCELERATOR (DLEA)

The DLEA has for several years been utilized in research programs requiring charged particles (protons, deuterons, etc.) and monoenergetic neutrons. In recent months, significant modifications and additions have been made to the beam tube in order to accommodate an experiment designed to study the stopping of protons as they traverse an interaction region of the beam tube filled with tissue-constituent gases. Proper gas pressure is maintained by differential pumping.

ORNL 3-MV VAN DE GRAAFF ACCELERATOR

This accelerator serves as a pulsed source of swift particles (protons with energy to 2.5 MeV) for studies

ORNL-DWG 74-1260

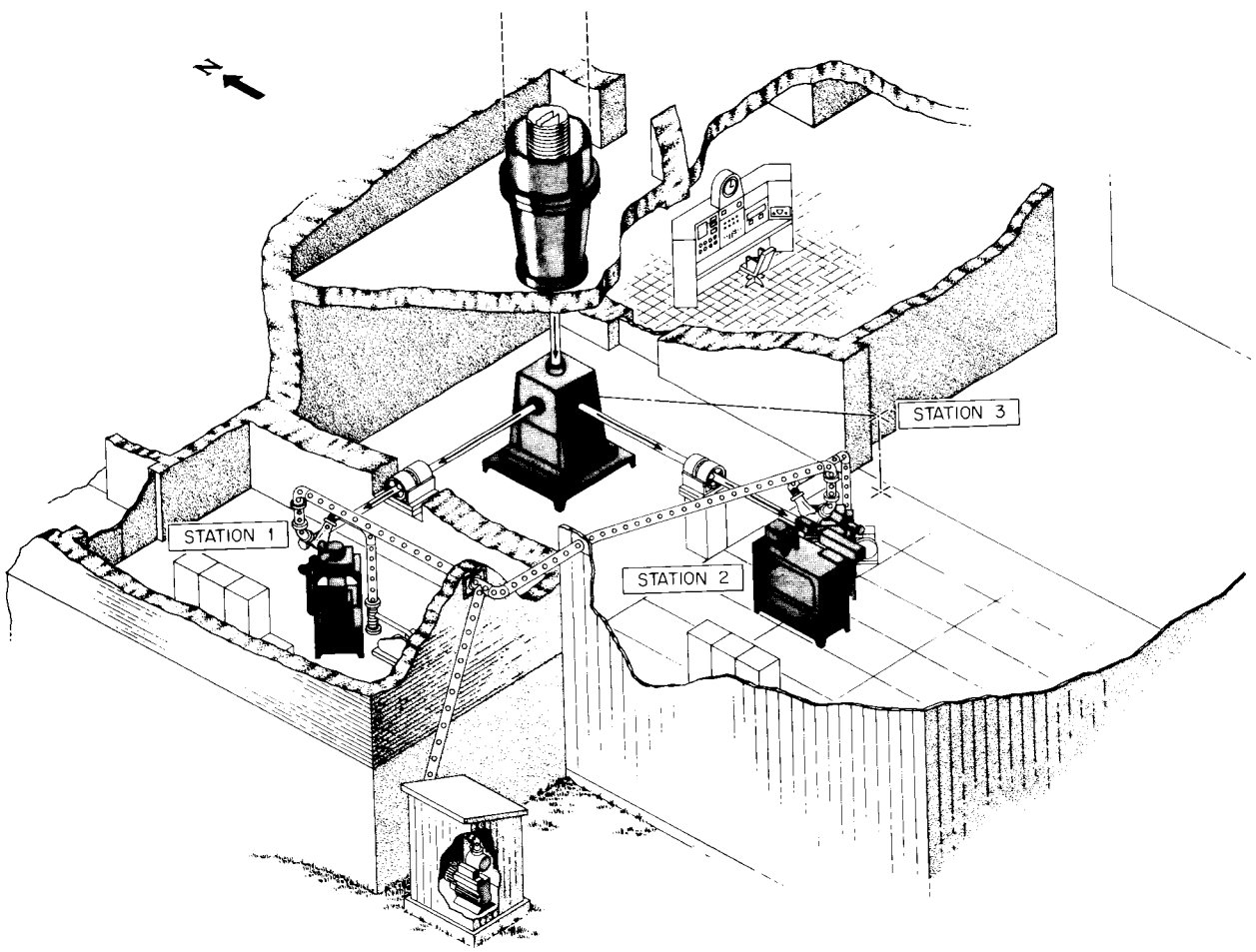

Fig. 29.2. Diagram of the 3-MV Van de Graaff experimental area.

on energy pathways in noble gases. During the last four years, all the experimental work has been done at one experiment station. The Atomic Physics Program is expected to expand in the next few years to include studies related to laser action in noble gases and to the characterization of pollution in the modern atmosphere. In order to conduct these new experiments in the most efficient manner, it is necessary to expand the facilities of the Van de Graaff work area. A diagram of the proposed experimental layout, including a new spectrometer system (station 2) complete with differential pumping, is shown in Fig. 29.2. A plan view of this station is shown in Fig. 29.3. It is seen that there will be a pulsed dye laser, a visible and uv monochromator, and a vacuum uv scanning monochromator attached to the interaction cell. The dye laser will be controlled so that pulses of tuned laser light will follow closely after the pulse of protons from the Van de Graaff.

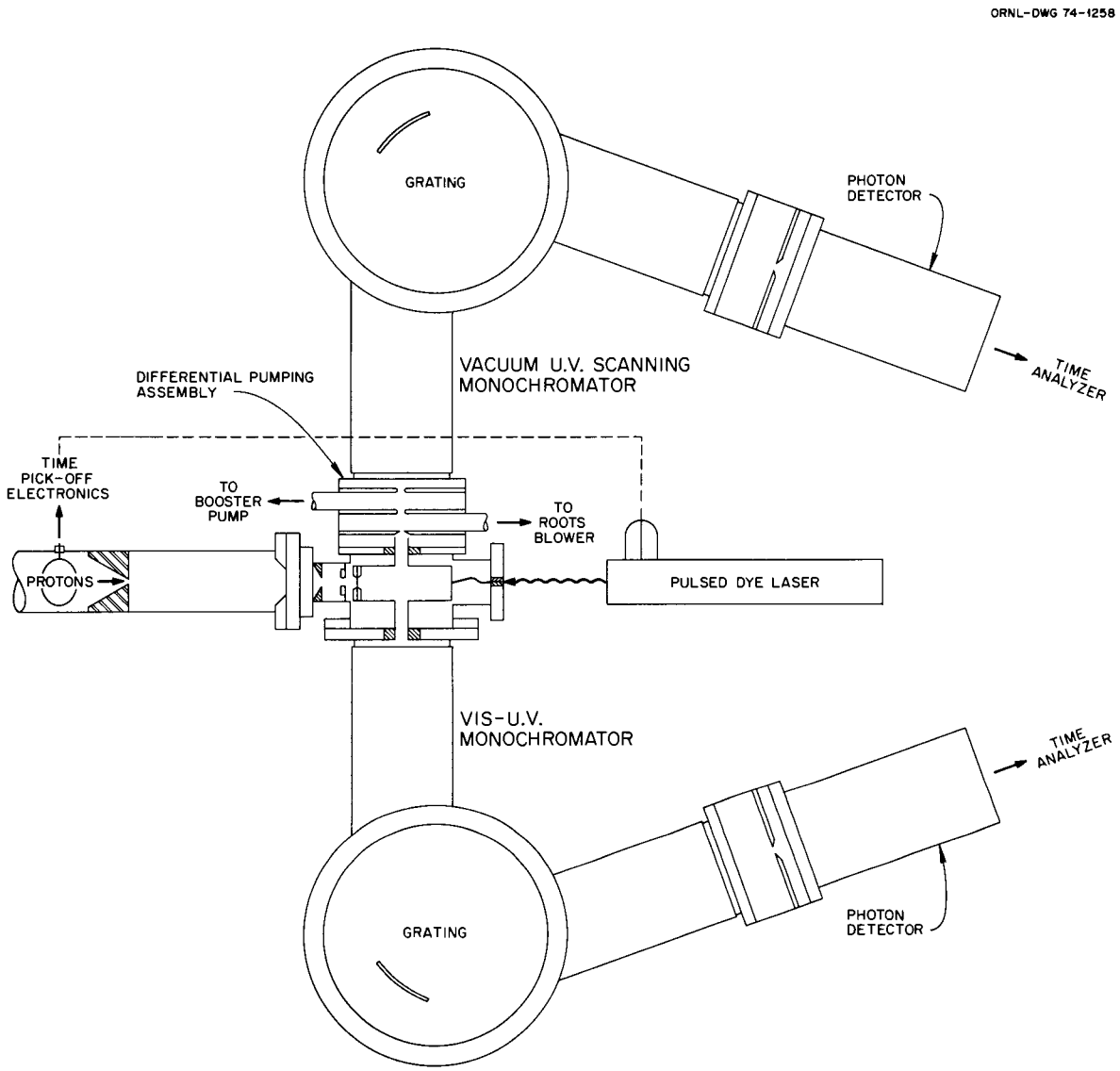

Fig. 29.3. Plan view of the Van de Graaff experimental station 2 showing beam tube, dye laser, and spectrometers for both visible and uv radiation from the interaction region.

Part V. Education and Information

J. C. Hart

The Education and Information Section plans and coordinates the Division's educational programs and operates the Health Physics Information System, which ministers to the Division, parts of the AEC, and the profession of health physics.

30. Education and Vocational Training

M. F. Fair J. C. Hart J. E. Turner

The need for training in health physics continues to grow at an accelerated pace. As in the past, education at the Ph.D. level provides personnel for key positions in industry, in medicine, and in the academic field; training at the master's level is required in many areas of applied health physics where there is an emphasis on instrumentation and regulatory compliance; but the anticipated expansion in the nuclear power industry and other nuclear-related fields requires that more attention be directed toward developing B.S.-degree-level technologists.

Surveys show[1] that only 49 undergraduates were enrolled in the fall of 1971 in all subfields of radiation protection among the principal schools that offer radiological training programs. In contrast, 449 graduate students were enrolled. Four bachelor's and 201 graduate degrees were awarded in radiation protection fields between July 1, 1970, and June 30, 1971.

Estimates of the numbers of new B.S.-level health physics technologists needed for various activities by 1985 are shown in Table 30.1. Through 1985 the average number of new B.S.-level technologists needed annually is between 300 and 500. The need occurs rather evenly for each activity. The nuclear power program, including fuel recycling operations, requires between 950 and 1500 health physics technologists. Nuclear medicine and "other" nuclear applications will require between 1200 and 2500. An anticipated increase in Federal, State, and local regulatory activities will require an additional 500 to 1000. Between 650 and 1000 additional persons will be needed to replace present workers who will retire, die, or change their specialty.

In 1973 the Division conducted two training sessions for 12 bachelor of science students. Each session involved a 12-week (one academic quarter) on-the-job training period. Participants were required to be science or engineering majors, and the Oak Ridge training was given in addition to normal academic requirements for a

Table 30.1. Newly trained health physics B.S.-level technologists needed by the year 1985

	Minimum	Maximum
Nuclear power industry	750[a]	1000
Nuclear fuel cycles	200	500
Nuclear medicine	500	1500
Regulatory operations	500	1000
Staff replacements (AEC)	650	1000
Others	700	1000
	3300	6000

[a]Based on 150 reactors to be built and assuming a demand for five health physics technologists per reactor complex (reference: *Nuclear Reactors Built, Being Built, or Planned in the U.S. as of December 31, 1972*, TID-8200-R27, USAEC Technical Information Center.)

1. U.S. Atomic Energy Commission, Division of Nuclear Education and Training, *Radiation Protection Enrollment and Degree Survey*, WASH-1229 (November 1972).

bachelor's degree. The program was funded by the AEC for only one year during the spring and summer months of 1973. A single recruiting trip made in the fall of 1972 to seven campuses in the Appalachian region was sufficient to show that there was considerable interest in the program. In fact, one institution alone proposed 15 applicants.

Although a survey of 37 campuses (Table 30.2) indicates that an average of 150 advanced radiological degrees were awarded during each of the six years, bachelor of science graduates averaged only three per year with no increase in trend by 1971. In looking at the problem in depth, our evaluation indicated that on-the-job training alone could not meet the requirements for health physics technologists, and we concluded that many more of the nation's colleges and universities should develop suitable curricula for educating and training these persons. Consequently, many newly trained faculty members are needed to teach B.S. degree work in health physics.

If one evaluates the manpower projections indicated in Table 30.1 on the basis of startup schedules, a minimum of 1000 new health physics technologists will be required to meet the scheduled demand by 1980. Then, an additional 3000 persons will be required by 1985, when the approximately 150 power reactors will be in operation. If college instructors qualified to handle a B.S.-level curriculum are made available at an average rate of ten per year starting in 1975, by the year 1980 approximately 1000 B.S.-level health physics technologists could be produced. This estimate assumes that each qualified instructor would turn out about ten graduates per year.

In an effort to promote the development of a B.S.-level curriculum on selected college campuses, the Division established a Faculty Institute that began on June 17, 1974, with nine college faculty members participating. The principal purpose of the program is to make research facilities and staff leadership from within the ORNL Health Physics Division available to faculty members associated with educational institutions that have, or expect to develop, health physics curricula at the B.S. level which will produce graduates who can be certified by the American Board of Health Physics early in their careers. The Institute operates as follows:

Table 30.2. Radiological degrees granted, 1966–71

Survey of 37 institutions, WASH-1229

Year	Bachelor's	Master's	Doctorate
1966	1	101	24
1967	1	122	27
1968	5	105	42
1969	2	107	44
1970	5	121	48
1971	4	141	60
	18	697	245

1. Up to ten participants are brought into the program during the summer months each year, beginning in FY 1975 and extending through FY 1980.
2. Faculty members who participate in the Institute spend approximately 12 weeks at ORNL.
3. Stipends, travel reimbursement, and assistance with recruitment are handled by Oak Ridge Associated Universities.
4. Particular projects assigned to each individual participant are based on *what the participant needs* to qualify as a capable instructor in health physics techniques under the assumption that most participants already possess basic training in one or more of the scientific disciplines that are prerequisite to degree work in health physics technology.

The first B.S.-degree graduates to receive instruction from participants in the Faculty Institute program should be available for employment by the summer of 1975. The program will be in full operation by 1977.

31. Health Physics Information System (HPIS)

J. C. Hart C. F. Holoway B. L. Houser J. E. Turner

The development of a computerized information system capable of providing input and output for disciplines that make up the health physics profession was undertaken by the Division in 1972. The Medical Physics and Internal Dosimetry Section of the Division had utilized a manual technique in the operation of the Information Center for Internal Exposure (ICIE), but this program was limited almost exclusively to internal dose matters. Early in 1973, through the cooperation of all sections of the Division, the Health Physics Information System (HPIS) was put into operation. Almost immediately the HPIS interfaced with other technical information systems maintained in the Oak Ridge area so as to provide for more extensive interchange of data.

During the past year the Nuclear Safety Information Center (NSIC) dropped its efforts in areas concerned with ecology, thermal pollution, mammalian metabolism, monitoring, and waste management. The HPIS assumed responsibility for mammalian metabolism, monitoring, and waste management as part of its analytical work, with particular reference to external exposure. Included in mammalian metabolism are both normal and abnormal metabolism (physiology and pathology).

The HPIS is interfaced with NSIC, Environmental Information Sciences Office (EISO), Comparative Animal Research Laboratory (CARL), Environmental Plutonium Data Base (EPDB), and Computer Sciences Division (CSD). This relationship is in keeping with the unification of information systems at the Oak Ridge facilities so as to minimize duplication of effort.

HPIS has moved from the design pilot stage to an operational stage with partial capability on video terminals via the ORLOOK program of the Computer Sciences Division. The staff responded to a wide range of queries during the 12-month period that ended in July 1974. Sample subjects that illustrate the range of topics are:

1. radiation exposures from accelerators,
2. carbon-14 waste management,
3. critique of Eniwetok Radiological Survey volumes,
4. health physics aspects of plutonium (LWRs),
5. plutonium hot-particle-in-lung problem,
6. biohazard of thorium in welding rods,
7. carcinogens from liquefaction of coal,
8. mammalian genetic effects of ionizing radiation,
9. fetal pathology of iodine-131 diagnostics,
10. biological hazard of niobium-94 produced in thermonuclear reactors.

Theses, Papers, Publications, and Lectures

Theses

Liliana Deleanu
Dissociative Ionization of Molecules by Electron Impact (University of Tennessee) (in preparation)

K. Gant
Electron Capture and Drift in Organic Liquids (University of Tennessee) (in preparation)

S. M. Garry
Measurement of Absorbed Fractions for Photon Sources Distributed Uniformly in Various Organs of a Heterogeneous Phantom, ORNL-TM-4411 (University of Tennessee) (January 1974)

R. E. Goans
Electron Attachment to Molecules in High Pressure Gases (University of Tennessee) (June 1974)

Der Y. Hsia
A Study of the Fission Product Release from a Badly Damaged Water-Cooled Reactor (University of Tennessee) (June 1974)

J. R. McNeeley
Time-Resolved Quenching of Argon Resonance Radiation by Nitrogen Molecules (University of Tennessee) (in preparation)

V. N. Neelavathi
Collective Effects in Charged Particle Track Structure (University of Tennessee) (in preparation)

J. E. Talmage
Transport of Resonance Radiation in Argon, ORNL-TM-4368 (University of Kentucky)

I-Lan Tang
Optical Properties of Guanine, Thymine, Adenine, and Cytosine (University of Tennessee) (in preparation)

Papers

J. C. Ashley and L. C. Emerson
"Dispersion Relations for Non-Radiative Surface Plasmons on Cylinders," Southeastern Section of the American Physical Society, Winston-Salem, N.C., Nov. 8–10, 1973.

J. C. Ashley, R. H. Ritchie, and Werner Brandt
"$Z_1{}^3$-Dependent Stopping Power and Range Contributions," Third International Conference on Atomic Collisions in Solids, Gatlinburg, Tenn., Sept. 23–28, 1973.

J. K. Baird
"Reflection and Transmission of a Traveling Wave at a Transmission Line–Power Transformer Junction," Joint Electromagnetic Pulse Technical Meeting, Kirtland AFB, N.M., Sept. 25–27, 1973.

Klaus Becker

"Applications of Exoelectron Emission in Radiation Dosimetry," Symposium on Exoelectron Phenomena, Detroit, Mich., June 28–29, 1973.

"Personnel Dosimetry of Radon and Radon Daughters," Noble Gases Symposium, Las Vegas, Nev., Sept. 24–28, 1973.

"LET Response and Fast Neutron Dosimetry with TSEE and TLD," Fourth Symposium on Microdosimetry, Verbania, Italy, Sept. 24–27, 1973.

"Progress in the Dosimetric Applications of Exoelectron Emission," Fourth International Symposium on Exoelectron Emission and Dosimetry, Liblice, Czechoslovakia, Oct. 1–3, 1973.

"Current Studies on Integrating Environmental Monitoring at ORNL," Second Environmental Radiation Workshop, New York, N.Y., Feb. 20–21, 1974.

"Recent Progress in Solid-State Research and Applications," USAEC/DBER Health Physics Research Program Review, Airlie House, Warrenton, Va., Mar. 12–14, 1974.

Klaus Becker and M. M. Abdel Razek

"Spark Counting of Neutron-Induced Recoil Particle Tracks in Polymers," American Nuclear Society Meeting, Philadelphia, Pa., June 1974 (presented by Klaus Becker).

"Automatic Spark Counting of Fast Neutron Induced Recoil Particle Tracks in Polymer Foils," Fifth International Congress of Radiation Research, Seattle, Wash., July 14–20, 1974 (presented by Klaus Becker).

Klaus Becker and J. S. Jun

"TLD Measurements with Terbium-Activated Magnesium Orthosilicate," Fifth International Congress of Radiation Research, Seattle, Wash., July 14–20, 1974 (presented by Klaus Becker).

Klaus Becker and A. Moreno y Moreno

"Long-Term Environmental Dosimetry by Thermoluminescence Measurements in Ancient Ceramics," Health Physics Society Annual Meeting, Houston, Tex., July 7–11, 1974 (Presented by Klaus Becker).

Klaus Becker, T. D. Tham, and F. F. Haywood

"Compounds of TLD's and High-Melting Organics for Fast Neutron Personnel Dosimetry," IRPA Congress, Washington, D.C., September 1973 (presented by Klaus Becker).

S. R. Bernard

"A Metabolic Model for Copper Useful in Estimation of Internal Radiation Dose," Conference on Bioassay, Environmental and Analytical Chemistry, Jackson Lake Lodge, Wyo., Sept. 4–6, 1973.

S. R. Bernard and W. S. Snyder

"A Generalized Compartment Model with an Application to Dose from ^{55}Fe and ^{59}Fe," Health Physics Society Meeting, Miami Beach, Fla., June 17–21, 1973.

J. G. Carter, L. G. Christophorou, and D. L. McCorkle

"Long-Lived Organic Negative Ions," Fifth International Congress for Radiation Research, Seattle, Wash., July 14–20, 1974.

C. V. Chester

"Research Support for DCPA's Evacuation Program," Oct. 15, 1973, to R. Park, National Academy of Sciences.

C. V. Chester and E. P. Wigner

"Comparative Status of U.S. and Soviet Civil Defense Programs," Aug. 29, 1973, to Senator Howard H. Baker.

L. G. Christophorou

"Electron Mobilities in Gases and Liquids," Fifth International Congress of Radiation Research, Seattle, Wash., July 14–20, 1974.

"Role of Basic Physicochemical Studies on the Atomic and Molecular Level," First Conference on the Analysis of Multi-Component Mixtures and Their Applications to Health Related Problems, Washington, D.C., June 10–12, 1973.

C. D. Cooper and R. N. Compton
"Electron Affinities of Selected Hexafluorides," 22nd Annual Conference on Mass Spectrometry and Allied Topics, Philadelphia, Pa., May 19–24, 1974.

H. W. Dickson, S. A. Abdullah, and W. F. Fox
"Environmental Gamma-Ray Measurements," Health Physics Society Annual Meeting, Houston, Tex., July 7–11, 1974 (presented by H. W. Dickson).

J. Dutrannois, J. E. Turner, R. N. Hamm, and H. A. Wright
"Influence of Beam Characteristics on Calculated Negative-Pion Depth-Dose Distributions in Water," Health Physics Society Annual Meeting, Houston, Tex., July 7–11, 1974.

R. B. Gammage and J. S. Cheka
"Exoelectron Emitting Dosimeters as Tritium Detectors," Health Physics Society Annual Meeting, Houston, Tex., July 7–11, 1974 (presented by R. B. Gammage).

"A Practical TSEE Dosimetry System Based on BeO Ceramic," Fourth International Symposium on Exoelectrons, Liblice, Czechoslovakia, Oct. 1–4, 1973 (presented by R. B. Gammage).

R. B. Gammage and A. K. Garrison
"Trapping Centers and Activators in Thermalox BeO," Fourth International Symposium on Exoelectrons, Liblice, Czechoslovakia, Oct. 1–4, 1973 (presented by R. B. Gammage).

R. B. Gammage, F. F. Haywood, M. H. Lee, and J. S. Cheka
"Fast Neutron Monitoring with Exoelectron Emitting BeO Dosimeters," Health Physics Society Annual Meeting, Houston, Tex., July 7–11, 1974 (presented by F. F. Haywood).

W. R. Garrett and M. G. Payne
"Example of Cell Survival Models Incorporating the Fixation Time Concept," Fifth International Congress of Radiation Research, Seattle, Wash., July 14–20, 1974.

C. M. Haaland and E. P. Wigner
"Defense of Cities by ABM," Operations Research Society of America Meeting, Boston, Mass., Apr. 22–24, 1974.

R. N. Hamm, H. A. Wright, and J. E. Turner
"Effects of Inhomogeneities on Dose Distributions from Pion Beams," Fifth International Congress of Radiation Research, Seattle, Wash., July 14–20, 1974.

F. F. Haywood
"ORNL Health Physics Research Reactor and External Dosimetry Studies," USAEC/DBER Health Physics Research Program Review, Airlie House, Warrenton, Va., Mar. 12–14, 1974.

J. M. Heller, R. N. Hamm, R. D. Birkhoff, and L. R. Painter
"Collective Oscillation in Liquid Water," American Physical Society Meeting, Winston-Salem, N.C., Nov. 8–10, 1973.

H. F. Holmes, E. L. Fuller, Jr., and R. B. Gammage
"Some Surface Properties of Apollo 17 Soils," Fifth Lunar Science Conference, Houston, Tex., Mar. 18–22, 1974 (presented by H. F. Holmes).

G. S. Hurst
"Energy Transfer from Argon Resonance States to Molecules," 26th Annual Gaseous Electronics Conference, Madison, Wis., Oct. 16–19, 1973.

"Energy Pathways, Including the Jesse Effect, in Noble Gases," Symposium on the Jesse Effect and Related Phenomena, Gatlinburg, Tenn., Nov. 9–10, 1973.

"Health Physics Research at ONRL," Health Physics Society, Blue Grass Chapter, Lexington, Ky., May 18, 1974.

T. Inagaki, R. N. Hamm, and E. T. Arakawa
"Optical and Dielectric Properties of Deoxyribonucleic Acid in the Extreme Ultraviolet," American Physical Society Meeting, Philadelphia, Pa., Mar. 25–28. 1974.

D. G. Jacobs

"Management of Radioactive Wastes – International Concerns and Programs," Symposium on Waste Management, Tucson, Ariz., Apr. 22, 1974.

"Waste Management," presented at the combined meeting of the North Carolina, South Carolina, and Tennessee Chapters of the Health Physics Society, Appalachian State University, Boone, N.C., Oct. 27, 1973.

J. S. Jun, J. E. Talmage, and K. Becker

"Computational Extension of the Dynamic Range of TL and TSEE Readers," Health Physics Society Annual Meeting, Houston, Tex., July 7–11, 1974 (presented by J. S. Jun).

G. D. Kerr

"Measurement of Radon Progeny Concentrations in Air," Annual Meeting of the American Nuclear Society, San Francisco, Calif., November 1973

"Measurement of Radon Progeny Concentrations in Air by Alpha Particle Spectrometry," Workshop on the Natural Radiation Environment at the USAEC Health and Safety Laboratory, New York, N.Y., Feb. 20–22, 1974.

"Dosimetry for Human Exposures and Studies Related to the Estimation of Radiation Exposure to Japanese Survivors," USAEC/DBER Health Physics Research Program Review, Airlie House, Warrenton, Va., Mar. 12–14, 1974.

Studies Related to the Estimation of Radiation Exposure of Atomic-Bomb Survivors of Hiroshima and Nagasaki, Japan, Residing in the United States," presented to the staff of the Department of Public Health, City and County of San Francisco, Calif., Apr. 1, 1974.

C. E. Klots

"Theory of Ionic Fragmentation: Recent Developments," International Mass Spectrometry Conference, Edinburgh, Scotland, Sept. 10–14, 1973.

C. E. Klots and R. N. Compton

"Electronic and Ionic Properties of Molecular TTF and TCNQ," 22nd Annual Conference on Mass Spectrometry and Allied Topics, Philadelphia, Pa., May 19–24, 1974.

C. E. Klots, M. G. Payne, and G. S. Hurst

"New Mechanisms for the Jesse Effect," Fifth International Congress of Radiation Research, Seattle, Wash., July 14–20, 1974.

S. B. Lupica and G. D. Kerr

"Thin Cellulose Nitrate Films for Use in Alpha Particle Detection," Health Physics Society Annual Meeting, Houston, Tex., July 7–11, 1974 (presented by G. D. Kerr).

V. N. Neelavathi and R. H. Ritchie

"Surf-Riding Electron States: Polarization Charge Density Effects Associated with Ion Motion in Solids," Third International Conference on Atomic Collisions in Solids, Gatlinburg, Tenn., Sept. 23–28, 1973.

V. N. Neelavathi, J. E. Turner, D. Arora, J. S. Bisht, R. K. Kher, and R. B. Vora

"Ultrarelativistic Stopping Power Theory for Nucleons: Application to Neutrons," Southeastern Section of the American Physical Society, Winston-Salem, N.C., Nov. 8–11, 1973.

M. G. Payne

"A Family of Cell Survival Models for Low LET Radiation," Fifth International Congress of Radiation Research, Seattle, Wash., July 14–20, 1974.

"Transport of Resonance Radiation," Symposium on the Jesse Effect and Related Phenomena, Gatlinburg, Tenn., Nov. 9–10, 1973.

P. T. Perdue and W. H. Baldwin

"Development of a Stable, High Melting Point Organic Scintillator for Applications in Radioprotection," Health Physics Society Annual Meeting, Houston, Tex., July 7–11, 1974 (presented by P. T. Perdue).

R. H. Ritchie

"Plasmons in Condensed Matter," DBER Radiological and Chemical Physical Contractor's Meeting, ORNL, Feb. 14–15, 1974.

"Primary Processes and Track Effects in Irradiated Media," Fifth International Congress of Radiation Research, Seattle, Wash., July 14–20, 1974.

J. G. Skofronick, D. B. Greene, E. A. Halprin, and R. N. Compton
"A Chemical Accelerator for Studying the Collisional Behavior of Large Molecules: SF_6 + CO_2 Total Cross Sections," Eighth International Conference on the Physics of Electronic and Atomic Collisions, Belgrade, Yugoslavia, July 16–20, 1973.

W. S. Snyder
"Dosimetric Aspects of a Forthcoming Report of ICRP on Internal Emitters," Third Congress of the International Radiation Protection Association, Washington, D.C., Sept. 9–14, 1973.

W. S. Snyder, L. T. Dillman, M. R. Ford, and J. W. Poston
"Calculations of the Absorbed Dose to a Man Immersed in an Infinite Cloud of ^{85}Kr," Noble Gases Symposium, Las Vegas, Nev., Sept. 24–28, 1973.

J. A. D. Stockdale and R. N. Compton
"Dissociative Ionization of Sulfur Hexafluoride," 22nd Annual Conference on Mass Spectrometry and Allied Topics, Philadelphia, Pa., May 19–24, 1974.

"Dissociative Ionization of Molecules by Electron Impact," Fifth International Congress of Radiation Research, Seattle, Wash., July 14–20, 1974.

J. A. D. Stockdale, F. J. Davis, R. N. Compton, and C. E. Klots
"Production of Negative Ions from CH_3X ($X = NO_2$, CN, I, Br) Molecules by Electron Impact, and by Collisions with Rare Gas Atoms in Excited Rydberg States," Annual Meeting of the Division of Electron and Atomic Physics, APS, New Haven, Conn., Dec. 10–12, 1973.

J. A. D. Stockdale, Liliana Deleanu, and R. N. Compton
"Dissociative Ionization of N_2 by Electron Impact," 26th Annual Gaseous Electronics Conference, Madison, Wis., Oct. 16–19, 1973.

J. H. Thorngate
"Monoenergetic Radiation and Spectrometry Studies in the Health Physics Division of Oak Ridge National Laboratory," USAEC/DBER Health Physics Research Program Review, Airlie House, Warrenton, Va., Mar. 12–14, 1974.

J. E. Turner, H. A. Wright, and R. N. Hamm
"Calculational Methods for High-Energy Radiation Dosimetry," Working Party on Space Biophysics, Fontenay aux Roses, France, Oct. 4–6, 1973.

C. E. Wheeler, E. T. Arakawa, and R. H. Ritchie
"Coupling of Photons and Surface Plasmons at Interfaces of Known Profile," American Physical Society Meeting, Philadelphia, Pa., Mar. 25–28, 1974.

M. W. Williams, E. T. Arakawa, R. D. Birkhoff, R. N. Hamm, H. C. Schweinler, and R. A. McRay
"Optical Properties of Chloroplasts and Red Blood Cells in the Vacuum UV," Fifth International Congress of Radiation Research, Seattle, Wash., July 14–20, 1974.

J. F. Wilson and R. N. Compton
"Mass Analysis of Negative Ions Produced in Electron Swarm Experiments: H_2O (D_2O) and NH_3 (ND_3)," 26th Annual Gaseous Electronics Conference, Madison, Wis., Oct. 16–19, 1973.

H. A. Wright, R. N. Hamm, and J. E. Turner
"^{11}C Activity to Dose and Dose Equivalent Conversion Factors," Health Physics Society Annual Meeting, Miami Beach, Fla., June 17–21, 1973.

"Dose, Dose Equivalent, Effective Dose and Cell Survival from Negative Pions," Third International Congress of the International Radiation Protection Association, Washington, D.C., Sept. 9–14, 1973.

"Effects of π^- Beam Parameters on Calculated Dose Distributions in Tissue," Fifth International Congress of Radiation Research, Seattle, Wash., July 14–20, 1974.

Publications

V. E. Anderson, R. N. Hamm, J. E. Turner, H. A. Wright, R. G. Alsmiller, Jr., and T. W. Armstrong
Isodata: A Computer Program for Calculating Isodata Contours, ORNL-TM-4296 (February 1974).

E. T. Arakawa, R. N. Hamm, and M. W. Williams
"Optical Properties and Electron Attenuation Lengths from Photoelectric Yield Measurements," *J. Opt. Soc. Amer.* **63**, 1131–34 (1973).

E. T. Arakawa and M. W. Williams
"Satellites in the X-Ray Emission Spectra of Li, Be, and Na," *Phys. Rev.* **8**, 4075–78 (1973).

E. T. Arakawa, M. W. Williams, R. N. Hamm, and R. H. Ritchie
"Effect of Damping on Surface Plasmon Dispersion," *Phys. Rev. Lett.* **31**, 1127–29 (1973).

J. C. Ashley
"The Influence of the Z_1^3 Contribution to Stopping Power on the Evaluation of Mean Excitation Potentials and Shell Corrections," *Phys. Rev.* (Comments and Addenda Section) **39**, 334–36 (1974).

J. C. Ashley, V. E. Anderson, R. H. Ritchie, and Werner Brandt
"Z_1^3 Effect in the Stopping Power of Matter for Charged Particles: Tables of Functions," National Auxiliary Publications Service, NAPS Document No. 02195.

J. C. Ashley and L. C. Emerson
"Dispersion Relations for Non-Radiative Surface Plasmons on Cylinders," *Surface Sci.* (Letter to Editor) **41**, 615–18 (1974).

J. C. Ashley, T. L. Ferrell, and R. H. Ritchie
"X-Ray Excitation of Surface Plasmons in Metallic Spheres," submitted for publication in the *Physical Review.*

J. C. Ashley and R. H. Ritchie
"The Influence of Plasmon Damping on the Mean Free Path of Electrons for Plasmon Excitation," *Phys. Status Solidi b* **62**, 253–60 (1974).

J. C. Ashley, R. H. Ritchie, and Werner Brandt
"Z_1^3-Dependent Stopping Power and Range Contributions," *Phys. Rev. A* **8**, 2402–2408 (1973).

"Z_1^3-Dependent Stopping Power and Range Contributions," in Proceedings of Fifth International Conference on Atomic Collisions in Solids, Gatlinburg, Tennessee, September 23–28, 1973 (to be published).

"Z_1^3-Dependent Range Contributions," *Phys. Rev. A* (Comments and Addenda Section) (to be published).

J. K. Baird and N. J. Frigo
Effects of Electromagnetic Pulse (EMP) on the Supervisory Control Equipment of a Power System, ORNL-4899 (October 1973).

P. R. Barnes
"On the Singularity Expansion Method as Applied to the Cylindrical Dipole Receiving Antenna," *Proceedings IEEE/G-AP Symposium, University of Colorada, August 21–24, 1973.*

The Analysis and Simulation of the Electric Dipole Antenna Response to EMP, ORNL-TM-4086 (September 1973).

"On the Singularity Expansion Method as Applied to the EMP Analysis and Simulation of the Cylindrical Dipole Antenna," *Interaction Note 146,* Air Force Weapons Laboratory, November 1973.

The Effects of Nuclear Electromagnetic Pulse (EMP) on Civil Defense Two-Way Radio Communications, ORNL-4873 (February 1974).

"On the Input Admittance of an Infinitely Long Cylindrical Dipole Antenna Excited by a Finite Uniform Distributed Source," *Interaction Note 154,* Air Force Weapons Laboratory, February 1974.

"On the Response of an Infinitely Long, Perfectly Conducting, Cylindrical Antenna to an Electromagnetic Plane Wave Pulse," *Interaction Note 157,* Air Force Weapons Laboratory, February 1974.

P. B. Barnes and D. B. Nelson

"Transient Response of Low Frequency Vertical Antennas to High Altitude Nuclear Electromagnetic Pulse (EMP)," *Interaction Note 160,* Air Force Weapons Laboratory, March 1974.

Transient Response of Low Frequency Vertical Antennas to High Altitude Nuclear Electromagnetic Pulse (EMP), ORNL-4960 (June 1974).

George Basbas, Werner Brandt, and R. H. Ritchie

"Perturbed-Stationary-State Theory of Atomic Inner-Shell Ionization by Heavy Charged Particles," *Phys. Rev. A* **7**, 1971–76 (1973).

Klaus Becker

"Solid-State Neutron Personnel Dosimetry Research at ORNL," *Proceedings of Fourth AEC Workshop on Neutron Dosimetry, Miami, Florida, June 14–15, 1973,* BNWL-1777 (1973).

"Progress in the Dosimetric Applications of Exoelectron Emission," *Proceedings of Fourth International Symposium on Exoelectron Emission and Dosimetry, Liblice, Czechoslovakia, October 1–3, 1973,* p. 218.

"Personnel Dosimetry of Radon and Radon Daughters," *Proceedings of Symposium on Noble Gases, Las Vegas, Nevada, September 24–28, 1973.*

"The LET Response of Solid-State Detectors – a Review," *Proceedings of Fourth International Symposium on Microdosimetry, Verbania, Italy, September 27, 1973,* EUR-5122, vol. II, p. 899.

Solid State Dosimetry, CRC Press, Cleveland, Ohio, November 1973.

Book review: "On the Possible Application of Exoelectrons in Dosimetry," *Proceedings of a Workshop, Braunschweig, 1972,* ed. by H. Riskat and H. Seguin, EUR-4904, appearing in *Health Phys.* **25**(5), 530 (1973).

"Current Studies on Integrating Environmental Monitoring at ORNL," *Proceedings of Second Environmental Radiation Workshop, New York, February 20–21, 1974.*

Book review: *Radiosterilization – Principles and Applications in Medicine and Pharmaceutical Manufacturing* (in German), J. A. Barth, Leipzig, East Germany, 1972, appearing in *Health Phys.* **26**(3), 271 (1974).

"Some Reflections on the Health Physics Publication Explosion," *Health Phys.* **26**(3), 267 (1974) (letter to editor).

"On the Discovery of Thermoluminescence," *Health Phys.*, in press (letter to editor).

"Stability of Film and Thermoluminescence Dosimeters in Warm and Humid Climates," *Atomkernenergie* (in press).

"The LET Response of Solid-State Detectors – a Review," *J. Radiat. Eng.* (Israel) (in press).

"Conferences on Exoelectron Emission and Dosimetry," *Health Phys.* (in press) (new item).

Long-Term Stability of Film, TLD, and Other Integrating Dosimeters in Warm and Humid Climates, ORNL-TM-4297 (August 1973).

Report of Foreign Travel to Europe, September 10–October 9, 1973, ORNL-CF-73-12-25 (Dec. 20, 1973).

Klaus Becker and M. Abdel Razek

"Fast Neutron Response Characteristics of TSEE Dosimeters," *Nucl. Instrum. Methods* **113**, 611–14 (1973).

Automatic Spark Counting of Fast Neutron Induced Recoil Particle Tracks in Polymer Foils, ORNL-TM-4460 (March 1974).

Klaus Becker, F. F. Haywood, and T. D. Tham

"Compounds of TLD's and High-Melting Organics for Fast Neutron Personnel Dosimetry," *Proceedings of IRPA Congress, Washington, D.C., September 10–24, 1973.*

Klaus Becker and A. Moreno y Moreno

Applications of Thermoluminescence Measurements in Ancient Ceramics, ORNL-TM-4572 (June 1974).

G. M. Begun and R. N. Compton

"Electron Impact Ionization Studies of Ferrocene, Cobaltocene, Nickelocene, and Magnesocene," *J. Chem. Phys.* **58**, 2271–80 (1973).

S. R. Bernard
"Estimates of Microcurie-Days Residence, Bone Dose Equivalent, and $(MPC)_w$ for Thorium-232 in Man Using a Mammillary Model," *Bull. Math. Biol.* **35**, 129 (1973).

R. D. Birkhoff
Review of ICRU Report 21: "Radiation Dosimetry: Electrons with Initial Energies between 1 and 50 eV," *Nucl. Safety* **14**(1), 76–77 (January–February 1973).

R. D. Birkhoff, R. N. Hamm, M. W. Williams, E. T. Arakawa, and L. R. Painter
"Optical Properties of Liquids in the Vacuum UV," *Proceedings of NATO–Advanced Study Institute on Chemical Spectroscopy and Photochemistry in the Vacuum Ultraviolet, Valmorin, Quebec, August 5–17, 1973,* pp. 129–47.

Werner Brandt and R. H. Ritchie
"Primary Processes in the Physical Stage," in *Proceedings of Conference on Physical Mechanisms in Radiation Biology, Airlie, Virginia, October 10–14, 1972.*

A. J. Braundmeier and E. T. Arakawa
"Effect of Surface Roughness on Surface Plasmon Resonance Absorption," *J. Phys. Chem. Solids* **35**, 517–20 (1974).

T. A. Callcott and E. T. Arakawa
"Ultraviolet Optical Properties of Li," submitted for publication in the *Journal of the Optical Society of America.*

C. V. Chester
The Need for a Third Contingency Plan for Civil Defense, ORNL-CF-73-11-73 (Oct. 26, 1973).

C. V. Chester and R. O. Chester
"Civil Defense Implications of an LMFBR in a Thermonuclear Target Area," *Nucl. Technol.* **21**(3), 190–200 (1974).

C. V. Chester, G. A. Cristy, and C. M. Haaland
Strategic Considerations in Planning a Counterevacuation, ORNL-4888 (in preparation).

R. O. Chester
Dose and Deposition from a Nuclear Reactor Core Meltdown, ORNL-4944 (1974).

D. J. Christian and J. H. Thorngate
A Compact Electronic System for an Improved Alpha Air Monitor, ORNL-TM-4346 (September 1973).

L. G. Christophorou, R. P. Blaunstein, and D. Pittman
"Mobilities of Thermal Electrons in Gases and Liquids," *Chem. Phys. Lett.* **18**, 509–14 (Feb. 15, 1973).

L. G. Christophorou, J. G. Carter, E. L. Chaney, and P. M. Collins
"Long-Lived Parent Negative Ions Formed by Capture of Low-Energy Electrons (0 to 3 eV) in the Field of the Ground and Excited Electronic States of Organic Molecules," pp. 145–57 in *Advances in Radiation Research,* ed. by Duplan and Chapiro (Proceedings of Fourth International Congress of Radiation Research, Evian, France, June 29–July 4, 1970), Gordon and Breach, London, 1973.

L. G. Christophorou and R. E. Goans
"Low-Energy (<1 eV) Electron Attachment to Molecules in Very-High Pressure Gases: C_6H_6," submitted for publication in the *Journal of Chemical Physics.*

L. G. Christophorou, A. A. Hadjiantoniou, and J. G. Carter
"Long-Lived Parent Negative Ions Formed via Nuclear-Excited Feshbach Resonances. Part III – Variation of the Autodetachment Lifetime with Incident Electron Energy," *J. Chem. Soc., Faraday Trans.* **69**, 1713–22 (1973).

L. G. Christophorou, D. L. McCorkle, and J. G. Carter
"Compound-Negative-Ion Resonant States and Threshold-Electron Excitation Spectra of Monosubstituted Benzene Derivatives," Proceedings of the International Conference on the Excited States of Biological Molecules, Lisbon, Portugal, April 18–24, 1974 (to be published).

"Compound-Negative-Ion-Resonant States and Threshold-Electron-Excitation Spectra of Monosubstituted Benzene Derivatives," submitted for publication in the *Journal of Chemical Physics.*

L. G. Christophorou, D. L. McCorkle, and D. Pittman
"Electron Attachment to c-C_4F_8, CCl_2F_2, and C_2H_5Cl below ~2 eV; a Comparison of the Electron Swarm and the Microwave Methods," *J. Chem. Phys.* **60**, 1183–84 (Feb. 1, 1974).

R. J. Cloutier, S. A. Smith, E. E. Watson, W. S. Snyder, and G. G. Warner
"Dose to the Fetus from Radionuclides in the Bladder," *Health Phys.* **15**(2), 147 (1973).

R. N. Compton and C. D. Cooper
"Molecular Electron Affinities from Collisional Ionization of Cesium: SF_6 and TeF_6," *J. Chem. Phys.* **59**, 4140–44 (October 1973).

R. N. Compton, P. W. Reinhardt, and C. D. Cooper
"Mass Spectrometry Utilizing Collisional Ionization of Cesium: Maleic Anyhdride and Succinic Anhydride," *J. Chem. Phys.* **60**, 2953–57 (Apr. 15, 1974).

C. D. Cooper and R. N. Compton
"Electron Attachment to Cyclic Anhydrides and Related Compounds," *J. Chem. Phys.* **59**, 3550–65 (Oct. 1, 1973).

"Electron Attachment and Cesium Collisional Ionization Studies of Tetrafluorosuccinic and Hexafluoroglutaric Anhydrides: Molecular Electron Affinities," *J. Chem. Phys.* **60**, 2424–29 (Mar. 15, 1974).

G. A. Cristy
"Blast Shelters? Why Not?" *Survive,* vol. 6, No. 5 (September–October 1973).

Expedient Shelter Handbook, ORNL-4941 (in press).

TW-1966 Technical Directives for the Construction of Private Air Raid Shelters (Swiss translation), ORNL-TR-2707 (July 1974) (ed. by G. A. Christy).

F. J. Davis, R. N. Compton, and D. R. Nelson
"Thermal Energy Electron Attachment Rates for Some Polyatomic Molecules," *J. Chem. Phys.* **59**, 2324–29 (Sept. 1, 1973).

H. W. Dickson and D. J. Christian
Results of ORNL Measurements Made during the International Neutron Dosimetry Intercomparison, ORNL-4441 (February 1974).

H. W. Dickson and F. F. Haywood
Results of Measurements during the Third IAEA Intercomparison Study, ORNL-TM-4418 (January 1974).

J. R. Dutrannois, H. A. Wright, J. E. Turner, and R. N. Hamm
"Estimations of RBE for π^- and π^+ from Survival Data of T-1 Human Kidney Cells," *Int. J. Radiat. Biol.* **23**, 421 (1973).

C. E. Easterly and L. G. Christophorou
"Fluorescence Emission from the First- and the Second-Excited π-Singlet States of Aromatic Hydrocarbons in Solution, and Their Temperature Dependences," *J. Chem. Soc., Faraday Trans. 2* (Chem. Phys.) **70**, 267–73 (1974).

C. E. Easterly, L. G. Christophorou, and J. G. Carter
"Fluorescence from the Second Excited π-Singlet State of Aromatic Hydrocarbons in Solution," *J. Chem. Soc., Faraday Trans. 2* **69**, 471–83 (1973).

J. M. Elson and R. H. Ritchie
"Diffuse Scattering and Surface Plasmon Generation by Photons at a Rough Dielectric Surface," *Phys. Status Solidi b* **62**, 461–68 (1974).

L. C. Emerson, R. D. Birkhoff, V. E. Anderson, and R. H. Ritchie
"Electron Slowing-Down Spectrum in Irradiated Silicon," *Phys. Rev. B* **7**, 1798–1811 (Mar. 1, 1973).

W. F. Frey, R. N. Compton, W. T. Naff, and H. C. Schweinler
"Electron Impact Studies of Some Cyclic Hydrocarbons," *Int. J. Mass Spectrom. Ion Phys.* **12**, 19–32 (1973).

J. S. Gailar
"The 'Why' of Soviet Civil Defense," *Survive,* vol. 6, No. 5 (September–October 1973).

"The New 1973 Soviet CD Training Program," *Survive,* vol. 6, No. 6 (November–December 1973).

"ORNL Publishes 1970 Soviet CD Handbook," *Survive,* vol. 7, No. 1 (January–February 1974).

"Soviet Populace Instructed in Shelter Building," *Survive,* vol. 7, No. 2 (March–April 1974).

J. S. Gailar and C. H. Kearny, eds.
Antiradiation Shelters in Rural Areas (Russian translation), ORNL-TR-2745 (October 1973).

J. S. Gailar, C. H. Kearny, and C. V. Chester, eds.
Civil Defense (Moscow 1970) (Russian translation), ORNL-TR-2793 (December 1973).

J. S. Gailar and E. P. Wigner
"Civil Defense in the Soviet Union," *Foresight,* vol. 1, No. 3 (May–June 1974).

R. B. Gammage
Report of Foreign Travel – Czechoslovakia, England, September 4–October 5, 1973, ORNL-CF-73-12-24 (Dec. 20, 1973).

R. B. Gammage and J. S. Cheka
"A Practical TSEE Dosimetry System Based on BeO Ceramic," p. 247 in *Proceedings of the Fourth International Symposium on Exoelectrons, Liblice, Czechoslovakia, October 1–4, 1973,* Czechoslovakia Academy of Sciences, Prague, Czechoslovakia.

R. B. Gammage and A. K. Garrison
"Trapping Centers and Activators in Thermalox BeO," p. 93 in *Proceedings of the Fourth International Symposium on Exoelectrons, Liblice, Czechoslovakia, October 1–4, 1973,* Czechoslovakia Academy of Sciences, Prague, Czechoslovakia.

R. B. Gammage, H. F. Holmes, and E. L. Fuller, Jr.
"Pore Structures Induced in Lunar Fines by Adsorbed Water," *Proceedings of RILEM/IUPAC International Symposium on Pore Structure and Properties of Materials, Prague, Czechoslovakia, October 1–3, 1973,* Academia, Prague, Czechoslovakia, 1973.

R. B. Gammage, H. F. Holmes, E. L. Fuller, Jr., and D. R. Glasson
"Pore Structures Induced by Water Vapor Adsorbed on Nonporous Lunar Fines and Ground Calcite," *J. Colloid Interface Sci.* **47**(2) (1974).

W. R. Garrett
Book review: Joel Griffiths and Richard Ballentine, *Silent Slaughter,* Henry Regnery Co., Chicago, 1972, appearing in *Health Phys.* **25**, 616 (1973).

T. F. Gesell, E. T. Arakawa, and M. W. Williams
"Optical and Photoelectric Properties of Mg in the Vacuum UV," *Phys. Rev. B* **7**, 5141–46 (June 15, 1973).

R. E. Goans and L. G. Christophorou
"Attachment of Slow (<1 eV) Electrons to O_2 in Very-High-Pressures of Nitrogen, Ethylene and Ethane," *J. Chem. Phys.* **60**, 1036–45 (February 1974).

C. M. Haaland
"Isometric View of Northeast Corridor Population Density," *SIGSOC Bulletin* (Special Interest Group on Social and Behavioral Science Computing), vol. 5, No. 2 (Fall 1973).

C. M. Haaland and M. T. Heath
"Mapping of Population Density," *Demography,* May 1974.

A. Hadjiantoniou, L. G. Christophorou, and J. G. Carter
"Long-Lived Parent Negative Ions Formed via Nuclear-Excited Feshbach Resonances. Part I – Benzene Derivatives," *J. Chem. Soc., Faraday Trans. 2* **69**, 1691–1703 (1973).

"Long-Lived Parent Negative Ions Formed via Nuclear-Excited Feshbach Resonances. Part II – Aromatic Molecules Other than Benzene Derivatives and Non-Aromatic Organic Structures," *J. Chem. Soc., Faraday Trans. 2* **69**, 1704–12 (1973).

F. F. Haywood
"Intercomparisons of Neutron Monitors under Conditions of Simulated Nuclear Accidents," *Proceedings of the IAEA Symposium on Neutron Monitoring for Radiation Protection Purposes, Vienna, Austria, December 11–15, 1972,* IAEA-SM-167/81 (1973).

H. F. Holmes, E. L. Fuller, Jr., and R. B. Gammage
"Alternation of an Apollo 12 Sample by Adsorption of Water Vapor," *Earth Planet Sci. Lett.* **19**, 90 (1973).

"Interaction of Gases with Lunar Materials: Apollo 12, 14, and 16 Samples," in Proceedings of the Fourth Lunar Science Conference, Houston, Texas, March 5–8, 1973, *Geochim. Cosmochim. Acta,* **Suppl. 4**, 2413–23 (December 1973).

R. H. Huebner, W. F. Frey, and R. N. Compton
"Threshold Electron Excitation of Azulene," *Chem. Phys. Lett.* **23**, 587–91 (Dec. 15, 1973).

G. S. Hurst
"History and Use" and "Gas Mixtures," submitted for publication in *Report of the ICRU Committee on the Average Energy Required to Produce an Ion Pair,* a report of the International Commission on Radiation Units and Measurements.

"Energy Pathways, Including the Jesse Effect, in Noble Gases," *Radiat. Res.* (in press).

G. S. Hurst, W. R. Garrett, and M. G. Payne
"Rationale for Radiation Protection," *Health Phys.* **26**, 313–18 (April 1974).

G. S. Hurst and C. E. Klots
"Elementary Processes in Irradiated Noble Gases," to be published in vol. 4 of *Advances in Radiation Chemistry,* ed. by M. Burton and J. L. Magee, Wiley-Interscience, New York.

G. S. Hurst, M. G. Payne, and E. B. Wagner
"Resonance Ionization Spectroscopy," submitted for publication in *Physical Review Letters.*

G. S. Hurst, E. B. Wagner, and M. G. Payne
"Energy Transfer from the Resonance States $Ar(^1P_1)$ and $Ar(^3P_1)$ to Ethylene," submitted for publication in the *Journal of Chemical Physics.*

D. G. Jacobs
"Environmental Behavior of Radionuclides Released in the Nuclear Industry – Report on the International Symposium Held in Aix-en-Provence from May 14–18, 1973," *At. Energy Rev.* **11**(3), 691–97 (October 1973).

C. H. Kearny
Trans-Pacific Fallout and Protective Countermeasures, ORNL-4900 (November 1973).

C. H. Kearny and C. V. Chester
Blast Test of Expedient Shelters, ORNL-4905 (January 1974).

G. D. Kerr
"Measurement of Radon Progeny Concentrations in Air," *Trans. Amer. Nucl. Soc.* **17**, 541 (1973).

Report of Foreign Travel to Atomic Bomb Casualty Commission in Hiroshima and Nagasaki, Japan, April 26–May 30, 1973, ORNL-CF-73-6-35 (June 28, 1973).

C. E. Klots
Book review: A. R. Denaro and G. S. Jayson, *Fundamentals of Radiation Chemistry,* Butterworths, London, 1972, appearing in *Health Phys.* **24**, 457–58 (1973).

"Comparison of Photoabsorption and Resonance Energy Transfer Processes," pp. 61–68 in *Advances in Radiation Research,* ed. by Duplan and Chapiro (Proceedings of Fourth International Congress of Radiation Research, Evian, France, June 29–July 4, 1970), Gordon and Breach, London, 1973.

"Theory of Ionic Fragmentations: Recent Developments," submitted for publication in *Advances in Mass Spectrometry.*

"Thermochemical and Kinetic Information from Metastable Decompositions," *J. Chem. Phys.* **58**, 5364–67 (June 15, 1973).

C. E. Klots, R. N. Compton, and V. F. Raaen
"Electronic and Ionic Properties of Molecular TTF and TCNQ," *J. Chem. Phys.* **60**, 1177–78 (Feb. 1, 1974).

C. E. Klots and L. W. Sieck
"Argon Sensitized Formation of Xe_2^+: A New Mechanism for the Jesse Effect," in Proceedings of Symposium on the Jesse Effect and Related Phenomena, Gatlinburg, Tennessee, November 9–10, 1973 (to be published).

"Argon Sensitized Formation of Xe_2^+: A New Mechanism for the Jesse Effect," submitted for publication in *Chemical Physics Letters.*

R. A. MacRae, M. W. Williams, and E. T. Arakawa
"Optical Properties of Some Aromatic Liquids in the Vacuum Ultraviolet," submitted for publication in the *Journal of Chemical Physics.*

R. W. Manweiler, C. V. Chester, and C. H. Kearny
Measurement of Shock Overpressure in Air by a Yielding Foil Membrane Blast Gauge, ORNL-4868 (September 1973).

J. H. Marable
"Electromagnetic Pulse Coupling to Power Lines," *Joint EMP Technical Meeting, First Annual Nuclear EMP Meeting, NEM 1973 Abstracts of Technical Papers,* sponsored by Army (HDL), Navy (NOL), Air Force (AFWL), and Defense Nuclear Agency, Sept. 25–27, 1973.

J. H. Marable et al.
"Effects of Electromagnetic Pulse (EMP) on a Power System," *Interaction Note 173,* Air Force Weapons Laboratory, March 1974.

The Protection of the Electric Power System against the Threat of Electromagnetic Pulse (EMP), ORNL-4958 (in preparation).

S. J. Nalley, R. N. Compton, H. C. Schweinler, and V. E. Anderson
"Molecular Electron Affinities from Collisional Ionization of Cesium, Part I. NO, NO_2, and N_2O," *J. Chem. Phys.* **59**, 4125–39 (Oct. 1, 1973).

V. N. Neelavathi and R. H. Ritchie
"Surf-Riding Electron States: Polarization Charge Density Effects Associated with Ion Motion in Solids," in Proceedings of Third International Conference on Atomic Collisions in Solids, Gatlinburg, Tennessee, September 23–28, 1973 (to be published).

Jacob Neufeld
"Absorbed Dose and Tissue Dose," *Health Phys.* **24**, 101–3 (1973).

"Comments on the Theory of Radiation Risk, Parts 1 and 2," *Health Phys.* **26**, 229–43 (March 1974).

Jacob Neufeld, H. A. Wright, and R. N. Hamm
"A Comparison of Two-Component Models of Cellular Survival," in Proceedings of Fourth Symposium on Microdosimetry, Verbania Pallanza, Italy, September 24–28, 1973 (to be published).

M. G. Payne and W. R. Garrett
"General Models for Cell Survival with Low LET Radiation, Part I," submitted for publication in *Radiation Research.*

"General Models for Cell Survival with Low LET Radiation. Part II," submitted for publication in *Radiation Research.*

"Statistical Pitfalls in the Modelling of Cell Survival," submitted for publication in *Radiation Research.*

M. G. Payne, J. E. Talmage, G. S. Hurst, and E. B. Wagner
"Effect of Correlations between Absorbed and Emitted Frequencies on the Transport of Resonance Radiation," *Phys. Rev. A* **9**, 1050–69 (1974).

P. T. Perdue, W. H. Shinpaugh, J. H. Thorngate, and J. A. Auxier
"A Convenient Counter for Measuring Alpha Activity of Smear and Air Samples," *Health Phys.* **26**, 114–16 (January 1974).

M. N. Pisanias, L. G. Christophorou, J. G. Carter, and D. L. McCorkle
"Compound-Negative-Ion Resonance States and Threshold-Electron Excitation Spectra of N-Heterocyclic Molecules: Pyridine, Pyridazine, Pyrimidine, Pyrazine, and sym-Triazine," *J. Chem. Phys.* **58**, 2110–24 (Mar. 1, 1973).

J. W. Poston and W. S. Snyder
"A Model for Exposure to a Semi-Infinite Cloud of a Photon Emitter," *Health Phys.* **26**(4), 287 (April 1974).

R. H. Ritchie
"Plasmons in Solids," *Interaction of Energetic Charged Particles with Solids, NATO Advanced Study Institute, Istanbul, Turkey, August 1971,* BNL-50336 (February 1973).

Book review: M. L. Ter-Mikaelian, *High-Energy Electromagnetic Processes in Condensed Media,* Wiley-Interscience Tract on Physics and Astronomy, No. 29, 1972, appearing in *Nucl. Technol.* **18**, 312 (1973).

"Surface Polaritons," in Proceedings of Taormina Research Conference on the Structure of Matter, Taormina, Sicily, October 2–6, 1972 (to be published).

"Surface Plasmons in Solids," in Proceedings of Conference on Surface Plasmons, University of Missouri, Rolla, June 1972, *Surface Sci.* **34**, 1–19 (January 1973).

"Isotropic Incident Flux in Monte Carlo Calculations," *Health Phys.* **24**, 571–72 (May 1973).

R. H. Ritchie, J. C. Ashley, and Dayashankar
"Generalized Oscillator Strength of an Atomic System Based on the Binary Encounter Model I," submitted for publication in *Physical Review A.*

H. C. Schweinler and J. W. McKeever
"Diatomic Potential Energy by Maximum Transform," to be submitted to the *Journal of Chemical Physics* for publication.

W. S. Snyder
"Mathematical Procedures for Estimating Dose from an Internally Deposited Emitter," p. 33 in *Health Physics Problems of Internal Contamination,* Akadémiai Kiadó, Budapest, Hungary, 1973.

W. S. Snyder, M. R. Ford, and G. G. Warner
"Estimates of Absorbed Fractions for Photon Emitters within the Body," *Health Phys. Div. Annu. Progr. Rep. July 31, 1972,* ORNL-4822, p. 86.

W. S. Snyder and T. D. Jones
"Depth Dose Due to Neutrons as Calculated for a Tissue Phantom and Man," p. 597 in *Proceedings of the First Symposium on Neutron Dosimetry in Biology and Medicine, Neuherberg/München (Germany), May 15–19, 1972,* EUR 4896 d-f-e.

J. A. D. Stockdale
"Thermal Energy Ion Condensation Reactions in Benzene Vapor," *J. Chem. Phys.* **58**, 3881–83 (May 1, 1973).

J. A. D. Stockdale, F. J. Davis, R. N. Compton, and C. E. Klots
"Production of Negative Ions from CH_3X ($X = NO_2$, CN, I, Br) Molecules by Electron Impact and by Collisions with Atoms in Excited Rydberg States," submitted for publication in the *Journal of Chemical Physics.*

J. A. D. Stockdale and Liliana Deleanu
"Dissociative Ionization of O_2 and N_2 by Electron Impact: N^+ and O^+ Energies and Angular Distributions," *Chem. Phys. Lett.* **22**, 204–8 (Sept. 15, 1973).

"Vibrational Structure in Kinetic Energy Spectra of O^+ Ions from Electron Impact Dissociative Ionization of O_2: Predissociation of the $B^2\Sigma_g^-$ State of O_2^+," submitted for publication in *Chemical Physics Letters.*

J. H. Thorngate, W. J. McDowell, and D. J. Christian
"An Application of Pulse Shape Discrimination to Liquid Scintillation Alpha Spectroscopy," Note, *Health Phys.* (in press).

J. E. Turner
Book review: Eberhard Freytag, *Strahlenschutz an Hochenergiebeschleunigern,* G. Braun, Publishers, Karlsruhe, Germany, 1972, appearing in *Health Phys.* **25**, 530 (1973).

News item: "Fourth Symposium on Microdosimetry," *Health Phys.* **26**, 274 (1974).

Book review: *Topics in Radiation Dosimetry (Radiation Dosimetry, Supplement 1),* F. H. Attix, ed., Academic Press, New York, 1974, to be published in *Nuclear Science and Engineering.*

J. E. Turner, R. N. Hamm, and H. A. Wright
"Microscopic Description of Energy Deposition in Tissue by Pion Beams," p. 75 in *Proceedings of Fourth Symposium on Microdosimetry, Verbania Pallanza, Italy, September 24–28, 1973,* EURATOM, Brussels, Belgium, 1974.

J. E. Turner, R. K. Kher, D. Arora, J. S. Bisht, V. N. Neelavathi, and R. B. Vora
"Quantum-Mechanical Calculation of Neutron Stopping Power," *Phys. Rev. B* **8**, 4057–62 (Nov. 1, 1973).

J. E. Turner, V. N. Neelavathi, R. B. Vora, J. S. Bisht, and D. Arora
"Generalized Formulation of Stopping-Power Theory for Nucleons in the First Born Approximation," *Phys. Rev. B* **8**, 4053–56 (Nov. 1, 1973).

J. E. Turner, H. A. Wright, and R. N. Hamm
"Estimation of W-Values in Nitrogen and Argon for Use in Negative Pion Dosimetry," submitted to *Radiation Research.*

"Calculations for High-Energy Radiations," submitted to *Radioprotection.*

R. B. Vora, J. E. Turner, and R. N. Compton
"Single-Electron Excitation and Transfer in Collisions of Alkali-Metal and Oxygen Atoms," *Phys. Rev. A* **9**, 2532 (1974).

U. S. Whang, R. N. Hamm, E. T. Arakawa, and M. W. Williams
"A Slope Method for Determining Extinction Coefficients," *J. Opt. Soc. Amer.* **63**, 305–8 (March 1973).

M. W. Williams, E. T. Arakawa, R. D. Birkhoff, R. N. Hamm, H. C. Schweinler, and R. A. MacRae
"Optical Properties of Chloroplasts and Red Blood Cells in the Vacuum UV," submitted for publication in *Radiation Research.*

H. A. Wright, R. N. Hamm, and J. E. Turner
"Dose, Dose Equivalent, Effective Dose and Cell Survival from Negative Pions," in Proceedings of Third International Congress of the International Radiation Protection Association, Washington, D.C., September 9–14, 1973 (to be published).

"Estimation of Dose Equivalent and Quality Factors for π^- and π^+ Beams," to be published in *Health Physics.*

Lectures

P. R. Barnes
"On the Singularity Expansion Method as Applied to the Cylindrical Dipole Receiving Antenna," IEEE G–AP Symposium, University of Colorado, Aug. 21–24, 1973, Boulder, Colorado.

"The Early Time Response of the Low-Frequency Vertical Radiator to a Transient Electromagnetic Plane Wave," Joint EMP Technical Meeting, Kirtland AFB, New Mexico, Sept. 25–27, 1973.

"The Electromagnetic Pulse (EMP) Susceptibility of Two-Way Radio Communications," Defense Nuclear Agency's EMP Conference, May 15–16, 1974.

Klaus Becker

"Current Solid-State Dosimetry Research at ORNL," Department of Physics, University of Giessen, Giessen, Germany, Sept. 18, 1973.

"Solid-State Dosimetry Research at ORNL," Institute of Physics, University of Giessen, Giessen, Germany, Sept. 20, 1973.

"Current Solid-State Dosimetry Research at ORNL," Institute for Nuclear Research, Cracow, Poland, Oct. 5, 1973.

"Modern Techniques in Personnel Dosimetry," ORAU Ten-Week Course in Health Physics, Mar. 8, 1974.

C. V. Chester

"Russian Civil Defense," briefing for Senator Howard Baker, Huntsville, Tennessee, Aug. 21, 1973.

"Activities of the Civil Defense Research Section," briefing for J. M. Teem, Assistant General Manager for Research, U.S. Atomic Energy Commission, Oak Ridge National Laboratory, Sept. 5, 1973.

"U.S. and Soviet Civil Defense," briefing for R. Mossbacher of Sen. H. Baker's staff, Washington, D.C., Sept. 24, 1973.

"U.S. and Soviet Civil Defense," briefing for Senator Howard Baker, H. Sonnenfelt, Chief Counsel, State Department, and F. C. Ikle, Director of ACDA, Washington, D.C., Feb. 5, 1974.

"Strategic Balance," Optimist Club, Oak Ridge, Tennessee, Feb. 14, 1974.

"Strategic Implications of a Counterevacuation," Special Committee on Evacuation, National Academy of Sciences Subcommittee on Civil Defense, Washington, D.C., Feb. 28, 1974.

"The Terrorist Problem for Nuclear Power," Chemical Technology Seminar, Oak Ridge National Laboratory, Mar. 6, 1974.

"Terrorist Alternatives," briefing for C. Bennett (Battelle), N. Barr, C. T. McDowell, W. W. Schroebel, and R. W. Wood, U.S. Atomic Energy Commission, Washington, D.C., Apr. 4, 1974.

"Expedient Shelter and Strategic Consideration," Defense Civil Preparedness Agency Contractors' Conference, San Francisco, Apr. 22–25, 1974.

"Analysis of the Soviet Civil Defense Program," briefing for Commissioner W. E. Kriegman, GM J. A. Erlewine, AGM E. B. Giller, and E. Graves, U.S. Atomic Energy Commission, Washington, D.C., May 2, 1974.

R. N. Compton

"The Formation and Structure of Negative Ions," Columbia University, New York, New York, Nov. 10, 1972.

J. S. Gailar

"Civil Defense in the USSR," Daughters of the American Revolution (DAR), Knoxville, Tennessee, Jan. 12, 1974.

R. B. Gammage

"Dosimetry with Exoelectron Emitters," Atomic Energy Research Establishment, Harwell, England, October 1973.

W. R. Garrett

"Mechanisms for and Mathematical Modelling of Effects in Low LET Cell Survival Studies," Oak Ridge National Laboratory, Biology Division, Jan. 14, 1974.

C. M. Haaland

"Defense of Cities by ABM," Operations Research Society of America Meeting, Boston, Apr. 22–24, 1974.

J. C. Hart

"A Moot Court Trial Involving Radiation Injury" (2 lectures), TVA Medical Department, Chattanooga, Tennessee, Aug. 12, 1973; and Blue Grass Chapter of the Health Physics Society (HPS), Jamestown, Kentucky, Sept. 7, 1973.

Vice-Chairman of the session on "Public Information, Legal Aspects, Education and Training," Third Congress of the IRPA, Washington, D.C., Sept. 14, 1973.

"Health Physics over the Next Decade," Joint Meeting of the East Tennessee and North Carolina Chapters of the HPS, Boone, North Carolina, Oct. 26, 1973.

Moderator of a panel discussion on "Low-Level Population Exposures," Joint Meeting of Cincinnati Radiation Society and Blue Grass Chapter of the HPS, Louisville, Kentucky, Nov. 3, 1973.

"A Candid Look at the Scientist-Juror" (4 lectures), Western Pennsylvania Chapter of the HPS, Pittsburgh, Pennsylvania, Dec. 2, 1973; Northeastern New York Chapter of the HPS, Albany, New York, Dec. 3, 1973; Midwest Chapter of the HPS, Chicago, Illinois, May 8, 1974; and Cincinnati Radiation Society, Cincinnati, Ohio, May 9, 1974.

"Legalistic Aspects of the Radiation Exposure Record," Lowell Technical Institute, Lowell, Massachusetts, Dec. 4, 1973.

"Legal Aspects of Operational Health Physics," Nuclear Engineering Department, University of Virginia, Charlottesville, Virginia, Feb. 25, 1974 (ORAU Visiting Lecturer Series).

"Las Vegas Revisited: A Candid Look at the Scientist-Juror" (2 lectures), Baltimore-Washington Chapter of the HPS, Washington D.C., Feb. 26, 1974; and Alabama Chapter of the HPS, Huntsville, Alabama, May 31, 1974.

"Legal Requirements for Operational Health Physics," ORAU Health Physics Training Series, Oak Ridge, Tennessee, March 1974.

"Legal Problems Associated with the Medical Aspects of the Radiation Exposure Record," Medical School, University of Cincinnati, Cincinnati, Ohio, May 9, 1974.

Chairman of the workshop discussion on "Recent Standards and Radiation Practices," 19th Annual Meeting of the HPS, Houston, Texas, July 7–11, 1974.

G. S. Hurst

"Energy Transfer Processes in Noble Gases," Department of Physics, University of Tennessee, Knoxville, Tennessee, May 7, 1974.

"Energy Pathways in Noble Gases," Department of Physics, University of Kentucky, Lexington, Kentucky, May 20, 1974.

D. G. Jacobs

"Impacts in Groundwater of Effluents Arising in the Nuclear Industry," presented at the course on Environmental Impact Assessment of Nuclear Power Generation, University of California, Berkeley, California, Sept. 12, 1973.

"Long-Term Management of High-Level Radioactive Wastes," School of Nuclear Engineering, Georgia Institute of Technology, Atlanta, Georgia, Feb. 14, 1974.

"Environmental Impact of Radioactive Wastes from Nuclear Power Plants," Workshop on the Energy Crisis and Its Effect on the Environment, Georgia Institute of Technology, Atlanta, Georgia, June 18, 1974.

C. E. Klots

"Reactions of Excited Atoms," Université de Paris-Sud, Orsay, France, Sept. 17, 1973.

"Reactions of Excited Atoms," Hahn-Meitner Institut für Kernforschung, Berlin, Germany, Sept. 20, 1973.

"Theory of Unimolecular Decompositions," Physikalisch-Technische Bundesanstalt, Braunschweig, Germany, Sept. 7, 1973.

J. H. Marable

"Electromagnetic Pulse Coupling to Power Lines," Joint EMP Technical Meeting, Kirtland Air Force Base, New Mexico, Sept. 25–27, 1973.

"The Vulnerability of the Electric Power System to EMP," Oak Ridge Civil Defense Society, Oak Ridge, Tennessee, January 1974.

M. G. Payne

"Transport of Resonance Radiation," Department of Physics, University of Kentucky, Lexington, Kentucky, May 21, 1974.

J. W. Poston

"Health Physics Research at ORNL: Past, Present, and Future," School of Nuclear Engineering, Georgia Institute of Technology, Atlanta, Georgia, Oct. 4, 1973.

"Estimation of Dose to Selected Organs from X-Ray Exposure," Physics and Astronomy Department, Clemson University, Clemson, South Carolina, Mar. 28, 1974.

"Health Physics Research at ORNL," Nuclear Science and Engineering Department, Virginia Polytechnic Institute, Blacksburg, Virginia, May 13, 1974.

R. H. Ritchie

"Collective Effects in Absorption of Energy From Ionizing Radiation," Solid-State Biophysics Seminar, Oak Ridge National Laboratory, May 7, 1973.

"Some Properties of Surface Plasmon States," University of Rolla, Rolla, Missouri, Sept. 13, 1973.

"Surface Plasmons Effects in Solids," Department of Physics, Indiana University, Bloomington, Indiana, Feb. 22, 1974.

H. C. Schweinler

"Super-High Conductivity in Molecular Ionic Crystals at 60°K," Clemson University (Joint Physics-Chemistry Colloquium), Clemson, South Carolina, June 7, 1973.

W. S. Snyder

"Age Dependence of Uptake and Retention of Radionuclides, Biological Differences of Segments of the Population and Their Effect on Dose Estimates for Individuals, Environmental Pathways from Reactor to Man, and Physical Dosimetry Involved in Making Dose Estimates for Population Exposures," Second International Summer School on Radiation Protection, Herceg Novi, Yugoslavia, Aug. 21–31, 1973.

"Internal Dosimetry," ORAU Course on Radiation Protection and Health Physics, Oak Ridge, Tennessee, Feb. 22, 1974.

Miscellaneous Staff Activities

Academic Appointments

K. Becker
Adjunct Professor, University of Tennessee

R. D. Birkhoff
Ford Professor, University of Tennessee

L. G. Christophorou
Ford Professor, University of Tennessee

M. F. Fair
Visiting Assistant Professor of Physics, University of Tennessee

G. S. Hurst
Adjunct Professor, University of Kentucky

R. H. Ritchie
Ford Professor, University of Tennessee

H. C. Schweinler
Ford Professor, University of Tennessee

J. E. Turner
Professor of Physics (part-time), University of Tennessee

Service in Professional Organizations

J. A. Auxier
National Academy of Sciences Advisory Committee on Civil Defense; National Academy of Sciences Subcommittee on Radiation Shielding; ICRU Task Group on Neutron Instrumentation; USASI Subcommittee N-13.8; NCRP Subcommittee 28; IAEA Panel on Nuclear Accident Dosimetry Systems; AEC-DBER Cf-252 Biomedical Advisory Panel; ICRP Task Group on Emergency and Accidental Exposures; and Joint SNS/BER Biomedical Working Group.

K. Becker
Organization Committee, Fourth International Symposium on Exoelectrons and Dosimetry, Liblice, Czechoslovakia, 1973; Vice-President and Member of Program Committee, Fourth International Conference on Luminescence Dosimetry, Krakow, Poland, 1974.

C. V. Chester
Special Committee on Evacuation, Advisory Committee on Civil Defense, National Academy of Sciences.

R. N. Compton
National Science Foundation Committee on Gas Phase Molecular Interactions and the Nation's Energy Problem.

M. R. Ford
NCRP Scientific Committee 32 and NCRP Scientific Committee 33.

J. C. Hart
President-Elect, Health Physics Society, 1973–74; President, HPS, 1974–75; Executive Committee, HPS, 1973–74, 1974–75; Judiciary Committee, International Radiation Protection Association; Advisor, Rules Committee, IRPA; Parliamentarian, IRPA Congress (Washington, D.C.), 1973; Utilities Committee, Ruritan National.

F. F. Haywood
Subcommittee on Radiation Shielding, National Academy of Sciences Advisory Committee on Civil Defense; Standards Committee N-16, American National Standards Institute (Alternate Member); IAEA Panel of Experts for Nuclear Accident Dosimetry.

G. S. Hurst
Report Committee on Average Energy Required to Produce an Ion Pair, ICRU; Affiliates Committee of Health Physics Society.

D. B. Nelson
Technical Advisory Committee for the Air Force Weapons Laboratory's C^3 Program; Advisory Committee on Civil Defense and EMP Subcommittee, National Academy of Sciences.

J. W. Poston
NCRP Ad Hoc Committee on the Experimental Verification of Internal Dosimetry Calculations; Secretary, Health Physics Society; Medical Internal Radiation Dose Committee (ex officio); MIRD Task Group on Cardiac Modeling; ICRP Task Group on Dosimetry Calculations for Committee 2.

W. S. Snyder
Committee 2 Member, ICRP; NCRP Member; Chairman, Scientific Committee 23, NCRP; Chairman, Scientific Committee 33, NCRP; SNM-MIRD Committee Member; Editor, *Health Physics* Journal; Publications Director, IRPA.

N. E. Tarr
Publications Committee, Health Physics Society; History Committee, HPS.

J. E. Turner
Publications Committee, Health Physics Society; Intersociety Liaison Committee, HPS.

Guests and Trainees

FACULTY INSTITUTE PARTICIPANTS

H. W. Berk, *University of Virginia*

J. G. Lindsay, Jr., *Appalachian State University*

S. H. Lott, *Vanderbilt University*

L. B. O'Kelly, *Memphis State University*

C. E. Roessler, *University of Florida*

B. L. Sloan, *Carson-Newman College*

A. W. Spear, *Southwest Texas State University*

R. J. Vetter, *Purdue University*

J. E. Wiest, *West Virginia Wesleyan College*

HEALTH PHYSICS TECHNOLOGISTS

P. L. Baker, D. E. Coate, B. J. Dionne, R. C. Edwards, C. R. Flynn, A. R. Hawthorne, J. D. Kizer, J. S. Lorber, Serafin G. Menocal, F. H. Moore, T. W. Oakes, D. A. Padula, D. L. Padula, B. A. Snell, B. R. Thomas, C. R. Tuley, S. D. Van Hoesen

ORAU TRAINEES

S. D. Attaya, M. A. Cummins, A. E. Dembe, L. A. Huskey, S. S. Jaeger, J. T. McMillan, G. K. Sumner, J. S. Wakefield

GRADUATE STUDENTS

J. R. Frazier, *AEC Fellow, University of Tennessee*

K. S. Gant, *University of Tennessee*

S. M. Garry, *University of Tennessee*

J. P. Johnson, *University of Tennessee*

D. G. Hall, *University of Tennessee*

J. J. Shonka, *Georgia Institute of Technology*

P. S. Stansbury, *Georgia Institute of Technology*

R. J. Warmack, *University of Tennessee*

C. E. Wheeler, *University of Tennessee*

FOREIGN GUESTS

M. M. Abdel Razek, *Atomic Energy Establishment, Cairo, Egypt*

S. A. Abdullah, *Atomic Energy Center, Dacca, Bangladesh*

S. L. Chu, *Institute of Nuclear Energy Research, Atomic Energy Council, Taiwan, Republic of China*

Liliana Deleanu, *Rumania*

D. Y. Hsia, *Republic of China*

T. Inagaki, *Osaka Kyoiku University, Osaka, Japan*

Sung-I Juan, *Republic of China*

J. S. Jun, *Korean Atomic Energy Research Institute, Seoul, Korea*

N. H. Mei, *Republic of China*

A. Moreno y Moreno, *Instituto de Fisica, Universidad Nacional Autonoma de Mexico, Mexico City, Mexico*

V. N. Neelavathi, *Bhabha Atomic Research Centre, Bombay, India*

N. P. Saheli, *Tehran University Nuclear Centre, Tehran, Iran*

C. J. Tung, *Republic of China*

HEALTH PHYSICS DIVISION

JULY 1, 1974

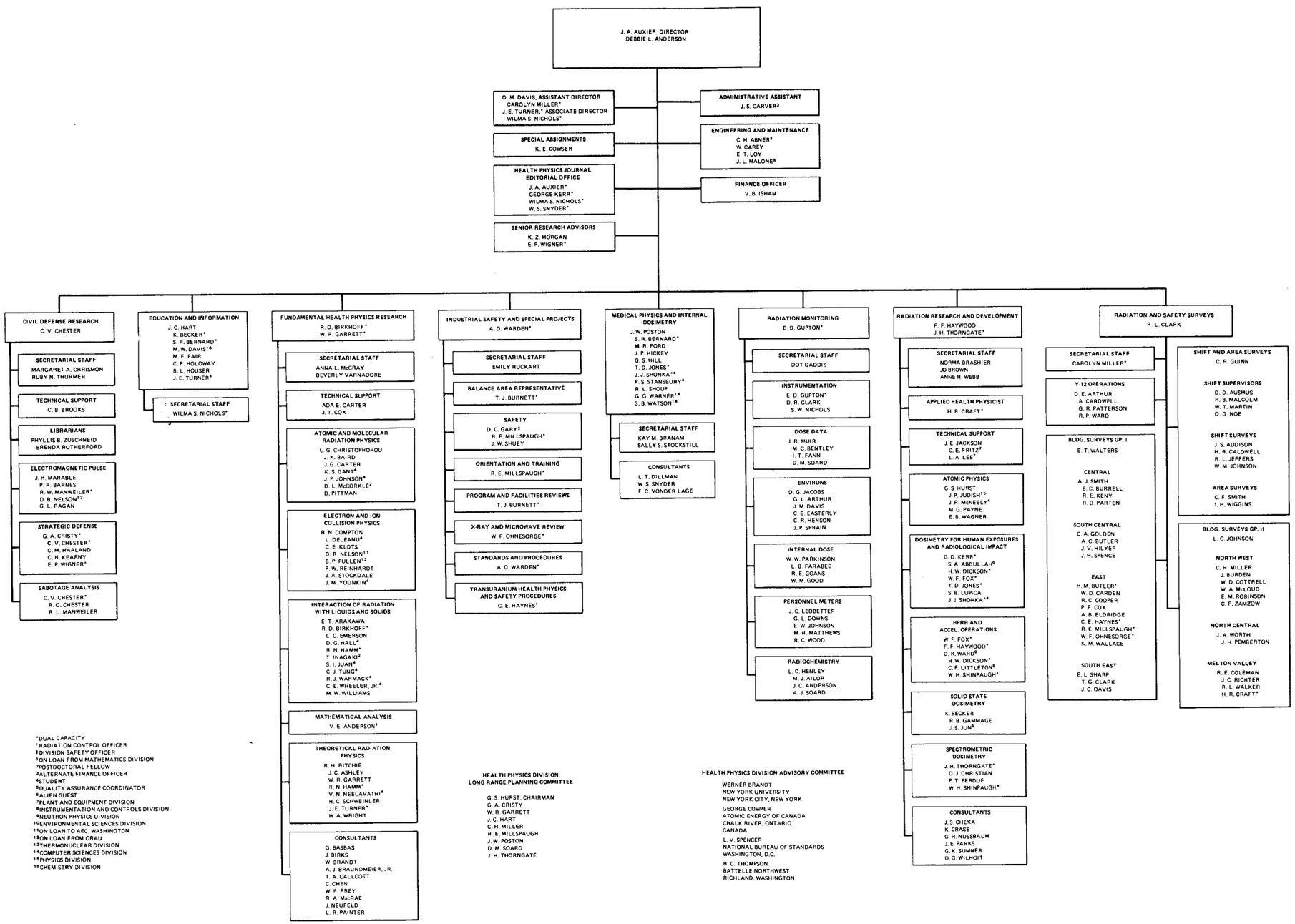

*DUAL CAPACITY
[1]RADIATION CONTROL OFFICER
[2]DIVISION SAFETY OFFICER
[3]ON LOAN FROM MATHEMATICS DIVISION
[4]POSTDOCTORAL FELLOW
[5]ALTERNATE FINANCE OFFICER
[6]STUDENT
[7]QUALITY ASSURANCE COORDINATOR
[8]ALIEN GUEST
[9]PLANT AND EQUIPMENT DIVISION
[10]INSTRUMENTATION AND CONTROLS DIVISION
[11]NEUTRON PHYSICS DIVISION
[12]ENVIRONMENTAL SCIENCES DIVISION
[13]ON LOAN TO AEC, WASHINGTON
[14]ON LOAN FROM ORAU
[15]THERMONUCLEAR DIVISION
[16]COMPUTER SCIENCES DIVISION
[17]PHYSICS DIVISION
[18]CHEMISTRY DIVISION

HEALTH PHYSICS DIVISION LONG RANGE PLANNING COMMITTEE

G. S. HURST, CHAIRMAN
G. A. CRISTY
W. R. GARRETT
J. C. HART
C. H. MILLER
R. E. MILLSPAUGH
J. W. POSTON
D. M. SOARD
J. H. THORNGATE

HEALTH PHYSICS DIVISION ADVISORY COMMITTEE

WERNER BRANDT
NEW YORK UNIVERSITY
NEW YORK CITY, NEW YORK

GEORGE COWPER
ATOMIC ENERGY OF CANADA
CHALK RIVER, ONTARIO
CANADA

L. V. SPENCER
NATIONAL BUREAU OF STANDARDS
WASHINGTON, D.C.

R. C. THOMPSON
BATTELLE NORTHWEST
RICHLAND, WASHINGTON